Paris Saclay University and Osaka University

Doctoral Thesis

High quality laser driven electron beams for undulator and free electron laser radiation

(自由電子レ-ザ-ならびにアンジュレ-タ-放射光源のための高品質レ-ザ-加速電子ビ-ムに関する研究)

Author:
Driss Oumbarek Espinos

Supervisors:
Dr. Marie Emmanuelle Couprie
Dr. Ryosuke Kodama

A thesis submitted in fulfillment of the requirements for the degree of Doctor of Philosophy in Engineering

in the

Graduate school of engineering, Osaka university and Ecole doctorale PHENIICS, Université Paris-Saclay

Jury members:

Marie Emmanuelle Couprie, Synchrotron SOLEIL	Thesis supervisor
Ryosuke Kodama, Graduate school of Engineering, Osaka university	Thesis supervisor
Masaki Kando, QST, Kansai Photon Science Institute	Rapporteur
Hiroyuki Hama, Tohoku university	Rapporteur
Yasuhiro Kuramitsu, Graduate school of Engineering, Osaka University	Rapporteur
Sophie Kazamias, Paris-Saclay university	Examiner
Yoshio Ueda, Graduate school of Engineering, Osaka university	Examiner
Yasuhiko Sentoku, Institute of Laser Engineering, Osaka university	Examiner

July 26, 2021

Thèse de doctorat

NNT: 2021UPASP063

Electrons de haute qualité produits par accélération laser plasma pour rayonnement onduleur et laser à électrons libres

(High quality laser driven electron beams for undulator and free electron laser radiation)

(自由電子レ-ザ-ならびにアンジュレ-タ-放射光源のための高品質レ-ザ-加速電子ビ-ムに関する研究)

Thèse de doctorat de l'Université Paris-Saclay

École doctorale n° 576, Particules, Hadrons, Énergie, Noyaux, Instrumentation, Imagerie, Cosmos et Simulation (PHENIICS)
Spécialité de doctorat: Physique des accélérateurs
Unité de recherche: Synchrotron SOLEIL
Référent: Faculté d'Orsay, Université Paris-Sud

Thèse présentée et soutenue à Osaka, le 27 Juillet 2021, par

Driss Oumbarek Espinos

Composition du jury:

Ryosuke Kodama Professeur, Graduate School of Engineering, Osaka University	Président et Codirecteur
Marie Emmanuelle Couprie Directrice de recherche, Synchrotron SOLEIL	Directrice
Masaki Kando Directeur de recherche, QST, Kansai Photon Science Institute	Rapporteur
Hiroyuki Hama Professeur, Tohoku University	Rapporteur
Yasuhiro Kuramitsu Professeur, Graduate School of Engineering, Osaka University	Rapporteur
Sophie Kazamias Professeure, Universite Paris-Saclay	Examinatrice
Yoshio Ueda Professeur, Graduate School of Engineering, Osaka University	Examinateur
Yasuhiko Sentoku Professeur, Institute of Laser Engineering	Examinateur

"*There is nothing either good or bad, but thinking makes it so.* "

William Shakespear, Hamlet, Act 2, Scene 2

Titre: Electrons de haute qualité produits par accélération laser plasma pour rayonnement onduleur et laser à électrons libres

Mots clés: LEL, acceleration laser plasma, dynamique du faisceaux

Résumé: Les laser à électrons libres (LEL) sont sources de rayons X accordables les plus brillantes disponibles. Les LEL visant les courtes longueurs d'onde nécessitent de longues installations d'accélération pour fournir les énergies des électrons nécessaires. Les progrès récents dans le domaine de l'accélération laser-plasma (LPA) rendent cette technologie intéressante pour l'utilisation dans des LEL grâce à ses faisceaux femtosecondes avec GeV dans des centimètres. La divergence, la densité d'énergie et la dispersion de l'énergie des faisceaux LPA ne sont pas comparables à celles des faisceaux utilisés dans les LEL. Le transport des faisceaux LPA reste difficile en raison de la grande divergence initiale et de la dispersion de l'énergie. Pour une application LEL, la dispersion de l'énergie doit être adaptée pour atteindre la valeur requise et la divergence du faisceau doit être compensée pour éviter des effets chromatiques et la croissance de l'émittance avec des éléments de focalisation puissants.

La ligne COXINEL vise à faire la démonstration d'un LEL basé sur le LPA. La ligne transporte et focalise le faisceau d'électrons à l'onduleur avec de dispositifs magnétiques classiques. Premièrement, un triplet de quadrupôles à gradient variable spécialement conçus (QUAPEVA) compensent la divergence initiale. Le faisceau est transporté dans une chicane magnétique pour la sélection de l'énergie, suivie d'un ensemble de quatre quadrupôles électro-magnétiques pour une focalisation à l'intérieur d'un onduleur. Après l'onduleur, un dipôle «dump» évacue les électrons. Dans cette thèse, la qualification et l'évolution pendant le transport des faisceaux d'électrons produits par LPA pour la génération du LEL sur l'expérience COXINEL est explorée. La source LPA expérimentale a été modélisée par des simulations « Particle in cell » afin de déterminer ses performances. La simulation montre des faisceaux avec des divergences RMS de 2 mrad, des dispersions de l'énergie de 10 % et des énergies de pointe autour de 170 MeV dans les meilleurs cas. L'expérience COXINEL a été conçue pour un faisceau d'électrons de référence dont les paramètres sont capables de produire un rayonnement LEL dans les simulations, mais des écarts entraînent une chute rapide de la puissance LEL ou sa disparition. A chaque campagne expérimentale, les performances du LPA se sont améliorées. Mais, les paramètres du faisceau trouvés à la source sont encore loin du faisceau de référence. Les simulations montrent une dégradation considérable du transport en raison de la divergence et du pointage expérimentaux élevés, mais la ligne COXINEL est toujours capable de transporter la tranche d'énergie de référence sans pertes. En utilisant les diagnostics le long de la ligne COXINEL, l'évolution des paramètres du faisceau ont été suivie. Une forte dégradation du faisceau au cours de l'expérience a été observée en raison de la dégradation du laser à l'usage. Ainsi, le faisceau arrivant à l'onduleur pendant les expériences de recherche LEL présente une émittance plus élevée et une charge plus faible que celle mesurée au spectromètre au début de l'expérience. La divergence du faisceau, la dispersion de l'énergie et le pointage initial se sont avérés être les principales causes de la dégradation du transport. Leurs effets ont été quantifiés par des simulations et confirmés expérimentalement.

Ce travail de thèse montre que les caractéristiques des électrons peuvent être mesurées le long de la ligne. A partir de la taille transversale du faisceau mesurée au milieu de la chicane et des équations de transport, l'émittance verticale moyenne RMS de la tranche de référence a été trouvée de 3,2 mm.mrad et la divergence RMS de 2 mrad. La mesure du faisceau au niveau du dipôle «dump» a permis d'observer la charge de la tranche d'énergie de référence à la fin de la ligne. La meilleure valeur moyenne de la charge de tranche était de 0,27 pC. Avec telles valeurs de faisceau qu'aucun LEL ne peut être atteinte.

Title: High quality laser driven electron beams for undulator and free electron laser radiation

Keywords: FEL, laser plasma acceleration, beam dynamics

Abstract: Particle accelerators are a cornerstone of today science for research and industrial applications. They are used for example for radiation sources such as undulator radiation and free electron laser (FEL), the brightest tunable x-ray sources available. FEL aiming at short wavelengths require of long accelerator facilities (up to km) to provide the electron energies needed. The recent progress in Laser Plasma Acceleration (LPA) makes it attractive for FEL usage thanks to its capacity to produce femtosecond, GeV beams in cm scale distances. However, the LPA beams slice divergence, energy density and energy spread are not on par with the standard beams utilized for FELs. Moreover, LPA beams transport is still challenging due to the large initial divergence and energy spread. In view of a FEL application, the energy spread has to be adapted to reach the required small slice value while the beam divergence has to be controlled to avoid chromatic effects and emittance growth with strong focusing elements.

The COXINEL line aims to demonstrate LPA based FEL. The line transports the electron beam from the source to the undulator while compensating the initial divergence, manipulating and focusing the beam at the undulator using classic magnetic devices. Following the electron beam path, a triplet of specially designed variable gradient quadrupoles called QUAPEVA compensate the initial divergence. The beam is transported in a magnetic chicane for energy selection, followed by a set of four electro-magnet quadrupoles for proper focusing inside a cryo-ready undulator. After the undulator a dipole dump evacuates the electrons.

In this thesis, the qualification and evolution during transport of the LPA produced electron beams for FEL generation on the COXINEL experiment is explored. The experimental LPA source has been modeled via particle in cell simulations to find the setup performance and generated electron beam parameters dependance on the gas target characteristics. The simulation shows beams with mean RMS slice divergences of 2 mrad, energy spreads of 10 % and peak energies around 170 MeV in the best cases. The experiment was designed for a baseline electron beam parameters that are able to produce FEL radiation in simulations, but deviations from them cause a fast drop in FEL power or completely nullifies it. At each experimental campaign the LPA performance have improved steadily. But, during the multiple experimental campaigns, the beam parameters found at the source are still far from the baseline. Simulations exhibit a considerable degradation of the transport due to the high experimental divergence and pointing but the COXINEL line is still able to transport the reference energy slice without losses. Utilizing the diagnostics along the COXINEL line, the beam parameters evolution has been monitored. A strong beam worsening during experiment has been observed due to laser degradation with use. Thus, the beam arriving at the undulator during the FEL search experiments presents a higher emittance and lower charge than the measured at the spectrometer in the beginning of the experiment. The beam divergence, energy spread and initial pointing have been found to be the main causes of transport degradation. its effects have been quantified by simulations and confirmed experimentally. This thesis works shows that the electron beam characteristics can be measured along the line. From the beam transverse size measured at the middle of the chicane and transport equations the mean reference slice RMS vertical emittance has been found to be of 3.2 mm.mrad and the RMS divergence 2 mrad. The measurement of the beam at the dipole dump permitted to observe the reference energy slice charge that crossed the undulator. The best mean reference slice charge value was 0.27 pC. The simulation and calculations of radiation with such beam values confirm that no FEL can be reached. Further improvements of the LPA beam are still necessary to achieve FEL.

Acknowledgements

First of all i want to thank Marie Emmanuelle Couprie. She has been like my scientific mother, deeply influencing how i work and think about physics. She also gave me the opportunity to work with her, do this thesis and helped me come to Japan. She has invested so much time and effort that i don't know if I can ever make it back to her but I will do my best to make her effort worthwhile.

Thanks also to Kodama 先生 for accepting being my supervisor and his support during this three years. Without you i could have never been able to discover such a great country, people and laboratory.

I am deeply grateful to Sophie Kazamias for helping me during my time of doubts and giving her support that allowed my to know Marie Emmanuelle and to start this thesis.

I want to thank Amin, you really made me feel at home in SOLEIL with our discussions. You always made time to answer all my doubts making things much easier for me during all our experiments together. You are a great friend and I wish you the best.

本当にありがとうございます Yano, for the innumerable fun times that we have had, to teaching me important japanese words, helping me with a lot of bureaucracy in Japanese and basically for being a true friend.

Also thank you Yasuo, being in the experiment or outside it with you is always a joy, is a shame that we couldn't work more together. I hope I see you soon!

I am grateful to Sentoku 先生 for letting me be in his group and taking so much time to help me with the simulations and more.

Thanks to the COXINEL team, Marie, Éléonore and Alexandre, i can't imagine better colleagues to stay all day inside the control room. I have learn a lot from you and without you this could not have been done.

A huge thanks to the whole team of GMI at SOLEIL, all and every single one of you is awesome and thanks to you being at GMI is always a great time.

Thank you Lena for all your efforts during the experiment and for staying until late at night with us and for all the small COXINEL parties.

Thanks to the rest of the team at LOA, Sébastien, Cédric, Julien and Guillaume, it has been a pleasure to work with you during these three years.

Thanks to Monno さん, Kurisu さん and Kaori さん for helping me beyond their obligations making my life in Osaka much easier.

Thanks to Sabine for always helping with my paper work with a smile

Thanks to all the members of the jury Kando 先生, Hama 先生, Kuramitsu 先生 and Ueda 先生 for accepting to review my work.

Finally, I want to thank my family. without my father i wouldn't have had the opportunity to go to study in Paris which started this amazing journey. Also without my sister's support I wouldn't have been able to make it through some hard times. There are not enough words to describe all the things my mother has done to help and support me, so the only thing I can do is to make her proud, Thank you.

Contents

Chapter 1

Introduction

1.1 Context

Since the first accelerators in 1930 producing particles of hundreds of KeV, the accelerator technologies have improved steadily with current facilities offering particle energies above the TeV. Nowadays particle accelerators are a cornerstone of science, they are used for research and industrial applications in domains from atomic physics to nanotechnology or medicine. The acceleration of particles above MeV energies can be used in multiple ways, e.g., collision of particles, probing materials or radiation sources. For example, one of such applications are the undulator type light sources. When a relativistic particle is bent in a magnetic field, synchrotron radiation is emitted. Synchrotron radiation facilities use accelerated electrons from storage rings and are widely used for structural analysis of matter. Invented in the 1970s, the free electron laser (FEL) [1] takes this principle a step further. FELs use high energy electrons to produce coherent radiation as they pass through an undulator. The FEL produced radiation wavelength ranges from mm to X-rays, based on the electron energy. FELs are the brightest tunable x-ray undulator radiation light sources, they opened a new way to explore ultra-fast phenomena with high time resolution. Such sources have a vast number of applications in fundamental research and industry. FEL aiming at short wavelengths need long linear accelerators (LINAC) that provide high peak charge, quality and stable electron beams.

The laser plasma acceleration technique (LPA) [2] has gained traction thanks to the progress in high power lasers systems, in part due to the remarkable invention of the chirped pulse amplification [3] that permitted the generation of femtosecond laser pulses. LPA consists on the production and acceleration of electrons via a density structure created by the ponderomotive push appearing when a femtosecond high power laser pulse is focused on a gas target. Acceleration fields (1 GeV/cm) three orders of magnitude superior to the radio-frequency cavities breakdown limit (100 MeV/m) can be reached with LPA because the plasma is ionized, thus, making possible the production of high energy particles in cm scales plus the laser system size. In the last 20 years, LPA has drawn the interest of multiple fields as its performance improved. Electron beam energies of up to 8 GeV [4], charges of hundreds of pC [4, 5] with percent energy spread [6, 7] and FWHM divergences of the order of mrad [4, 7] have already been produced and continue to ameliorate. Recently, great progress in stability is also being done [8]. The complexity and high non linearity of the phenomena inside the plasma makes the LPA analytical treatment really difficult thus, the need of substantial experimental and simulation work to understand the underlying processes. Precise LPA simulations require huge computational facilities as full 3D simulation can use more than a hundred hours with thousands of cores. The achieved LPA electron beams have awoken interest and the possibility of future use of LPA as sources or secondary accelerators for FEL and other applications is being considered. However, in view for a FEL application, LPA electron beams are still far from the quality (mrad divergence, pC/MeV charge and percent energy spread) and stability offered by a LINAC. Nonetheless, in their current state they are good enough to try to demonstrate their application for FEL. But there are still crucial challenges to surpass to succeed.

The COherent Xray source INferred from Electrons accelerated by Laser (COXINEL) experiment [9] aims at qualifying LPA with a FEL application. An 8 meters long transport line based on reliable conventional accelerator magnet technologies (COXINEL line) has been developed at SOLEIL [10] to manipulate the LPA beam, ensuring the best quality possible at the undulator for radiation experiments. As LPA based FEL is still under research, the COXINEL experiment has multiple middle term objectives, required before the FEL generation. The strategy steps followed in COXINEL are the design a solution for FEL with baseline parameters, demonstration of proper transport and manipulation of the electron beam, observation of radiation at the end of the line and re-iteration if the baseline is different from the measured LPA beam. The line was conceived for a baseline parameters set with a reference electron energy of 176 MeV, 1 mrad RMS divergence, 1 mm.mrad RMS emittance, 1 % energy spread and 34 pC total charge. The baseline was established from previous experimental

LPA results with the colliding pulse injection in the LOA facility [11] without systematic simulations. The LPA source used for the COXINEL line is the "Salle Jaune" facility of "Laboratoire d'Optique Applique" (LOA). In total, seven experimental campaigns have been done in the COXINEL line (2016 - 2020). The inability to use the colliding pulse injection in a reliable and stable way led to a change of injection scheme to ionization injection. The new scheme offered a more robust and stable operation in exchange of worse beam parameters. The lack of experimental or simulated data of the new scheme performance lead to a more difficult line operation and the need of modifications in the transport line. The transport line underwent various mechanical (quadrupole triplet displacement system to take them out of the beam axis) and technical changes (beam pointing alignment compensation method developed [12]) prior to the start of this thesis. Until now, seven experimental campaigns have been done in the COXINEL line. In the first one (March 2016) the electrons were created with the LPA source by ionization injection and transported. During the second campaign (November 2016), the LPA shock injection configuration was tested but due to poor stability was discarded. In the third campaign (March 2017), the chicane was added and the beam pointing compensation approach was established permitting the beam dispersion correction.

This thesis started on time for the fourth experimental campaign and covers the experiments until the seventh campaign, so, the details from previous ones are not addressed. Therefore, the line design, construction and expected baseline beam transport studies were done before this thesis and thus, the line elements available were used for the present work. Multiple feats have been done in COXINEL, including the measurement of undulator radiation [13]. In this thesis the full characterization of the LPA beam at the source, the transport and the undulator is achieved, the effect of multiple deviations from the ideal line and LPA beam are studied, quantified and used to understand the observations and the line diagnostics are improved. Different groups around the world are also aiming at the FEL demonstration.

1.2 Thesis motivation

This work constitutes a step towards the search of a demonstration of FEL radiation generation with an LPA source inside the COXINEL experiment. The motivation is to approach conditions for a Free Electron Laser demonstration. This quest adopts different strategies: Firstly, I modeled the LPA source with particle in cell simulations to understand the expected performance and to compare with the measured one, as no previous formal analysis was performed before the start of the experiments. Secondly, I qualified the electron beam along its transport throughout the line. I examined the transport along the COXINEL line with experimental LPA beam parameters deviating from the baseline ones used to optimize. Thirdly, I measured the electron beam quality at the undulator location and explored the FEL feasibility. I did my own measurement treatment codes and calibrated diagnostics already in place to extract the most information with the best precision possible. I estimated whether FEL demonstrations is reachable with the measured beam parameters. If not, steps for improved performances were investigated.

1.3 Thesis outline

In Chapter 2, the basic theoretical concepts of LPA, electron beam transport via magnetic elements, FEL and the state-of-the-art facilities are presented. The chapter finishes with a discussion of the problematic and requirements of the use of an LPA electron beam as a source for an FEL.

In chapter 3, first, the beam emittance growth due to the transport is analyzed analytically. Then the COXINEL transport line baseline design and its different optics configurations are presented as well as their effect on the electron beam via simulations. The baseline electron beam sensitivity during transport is reported and the beam requirements for FEL studied by simulations. Finally, the components of the line are introduced in more detail.

In chapter 4, I analyze the measurements of the electron beam energy distribution, divergence and stability taken at the electron spectrometer and an imager close to the LPA gas target for multiple experimental campaigns. The usefulness of the electron beams obtained for the FEL application is studied.

In chapter 5, I study the performance of the LPA configuration used in COXINEL via 2D particle in cell simulations with the PICLS code. The effect of the plasma ramp at entrance and exit on the beam parameters is analyzed. A relative beam charge and the main bunch energy versus plasma density and gas composition map is produced. The consequence of an increase of laser power is studied. The chapter closes with a short

discussion about possible improvements like the addition of a shock at the start of the plasma density distribution.

In chapter 6, I simulate the transport with an experimental like electron beam and compared to the baseline case. The sensitivity of the beam charge and transverse space along the transport is studied for initial beam and quadrupole defects. In the last section, measurements are reproduced via simulation by identifying the main initial experimental deviations and applying them to the simulation.

In chapter 7, the beam parameters are monitored along the line with the different imagers and integrated current transformers (ICT). I study the total charge evolution from the source to the undulator with the ICTs. I validate via simulation and present the experimental results of a single shot emittance diagnostic using the imager at the center of the magnetic chicane. The calibration of the imagers after the undulator is introduced. I study the reference energy slice beam evolution along the transport line (i.e., from source to the beam evacuation) and compare it at the different experimental campaigns.

Chapter 8 summarizes the main results of the thesis and the possibilities of FEL based LPA are discussed.

Chapter 2

LPA based FEL: Theory and state of the art

The development of a free electron laser based on laser plasma accelerated electrons requires the knowledge of different physics fields. This chapter aims to introduce the basics and relevant concepts of plasmas, lasers, electron beam transport and free electron laser generation in a succinct but understandable manner.

2.1 Introduction to plasma physics

Plasmas are generally defined as partially ionized matter displaying a collective behavior through electromagnetic (EM) interactions of its charges and quasi-neutrality. The collective behaviour arises from the $1/r$ long-range Coulomb interaction (with r a distance) between the plasma charges. Thus, a local perturbation inside the plasma could influence distant regions. The quasi-neutrality implies that the overall charge densities of the electrons and ions forming the plasma cancel each other:

$$n_e = Zn_i \tag{2.1}$$

with n_e the electron density, n_i the ion density and Z the ion ionization state.

Plasma dynamics require the resolution of non-linear and self-consistent problems where EM fields interact with charged particles vice-versa. The sheer quantity of charges interacting at the same time inside a plasma requires the use of statistical mechanics to go from the information of individual particles to the plasma macroscopic quantities.
All plasma events are a combination of a mechanical part and an electromagnetic part. The mechanical part corresponds to the dynamics equation:

$$\frac{d\vec{p}}{dt} = m\frac{d\vec{v}}{dt} = q(\vec{E} + \vec{v} \times \vec{B}) \tag{2.2}$$

where $\vec{p} = m\vec{v}$ represents the particle momentum vector, q the particle charge, $\vec{v}$ its velocity and m its mass, $\vec{E}$ an electric field and $\vec{B}$ a magnetic field.
The electromagnetic part is described by the Maxwell equations [14]:

$$\vec{\nabla} \cdot \vec{E} = \frac{\rho}{\epsilon_0} = \frac{e(n_i - n_e)}{\epsilon_0} [Poisson's\ equation] \tag{2.3}$$

$$\vec{\nabla} \cdot \vec{B} = 0 \tag{2.4}$$

$$\vec{\nabla} \times \vec{E} = -\frac{\partial \vec{B}}{\partial t} [Faraday's\ law] \tag{2.5}$$

$$\vec{\nabla} \times \vec{B} = \mu_0 \vec{j} + \epsilon_0 \mu_0 \frac{\partial \vec{E}}{\partial t} [Ampere's\ equation] \tag{2.6}$$

with e the elementary charge, $\vec{j}$ the current density, ϵ_0 the vacuum permittivity and μ_0 vacuum susceptibility. Equation 2.3 shows that the source of $\vec{E}$ is the spatial charge density; Equation 2.4 assumes the non-existence of magnetic charges (magnetic monopole); Equations 2.5 and 2.6 express the coupling between the electric and magnetic fields via their space-time variations.

The grand number of particles interacting with themselves and external fields plus the non-linearity introduced by the aforementioned equations, make plasmas a rich and highly complex medium to study. The various kinds of interactions give place to multiple phenomena that occurs at different timescales. Bogoliubov [15] differentiates four timescales: correlation, kinetic, hydrodynamics and diffusion. Depending on the phenomena to be studied and the possible approximations, there are four approaches to plasma physics. From short to long timescales they are:

- Theory of orbits: where the individual motion of a particle is studied.
- Kinetic theory: a statistical approach is taken for the study of N particles, thus, the problem is reduced to the solution of the distribution function.
- Multi-fluid theory: where the particles of each species are considered in a local thermodynamic equilibrium and thus, it can be described as a fluid with a density velocity and local temperature.
- Magneto-hydrodynamics theory: In the very long time scale limit, the plasma can be treated as a single globally conducting fluid.

2.1.1 Ionization mechanisms

To generate a plasma, first a gas should be ionized. Multiple ways exist to cause the gas ionization, for example, through collision of fast particles with atoms, photo-ionization or electrical breakdown. Let's focus on the photo-ionization by the photoelectric effect [16, 17]. An atom can be ionized by light if the following relation is fulfilled:

$$\hbar \frac{2\pi c}{\lambda_{photon}} = W_A \tag{2.7}$$

with c the speed of light, $\hbar$ the Planck constant and W_A the work function. If the photon energy is superior to W_A, the extra energy is transformed into electron kinetic energy. For a Titanium:Sapphire (Ti:Sa) laser (wavelength $\lambda_L = 800\ nm$), the photon energy is of 1.55 eV. Thus, a Ti:Sa laser cannot ionize most atoms [18].

The advantage of the use of lasers is their high intensity, i.e., large number of photons in a small space. For high enough intensities the atoms interact with multiple photons at the same time which can trigger multiple photon ionization (MPI). For an He atom, the work function is of 24.6 eV, so at least 16 photons of a Ti:Sa laser are needed to trigger the ionization. The ionization rate Γ_n is given by:

$$\Gamma_n = \sigma_n I_L^n \tag{2.8}$$

with σ_n the cross section for the photon-atom interaction and I_L the laser intensity.

The superposition of the laser field and the atom field can cause modifications on the Coulomb potential of the atom. If the laser electric field is strong enough, the Coulomb potential can be reduced so the electron can escape easier. This process is called tunneling ionization [17]. The tunneling rate Γ is:

$$\Gamma = exp(-2\int_{x1}^{x2} \frac{\sqrt{2m(V_{(x)} - E)}}{\hbar} dx) \tag{2.9}$$

with V the potential of an atom, x the position in the x axis of a orthogonal base x, y and z. If the laser field is even higher, then the electron can leave the atom directly. This process is called barrier suppression ionization (BSI) [19]. This process starts to dominate for intensities above $10^{15}\ W/cm^2$.

2.1.2 Plasma characteristic time and length

Inside a plasma the charges are free to move. Ions are considered stationary because of their large difference in mass and thus in velocity. In thermal equilibrium, the electron density follows a Boltzmann distribution [20]:

$$n_e = n_i e^{e\phi/k_B T_e} \tag{2.10}$$

with $\phi_{(r)}$ the local potential, k_B the Boltzmann constant and T_e the electron distribution temperature. Supposing $\phi \to 0$ at $r = \infty$, one can combine Equations 2.3 and 2.10 in spherical geometry to obtain the expression of the maximal distance at which an electron will be screened by other charges, also called Debye length:

$$\lambda_D = (\frac{\epsilon_0 k_B T_e}{e^2 n_e})^{1/2} \tag{2.11}$$

So, while globally ($L \gg \lambda_D$) the plasma is neutral, locally ($L = \lambda_D$) it is not necessarily the case.

The plasma actively tries to achieve neutrality. If a supplementary charge is added, the search for neutrality causes a perturbation that leads to neutrality. As the ions are much slower than the electrons, the timescale to reach neutrality is defined by the electrons. Let's consider a 1D plasma, without external forces and pure electrostatic oscillations (i.e., $\nabla \times E = 0$). Supposing an initial plasma at rest ($v_{e0} = 0$) and neutral ($E_0 = 0$), the addition of a charge can be considered as a small perturbation of the system, which can be written to first order as:

$$\begin{aligned} n_e &= n_0 + n_1 \\ v_e &= v_{e1} \\ E &= E_1 \end{aligned} \tag{2.12}$$

with the index 1 referring to the first order terms. The system continuity equation is defined as:

$$\frac{\partial n_e}{\partial t} + \frac{\partial}{\partial x}(n_e v_e) = 0 \tag{2.13}$$

To first order, Equations 2.2, 2.13 and 2.3 become:

$$m_e \frac{\partial v_1}{\partial t} = -eE_1 \tag{2.14}$$

$$\frac{\partial n_1}{\partial t} + n_e \frac{\partial v_1}{\partial x} = 0 \tag{2.15}$$

$$\epsilon_0 \frac{\partial E_1}{\partial t} = -en_1 \tag{2.16}$$

with m_e the electron mass. Supposing the perturbation has a planar wave form:

$$X_1 = X_{10} e^{i(kx - \omega t)} \tag{2.17}$$

with X being any of the 1st order terms n_1, v_1 or E_1, k the wave number and ω the frequency. Substituting the perturbations by the planar wave form in 2.14, 2.15 and 2.16, the electron plasma frequency ω_p is found to be:

$$\omega_p = \sqrt{\frac{n_e e^2}{\epsilon_0 m_e}} \tag{2.18}$$

The electron plasma frequency is the response time of the plasma to the external perturbation The Debye length can be defined also as the distance of an electron with thermal velocity $v_{th,e}$ traveling during $1/\omega_p$:

$$\omega_p \lambda_D = \sqrt{\frac{k_B T_e}{m_e}} \approx v_{th,e} \tag{2.19}$$

2.1.3 Electro-magnetic fields propagation in plasmas

An EM wave can be defined by Faraday's law (Equation 2.5) and Ampere's equation (Equation 2.6). Let's again use the perturbation analysis, i.e., the EM wave field is composed of a static part (E_0 and B_0) and a variable perturbation (E_1 and B_1). To first order Equations 2.5 and 2.6 become:

$$\vec{\nabla} \times \vec{E_1} = -\frac{\partial \vec{B_1}}{\partial t} \tag{2.20}$$

$$\vec{\nabla} \times \vec{B_1} = \mu_0 \vec{j_1} + \epsilon_0 \mu_0 \frac{\partial \vec{E_1}}{\partial t} \tag{2.21}$$

with j_1 the term accounting for the currents inside the plasma to respond to external perturbations. Considering the ansatz Equation 2.17 for the perturbations terms and summing the partial time derivative of Equation 2.21 to the rotational of Equation 2.20, one obtains the expression:

$$(\omega_L^2 - c^2k^2)\vec{E_1} = -\frac{i\omega_L}{\epsilon_0}\vec{j_1} \tag{2.22}$$

with ω_L the laser frequency. Assuming that $\vec{E_1}$ is rapidly varying, the plasma response is dominated by the electrons and thus, the perturbed electric field and electron current are:

$$\begin{aligned} \vec{E_1} &= \frac{m_e}{e}\frac{\partial \vec{v_{e1}}}{\partial t} \\ \vec{j_1} &= -en_0\vec{v_{e1}} \end{aligned} \tag{2.23}$$

with $\vec{v_{e1}}$ the electrons perturbation velocity and j_1 the perturbation current density caused by the electrons. Inserting Equations 2.23 into Equation 2.22 yields the dispersion relation for the plane EM wave in a plasma:

$$\omega_L^2 = \omega_p^2 + k^2c^2 \tag{2.24}$$

From the dispersion relation one can deduce multiple features of the EM wave in plasma, like the phase and group velocities:

$$v_{ph} = \frac{\omega_L}{k} = \frac{c}{\sqrt{1 - \frac{\omega_p^2}{\omega_L^2}}} \tag{2.25}$$

$$v_{gr} = \frac{\partial \omega_L}{\partial k} = \frac{kc^2}{\omega_L} \tag{2.26}$$

and also the plasma refractive index:

$$\eta = \sqrt{1 - \frac{\omega_p^2}{\omega_L^2}} = \frac{kc}{\omega_L} \tag{2.27}$$

Thus, for $\omega_L < \omega_p$ the refractive index is imaginary and the EM wave cannot propagate inside the plasma and drops exponentially inside it. For $\omega_L \geq \omega_p$ the refractive index is less than one and the EM wave can propagate inside the plasma. The physical phenomena occurring when $\omega_L \geq \omega_p$ is that the electrons cannot react fast enough to compensate the wave perturbation. The propagation condition can be translated in terms of the electron density by the definition of the critical density:

$$n_c = \frac{\omega_L^2 \epsilon^2 m_e}{e^2} \tag{2.28}$$

For a laser of frequency ω_L, if the plasma density is lower than the critical density, then the EM wave is able to propagate inside. For a Ti:Sa laser of $\lambda_L = 800\ nm$, the critical density is $1.74 \times 10^{21}\ cm^{-3}$.

2.2 Strong laser fields in plasmas

A finite high power laser fulfilling the propagation condition $\omega_L \geq \omega_p$ can propagate in a plasma and leads to a plethora of interesting phenomena.

2.2.1 Laser fields description

Some concepts should be introduced about the laser fields in order to continue with the interaction between electrons and EM waves inside the plasma.

Due to the fact that the divergence of a curl is equal to zero ($\vec{\nabla} \cdot \vec{\nabla} \times \vec{B} = 0$), Equation 2.4 allows to express $\vec{B}$ as the rotational of an arbitrary vector potential $\vec{A}$:

$$\vec{B} = \vec{\nabla} \times \vec{A} \tag{2.29}$$

From the potential vector $\vec{A}$ one can define the normalized vector potential a_0 as:

$$a_0 = \frac{eA_0}{m_e c} \tag{2.30}$$

with A_0 the maximum amplitude of $\vec{A}$.

Inserting Equation 2.29 into Equation 2.5, the following expression of the electric field is obtained:

$$\vec{E} = -\frac{\partial \vec{A}}{\partial t} - \vec{\nabla}\phi \tag{2.31}$$

where $\vec{\nabla}\phi$ is the integration constant equal to 0 if there is no free charges. ϕ is called the scalar potential.

The laser intensity is defined as the temporal average ($\langle ... \rangle_T = \frac{1}{T}\int_0^\tau ...dt$) of the modulus ($\|...\|$) of the Poynting vector:

$$I_L = \langle \| \vec{E}(x,t) \times \frac{1}{c}\vec{B}(x,t) \| \rangle_T \tag{2.32}$$

which for a planar wave $\vec{E}$ and $\vec{B}$ fields can be written as:

$$I_L = \frac{\epsilon_0 c}{2} E_0^2 \tag{2.33}$$

The normalized vector potential (Equation 2.30) can be used to describe the $\vec{E}$ field amplitude and thus the intensity:

$$\begin{aligned} E_0 &= \frac{a_0 \omega_L m_e c}{e} \\ I_L &= 1.37 \times 10^{18} \frac{a_0^2}{\lambda_L^2} \quad [\frac{W}{cm^2}\mu m^2] \end{aligned} \tag{2.34}$$

Calculation of the electron motion in a plane wave in a classical way yields a limitation on this approach. For $a_0 >\sim 1$, the classical description is insufficient and a relativistic treatment is necessary. In high power lasers cases the focused beams exceeds $a_0 = 1$.

2.2.2 Relativistic electron electromagnetic wave interaction

The momentum of a relativistic electron is defined as:

$$\vec{p} = \gamma m_e \vec{v_e} \tag{2.35}$$

with γ the relativistic factor defined as:

$$\gamma = (\sqrt{1-\beta^2})^{-1} \tag{2.36}$$

where β is the normalized velocity:

$$\beta = \frac{v_e}{c} \tag{2.37}$$

Thus, for a relativistic electron Equation 2.2 becomes:

$$\frac{d(\gamma m_e \vec{v_e})}{dt} = q(\vec{E} + \vec{v} \times \vec{B}) \tag{2.38}$$

Multiplying Equation 2.38 by $\vec{p}$ yields the energy equation:

$$\frac{dE_{kin}}{dt} = -e\vec{v_e}\vec{E} \tag{2.39}$$

where E_{kin} is the kinetic energy:

$$E_{kin} = (\gamma - 1) m_e c^2 \tag{2.40}$$

Going back to the equation of motion (Equation 2.38), by using the total differential definition ($\frac{d\vec{A}}{dt} = \frac{\partial \vec{A}}{\partial t} + \frac{\partial \vec{A}}{\partial \vec{u}}\frac{\partial \vec{u}}{\partial t}$, with $\vec{u}$ an arbitrary coordinate vector) in $\vec{E} = -\frac{\partial \vec{A}}{\partial t}$ and inserting the result in Equation 2.38, one obtains:

$$\frac{d\vec{p}}{dt} = e\frac{d\vec{A}}{dt} - \vec{\nabla}(\vec{v}_e\vec{A}) \tag{2.41}$$

Let's consider the y-component only, i.e., $\vec{A} = A_0\vec{e_y}sin(\phi)$ with $\phi = -\omega_L t + k_L x$. $\vec{A}$ and $\vec{v}_e$ are both functions of time and in a plane wave the transverse position does not change the interdependence between both, hence, the term $\vec{\nabla}(\vec{v}_e\vec{A})$ becomes 0 and Equation 2.41:

$$p_y - eA_y = C_1 \tag{2.42}$$

with the integration constant, also called the "first constant of the electron motion". If the electron is at rest at $t = 0$ then $C_1 = 0$.

Let's analyze the motion and energy equations for all components:

$$\begin{aligned}\frac{d}{dt}\begin{pmatrix}\tilde{p_x}\\ \tilde{p_y}\\ \tilde{p_z}\end{pmatrix} &= \frac{-e}{m_e c}\left(\begin{pmatrix}0\\ E_0\\ 0\end{pmatrix} + \begin{pmatrix}v_x\\ v_y\\ v_z\end{pmatrix} \times \begin{pmatrix}0\\ 0\\ B_0\end{pmatrix}\right)cos(\phi)\\ &= -a_0\omega_L\begin{pmatrix}v_x/c\\ 1 - v_y/c\\ 0\end{pmatrix}cos(\phi)\end{aligned} \tag{2.43}$$

$$\frac{d\gamma}{dt} = \frac{-e}{m_e c^2}\vec{v}_e\begin{pmatrix}0\\ E_0\\ 0\end{pmatrix}cos(\phi) = -a_0\omega_L\frac{v_y}{c}cos(\phi) \tag{2.44}$$

Comparing the y component of Equation 2.44 to the x component of Equation 2.43 results in the relation:

$$\gamma - \tilde{p_x} = C_2 \tag{2.45}$$

with C_2 being the second constant of electron motion. Equation 2.45 shows that the electron energy and its forward momentum are always correlated. For an electron at rest $C_2 = 1$, thus, from Equation 2.35, 2.36 and 2.45 one can find the following relation between the longitudinal and transverse momentum:

$$\tilde{p_x} = \frac{1}{2}\tilde{p_y}^2 \tag{2.46}$$

If $\tilde{p_y} \gg 1$ the longitudinal momentum is the main movement, if $\tilde{p_y} \ll 1$ then the transverse momentum dominates.
From Equations 2.40, 2.45 and 2.46 the following relations are obtained:

$$\begin{aligned}E_{kin} &= m_e c^2\frac{a^2}{2}\\ \gamma &= 1 + \frac{1}{2}a^2\\ \tilde{p_y} &= a\end{aligned} \tag{2.47}$$

From the momentum definition ($p_u = \gamma m_e v_u$, with u an arbitrary direction) and Equation 2.47 the electron motion equations can be obtained:

$$\begin{aligned}\tilde{p_x} &= \frac{a^2}{2}\\ \tilde{p_y} &= a\\ \tilde{p_z} &= 0\end{aligned} \tag{2.48}$$

To simplify the following calculations, let's transform the coordinate system to the co-moving frame of the electrons:

$$\tau = t - \frac{x}{c} \tag{2.49}$$

Thus, $\phi = -\omega_L \tau$ and $\vec{a}_\tau = -\vec{e_y} a_0 sin(\omega_L \tau)$. Equations 2.48 integration become easier, yielding:

$$\begin{aligned} x_{(\tau)} &= \frac{c a_0}{\omega_L}(1 - cos(\omega_L \tau)) \\ y_{(\tau)} &= \frac{c a_0^2}{4}(\tau - \frac{1}{2\omega_L} sin(2\omega_L \tau)) \\ z_{(\tau)} &= 0 \end{aligned} \tag{2.50}$$

The y-coordinate is an oscillation motion. The x-coordinate motion is the combination of an oscillation with the second laser field harmonic and a longitudinal drift of velocity:

$$v_{drift} = \frac{a_0^2 c}{4 + a_0^2} \tag{2.51}$$

In the case of a finite laser pulse of the form:

$$a_{(\tau)} = a_0 e^{-\frac{\tau}{\tau_0}^2} sin(\omega_L \tau) \tag{2.52}$$

with τ_0 an arbitrary time. When the laser pulse arrives to the electron first the electron is pushed forward, then the laser pulse overtakes it leaving the electron at rest again. Thus, the electron gains energy from the laser and then gives it back, i.e., the total energy gain is 0.

2.2.2.1 Ponderomotive force

A focused laser achieves high a_0. The fields at the center (on-axis) is at its highest, thus, an electron on-axis suffers a deflection force that pushes it out of the focal region while oscillating. The electron obtains a non-zero kinetic energy from this interaction. This process is called ponderomotive scattering and is proportional to the pressure exerted by the laser field:

$$P_L = \frac{I_L}{c} \tag{2.53}$$

The ponderomotive force expression can be derived from the equation of motion, taking into account the linear terms as well as their quadratic variation (second order). For a relativistic case the calculation is complex so, only the result is presented here:

$$\vec{F}_{pond} = -\vec{\nabla}\Phi_{pond} \tag{2.54}$$

$$\Phi_{pond} = m_e c^2 \frac{a_0^2}{4 + a_0^2} \tag{2.55}$$

with $\vec{F}_{pond}$ the ponderomotive force and Φ_{pond} the ponderomotive potential. The ponderomotive force pushes the electrons from a high gradient zones to low gradient ones. Thus, it drives electrons away from high field zones.

2.2.2.2 Lawson-Woodward theorem

The Lawson-Woodward theorem establishes the conditions in which an electron interacting with an EM wave does not gain energy. If any of the conditions is broken the energy gain becomes possible [21]. The conditions are the following:

- The interaction takes place in vacuum

- The electron is highly relativistic during the process
- There are no static fields
- The laser field is a plane wave (infinite interaction region)
- The ponderomotive forces can be neglected

If the interaction takes place in a plasma the first condition is broken. For a high power focused laser the fourth and fifth conditions are also broken. A laser inside the plasma usually generates static fields thus, the third condition is also broken. So, electron acceleration via laser-plasma interaction is possible.

2.2.3 Non-linear optics

In a focused high power laser propagating inside a plasma, the electrons become relativistic, thus, their mass change should be taken into account. The plasma frequency in such case becomes:

$$\omega_p = \sqrt{\frac{n_e e^2}{\epsilon_0 \langle\gamma\rangle m_e}} \tag{2.56}$$

and in consequence the refractive index becomes a function of the γ, i.e., depends on the laser intensity that at the same time is a function of time and space:

$$\eta = \sqrt{1 - \frac{\omega_p^2}{\langle\gamma\rangle \omega_L^2}} = \eta_{I(u,t)} \tag{2.57}$$

with u an arbitrary position in space. This dependence of the plasma medium particles on the laser intensity and vice-versa generates a number of non-linear phenomena that can change the laser during its propagation. In this section, a quick description of the effects of such non-linear effects on the plasma is given.

2.2.3.1 Ionization defocusing

A laser pulse focused into a gas has a high intensity on-axis, specially when is close to focus [16, 22]. Thus, close to focus the ionization rate is higher and in consequence also the electron density. From Equations 2.27 and 2.28 one can write the refractive index as $\eta = \sqrt{1 - \frac{n_e}{n_c}}$, so the refractive index is lower on-axis and when close to focus, ergo, the phase velocity v_{ph} is higher. The ionization of the gas at the front of the laser pulse counters the focusing of the laser and does not allow it to achieve its maximum intensity. So, maximum focus requires of propagation in vacuum or in a fully ionized plasma.

2.2.3.2 Relativistic self-focusing

The change in the refractive index due to the generation of relativistic electrons affects the focus of the laser inside the plasma [16, 22, 23]. Let $w_{(x)}$ be the beam waist and w_0 the minimum beam waist, defined as:

$$w_{(x)} = w_0 (1 + \frac{x^2}{x_R^2})^{1/2} \tag{2.58}$$

$$w_0 = \frac{\lambda_L}{\pi \frac{D}{2f}} \tag{2.59}$$

with f the focal length, D beam diameter and x_R the Rayleigh length defined by:

$$x_R = \frac{\pi w_0^2}{\lambda_L} \tag{2.60}$$

From the analysis of the laser plane wavefront evolution inside a plasma between a time t and $t + \Delta t$ taking into account the refractive index variations, one can find the power threshold in which the laser gets focused by relativistic effects [22, 24]:

$$P_c = 17.4\frac{\omega_L^2}{\omega_p^2}[GW] = 17.4\frac{n_c}{n_e}[GW] \tag{2.61}$$

For a power superior to P_c the relativistic self-focusing occurs. The self-focusing is stronger if the laser power or the plasma density are increased. For a determined P_c, the beam waist evolution can be described as a function of the power. To first order the waist evolution is:

$$w_{(x)} = w_0(1 + (1 - \frac{P}{P_c})\frac{x^2}{x_R^2}) \tag{2.62}$$

However, this expression is not valid for $P \geq P_c$, for which higher orders are needed.

2.2.3.3 Pulse compression

Due to the spatial variations of the laser field, the focusing, ionization and plasma-pulse interaction can occur at different positions. Thus, the electron density seen by different parts of the pulse varies spatially and temporally. The refractive index seen by the laser varies locally and so does the phase velocity (Equation 2.25, $v_{ph} = \frac{c}{\eta}$). The locality of the phase group derives into two main effects:

The ionization occurring mainly at the front half of the laser pulse increases the electron density in that zone. The rise of density decreases the local refractive index and increases the phase velocity. The growth of phase velocity of the later part of the pulse causes the compression of the pulse [16, 23, 25].

The ponderomotive force is stronger in the higher field zone of the pulse. It expels electrons from the high field zone to the lower ones reducing the local electron density and increasing the refractive index. Thus, the local phase velocity of the later part of the pulse travels slower potentially causing pulse elongation[25].

2.2.3.4 Self-phase modulation

The propagation of a laser inside the plasma can excite a plasma wave. The plasma wave causes a periodic variation of the electron density and thus, a periodic variation of the phase velocity. Such periodic structure can originate a splitting of the laser pulse into smaller sub-pulses with a separation distance equal to the plasma wavelength λ_p. For pulses of $c\tau_L < \lambda_P$, the splitting does not take place and the pulse is compressed instead. The modulation can generate new frequency components of $\omega = \omega_L \pm n\omega_p$ (Raman sidebands) [26].

2.3 Laser plasma acceleration

The Lawson-Woodward theorem (Section 2.2.2.2) proves the possibility to use lasers inside plasma to accelerate electrons. In 1979, T. Tajima and J.M. Dawson proposed the use of a plasma wave generated by the non-linear ponderomotive force from an intense short EM pulse of frequency higher than the plasma one for electron acceleration [27]. Nowadays, thanks to the ultra-short high power lasers available, the electron acceleration via laser plasma interaction has been achieved [28] as proposed in the original article [2, 27].

2.3.1 Wakefield

The non-linearities arising from the laser and plasma interaction can be daunting for calculations, however, through the use of certain assumptions about the pulse shape one can describe the basic phenomena in a simple way. Let's consider a plane wave that varies in space:

$$E(t) = (E_0 + x_{(t)}\frac{\partial E_{0(x)}}{\partial x})cos(\omega t) \tag{2.63}$$

with E_0, the wave amplitude and ω its frequency. For a non-relativistic electron the equation of motion in the x-component is:

$$m_e\frac{d^2x}{dt^2} = -eE_{0(x)}cos(\omega t) - \frac{e^2}{m_e\omega^2}E_{0(x)}cos^2(\omega t)\frac{\partial}{\partial x}E_{0(x)} \tag{2.64}$$

Averaging Equation 2.64 over a period:

$$m_e \frac{d^2x}{dt^2} = -\frac{1}{4}\frac{e^2}{m_e\omega^2}\frac{\partial}{\partial x}E^2_{0(x)} \tag{2.65}$$

and in 3D it becomes:

$$F_{pond} = -\frac{1}{4}\frac{e^2}{m_e\omega^2}\nabla E^2_{0(x,y,z)} \tag{2.66}$$

with F_{pond} the ponderomotive force.

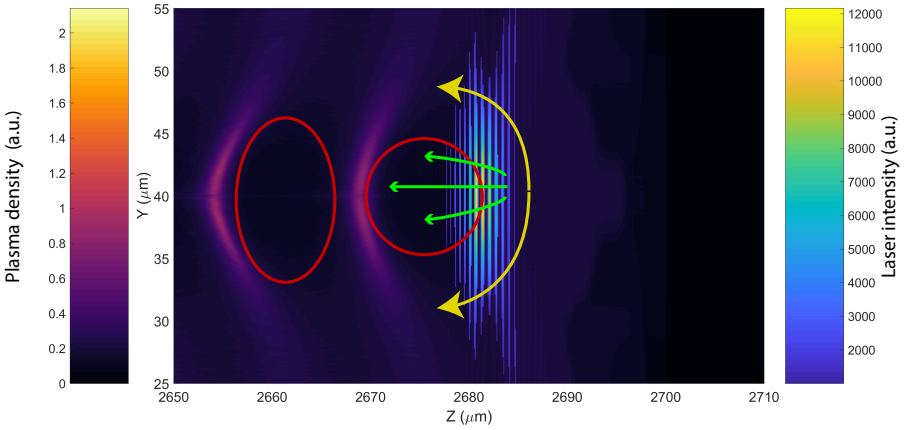

FIGURE 2.1: Representation of a wakefield generated by a laser pulse propagating to the right. The plasma density is represented in the left colormap scale, the laser pulse to the right colormap, the red circles represent the wakes, the yellow arrows represent electrons expelled by the laser pulse and the green ones electrons going into the wakefield.

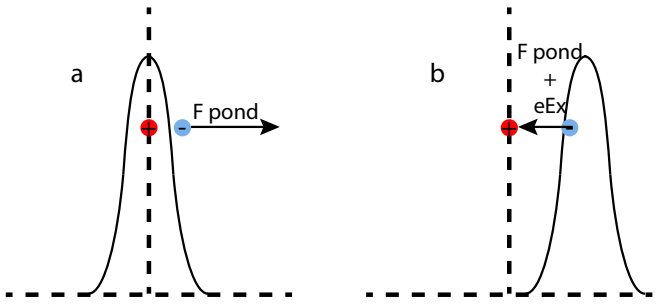

FIGURE 2.2: Ponderomotive force of a laser pulse on electrons inside plasma.

F_{pond} pushes the electrons from a high intensity region to low intensity one (Figure 2.1 yellow arrow) causing them to oscillate. When the front of the laser enters in contact with the electrons, they are moved in the pulse propagation direction (Figure 2.2a). Let's consider a group of electrons interacting with the front of the laser at the same time as a slab of width L_e being impelled a small distance $\delta \ll L_e$. As the ions are much slower, the electrons push creates a positive charge plasma zone (Figure 2.2b) and thus, a restoring force from the charge separation:

$$F_{restore} = -q_{dis}E = m_{dis}\frac{d^2\delta}{dt^2} \tag{2.67}$$

$$q_{dis} = -en_eA_{dis}\delta \tag{2.68}$$

$$m_{dis} = m_en_eA_{dis}\delta \tag{2.69}$$

with $F_{restore}$ the restoring force, q_{dis} the displaced charge, m_{dis} the displaced mass and A_{dis} the physical area of the displaced electron volume. The equation of motion per unit area A_{dis} is:

$$\frac{d^2\delta}{dt^2} = \frac{n_e e^2}{m\epsilon_0}\delta \tag{2.70}$$

which is an harmonic oscillator of frequency ω_p.

In addition to the restoring force, when the electrons are at the falling edge of the pulse, the ponderomotive force pushes them to the direction opposite to the pulse propagation one. Through the ponderomotive force, a separation of charges inside the plasma is generated (Figure 2.1 red circle) and with it a strong longitudinal electric field. The wave structure advances behind the laser pulse with a group velocity $v_{gr} = c\eta$ and can be used to accelerate electrons.

Let's consider a Gaussian laser pulse

$$a(z,t) = a_0 e^{-(\omega_L t - \frac{\omega_L z}{v_{gr}})^2} \tag{2.71}$$

with $a_0 = \frac{eE_0}{m\omega_L c}$ the normalized field amplitude and relativistic electrons. The electric field is approximately equal to the ponderomotive force (Equation 2.66):

$$F_{pond} \approx eE_{\parallel} \tag{2.72}$$

$$eE_{\parallel} = \frac{e^2}{4m_e\omega^2{}_L\langle\gamma\rangle}\vec{\nabla}\vec{E}^2 = \frac{m_e c^2}{4\langle\gamma\rangle}\vec{\nabla}_{\parallel}a_0^2 \tag{2.73}$$

with $E_{\parallel}$ the longitudinal electric field. Derivating a_0 in z and using Equation 2.47, Equation 2.73 becomes:

$$E_{\parallel} = \frac{m_e c\omega_p}{e}\frac{a_0^2/2}{\sqrt{1+a_0^2/2}} \tag{2.74}$$

So, the electric field of the wake depends on the plasma density n_e through the plasma frequency and the laser intensity. By itself this electric field does not accelerate electrons and only oscillate around their rest position. In order to achieve longitudinal acceleration, the electrons have to properly enter the wake structure and be trapped by it (Figure 2.1).

2.3.2 Injection schemes

Multiple ways to inject electrons in the wake have been developed over time. Here, some of those schemes will be quickly introduced.

2.3.2.1 External injection

The electrons can be injected into the wakefield if given enough velocity and if the bunch formed by them is shorter than $\approx 1/\omega_L$ longitudinally and $\approx \lambda_P$ transversely. These requirements are not easy to achieve [16, 29].

2.3.2.2 Wavebreaking injection

When the ponderomotive force generates a parallel electric field that exceeds the wavebreaking threshold, the plasma wave is driven into breaking to structures of scales much smaller than λ_p. The wavebreaking electric field threshold in the relativistic case is [16, 22, 26, 29]:

$$E_{wb} = \frac{m\omega_p c}{e}\sqrt{2(\gamma_p - 1)} = \frac{m\omega_p c}{e}\sqrt{2(\frac{\omega_L}{\omega_p} - 1)} \tag{2.75}$$

with $\gamma_p = \sqrt{1-(v_{ph,p}/c)} = \omega_L/\omega_p$ the relativistic factor of the plasma wave and $v_{ph,p} = c\eta$ its phase velocity which is equal to the laser group velocity. Increasing the electron density rises the wavebreaking threshold field, i.e., $E_{wb} \propto \sqrt{\omega_p}$, except if $\omega_p \approx \omega_L$, where it decreases until $\omega_p = \omega_L$. Therefore, for sufficiently low density the wavebreaking threshold increases with density ($E_{wb} \propto \sqrt{\omega_p}$) however, the intensity to reach a certain parallel field $E_{\parallel} \propto \omega_p$ drops faster with density. Thus, wavebreaking is easier at high density. Wavebreaking can also happen transversally. Once wavebreaking occurs the wave stays broken allowing continuous electron injection into the wakefield. A continuous injection yields a high charge and large energy spread electron beam.

2.3.2.3 Downramp injection

A decreasing plasma density ramp increases the pulse group velocity and the plasma wave λ_p, causing an elongation of the wakes and reduction of the phase velocity of the plasma wave. Both wake changes facilitate the electron injection. The phase velocity change is different for each wake. Thus, the injection in later wakes becomes easier than in the first one but, as the field amplitude is also lower in the later buckets, most injected electrons will be in the first wakes [16, 29].

The shaping of the plasma density distribution makes possible a better control on the injection process caused by wavebreaking [30–37]. The use of a density shock followed by a downramp permits to better localize the injection event resulting in lower energy spreads. In practice, the laser enters the plasma and forms the wake then, it encounters a density shock, and in its steep downramp wavebreaking occurs and the wake elongates causing a large injection event. After the steep downramp a much less steep gradient reduces the density until the interface plasma vacuum and is in this zone where the injected electrons are accelerated. The final beam charge and energy can be tuned via the shock position, density and acceleration zone length.

2.3.2.4 Ionization injection

The front of a high intensity laser can completely ionize low Z gases like *He*, via tunnel ionization. Thus, the laser sees a fully ionized plasma and pushes the electrons via the ponderomotive force creating the wakefield behind the pulse. The injection of electrons in the wakefield requires of them being at the correct position and having a similar velocity to the wakefield. The electrons pushed by the front of the laser do not acquire a high velocity, therefore are rarely injected. Doping the gas with a low percentage of a high Z element can lead to injection. The external electrons of the high Z atoms are stripped at the front of the laser, however, the deeper electron are ionized at the maximum intensity zone of the laser pulse. The deeper electrons are then born with a velocity similar to the wakefield one and receive only a relatively small backwards push towards the wake. These electrons can be trapped in the first wakes. Multiple high Z gases have been tested [38] like N_2, *Ne* and *Ar*, and it has been shown that even a doping of 1 % increases significantly the charge obtained and the energy distribution shape. The ionization injection scheme leads to a continuous injection along the entire plasma which creates beams with high energy spread and high charge [39–41], however, at lower gas densities it is possible to obtain low energy spreads at the cost of total charge [42].

2.3.2.5 Colliding pulse injection

The colliding pulse injection method is based in the use of two laser pulses [43] propagating in opposite directions [44], where the driver pulse of amplitude a_0 generates a non-breaking wakefield, thus not trapping electrons, and an injection pulse of amplitude $a_1 < a_0$ that collides with the driver injects electrons. At the collision event position a standing wave, of $v_{ph} = 0$ and scale $\lambda_L/2$, is generated and a ponderomotive force proportional to $\frac{2a_0a_1}{\lambda_L}$ appears. Therefore, the ponderomotive force can achieve high values even for modest laser amplitudes. The interaction between the ponderomotive force and the background electrons increase their momentum enough to allow for trapping and injection into the driver pulse wakefield. As the injection occurs in short time scales, the energy spread of the resulting beam is low, permits the generation of quasi monoenergetic electron beams. The collision position inside the plasma determines the injection position and therefore, the acceleration distance available. The injection pulse allows the charge injected to be controlled to certain extent. The beam loading effect limits the minimum energy spread achievable. The control of the collision position enables for beam energy tuning [45–50].

2.3.3 Dephasing length

Once the electrons are trapped in the wakefield, they exchange energy with the laser pulse through the wakefield gaining momentum. Eventually, the electron velocity reaches values superior to v_{ph} and starts to overtake the laser, reaching an opposite field region. As soon as the electrons reach the opposite field region they start to lose energy. The dephasing process limits the distance during which an electron can gain energy.

The dephasing limit can be easily calculated. Considering a plasma wave of phase velocity v_{ph} and length between its maximum and minimum amplitude $\lambda_p/2$, the time t_{DL} for an electron of velocity $v_e \approx v_{ph}$ to achieve the opposite field region is:

$$t_{DL} = \frac{\lambda_p}{2}\frac{1}{v_e - v_{ph}} = \frac{\lambda_p}{2c}\frac{1}{\beta_e - \beta_{ph}} \tag{2.76}$$

For a high energy electron $\beta_e \approx 1$ and for the plasma wave:

$$\beta_{ph} = \frac{v_{gr}}{c} = \eta = \sqrt{1 - \frac{n_e}{n_c}} \approx 1 - \frac{n_e}{2n_c} \tag{2.77}$$

Using Equations 2.77 into Equation 2.76 yields:

$$t_{DL} = \frac{\lambda_p n_c}{c n_e} \tag{2.78}$$

And therefore the dephasing length is:

$$d_{DL} = c t_{DL} = \frac{\lambda_p n_c}{n_e} = \frac{2\pi c n_c}{\omega_p n_e} \tag{2.79}$$

Since ω_p is proportional to n_e (Equation 2.18), the dephasing length is proportional to $\frac{1}{n^{3/2}}$. For a given laser, the acceleration length of the electrons is inversely proportional to the plasma electron density.

2.3.4 Depletion length

The generation of the plasma wave occurs at the pulse front and utilizes energy from the laser pulse. Thus, slowly the laser front is consumed with the so-called etching velocity, defined as [51]:

$$v_{etch} = c\frac{\omega_p^2}{\omega_L^2} \tag{2.80}$$

and the distance by which the laser is depleted is:

$$L_{depl} = \frac{c}{v_{etch}} c\tau_{L,(FWHM)} = \frac{\omega_p^2}{\omega_L^2} c\tau_{L,(FWHM)} \tag{2.81}$$

with $\tau_{L,(FWHM)}$ the laser pulse duration. The depletion of the laser also causes a change in the phase velocity:

$$v_{ph} = v_{gr,L} - v_{etch} \tag{2.82}$$

Therefore, the dephasing length (Equation 2.79) is also modified becoming:

$$d_{DL} \simeq \frac{2}{3k_p}\frac{\omega_p^2}{\omega_L^2}\sqrt{a_0} \tag{2.83}$$

2.3.5 Maximum electron energy gain

The maximum energy gain for an electron can be calculated from the longitudinal field $E_\parallel$:

$$W_{gain} = e\int E_\parallel dx \tag{2.84}$$

One can simplify the integral by just considering that the field is constant and equal to half of its maximum amplitude (Equation 2.73) during interaction [16, 22], which yield the approximation:

$$W_{gain} \approx \pi m_e c^2 \frac{a_0^2}{2}\frac{n_c}{n_e}\frac{1}{\sqrt{1 + a_0^2/2}} \tag{2.85}$$

A more exact calculation [16, 22] taking into account the field evolution gives the expression:

$$W_{gain} \approx m_e c^2 a_0^2 \frac{n_c}{n_e}\frac{1}{\sqrt{1 + a_0^2/2}} \tag{2.86}$$

For a Ti:Sa laser of $\lambda_L = 800$ nm a electron density of $n_e = 5 \times 10^{18}\ cm^{-3}$ and $a_0 = 1.5$ the maximum electron energy gain is of 274 MeV. In Equation 2.86 there is a lot of non-linear phenomena that is not taken into account, moreover, in the case of a ionization injection the laser energy is also consumed in order to ionize the gas at the front and maximum amplitude position in case of high Z atoms. Nevertheless, is an approximation of what accelerations one can expect.

2.3.6 Bubble regime

The wakefield features change dramatically depending on the driver laser pulse a_0. For $a_0 < 1$, the wakefield is similar to a small plasma perturbation (Equation 2.12) of first-order. This is the so-called linear regime in which no electron trajectory crossing occurs [52, 53] and for a plasma density of $n_e = 10^{18}$ the accelerating field is:

$$E_{max} \approx 36 a_0^2 \; GV.m^{-1} \tag{2.87}$$

If $a_0 \geq 1$, the wakefield cannot be treated as a weak perturbation. The strength of the ponderomotive force is enough to push all electrons from the first wake, leaving only the ion. The expelled electrons form a thin sheath around the cavity. This regime is called "cavern", "blow-out" or "bubble" [54–57] due to its electron free quasi-spherical shape. Significant trajectory crossing is present in this non-linear regime [56]. The first wake radius is proportional to the driver laser pulse as [58]:

$$r_b \approx 2\sqrt{a_0} \tag{2.88}$$

From r_b a beam spot size condition can be found by balancing the laser ponderomotive force with the ion channel force[56]:

$$k_p r_b \approx 2\sqrt{a_0} \tag{2.89}$$

If the laser pulse spot size is superior to the matched spot size, a_0 is not enough to cause blowout initially and only self-focusing of the laser pulse inside the plasma could trigger it. From phenomenological data and simulation the first wake length can be written as [51]:

$$L_b = 4\sqrt{a_0}\frac{c}{w_p} \tag{2.90}$$

The maximum accelerating field for $n_e = 10^{18}$ [51]:

$$E_{max} \approx 96\sqrt{a_0} \; GV.m^{-1} \tag{2.91}$$

And the maximum number of electrons that can be accelerated [51]:

$$N_{max} \approx 2.5 \times 10^9 \frac{\lambda_l \; [\mu m]}{0.8}\sqrt{P \; [TW]/100} \tag{2.92}$$

2.3.7 LPA state of the art

In the last decade the LPA beam parameters have improved steadily, thanks to the highly nonlinear regime and the advances in laser power. Table 2.1 documents some of the main laser plasma accelerator advances since 20 years ago with the experimental parameters and the measured beam results. Energies from hundreds MeV to close to tens of GeV can now be produced with hundreds of pC total beam charge and energy spreads on the % levels with FWHM divergences around the mrad. The achieved single shot energy record is 8 GeV with close to 0.5 nC total charge and 5 pC on the 8 GeV peak. Beam stability has been also a growing concern that is being addressed, e.g., 24 hours continuous LPA operation while correcting electron energy drift and jitter [8].

TABLE 2.1: LPA beam experimental results.

Facility (REF)	year	a_0	Laser Intensity W/cm^2	Power TW	Laser energy J	Beam size fs (FWHM)	Gas density cm^{-3}	Beam energy MeV	Charge Total pC	Divergence/Energy spread/ Emittance mrad/−/mm.mrad (RMS)
RAL ([59])	1998	2	5×10^{18}	20	20	10^3	$1.7 - 2 \times 10^{19}$	70		
MPI ([60])	1999		4×10^{18}		0.25	200	3×10^{19}	12.5	$3.2{\times}10^3$	
LOA ([5])	2004	1.3	3.2×10^{18}		1	33	6×10^{18}	170	$2{\pm}0.5{\times}10^3$ ($0.5{\pm}0.2{\times}10^3$ on peak)	10 (FWHM) / 24 % (FWHM) / −
Berkeley ([6])	2004		1.1×10^{19}	10	0.5	55	4.5×10^{19}	86	320	3 (FWHM) / 2 % (FWHM) / $<2\pi$ (FWHM)
Berkeley ([61])	2006		10^{18}	40		38	3×10^{18}	10^3	30	1.6 / 2.5% / −
Berkeley	2006		10^{18}	12		73	3×10^{18}	500	50	2 / 5.6% / −
JETI laser ([62])	2008	1.5	5×10^{18}			85	2×10^{19}	65	28	1.6 / 5 % (FWHM) / 1.3π
BELLA ([7])	2014	1.6+-0.1		300	16	40	7.5×10^{17}	$4.2{\times}10^3$	6	0.3 / 6 % /-
BELLA ([4])	2019	2.2		850	31	35	3.4×10^{17}	$7.8{\times}10^3$	420 (5 on peak)	0.2-0.6 /-/-
BELLA	2019	2.2		850	31	35	3.4×10^{17}	$6{\times}10^3$	210 (62 on peak)	0.2-0.6 /-/-

2.4 Particle in cell simulation method

As seen in the previous section, the interaction between the electrons and ions fields in the LPA process can be described by Lorentz and Maxwell equations (Equations 2.3-2.6) in a self consistent way. The number of interactions happening at the same time and the non-linearity of the system makes the direct calculation of the problem impossible. Thus, simulations to probe the underlying non-linear physics are needed.

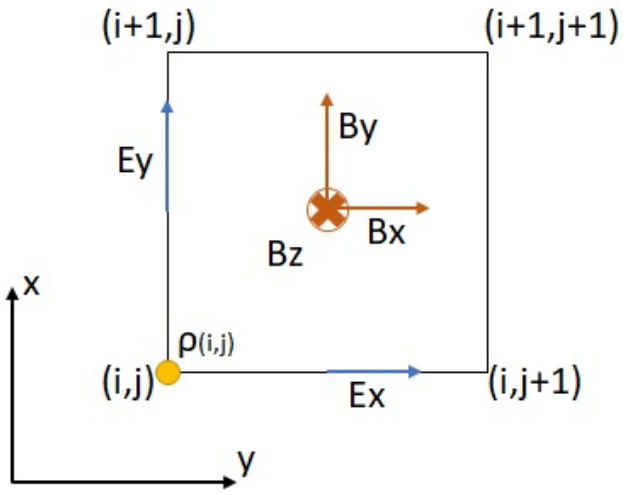

FIGURE 2.3: Example of a 2D PIC cell.

The Particle in cell (PIC) [63, 64] is an effective technique to simulate the plasma behavior with a much lower number of particles than in reality. The plasma is reduced to an ensemble of macroparticles, each representing a small portion of the phase space, that moves on a grid (see Figure 2.4). Each grid contains the weighted charge density information from which the electromagnetic forces can be extrapolated to any position.

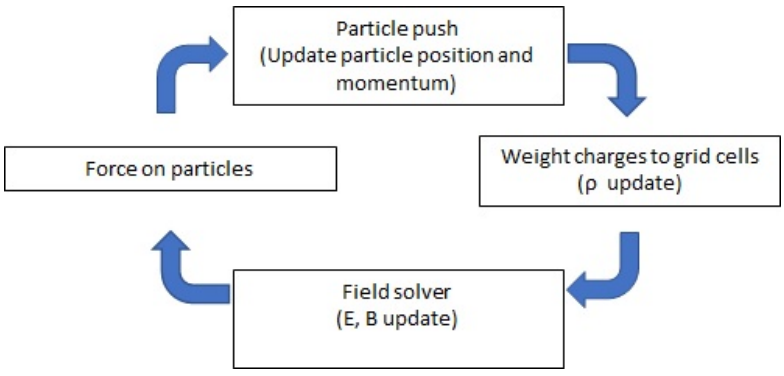

FIGURE 2.4: PIC code time-step calculation loop.

Figure 2.4 illustrates the basic cycle of a PIC code [63, 64]. First, the charge density is calculated at each cell from the macroparticles position. Secondly, the fields are computed on the grid with the Maxwell equations. Then, the forces on each macroparticle is calculated with the Lorentz equation at the grid. Finally, the time step advances and the macroparticles new position and momentum are deduced. While the main equations are straight forward the order of the operations and the way to extrapolate in the grid and advance the time step is not. For different numerical schemes are used, with the most common one being the leap-frog method [63]. There are also multiple ways to treat additional effects like ionization [65], recombination, collisions [66, 67], etc in PIC codes with different strengths and weaknesses. During this thesis, some research was done in the calculation of elastic collisions in plasma for PIC simulations. Such research yielded a method of calculations of coulomb collision usable also in non-maxwellian plasmas and multiple plasma populations that allows to conserve the mean velocities, calculation of runaway flux, conductivity, etc. An article was published from it (Appendix E).

For the present work the fully relativistic PIC code PICLS [65, 66] has been used. The PICLS code has been utilized before for laser research in laser-plasma interactions including laser-solid interaction, plasma formation, and laser wakefield acceleration (LWA) [68, 69]. The PICLS code features a current-conserving integration scheme [70], a numerical dispersion free Maxwell solver with the directional splitting scheme [63], which has been extended to the multidimensional problems. Also PICLS has a fourth order current/force interpolation to suppress the numerical instability causing under-resolving the Debye length.

2.5 Recall of electron beam transport

Once outside the source, the manipulation and transport of the relativistic electrons requires a high precision. Through the use of magnetic fields, one can control the direction and compensate the defocusing of the beam due to its divergence. Thus, it is necessary to do careful calculation of the electron path and reaction to the magnetic elements. In this section is recalled the basic modeling of the electron beam transport.

2.5.1 Beam dynamics

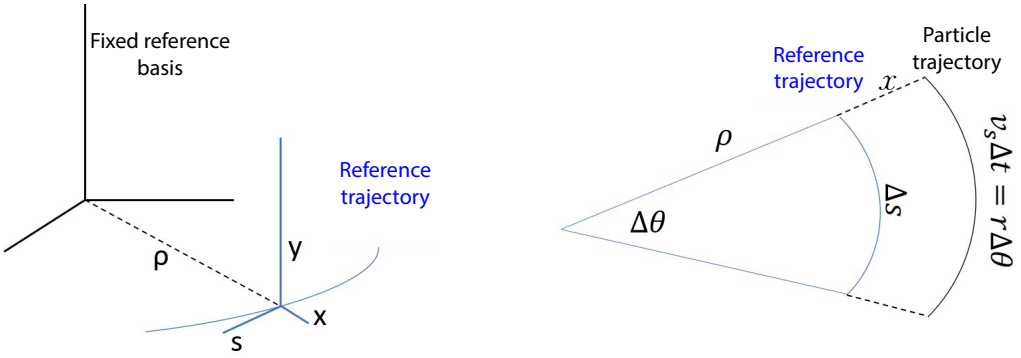

FIGURE 2.5: Moving frame based on a particle reference trajectory. For a time step Δt, a particle of longitudinal velocity v_s will advance a distance $r\Delta\theta = (\rho + x)\Delta\theta$ with θ the angle of rotation with respect to the fixed reference basis origin.

The electron motion is here described in a moving frame (Figure 2.5), centered on the orthogonal projection of the particle on a reference trajectory defined for the reference electron energy (on-momentum). Figure 2.5 indicates the moving frame with x the horizontal direction, y the vertical direction and s the longitudinal one and $\vec{u_x}$, $\vec{u_y}$ and $\vec{u_s}$ their orthonormal basis. The absolute vector position of an electron is given by $\vec{r}$ and the absolute vector position of the reference electron is given by $\vec{r_0}$. The electron position relative to the reference $\delta\vec{r}$ can be obtained by:

$$\delta\vec{r} = \vec{r} - \vec{r_0} = x\vec{u_x} + y\vec{u_y} \tag{2.93}$$

with x and y the x and y components of $\delta\vec{r}$. The unit vectors derivatives are:

$$\begin{aligned} \frac{d\vec{u_x}}{dt} &= \frac{\vec{u_s}}{\rho} = h\vec{u_s} \\ \frac{d\vec{u_y}}{dt} &= 0 \\ \frac{d\vec{u_s}}{dt} &= -\frac{\vec{u_x}}{\rho} = -h\vec{u_x} \end{aligned} \tag{2.94}$$

with ρ the curvature radius and $h = 1/\rho$ the local curvature. One can also define the longitudinal component of the position s derivative in time (Figure 2.5):

$$\frac{ds}{dt} = \frac{v_s}{1 + hx} \tag{2.95}$$

with v_s the velocity in the s direction. Equation 2.95 can be rewritten as:

$$\frac{ds}{dt} = \frac{v}{(1+hx)\sqrt{1+x'^2+y'^2}} = \frac{v}{l'} \tag{2.96}$$

with v the particle total velocity, l the length of the particle trajectory and l' its first derivative. The electron motion in a magnetic field $\vec{B}(x,y) = B_x(x,y)\vec{u_x} + B_y(x,y)\vec{u_y}$; from now on written without (x,y); equation is:

$$\frac{d^2\vec{r}}{dt^2} = \frac{q}{\gamma m_0}(\vec{v} \times \vec{B}) \tag{2.97}$$

with q the charge, m_0 the rest mass and γ the Lorentz factor of the particle. Using Equation 2.96, the time derivative of Equation 2.97 is replaced by an s derivative [71]

$$\frac{d^2\vec{r}}{ds^2} - \frac{l''d\vec{r}}{l'ds} = \frac{q}{p}l'(\frac{d\vec{r}}{ds} \times \vec{B}) \tag{2.98}$$

with p the particle momentum and l'' the length second derivative. By projecting Equation 2.98 along the transverse directions:

$$\begin{aligned} \frac{d^2x}{ds^2} - \frac{l''dx}{l'ds} &= (1+hx)(h - \frac{q}{p}l'B_y) \\ \frac{d^2y}{ds^2} - \frac{l''dy}{l'ds} &= (1+hx)(\frac{q}{p}l'B_x) \end{aligned} \tag{2.99}$$

The particle momentum can be defined in relation to the reference trajectory as:

$$\delta = \frac{p - p_0}{p_0} \tag{2.100}$$

with p_0 the reference particle momentum and δ the relative momentum. Equation 2.99 can be simplified by considering three approximations: The electron relative horizontal position is smaller than the local curvature radius ($(hx)^2 << hx$). The beam propagates mostly parallel to the longitudinal axis i.e. $x'^2 + y'^2 << 1$ (the paraxial approximation). The electron momentum p is close to the reference one p_0 i.e. $\delta \approx 0$. Thus, a linear expansion can be made:

$$\begin{aligned} l' &\approx 1 + hx \\ \frac{q}{p} &\approx \frac{q}{p_0}(1-\delta) \\ h &\approx h_0(1-\delta) \end{aligned} \tag{2.101}$$

with h_0 the reference particle local curvature. Maxwell equation $\nabla \times \vec{B} = 0$ gives the relation:

$$\frac{\partial B_y}{\partial x} = \frac{\partial B_x}{\partial y} \tag{2.102}$$

Considering that there is no field on axis, $B_x(0,0) = B_y(0,0) = 0$, the magnetic field can be written as:

$$\begin{aligned} \vec{B} &= B_x\vec{u_x} + B_y\vec{u_y} \\ &= (\frac{\partial B_x}{\partial y}y + \frac{\partial B_x}{\partial x}x)\vec{u_x} + (\frac{\partial B_y}{\partial x}x + \frac{\partial B_y}{\partial y}y)\vec{u_y} \end{aligned} \tag{2.103}$$

Let's define the skew normalized gradient $\bar{K_0}$ and the normalized gradient K_0 [72, 73] as:

$$\begin{aligned} K_0 &= \frac{q}{p_0}\frac{\partial B_y}{\partial x} \\ \bar{K_0} &= \frac{q}{p_0}\frac{\partial B_x}{\partial x} \end{aligned} \tag{2.104}$$

By the relation established in Equation 2.102:

$$\begin{aligned} K_0 &= \frac{q}{p_0}\frac{\partial B_y}{\partial x} = \frac{q}{p_0}\frac{\partial B_x}{\partial y} \\ \bar{K_0} &= \frac{q}{p_0}\frac{\partial B_x}{\partial x} = -\frac{q}{p_0}\frac{\partial B_y}{\partial y} \end{aligned} \tag{2.105}$$

So, one can rewrite Equation 2.103 as:

$$\begin{aligned} \frac{q}{p_0}B_x &= K_0 y + \bar{K_0} x \\ \frac{q}{p_0}B_y &= h_0 - \bar{K_0} y + K_0 x \end{aligned} \tag{2.106}$$

with $\bar{K_0}$ inducing a linear coupling. Using Equation 2.106 in Equation 2.99, one finds:

$$\begin{aligned} \frac{d^2x}{ds^2} + (K_0 + h^2)x &= h\delta + \bar{K_0} y \\ \frac{d^2y}{ds^2} - K_0 y &= \bar{K_0} x \end{aligned} \tag{2.107}$$

The $h\delta$ term gives the influence of the relative energy in the horizontal direction (chromatic term).

If one considers an on-momentum electron; i.e. $\delta = 0$; without horizontal and vertical coupling, the motion given by Equation 2.107 simplifies to an harmonic oscillator one of "spring constant" $K(s)$:

$$\frac{d^2u}{ds^2} + K(s)u = 0 \tag{2.108}$$

with u representing a transversal direction. The solutions of Equation 2.108 can be written in matrix form for a transport from a position $s = 0$ to s:

$$\begin{pmatrix} u(s) \\ u'(s) \end{pmatrix} = \begin{pmatrix} cos(\sqrt{K(s)}s) & \frac{1}{\sqrt{K(s)}}sin(\sqrt{K(s)}s) \\ -\sqrt{K(s)}cos(\sqrt{K(s)}s) & sin(\sqrt{K(s)}s) \end{pmatrix} \begin{pmatrix} u(0) \\ u'(0) \end{pmatrix} = M_{0/s} \begin{pmatrix} u(0) \\ u'(0) \end{pmatrix} \tag{2.109}$$

$$M_{0:s} = \begin{pmatrix} C(0:s) & S(0:s) \\ C'(0:s) & S'(0:s) \end{pmatrix} = \begin{pmatrix} R_{11} & R_{12} \\ R_{21} & R_{22} \end{pmatrix} \tag{2.110}$$

with the index $(0 : s)$ referring to the path from an initial longitudinal position 0 to a position s, $S(s) = cos(\sqrt{K(s)}s)$, $C(s) = cos(\sqrt{K(s)}s)$ and R_{ij} refering to the transport matrix term at the row i and column j. So a transport of an electron through a line can be calculated via the product of the different magnetic element matrices $M_{s_n:s_0}$:

$$M_{s_n:s_0} = M_{s_n:s_{n-1}} \cdot ... \cdot M_{s_2:s_1} \cdot M_{s_1:s_0} \tag{2.111}$$

For an off-momentum electron, i.e. $\delta \neq 0$, in the horizontal plane, Equation 2.107 becomes:

$$\begin{aligned} \frac{d^2x}{ds^2} + K(s)x &= h\delta \\ P''(s) + K(s)P(s) &= p(s) \end{aligned} \tag{2.112}$$

with $P(s)$ the particular solution and $p(s)$ the perturbation term. The solution of the homogeneous equation given in Equation 2.110 enables to find particular solutions $P(s)$ for the inhomogeneous differential equation, thus, a solution of $P(s)$ can be found from:

$$P(s) = \int_0^s p(\tilde{s})G(s,\tilde{s})d\tilde{s} \tag{2.113}$$

with $G(s,\tilde{s})$ the Green's function deduced from the homogeneous case solution (Equation 2.110):

$$G(s,\tilde{s}) = S(s)C(\tilde{s}) - C(s)S(\tilde{s}) \tag{2.114}$$

Thus, inserting Equation 2.114 into Equation 2.113 gives:

$$P(s) = S(s)\int_0^s p(\tilde{s})C(\tilde{s})d\tilde{s} - C(s)\int_0^s p(\tilde{s})S(\tilde{s})d\tilde{s} \tag{2.115}$$

The general solution of the equation of motion is a combination of the homogeneous case solutions (Equation 2.110) and a particular solution of the inhomogeneous differential equation (Equation 2.115):

$$u(s) = aC_u(s) + bS_u(s) + P_u(s) \tag{2.116}$$

where a and b are constants that depend on the initial parameters of the trajectory. Following the Equation 2.115, one can define the dispersion function $D_u(s)$ as:

$$D_u(s) = \frac{P_u(s)}{\delta} \tag{2.117}$$

and using 2.112:

$$D_u(s) = \int_0^s h(\tilde{s})(S_u(s)C_u(\tilde{s}) - C_u(s)S_u(\tilde{s}))d\tilde{s} \tag{2.118}$$

$\delta D_u(s)$ gives the off momentum trajectory offset with respect to the reference trajectory. One can expand the transport matrix Equation 2.110 as:

$$\begin{pmatrix} u(s) \\ u'(s) \\ \delta(s) \end{pmatrix} = \begin{pmatrix} C_u(0:s) & S_u(0:s) & D_u(0:s) \\ C'_u(0:s) & S'_u(0:s) & D'_u(0:s) \\ 0 & 0 & 1 \end{pmatrix} \begin{pmatrix} u(0) \\ u'(0) \\ \delta(0) \end{pmatrix} = M_{0:s} \begin{pmatrix} u(0) \\ u'(0) \\ \delta(0) \end{pmatrix} \tag{2.119}$$

The matrix formalism can be extended to second order [74]. The transport matrix of 2nd order in δ for an electron in the horizontal direction takes the following form:

$$M = \begin{pmatrix} R_{11} & R_{12} & R_{16} \\ R_{21} & R_{22} & R_{26} \end{pmatrix} + \delta \begin{pmatrix} R_{116} & R_{126} & R_{166} \\ R_{216} & R_{226} & R_{266} \end{pmatrix} \tag{2.120}$$

Adding correlations between all first order terms and the electron relative energy in the form of the terms R_{ij6}.

2.5.2 Betatron function

Let's consider an on-momentum uncoupled electron in a periodic channel ($K(s) = K(s+L_p)$, with L_p the period) [71]. Equation 2.108 with a periodic condition is known as Hill's equation [75]. Its solution has been formulated in Floquet's theorem. Let's define $\beta_T(s)$, the betatron function of the particle motion, as

$$\beta_T(s+L_p) = \beta_T(s) \tag{2.121}$$

A simplified version of Floquet's theorem [76] can be written as:

$$u(s) = \sqrt{U\beta_T(s)}cos(\Phi(s)) \tag{2.122}$$

with $\mu(s:s_0) = \Phi(s) - \Phi(s_0) = \int_{s_0}^{s} \frac{ds}{\beta_T(s)}$ the phase advance of the particle from a position s to another s_0, Φ the particle phase and U an invariant dependent on the initial conditions. This motion is named betatron oscillation. Using Equation 2.122 in Equation 2.108 gives:

$$(-\frac{\beta_T'^2}{4\beta_T^2} + \frac{\beta_T''}{2\beta_T} - \Phi'^2 + K)cos(\Phi) - (\frac{\beta_T'\Phi'}{\beta_T} + \Phi'')sin(\Phi) = 0 \tag{2.123}$$

With $\beta_T(s) = \beta_T$, $\Phi(s) = \Phi$, β_T' and β_T'' the first and second derivatives in s respectively and idem for Φ' and Φ''. As one can't make any assumptions over Φ for an arbitrary particle, the terms in front of the cosine and sine have to be equal to 0.

$$\frac{1}{2}(\beta_T\beta_T' - \frac{1}{2}\beta_T'^2) - \beta_T^2\Phi'^2 + \beta_T^2 K = 0$$
$$\beta_T'\Phi' + \beta_T\Phi'' = 0$$

The right parenthesis of Equation 2.123 can be easily integrated, and by choosing $\beta_T\Phi' = cte = 1$, one finds:

$$\Phi(s) = \int_0^s \frac{ds}{\beta_T(s)} + \Phi_0 \tag{2.124}$$

Using this new Φ expression in the left parenthesis of Equation 2.123 gives:

$$\frac{1}{2}\beta_T\beta_T' - \frac{1}{4}\beta_T'^2 + \beta_T^2 K = 1 \tag{2.125}$$

which is the envelope equation. From here the so-called Twiss parameters α_T and γ_T can be defined from β_T:

$$\alpha_T(s) = -\frac{\beta_T'(s)}{2}$$
$$\gamma_T(s) = \frac{1+\alpha_T^2(s)}{\beta_T(s)} \tag{2.126}$$

Equation 2.125 can be rewritten as:

$$\beta_T'' + 2K\beta_T - 2\gamma_T = 0 \tag{2.127}$$

Every β_T and Φ satisfying Equation 2.124 and Equation 2.127 makes Equation 2.122 real. Equation 2.127 can be rewritten as:

$$\gamma_T u^2 + 2\alpha_T u u' + \beta_T u'^2 = U \tag{2.128}$$

Equation 2.128 is like an ellipse equation in the phase-space (u, u') with U a constant of motion that defines the periodical trajectory of an electron in (u, u').

2.5.3 Particle beam dynamics

Until now, the case of individual electrons have been considered. An electron beam is constituted by a group of particles with a momentum in the s direction much higher in average than in the other directions:

$$\langle p_s\rangle^2 > \langle p_x\rangle^2 + \langle p_y\rangle^2 + \langle(p_s - \langle p_s\rangle)^2\rangle$$

with $\langle X\rangle$ the average of a variable X. The beam then can be represented as a 6D particle distribution in the phase-space $(x, x', y, y', l, \delta)$ with l the relative longitudinal position. The electron beam occupies a volume in the phase-space, which is an invariant of motion in Hamiltonian systems. It can be used as a beam quality indicator and it is called emittance ϵ_u. Without correlation between the horizontal and vertical axis, one can define separated 2D phase-spaces and an emittance for each by surrounding all particles of the beam by an ellipse following Equation 2.128 with the constant $U = \epsilon_u$:

$$\gamma_{T,u} u^2 + 2\alpha_{T,u} u u' + \beta_{T,u} u'^2 = \epsilon_u \tag{2.129}$$

Figure 2.6 presents a 2D phase space (u, u') with a red ellipse surrounding the particles. The area enclosed by the ellipse is $\pi\epsilon_u$, and the Twiss parameters determine the shape and orientation of the ellipse. $\alpha_{T,u}$ is related to the ellipse tilt, $\beta_{T,u}$ to the ellipse shape and size and ϵ_u to the ellipse size. The definition in relation to the ellipse

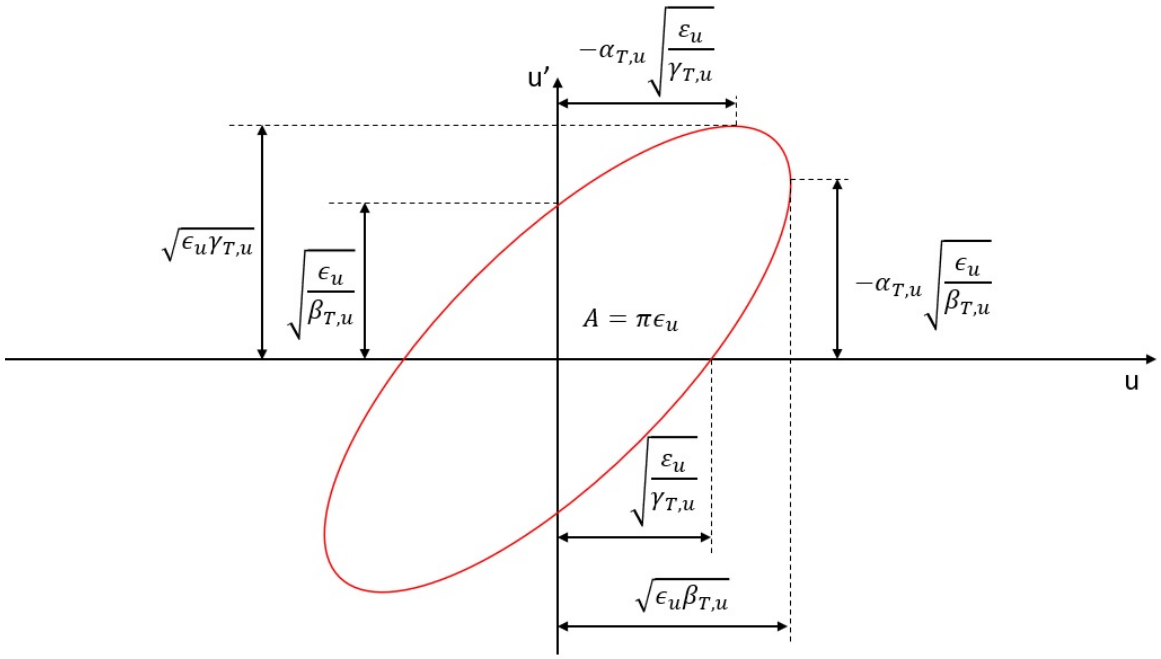

FIGURE 2.6: Elliptic area enclosing the beam in a 2D phase-space.

shape of the beam parameters (Figure 2.6) has limitations when the phase-space doesn't resemble an ellipsoid. Thus, the emittance and Twiss parameters can be more accurately defined using the moments of the position and moments of the electrons [77]. For $\Psi(x,x',y,y',l,\delta)$ the particle density in 6D phase space, the first and second moments and the coupling of variables are defined as follows:

$$\langle u\rangle = \frac{\int u\Psi(x,x',y,y',l,\delta)dxdx'dydy'dld\delta}{\int \Psi(x,x',y,y',l,\delta)dxdx'dydy'dld\delta} \tag{2.130}$$

$$\langle u^2\rangle = \frac{\int (u-\langle u\rangle)^2\Psi(x,x',y,y',l,\delta)dxdx'dydy'dld\delta}{\int \Psi(x,x',y,y',l,\delta)dxdx'dydy'dld\delta} \tag{2.131}$$

$$\langle uv\rangle = \frac{\int (u-\langle u\rangle)(v-\langle v\rangle)\Psi(x,x',y,y',l,\delta)dxdx'dydy'dld\delta}{\int \Psi(x,x',y,y',l,\delta)dxdx'dydy'dld\delta} \tag{2.132}$$

In the 2D phase-space (x,x') case, $\langle u\rangle$ gives the center of gravity of the distribution, $\langle u^2\rangle$ the variances, the square-root of the variances $\sqrt{\langle u^2\rangle}$ provides the RMS beam sizes and $\langle uv\rangle$ the correlation between the parameters u and v. The so-called "covariance matrix" is introduced:

$$\sigma_{beam} = \begin{pmatrix}\sigma_{11} & \sigma_{12}\\ \sigma_{21} & \sigma_{22}\end{pmatrix} = \epsilon_x^2\begin{pmatrix}\langle x^2\rangle & \langle xx'\rangle\\ \langle x'x\rangle & \langle x'^2\rangle\end{pmatrix} \tag{2.133}$$

By using Equations 2.129 and 2.110 one can define the RMS Twiss parameters of the beam $\tilde{\beta_T}$, $\tilde{\alpha_T}$ and $\tilde{\gamma_T}$ as:

$$\begin{aligned}\tilde{\beta_T} &= \langle x^2\rangle/\epsilon_{rms} = \sigma_{11}/\epsilon_{rms}\\ \tilde{\gamma_T} &= \langle x'^2\rangle/\epsilon_{rms} = \sigma_{22}/\epsilon_{rms}\\ \tilde{\alpha_T} &= \langle xx'\rangle/\epsilon_{rms} = \sigma_{12}/\epsilon_{rms}\\ \epsilon_{rms} &= \sqrt{\langle x^2\rangle\langle x'^2\rangle - \langle xx'\rangle^2}\end{aligned} \tag{2.134}$$

If there is acceleration or deceleration, the emittance is no longer constant (Liouville theorem [78]), and the change is proportional to $\gamma\beta$, the Lorentz factor and the reduced speed ($\frac{v}{c}$) respectively. Thus, one can introduce the normalized emittance:

$$\epsilon_{norm} = \beta\gamma\epsilon_{rms} \tag{2.135}$$

2.5.4 Transport matrix for on-momentum electrons

Following Equation 2.119, the transport matrices can be calculated for the different magnetic elements used along the line (Equations 2.136-2.145) [71]. During a drift no magnetic field is present thus, by taking the limit of $K(s) \to 0$ and the transport matrix is given by:

$$R_{drift} = \begin{pmatrix} 1 & l_d & 0 & 0 & 0 & 0 \\ 0 & 1 & 0 & 0 & 0 & 0 \\ 0 & 0 & 1 & l_d & 0 & 0 \\ 0 & 0 & 0 & 1 & 0 & 0 \\ 0 & 0 & 0 & 0 & 1 & 0 \\ 0 & 0 & 0 & 0 & 0 & 1 \end{pmatrix} \tag{2.136}$$

with l_d the drift length.

Let a quadrupole of magnet of length l_q and $G = \frac{\partial B_x}{\partial y}$ the magnetic gradient. Thus, the remaining term is the focusing gradient (Equation 2.104) of the quadrupole $k_q = G/(B\rho)$ in m^{-2}. Equation 2.108 for a quadrupole gives the following transport matrix:

$$R_{Quadrupole,k_q<0} = \begin{pmatrix} cosh(\sqrt{-k_q} \times l_q) & \frac{sinh(\sqrt{-k_q} \times l_q)}{\sqrt{-k_q}} & 0 & 0 & 0\,0 \\ \sqrt{-k_q} sinh(\sqrt{-k_q} \times l_q) & cosh(\sqrt{-k_q} \times l_q) & 0 & 0 & 0\,0 \\ 0 & 0 & cos(\sqrt{-k_q} \times l_q) & \frac{sin(\sqrt{-k_q} \times l_q)}{\sqrt{-k_q}} & 0\,0 \\ 0 & 0 & -\sqrt{-k_q} sin(\sqrt{-k_q} \times l_q) & cos(\sqrt{-k_q} \times l_q) & 0\,0 \\ 0 & 0 & 0 & 0 & 1\,0 \\ 0 & 0 & 0 & 0 & 0\,1 \end{pmatrix} \tag{2.137}$$

for a vertically focusing quadrupole.

$$R_{Quadrupole,k_q>0} = \begin{pmatrix} cos(\sqrt{k_q} \times l_q) & \frac{sin(\sqrt{k_q} \times l_q)}{\sqrt{k_q}} & 0 & 0 & 0\,0 \\ -\sqrt{k_q} sin(\sqrt{k_q} \times l_q) & cos(\sqrt{k_q} \times l_q) & 0 & 0 & 0\,0 \\ 0 & 0 & cosh(\sqrt{k_q} \times l_q) & \frac{sinh(\sqrt{k_q} \times l_q)}{\sqrt{k_q}} & 0\,0 \\ 0 & 0 & \sqrt{k_q} sinh(\sqrt{k_q} \times l_q) & cosh(\sqrt{k_q} \times l_q) & 0\,0 \\ 0 & 0 & 0 & 0 & 1\,0 \\ 0 & 0 & 0 & 0 & 0\,1 \end{pmatrix} \tag{2.138}$$

For a horizontally focusing quadrupole.
The magnetic field as seen from the beam can be expressed as a series of multipoles [79]:

$$B(c) = \sum_{n=1}^{\infty} (B_n + iA_n) \frac{c^{n-1}}{r_0^{n-1}} \tag{2.139}$$

with n the multipolar order, the complex number $c = x + iz$, B_n the normal multipolar, A_n the skew component, and r_0 the radius. Each multipolar term corresponds to a magnetic flux distribution [80]. A quadrupole comports the desired normal terms (B_2), and unwanted components such as skew contributions (A_2) and higher order multipoles. The integrated components are defined as:

$$a_n = \int A_n \cdot dl; b_n = \int B_n \cdot dl \tag{2.140}$$

with l as the longitudinal direction. The skew real component a_2 can be characterized by an angle, defined as:

$$\theta_{skew} = \frac{1}{2} arctan(\frac{a_2}{b_2}) \tag{2.141}$$

If the quadrupole presents a skew θ_{skew} on the magnet structure in the transverse plane (x,y), its effect on the electron beam can be taken into account with a simple rotation matrix:

$$R_{QuadrupoleSkewEntrance} = \begin{pmatrix} 1 & 0 & \theta_{skew} & 0 & 0 & 0 \\ 0 & 1 & 0 & \theta_{skew} & 0 & 0 \\ -\theta_{skew} & 0 & 1 & 0 & 0 & 0 \\ 0 & -\theta_{skew} & 0 & 1 & 0 & 0 \\ 0 & 1 & 0 & 0 & 1 & 0 \\ 0 & 0 & 0 & 0 & 0 & 1 \end{pmatrix} \tag{2.142}$$

$$R_{QuadrupoleSkewExit} = \begin{pmatrix} 1 & 0 & -\theta_{skew} & 0 & 0 & 0 \\ 0 & 1 & 0 & -\theta_{skew} & 0 & 0 \\ \theta_{skew} & 0 & 1 & 0 & 0 & 0 \\ 0 & \theta_{skew} & 0 & 1 & 0 & 0 \\ 0 & 1 & 0 & 0 & 1 & 0 \\ 0 & 0 & 0 & 0 & 0 & 1 \end{pmatrix} \tag{2.143}$$

A bending magnet presents a magnetic field in the direction that crosses both magnets, thus, perpendicular to the electron velocity. The strength is $k_b = K_0(bending - magnet)$ and $k_b = |h^2|$, from the h^2 contribution in Equation 2.107, with $||$ the module. For a bending magnet of strength k_b, curvature radius ρ and bending magnet length l_b, the transport matrix is:

$$R_{Bending} = \begin{pmatrix} cos(l_b \times k_b) & \frac{sin(l_b \times k_b)}{k_0} & 0 & 0 & 0 & h\frac{1-cos(l_b \times k_b)}{k_b^2} \\ -k_b sin(l_b \times k_b) & cos(l_b \times k_b) & 0 & 0 & 0 & sin(l_b \times k_b) \\ 0 & 0 & 1 & l_b & 0 & 0 \\ 0 & 0 & 0 & 1 & 0 & 0 \\ -sin(l_b \times k_b) & h\frac{cos(l_b \times k_b)-1}{k_b^2} & 0 & 0 & 1 & \frac{k_b l_b - sin(l_b \times k_b)}{-k_b} \\ 0 & 0 & 0 & 0 & 0 & 1 \end{pmatrix} \tag{2.144}$$

Electrons that do not enter with a velocity perpendicular to the dipole edge see a different magnetic field at the edge, thus, a correction on the dipole magnetic field effect has to be done upon entry and exit of the dipole, according to:

$$R_{BendingEdge} = \begin{pmatrix} 1 & 0 & 0 & 0 & 0 & 0 \\ tg(\theta_{be})/\rho & 1 & 0 & 0 & 0 & 0 \\ 0 & -tg(\theta_{be} - \Phi_{be})/\rho & 1 & 0 & 0 & 0 \\ 0 & 0 & 0 & 1 & 0 & 0 \\ 0 & 0 & 0 & 0 & 1 & 0 \\ 0 & 0 & 0 & 0 & 0 & 1 \end{pmatrix} \tag{2.145}$$

with θ_{be} = dipole face rotation, $\Phi_{be} = \frac{k_{be}}{\rho}(1 + sin^2(\theta_{be})/cos(\theta_{be}))$, $k_{be} = L_{ff}/6$ and L_{ff} fringe effect [81].

2.5.5 Exact Hamiltonian integration

The equations of motion for an electron going through magnetic lattices can be exactly integrated from the Hamiltonian [82], as:

$$H(\vec{q}, \vec{p}) = c\sqrt{(\vec{p} - e\vec{A}(\vec{q}))^2 + m^2c^2} + e\phi(\vec{q}) \tag{2.146}$$

with $\vec{q}$ the coordinates vector and $\vec{p}$ the momentum vector, $\vec{A}$ the potential vector and ϕ the scalar potential of the field. Transforming this Hamiltonian to the moving reference frame, one obtains:

$$H(x, y, l, p_x, p_y, \delta; s) = -(1 + h(s)x)\sqrt{(1+\delta)^2 - p_x^2 - p_y^2} - eA_s + \delta + 1 \tag{2.147}$$

Thus, from the Hamiltonian definition [83], the derivatives are:

$$\begin{aligned} \frac{du}{ds} &= \frac{\partial H}{\partial p_u} \\ \frac{dp_u}{ds} &= -\frac{\partial H}{\partial u} \end{aligned} \tag{2.148}$$

The exact dynamics of the particles for each magnetic element can be calculated by integrating the general equations of motion. Let's define the index 0 as the initial state of the particle and 1 as the state after the element action. For a drift of length l_d the equations of motion are:

$$\begin{aligned} x_1 &= x_0 + \frac{p_{x,0} l_d}{\sqrt{(1+\delta)^2 - p_{x,0}^2 - p_{y,0}^2}} \\ y_1 &= y_0 + \frac{p_{y,0} l_d}{\sqrt{(1+\delta)^2 - p_{x,0}^2 - p_{y,0}^2}} \\ l_1 &= l_0 + \frac{(1+\delta) l_d}{\sqrt{(1+\delta)^2 - p_{x,0}^2 - p_{y,0}^2}} \end{aligned} \tag{2.149}$$

for a dipole of length l_b:

$$\begin{aligned} p_{x,1} &= p_{x,0} cos(h l_b) + (\sqrt{(1+\delta)^2 - p_{x,0}^2 - p_{y,0}^2} - b_1 (h^{-1} + x_0)) \\ x_1 &= \frac{1}{h b_1} (h \sqrt{(1+\delta)^2 - p_{x,0}^2 - p_{y,0}^2} - \frac{dp_{x,1}}{ds} - b_1) \\ y_1 &= y_0 + \frac{p_{y,0}}{b_1} (asin(\frac{p_{x,0}}{\sqrt{(1+\delta)^2 - p_y^2}} - asin(\frac{p_{x,1}}{\sqrt{(1+\delta)^2 - p_y^2}})) + \frac{p_{y,0} h}{b_1} l_b \\ l_1 &= l_0 + \frac{(1+\delta)}{b_1} (asin(\frac{p_{x,0}}{\sqrt{(1+\delta)^2 - p_y^2}} - asin(\frac{p_{x,1}}{\sqrt{(1+\delta)^2 - p_y^2}})) + \frac{(1+\delta) h}{b_1} l_b \end{aligned} \tag{2.150}$$

For a particle with velocity non-perpendicular to the dipole edge by an angle θ_u, the correction at the dipole's entrance and exit is:

$$\begin{aligned} p_{x,1} &= p_{x,0} + h x_0 tan(\theta_u) \\ p_{y,1} &= p_{y,0} + h y_0 tan(\theta_u) \end{aligned} \tag{2.151}$$

For a quadrupole of l_q length and strength k_q, the equations are:

$$
\begin{aligned}
\omega &= \sqrt{\frac{k_q}{1+\delta}} \\
x_1 &= x_0 cos(\omega l_q) + \frac{1}{\omega(1+\delta)} sin(\omega l_q) p_{x,0} \\
p_{x,1} &= -\omega(1+\delta) sin(\omega l_q) x_0 + cos(\omega l_q) p_{x,0} \\
y_1 &= y_0 cosh(\omega l_q) + \frac{1}{\omega(1+\delta)} sinh(\omega l_q) p_{y,0} \\
p_{y,1} &= \omega(1+\delta) sinh(\omega l_q) y_0 + cosh(\omega l_q) p_{y,0} \\
l_1 &= l_0 + \Delta l \\
\Delta l = \frac{1}{4}\omega(\frac{1}{2} sin(2\omega l_q) - \omega l_q) x_0^2 - \frac{1}{4}\omega(\frac{1}{2} sinh(2\omega l_q) - \omega l_q) y_0^2 - \\
\frac{1}{4}\frac{1}{(1+\delta)^2}(\frac{sin(2\omega l_q)}{2\omega} + l_q) p_{x,0}^2 - \frac{1}{4}\frac{1}{(1+\delta)^2}(\frac{sin(2\omega l_q)}{2\omega} + l_q) p_{y,0}^2 \\
+\frac{1}{2}\frac{sin^2(\omega l_q)}{1+\delta} x_0 p_{x,0} + \frac{1}{2}\frac{sinh^2(\omega l_q)}{1+\delta} y_0 p_{y,0}
\end{aligned}
\tag{2.152}
$$

If the quadrupole strength is negative, the strength k_q in Equation 2.152 should be changed to $-k_q$. The axis without any equation are the ones not affected by the magnetic lattice, i.e. $u_1 = u_0$

The Hamiltonian and matrix formalism allow for an accurate calculation of the electron beam dynamics through magnetic elements.

2.6 Application of laser plasma acceleration to free electron laser

Free electron laser (FEL) is based on the transformation of a relativistic electron beam kinetic energy into electromagnetic radiation (EM radiation) via an alternating magnetic field generated by an undulator, that forces the electrons to oscillate along their trajectory. During the electron beam propagation inside the undulator, the beam and EM radiation interact by exchanging energy. The FEL can be described as a conventional laser in which the role of active medium and energy pump are taken by the electron beam and an optical resonator can be used for visible and infrared radiation.

The conception of the FEL was developed in the 50s and 60s [1, 84, 85] with the objective to achieve shorter wavelength radiation sources and the first working FEL was developed by Madey and his team at Stanford University [86, 87] with a helical undulator [88, 89]. An FEL has two main components: Electron source and acceleration section and undulator section.

2.6.1 Basics of free electron lasers

While originally the FEL equations used a quantum mechanics description [1], in most cases a classical description is enough. The description of the interaction between the undulator magnetic field, the electron beam and the radiation requires the solution of the Lorentz force equation (Equation 2.2) and the Maxwell equations (Equation 2.3-2.6) in a self-consistent way [90].

2.6.1.1 Electron dynamics in an undulator magnetic field

An undulator [91, 92] is a periodic structure of magnets producing an alternating sinusoidal field distribution along the longitudinal axis. There are two main undulator types: helical and planar. The helical undulator [88, 89] generates a magnetic field with a vector that rotates around as a function of the longitudinal axis distance. For the planar undulator the magnetic field equation can be written as:

$$
\vec{B} = B_u[\vec{e}_y sin(2\pi \frac{z}{\lambda_u})]
\tag{2.153}
$$

with B_u the field amplitude, z the longitudinal direction along the undulator, y the perpendicular direction, $\vec{e}_y$ the unit vector along y and λ_u the undulator period. The electron velocity normalized by c in the undulator field is:

$$\beta_{e^-} = \frac{K_u}{\gamma_{e^-}}[\vec{e}_x sin(2\pi\frac{z}{\lambda_u})] + \vec{e}_z\beta_{e^-,z} \tag{2.154}$$

with $\beta_{e^-,z}$ the electron velocity z component, x the transverse direction, $\vec{e}_x$ the unit vector along it, $\frac{K_u}{\gamma_{e^-}}$ the amplitude of the transverse velocity and K_u the deflection parameter expressed as:

$$K_u = \frac{eB_u\lambda_u}{2\pi mc} \tag{2.155}$$

which in practical units can be rewritten as:

$$K_u = 93.4B_0[T]\lambda_u[m] \tag{2.156}$$

$\frac{K_u}{\gamma_{e^-}}$ represents the maximum angle between the electron trajectory and the undulator axis. For relativistic electrons, $\frac{K_u}{\gamma_{e^-}} << 1$. Thus, the electron trajectory is a sinusoidal in the perpendicular plane to the magnetic field. In the moving electron frame, the wavelength of the emitted dipole radiation λ_l by the electrons is:

$$\lambda_l^* = \lambda_u/\overline{\gamma} \tag{2.157}$$

with $*$ indicating the moving frame and $\overline{\gamma}$ the average electron bunch relativistic factor. For a planar undulator of $\vec{B} = -B_u sin(2\pi\frac{z}{\lambda_u})\vec{e}_y$, going back to the laboratory system in Equation 2.157 and using the expansion $cos\theta = 1 - \theta^2/2$, it comes [93]:

$$\lambda_l = \frac{\lambda_u}{2\gamma^2}(1 + \frac{K_u^2}{2} + \gamma^2\theta^2) \tag{2.158}$$

with θ the emission angle observed with respect to the undulator axis. The radiation is emitted in a narrow cone in the electron beam propagation direction with a vertical aperture $\approx 1/\gamma$ [94], thus, for relativistic electrons the emission cone aperture is small. On-axis, the fundamental and all odd harmonics can be observed and off-axis even and odd harmonics appear. The radiation linewidth of the first harmonics depends on the undulator periods N_u and it is equal to:

$$\frac{\Delta\lambda_l}{\lambda_l} = \frac{1}{2N_u} \tag{2.159}$$

2.6.1.2 FEL principle

In principle, an electron beam passing through an undulator emits spontaneous radiation without phase correlation. So, the total radiation is the sum of the individual electrons radiation, i.e, proportional to the number of electrons N_e. In an FEL, there is a phase correlation between the electrons, which is achieved by a longitudinal electron beam density modulation on the scale of the radiation wavelength. Electrons in the correct phase transfer their energy to the electromagnetic (EM) wave while dephased electrons take energy from it. The kinetic energy difference between electrons due to the EM wave-electron exchange separates them causing the spatial density modulation, a process called bunching [91]. When the bunching process starts, the coherent level of the radiation emitted by the electrons increases. The rise in emission level grows the modulation which, in exchange, enhances the bunching. When the density modulation limit is achieved the FEL amplification reaches saturation. At saturation all electrons emit in phase and the radiation is completely coherent.

2.6.1.3 FEL configurations

FELs can be operated in three configurations [95], differing mainly how the coherent radiation of the electron beam is attained.

2.6.1.3.1 Resonator

In the resonator configuration [96] an optical cavity is used to trap the incoherent radiation produced in the undulator (Figure 2.7a). The pass of multiple electron beams across the undulator increases the radiation intensity and thus, the density modulation due to the energy exchange between beam and EM radiation. This configuration is limited to vacuum ultraviolet to infrared FELs (i.e. from 109 nm up to 9 μm [86, 97]) due to the need of mirrors.

2.6.1.3.2 Seeded amplifier FEL

In the seeded FEL [98–100] a laser pulse (seed) co-propagates along the undulator with the electron beam (Figure 2.7b). The laser starts the beam density modulation.

2.6.1.3.3 Self amplified spontaneous emission

The self amplified spontaneous emission (SASE) configuration [101–104] (Figure 2.7c) is similar to the seeded FEL with the spontaneous emission of the electron beam taking the role of the laser. Due to the random nature of the noise needed to start the SASE, its output lacks temporal coherence, i.e., spiky longitudinal temporal profile [90].

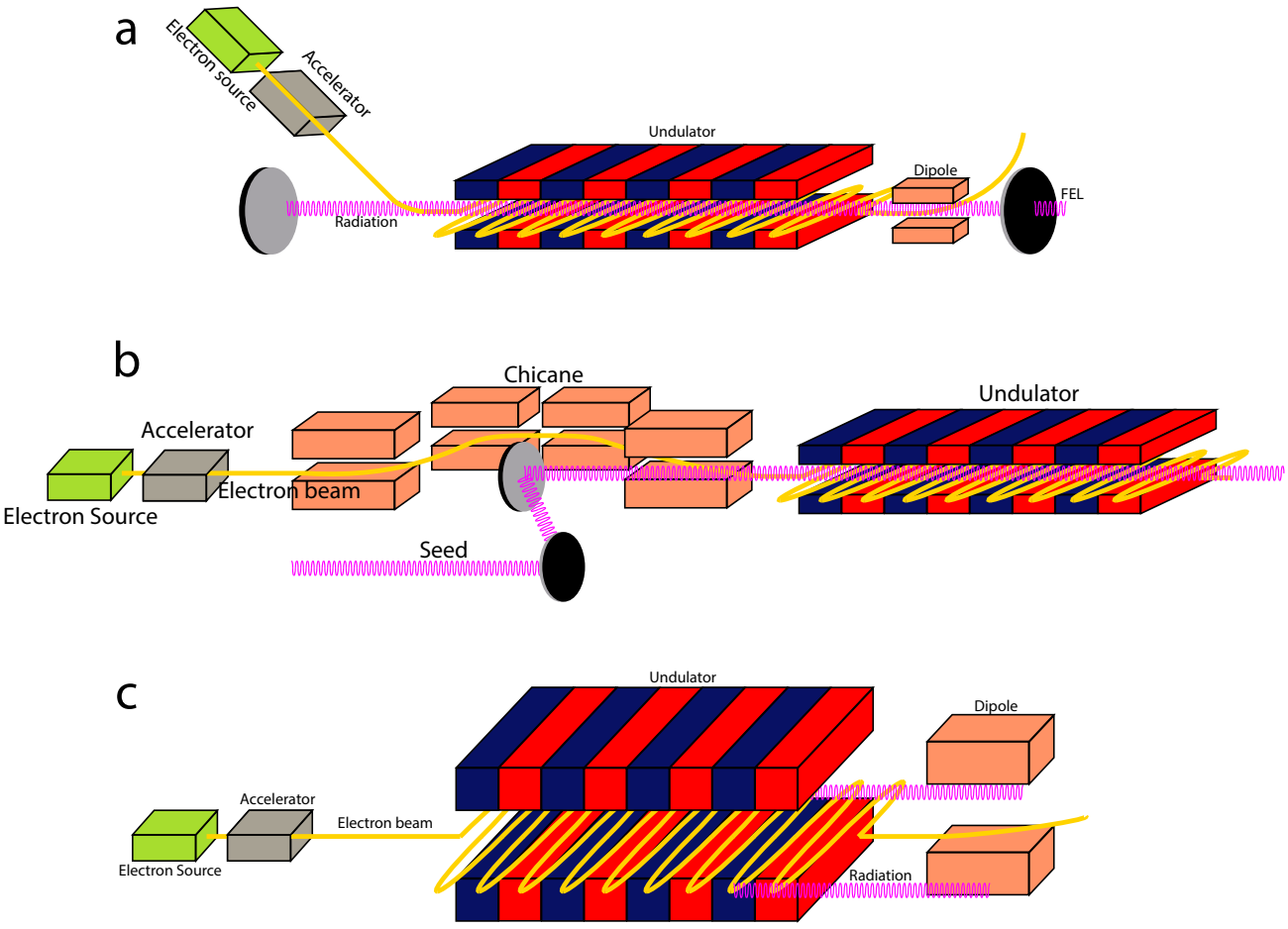

FIGURE 2.7: (a) Resonator, (b) seeded and (c) self amplified spontaneous emission free electron laser scheme. Electron beam source (lime), accelerator (grey), electron beam (yellow), dipoles (orange), resonator and seed focus mirrors (silver/black), undulator (red/blue), generated radiation in the undulator (pink), dipole to evacuate the electron beam (orange)

2.6.1.4 FEL 1D model

A simplified model of the EM wave-electron interaction can be developed by ignoring the transverse effects, e.g., radiation diffraction. Let's consider a planar undulator and a seeded FEL configuration with a light source of wavelength λ_l and electric field:

$$E_x(z,t) = E_0 cos(k_l z - \omega_l t + \psi_0) \tag{2.160}$$

with ψ_0 the initial phase of the radiation field at $t, z = 0$. From Equations 2.153 and 2.160, one finds:

$$\frac{dW}{dt} = m_e c^2 \frac{d\gamma}{dt} = -\frac{ecK_u E_0}{2\gamma}[cos(\psi) + cos(\chi)] \tag{2.161}$$

with W the electron energy, ψ the ponderomotive phase [105] and χ a rapidly oscillating phase:

$$\psi = (k_l + k_u)z(t) - \omega_l t + \psi_0 \tag{2.162}$$

$$\chi = (k_l - k_u)\overline{\beta}ct - \omega_l t + \psi_0 \tag{2.163}$$

Continuous energy exchange from the electron to the EM wave can take place if ψ is constant, i.e., $\frac{d\psi}{dt} = 0$ (synchronism condition). Neglecting the electron beam longitudinal variations of velocity ($v_z = \overline{v_z}$) and taking into account that $k_u \ll k_l$, the synchronism condition is fulfilled for the wavelength:

$$\lambda_l = \frac{\lambda_u}{2\gamma^2}(1 + \frac{K_u^2}{2}) \tag{2.164}$$

which is the undulator fundamental wavelength at an observation angle of zero (Equation 2.158). The rapidly oscillating term $cos(\chi)$ averages to zero over a few periods. When the different electron velocities inside the beam are considered, one finds that a beam with velocities close or equal to the resonant velocity, thanks to the interaction with the EM wave, ends up with a sinusoidal density modulation. Electrons with a χ phase between $[\chi, \chi + \pi]$, gain energy ($d\psi/dt > 0$), while electrons with a χ phase between $[\chi + \pi, \chi + 2\pi]$, lose energy ($d\psi/dt < 0$). In the end the electrons are driven to the phase $\chi = \pi$ resulting in bunching with the periodicity of the radiation field. Due to the constant interaction, the radiation field phase χ also changes with time. The EM wave evolution self-consistent described with the Maxwell equations (Equations 2.3-2.6), yielding [106]:

$$(\frac{\partial}{c\partial t} + \frac{\partial}{\partial z})E = i\frac{\mu_0}{2}K_u \sum_j \frac{e^{-i\psi_j}}{\gamma_j} \tag{2.165}$$

with μ_0 the magnetic permeability and $\sum_j$ the sum over all electrons. The right hand of Equation 2.165 is maximum when all electrons have the same phase ψ_j, i.e., maximum bunching. Equations 2.161, 2.162 and 2.165 represent the basic process of interaction between the EM wave and the electron beam inside the undulator. The strength of the coupling between the electrons and the radiation amplification scales proportionally to the Pierce parameter ρ_p (also called FEL paramater) [107, 108]:

$$\rho_p = (\frac{I}{8\gamma^3 I_A}(\frac{\lambda_u K_u [JJ]}{2\pi\sigma_x})^2)^{1/3} \tag{2.166}$$

with I the beam current, $I_A = 17$ kA the Alfven current, $[JJ] = |J_1(Y) - J_0(Y)|^2$, J the Bessel function and $Y = \frac{K_u^2}{4(1+K_u^2/2)}$. The solutions of the Equations 2.161, 2.162 and 2.165 are of the form:

$$E \propto e^{i\Lambda 2\omega_u \rho_p t} \tag{2.167}$$

with Λ the growth rate proportional to the electron beam density energy distribution. For a mono-energetic beam Λ is the solution of the dispersion equation $\Lambda^3 = 1$ [109]. The dispersion equation solution with a negative imaginary part gives an exponentially growth mode with a maximum growth rate of $-Re(i\Lambda) = \sqrt{3}/2$. Using the ansatz of Equation 2.167, the gain length can be deduced [110]:

$$L_g = \frac{\lambda_u}{4\pi\sqrt{3}\rho_p} \tag{2.168}$$

Two other modes are found from the dispersion equation, oscillating modes and decaying ones. At the start of the FEL no mode is dominant, then, after some gain lengths (lethargic regime [107]), the exponentially growing mode dominates. This growth continues until saturation, where the beam is divided in microbunches with a spacing equal to the radiation wavelength.

2.6.1.4.1 Low gain

In the low gain regime the undulator length is shorter than the gain length and the enhancement of the radiation over the seeding radiation field is of a couple of times at maximum. During this regime exponential growth is not reached. The low gain FEL gain function was derivated by J. M. Madey [1]. For an initial small amplitude EM wave and an initially monochromatic electron beam, the gain in the low regime is:

$$G_s = 4\sqrt{2}\pi\frac{\lambda_l\lambda_u}{\omega_u^2}\frac{K_u^2}{\sqrt{(1+K_u^2)^3}}\frac{I_b}{I_A}N_u^3 \times \frac{d}{d(g_x/2)}\left(\frac{sin^2(g_x/2)}{(g_x/2)^2}\right) \tag{2.169}$$

with $g_x = 2\pi N_u \Delta\omega_l/\omega_l$, I_b the beam current and $\pi\omega_l^2$ the transverse EM wave cross section. The FEL gain given by Equation 2.169 curve is proportional to the derivative of the spontaneous radiation spectrum so-called Madey theorem [111]. For $g_x = 0$ the gain is zero and for $g_x \approx 2.6$ the gain is maximum. g_x can be defined for a particular frequency, becoming $g_x = 4\pi N_u \Delta\gamma/\gamma$ [91]. When the exchange of electron kinetic energy to radiation field ratio is about $1/2N_u$ the gain becomes zero. Therefore, the FEL maximum efficiency can be defined as a ratio between the radiation intensity and the beam kinetic energy and is $\approx 1/N_u$.

2.6.1.4.2 High gain

For an undulator of several gain lengths long, the FEL can achieve an exponential growth regime [110], called high gain regime, that continues until saturation. The energy spread of an electron beam impedes the bunching of all electrons at the same phase due to the difference in longitudinal velocity. Not all electron energies take part in the FEL amplification process. The energy range contributing to the FEL can be determined through the Pierce parameter. A larger ρ_p signifies that the electron-EM wave exchange is stronger, thus, the gain length is shorter (Equation 2.168). Due to the smaller gain length the difference in velocities of the electrons have a lower impact and the energy spread participating in FEL is higher. To avoid unreasonable gain lengths, the condition on the initial electron beam energy spread is:

$$\sigma_\gamma \ll \rho_p \tag{2.170}$$

For high gain FEL, the lower the energy spread, the higher the gain. Only electrons inside an energy bandwidth of $\approx \rho_p$ around the reference energy contribute to the FEL. As more energy is transfered from the electrons to the radiation field, electrons start to exit the energy bandwidth and thus, the gain drops. The energy transfer efficiency is ρ_p and the saturation power of the radiation field is [112, 113]:

$$P_{sat} = \rho_p P_{beam} \tag{2.171}$$

with $P_{beam} = \langle\gamma\rangle I_p m_e c^2/e$ the electron beam power and I_p the peak current.

2.6.1.5 FEL equation three dimensional corrections

If one considers the transverse plane dynamics, the main degradation sources of FEL are the electron beam transversal spread and the radiation field diffraction.

Transverse emittance growth [114] inside the undulator reduces the beam density and therefore, the FEL gain. Thus, the beam should be properly focused in the undulator. The spread and the undulator field originates betatron oscillations on the electrons. The electrons suffering betatron oscillations lose energy in the process, decreasing their momentum in the longitudinal direction, which causes an additional spread, enhanced by higher emittance. To avoid a substantial impact, a condition on the normalized emittance can be set as [91]:

$$\epsilon_n \ll \frac{4\lambda_l\beta_T\langle\gamma\rangle}{\lambda_u}\rho_p \tag{2.172}$$

One can optimize the emittance value so the beam does not divergence faster than the radiation field [91], yielding the limit $\epsilon = \epsilon_n/\gamma < \lambda_l/4\pi$.

The radiation field transverse diffraction can reduce the interaction between the electrons and the EM wave [91]. So, the FEL amplification can counteract this diffraction (gain guiding). After the lethargy regime, an equilibrium between diffraction and amplifications is reached and the transverse radiation profile becomes constant while the amplitude rises exponentially (gain guiding [115, 116]).

2.6.2 Ming Xie FEL radiation equations

From the 1D approximation of the FEL process, a 1D model [117, 118] of the amplification expected from a given undulator can be achieved, giving a group of formulas to predict SASE performance. In the following section, the 1D equations derivated by Ming Xie [119] are briefly presented.

Let P_{SR} be the synchrotron radiation power in a FEL generated in the first the gain length L_g [117, 120]. The SASE power amplification can be described by:

$$P = \alpha P_{SR} e^{z/L_g} < P_{sat} \tag{2.173}$$

with z the longitudinal distance, α the coupling coefficient representing the fraction of P_{SR} coupled to the exponential growth and P_{sat} the saturation power. The required length to reach saturation is:

$$L_{sat} = L_g ln(\frac{P_{sat}}{\alpha P_{SR}}) \tag{2.174}$$

P_{sat}, L_{sat} and L_g are the main parameters determining SASE performance.

For the following equations, the beam is considered Gaussian in all dimensions except longitudinally where it is taken as uniform. The electron beam is characterized by four parameters: energy $E_0 = \gamma m_e c^2$, current I, normalized RMS emittance ϵ_n and RMS energy spread σ_γ. The undulator is defined by its period λ_u and undulator parameter $K_u = 0.934\lambda_u[cm]B_u[T]$, with B_u the undulator peak field. In addition, β_T is considered constant. In the 1D model [117, 118] the emittance and energy spread is assumed to be zero and the Equation 2.173 quantities become:

$$\begin{aligned} \alpha &= 1/9 \\ P_{SR} &\approx \rho_p^2 c E_0/\lambda_l \\ L_g &= \lambda_u/4\pi\sqrt{3}\rho_p \\ P_{sat} &= \rho_p P_{beam} \end{aligned} \tag{2.175}$$

with $P_{beam}[TW] = E_0[GeV]I[kA]$ the electron beam power. The 1D model gives the highest possible FEL gain. The ratio between the gain length and its 1D model counterpart ($L_{g,1D}$) can be expressed as [121, 122]:

$$\frac{L_{g,1D}}{L_g} = \frac{1}{1+\eta_L} \tag{2.176}$$

with η_L fitted from numerical solutions given by [119]:

$$\eta_L = a_1\eta_d^{a_2} + a_3\eta_\epsilon^{a_4} + a_5\eta_\gamma^{a_6} + a_7\eta_\epsilon^{a_8}\eta_\gamma^{a_9} + a_{10}\eta_d^{a_{11}}\eta_\gamma^{a_{12}} + a_{13}\eta_d^{a_{14}}\eta_\epsilon^{a_{15}} + a_{16}\eta_d^{a_{17}}\eta_\epsilon^{a_{18}}\eta_\gamma^{a_{19}} \tag{2.177}$$

$$\eta_d = \frac{L_{1D}}{L_r};\quad \eta_\epsilon = \frac{L_{1D}}{\beta_T}\frac{4\pi\epsilon}{\lambda_l};\quad \eta_\gamma = 4\pi\frac{L_{1D}}{\lambda_u}\frac{\sigma_\gamma}{E_0}$$

with a_i fitting parameters:

$$\begin{aligned} &a_1 = 0.45 \quad a_2 = 0.57 \quad a_3 = 0.55 \quad a_4 = 1.6 \quad a_5 = 3 \quad a_6 = 2 \quad a_7 = 0.35 \quad a_8 = 2.9 \quad a_9 = 2.4 \quad a_{10} = 51 \\ &a_{11} = 0.95 \quad a_{12} = 3 \quad a_{13} = 5.4 \quad a_{14} = 0.7 \quad a_{15} = 1.9 \quad a_{16} = 1140 \quad a_{17} = 2.2 \quad a_{18} = 2.9 \quad a_{19} = 3.2 \end{aligned}$$

η_d expresses the gain reduction due to diffraction, η_ϵ and η_γ represent the gain reduction due to electron longitudinal spread by emittance and energy spread respectively. The numerical fitting also yields the saturation power [123]:

$$P_{sat} \approx 1.6\rho_p(\frac{L_{1D}}{L_g})^2 P_{beam} \tag{2.178}$$

The noise power Equation 2.175 is used due to the lack of a non-ideal beam case one.

2.6.3 FEL state of the art

Current FELs [124–128] offer a wide range of wavelengths [129–131] (from mm to nm), high power, tunability and stability. Nowadays, only FELs offer a high quality, peak power (GW) and tunable x-ray source for users, achieved after forty years of development since the first FEL. Table 2.2 presents examples of FEL facilities of multiple wavelengths and their beam parameters. The electron beams energies range from the $\approx$ 40 MeV to GeV [132–137] with normalized RMS emittances around the mm.mrad and relative energy spreads below 0.2 % with nC charges. Moreover, FEL amplification requires high quality electron beams (Table 2.2), which can be quantified by the peak brightness [138]:

$$B_{bright} = \frac{2 \times I}{\pi^2 \epsilon_y \epsilon_x} \tag{2.179}$$

Therefore, the electron beams should also have high current in addition to low transverse emittance to provide as high brightness as possible. The brightness can be related to the Pierce parameter through Equation 2.172 yielding $\frac{1}{B_{bright}} \ll \frac{\rho_p}{I}$.

As the FEL radiation depends not only on the undulator but also on the electron beam energy and intensity, X-ray FELs need long radio frequency (RF) linear accelerators [124] or storage rings [127].

TABLE 2.2: Free electron laser facilities.

Facility	Wavelength (nm)	Energy (MeV)	Beam RMS normalized emittance (mm.mrad)	Relative Energy spread (%)
Shanghai FEL [139]	0.05-3	8000	0.4	< 0.1
Pohang FEL [140, 141]	0.06-0.1	10000	0.5	0.1
SACLA [132, 142]	0.06-0.3	8500	1	< 0.1
SwissFEL [143]	0.1-0.7	2100-5800	0.4	< 0.02
LCLS [144, 145]	0.15	$2500 - 15000$	0.45	0.25
European XFEL [135]	0.05-4.7	17500	1.2	-
FLASH2 [146, 147]	4-80	500-1250	1.4	< 0.1
FERMI [148]	4-100	1800	1	-
Shanghai FEL [149, 150]	8.8-265	840-1500	<1.5	0.06
SPARC [151, 152]	66-800	80-177	< 1	0.2
UCLA [133]	800	72	2	0.17
CLIO [153]	1750	45	80	0.7
FELIX [154]	5000	45	-	-

2.6.4 Challenges of LPA X-ray FEL

LPA electron beams of up to 10 GeV have been generated [155], however, the beam brightness is not up to the levels of current accelerator facilities (Table 2.2). While LPA beam (Table 2.1) transversal emittance can be of the order of the mm.mrad [156], the charge ($\leq$ 500 pC [157, 158]) and energy spread (FWHM $\geq$ 2 %) are far from optimum. Such values are over the limits imposed by the conditions in Equation 2.170 and 2.172 for usual undulators. So, in their current state LPA sources still require improvements to be able to offer characteristics for FEL generation and even more refinement to provide them reliably. Even though actual LPA electron beam

parameters are not up to the classic accelerator standards, in the following years it could become an alternative compact electron beam source usable for FEL [159–161]. Thus, it is worth trying to start the FEL generation demonstration with the available LPA systems.

2.7 Summary

In this chapter the basic equations to describe the LPA, electron beam transport and FEL processes have been presented. The state of the art LPA facilities show a great progress being able to produce high energy, short length, low emittance electron beams. The best LPA parameters at the source (GeV energies, under 1.6 mrad divergence RMS and above 5 pC on the energy peak) are reached in modern PW laser facilities but multi TW laser facilities offer less charge density and electron energies. However, the reported energy spreads seem to be always above 5 %, higher than usual FEL requirements.

2.8 Conclusion

For an FEL application, the LPA parameters could be enough for a demonstration of the FEL generation, especially in the the TW facilities. In a real application the LPA beam transport and focus at the undulator is already a challenge and the beam parameters at the undulator could not be the same as at the source. Therefore, experimental and analytical work is necessary to understand the real behavior of the LPA beam and capacity to achieve FEL.

Chapter 3

COXINEL, a solution answering the LPA based FEL challenge

The transport of the electron beam from the LPA source to the undulator is a critical step to achieve FEL. Under external forces driven by magnetic fields, a beam with mrad divergence sees an chromatic emittance increase, which reduces the quality of the beam and increases the difficulty of achieving FEL if it is not compensated [162, 163]. Moreover, the FEL imposes strict limits to the energy spread of the electron beams and LPA electron beams obtained by ionization injection tend to have broad energy distributions [164], i.e., higher than percentage level energy spreads (Section 2.6.1.4.2). The electron beam has to be transported while avoiding the divergence defocusing, the chromatic emittance growth and manipulated to reduce its energy spread. The transport line has to be designed carefully taking into account its robustness, adaptability, the technology available and the expected beam parameters at the source and at the destination in addition to the alterations needed to reach the desired beam. Technologically wise, the use of plasma based optics for such beams is being researched with good results [165–167], however, this adds an extra layer of technical complexity to an already challenging feat thus, more robust and understood options are preferable for a first step. The use of classic magnetic elements (dipoles and quadrupoles) technologies is a safe and reliable choice for the electron beam transport, thanks to the years of use and development on a grand number of operational machines [10, 168–170]. The COXINEL line has thus been conceived under this premise using baseline reference parameters . In this chapter, the chromatic emittance growth caused by the initial beam parameters and requirements of the FEL are presented. Then, the COXINEL line design choices to manipulate the beam to fulfill the necessary characteristics for FEL is shown for a baseline electron beam set of parameters (reference electron energy of 176 MeV, 1 mrad RMS divergence, 1 mm.mrad RMS emittance, 1 % energy spread and 34 pC total charge). The different optics of COXINEL and a sensitivity to deviations study are developed. The chapter ends with the description of the multiple elements of the line.

3.1 COXINEL line design

The COXINEL line has been designed to monitor and transport the LPA electron beam while manipulating the beam to suit the FEL requirements. For that in-dept studies of the expected beam dynamics during transport are necessary. In this section, the LPA beam transport for LPA problematic is analyzed and the solutions offered in the COXINEL line presented.

3.1.1 LPA based FEL beam transport issues and COXINEL specifications

3.1.1.1 Beam quality deterioration during transport

The electron beam generated by LPA is very sensitive [8] (see Chapter 5) and can degrade during transport (Chapter 2.5.4). The transport calculations show the constant change of the beam 2D phase space. Due to the importance of the emittance for the beam quality, it is necessary to understand its evolution to plan and design a transport line.

The effect of a quadrupole on an electron beam of energy spread σ_γ can be calculated with the matrix given in Equation 2.137. To simplify the calculations let's take into account only the horizontal axis x in the thin lens approximation, i.e., $l_q \approx 0$. An off-momentum particle ($\delta \neq 0$; Equation 2.100) entering a quadrupole sees the gradient changed by $\Delta k_q = \frac{qG}{p_0}\delta$, using Equation 2.101 in Equation 2.105. Thus, for an off-momentum particle the additional term $k_q\delta$ has to be added to adjust the quadrupole strength k_q. The matrix is written as:

$$R_Q = \begin{pmatrix} 1 & 0 \\ -k_q(1-\delta) & 1 \end{pmatrix} = \begin{pmatrix} A & B \\ C & D \end{pmatrix} \tag{3.1}$$

with A, B, C and D the different matrix terms. For an electron of initial phase space position (x_0, x'_0), the new position (x_1, x'_1) after the quadrupole is:

$$\begin{aligned} x_1 &= Ax_0 + Bx'_0 \\ x'_1 &= Cx_0 + Dx'_0 \end{aligned} \tag{3.2}$$

with the indexes 0 and 1 indicating the initial state and the state after transport respectively. The emittance can be then calculated as in Equation 2.134. As $\langle\delta\rangle = 0$ and $\langle Ax_0\rangle = \langle A\rangle\langle x_0\rangle$, and similarly for $\langle x'_0\rangle$ and B, C and D:

$$\begin{aligned} \langle x_1^2\rangle &= \langle A^2\rangle\langle x_0^2\rangle + 2\langle AB\rangle\langle x'_0x_0\rangle + \langle B^2\rangle\langle x_0'^2\rangle \\ \langle x_1'^2\rangle &= \langle C^2\rangle\langle x_0^2\rangle + 2\langle CD\rangle\langle x'_0x_0\rangle + \langle D^2\rangle\langle x_0'^2\rangle \\ \langle x_1x'_1\rangle^2 &= \langle A^2C^2\rangle\langle x_0^2\rangle^2 + 2\langle AC\rangle\langle BC\rangle\langle x'_0x_0\rangle\langle x_0^2\rangle + 2\langle AC\rangle\langle AD\rangle\langle x_0'^2\rangle\langle x_0^2\rangle \\ &+\langle B^2C^2\rangle\langle x'_0x_0\rangle^2 + 2\langle BC\rangle\langle BD\rangle\langle x_0'^2\rangle\langle x'_0x_0\rangle + \langle A^2D^2\rangle\langle x'_0x_0\rangle^2 \\ &+2\langle AD\rangle\langle BD\rangle\langle x_0'^2\rangle\langle x'_0x_0\rangle + \langle B^2D^2\rangle\langle x_0'^2\rangle^2 \end{aligned} \tag{3.3}$$

The new emittance $\epsilon_{x,1}$ can be written as:

$$\epsilon_{x,1}^2 = \epsilon_{x,0}^2 + k_q^2\sigma_\gamma^2\sigma_{x,0}^4 \tag{3.4}$$

with $\langle\delta^2\rangle = \sigma_\gamma^2$ and $\langle x^2\rangle = \sigma_{x,i}^2$ and $\sigma_{x,i}$ the beam size and the index i equal to 0 or 1. The second term $(k_q^2\sigma_\gamma^2\sigma_{x,0}^4)$ is called chromatic [171] emittance. The chromatic term increases the emittance proportionally to the energy spread, the quadrupole k_q and the square of the beam size. Therefore, for an ideal beam going through the magnetic center with no energy spread or infinitely small the emittance is not affected by a quadrupole. The use of a doublet or triplet of quadrupoles with the right strengths k_q can compensate this chromatic emittance growth [172]. However, before the beam arrives to the quadrupole from the source it has to go through a drift stage. Adding a drift (Equation 2.136) of length L_{drift} before a quadrupole of strength $k_q = 1/L_{drift}$, to compensate the beam divergence and simplifying the expressions, gives the following transport matrix:

$$R_QR_{drift} = \begin{pmatrix} 1 & 0 \\ -k_q(1-\delta) & 1 \end{pmatrix}\begin{pmatrix} 1 & L_{drift} \\ 0 & 1 \end{pmatrix} = \begin{pmatrix} 1 & L_{drift} \\ -k_q(1-\delta) & \delta \end{pmatrix} \tag{3.5}$$

After propagation through this simple system and using the Equations 3.3, the final beam emittance can be calculated:

$$\begin{aligned} \epsilon_{x,1}^2 &= \epsilon_{x,0}^2 + k_q^2\sigma_\gamma^2\sigma_{x,0}^4 + 2\sigma_\gamma^2\sigma_{x,0}^2\sigma_{x,0}'^2 + L_{drift}^2\sigma_{x,0}'^4\sigma_\gamma^2 + 4k_q\sigma_\gamma^2\sigma_{x,0}^2\langle x'_0x_0\rangle + 4L_{drift}\sigma_\gamma^2\sigma_{x,0}^2\langle x'_0x_0\rangle + 4\sigma_\gamma^2\langle x'_0x_0\rangle^2 \\ &\approx \epsilon_{x,0}^2 + L_{drift}^2\sigma_{x,0}'^4\sigma_\gamma^2 \end{aligned} \tag{3.6}$$

with $\langle x'^2\rangle = \sigma_{x,i}'^2$ and $\sigma'_{x,i}$ the beam divergence. In addition to the previous chromatic term (Equation 3.4), two additional ones are introduced: one $(2\sigma_\gamma^2\sigma_{x,0}^2\sigma_{x,0}'^2)$ proportional to the beam divergence, size and energy spread and another $(L_{drift}^2\sigma_{x,0}'^4\sigma_\gamma^2)$ to the drift length and energy spread and square of initial beam divergence. The divergences in LPA being of the order of mrad and the beam sizes of the order of the μm, the emittance terms depend on the divergence dominate over the ones with a dependence on the beam size. The three terms $4k_q\sigma_\gamma^2\sigma_{x,0}^2\langle x'_0x_0\rangle + 4L_{drift}\sigma_\gamma^2\sigma_{x,0}^2\langle x'_0x_0\rangle + 4\sigma_\gamma^2\langle x'_0x_0\rangle^2$ proportional to the correlation term $\langle x'_0x_0\rangle$ can be neglected after the source for μm beam sizes with a couple of hundreds of pC (see Chapter 5). To counter the huge chromatic emittance growth due to mrad divergences and the dependence on the drift length $(L_{drift}^2\sigma_{x,0}'^4\sigma_\gamma^2)$, the distance between magnetic elements should be reduced as much as possible. For a 1 mrad divergence, 1 % energy

spread and $\epsilon_{x,0} = 0.2$ mm.mrad, a 35 mm drift causes the initial emittance to double. For a divergence of 1.5 mrad the final emittance value becomes four times the initial one ($\epsilon_{x,1} = 0.815$ mm.mrad).

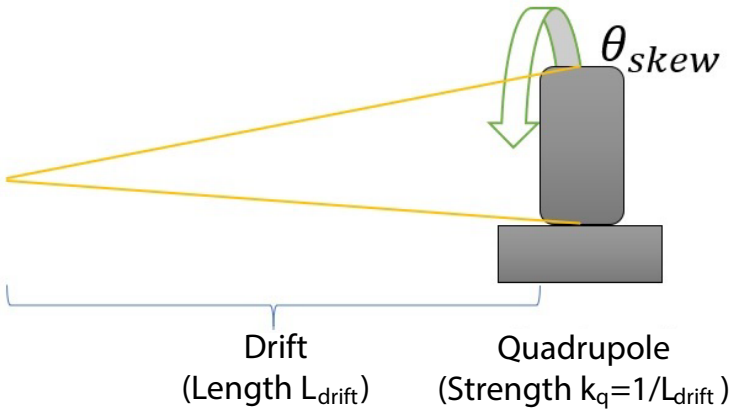

FIGURE 3.1: Example of propagation of a beam through a drift and a skewed quadrupole.

The consideration of a skew angle θ_{skew} (Equation 2.141) in the quadrupole, adds coupling between the horizontal and vertical direction. Figure 3.1 shows the system configuration of drift followed by a skewed quadrupole. The motion equation in the horizontal 2D phase space can be calculated with the transport matrices in Equation 2.136, 2.137 and 2.142:

$$\begin{aligned} R_{drift} &= \begin{pmatrix} 1 & L_{drift} & 0 & 0 \\ 0 & 1 & 0 & 0 \end{pmatrix} \quad R_{QSkewIn} = \begin{pmatrix} 1 & 0 & \theta_{skew} & 0 \\ 0 & 1 & 0 & \theta_{skew} \end{pmatrix} \\ R_Q &= \begin{pmatrix} 1 & 0 & 0 & 0 \\ -k_q(1-\delta) & 1 & 0 & 0 \end{pmatrix} \quad R_{QSkewOut} = \begin{pmatrix} 1 & 0 & -\theta_{skew} & 0 \\ 0 & 1 & 0 & -\theta_{skew} \end{pmatrix} \end{aligned} \tag{3.7}$$

Thus, the transport matrix for the system is:

$$\begin{aligned} R_{QSkewOut}R_QR_{QSkewIn}R_{drift}\begin{pmatrix} x_0 \\ x'_0 \\ y_0 \\ y'_0 \end{pmatrix} &= \begin{pmatrix} 1 & L_{drift} & 0 & 0 \\ -k_q(1-\delta) & \delta & -2k_q\theta_{skew}(-1+\delta) & -2(-1+\delta)\theta_{skew} \end{pmatrix}\begin{pmatrix} x_0 \\ x'_0 \\ y_0 \\ y'_0 \end{pmatrix} \\ &= \begin{pmatrix} A & B & E & F \\ C & D & G & H \end{pmatrix}\begin{pmatrix} x_0 \\ x'_0 \\ y_0 \\ y'_0 \end{pmatrix} \end{aligned} \tag{3.8}$$

Due to the additional terms in the matrix E, F, G and H, Equation 3.3 has to be recalculated. Neglecting the correlation terms between size and divergence and between the horizontal direction and the vertical direction, the final emittance is:

$$\begin{aligned} \epsilon_{x,1}^2 = \epsilon_{x,0}^2 + k_q^2\sigma_{x,0}^4 - k_q^2\sigma_{x,0}'^4 + 4k_q^2\theta_{skew}^2\sigma_{x,0}^2\sigma_{y,0}^2 + 4\theta_{skew}^2\sigma_{x,0}'^2\sigma_{y,0}^2 + 4\theta_{skew}^2\sigma_{x,0}^2\sigma_{y,0}'^2 \\ +4L_{drift}^2\theta_{skew}^2\sigma_{x,0}'^2\sigma_{y,0}'^2 + k^2\sigma_{x,0}^4\sigma_\gamma^2 + 2\sigma_{x,0}^2\sigma_{x,0}'^2\sigma_\gamma^2 + L_{drift}^2\sigma_{x,0}'^4\sigma_\gamma^2 + 4k^2\theta_{skew}^2\sigma_\gamma^2\sigma_{x,0}^2\sigma_{y,0}^2 \\ +4\theta_{skew}^2\sigma_\gamma^2\sigma_{x,0}'^2\sigma_{y,0}^2 + 4\theta_{skew}^2\sigma_\gamma^2\sigma_{x,0}^2\sigma_{y,0}'^2 + 4\theta_{skew}^2L_{drift}^2\sigma_\gamma^2\sigma_{x,0}'^2\sigma_{y,0}'^2 \end{aligned} \tag{3.9}$$

The main terms causing the emittance increase due to their dependence in the beam divergence and energy spread are colored. The term $k_q^2\sigma_{x,0}'^4$, even though is proportional to the square of the divergence, for mrad divergences and drifts of cm distances, becomes negligible. One can approximate the emittance to:

$$\epsilon_{x,1}^2 \approx \epsilon_{x,0}^2 + L_{drift}^2 \sigma_{x,0}'^4 \sigma_\gamma^2 + (1+\sigma_\gamma^2) 4\theta_{skew}^2 L_{drift}^2 \sigma_{x,0}'^2 \sigma_{y,0}'^2 \tag{3.10}$$

with the first term ($L_{drift}^2 \sigma_{x,0}'^4 \sigma_\gamma^2$) being the main chromatic emittance and the second term ($(1+\sigma_\gamma^2) 4\theta_{skew}^2 L_{drift}^2 \sigma_{x,0}'^2 \sigma_{y,0}'^2$) the tilt emittance. For θ_{skew}, $\sigma_{x,0}'$, $\sigma_{y,0}' = 1$ mrad, $\sigma_\gamma = 1\%$, $\epsilon_{x,0} = 0.2$ mm.mrad, and $L_{drift} = 35$ mm, the usual distance between source and the quadrupole, the tilt term yields a value of ≈ 0.49 mm.mrad and the chromatic term ≈ 0.12 mm.mrad; giving $\epsilon_{x,1} \approx 0.81$ mm.mrad. So, these two terms ($L_{drift}^2 \sigma_{x,0}'^4 \sigma_\gamma^2 + (1+\sigma_\gamma^2) 4\theta_{skew}^2 L^2 \sigma_{x,0}'^2 \sigma_{y,0}'^2$) dominate the emittance evolution for mrad initial divergences. For a large initial divergence, the presence of a skew quadrupolar term leads to a significant chromatic emittance growth. Thus, maximum care has to be taken while installing the magnetic elements, however, it is not possible to avoid completely a substantial chromatic emittance growth due to the mrad divergence beams.

3.1.1.2 COXINEL design considerations

The COXINEL line [173, 174] aims at demonstrating FEL capabilities from an LPA based electron beam [164, 175–177]. The line has to be able to transport the beam focusing it at the center of the undulator and manipulate it to be inside the energy spread limits imposed by the FEL while avoiding the beam quality degradation due to the beam initial divergence.

One can classify the line requirements into two categories: caused by FEL or by the transport from source to the undulator.

3.1.1.2.1 FEL requirements

To achieve FEL the relative energy spread over one coherent length should fulfill the following condition:

$$\sigma_\gamma < \rho_p \tag{3.11}$$

with ρ_p the Pierce parameter (Equation 2.166) [107, 108]. A higher σ_γ deteriorates the micro-bunching caused by the interaction between photon and electrons inside the undulator. The Pierce parameter is of the order of 10^{-3}, which imposes an upper limit of the σ_γ of around 0.1 %.

3.1.1.2.2 Transport requirements

During transport, the beam degradation due to its initial divergence has to be compensated as much as possible. The COXINEL line achieves a proper transport of the electron beam, i.e., it compensates the defocusing due to the beam divergence and limits the chromatic emittance growth. The line is also capable of reducing the LPA beam energy spread to adapt it to acceptable levels for FEL operation. Taking into account the sensitivity of the beam to the transport after exiting the source, the COXINEL line has been conceived to properly transport the LPA electron beam to the center of an undulator and evacuate it afterwards.

3.1.1.3 COXINEL design

As developed in sections 2.5.4 and 2.5.5, the transport of an electron beam in a line can be modeled via the matrix formalism or with the Hamiltonians representing the effect of each magnetic element. The transport matrix of the COXINEL line can be created with the use of drifts (Equation 2.136), dipoles (Equations 2.144, 2.145) and quadrupoles (Equations 2.137, 2.138, 2.143, 2.142) matrices.

TABLE 3.1: Baseline parameters at the source of the COXINEL line design.

Total charge Q_t pC	Energy spread σ_γ	Divergence RMS σ_x', σ_z' *mrad*	Normalized Emittance RMS ϵ_x, ϵ_z *mm.mrad*	Bunch length σ_s *μm*	Central Energy E_0 MeV
34	1%	1	1	1	176

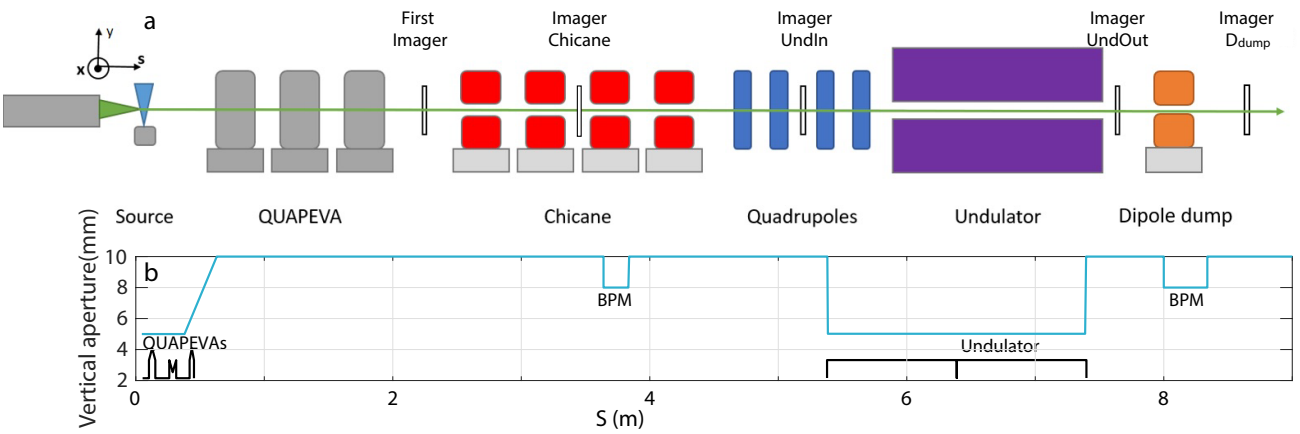

FIGURE 3.2: (**a**) COXINEL transport line scheme. Left to right: Laser pulse focused on a gas jet (blue), triplet of QUAPEVAs (grey), chicane (red), a second set of electro-magnetic quadrupoles (blue), undulator (purple), dipole dump (orange) and imagers along the line (white). (**b**) Vertical aperture along the longitudinal direction of the transport line [178].

For COXINEL experiment, electrons are produced and accelerated by a Titanium:Sapphire laser focused on a gas jet. Figure 3.2 shows a scheme of the COXINEL line, with a total length of 8 m, designed at SOLEIL for the baseline parameters in Table 3.1, given from LPA colliding pulse injection experiments done previously. The line design is based in the source-to-image optics [179], i.e., the optics ensures minimum beam size for reference energy ($\delta = 0$) electrons in the focusing positions. The transport matrix u and u' coupling terms are neglected, with u equal to x or y. In terms of the transport matrix, R_{12} and R_{21} for the horizontal direction and R_{43} and R_{34} for the vertical are considered equal to 0, thus, Equation 2.110 in the horizontal direction becomes:

$$M_{0:s}|_x = \begin{pmatrix} R_{11} & 0 \\ 0 & R_{22} \end{pmatrix} \tag{3.12}$$

with $|_x$ indicating the horizontal projection. Figure 3.2b presents the vertical aperture along the transport line: 10 mm in the QUAPEVAs, 20 mm in the vacuum pipe, 5 mm in the undulator.

3.1.1.3.1 Handling of the divergence

If the beam is let to freely propagate after the source, its beam size quickly increases to values superior to the line aperture due to the divergence (Equation 2.136). Figure 3.3 presents the simulated propagation in a 60 cm drift of a beam with the baseline parameters and an energy spread of 15 %. The beam at the source presents a small round spot of μm size and after propagation the beam size rises to mm levels.

To handle the initial mrad divergence of the electron beam a triplet of permanent magnet quadrupoles with tunable gradient named QUAPEVA [180, 181] are positioned as close as possible (5 cm), to shorten the drift. Their strong magnetic field insures a proper beam focusing. In terms of transport matrix, by using Equations 2.136, 2.137, 2.138, 2.143 and 2.142 ,i.e., drift and quadrupoles, the first part of the line can be model as:

$$\begin{aligned} M_{COX,1} &= R_{QAll,QAP3} R_{Drift} R_{QAll,QAP2} R_{Drift} R_{QAll,QAP1} R_{Drift} \\ R_{QAll,QAP} &= R_{QSkewOut} R_Q R_{QSkewIn} \end{aligned} \tag{3.13}$$

with $R_{QAll,QAPi}$ the ith QUAPEVA transport matrix taking into account a possible skew angle θ_{skew}.

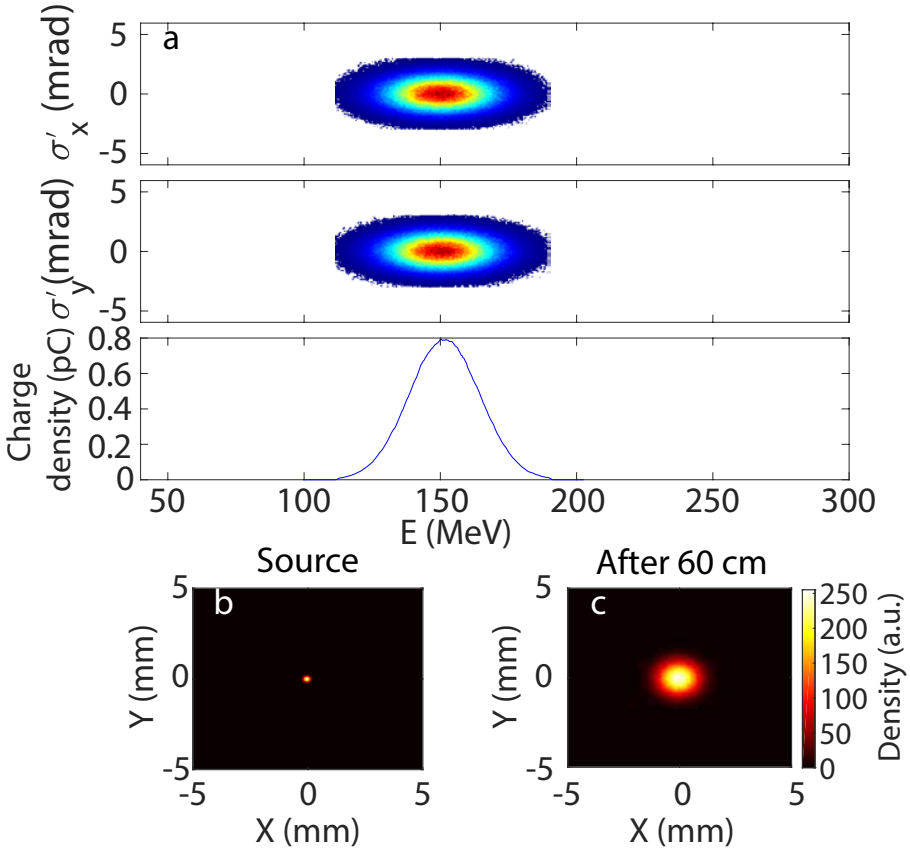

FIGURE 3.3: (a) Initial beam used for simulation with $\epsilon = 1$ mm.mrad, $\sigma_s = 1$ μm and $\sigma_\gamma = 15$ %. Simulated transport of the beam at the source (b) and at the "first imager" (c) without QUAPEVAs.

3.1.1.3.2 Handling of the energy spread

LPA beams by ionization injection exhibit usually a wide energy spread [42, 182, 183] over percentage level, that poses a problem for the transport and for the efficiency of the FEL effect. To reduce the slice energy spread after the QUAPEVA triplet, a demixing chicane [179, 184] consisting of four electro-magnetic dipoles accompanied with a removable slit of variable width placed in the middle is used. The chicane stretches the beam longitudinally and sorts electrons by energy. Figure 3.4 shows how under the dipoles magnetic field, the electrons of lower energy take a longer path through the chicane delaying them with respect to the electrons with higher energies. The slit reduces the energy spread of the electron beam reaching the undulator by selecting the desired energies. [12, 179, 185–190]. When the electron beam passes through the first two dipoles of the electromagnetic chicane, the electron beam is horizontally dispersed and the electrons are sorted in energy. Upon arrival to the slit (see Figure 3.4 insert), the reference energy goes through the center of the slit and the energies at certain distance from it collides with the slit borders. The beam left goes through and is recombined horizontally by the other half of the chicane (Figure 3.4).

Thus, thanks to Equations 2.136, 2.144 and 2.145 the chicane can be written as the following transport matrix:

$$\begin{aligned} M_{COX,2} &= R_{Drift} R_{Chicane} R_{Drift} \\ R_{Chicane} &= R_{DipoleAll4} R_{Drift3} R_{DipoleAll3} R_{Drift2} R_{DipoleAll2} R_{Drift1} R_{DipoleAll1} \\ R_{DipoleAll} &= R_{BendingEdgeOut} R_{Dipole} R_{BendingEdgeIn} \end{aligned} \tag{3.14}$$

with $R_{Chicane}$ the chicane transport matrix taking into account the four dipoles, $R_{DipoleAll}$, and the face correction if the electron beam velocity is not perpendicular to it.

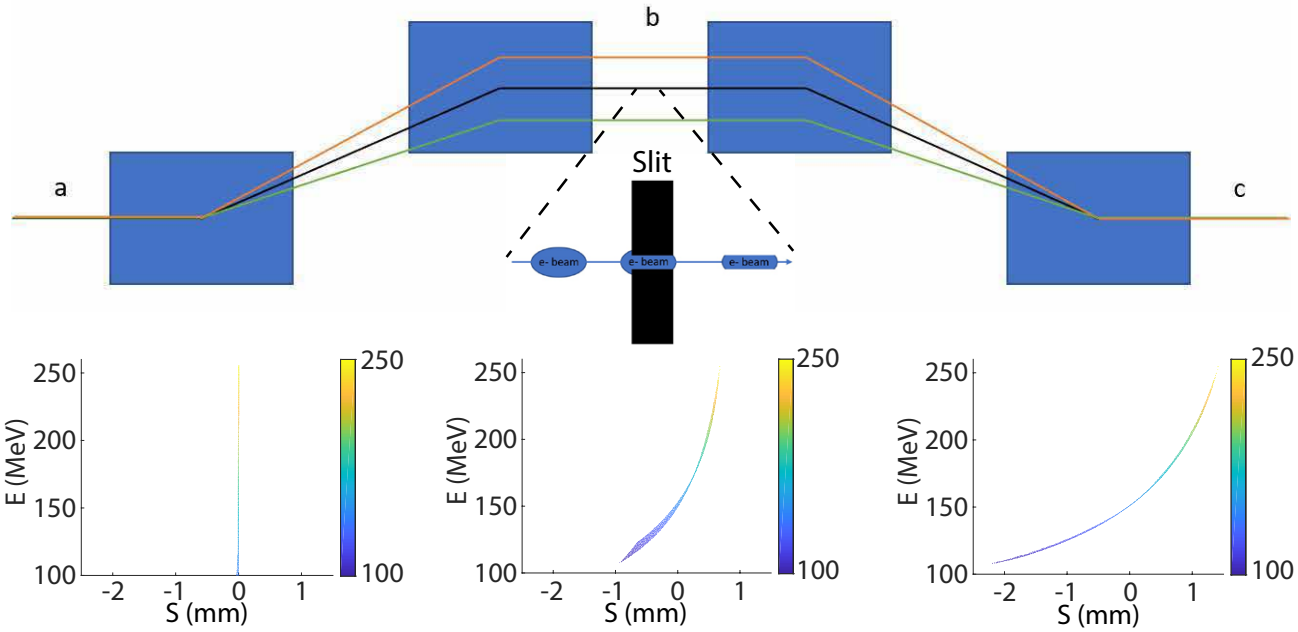

FIGURE 3.4: Magnetic chicane and example of the path taken by the reference energy (black), lower (orange) and higher energies (green). The three figures at the bottom show the electron energy versus longitudinal position in a beam at the positions a, b and c. Baseline parameters (Table 3.1) used. (insert) Scheme of the electron slit at the center of the chicane principle.

3.1.1.3.3 Chromatic matching

To reduce the chromatic effects of the electron beam, an energy dependent focusing position strategy is used [179]. By canceling the second order in energy transport matrix terms that relates the beam vertical and horizontal sizes to the beam relative energy, the various energies are focused at different longitudinal positions inside the undulator. Thus, R_{116} and R_{226} and R_{336} and R_{446} are set to 0 in the second order transport matrix Equation 2.120:

$$M_{0:s}|_x = \begin{pmatrix} R_{11} & 0 & R_{16} \\ 0 & R_{22} & R_{26} \end{pmatrix} + \delta \begin{pmatrix} 0 & R_{126} & R_{166} \\ R_{216} & 0 & R_{266} \end{pmatrix} \tag{3.15}$$

In addition, fixing $R_{11} = R_{33}$ sets a round electron beam and fixes the chicane gradient [179]. Thus, it is possible to synchronize the FEL wave slippage over the electron beam with the multiple beam energies slices. Although, the chicane is able to sort longitudinally the energy to effectively put in place such optics, additional quadrupoles are necessary. So, a second set of four electromagnetic quadrupoles (EMQs) is set between the chicane and the undulator. The four quadrupoles set transport matrix is written as:

$$\begin{aligned} M_{COX,3} = R_{Drift} R_{QAll,EMQ4} R_{Drift} R_{QAll,EMQ3} R_{Drift} R_{QAll,EMQ2} R_{Drift} R_{QAll,EMQ1} \\ R_{QAll,EMQ} = R_Q \end{aligned} \tag{3.16}$$

with $R_{QAll,EMQi}$ the ith EMQ matrix. After the undulator, the beam exits the line thanks to a dipole dump and the radiation is focused to a UV spectrometer. Along the line, there are multiple beam diagnostics to be able to monitor the beam charge, position, size and divergence at different positions.

3.1.2 COXINEL baseline reference case

The COXINEL line has been designed considering baseline reference parameters given in Table 3.1. This section reports on the optics, the reference transport and on the tolerance study.

3.1.2.1 Optics

The high tunability of the QUAPEVA triplet offers a large flexibility for the manipulation of the electron beam. Different optics are designed for both for the step by step optimization of the electron beam transport along

the line and FEL operation. Equations 3.13, 3.1.1.3.2 and 3.16 lead to the following expression of the transport matrix from the source to the undulator:

$$M_{S:Und} = M_{COX,3}M_{COX,2}M_{COX,1} = R_{Drift}R_{QAll,EMQ4}R_{Drift}R_{QAll,EMQ3}R_{Drift}R_{QAll,EMQ2}R_{Drift}R_{QAll,EMQ1} R_{Drift}R_{Chicane}R_{Drift}R_{QAll,QAP3}R_{Drift}R_{QAll,QAP2}R_{Drift}R_{QAll,QAP1}R_{Drift} \quad (3.17)$$

$$(3.18)$$

This long expression can be easily solved computationally, as for the Hamiltonian formalism. So, the design of the COXINEL line optics is done via simulation. The electron beam transport is modeled up to the second order in energy with BETA [191], where using a multiparticle tracking code, based on sympletic mapping, the electron beam is tracked in the 6D phase space, describing position, momenta, and energy at any location along the line. The code uses the Hamiltonian formalism as described (section 2.5.5), to calculate the 6D phase space of all particles. The code was benchmarked on COXINEL case with multiple codes [175, 192–194].

3.1.2.1.1 The supermatching optics

The main optics for the generation of FEL radiation is the "supermatching optics" [179]. This optics focuses the reference energy at the center of the undulator and the lower (higher) energies before (after) in order to synchronize the FEL wave slippage with the different energies. For this, the chromatic matching conditions (Section 3.1.1.3.3, i.e., $R_{116} = R_{226} = R_{336} = R_{446} = 0$, $R_{11} = R_{33}$ and $R_{12} = R_{21} = R_{34} = R_{43} = 0$) are used, yielding the transport matrix Equation 3.15.

3.1.2.1.1.1 Baseline reference case transport

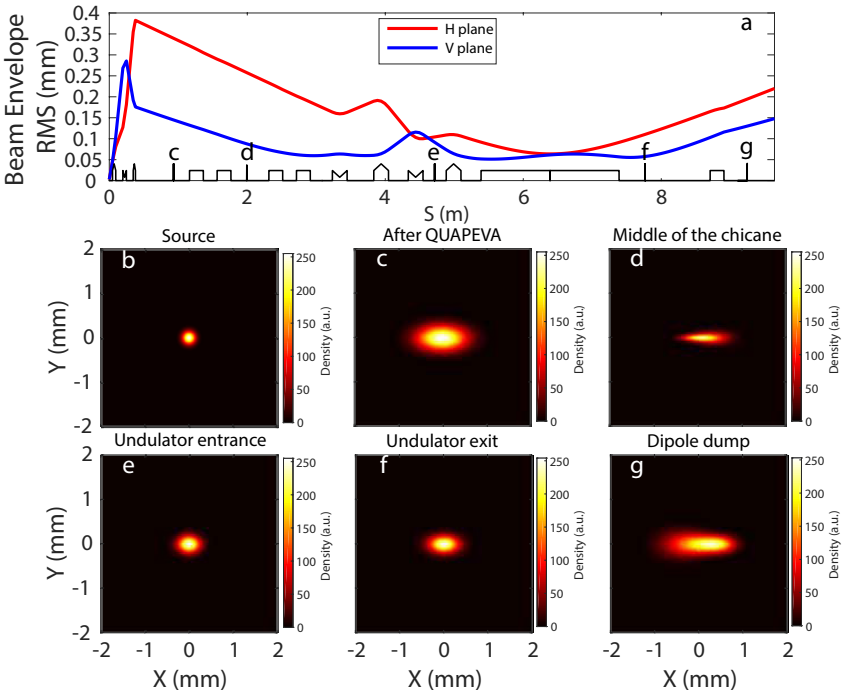

FIGURE 3.5: (a) Beam envelope evolution along the line and transversal shape at (b) the source and at the imagers (c) after the QUAPEVA triplet, (d) in the middle of the chicane, (e) at the entrance and (f) exit of the undulator and (g) after the dipole dump for the "supermatching" optics with a flat-top energy spectrum beam centered at 176, σ_γ =1 %, ϵ_{RMS} =1 mm.mrad, $\sigma'_{y,RMS,i}$ = 1 mrad and $\sigma'_{x,RMS,i}$ = 1 mrad (Table 3.1). Transport line elements representation (**black**) with screens (**vertical line**), dipoles (**rectangle**), and focusing (**rectangle with indentation**) and defocusing quadrupoles (**triangle on top**).

Figure 3.5a presents the beam transversal envelope evolution along the line for the "supermatching" optics and a flat-top beam with the baseline parameters (Table 3.1). The initial transversal shape of the beam used for the transport simulation (Figure 3.5b) is a Gaussian profile in all spatial directions while the energy distribution is flat-top. From the source to the QUAPEVA triplet, due to the initial beam divergence, the beam transversal size quickly increases from $\approx 3\ \mu m$ to around 0.3 mm, i.e., by two orders of magnitude. Thanks to the QUAPEVA triplet, the divergence beam defocus is compensated and the transversal beam size decreases along the line. The chicane does not affect the reference energy transversal size, however, it elongates the beam longitudinally. The electromagnetic quadrupole quadruplet (EMQ) then transversally focuses the beam at the center of the undulator. Figure 3.5c presents the transversal shape at the simulated imager after the QUAPEVA triplet ("first imager"). The beam is centered in the imager and the horizontal size is longer than the vertical one. In the middle of the chicane (imager "chicane") (Figure 3.5d), the beam is sorted horizontally by energy and the differences between energies in vertical focus can be appreciated. At imager "UndIn" (Figure 3.5e), the transversal beam size is greatly reduced in respect to the one at the "first imager". According to the simulated beam on the imager at the undulator exit (imager "UndOut") (Figure 3.5f) the beam starts again to diverge, specially in the horizontal direction. At the simulated imager after the dipole dump (imager "D_{dump}") (Figure 3.5g), the beam is sorted by energy horizontally by the dipole dump like in imager "chicane", so, one can differentiate in the transversal image the different energy slices vertical sizes.

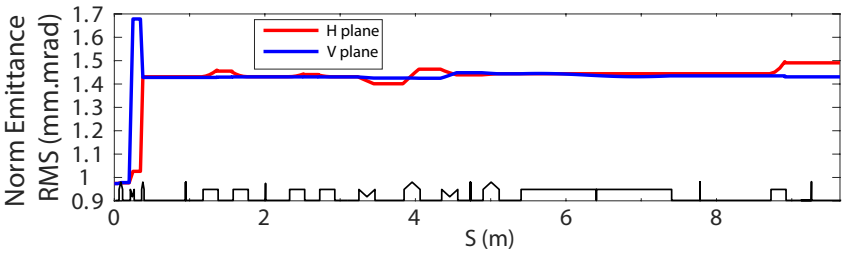

FIGURE 3.6: Beam emittance evolution along the line for the "supermatching" optics with a flat-top energy spectrum beam centered at 176, σ_γ =1 % , ϵ_{RMS} =1 mm.mrad, $\sigma'_{y,RMS,i} = 1$ mrad and $\sigma'_{x,RMS,i} =$ 1 mrad (Table 3.1). Transport line elements representation (**black**) with screens (**vertical line**), dipoles (**rectangle**), and focusing (**rectangle with indentation**) and defocusing quadrupoles (**triangle on top**).

Figure 3.6 presents the evolution of the transversal emittance of the beam along the COXINEL line: For an energy spread of 1 %, the emittance main increase occurs at the QUAPEVA triplet, by 1.5 times. If one considers the distance between QUAPEVAS of 10 cm and the baseline beam parameters (Table 3.1), Equation 3.10 ($\epsilon^2_{x,1} \approx \epsilon^2_{x,0} + L^2_{drift}\sigma'^4_{x,0}\sigma^2_\gamma + (1+\sigma^2_\gamma)4\theta^2_{skew}L^2\sigma'^2_{x,0}\sigma'^2_{y,0}$) leads to an emittance of 1.57 mm.mrad, which is in good agreement with the simulation. After the QUAPEVA triplet, the emittance remains mostly stable with slight variations.

3.1.2.1.1.2 Energy dependent focusing position

The "supermatching" optics design makes the horizontal and vertical focusing longitudinal position dependent on the electron energy.

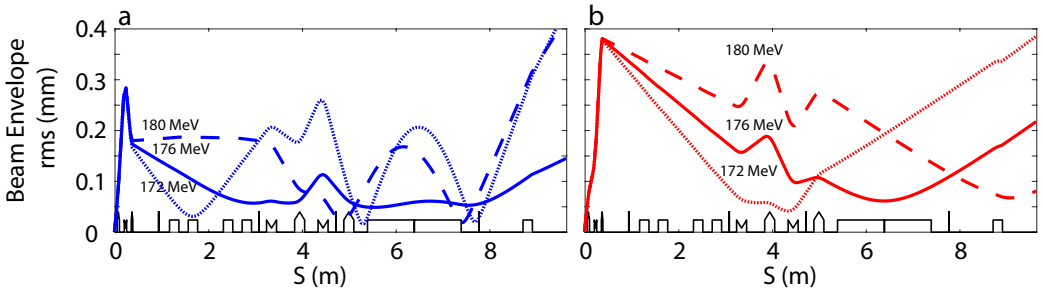

FIGURE 3.7: Simulated vertical (**a**) horizontal (**b**) RMS beam envelope along the line. (**c**) Vertical (**blue**) and horizontal (**red**) normalized emittance at the undulator center and total beam charge (**green**). Case of flat-top beams of 180 MeV (**dashed line**), 176 MeV (**solid line**), and 172 MeV (**dotted line**), with the "supermatching" optics, and baseline parameters Table 3.1 [178].

Figure 3.7a,b presents the beam envelope evolution with the "supermatching" optics for a flat-top distribution and no energy spread for three different energies: The nominal energy (176 MeV) electrons are focused at the center of the undulator, while the lower energy (172 MeV) (resp. higher energy (180 MeV)) ones are focused before (after) the undulator.

3.1.2.1.2 The COXINEL different optics

Thanks to the adaptability of the COXINEL line multiple optics based on the source-to-image principle have been designed with different intents. Figure 3.8 shows the main optics configurations (Figure 3.8a–d) and the associated simulated beam transverse shape observed at the entrance ("UndIn"), center and exit ("UndOut") of the undulator (Figure 3.8a1–d3). The beam envelope is modeled using the baseline parameters (Table 3.1) and the magnetic elements settings given in Table 3.2. The optics of the COXINEL line can be divided in two groups by purpose: Radiation generation optics and Line adjustment optics.

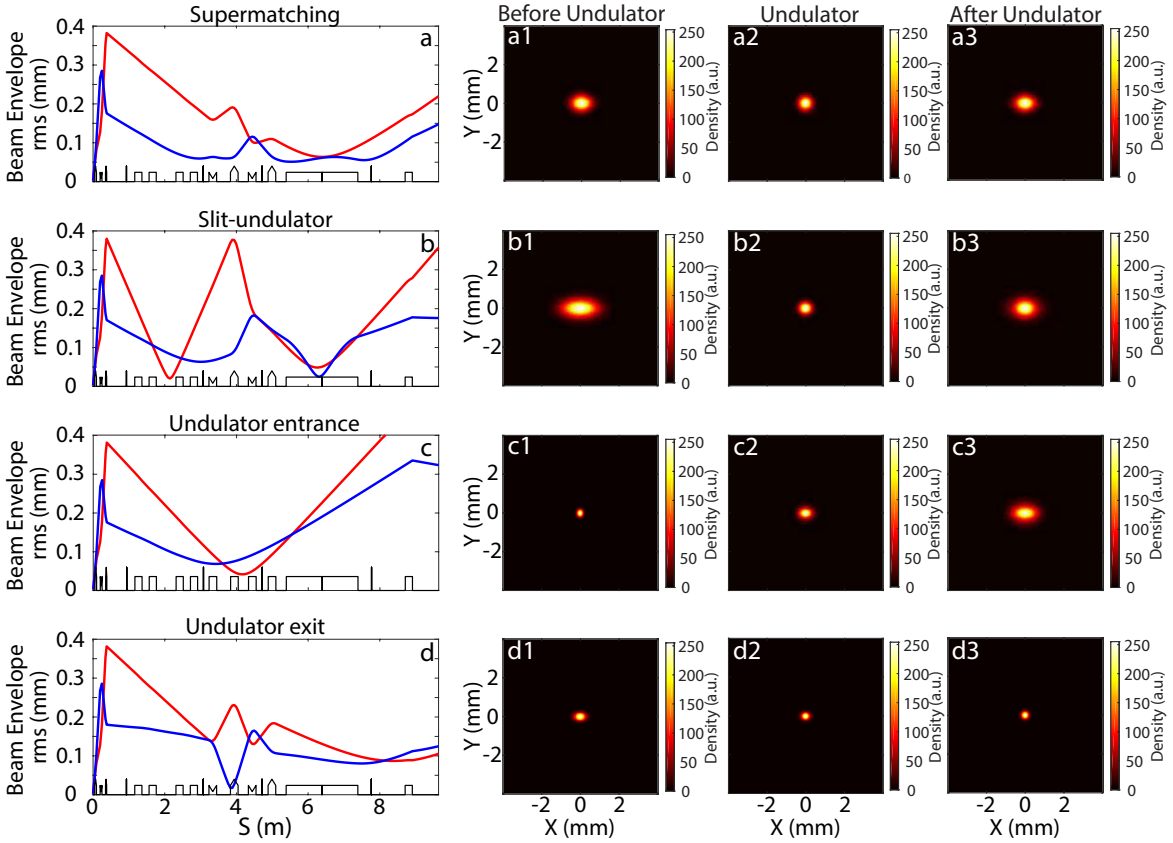

FIGURE 3.8: Simulation of the horizontal (**red**) and vertical (**blue**) beam envelope of the optics (**a**) "supermatching", (**b**) "slit-undulator", (**c**) "undulator-entrance", and (**d**) "undulator-exit" along the line for a flat-top energy spectrum beam of 176 ± 1 % MeV, with the baseline parameters (Table 3.1). Transversal distribution of the electron beam at the undulator entrance (**a1**–**d1**), center (**a2**–**d2**), and exit (**a3**–**d3**) associated with the corresponding magnetic elements settings given in Table 3.2. Transport line elements representation (**black**) with screens (**vertical line**), dipoles (**rectangle**), and focusing (**rectangle with indentation**) and defocusing quadrupoles (**triangle on top**).

TABLE 3.2: Magnetic elements characteristics per optics configuration.

Optics	QUAPEVAs (QAP)			Chicane Dipoles				Electro-Magnetic Quadrupoles (QEM)			
Unit	Gradient T/m			B Field	Gap	Current	r_{56}	Gradient T/m			
Component	QAP1	QAP2	QAP3	T	mm	A	mm	QEM1	QEM2	QEM3	QEM4
"Slit"	+104.8	−104.3	+97.36	0.24	25	46.5	4.3	0	0	0	0
"Supermatching"	+102.68	−101.14	+89.10	0.24	25	46.5	4.3	−0.52	0.85	−1.23	0.46
"Slit-undulator"	+104.1	−103	+96.43	0.24	25	46.5	4.3	−0.01	4.70	−4.40	0.29
"Undulator entrance"	+102.8	−101.2	+90.26	0.24	25	46.5	4.3	0	0	0	0
"Undulator exit"	+102.41	−100.74	+89.78	0.24	25	46.5	4.3	−1.74	1.26	−1.36	0.41

3.1.2.1.2.1 Line adjustment optics

The aim of the line adjustment optics is to align the beam step by step and to detect laser or magnetic elements misalignment. The beam is focused on the different imagers for observing the transversal shape and to identify and correct the beam errors.

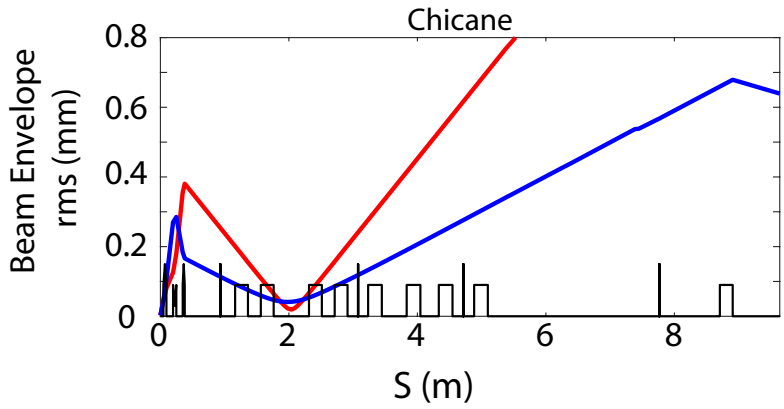

FIGURE 3.9: Simulation of the horizontal (**red**) and vertical (**blue**) beam envelope of the "Chicane" optics along the line for a flat-top energy spectrum beam of 176 ± 1 % MeV, with the baseline parameters (Table 3.1). Transport line elements representation (**black**) with screens (**vertical line**), dipoles (**rectangle**), and focusing (**rectangle with indentation**) and defocusing quadrupoles (**triangle on top**).

The "chicane" optics focus the beam transversally in the middle of the chicane, as shown in the beam envelope evolution in Figure 3.9. This optics are used with the imager "chicane" inserted, therefore, the beam stops in the focus position. The "undulator-entrance" optics (Figure 3.8c) focuses the beam onto the imager "UndIn" at the undulator entrance. Figure 3.8c shows the "undulator-entrance" optics transport for the baseline parameters. Figures 3.8c shows the beam envelope focusing onto the imager "UndIn" by the QUAPEVA triplet. The transverse shape at the imager "UndIn" shown in Figure 3.8c1 exhibits a tiny spot, and at the undulator center and imager "UndOut" in Figures 3.8c2, c3, the beam diverges. Figures 3.8d shows the "undulator-exit" optics for the baseline parameters. The beam is focused onto imager "UndOut" at the undulator exit. The beam is well focused along the undulator with its minimum size being achieved at the imager "UndOut".

A possible initial pointing defect of the beam can lead to misalignment from the QUAPEVAs magnetic center and thus, the rest of the line. The "chicane" optics (Figure 3.8b) and the "undulator entrance" optics (Figures 3.8c, 3.18) are the main ones used to adjust the alignment. The "undulator entrance" optics is also used to check the focusing of the beam energies, i.e., the apparition of a cross shape instead of a focused round beam. The "undulator exit" optics (Figures 3.8d, 3.19), in conjunction with the "undulator entrance" optics (Figures 3.8c, 3.18) is mainly used for the alignment of the beam through the undulator. Once a misalignment of the beam has been identified, a method of compensation via the QUAPEVA triplet has been created to correct the alignment. This method is called Beam pointing alignment compensation (BPAC) [12].

3.1.2.1.2.2 Beam pointing alignment compensation

By transport calculations, one can determine the effect of the misalignment with respect to all magnetic elements on the electron beam path. So, for each element, the matrices correlating the orbit and dispersion of the beam to the elements position can be obtained. The correlation matrices show that the misalignment can be corrected through horizontal and vertical axis displacements of the QUAPEVA triplet [12]. First one determines the on-momentum and off-momentum particle transport for the QUAPEVA triplet position offset and then the orbit and dispersion can be calculated as:

$$\begin{aligned} x_i(s) &= \langle x_i(s, \delta = 0) \rangle \\ y_i(s) &= \langle y_i(s, \delta = 0) \rangle \\ D_{x,i}(s) &= \frac{\langle x_i(s, \delta \neq 0) \rangle - \langle x_i(s, \delta = 0) \rangle}{\delta} \\ D_{y,i}(s) &= \frac{\langle y_i(s, \delta \neq 0) \rangle - \langle y_i(s, \delta = 0) \rangle}{\delta} \end{aligned}$$

with the index i corresponding to the QUAPEVA 1, 2 or 3. Then, the correlation matrix between the orbit and dispersion and the QUAPEVAs position offset is:

$$\begin{pmatrix} x(s) \\ D_x(s) \end{pmatrix} = \begin{pmatrix} x_1(s) & x_2(s) & x_3(s) \\ D_{x,1}(s) & D_{x,2}(s) & D_{x,3}(s) \end{pmatrix} \begin{pmatrix} \Delta Tx1 \\ \Delta Tx2 \\ \Delta Tx3 \end{pmatrix} \tag{3.19}$$

$$\begin{pmatrix} y(s) \\ D_y(s) \end{pmatrix} = \begin{pmatrix} y_1(s) & y_2(s) & y_3(s) \\ D_{y,1}(s) & D_{y,2}(s) & D_{y,3}(s) \end{pmatrix} \begin{pmatrix} \Delta Ty1 \\ \Delta Ty2 \\ \Delta Ty3 \end{pmatrix} \tag{3.20}$$

with $\Delta T_{u,i}$ the displacement in u of the QUAPEVA i. Equations 3.20, 3.19, are solved using the least squares method is used.

3.1.2.1.2.3 Radiation generation optics

The so-called "slit-undulator" optics aims at observing undulator spontaneous emission which can also be used as a diagnostic of the energy slice passing through the slit [195]. It transversally focuses the beam at the center of the undulator and at the slit placed in the center of the chicane, allowing its use for energy spread manipulation. For the baseline case in Figure 3.8b, the beam is horizontally focused in the middle of the chicane and then vertically and horizontally in the middle of the chicane. At imager "UndIn" (Figure 3.8b1), the beam is more vertically than horizontally focused. In the undulator center (Figure 3.8b2) the beam is tightly focused in both directions giving a small round spot. In imager "UndOut" (Figure 3.8b3), the beam is more defocused horizontally than vertically. As shown by Equation 3.10, the transport is affected by energy spreads of some percents.

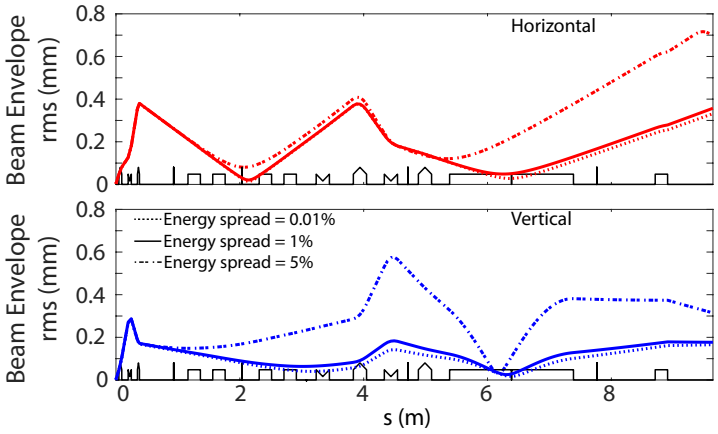

FIGURE 3.10: Simulation of the horizontal (red) and vertical (blue) beam envelopes versus longitudinal position 's' for the optics "slit-undulator" along the transport line for a flat-top energy spectrum centered at 176 MeV with $\sigma_\gamma = 5\%, 1\%, 0.01\%$ and the baseline parameters Table 3.1. Transport line elements representation (black) with screens (vertical line), dipoles (rectangle), focusing (rectangle with indentation) and defocusing (triangle on top) quadrupoles [196].

Figure 3.10 shows the horizontal and vertical beam envelope along the entire line for the "slit-undulator" optics for a beam centered around the 176 MeV reference energy and energy spread σ_γ = 5%, 1%, 0.01%. When the energy spread increases, the beam is focused before the undulator, with a larger focus size. Therefore, for a non zero energy spread beam, its minimum transversal size position can differ from the reference energy maximum focus one.

TABLE 3.3: Baseline parameters at the source of the COXINEL line design, beam RMS characteristics at the undulator center after transport for a flat-top initial beam with the "slit-undulator" optics and the slit opened at 3.6 mm and 1 mm [196].

Position	**Slit**	**Total charge** Q_t	**176 ± 0.5 MeV slice charge** $Q_{176\pm0.5MeV}$	**Energy spread** σ_γ	**Divergence** σ'_x, σ'_y	**Emittance x** ϵ_x	**Emittance y** ϵ_y	**Beam length** σ_s	**Beam size x** σ_x	**Beam size y** σ_y	**Central energy**
	mm	*pC*	*pC*		*mrad*	*mm.mrad*	*mm.mrad*	*μm*	*mm*	*mm*	*MeV*
Source	—	34	10.9	1%	1	1	1	1	—	—	176
Undulator center $\sigma_{\gamma,initial}$ = 1 %	3.6	34	10.9	1%	—	1.7	1.4	—	0.07	0.03	—
Undulator center $\sigma_{\gamma,initial}$ = 10 %	3.6	19.53	0.97	5.8%	—	7.8	4.9	—	0.3	0.1	—
Undulator center $\sigma_{\gamma,initial}$ = 10 %	1	5.4	0.97	1.6%	—	2.5	1.9	—	0.1	0.06	—

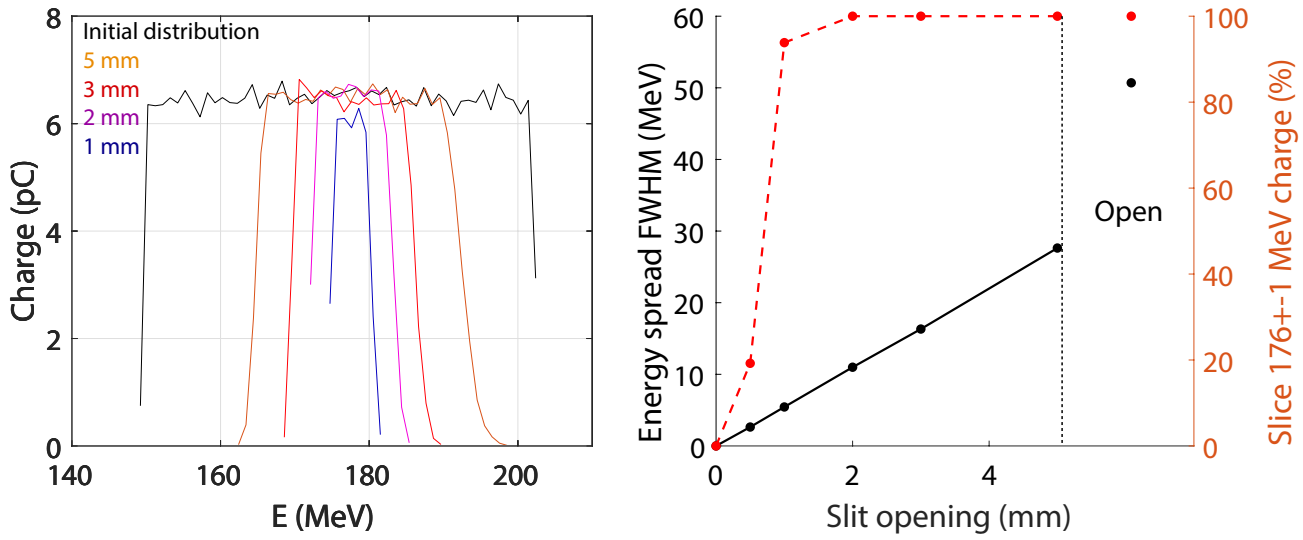

FIGURE 3.11: (a) Initial flat-top beam energy distribution and remaining at the center of the undulator for different slit openings. (b) Energy spread σ_γ FWHM at the center of the undulator and 176 ± 0.5 MeV slice charge arriving to the center of the undulator for different slit openings for the 'slit-undulator' optics. Initial beam; flat-top, σ_γ = 15%, ϵ = 1 mm.mrad, σ' = 1 mrad.

In addition to worsen the total beam transport, low energy spreads are required for FEL applications. Figure 3.11 shows the evolution of the energy distribution function of the beam at the middle of the undulator for different slit apertures from transport simulations with the "slit-undulator" optics. The distribution is properly cut around the energy of interest of 176 MeV (see Figure 3.11a). The slit effectively reduces the energy spread σ_γ (see Figure 3.11b) at the expenses of the total beam charge, nevertheless the lost charge corresponds to energies far from the reference one. The charge for the slice 176 ± 0.5 MeV is conserved except for slits closed at a value smaller than 1 mm.

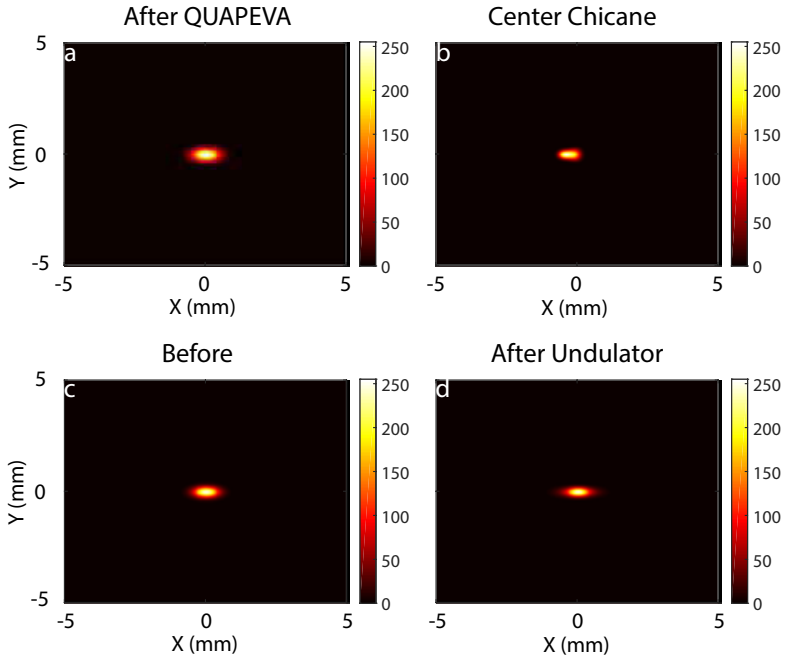

FIGURE 3.12: Electron beam transverse shape simulated after the QUAPEVA triplet (a), center of the chicane (b), undulator entrance (c) and exit (d) for a flat-top beam centered at 176 MeV with an energy spread of 10 %, the baseline parameters (Table 3.3) with the "slit-undulator" optics with the slit open to 3.6 mm.

Figure 3.12 shows the transport along the line for a beam with an energy spread of 10 %, the baseline parameters (Table 3.3) and the "slit-undulator" optics with the slit opened at 3.6 mm. Table 3.3 shows the beam parameters at the undulator center. For a beam of 1% energy spread at the reference energy, a small increase of the emittance occurs while the charge is conserved at the undulator center and the beam is properly focused. For a flat-top beam of 10% energy spread around the reference energy 176 MeV, for the slit opened at 3.6 mm (1 mm) σ_γ is reduced to 5.8% (1.6%).
The versatility of the COXINEL line enables the design of multiple optics for alignement and diagnosing the beam and for spontaneous emission and FEL search. Through the use of these optics the beam is properly characterized, transported and manipulated to satisfy the requirements imposed for FEL.

3.1.2.2 Sensitivity to parameters

The COXINEL line and its optics have been designed with the baseline parameters (Table 3.1). Nevertheless, the line is capable to still transport to the undulator beams with degraded parameters or slight errors in the experimental optics configuration. Therefore, a study of the limits of the transport and how is the FEL affected is required to set the acceptable limits of the deviations from the ideal baseline case. In this section, a quick review of the influence of slight variations from the baseline beam parameters and the optics is presented from [176], and a beam charge-divergence FEL amplification zone is defined from FEL simulations to be able to infer the experimental electron beam capabilities for FEL. The ideal case can be affected by two kind of variations, changes in the LPA beam or changes in the line magnets.

3.1.2.2.1 COXINEL line sensitivity to LPA parameters in the baseline reference case

For this studies the baseline beam is considered Gaussian in the 6D phase-space with the "supermatching" optics. For the FEL enhancement via a seed to occur a minimum of charge per energy slice and divergence is required A baseline beam (Table 3.1) with 0.56 pC/MeV of energy bandwidth presents a small amplification while increasing the charge to 2.8 pC/MeV produces an amplification of 2 orders of magnitude. Figure 3.13 presents the normalized peak power versus the total beam divergence and charge from GENESIS [197] and CHIMERA [198] seeded FEL simulations. Changes of the order of 1 mrad or 10 pC on the total beam charge can reduce the power by an order of magnitude.

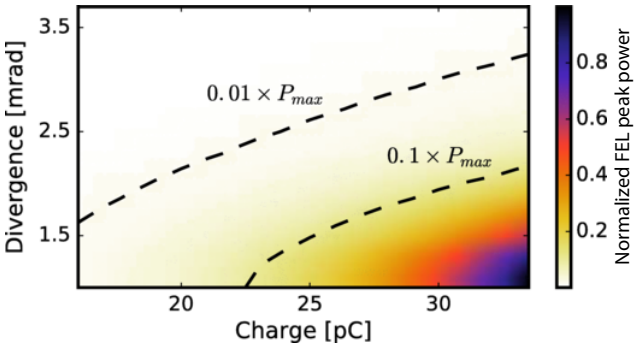

FIGURE 3.13: Normalized FEL peak power at 200 nm versus electron beam charge and divergence. Beam transport simulation with OCELOT [199] without collective effects using the "supermatching" optics with R_{11}=R_{33}=10 and R_{56}=0.4 mm/ Normalized emittance preserved at 1 mm.mrad. FEl simulation with CHIMERA. Figure extracted from [176].

High power lasers beams suffer from spatial jitters. Let's suppose a baseline beam with a 5 μm RMS transversal position, 1 mrad RMS pointing angle and 1 % energy spread jitters. At the undulator center, the 1 mrad pointing angle dominates the beam orbit degradation. Moreover, the jitters also cause transverse changes in the dispersion due to the beam passing off-axis through the quadrupoles. Dispersion values up to 10 mm in the undulator increase the beam size to 100 μm. The increase in size translates into an chromatic emittance growth by a factor 3 to 5 from the ideal case. Regarding the FEL output power, a displacement of 20 μm RMS or an angle of 2 mrad RMS yields a drop of one order of magnitude, originating mainly from the loss of overlap between the seed and the beam.

The transversal line acceptance is plotted in Figure 3.2b. The LPA beam acceptance is mainly proportional to its initial divergence and energy spread. A few mrad pointing causes a drastic rise of the beam losses. For an baseline beam (Table 3.1) with an energy spread of 10 %, the losses are negligible, however, by increasing the energy spread above 20 % less than 90 % of the beam arrives at the undulator exit.

3.1.2.2.2 Optics parameters sensitivity

During experiment systematic errors on magnet alignment can occur that if left uncorrected can lead to important degradation of the FEL amplification.

Let's consider random displacement of all quadrupoles by up to 100 μm, random tilt for the dipoles of up to 100 μm and random relative magnetic strength of up to 0.1 %. Up to 5 mrad slopes and 5 mm RMS orbit amplitudes in the undulator are found, i.e., the order of the undulator aperture. Via the use of beam steerers, the orbits can be reduced to 0.4 mm in the undulator. The dispersion function reaches 10 mm in the undulator and remains unaffected by the orbit correction but it can be corrected with the BPAC (Section 3.1.2.1.2.2). As for the jitters, the dispersion causes an chromatic emittance growth that can strongly affect the FEL amplification. An offset of 10 μm on the second QUAPEVA, i.e., the strongest one, leads to a drop of FEL power of 1 order of magnitude, because of the beam orbit change produced by the QUAPEVA misalignement, e.g., a 30 μm QUAPEVA 2 offset induces a 400 μm displacement of the beam and as the seed is 200 μm, therefore, the spatial overlapping between them does not occur. Using the BPAC, one can limit the power drop to less than a factor two for displacements of < 300 μm. Depending on the quadrupole, to achieve a FEL power drop of one order of magnitude an error between 1 % and 20 % is required. A detuning of the QUAPEVAs or EMQs yields important mismatches in the undulator and thus, significant FEL gain degradation. A realistic undulator magnetic field from measurements of an undulator U20 of SOLEIL [200] is modeled with the CHIMERA code. The electrons with moderated energies see a deviation in the horizontal axis throughout the undulator. A small beam entrance angle of 27 μrad is able to correct the deviation. Eventual small imperfections of the magnetic field can be compensated by orbit corrections at the undulator entrance and exit.

3.1.2.2.3 Electron beam reference slice requirements for FEL

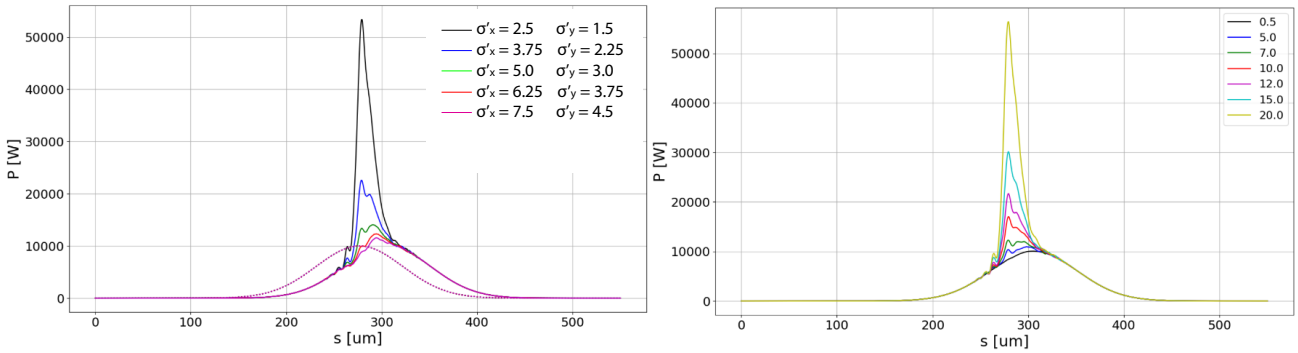

FIGURE 3.14: FEL properties versus electron beam initial (left) RMS divergence; 1.0, 1.5, 2.0, 2.5 and 3.0 times the initial reference value (2.5 mrad ; 1.5 mrad) and (right) versus charge: 0.5 pC, 5 pC, 7 pC, 10 pC, 12 pC, 15 pC, 20 pC on-axis temporal profiles. For power profiles and spectra: (dotted line) undulator entrance and (continuous line) undulator exit. Beam parameter setting #7 (From RUN 7): energy 151 MeV, σ_γ = 8 %, charge 20 pC, $\sigma'_{x,rms}$ = 2.5 mrad, $\sigma'_{y,rms}$ = 1.5 mrad, ϵ = 0.2 mm.mrad, $\sigma_{s,rms}$ = 0.1 μm. Figures from [201].

The FEL amplification is highly dependent on the beam parameters. If large deviations from the expected values are obtained, the FEL effect attained could be even jeopardized. Figure 3.14 presents the radiation power amplification due to an electron beam passing through the U18 undulator obtained via simulation for different initial divergences and beam slice charges. Let's define the amplification ratio f_{amp} as the ratio between the power at the undulator exit and the power at the undulator entrance ($P_{entrance}$ = 10000 W), i.e., amplification with respect to the seed:

$$f_{amp} = \frac{P_{UndExit}}{P_{entrance}} \tag{3.21}$$

The amplification ratio values are fitted to estimate the zone in the slice divergence-charge space where amplification is possible (Figure 3.15). The fit is found to be:

$$f_{amp}(\sigma'_y, Q_{slice}) = -5.41 + 12.25\sigma_y^{'-2} + 2.2Q_{slice}^{1.744} \tag{3.22}$$

with Q_{slice} the charge density at the reference energy in pC/MeV. The relation between the amplification and the slice divergence and slice charge allows for some flexibility in the beam parameters, i.e., there is multiple divergence and charge pairs that yield the same f_{amp}. For the baseline parameters of COXINEL (Table 3.3) the amplification ratio value is 146. The surface on Figure 3.15 represents the zone for FEL amplification ratio with respect to the seed higher than 1.5 is achieved. Provided there is sufficient signal-to-noise ratio and shot-to-shot reproducibility an amplification ratio of f_{amp} = 2 could be measured. For an experimental search of FEL effect, one aims at f_{amp} = 15, i.e., ten times less than the baseline reference case.

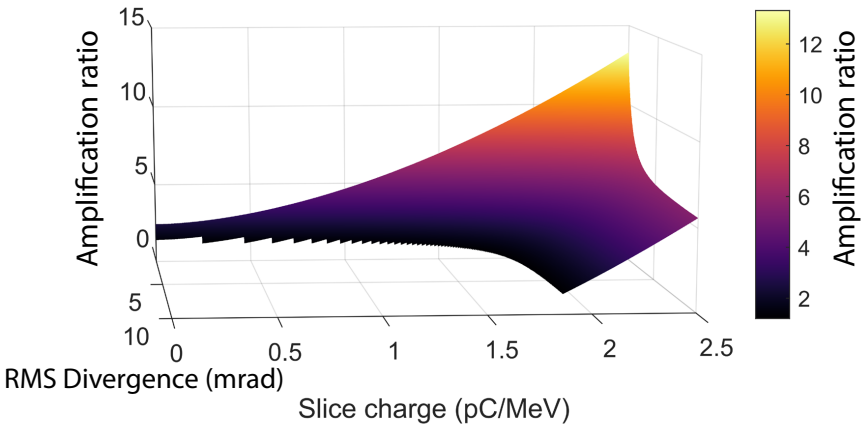

FIGURE 3.15: Low gain FEL amplification zone versus slice charge and divergence defined by the fit $f_{amp}(\sigma'_y, Q_{slice}) = -5.41 + 12.25\sigma_y^{'-2} + 2.2Q_{slice}^{1.744}$ from simulations (Figure 3.14) [201] for values $f_{amp} > 1.5$.

3.1.3 COXINEL with alternate initial electron beam characteristics

During the first COXINEL RUNs, the measurements of the electron beam characteristics appeared to deviate from the baseline reference case. To study the transport capacity of the different optics in the COXINEL line an alternative degraded beam with a 176 ± 1 % MeV flat-top energy distribution, higher divergence ($\sigma'_{y,i} = 2$ mrad RMS and $\sigma'_{x,i} = 3.12$ mrad RMS) and lower emittance ($\epsilon_{x,i}$,$\epsilon_{y,i} = 0.2$ mm.mrad) with respect to the baseline (Table 3.1) is studied in this section.

3.1.3.1 The supermatching optics

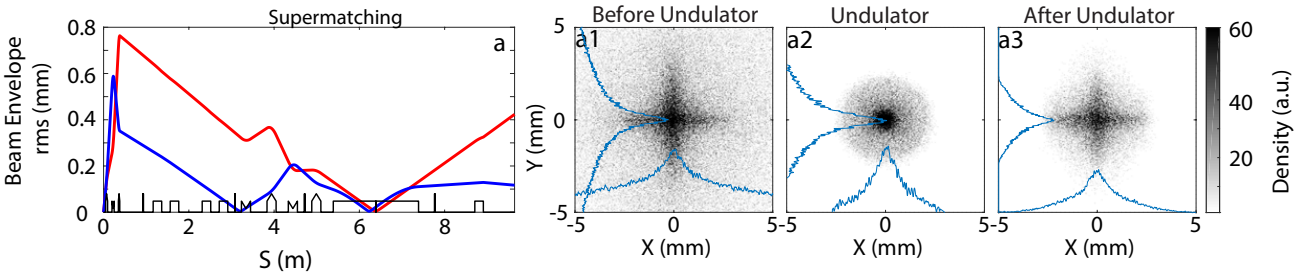

FIGURE 3.16: Simulation of the horizontal (**red**) and vertical (**blue**) beam envelope of the (**a**) "supermatching" optics along the line for a flat-top energy spectrum beam of (a) 176 ± 0.3 MeV and (a1-a3) 176 ± 5 % MeV, with $\sigma'_{y,i} = 2$ mrad RMS and $\sigma'_{x,i} = 3.12$ mrad RMS. Transversal distribution of the electron beam at the undulator entrance (**a1**), center (**a2**), and exit (**a3**) associated with the corresponding "supermatching" optics magnetic elements settings given in Table 3.2. Transport line elements representation (**black**) with screens (**vertical line**), dipoles (**rectangle**), and focusing (**rectangle with indentation**) and defocusing quadrupoles (**triangle on top**) [178].

Figure 3.16 presents the "supermatching" optics transport for the degraded beam. For the simulated transverse shape images of the degraded beam, an initial 5 % energy spread is used for better visualization of the chromatic effect on the focusing. Figure 3.16a presents a more violent increase in beam size, up to twice the baseline case (Figure 3.5a). Nevertheless, the QUAPEVA triplet is still capable of compensating the divergence and reduce the beam to μm values at focus position. The chromatic dependence induces the observed cross shape on imagers "UndIn" and "UndOut" (Figure 3.16a1, a3), due to the various energies being focused at different horizontal and vertical positions instead of the center of the undulator (Figure 3.7). In the beam transversal shape at the undulator center presented in Figure 3.16a2, the reference energy is well focused and the other unfocused energies form a halo around it.

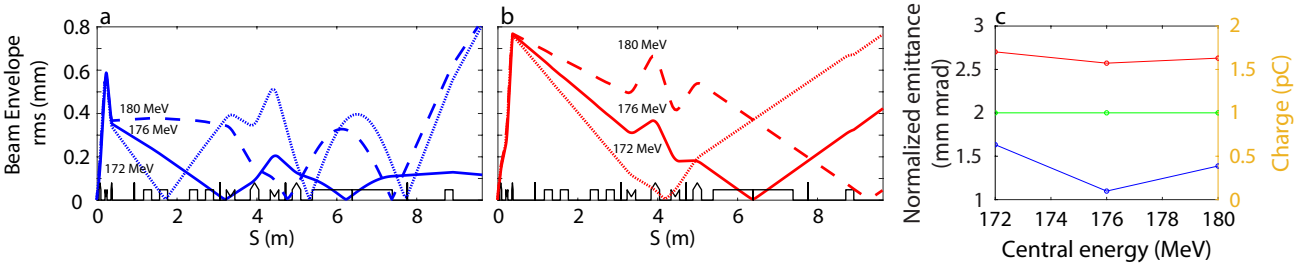

FIGURE 3.17: Simulated vertical (**a**) horizontal (**b**) RMS beam envelope along the line. (**c**) Vertical (**blue**) and horizontal (**red**) normalized emittance at the undulator center and total beam charge (**green**). Case of flat-top beams of 180 MeV (**dashed line**), 176 MeV (**solid line**), and 172 MeV (**dotted line**), with the "Undulator" optics, an $\sigma'_{y,i} = 2$ mrad RMS and $\sigma'_{x,i} = 3.12$ mrad RMS, charge of 1 pC, $\epsilon_{x,i}$,$\epsilon_{y,i} = 0.2$ mm.mrad [178].

Figure 3.17a,b shows the beam envelope for the 172 ± 0.3 MeV, 176 ± 0.3 MeV and 180 ± 0.3 MeV slices with the degraded beam characteristics and the "supermatching" optics. The same chromatic behavior of the focus as in the baseline is observed. Due to the higher divergence, the sizes achieved are higher than in Figure 3.7. However, thanks to the lower emittance, the beam is focused into a smaller spot than in the baseline case. Thus, the initial beam size limits the minimum focusing size possible for the optics. Figure 3.17c shows the emittance

and the charge at the undulator center for the different energies. The emittance is minimum at 176 MeV, for which the optics has been designed. The vertical (horizontal) emittance increases by a factor of 1.5 (1.05) for 172 ± 0.3 MeV and by a factor of 1.26 (1.02) for 180 ± 0.3 MeV. No charge is lost in any of the three cases.

3.1.3.2 Line adjustment optics

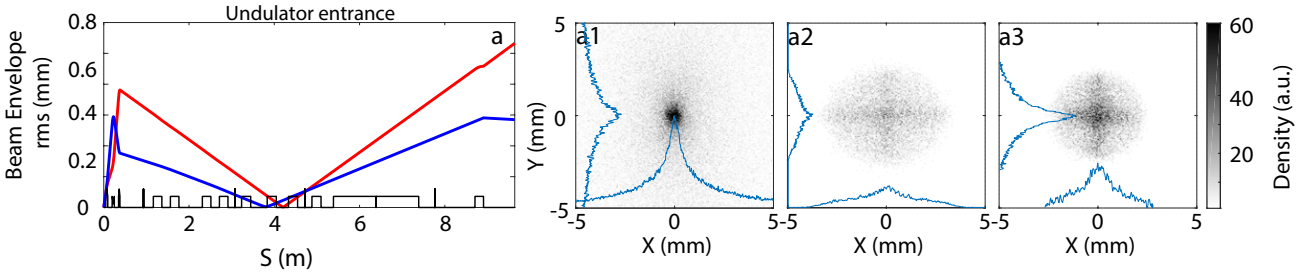

FIGURE 3.18: Simulation of the horizontal (**red**) and vertical (**blue**) beam envelope of the (**a**) "undulator entrance" optics along the line for a flat-top energy spectrum beam of (a) 176 ± 0.3 MeV and (a1-a3) 176 ± 5 % MeV, with $\sigma'_{y,i}$ = 2 mrad RMS and $\sigma'_{x,i}$ = 3.12 mrad RMS. Transversal distribution of the electron beam at the undulator entrance (**a1**), center (**a2**), and exit (**a3**) associated with the corresponding magnetic elements settings given in Table 3.2. Transport line elements representation (**black**) with screens (**vertical line**), dipoles (**rectangle**), and focusing (**rectangle with indentation**) and defocusing quadrupoles (**triangle on top**) [178].

Figure 3.18 presents the "undulator-entrance" optics transport in the case of a degraded beam. The beam envelope evolution (Figure 3.18a) is similar to the baseline case (Figure 3.8c). The transverse beam shape in imager "UndIn" (Figure 3.18a1) presents a focused round spot surrounded by a halo composed of higher and lower non focused energies. In the undulator center and imager "UndOut" (Figure 3.18a2, a3) the cross shape can be observed.

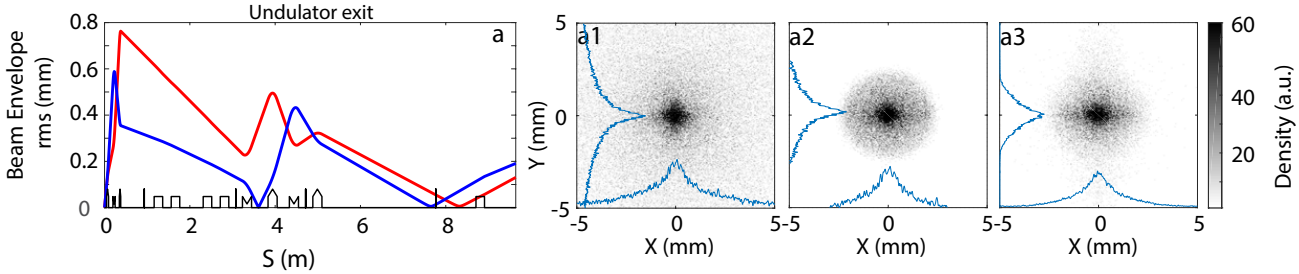

FIGURE 3.19: Simulation of the horizontal (**red**) and vertical (**blue**) beam envelope of the (**a**) "undulator exit" optics along the line for a flat-top energy spectrum beam of (a) 176 ± 0.3 MeV and (a1-a3) 176 ± 5 % MeV, with $\sigma'_{y,i}$ = 2 mrad RMS and $\sigma'_{x,i}$ = 3.12 mrad RMS. Transversal distribution of the electron beam at the undulator entrance (**a1**), center (**a2**), and exit (**a3**) associated with the corresponding magnetic elements settings given in Table 3.2. Transport line elements representation (**black**) with screens (**vertical line**), dipoles (**rectangle**), and focusing (**rectangle with indentation**) and defocusing quadrupoles (**triangle on top**) [178].

Figure 3.19 presents the "undulator-exit" optics transport in the case of a degraded beam. The envelope evolution is similar to the baseline case (Figure 3.8d) except at the imager "UndOut" where the larger energy spread causes the maximum horizontal beam focus to happen after the imager. The beam transverse shape in the imager "UndIn" (Figure 3.19a1) presents a round beam with a halo of high and low energies occupying the entire screen. In the undulator center (Figure 3.19a2) the beam is better focused and the halo size greatly reduced. In the imager "UndOut" (Figure 3.19a3) the beam reference energy is a well focused spot like shape and the halo is slightly reduced compared to the undulator center.

3.1.3.3 Radiation generation optics

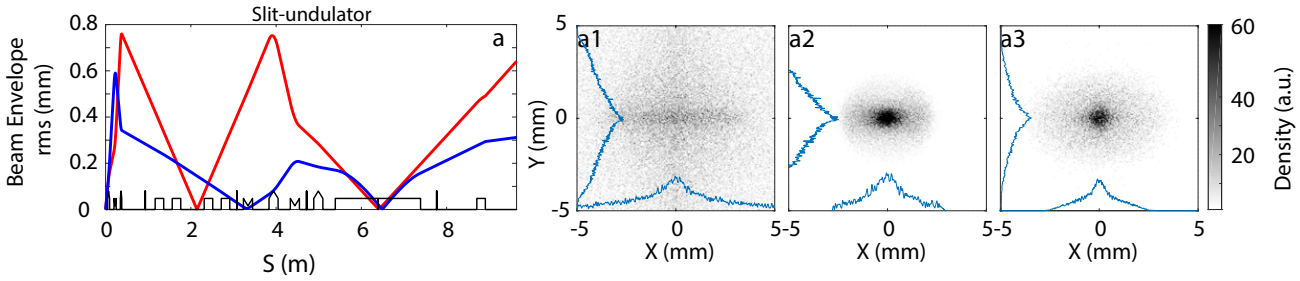

FIGURE 3.20: Simulation of the horizontal (**red**) and vertical (**blue**) beam envelope of the (**a**) "slit-undulator" optics along the line for a flat-top energy spectrum beam of (a) 176 ± 0.3 MeV and (a1-a3) 176 ± 5 % MeV, with $\sigma'_{y,i}$ = 2 mrad RMS and $\sigma'_{x,i}$ = 3.12 mrad RMS. Transversal distribution of the electron beam at the undulator entrance (**a1**), center (**a2**), and exit (**a3**) associated with the corresponding magnetic elements settings given in Table 3.2. Transport line elements representation (**black**) with screens (**vertical line**), dipoles (**rectangle**), and focusing (**rectangle with indentation**) and defocusing quadrupoles (**triangle on top**) [178].

The transport with the "slit-undulator" optics for a degraded beam is presented in Figure 3.20. The beam envelope in Figure 3.20a is similar to the baseline case. Figure 3.20a1, a2, a3 show the near elimination of the cross shape caused by the high energy spread (Figure 3.16), thanks to the action of the slit, i.e., the lower and higher energies with respect to the reference energy are cut. The beam is well focused in the undulator center.

3.1.4 COXINEL FEL estimation with baseline parameters

The Ming Xie radiation equations (Section 2.6.2) can give a first estimation of the FEL power that could be achieved in COXINEL undulator with a baseline like beam. An initial electron beam energy distribution resulting from the 2D PIC simulations for $a_{0,initial}$=1.75, $n_e = 4.56 \times 10^{18}\ cm^{-3}$and 1 % N_2 concentration (Figure 5.19) is utilized as it is close to experimental conditions and it shows a peak close to 176 MeV. The 176 ± 0.5 MeV slice initial charge and beam initial divergence and emittance are scaled to coincide with the baseline parameters (Table 3.1), i.e., $\sigma'_{x,y,RMS}$=1 mrad, $\epsilon_{x,y,RMS}$=1 mm.mrad, $Q_{176\pm0.5MeV}$=10.3 pC.

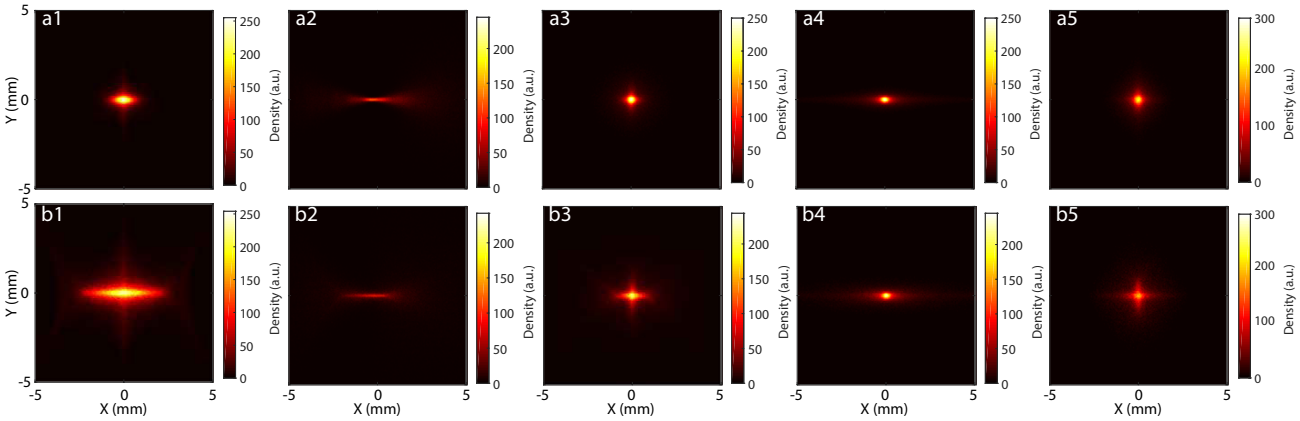

FIGURE 3.21: Simulated electron beam transverse shape at the (a1, b1) first imager, (a2, b2) "Chicane", (a3, b3) "UndIn", (a4, b4) undulator entrance and (a5, b5) "UndOut". Energy distribution from $a_{0,initial}$=1.75, $n_e = 4.56 \times 10^{18}$ and 1 % N_2 concentration (Figure 5.19) PIC simulation and initial electron beam characteristics $\epsilon_{x,y,RMS}$=1 mm.mrad, (a) $\sigma'_{x,y,RMS}$=1 mrad, $Q_{176\pm0.5MeV}$=10.3 pC, (b) $Q_{176\pm0.5MeV}$=1 pC, $\sigma'_{y,RMS}$=2 mrad, $\sigma'_{x,RMS}$=3.12 mrad.

Figure 3.21a exhibits the transport of the beam along the COXINEL line for the "supermatching" optics. The beam is well focused at the undulator and the faint side trails (cross on the first imager, "UndIn" and "UndOut") are due to the energy spread. At the undulator entrance, the electron beam 176 ± 0.5 MeV slice has a charge of 10.36 pC, RMS ϵ_y = 0.39 mm.mrad and RMS ϵ_x = 1.89 mm.mrad. With these parameters the Ming Xie equations predicts for the 176 ± 0.5 MeV slice a gain length of 2.1 m and average SASE power of 10.5 W for a wavelength of 235 nm (Table 3.4). A degraded initial parameters case, i.e., $Q_{176\pm0.5MeV}$=1 pC,

$\sigma'_{y,RMS}$=2 mrad, $\sigma'_{x,RMS}$=3.12 mrad and $\epsilon_{x,y,RMS}$=1 mm.mrad has also been tested with the same energy and divergence distribution (Figure 3.21b). The transverse beam shape is considerably more dispersed due to the higher divergence. At the undulator entrance the beam is still vertically focused but more horizontally defocused compared to the baseline like case. The degraded case leads to an average power significantly under the noise power and eight orders of magnitude lower than the baseline like case (Table 3.4).

TABLE 3.4: Gain length, noise power and average SASE power calculated from the Ming Xie equations (Section 2.6.2). Energy distribution from $a_{0,initial}$=1.75, $n_e = 4.56 \times 10^{18}$ and 1 % N_2 concentration (Figure 5.19) PIC simulation and initial electron beam characteristics $\epsilon_{x,y,RMS}$=1 mm.mrad, $\sigma'_{x,y,RMS}$=1 mrad, $Q_{176\pm0.5MeV}$=10.3 pC, $Q_{176\pm0.5MeV}$=1 pC, $\sigma'_{y,RMS}$=2 mrad, $\sigma'_{x,RMS}$=3.12 mrad.

PIC simulation parameters			Source parameters		Undulator parameters				Radiation		
$n_{e,norm}$	$a_{0,initial}$	N_2 concentration %	$Q_{151,source}$ pC/MeV	$\sigma'_{source,151,RMS}$ mrad	$Q_{151,und}$ pC/MeV	$\epsilon_{x,und,151,RMS}$ mm.mrad	$\sigma_{s,und,151,RMS}$ fs	$\sigma_{x,und,151,RMS}$ mm	L_{gain} m	$P_{SASE,mean}$ W	P_{noise} W
0.18	1.75	1	10.36	1	10.34	1.89	24.35	0.10	2.11	1.05×10^{1}	6.8×10^{-1}
$n_{e,norm}$	$a_{0,initial}$	N_2 concentration %	$Q_{151,source}$ pC	$\sigma'_{source,151,RMS}$ mrad	$Q_{151,und}$ pC/MeV	$\epsilon_{x,und,151,RMS}$ mm.mrad	$\sigma_{s,und,151,RMS}$ fs	$\sigma_{x,und,151,RMS}$ mm	L_{gain} (m) m	$P_{SASE,mean}$ (W) W	P_{noise} (W) W
0.18	1.75	1	1	2	1	50	24.18	0.91	1.45×10^{4}	2.03×10^{-7}	7.79×10^{-3}

The Ming Xie equations confirm that with the baseline parameters SASE FEL generation can be possible however, that is not a case with the degraded case. More accurate analysis including the seed proper radiation simulations are done with radiation simulations. While the estimations show possible SASE amplification in the baseline parameters, the seeded configuration simulations (Section 3.1.2.2.3) present more than an order of magnitude higher achieved amplification. Thus, taking into account the important effect of electron parameters degradation, the use of the seed FEL configuration for the search of LPA based FEL is more appropriate.

3.2 COXINEL experimental components

The modeling of the COXINEL line leads to the specifications of the necessary equipment for the transport and FEL. The COXINEL line uses classic magnetic elements with innovations to tackle the LPA electron beam characteristics. At the same time multiple diagnostics are placed along the line to measure multiple properties of the electron beam at any point of the line with ease.

3.2.1 Set-up for the LPA generation

The LPA system can be divided into two parts, the laser used to drive the wakefield and the gas target.

3.2.1.1 Laser system

A laser system at " Salle Jaune" of Laboratoire d' optique Appliquée was used for the LPA source. The Titanium:Sapphire (Ti:Sa) laser system provides a linearly polarized light in the horizontal direction, 800 nm, 30 fs (FWHM), 1.5 J pulse to the interaction chamber where it is focused into a spot of 20 μm (FWHM) (Table 3.5), i.e, a factor $a_0 = \sqrt{\frac{\lambda_L^2 I_L}{1.37\times10^{18}}}$ $[\frac{W}{cm^2}\mu m^2]$ (Equation 2.30, 2.34) of $\approx$ 1.9. For RUN 7 (2020/02), the laser was upgraded achieving an energy on target of 2.5 J (Table 3.5) increasing the factor a_0 to $\approx$ 2.4. The laser beam diameter also increased but via spherical mirrors of higher focal length the beam size on target remained mostly unchanged. The laser is focused at the entrance of the gas target with slight variations for optimization of beam parameters.

In Ti:Sa high power lasers, the imperfections in many optical components and the thermal heating effect distortions in the amplification crystals can lead to deformations in the wave-front [202, 203]. Such wave-front quality degradation changes the transversal intensity distribution leading to non symmetrical wakefields inside the plasma [204, 205]. Wave-front measurements of the used laser system for COXINEL have indicated that the beam distribution is not a perfect Gaussian [206]. The real main intensity peak is closer to half the one of a Gaussian case, thus, giving a factor a_0 during experiment of around $\approx$ 1.5 before the upgrade and of $\approx$ 1.8 after it. In addition to wave-front deformations, the laser also presents shot-to-shot spatial variations [207], that affects the focusing position and the gas density profile seen by the laser. Such instabilities render difficult a continuous and stable use of complex LPA schemes like the colliding pulses [208] thus, the initial idea of using it was discarded.

TABLE 3.5: Laser system parameters.

Dates	Laser	λ_{laser} nm	Energy J	Intensity W/cm^2	Length fs	Focus spot size μm	a_0
Before 2020/02	Ti:Sa	800	1.5	7.48×10^{18}	30	20	≈ 1.5
After 2020/02	Ti:Sa	800	2.5	1.25×10^{19}	30	20	≈ 1.76

3.2.1.2 Gas targets

Even though the colliding pulses scheme offers good control of the injection and acceleration phases in the wakefield it was decided to use the ionization injection scheme for its robustness, simple setup, relatively high charge and short beams [39–41]. Two kinds of gas targets have been used during the different experimental campaigns. A supersonic gas jet with a millimeter scale nozzle (RUNs 1, 2, 3, 4, 6 and 7) offers a broad Gaussian like gas density distribution spanning $\approx$ 6 mm. A gas cell of adjustable length of the order of the mm, with an entrance and exit of a diameter equal to 500 μm (RUN 4) [209]. The gas cell allows for a more uniform gas density and eliminates long density gradients in the longitudinal direction, leading to a flat-top plasma density profile. The frontal shock configuration was tested during RUN 2 but abandoned because the electron beam was very unstable. The laser is carefully aligned with the cell entrance and exit. The gas mixture for both gas targets is composed of 99% He and 1% of N_2 (Table 3.6).

TABLE 3.6: Gas-jet parameters.

Length mm	Gas mixture He %	N_2 %	Shape
6	99	1	Broad Gaussian

3.2.2 Magnetic elements

The COXINEL line combines electromagnetic dipoles and variable gradient permanent magnets based quadrupoles. In the following, the numerous magnetic elements are described.

3.2.2.1 QUAPEVA triplet

The QUAPEVA triplet, positioned 5 cm from the source handles the mrad divergence of the beam. The QUAPEVA is composed of two quadrupoles embedded in one mechanical structure [180, 181] (see Figure 3.22, Table 3.7): a first Halbach hybrid structure with four $Nd_2Fe_{14}B$ permanent magnets (PM) (high remanence field ($\sim$1.26 T) and coercivity (1830 kA/m)) and four iron–cobalt alloy magnetic poles, and a second one composed of four PM cylinders with a radial magnetic moment orientation, which produces a variable gradient by the rotation around their axis. Four Fe–Co alloys are placed behind the cylinders to shield the magnetic field and redirect the lines into the core. The magnetic system is built into a dedicated aluminum support frame that maintains the elements in their positions due to the strong generated magnetic force. This design guarantees a gradient higher than 100 T/m with a large tunability, i.e., greater than 30%, for a bore radius of 6 mm, with magnetic lengths from 26 mm up to 100 mm to provide different integrated strengths. The usual gradients are around 100 $\pm$ 20 T/m for the first and third QUAPEVA, and -100$\pm$20 T/m for the second one Table 3.2.

TABLE 3.7: QUAPEVA parameters.

Main structure	Magnet material		$Nd_2Fe_{14}B$
	Pole Material		Fe-Co
	Bore radius	mm	6
	Magnetic length	mm	26 - 100
Coercivity		kA/m	1830
Remanence field		T	1.26
Gradient	Value	T/m	>100
	Tunability	%	>30

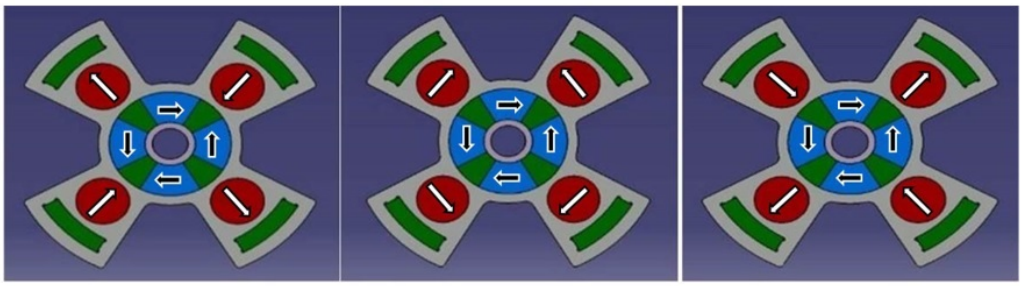

FIGURE 3.22: magnetic design with different orientation of the cylindrical magnets: maximum (**left**), intermediate (**middle**), minimum gradient (**right**) [178].

The quadrupole local magnetic field is given by Equation 2.139 [79] and the normal b_n and skew a_n multipolar terms by Equation 2.140. The gradients measured for the QUAPEVAs for different magnet angles (Figure 3.23) range between $[110, 190]$, $[-190, -110]$ and $[110, 205]$ T/m.

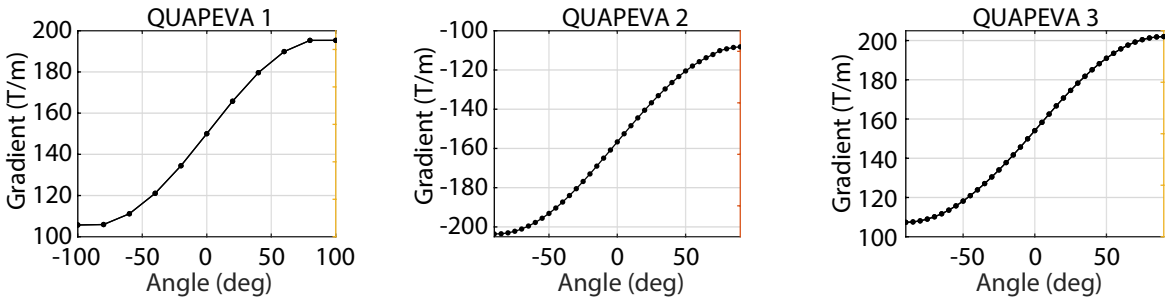

FIGURE 3.23: Gradient measured versus magnet angle, for the QUAPEVA triplet: 26 mm, 44.7 mm, and 40.7 mm from left to right respectively.

Because of the inherent uncertainty of the assembly process on the positions of the central Halbach ring, the QUAPEVA design is subject to the present default skew quadrupole contribution. After construction, the measured QUAPEVA multipolar terms using a stretched wire [210] (Table 3.8) present a non-negligible skew quadrupole contribution. The dodecapolar term (b_6) relative to the main quadrupolar term (b_2) is between 2% and 2.3 % for the three QUAPEVAs. The QUAPEVA transverse magnetic center offset error is limited to ± 10 μm [180]. The skew real component a_2 can be characterized by an angle (see Table 3.8), defined as $\theta_{skew} = \frac{1}{2} arctan(\frac{a_2}{b_2})$ (Equation 2.141). The skew quadrupole components, arising from the roll angle in the QUAPEVA, are corrected by introducing a small metallic plate (called shim) as thick as 500 μm between the QUAPEVA and the base. The measured skew quadrupolar term a_2 for the triplet used at COXINEL has been reduced by more than a factor of 10 by compensating the roll angle (see Table 3.8, Figure 3.24).

TABLE 3.8: Multipolar terms before (high skew terms case) and after (low skew terms case) correction [178].

	High Skew Term Case					**Low Skew Term Case**				
Magnetic Length	$\mathbf{a_2}$ *T.mm*	$\mathbf{a_6}$ T.mm	$\mathbf{b_2}$ T.mm	$\mathbf{b_6}$ T.mm	**Angle** mrad	$\mathbf{a_2}$ *T.mm*	$\mathbf{a_6}$ T.mm	$\mathbf{b_2}$ T.mm	$\mathbf{b_6}$ T.mm	**Angle** mrad
26 mm	0.073	−0.003	10.951	0.192	3.3	−0.007	−0.01	10.947	0.186	−0.3
40.7 mm	−0.325	−0.017	17.475	0.326	−9	0.027	−0	17.448	0.329	0.7
44.7 mm	0.362	0.012	−19.181	−0.363	−9.4	0.003	−0.004	−19.148	−0.357	0.05

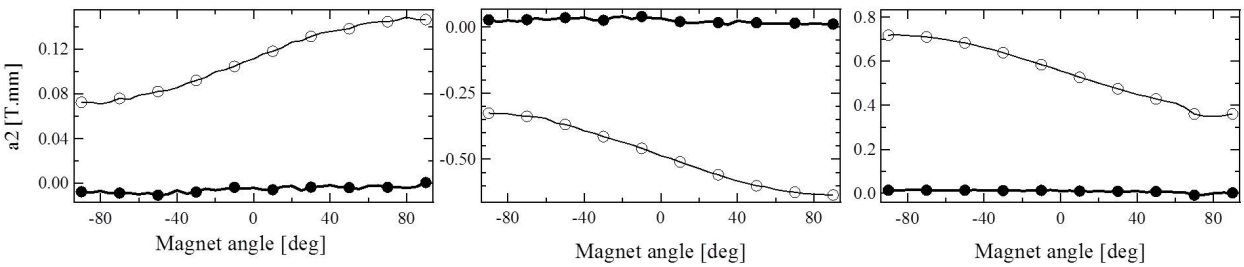

FIGURE 3.24: Skew quadrupolar term (a_2) measured with the stretched wire, before (○) and after (●) correction, for the QUAPEVA triplet: 26 mm (**left**), 40.7 mm (**middle**), and 44.7 mm (**right**), $r_0 = 4$ mm.

3.2.2.2 Chicane

The magnetic chicane (Figure 3.2), situated after the QUAPEVAs triplet, sorts the electron beam horizontally by energy and elongates longitudinally the beam. It is composed of four dipole magnets (made by SEF) all of equal field strength and magnetic length, water-cooled. The characteristics of the chicane are displayed in Table 3.9. The power supply has been procured by Sigmaphi Electronics and is also water-cooled.

TABLE 3.9: Magnetic chicane parameters.

Length mm	Aperture mm	Coils per magnet	Turns per coil	$\vec{B}$ field @ 150A T	$\Delta B/B$	Supply current A
200	25	2	11x4	0.55	0.2%	150

3.2.2.3 Electromagnetic quadrupoles

After the magnetic chicane, a quadruplet of electromagnetic quadrupoles (EMQ) is placed in order to focus the beam in the middle of the undulator. Thanks to the "energy - longitudinal position" correlation introduced by the chicane, the use of these four EMQs allow the different electron energies to be properly focused at different positions along the undulator, i.e., the "supermatching" optics configuration [179]. The EMQs parameters are shown in Table 3.10.

TABLE 3.10: Electromagnetic quadrupoles parameters.

Gradient		**Multipolar terms**			Bore radius	Length	Coils	Number of turns	Current
Maximum $\frac{T}{m}$	Tunability	B_6	B_{10}	B_{14}	mm	mm	mm^2		$A\ mm^2$
20	100%	$0.4\text{x}10^{-2}$	$0.07\text{x}10^{-2}$	$0.02\text{x}10^{-2}$	12	200	70x12	14x10	1.6

3.2.2.4 Steerers

Magnetic steerers are located at different positions along the line. The steerers adjust the horizontal and vertical position of the electron beam if needed to assure that it goes straight through the undulator. The parameters of the used steerers are shown in Table 3.11.

TABLE 3.11: Steerer parameters.

$\vec{B}_x$, $\vec{B}_z$ mT	Integrated Field Gm	Gap mm	Current Density $A \cdot mm^2$	Current A	Voltage V	Number of turns
3.5	31	340	1.6	10	3	72

3.2.2.5 Undulator

The under vacuum U18 undulator of 18 mm period made at SOLEIL [211] is used at the COXINEL line, and the parameters are shown at Table 3.12. The number of periods N_u of the undulator imposes another limitation to the energy spread. The homogeneous bandwidth ($\frac{\Delta\lambda}{\lambda} = \frac{1}{nN_u}$, with n the harmonic), should be higher than the energy spread contribution on the radiation bandwidth, thus giving, in COXINELs case, an upper limit of $176 \pm 0.5\%$ MeV, so, % level energy spread beams are an issue.

TABLE 3.12: Undulator U18 parameters.

Magnets	Material		$Pr_2Fe_{14}B$
Remanence	at 300 K	T	1.35
Pole	Material		Vanadium Permendur
Period	Lenght	mm	18
	Number		107
Gap		mm	5-30
Length		m	2

3.2.2.6 Dipole dump

A dipole dump takes out the electron beam off the line after the undulator by bending its trajectory. The dipole dump generates a magnetic field of 0.84 T when powered at 300 A.

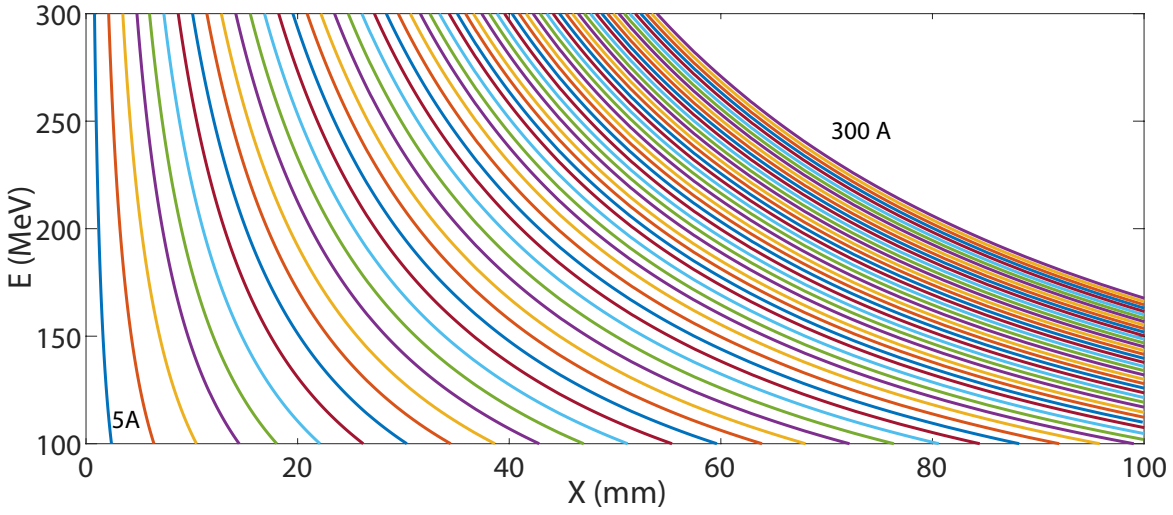

FIGURE 3.25: Imager "D_{dump}" energy position calibration for dipole dumps currents from 5 A to 300 A in steps of 5 A.

A charge q, traveling through a magnetic field $\vec{B}$ with a velocity $\vec{v}$ experiences a Lorentz force $\vec{F}$:

$$\vec{F} = q\vec{v} \times \vec{B} \tag{3.23}$$

For $\vec{v} \perp \vec{B}$ and $\vec{B}$ constant, the charge undergoes a circular motion with centripetal force:

$$\frac{mv^2}{\rho} = qvB \tag{3.24}$$

with m the mass and ρ the curvature radius. By defining m_0c^2 as the electron rest mass energy and E_{kin} as the kinetic energy in MeV, and taking into account the total energy equality $E = mc^2$ and $\beta = \frac{v}{c}$ (Equation 2.37), one can rewrite equation 3.24 as:

$$\rho[cm] = \frac{1}{0.02999B[T]}(E_{kin}^2 + 2E_{kin}m_0c^2)^{1/2} \tag{3.25}$$

Equation 3.25 shows that ρ depends only on E_{kin}. So, for a constant B, the angle of deflection ϕ is:

$$\phi = \frac{s}{\rho} \tag{3.26}$$

with s the path length through the magnet. Figure 3.25 presents the calibration of the electron energies horizontal positions at the imager "D_{dump}" for different currents of the dipole dump obtained via individual electron trajectory simulation.

3.2.3 Diagnostics

The COXINEL line counts with multiple beam diagnostics [212]. Two integrating current transformers (ICT) situated before and after the undulator. Two cavity beam position monitors (cBPM) located between the QUAPEVAs and after the undulator. Five removable imagers; positioned after the QUAPEVA triplet ("first imager"), at the chicane center (imager "Chicane"), undulator entrance (imager "UndIn") and exit (imager "UndOut") and after the dipole dump (imager "D_{dump}") (Figure 3.2).

3.2.3.1 Electron beam diagnostics

3.2.3.1.1 Electron Spectrometer

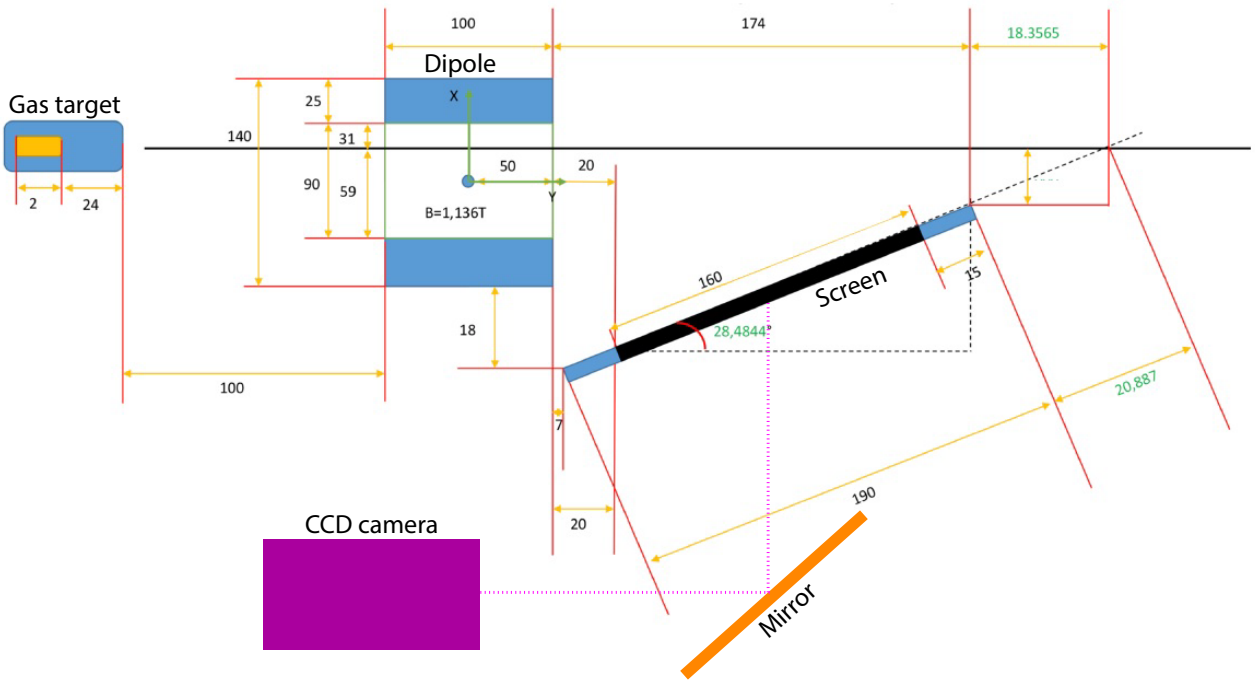

FIGURE 3.26: Experimental electron spectrometer setup with distances in mm (RUN 6; 2019/01/28 - 2019/02/15). The beam travels from the source (yellow) to the dipole (two blue blocks) which deviates them to the lanex screen (black), imaged from the back by a CCD camera HAMAMATSU ORCA Flash 4.0 V3 (magenta) via a mirror (orange). The green values refer to the values calculated.

TABLE 3.13: Electron spectrometer parameters.

Distance from gas jet *mm*	Dipole $\vec{B}$ *T*	dipole length *mm*
355	1.1	100

The electron beam energy distribution and vertical divergence is measured with a spectrometer equipped with a movable dipole, a lanex screen, a mirror and a CCD camera HAMAMATSU ORCA Flash 4.0 V3 [213]. The sketch of the configuration is presented in Figure 3.26 and Table 3.13 gives the parameters of its components.

3.2.3.1.2 ICT

Integrating Current Transformers are a non interceptive diagnostic of the beam charge. The measurement relies on the interaction between the ICT and the beam magnetic field to measure the charge. It can be described in the formalism of transformer circuit theory [214]. The ICTs used at COXINEL, provided by Bergoz [215], have fC resolution.

3.2.3.1.3 cBPM

The cavity beam position monitors cBPM [216] have an acceptance of 16 mm diameter and a length of 100 mm. They provide a sub-μm resolution with a 3.3 GHz frequency. The cBPM was used for charge measurements as the calibration for position monitoring requires more stable electron generation. Until the last experimental campaign, the cBPM were not used as position and charge were accurately measured by the imagers and ICTs respectively.

3.2.3.1.4 Imagers

An imager (Figure 3.27) is constituted by a screen turned 45° with respect to the beam axis. The screen is protected from the laser light by an aluminum foil of 25 μm. A CCD camera with a macro lens captures the image of the back of the screen. A band pass filter is placed between the camera and the screen in order to stop laser or plasma radiation residues. For the "first" imager instead of the filter various optical densities are place in front of the CCD camera.

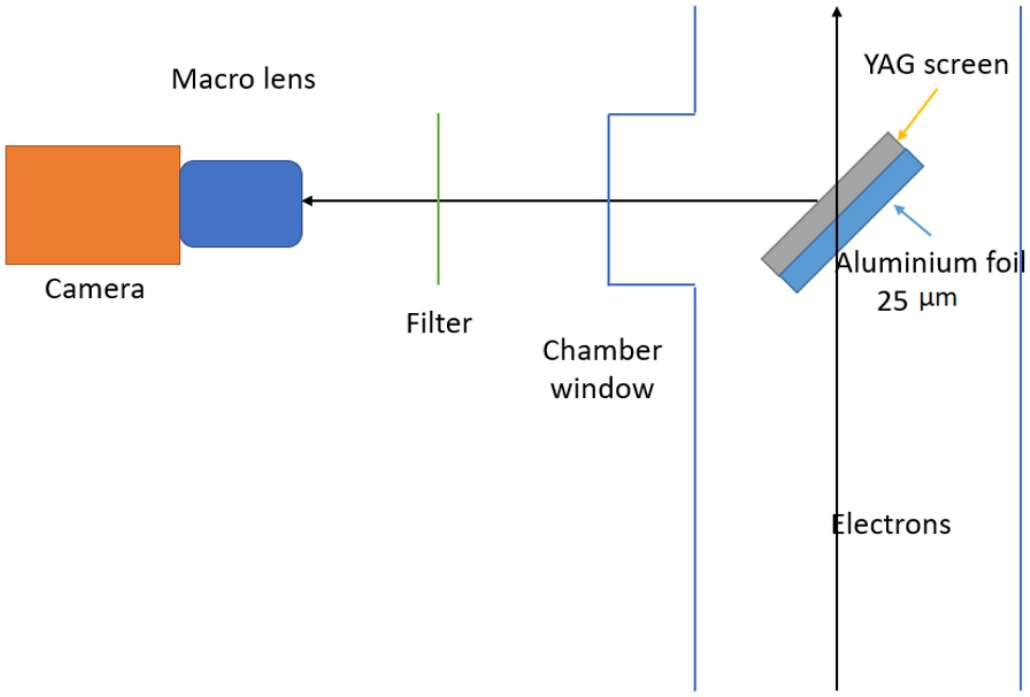

FIGURE 3.27: Scheme of the imagers.

TABLE 3.14: Properties of the screens for all imagers, used cameras and objective for the imagers.

	Symbol	Value	Unit
Kodak Lanex Fine screen (Imagers "First", "Chicane", "UndIn", "UndOut" and "D_{dump}")			
Surface density	ρ_{GOS}	7.44	g/cm^3
Surface charge	h_s	33x10^{-3}	g/cm^2
Photon energy	E_γ	2.27	eV
Efficiency in eV per cm traversed and electron	ξ	1.8x10^6	eV/cm
Fraction of photons exiting the screen	ζ	0.22	
Resolution	$\sigma_{granular}$	100	μm
YAG:Ce screen (Imagers "Chicane", "UndIn" and "UndOut")			
Photon energy	E_γ	2.26	eV
Thickness	e	10^{-2}	cm
Efficiency	R_{Yag}	2.26x10^{-6}	ph/eV
Resolution	$\sigma_{granular}$	30	μm
Basler scA640-70gm (Imagers "First imager")			
Quantic efficiency	QE	46@545nm	%
Conversion factor	CF	>1	
Pixel size (H x V)	σ_{px}	7.4 x 7.4	μm
Hamamatsu ORCA-FLASH 4.0 (Imagers "Chicane", "UndIn", "UndOut" and "D_{dump}")			
Quantic efficiency	QE	82@560nm	%
Conversion factor	CF	0.48	
Pixel size (H x V)	σ_{px}	6.5 x 6.5	μm
ZEISS MACRO (Imagers "D_{dump}")			
Aperture		2	
Transmission	T_{obj}	0.93	
Collect radious	R_{obj}	0.05	m
Collection surface	S_{coll}	0.079	m^2
Sigma 105 mm f/2.8 DG EX Macro OS HSM (Imagers "Chicane", "UndIn" and "UndOut")			
Aperture		2.8	
Transmission	T_{obj}	0.93	
Collect radious	R_{obj}	0.05	m
Collection surface	S_{coll}	0.079	m^2
Imagers constants			
Angle camera-screen	θ_{CCD}	$45\pi/180$	rad
Angle electrons-screen	$\theta_\perp$	$45\pi/180$	rad
Recollection angle	R_{coll}	0.4	m
Window transmission	T_{hub}	0.9	
Filter transmission	T_{filter}	0.85	

3.2.3.1.4.1 Imager resolution

The effects of the optics manifest in the difference between the real object size and the image obtained, called the magnification of the optical system:

$$M_{opt} = \frac{Image_{size}}{Object_{size}} = \frac{\sigma_{pix} s_i}{s_o} \tag{3.27}$$

with σ_{pix} the size of a pixel of the camera, s_i the image size in pixels and s_o the object size. In the imager 2 configuration used until the first part of RUN 7 case, the magnification is 0.45 ± 0.02 in horizontal and 0.17 ± 0.02 in vertical. The size measured in the imager can be written as:

$$\sigma_{x-measured} = \sqrt{\sigma_{real}^2 + \sigma_{resolution}^2} \times M_{opt} \tag{3.28}$$

with σ_{real} the real size on the imager screen and $\sigma_{resolution}$ the minimum size measurable by the system. M_{opt} and $\sigma_{resolution}$ are fixed by the experimental configuration. From Equation 3.28, the resolution of the used optical system is a limitation for such measurement of beam vertical divergence σ' and size σ, thus, a poor spatial resolution produces a result only usable as an upper limit for the real quantities. The magnification also affects the measured result.

The resolution of the imager can be written as:

$$\sigma_{resolution} = \sqrt{\sigma_{diff}^2 + \sigma_{gran}^2 + \sigma_{opt}^2} \tag{3.29}$$

with σ_{diff} the diffusion effect in the aluminum foil, σ_{gran} the granularity size of the scintillating screen and σ_{opt} the resolution of the camera defined as:

$$\sigma_{opt} = \sigma_{res-meas} \frac{\sigma_{pix}}{M_{opt}} \tag{3.30}$$

with $\sigma_{res-meas}$ the measured resolution. The effect of the diffusion in an aluminum foil, of the order of tens of nm, can be ignored. The granularity size of the screen is a value not well known. The incertitude is ± 3 μm for a granule of 30 μm in the case of the YAG screen. In the case of the COXINEL Hamamatsu camera, $\sigma_{pix} = 6.5$ μm and after measuring $\sigma_{res-meas}$ [217], one finds horizontally $\sigma_{opt} = 29$ μm at the center of the image, value valid for a zone of ± 100 px (± 1.3 mm). Vertically the value $\sigma_{opt} = 34$ μm and it is almost constant in the entire image.

For the imager "chicane" of COXINEL with the Sigma lens the obtained resolution is shown in Table 3.15. The resolution limit for the YAG screen appears to be 42 μm, any size below it can't be measured accurately.

Setup parameter				
σ_{diff} ≈ 10 nm	σ_{gran} 30 ± 3 μm	$\sigma_{opt,vertical}$ 34 μm	$\sigma_{opt,horizontal}$ 29 μm	
Magnification		Resolution		
Horizontal	Vertical	Screen	Horizontal (μm)	Vertical (μm)
0.45 ± 0.02	0.17 ± 0.02	YAG	42	42

Table 3.15: Magnification and resolution for the Yag screen in imager "chicane"

3.2.3.1.4.2 Imager "chicane" lenses

By changing the objective in front of the camera one can increase the magnification. Additional lenses were used in imager "chicane" during RUN 7 to increase the resolution. Table 3.16 shows the objectives [218] available in for imager "chicane".

Objective	Configuration	Field of view mm	M_{opt} ratio mm	Efficiency $Counts/ms/mm^2$
Sigma 105 mm f/2.8 DG EX Macro OS HSM [219]	Nominal	17x17	1	0.8
Trioptic Apo Rodagon D120 S1 Obj. [220]	Max zoom Min zoom	7x7 10x10	2.44 1.69	0.15
Navitar 12X S2 Obj. [221]	Zoom 0.58 Zoom 1 Zoom Max	8x8 5x5 3x3	2.13 3.45 5.56	0.01

Table 3.16: Field of view for different objectives with a distance between objective and target of 170 mm and the ratio between the Sigma M_{opt} and the other ones.

3.2.3.2 UV spectrometer photon diagnostic

Table 3.17: iHR320 HORIBA UV spectrometer parameters.

Focal length	320	mm
Aperture	78	mm
Gratings	600, 1200, 3600	grooves/mm
Slit	0.08 to 2	mm
Magnification	1.1	
Camera	SYNAPSE-354308	
Camera pixel size	26	μm
Camera pixel area	1024 x 256	$px \times px$
Camera image area	26.6 x 6.7	mm^2

The radiation emitted at the undulator is then measured by a UV spectrometer iHR320 from HORIBA [222]. The iHR320 is equipped with an adjustable slit at the entrance, three gratings of 600, 1200 and 3600 grooves per mm and a CCD camera. Table 3.17 presents the characteristics of the UV spectrometer.

3.2.4 FEL seed

COXINEL is designed to search an FEL effect in the seeded configuration [223] (Section 2.6.1.3.2). One can take advantage of splitting the Ti:Sa branch into two naturally synchronized branches, one being used for the electron generation of 1.5 J (2.5 J) before (after) the laser upgrade and another one for the seed generation of 15 mJ. The seed can be generated in the UV by harmonic generation in a crystal [224, 225], and further in the VUV by harmonic generation in gas [104, 226–229].
The first solution is the harmonic generation via a set of beta barium borate (BBO) crystals [224, 225], one for the second harmonic generation, another for the third harmonic and other non-linear optical components. The "Femtokit for Third Harmonic Generation of Ti:Sapphire Laser" from EKSMA OPTICS [230] was used. The use of crystals makes the setup robust and simple.
The second solution is the high harmonic generation (HHG) by focusing the seed-generation pulse in a gas cell with Ar gas, obtaining the third harmonic. HHG in gas originates from the interaction between the seed-generation pulse and gas atoms that causes the electrons to escape the atoms by tunnel ionization (Section 2.1.1). In the continuum the electrons are accelerated away from the parent atoms by the laser and then driven back to them when the laser field sign changes. The electrons gain kinetic energy from the process and when they recombine with the ionized atoms the gained kinetic energy is emitted (three-step model [229, 231, 232]). The use of a gas cell adds a laser pointing sensitivity to the setup.
The energy and transverse size of the seed-generation pulse can be reduced via an iris. After its generation the third harmonic pulse is isolated and introduced into the line by the utilization of multiple mirrors at the position of the chicane and focusing optics are used to focus the seed into the undulator.

In addition to the study of the seeded FEL case with the baseline parameters done in Section 3.1.2.2.3, numerical and empirical analysis of a 40 nm seeded FEL with 400 MeV electrons with the "supermatching" optics have been realized showing that with an undulator of 15 mm period and 1.5 T maximum field 5 m are necessary to achieve saturation in the GW peak power range for a 10 kW seed [179].

3.2.5 Integration

The chambers at the COXINEL line are made of stainless steel. The vacuum system is composed of two stages: a primary stage made of a dry scroll pump Edwards nWDS20i [233], that creates a 10^{-3} mbar vacuum; a secondary stage of four turbo molecular pumps PFEIFFER Vacuum HIPACE 80 [234] along the line and two more dedicated to the undulator, which achieves a 10^{-7} mbar vacuum.

In a rack, the XPS controllers for the different imagers motors are placed. Another two racks lodge the power supplies for the magnetic elements. One rack is dedicated to the vacuum pumps control. A last rack has the QUAPEVAs translation stage, the ICT controller and the control system.

The alignment of the girders and magnetic elements in respect to the theorectical laser axis has been done mainly by the use of a laser tracker (FARO VANTAGE [235]), a precision optic (LEICA N3 [236] and an inclinometer (WYLER [237]); with each having a precision of $\approx 0.020\ mm.m^{-1}$.

3.3 COXINEL typical transport procedure

Thanks to the multiple optics and the BPAC the experimental beam transport procedure is reduced to the following steps. First the electron beam is characterized at the spectrometer. Then, some shots at the "first imager" (Figure 3.2) are observed to confirm that the electron beam is on-axis or close. The QUAPEVA triplet is introduced, the "chicane" optics parameters of the line are applied and the beam is observed again on the "first imager" to make sure that its position of the beam has not changed. The "first imager" is taken out and the beam is observed at imager "chicane" (Figure 3.2) where with the BPAC procedure the vertical dispersion and the transverse positions of the beam are corrected. The horizontal dispersion cannot be adjusted in imager "chicane" due to the horizontal sorting caused by the dipoles. Once everything is optimized, imager "chicane" is taken out, the "Undulator-entrance" optics are applied and the beam is observed at imager "UndIn" (Figure 3.2). In this imager the beam transverse position and horizontal dispersion is corrected through the BPAC procedure. To finalize the transport, the "supermatching" or "slit-undulator" optics are applied to the line and the beam is observed at imager "UndOut" (Figure 3.2) to make sure that the beam passes through the undulator on-axis. A better look of the transverse electron beam observed on the imagers is given in Chapter 6.

3.4 Summary

The initial divergence of LPA beams spoil the emittance during transport if not controlled. The COXINEL line has been designed to transport and manipulate the baseline electron beam to fulfill FEL requirements while being able to adapt to beam parameters changes. Multiple optics have been designed for transport optimization and radiation generation. The optics can properly transport beams deviation from the baseline parameters however, total charge loss start to occur. The Ming Xie calculations and GENESIS simulations with the baseline beam show that FEL is possible in such conditions with the COXINEL line, however, for deviations from it makes the FEL power significantly drop or become negligible. Moreover, the seeded FEL configuration permits a significantly higher ($\approx$ 10 times) possible FEL amplification and thus, the FEL search is done with this configuration. The line can also monitor the beam at different positions along the line thanks to multiple diagnostics.

3.5 Conclusion

In Chapter 3, the design of the COXINEL line using the baseline parameters (Total beam charge 34 pC, 1 mrad, 1 mm.mrad, 1 % energy spread and reference energy 176 MeV), obtained beforehand experimentally with the LPA colliding pulse injection scheme (Section 2.3.2.5), has been described. The electron beam manipulation for enabling FEL demonstration along the line has been presented, together with the different components of the line. Multiple optics have been designed destined to the beam transport optimization or radiation generation. Simulations with the baseline electron beam in with the COXINEL line show that FEL is possible.

Chapter 4

Experimental LPA electron beam parameters

The COXINEL line has been designed for the baseline parameters (Table 3.1). Variations in these parameters, specially the divergence, charge and energy spread, can be critical for the performance of the line optics and the undulator radiation generation. The baseline was established from experimental results done at LOA with the colliding pulse scheme before COXINEL. However, due to the inability to utilize such scheme in a stable way (highly sensitive to laser variations) it was decided to use instead the ionization injection scheme for the LPA, that offered a simpler setup with a more robust performance, but, lower beam quality and control. This chapter presents the measurements of the beam characteristics at the source before the transport. The beam divergence, the initial beam energy and vertical divergence distributions measurement method are first shown in the two gas targets cases. The evolution of the beam features during the different experimental campaigns is then presented.

During the different RUNs (Table 4.1), the LPA source ensemble underwent various changes in order to improve the electron beam. The electron beam initial vertical divergence and energy distribution are measured thanks to a spectrometer.

Table 4.1: COXINEL line experimental campaigns dates.

Dates		Experimental campaign
Start	End	
20171123	20171130	RUN 4
20181206	20181221	RUN 5
20190130	20190215	RUN 6
20200901	20200925	RUN 7

4.1 Comparison between the gas cell and the gas jet configurations

4.1.1 Example of initial electron beam

During RUN 4, with a reference energy of 176 MeV, two gas target configurations for the LPA source are explored: a variable length gas cell (2017/11/06 - 2017/11/21) and a gas jet (from 2017/11/22 onward).

4.1.1.1 Gas jet case

The initial gas jet generated electron beam is characterized via the spectrometer (Appendix B) and the "first imager" (Appendix C).

4.1.1.1.1 Spectrometer data analysis

Figure 4.1 presents a single shot taken the 2017/11/30 (RUN 4). The different maximum intensity vertical positions for each energy slice seen in Figure 4.1a probably result from the existence of a halo on the laser wavefront, which causes the wakefield to wiggle around the reference trajectory [205] thus, generation such electron beam deformations. Figure 4.1b presents the charge and vertical divergence per energy slice. The FWHM energy spread is close to 50 %, much higher than the baseline. The charge density per slice (pC/MeV) is thus, more appropriate to be considered. The measured value 0.5 pC/MeV is significantly lower than the

baseline one (10.9 pC/MeV) The 176 MeV RMS slice vertical divergence is ≈ 1.8 mrad, nearly twice the baseline one. The electron beam is considerably far from the expected baseline parameters (Table 3.1) and following the fit in Figure 3.15, this shot is not apt for FEL.

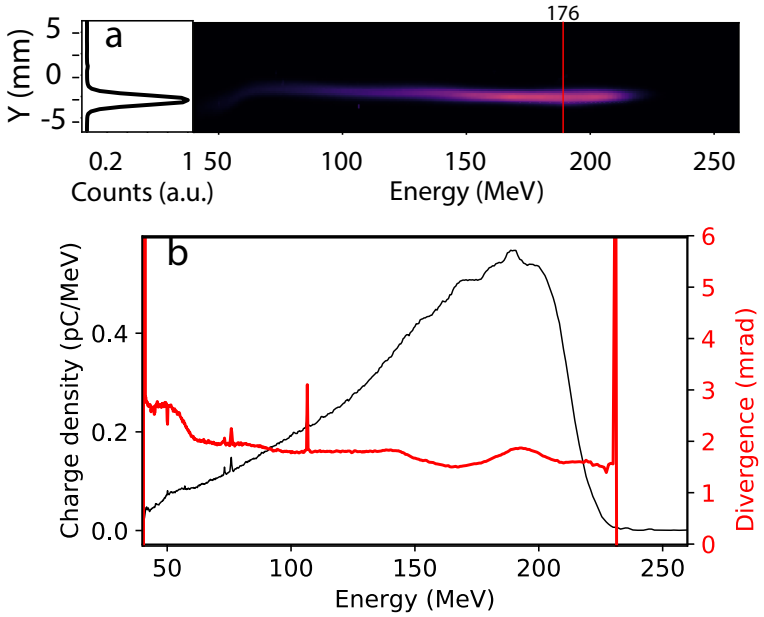

FIGURE 4.1: (a) Calibrated image, 176 ± 0.5 MeV slice vertical projection and (b) slice RMS vertical divergence and charge versus energy shot 10 of the first set taken the 2017/11/30 with gas jet.

TABLE 4.2: Beam and slice FWHM vertical divergence, total and slice experimental charge average at the spectrometer with the respective standard deviation for RUN 4 and the simulated beam with the baseline parameters (Table 3.3).

Date	Slice *MeV*	Slice mean charge (std) *pC*	Slice mean divergence (std) (FWHM) *mrad*	Beam mean divergence (std) (FWHM) *mrad*
Baseline	176 ± 0.5	10.3	2.35	2.35
2017/11/30 Set 1	176 ± 0.5	0.43 (0.08)	4.75 (0.5)	7.45 (0.91)

Figure 4.2a presents 20 shots during the first series taken the day 2017/11/30, with the gas jet target and Table 4.2 shows the series average slice divergence and charge of the set. The 20 shots respective vertical slice projection for the 176 MeV, shown in Figure 4.2b, have a Gaussian shape and an important shot-to-shot pointing variation. Figure 4.2c shows the measured 20 energy distributions. The energy distributions resemble to a flat-top from 50 MeV to ≈225 MeV with a peak around 180 MeV in some occasions. The slice vertical divergence per energy shown in Figure 4.2d presents a plateau between 3 mrad and 5 mrad FWHM from ≈ 60 MeV to ≈ 190 MeV and much higher peaks at 50 MeV and ≈ 220 MeV. The weighted mean of the vertical slice divergence for the energies with a slice charge superior to 0.1 pC yields a mean FWHM vertical beam divergence of 7.45 mrad with an std of 0.91 mrad. At the beginning of the day, with the laser in optimal condition, there is charge in the reference energy slice and the divergence can be compensated by the QUAPEVA triplet, thus, it can be transported to the undulator.

After intense use for extended periods of time, the laser power can decrease [206]. A lower laser power can shorten and delay the wakefield injection, thus, starting after a longer distance inside the plasma, leading to a much lower total charge and a shorter acceleration length. Figure 4.3 shows 20 shots during the last series measured the day 2017/11/30. The energy distributions shown in Figure 4.3b are quite different compared to the morning (Figure 4.2). The electrons barely achieve a maximum of 150 MeV and the distribution peak is mostly at 90 MeV. The decrease in laser power during the day is significant and causes a large decrease of maximum electron energy in the beam, to the point that is not possible to continue any undulator radiation experiment.

The weighted mean beam FWHM vertical divergence can be deduced, giving a value of 6.11 mrad and a std of 0.38 mrad.

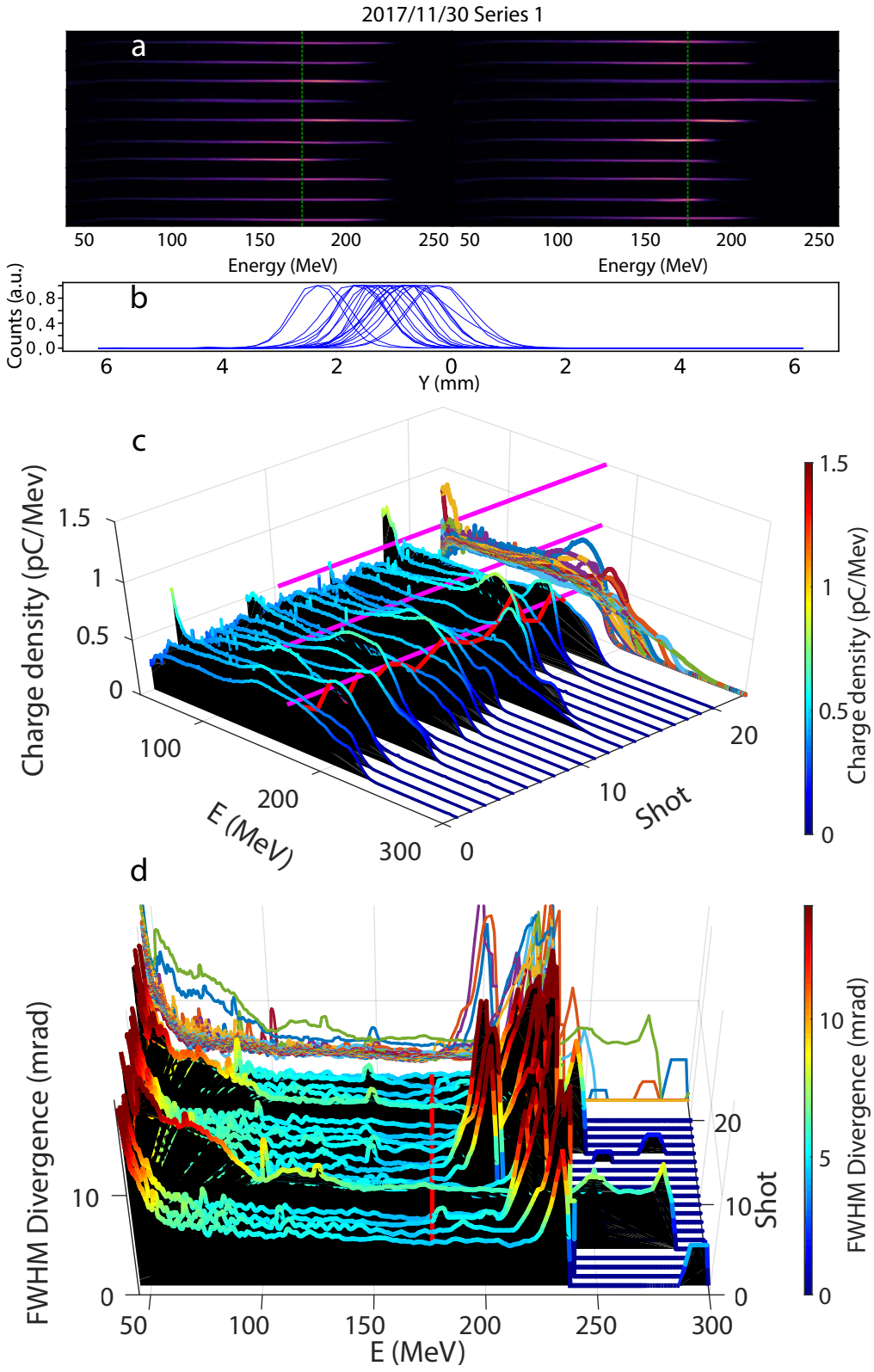

FIGURE 4.2: Beam measurements at the electron spectrometer of the first series of the day 2017/11/30. (a) Calibrated images with the green dotted line at 176 MeV. (b) Vertical projection of the 176 MeV slice for each shot. (c) Charge density versus electron beam energy for the successive shots (purple lines indicating the 0.5, 1 and 1.5 pC/MeV level at $E = 176$ MeV) and (d) 1 MeV width slice FWHM vertical divergence versus energy of each shot.

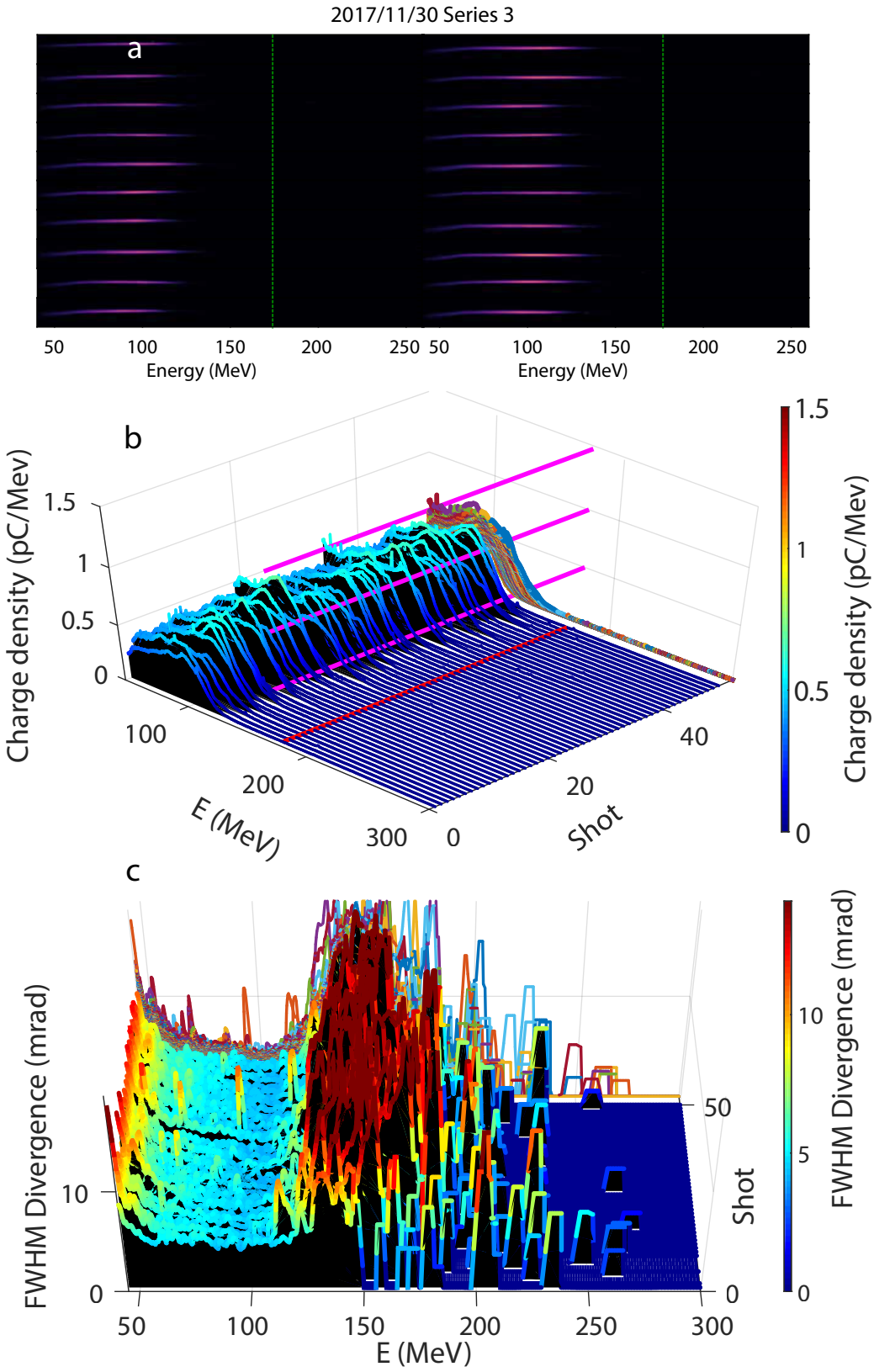

FIGURE 4.3: Beam measurements at the electron spectrometer of the last series of the day 2017/11/30. (a) Calibrated images with the green dotted line at 176 MeV. (b) Charge density versus electron beam energy for the successive shots (purple lines indicating the 0.5, 1 and 1.5 pC/MeV level at $E = 176$ MeV) and (c) 1 MeV width slice FWHM vertical divergence versus energy of each shot.

4.1.1.1.2 Determination of the horizontal divergence at "First imager"

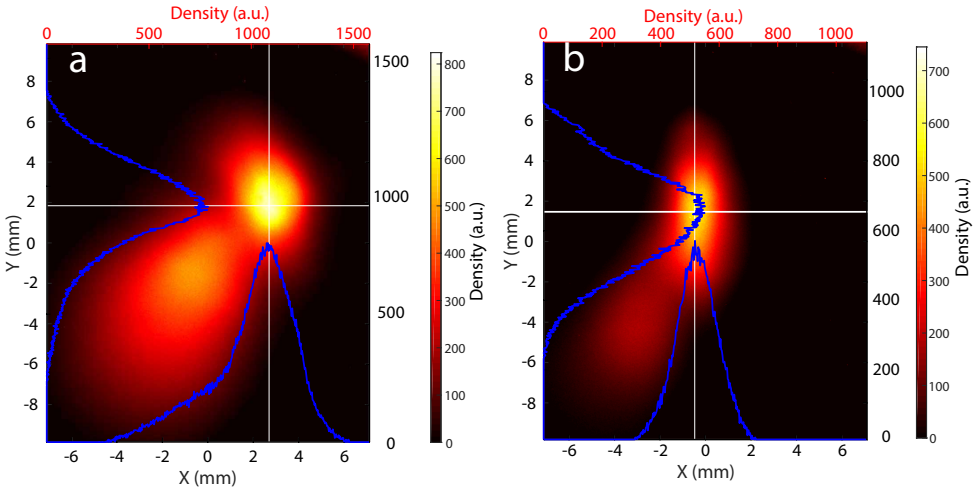

FIGURE 4.4: Measured transversal image taken at the "first imager" the (a) 2017/11/30 at 15:38:21 shot 4 and (b) 2017/11/30 at 18:12:18 shot 1 with white lines indicating the beam most intense pixel and their projections in blue.

Two shots separated by two hours and a half have been chosen to show the gas jet electron beam after a 60 cm drift, i.e., at the "first imager". Figure 4.4a presents a single shot at the "first imager". Two beams can be differentiated, a large with low intensity one and a more focused and intense one. The defocused one is considered being produced by the low energy electrons due to their higher quantity and vertical divergence displayed at the spectrometer compared to the other energy slices. The FWHM total beam horizontal (vertical) divergence is 6.46 mrad (4.39 mrad) yielding a divergence ratio of 1.4. Comparing the vertical beam divergence of the spectrometer set taken close in time (Figure 4.2), the "first imager" vertical beam divergence is 0.59 times lower. Figure 4.4b shows a shot recorded a couple of hours later. Again two beams can be distinguished and the more intense is considered the one containing the reference energy. Nevertheless, as seen in Figure 4.3, the laser degradation can reduce the maximum energy achieved in the electron beam to energies lower than the reference one. Therefore, the elongated more intense beam could correspond to the lower energies while the more round and faint one could be product of energies between 70 MeV to 150 MeV. Moreover, the elongated shape is more in accordance with the less intense beam in Figure 4.4a. Let's consider the more intense beam. The intensity is reduced by 1.5 times with respect to the previously shown shot (Figure 4.4a) and the FWHM total beam horizontal (vertical) divergence is 8.98 mrad (3.15 mrad). The difference between the horizontal and vertical beam sizes is substantially higher, achieving a ratio of 2.8. Therefore, the laser degradation through time affects also the ratio between horizontal and vertical divergence.

4.1.1.2 Gas cell case

The initial gas cell generated electron beam is characterized via the spectrometer and the "first imager".

4.1.1.2.1 Spectrometer data analysis

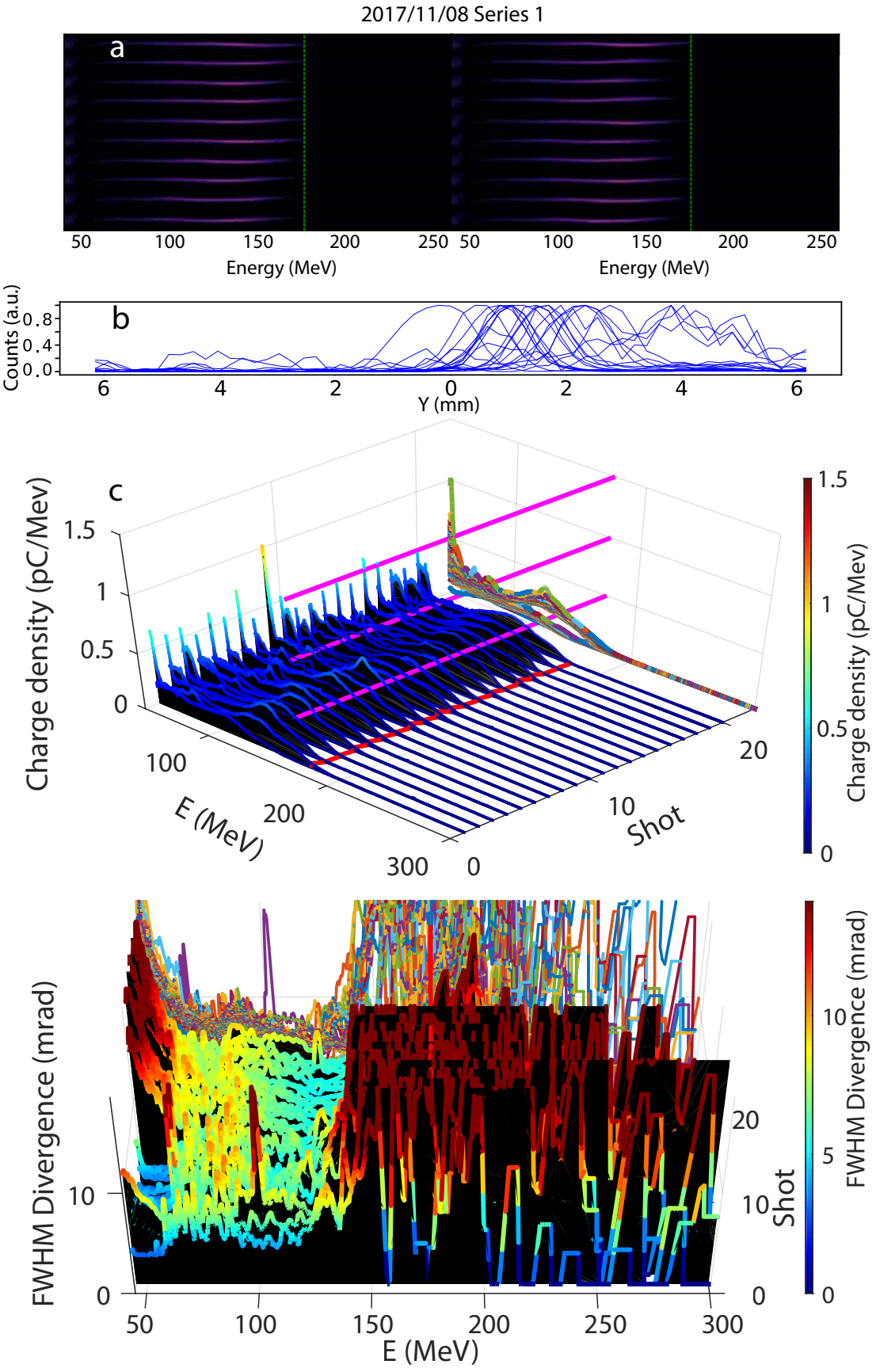

FIGURE 4.5: Beam measurements at the electron spectrometer of the first series of the day 2017/11/08. (a) Calibrated images with the green dotted line at 176 MeV. (b) Vertical projection of the 176 MeV slice for each shot. (c) Charge density versus electron beam energy for the successive shots (purple lines indicating the 0.5, 1 and 1.5 pC/MeV level at $E = 176$ MeV) and (d) 1 MeV width slice FWHM vertical divergence versus energy of each shot.

Figure 4.5a shows 20 shots during the last series measured the day 2017/11/08 with the gas cell target. The reference energy 176 MeV has barely any charge. The reference energy vertical slice projection in Figure 4.5b presents a more important shot-to-shot pointing variation than in the gas jet case (Figures 4.2b, 4.3b), the energy distributions of Figure 4.5c show a shape similar to the gas jet set (Figures 4.2b) but with a peak at $\approx$ 125 MeV and a recurrent low energies high peak. All energies have a much lower slice charge with respect to the gas jet case, with maximum $\approx$ 0.3 pC/MeV, except for the low energies peak. The reference energy is at the end of the high energies tail with barely any slice charge. The slice vertical divergence per energy distribution in Figure 4.5d presents an irregular peaked divergence distribution with FWHM values between 4 mrad and 10 mrad for the energies with some charge, i.e., $[60, 140]$ MeV. The weighted mean FWHM vertical beam divergence found in this set is of 13.46 mrad with an std of 0.19 mrad, higher than any of the previous gas jet sets. The gas cell target yields a much more unstable beam generation probably because of the laser shot-to-shot variation, since the gas cell was carefully prepared and maintained regularly.

4.1.1.2.2 "First imager" data analysis

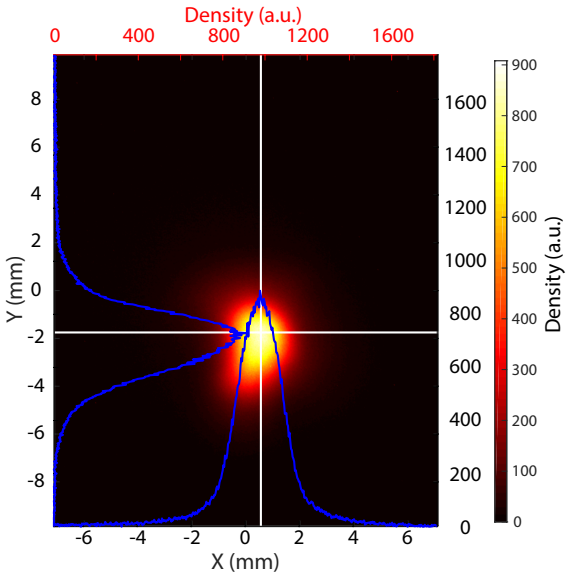

FIGURE 4.6: Measured transversal image taken at the "first imager" the 2017/11/10 at 18:06:07 shot 1 with white lines indicating the beam most intense pixel and their projections in blue.

Figure 4.6 presents a gas cell electron beam at the "first imager". A single beam is observed unlike the gas jet case (Figure 4.4). The horizontal and vertical total beam divergences deduced are 3.71 mrad and 2.42 mrad respectively, lower than the gas jet shots and the spectrometer data. The horizontal-vertical divergence ratio obtained for this shot is 1.5, similar to the gas jet in optimum conditions (Figure 4.4).

4.1.2 Systematic comparison between gas cell and jet (RUN 4)

During RUN 4 a substantial number of shots were done in both cell and jet targets. The analysis of all shots gives an accurate insight of the LPA beam average characteristics, variation and evolution in time for each gas target permitting their performance comparison.

4.1.2.1 Spectrometer data analysis

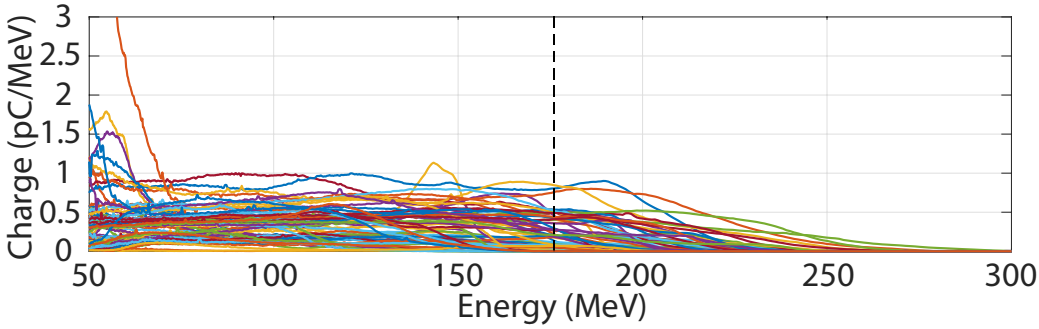

FIGURE 4.7: Examples beam energy distributions at the electron spectrometer during the RUN 4 for the gas jet. The black dotted line corresponds to the reference energy 176 MeV.

Figure 4.7 shows examples of beam energy distributions of RUN 4. The maximum energy achieved by the tail is ≈ 300 MeV. The reference energy 176 MeV is more often in the plateau of the distribution than in the peak. The beam distribution changes significantly from day to day and even in the same day (Figures 4.2 and 4.3).

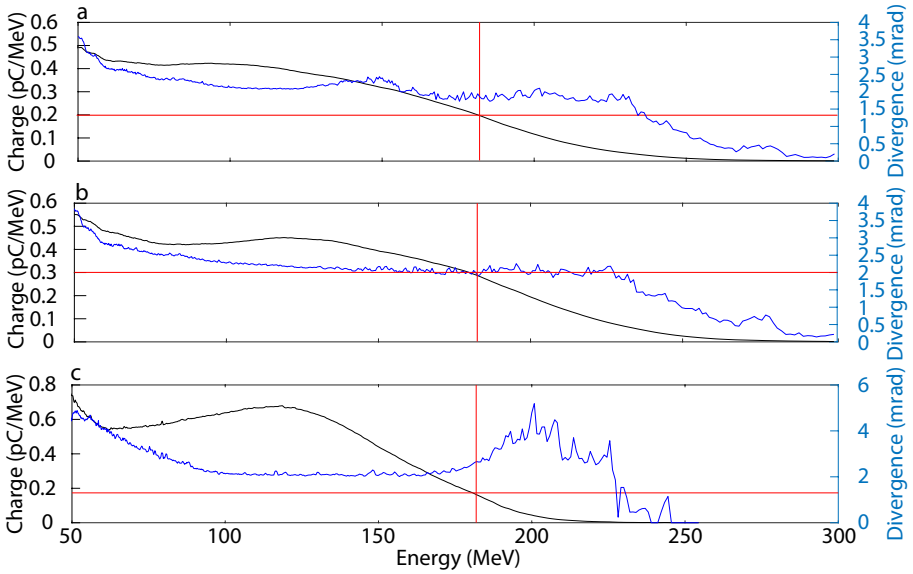

FIGURE 4.8: Initial beam energy distribution (black) and vertical (blue) RMS divergence for energy slices of ±0.5 MeV, spectrometer resolution. (a) Average of the gas jet shots of RUN 4, 370 shots (Figure 4.9), (b) without the worst days, 160 shots, (c) Average over a set of 20 distributions from the second set taken the 2017/11/30 [196].

TABLE 4.3: Total and slice experimental charge and vertical FWHM divergence of the energy distributions of Figure 4.8.

Distribution	Shots	Q_t pC	$Q_{176\pm0.5}$ pC	$\sigma'_{y,176\pm0.5}$ $mrad$
"All gas jet shots" (Figure 4.8a)	370	196	0.2	4.46
"Good shots" only (Figure 4.8b)	160	215	0.3	4.7
"Set average" (Figure 4.8c)	20	307	0.19	5.4

Figure 4.8 shows three average energy distributions and 1 MeV width slice vertical divergence deduced from data of RUN 4 with its values of total charge and reference slice charge and FWHM divergence in Table 4.3. Three data sets are used for the average: all gas jet shots (Figure 4.8a), best shots corresponding to 43% of all gas jet shots (Figure 4.8b) and a 20 shot series (Figure 4.8c). The shot-to-shot energy distribution variations

clearly translates into differences between Figure 4.8a and 4.8b. Ignoring the shots with almost no charge on the reference slice 176±0.5 MeV, the average reference slice charge sees increases 1.5 times with respect to the case with all gas jet shots (Table 4.3). Nevertheless, the reference slice divergence remains almost the same. The set average shows a high total charge with a vertical divergence and reference slice charge inside the RUN 4 average (Table 4.3).

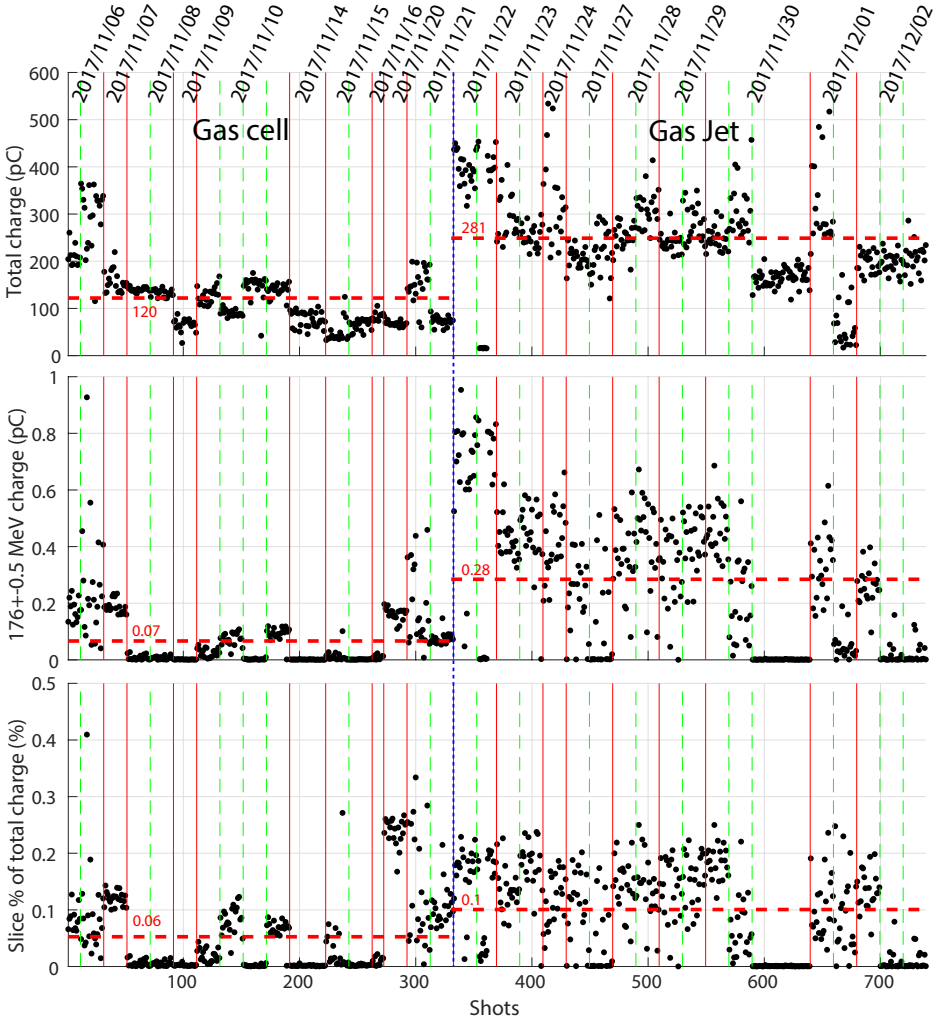

FIGURE 4.9: (a) Total beam charge, (b) 176 ± 0.5 MeV slice charge and (c) percentage of the total beam charge corresponding to the charge in the slice measured at the spectrometer during RUN 4 versus time, separation by configuration (blue dotted line), day (red line) and series (green dotted line).

Figure 4.9 shows the beam total and slice charge at the electron spectrometer for RUN 4, for 739 successive shots. The dates from 2017/11/06 to 2017/11/21 correspond to the gas cell target, while the rest corresponds to the gas jet target. The main difference between the gas cell and gas jet is in the gas distribution. The sharp density increase (Figure 5.1b) at the entrance of the gas cell affects the beam focusing over time and thus, the wakefield. In terms of the LPA main electron bunch, this translates into a single short injection and acceleration phases which yields a lower charge and energy but a much lower energy spread. While, the gas jet slow increase (Figure 5.1a, c) allows for a long injection and acceleration phases, resulting in a higher charge, energy spread and maximum electron energy. For the gas cell (2017/11/06-2017/11/21), a higher stability of the total and reference slice 176 ± 0.5 MeV charge can be observed. The energies obtained are too low and thus, the slice charge rarely goes above 0.2 pC. For the gas jet (2017/11/22-end), most shots offer a higher charge, with twice the average total charge and four times the average slice charge than the gas cell one. In average, 0.1 % of the beam charge corresponds to the reference slice charge. In both gas configurations, the slice 176 ± 0.5 MeV charge strongly evolves with time. On days where multiple series of consecutive shots were taken (e.g. 2017/11/30 or 2017/12/02), the charge even decreases by a factor two between series, leaving at the end of the day barely any charge in the slice 176 ± 0.5 MeV. The variations of shot-to-shot charge are larger in the gas jet than in the gas

cell case and in some days (e.g. 2017/12/01) there are many "bad" shots. The variation of laser power with time is one of the hardest experimental challenges, because it limits the operation time per day that one can use to prepare and execute FEL experiments.

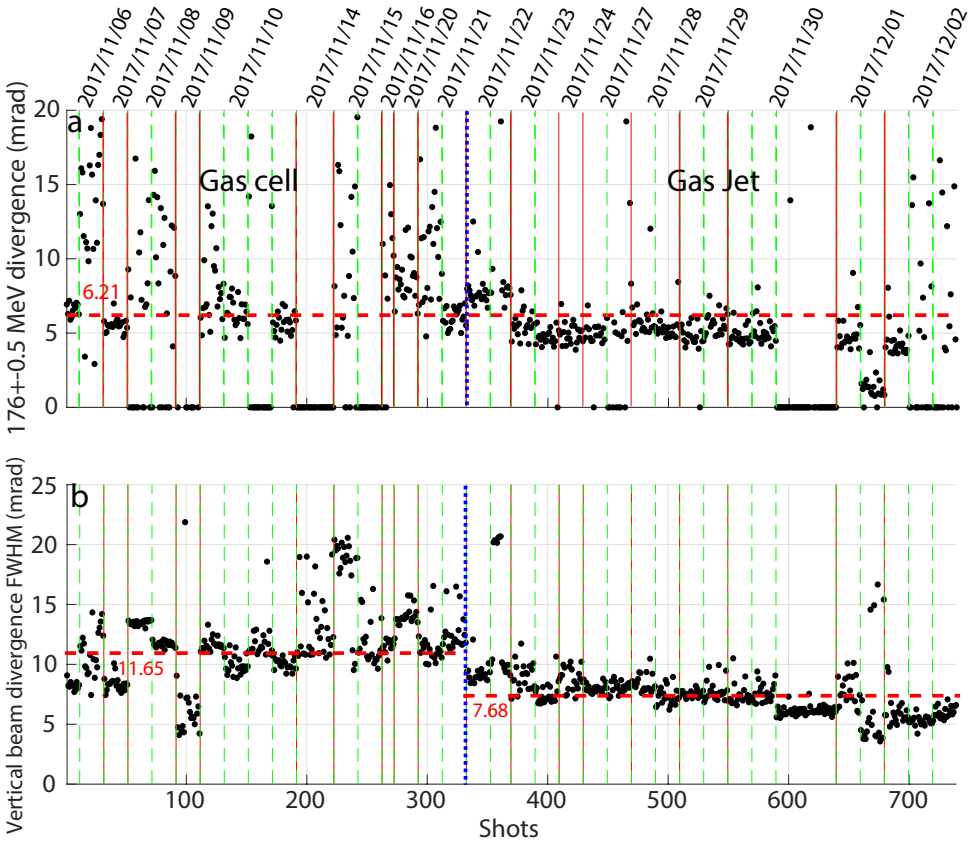

FIGURE 4.10: Measured FWHM (a) slice and (b) total vertical divergence with the electron spectrometer during RUN 4 versus time, separation configuration (blue dotted line), day (red line) and series (green dotted line).

Figure 4.10a presents the slice vertical divergence measurements during RUN 4 taken at the spectrometer. RUN 4 shows an average FWHM slice vertical divergence of 6.21 mrad with a low shot-to-shot stability (Table 4.4). The sudden 0 mrad and $>$ 10 mrad values of the vertical divergences are caused by a slice charge close or equal to 0 pC (see Figures 4.9, 4.7a). The gas cell gives an average FWHM slice vertical divergence of 7.35 mrad with an std of 2.87 mrad, more than three times the baseline one. The gas jet yields a higher shot-to-shot stability and the FWHM vertical slice divergence is lower than the gas cell one with a value of 5.26 mrad and a std of 2.08 mrad. The FWHM total beam vertical divergence in Figure 4.10b, shows for the gas cell a mean of 11.65 mrad with a std of 3.03 mrad when the day 2017/11/21 is included and a value of 11.59 mrad with an std of 3.17 mrad when excluded. The divergence is unstable shot-to-shot and also between days with jumps of more than 3 mrad in both cases. The gas jet, as in the slice case, presents a higher stability in general compared to the gas cell. The FWHM vertical beam divergence is significantly lower than the gas cell one with an average value of 7.68 mrad and a std of 2.37 mrad. The gas jet vertical beam divergence decreases with time achieving at the end of RUN 4 $\approx$ 5.9 mrad.

4.1.2.2 "First imager" data analysis

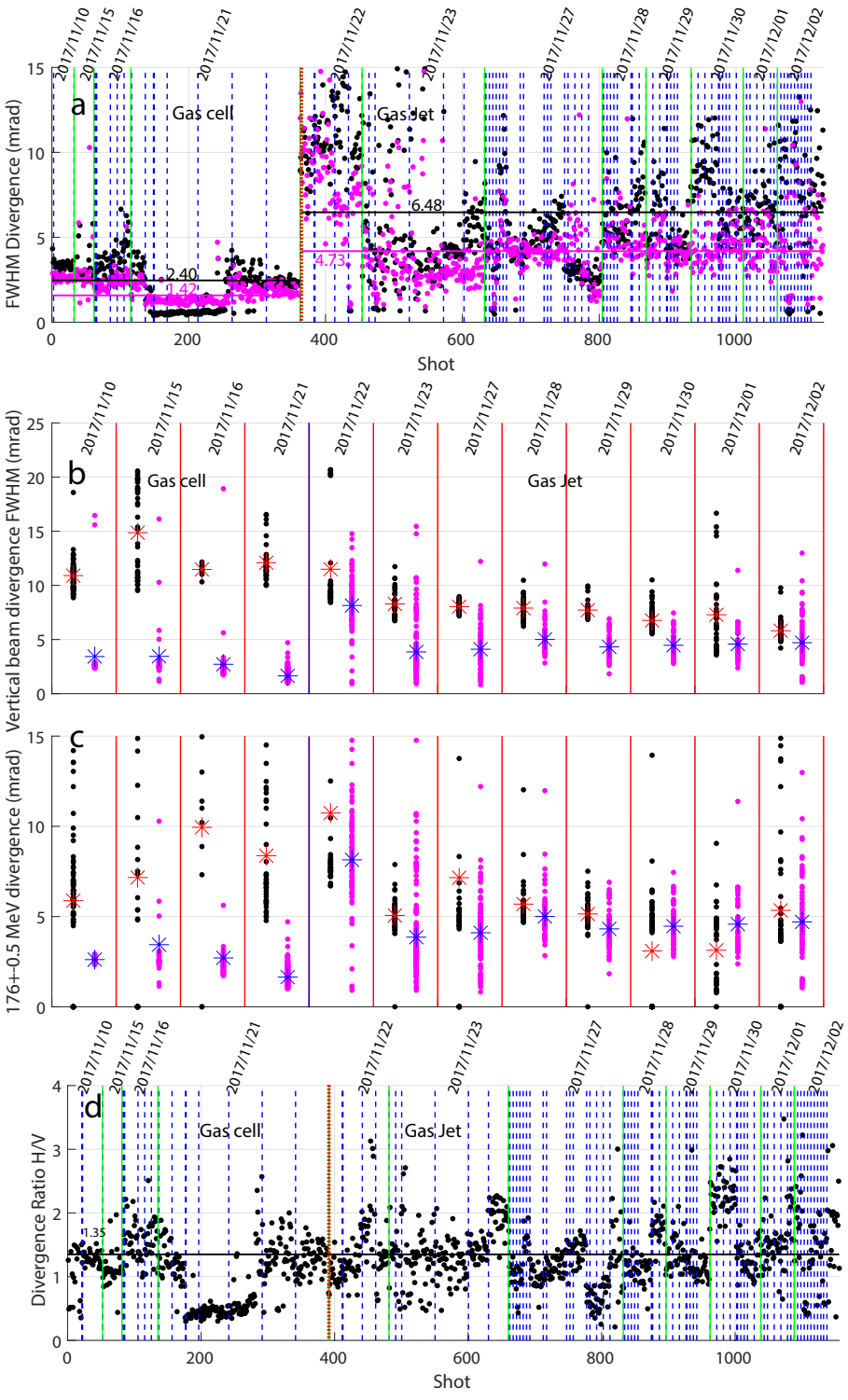

FIGURE 4.11: (a) Vertical (purple dots) and horizontal (black dots) total beam divergence measured at the "first imager" during RUN 4. (b) Vertical (purple dots) and horizontal (black dots) total beam divergence measured at the "first imager" during RUN 4. (c) FWHM vertical total beam divergence measured at the "first imager" (purple dots) and at the spectrometer (black dots) and their corresponding average values per day (spectrometer red stars; "first imager" blue stars) during RUN 4. (d) Divergence ratio σ'_x/σ'_y measured at the "first imager" during the entirety of RUN 4 in chronological order, separation configuration (red dotted line), day (green line) and series (blue dotted line).

The FWHM vertical and horizontal total beam divergences measured at the "first imager" are presented in Figure 4.11a. Globally the horizontal beam divergence is larger to the vertical one, with the exception of some sets during the 2017/11/21, due to the setup changes done on that day. The gas cell (2017/11/06 - 2017/11/21) offers a stable shot-to-shot beam divergence with an average horizontal and vertical FWHM divergence including (excluding) the day 2017/11/21 of 2.40 mrad and 2.03 mrad (2.87 mrad and 3.96 mrad) respectively and std of 1.42 mrad and 2.46 mrad (2.19 mrad and 3.64 mrad). The gas jet (2017/11/22 - 2017/12/02) has a significantly higher vertical (horizontal) FWHM beam divergence of 4.73 mrad (6.48 mrad) and std of 2.28 mrad (3.43 mrad). The shot-to-shot instability is also worse compared to the gas cell. The higher stability of the gas cell differs from the data of the spectrometer where the gas jet shots are more stable in the beam and slice vertical divergence (Figure 4.10).

Figure 4.11b compares the FWHM vertical total beam divergence measured at the spectrometer and at the "first imager" at each day. The gas cell spectrometer data presents a day average difference with the "first imager" between ≈ 7 mrad and ≈ 12 mrad which is outside the spectrometer and "first imager" std, i.e., 3.03 mrad and 2.19 mrad respectively. For the gas jet, the day average difference between the data is reduced to ≈ 3 mrad in the worst case (2017/11/23). In this case, the variations are inside the std for both the spectrometer and "first imager" data std, i.e., 2.37 mrad and 2.28 mrad respectively. Therefore, for the gas jet a fair agreement is found between both diagnostics. As seen in Section 4.1.1.1 a grand part of the beam electrons have vertical divergences withing a couple mrad with respect to each other with the exception of the low energy electrons. Therefore, one could expect the reference slice vertical divergence obtained from the spectrometer to not be far from the vertical total beam divergence deduced from the "first imager". Figure 4.11c presents the comparison between the reference slice vertical divergence and the vertical beam divergence data of each day. The mean vertical divergences differ by up to ≈ 8 mrad in the gas cell days while the gas jet shows a fair agreement of the means with at worst a difference of ≈ 3.5 mrad. The gas cell disparity comes from the less uniform and more spiked vertical divergence energy distribution observed (Figure 4.5). Thus, such comparison is not appropriate in the gas cell case. Figure 4.11d shows all measurements of the horizontal-vertical divergence ratio done during RUN 4 (1156 shots). Most shots ratios are between 1 and 2. The gas cell (2017/11/06 - 2017/11/21) shows an average ratio of 1.14 and std of 0.7. The 2017/11/21 data presents a more unstable beam with a lower ratio due to the modifications in the configuration before the change to the gas jet. The average ratio without the data from 2017/11/21 significantly rises to 1.49 with a std of 0.9. In terms of average FWHM reference slice horizontal divergence, the ratio yields 11 mrad (Table 4.4). The gas jet (2017/11/22 - 2017/12/02) shows a higher shot-to-shot instability. The average ratio is of 1.45 with a std of 1.1, which translates into a FWHM reference slice horizontal divergence of 7.6 mrad (Table 4.4). Comparing the gas jet results with the gas cell without the 2017/11/21 data, the average is close but the gas cell stability continues to be slightly higher. Variation of the divergence ratio during the day is observed. The time gradient of the ratio is irregular, with some days increasing (e.g., 2017/11/10 and 2017/11/23) and others decreasing (e.g., 2017/11/29). RUN 4 average values of the "first imager" measurements are summarized in Table 4.4.

TABLE 4.4: Beam 176 ± 0.5 MeV slice FWHM vertical divergence, total and slice experimental charge average at the spectrometer with the respective standard deviation and average beam divergences and horizontal-vertical divergence ratio for RUN 4 and the simulated beam with the baseline parameters (Table 3.3).

	Spectrometer				**"First imager"**		
RUN	**Mean charge (std)**		Mean divergence FWHM (std)		**Mean beam divergence FWHM (std)**		Mean $\frac{\sigma'_x}{\sigma'_y}$ (std)
	Total *pC*	Slice *pC*	Slice *mrad*	Total *mrad*	Vertical *mrad*	Horizontal *mrad*	
Baseline	34	10.9	2.35	2.35	1	1	1
4	193 (97)	0.19 (0.18)	6.21 (1.29)	9.47 (3.33)	2.03 (1.42)	2.40 (2.46)	1.10 (0.52)
4 (gas cell)	120.3 (66.8)	0.07 (0.11)	7.35 (2.87)	11.65 (3.03)	2.87 (2.19)	3.96 (3.64)	1.41 (0.47)
4 (gas jet)	280.7 (110.5)	0.27 (0.23)	5.26 (2.08)	7.68 (2.37)	4.73 (2.28)	6.48 (3.43)	1.45 (1.10)

4.1.2.3 FEL capabilities of the measured electron beams

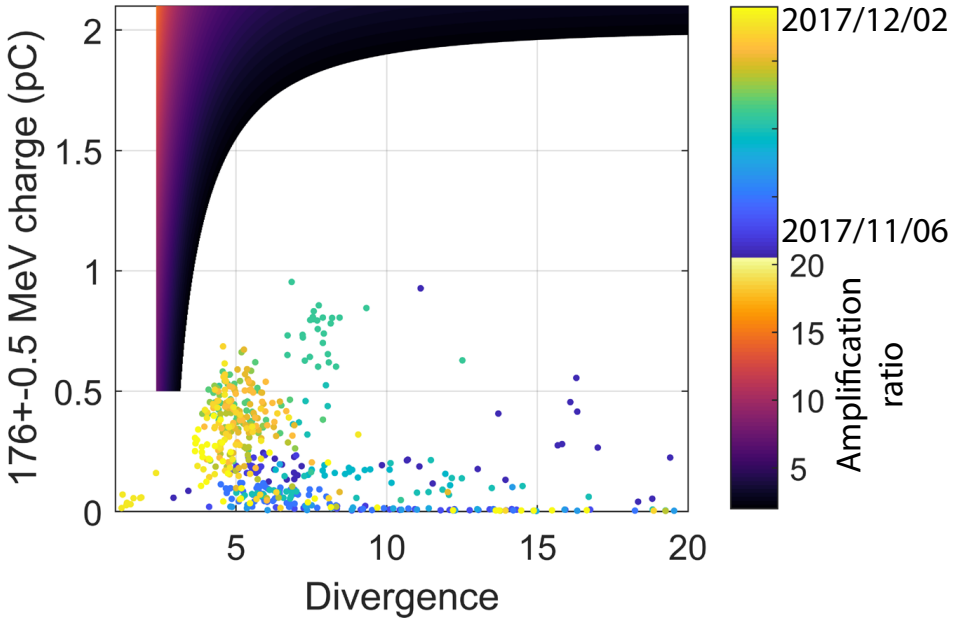

FIGURE 4.12: Slice charge versus FWHM divergence measured at the spectrometer for RUN 4. Shots sorted versus time when the series was taken according to the dots colormap with dark blue (yellow) corresponding to the start (end) if the RUN. Colored zone corresponding to low gain FEL zone deduced with the fit $f_{amp}(\sigma'_y, Q_{slice}) = -5.41 + 12.25\sigma_y^{'-2} + 2.2Q_{slice}^{1.744}$ (with Q_{slice} the slice charge and $f_{amp} \geq 2$) of the FEL radiation power achieved by a flat-top electron beam of 4 % energy spread with $\epsilon = 1$ mm.mrad and different initial divergences and beam slice charge obtained via simulations (Figure 3.14) [201]

Figure 4.12 shows the reference slice charge versus divergence for all shots of RUN 4 and the colored part corresponds to the $f_{amp} > 2$ zone where FEL should be achievable deduced from the simulation fit (Figure 3.15) [201]. None of the shots could be able to generate FEL. Thus, a higher slice charge or a lower divergence while keeping the same slice charge is needed for FEL. The gas cell target was abandoned to the gas jet setting, due to its produced beams of higher and more stable charge with a similar divergence. In both gas targets the beam charge and divergence were far from the baseline.

4.2 Case of the 161 MeV reference slice (RUN 5)

In RUN 5, some changes were done to the setup in search for improved LPA characteristics to approach the baseline parameters. The reference energy was shifted to 161 MeV. Aiming to a lower energy means that the acceleration length needed inside the plasma to obtain a peak centered at 161 MeV is reduced.

4.2.1 Spectrometer data analysis

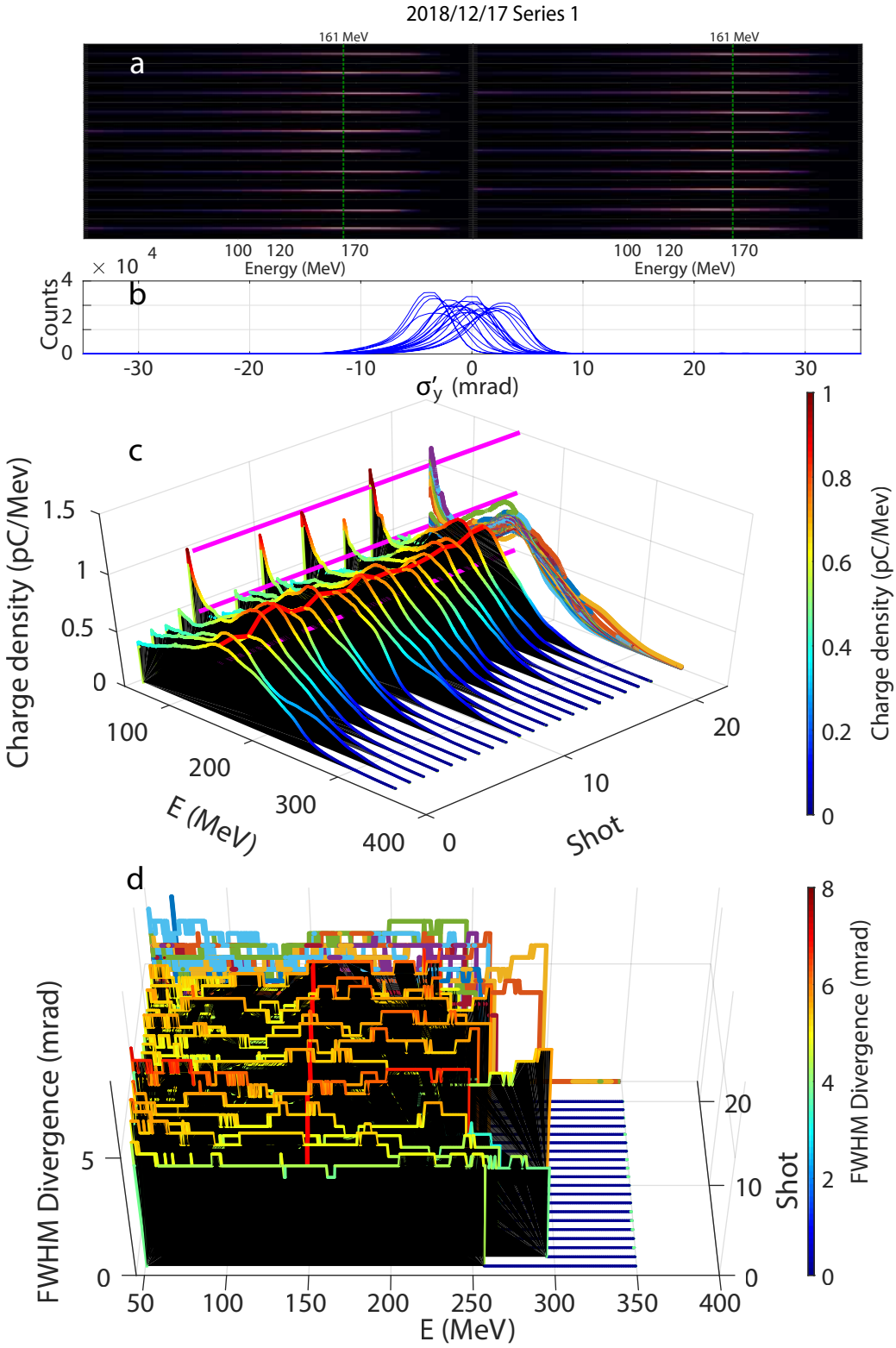

FIGURE 4.13: Beam measurements at the electron spectrometer of the first series of the day 2018/12/17. (a) Calibrated images with the green dotted line at 161 MeV. (b) Vertical projection of the 161 MeV slice for each shot. (c) Charge density versus electron beam energy (purple lines indicating the 0.5, 1 and 1.5 pC/MeV level at $E = 161$ MeV) (d) 1 MeV width slice FWHM vertical divergence versus energy for the successive shots

Figure 4.13a shows the first measured 20 shot series the 2018/12/17. The green dotted line corresponds to the screen horizontal position for the 161 MeV. All shots in the series show a broad energy range from 50 MeV to ≈ 270 MeV. The vertical projections of the 161 MeV slice are shown in Figure 4.13b. A reduction of shot-to-shot pointing can be appreciated with respect to RUN 4 (Figure 4.2b) thanks to the optimization of the gas density and the more stable laser. The 20 shots energy distribution (Figure 4.13c) are close to a broad Gaussian with its peak at the reference energy 161 MeV, with a tail into the high energies and in some occasions, with a large number of low energy electrons. The slice charge on peak is around 0.76 pC/MeV. The distribution is stable with the exception of the high peak in the 50 MeV energies in some shots due to the gas distribution and laser improvements. The FWHM divergence per MeV slice (Figure 4.13d) varies shot-to-shot between 4 mrad and 6 mrad and it is mostly flat. The FWHM vertical beam divergence can be obtained from the weighted mean of the slice divergences with a charge higher than 0.1 pC and it yields a set average value of 4.95 mrad with a std of 0.5 mrad.

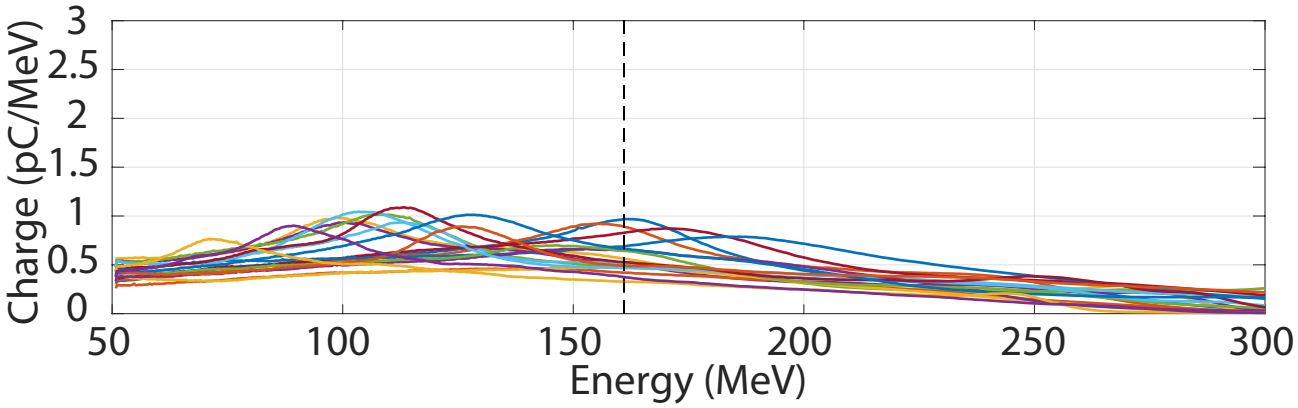

FIGURE 4.14: Examples beam energy distributions at the electron spectrometer during the RUN 5. The black dotted line corresponds to the reference energy 161 MeV.

Figure 4.14 presents some beam energy distributions of RUN 5. The broad Gaussian shape appears in all examples but the peak shifts between ≈ 120 MeV and ≈ 180 MeV. The peak is surrounded by long tails in both, high and low energy sides. Such a shape may indicate the existence of a single main electron injection event inside the gas and a less important continuous injection. The maximum electron energy exceeds in occasions 300 MeV.

Figure 4.15 presents the total and slice 161±0.5 MeV charges during RUN 5. A clear increase in shot-to-shot stability due to the laser optics improvements is observed. The total beam charge average is 107.69 pC, 2.5 times lower than in RUN 4, with an std of 23.3 pC (Table 4.5). Nevertheless, the reference slice 161±0.5 MeV charge average is 0.55 pC, twice the RUN 4's reference energy slice value, with an std of 0.19 pC (Table 4.5), also lower than the RUN 4 one. When multiple series were taken at different times of a same day (i.e., 2018/12/17, 2018/12/20 and 2018/12/21), a charge drop with time was observed. The lower total charge with a higher reference energy slice charge translates into a five times increase of the slice percentage of total charge with respect to RUN 4. Thus, the energy transfer between laser and electrons is more efficient due to a decrease of the wakefield radius or an increase of acceleration length. In some cases (2018/12/17), a drop in total charge occurs while the slice percentage of total charge sees an increase, meaning that higher or lower energies are the ones with a lower charge.

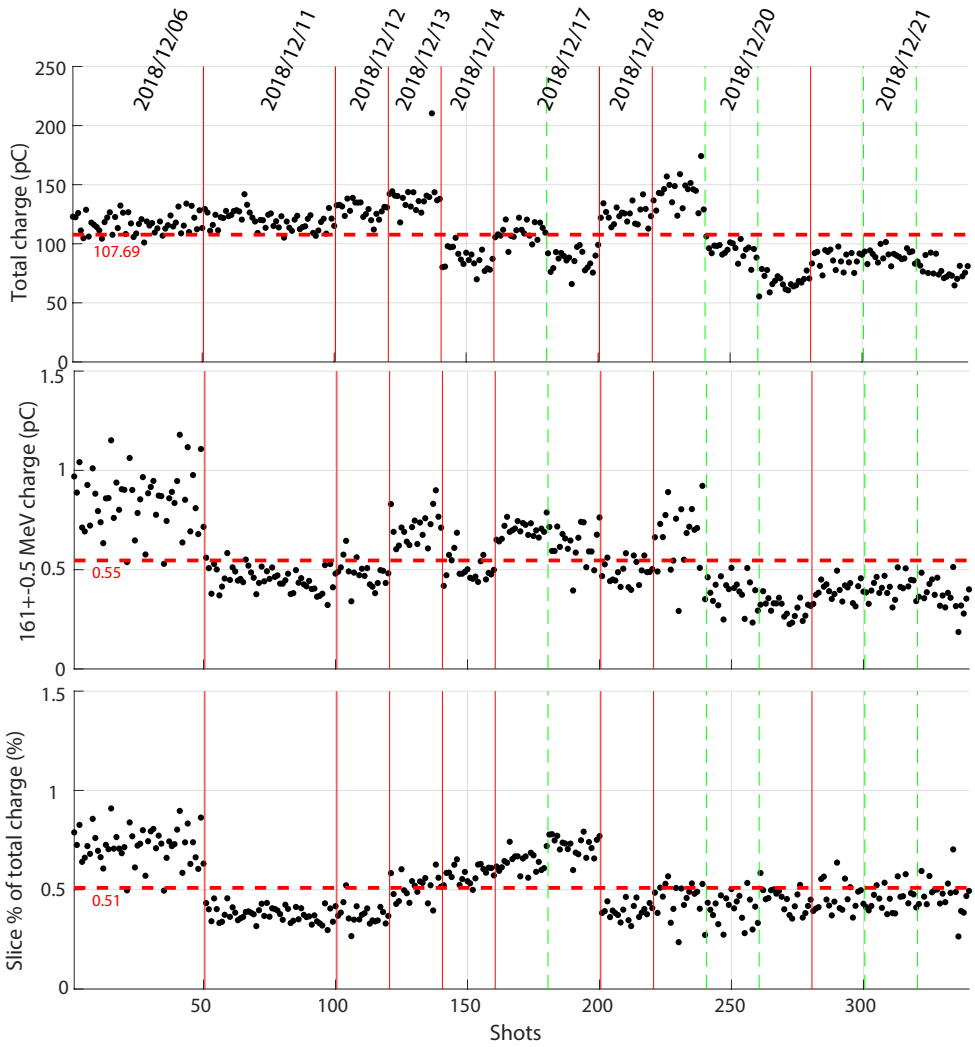

FIGURE 4.15: (a) Total beam charge, (b) 161 ± 0.5 MeV slice charge and (c) percentage of the total beam charge corresponding to the charge in the slice measured at the spectrometer during RUN 5 sorted by time and separated by day (red line) and series (green dotted line).

Figure 4.16a shows the FWHM divergence of the slice 161±0.5 MeV during RUN 5. The average divergence decreases with respect to RUN 4 data to a value of 4.54 mrad with a lower std of 1.29 mrad (Table 4.5). A clear decrease in divergence can be appreciated with time during each day. The average FWHM vertical beam divergence during RUN 5 in Figure 4.16b yields an average value of 4.9 mrad and a std of 1.23 mrad. The values are close to the vertical slice divergence (Figure 4.16a) due to the flat divergence energy distribution presented by the beams (Figure 4.13). The average vertical beam divergence is lower than in the gas jet case of RUN 4 (Figure 4.10b) by 2.78 mrad. As in RUN 4, the lowest values are found the last day of the RUN (2018/12/21).

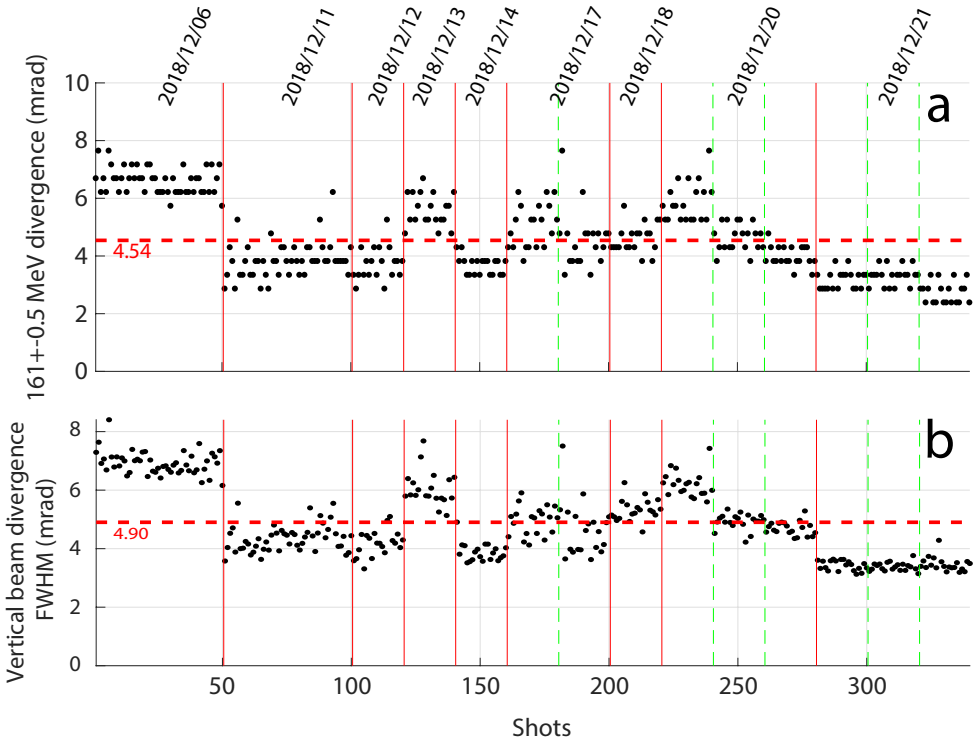

FIGURE 4.16: Measured FWHM (a) slice and (b) total vertical divergence at the electron spectrometer during RUN 5 sorted by time and separated by day (red line) and series (green dotted line).

4.2.2 "First imager" data analysis

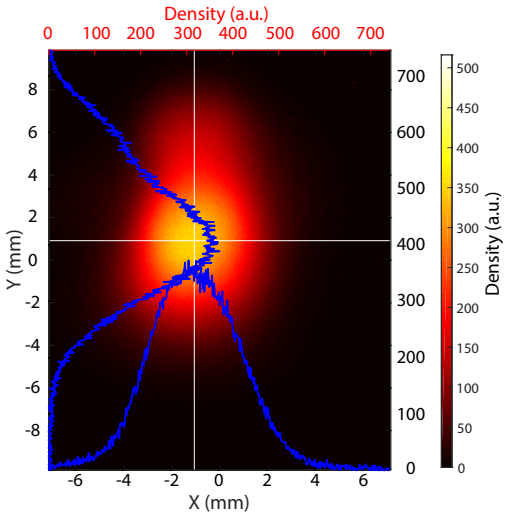

FIGURE 4.17: Measured transversal image taken at the "first imager" the 2018/12/14 at 18:12:33 shot 3 with white lines indicating the beam most intense pixel and their projections in blue.

The "first imager" shot presented in Figure 4.17 has a larger size and a lower intensity compared to RUN 4 examples. The beam shape is round with a vertical tail upwards. The deduced vertical (horizontal) FWHM total beam divergence is 6.9 mrad (10.93 mrad) and the horizontal-vertical divergence ratio is 1.58.

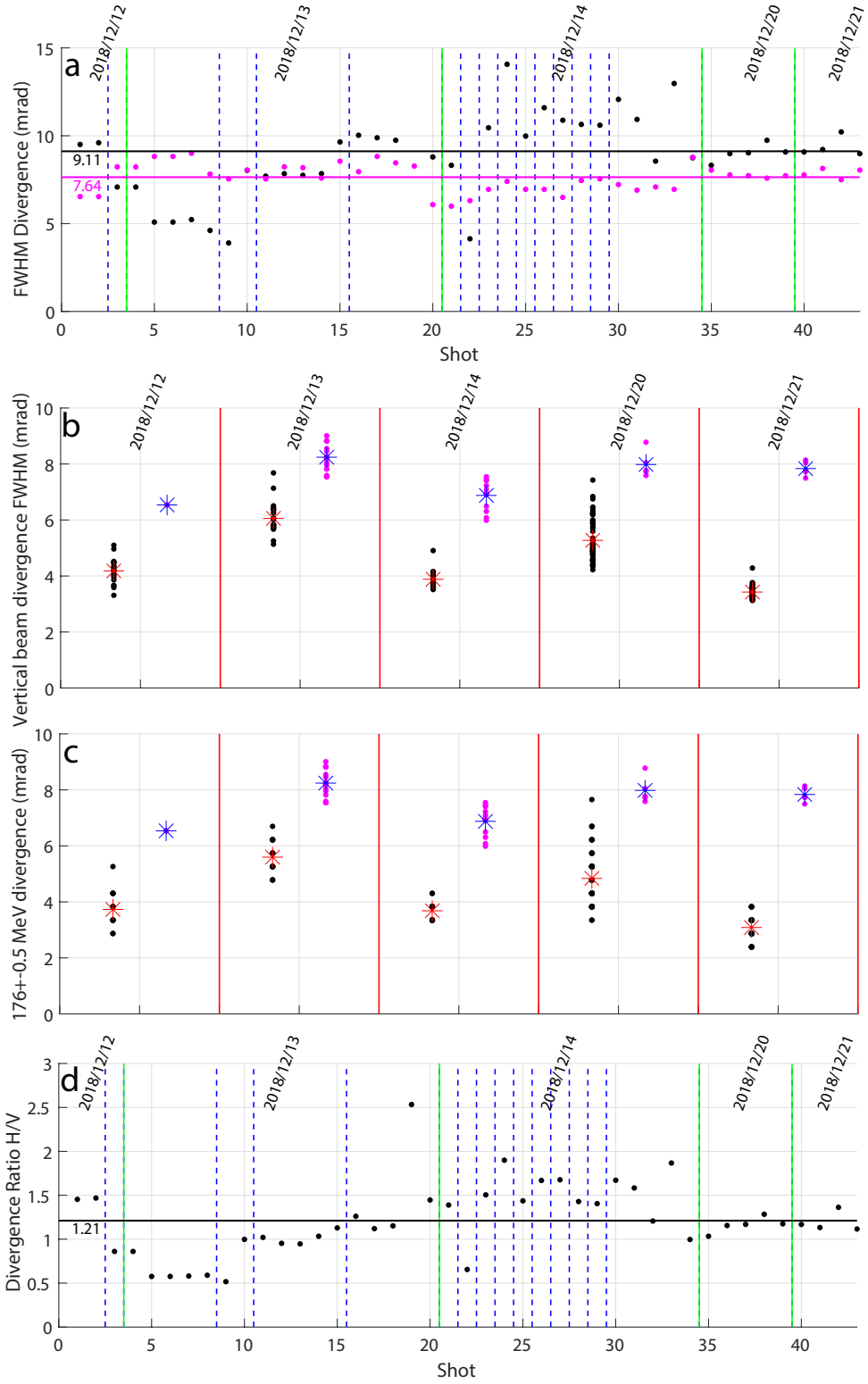

FIGURE 4.18: (a) Vertical (purple dots) and horizontal (black dots) FWHM total beam divergence measured at the "first imager" during RUN 5. (b) FWHM vertical total beam divergence measured at the "first imager" (purple dots) and at the spectrometer (black dots) and their corresponding average values per day (spectrometer red stars; "first imager" blue stars) during RUN 5. (c) FWHM vertical total beam divergence measured at the "first imager" (purple dots) and reference slice divergence at the spectrometer (black dots) and their corresponding average values per day (spectrometer red stars; "first imager" blue stars) during RUN 5. (d) Divergence ratio σ'_x/σ'_y measured at the "first imager" during the entirety of RUN 5 in chronological order, with the blue lines separating series of shots and the green lines separating days.

Figure 4.18a presents the FWHM vertical and horizontal total beam divergences at the "first imager". The

mean vertical beam divergence is 7.64 mrad with a std of 0.78 mrad, thus, offering a more stable shot-to-shot stability when compared to RUN 4 (Table 4.4). The horizontal beam divergence is in general higher than the vertical one with few exceptions. The horizontal beam divergence average is 9.11 mrad with a std of 2.89 mrad. The horizontal beam divergence stability is poorer than the vertical divergence one. No clear evolution of the values with time is observed probably due to the low number of shots taken. Figure 4.18b shows the day by day comparison of the measured spectrometer and "first imager" FWHM vertical total beam divergence throughout RUN 5. There is a difference between day averages of $\approx$ 2.5 mrad, with the exception of the day 2018/12/21 where they differ by $\approx$ 4.2 mrad. The cause of the rise in the values average disparity is difficult to pinpoint exactly as the shots at each diagnostic are taken at different times and the evolution. Nevertheless, neglecting the last day, the average value evolution per day is similar in both diagnostics. The comparison between the FWHM reference slice and total beam vertical divergence in Figure 4.18c is similar to the vertical beam divergence one (Figure 4.18b) due to the flat top like divergence energy slice distribution of the beams. A difference of $\approx$ 3 mrad between their day averages appears, except the 2018/12/21 where the difference achieves the $\approx$ 5 mrad. The evolution trend per day is similar in both cases. Figure 4.18d shows all measurements of the divergence ratio done during RUN 5 (43 shots). Although no much data was taken for this purpose during RUN 5, the average ratio is 1.21 with an std of 0.40, lower than the gas jet results of RUN 4. Using the average vertical divergence measured at the spectrometer (Table 4.5) the estimated FWHM reference slice horizontal divergence is 5.5 mrad, much lower than the average at the "first imager". The ratio variation during the day can only be analyzed for the 2018/12/13, where it increases by approximately 2.5 times with respect to the first set taken that day. RUN 5 average values of the "first imager" measurements are summarized in Table 4.5.

TABLE 4.5: Beam 161 ± 0.5 MeV slice FWHM vertical divergence, total and slice experimental charge average at the spectrometer with the respective standard deviation and average beam divergences and horizontal-vertical divergence ratio for RUN 5 and the simulated beam with the baseline parameters (Table 3.3).

	Spectrometer				**"First imager"**		
RUN	**Mean charge (std)**		Mean divergence FWHM (std)		**Mean beam divergence FWHM (std)**		Mean $\frac{\sigma'_x}{\sigma'_y}$ (std)
	Total *pC*	Slice *pC*	Slice *mrad*	Total *mrad*	Vertical *mrad*	Horizontal *mrad*	
Baseline	34	10.9	2.35	2.35	1	1	1
5	107.7 (23.3)	0.55 (0.19)	4.54 (1.29)	4.90 (1.23)	7.64 (0.78)	9.11 (2.89)	1.21 (0.40)

4.2.3 FEL capabilities of the measured electron beams

Figure 4.19 presents the reference slice charge versus divergence for all RUN 5 shots. The higher slice charge and lower divergence than in RUN 4 makes some shots enter the FEL zone at the border $f_{amp} = 2$, especially towards the end of the RUN. Nevertheless, only 1.4 % of the shots, i.e. three, are inside the $f_{amp} > 2$ fitted zone, the highest f_{amp} value achieved is $\approx$ 3.5 for two shots and they don't correspond to consecutive shots. The average is of 3.5 with a std of 0.08. The beam characteristics are still far from the baseline parameters. The best shots for the FEL search were achieved during the firsts day of RUN 5 (FWHM divergences of 3-4 mrad, slice energies of 1 - 1.2 pC). The reference slice charge decreased each day (Figure 4.19) halving by the end of the RUN. A way to improve f_{amp} is to increase the reference slice charge to $>$ 1.7 pC/MeV, therefore, giving more room for higher divergences.

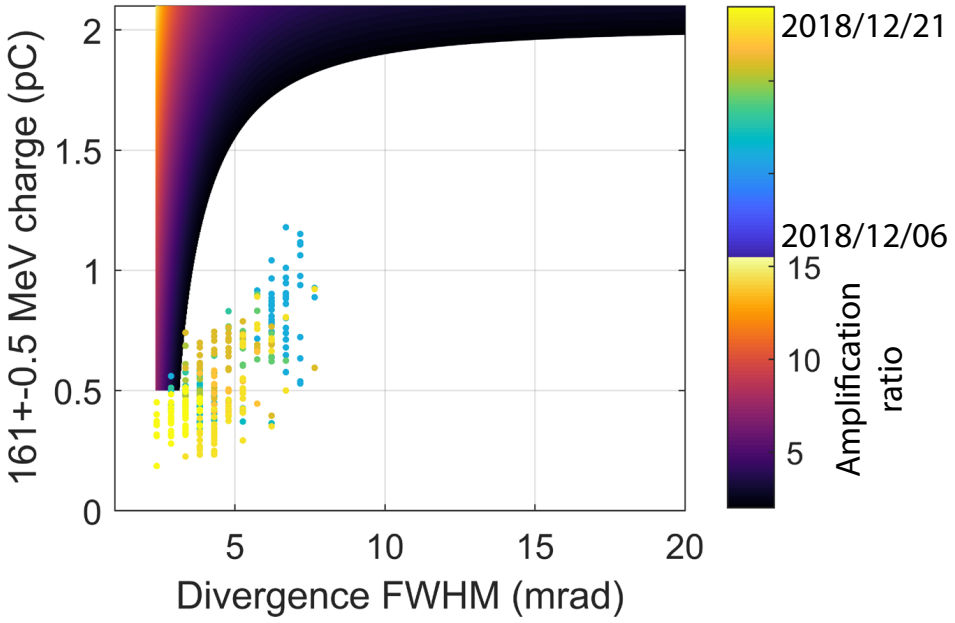

FIGURE 4.19: Slice charge versus FWHM divergence measured at the spectrometer for RUN 5. Shots sorted versus time when the series was taken according to the dots colormap with dark blue (yellow) corresponding to the start (end) if the RUN. Colored zone corresponding to low gain FEL zone deduced with the fit $f_{amp}(\sigma'_y, Q_{slice}) = -5.41 + 12.25\sigma_y'^{-2} + 2.2Q_{slice}^{1.744}$ (with Q_{slice} the slice charge and $f_{amp} \geq 2$) of the FEL radiation power achieved by a flat-top electron beam of 4 % energy spread with $\epsilon = 1$ mm.mrad and different initial divergences and beam slice charge obtained via simulations (Figures 3.14, 3.15) [201]

4.3 Case of the 151 MeV reference slice (RUN 6 and 7)

4.3.1 Systematic measurements of initial electron beam characteristics during RUN 6

During RUN 6 (2019/01/31 - 2019/02/15), to accomodate the line to the 151 MeV the QUAPEVA triplet was set 5 mm closer to the LPA source and the undulator gap was reduced to 4.7 mm to achieve an emission wavelength of 250 nm. Regarding the LPA system, the RUN 5 configuration was kept. In RUN 6 no "first imager" data was taken analyze.

4.3.1.1 Spectrometer data analysis

Figure 4.20a shows the first 20 shot series measured the 2019/02/15. The green dotted line corresponds to the screen horizontal position for the 151 MeV. The electron beam energies go from 50 MeV to $\approx$ 360 MeV. The corresponding 151$\pm$0.5 MeV vertical slice projections in Figure 4.20b exhibit a low shot-to-shot pointing variation. The 20 energy distributions of Figure 4.20c present a low energy peak followed by a lower peak at around 150 MeV with a slice charge density of $\approx$ 0.6 pC/MeV and a long high energy tail. The 20 shots show really similar distributions. For the divergence shown in Figure 4.20d, all energies have a similar FWHM divergence of around 4 mrad except the low energies peak. The average FWHM vertical beam divergence of the set is 3.20 mrad with a std of 0.15 mrad.

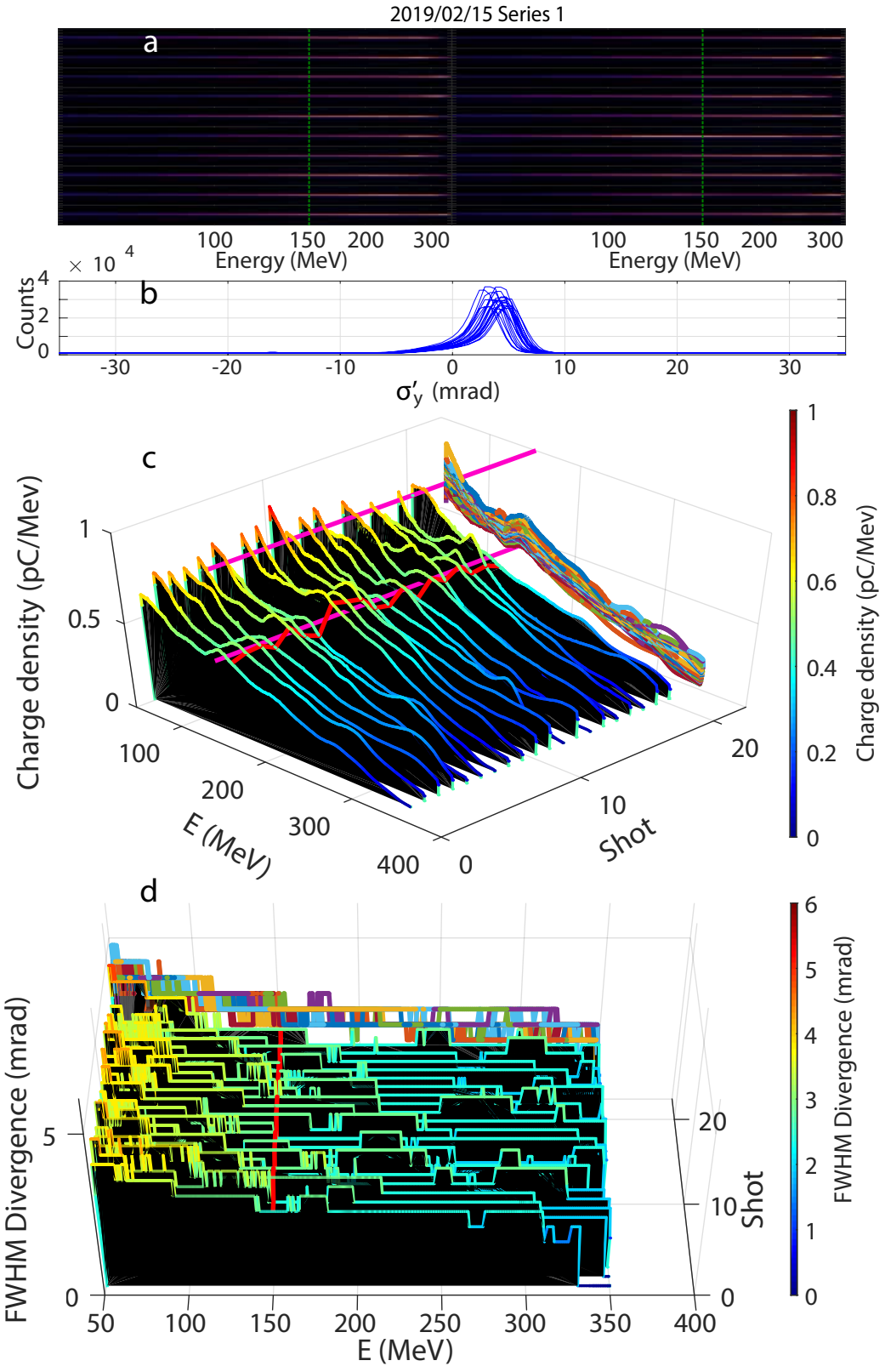

FIGURE 4.20: Beam measurements at the electron spectrometer of the first series of the day 2019/02/15. (a) Calibrated images with the green dotted line at 151 MeV. (b) Vertical projection of the 151 MeV slice for each shot. (c) Charge density versus electron beam energy (purple lines indicating the 0.5, 1 and 1.5 pC/MeV level at $E = 151$ MeV) and (d) 1 MeV width slice FWHM vertical divergence versus energy for the successive shots.

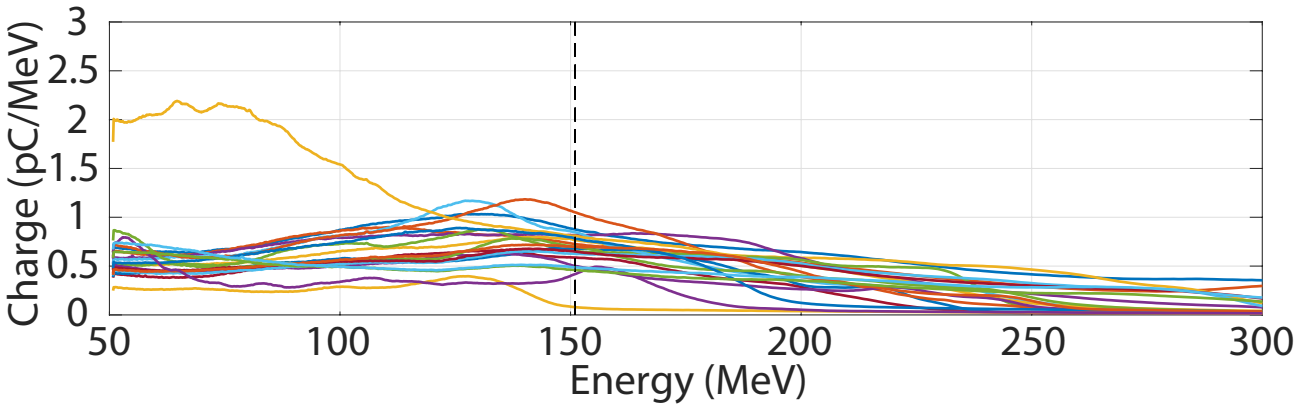

FIGURE 4.21: Examples beam energy distributions at the electron spectrometer during the RUN 6. The black dotted line corresponds to the reference energy 151 MeV.

Figure 4.21 shows how aforementioned lower peaks of the distribution are close to the reference energy 151 MeV in most occasions. The energy spread is always large.

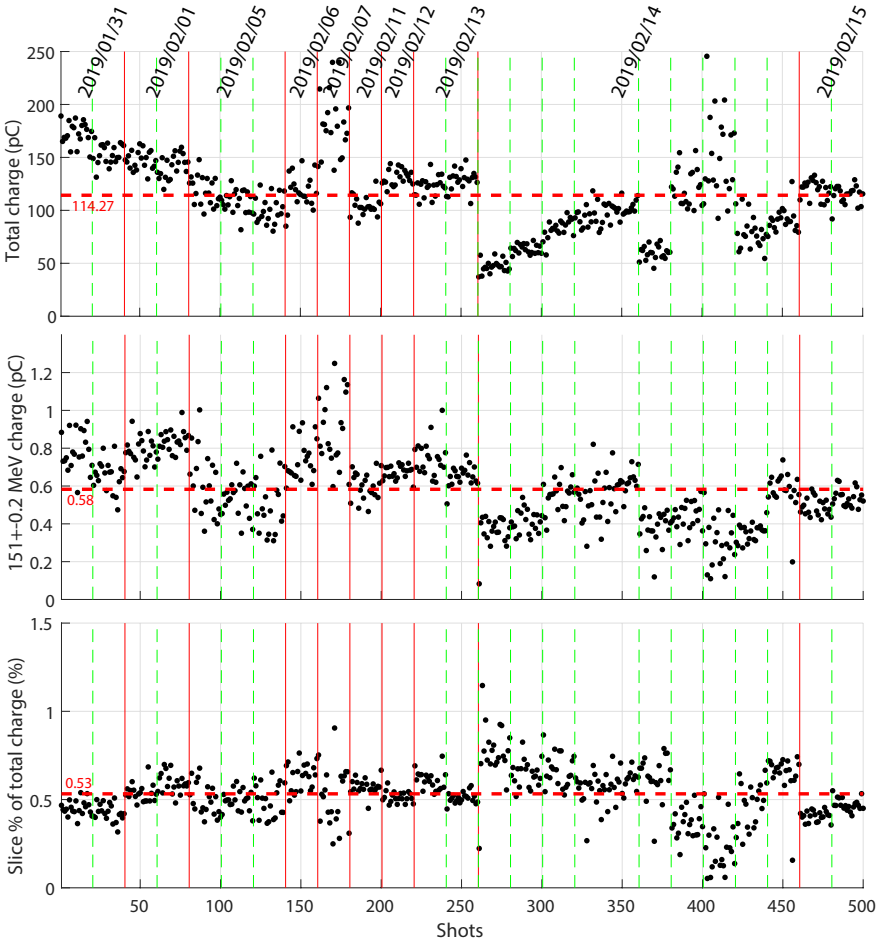

FIGURE 4.22: (a) Total beam charge, (b) 151 ± 0.2 MeV slice charge and (c) percentage of the total beam charge corresponding to the charge in the slice measured at the spectrometer during RUN 6 sorted by time and separated by day (red line) and series (green dotted line).

Figure 4.22 presents the total and 151 ± 0.5 MeV slice charge measured at the spectrometer for the 500 acquired shots. The total and reference slice charge are 114.27 pC and 0.58 pC/MeV with stds 35.75 pC and 0.18 pC respectively (Table 4.6). The slice charge density is slightly higher than RUN 5's one and the standard

deviation slightly lower. The percentage of the total beam charge corresponding to the reference energy slice sees a slight improvement from RUN 5 too. An important degradation of the electron beam was detected from 2019/01/31 to 2019/02/06. So, the 2019/02/07 the gas density was significantly increased to counter the charge loss. The 2019/02/12 was confirmed that the problem was due to the degradation of the laser optics and they were replaced the same day. The following two days (2019/02/13 - 14) the LPA system was optimized. Due to the multiple LPA source changes, the stability of the beam cannot be really analyzed except for the last day, where it seems on par with RUN 5.

TABLE 4.6: Beam slice FWHM vertical divergence, total and slice experimental charge average at the spectrometer with the respective standard deviation for RUN 6 and the simulated beam with the baseline parameters (Table 3.3).

RUN	Slice	**Mean charge (std)**		Mean divergence FWHM (std)	
		Total	Slice	Slice	Total
	MeV	*pC*	*pC*	*mrad*	*mrad*
Baseline	176 ± 0.5	34	10.9	2.35	2.35
6	151 ± 0.5	114.3 (35.7)	0.58 (0.18)	4.11 (4.63)	3.97 (0.65)

Figure 4.23a presents the FWHM divergence of all RUN 6 shots. The divergence improves to an average of 4.11 mrad and during the last day a consistent divergence of 3.4 mrad was achieved with a ≈ 0.58 pC/MeV slice charge. Figure 4.23b shows the FWHM vertical total beam divergence deduced from the spectrometer energy slice vertical divergence weighted mean. The RUN 6 average yields a value of 3.97 mrad with a std of 0.65 mrad, lower than RUN 5. Each day the vertical beam divergence decreased and as previously the lower average value is achieved the last day of the RUN with a value of ≈ 3.2 mrad.

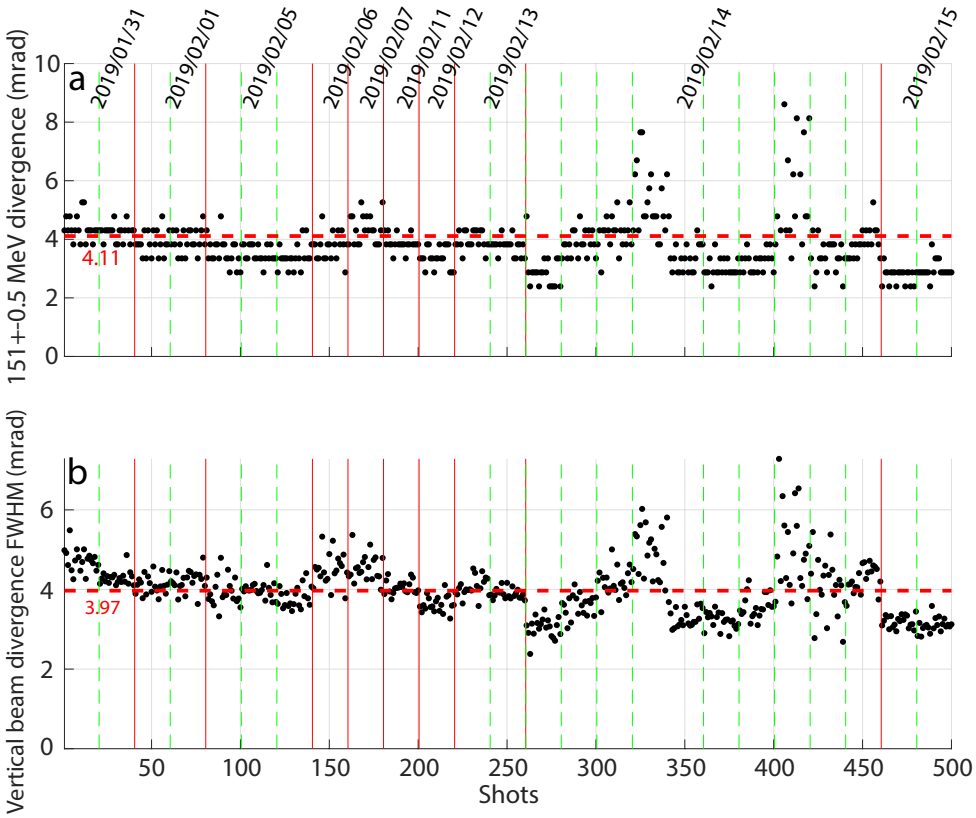

FIGURE 4.23: Measured FWHM (a) slice and (b) total vertical divergence at the electron spectrometer during RUN 6 sorted by time and separated by day (red line) and series (green dotted line).

4.3.1.2 FEL capabilities of the measured electron beams

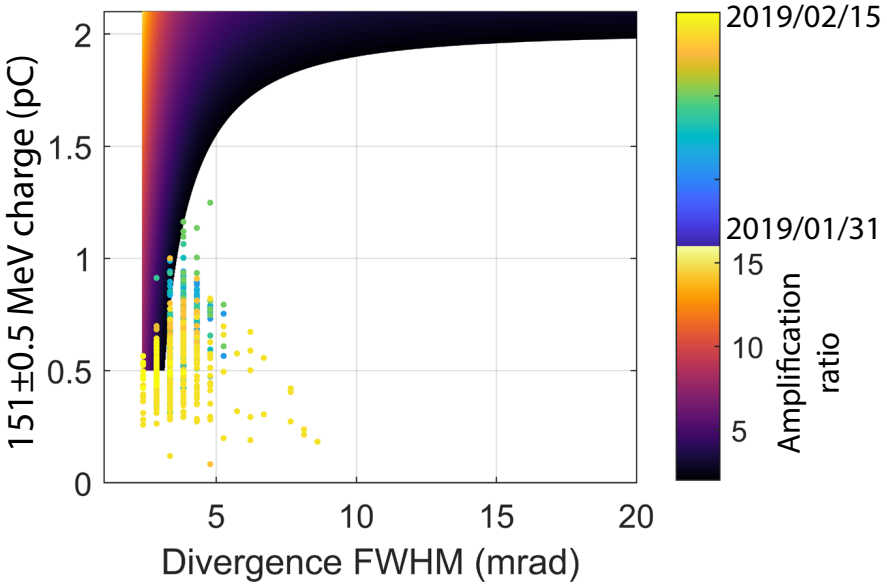

FIGURE 4.24: Slice charge versus FWHM divergence measured at the spectrometer for RUN 6. Shots sorted versus time when the series was taken according to the dots colormap with dark blue (yellow) corresponding to the start (end) if the RUN. Colored zone corresponding to low gain FEL zone deduced with the fit $f_{amp}(\sigma'_y, Q_{slice}) = -5.41 + 12.25\sigma_y^{'-2} + 2.2Q_{slice}^{1.744}$ (with Q_{slice} the slice charge and $f_{amp} \geq 2$) of the FEL radiation power achieved by a flat-top electron beam of 4 % energy spread with $\epsilon = 1$ mm.mrad and different initial divergences and beam slice charge obtained via simulations (Figures 3.14, 3.15) [201]

Figure 4.24 shows RUN 6 shots for the 151±0.5 MeV slice charge versus FWHM divergence. During the RUN, charges of 1 pC/MeV with less than 4 mrad were achieved. 10 % of all shots are found inside the $f_{amp} = 2$ FEL zone towards the border with an average of 3.55 and a std of 1.13. 8.8 % of the shots are under $f_{amp} = 5$ with a f_{amp} average of 3.3 and an std of 0.6. Only one shot is at $f_{amp} = 4.7$ and three at $f_{amp} \approx 7$. Such statistics are improved when compared to previous RUNs; however, in a single day, in average few shots enter the $f_{amp} = 2$ FEL zone. After the beam characterization via the spectrometer, the line has to be adjusted to transport to the undulator, which can take up to 100 shots and then the seeded FEL preparation has to be done. Moreover, once the line and seed are set, the search for FEL requires of additional parameters scans. As a result, the search for FEL, specially with beams that are barely in the $f_{amp} = 2$ FEL zone, requires of a high number of consecutive "suitable" shots. More realistically, as a perfectly stable system is not possible, one should aim to produce electrons around the threshold $f_{amp} = 15$ at the spectrometer, thus, facilitating FEL amplfication, observation and with a higher level of tolerance for laser degradation and instability. So, RUN 6 is closer to the $f_{amp} = 2$ FEL working zone than the previous RUNs, but, still more improvements in charge are needed.

4.3.2 Case of improved electron beam performances (RUN 7)

Before RUN 7 (2020/09/01 to 2020/09/25) the laser system was upgraded, increasing the energy output to 2.5 J and new spherical mirrors of higher focal length were added to keep the rest of the pulse parameters as in previous experiments. Thus, a higher average electron energy and charge are expected. The reference energy is kept at 151 MeV.

4.3.2.1 Spectrometer data analysis

Figure 4.25a shows 20 shots measured the 2020/09/25 in the middle of the experiments, corresponding to the twelve series. The energy spans a shorter range than in RUN 6, from 50 MeV to ≈ 280 MeV. The 151 MeV vertical projection in Figure 4.25b shows a shot-to-shot pointing stability similar to the RUN 6 (Figure 4.20). The energy distributions of Figure 4.25c present a broad Gaussian shape such as in RUN 5, centered around the reference energy 151 MeV, with a low energies high peak. The slice charge of the Gaussian peak is around 1.3 pC/MeV, which is higher than any RUN 6 shots. The slice FWHM vertical divergence per energy shown in Figure 4.25d presents a slope from 6 mrad at low energies to 3 mrad at high energies. For the reference energy

slice, the divergence is around 4 mrad. The FWHM vertical beam divergence of the set is of 4.12 mrad with a std of 0.8 mrad.

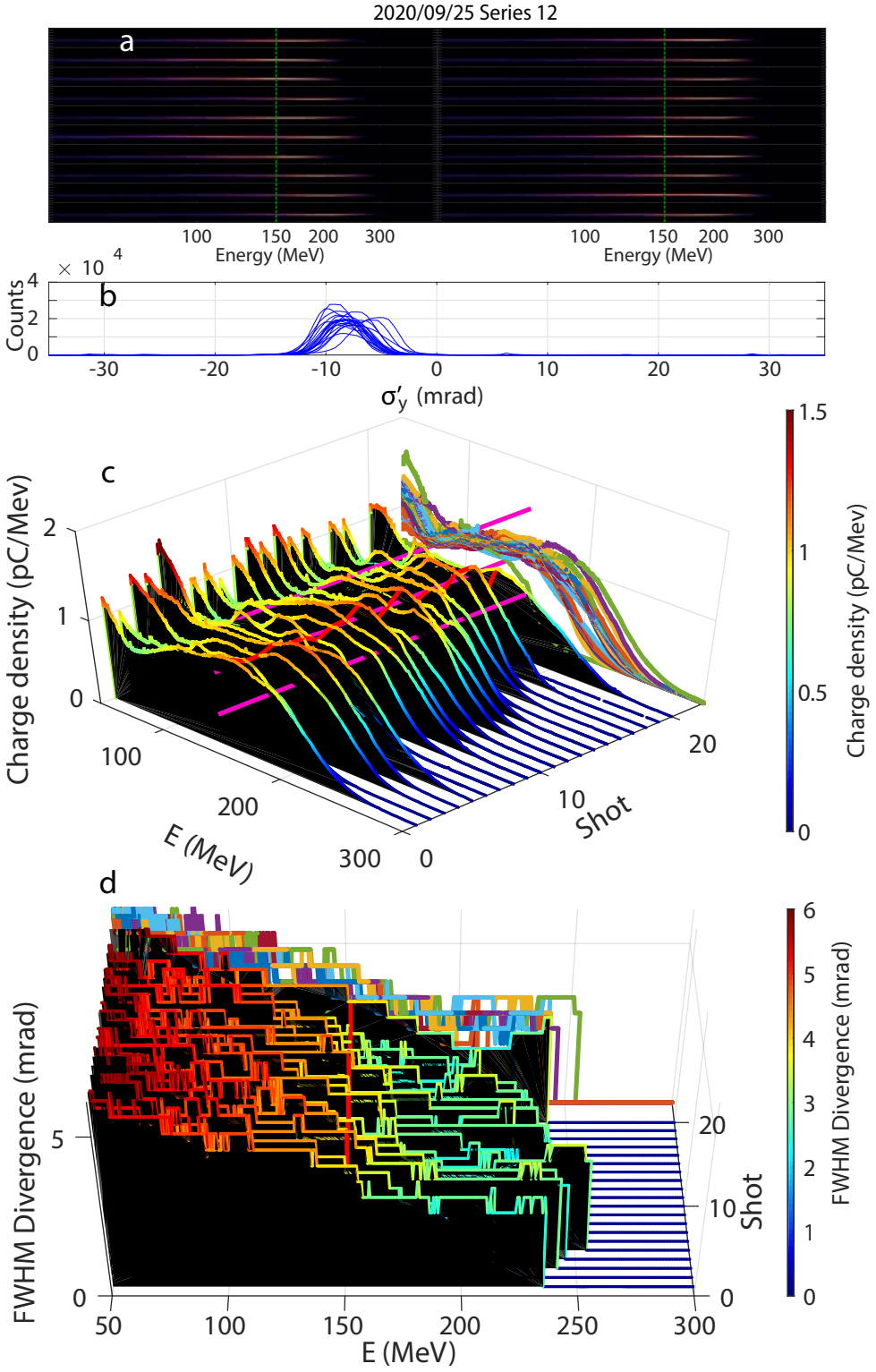

FIGURE 4.25: Beam measurements at the electron spectrometer of the day 2020/09/25 twelve series. (a) Calibrated images with the green dotted line at 151 MeV. Vertical projection of the 151 MeV slice for each shot. (c) Charge density versus electron beam energy (purple lines indicating the 0.5, 1 and 1.5 pC/MeV level at $E = 151$ MeV) and (d) 1 MeV width slice FWHM vertical divergence versus energy for the successive shots.

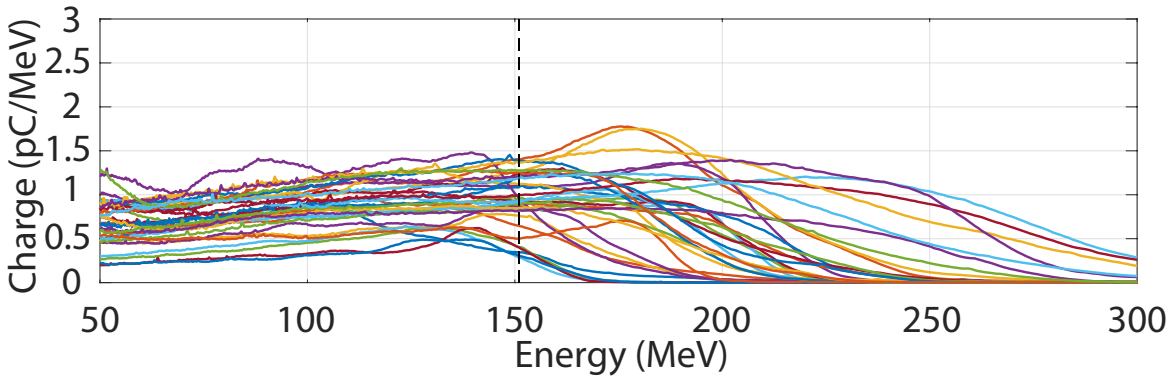

FIGURE 4.26: Examples beam energy distributions at the electron spectrometer during the RUN 7. The black dotted line corresponds to the reference energy 151 MeV.

Figure 4.26 presents some examples of RUN 7 shots. The energy distributions observed can be roughly divided in "long" and "short" energy range, with "short" meaning that the maximum energy is around 210 MeV and long when the maximum energy is superior to 210 MeV. For the short range cases, the reference energy 151 MeV is on the peak of the distribution or close to it. For the "long" range cases, the reference energy is found in the plateau before the main peak or at the start of the rise, and even though is not in such distributions peak, it yields more charge than in previous RUNs. The variations between "short" and "long" energy range can be originated by gas density changes between $4.5 \times 10^{18}\ cm^{-3}$ and $5 \times 10^{18}\ cm^{-3}$ as found in simulations (Figure 5.19, Section 5.2)

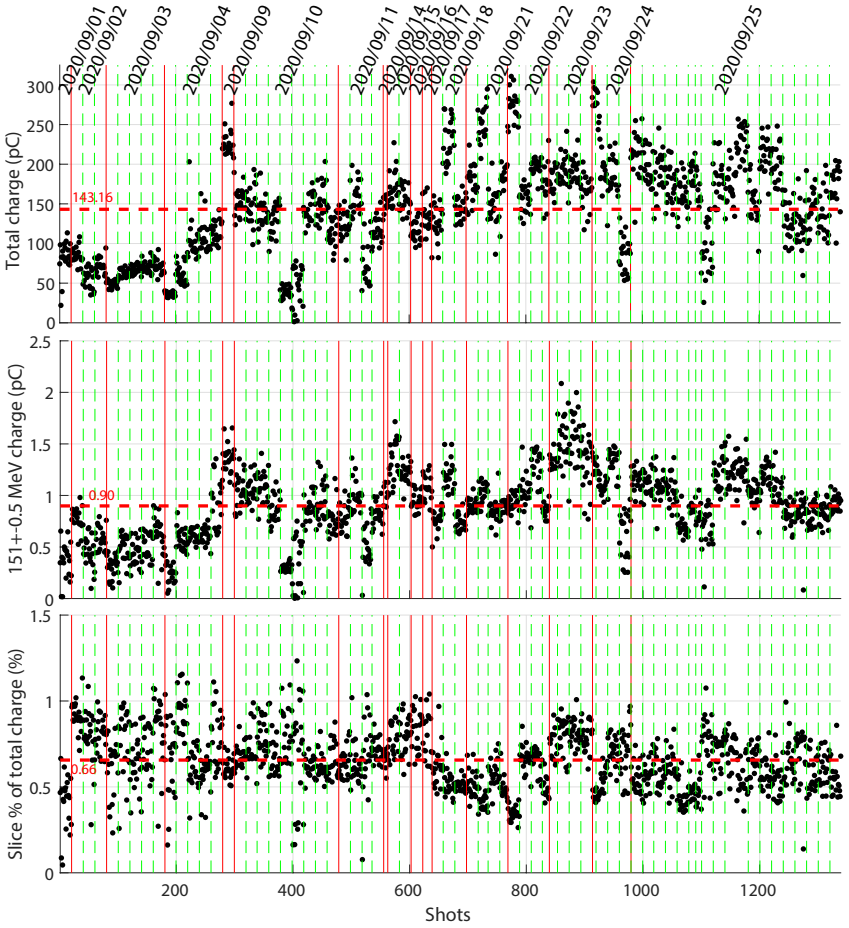

FIGURE 4.27: (a) Total beam charge, (b) 151 ± 0.5 MeV slice charge and (c) percentage of the total beam charge corresponding to the charge in the slice measured at the spectrometer during RUN 7 sorted by time and separated by day (red line) and series (green dotted line).

Figure 4.27 shows the total and 151 ± 0.5 MeV slice charge measured at the spectrometer for 1339 shots and Table 4.7 presents the RUN average values . The total charge improved with an average 1.5 times higher than in RUN 6, reaching 143.15 pC. The reference slice charge undergoes a similar increase, achieving an average of 0.9 with an std of 0.34. The percentage of the total charge corresponding to the slice 151 ± 0.5 MeV charge also increases, with an average of 0.66 % and going up to 1 % in some instances. One can still observe slice charge drops everyday during long periods of laser use (Figure 4.27).

Figure 4.28a shows the slice 151 ± 0.5 MeV FWHM divergence during RUN 7. The laser system upgrade and optimizations done throughout RUN 7 leads to a reduction of the average FWHM divergence to 3.76 mrad with an std of 1.53 mrad with an improved stability when compared to RUN 6. Figure 4.28b presents the FWHM vertical total beam divergence deduced from the spectrometer. The average value of RUN 7 is of 4.12 mrad with a std of 0.81 mrad, close to the one of RUN 6. Unlike in the previous RUNs the lowest divergence was achieved during the first days and kept increasing until the last day were the average is of 4.7 mrad.

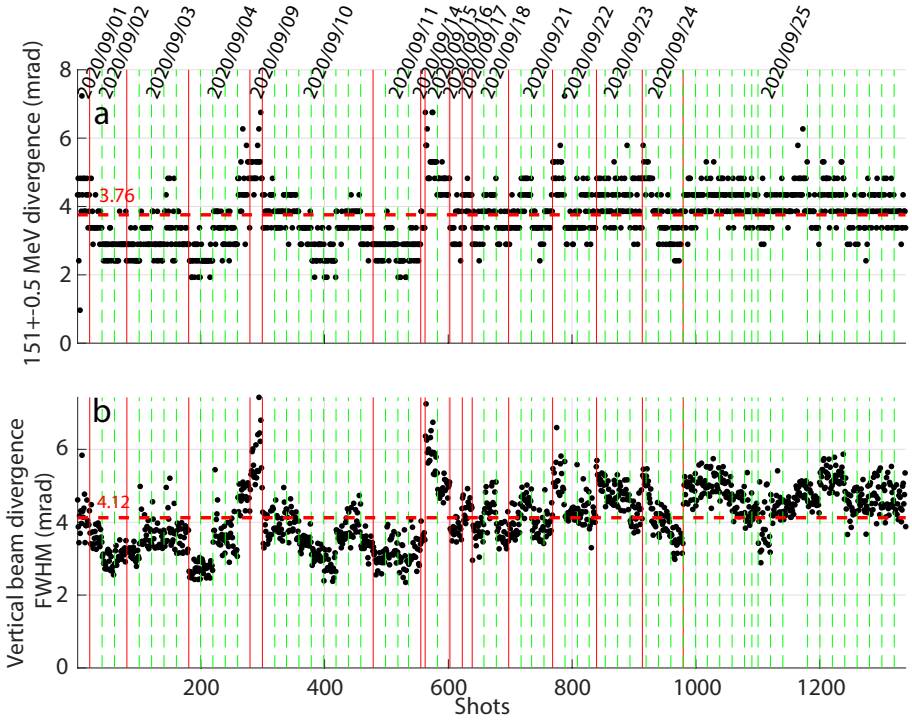

FIGURE 4.28: Measured FWHM (a) slice and (b) total vertical divergence at the electron spectrometer during RUN 7 sorted by time and separated by day (red line) and series (green dotted line).

4.3.2.2 "First imager" data analysis

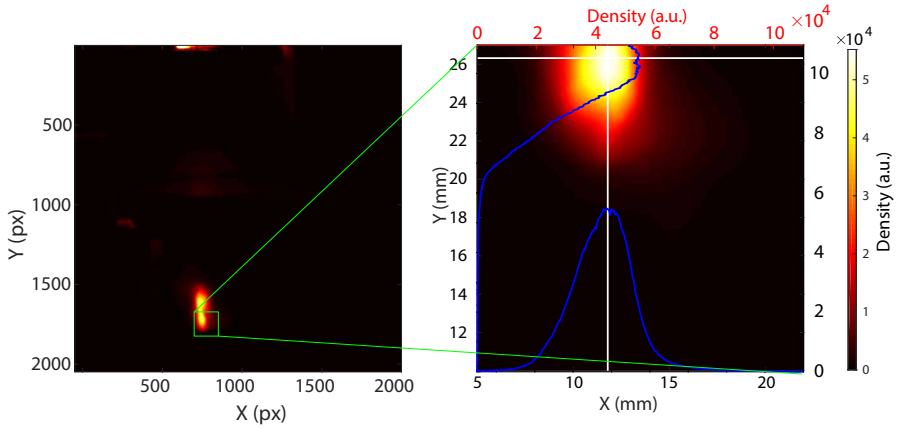

FIGURE 4.29: Measured transversal image taken at the "first imager" the 2019/09/25 at 13:57:28 shot 2 with white lines indicating the beam most intense pixel and their projections in blue.

Figure 4.29 shows a shot on the "first imager" taken the last day of RUN 7. Two beams are observed and the more focused is the one considered. The beam presents a much higher intensity compared to the previous RUNs due to the increase in beam charge. The FWHM total beam vertical and horizontal divergences found are 5.41 mrad and 7.78 mrad and the horizontal-vertical divergence ratio is 1.44.

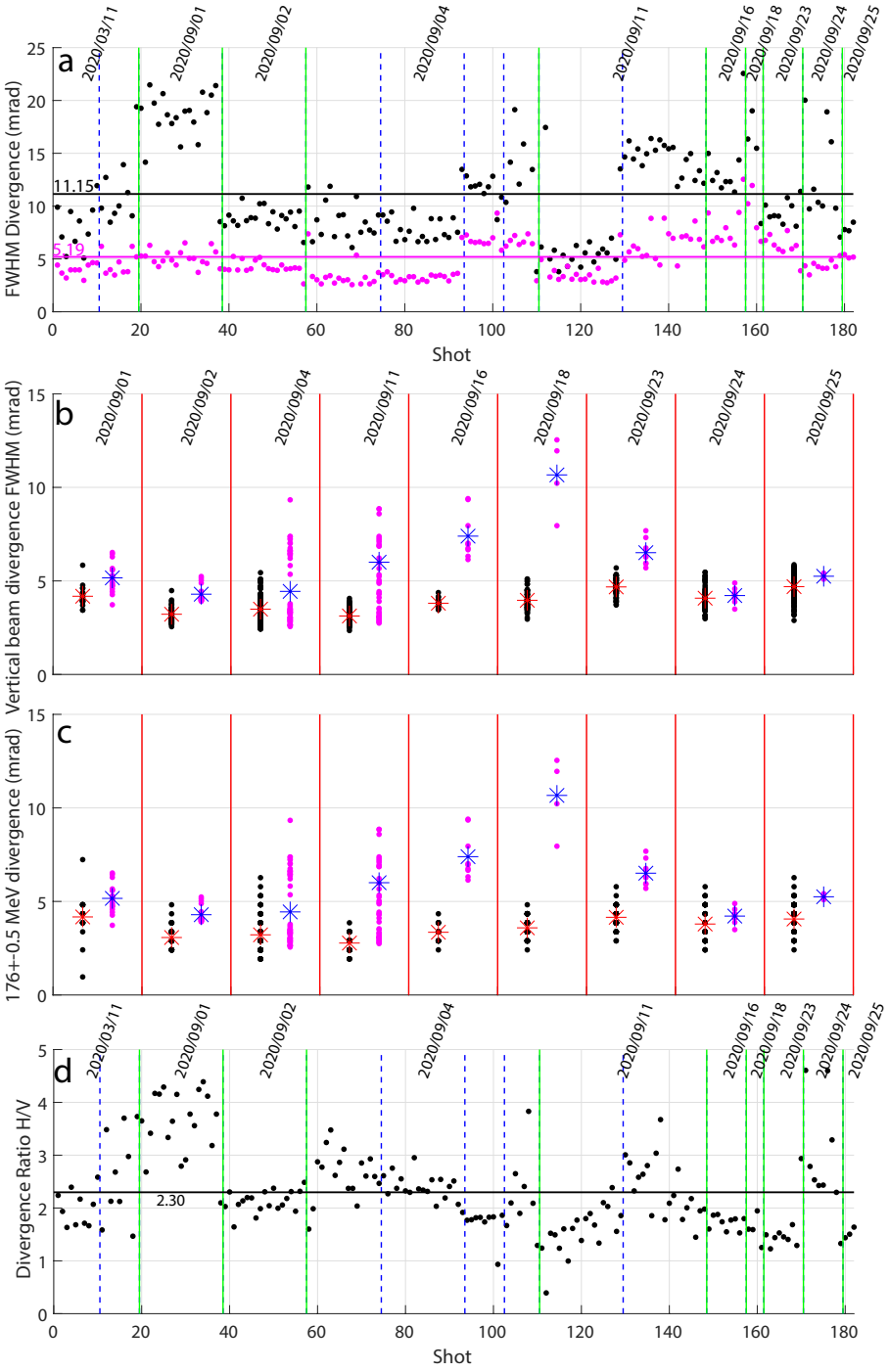

FIGURE 4.30: (a) Vertical (purple dots) and horizontal (black dots) total beam divergence measured at the "first imager" during RUN 7. (b) FWHM vertical total beam divergence measured at the "first imager" (purple dots) and at the spectrometer (black dots) and their corresponding average values per day (spectrometer red stars; "first imager" blue stars) during RUN 7. (c) FWHM vertical total beam divergence measured at the "first imager" (purple dots) and reference slice vertical divergence at the spectrometer (black dots) and their corresponding average values per day (spectrometer red stars; "first imager" blue stars) during RUN 7. (d) Divergence ratio σ'_x/σ'_y measured at the "first imager" during the entirety of RUN 7 in chronological order, with the blue lines separating series of shots and the green lines separating days.

Figure 4.30a presents the FWHM vertical and horizontal total beam divergences deduced at "first imager". The vertical beam divergence average value is 5.19 mrad, lower compared to the previous RUNs, with an std of 3.45 mrad. The horizontal beam divergence is in average more than twice the vertical one. The mean horizontal beam divergence is 11.14 mrad. Moreover, the shot-to-shot stability of the horizontal divergence is quite low, giving a std of 4.52 mrad. The comparison between the FWHM vertical total beam divergence per day at "first imager" and the spectrometer in Figure 4.30b exhibits a difference of their means of ≈ 1.5 mrad except during the days 2020/09/11-18 where the "first imager" data shows a sudden increase before going back to the lower values. The sudden changes could be caused by laser variations with time. During the same day sudden increases in the total beam charge can also be observed (Figure 4.27). In addition only four continuous shots were taken at the "first imager" on that day so is difficult to make a statement about the sudden increase. The FWHM vertical reference slice divergence versus total beam divergence in Figure 4.30c presents an agreement between their daily mean values withing ≈ 3 mrad with the exception of the days 2020/09/16 - 18. Again the eventual increase of their disparity could be caused by variations on the energy distribution or in the laser pointing. Figure 4.30d shows all measurements of the divergence ratio done in the course of RUN 7 (182 shots). The average ratio is significantly higher compared to the previous RUNs, with a value of 2.30 and a std of 0.78, i.e., a FWHM reference slice horizontal divergence of 8.51 mrad (Table 4.7). The LPA beam has thus, an average vertical divergence two times lower than the horizontal one. Compared to the gas jet data of RUN 4 and 5, RUN 7 offers the lowest shot-to-shot stability. The increased instability can be related to the higher laser intensity which could make the non-symmetries of the beam wavefront effect on the wakefield more important [204, 205]. As in RUN 4, the evolution of the ratio during the day has an irregular gradient, with some days increasing (e.g., 2020/03/11) and some days decreasing (e.g., 2020/09/11). RUN 7 average values of the "first imager" measurements are summarized in Table 4.7.

TABLE 4.7: Beam 151 ± 0.5 MeV slice FWHM vertical divergence, total and slice experimental charge average at the spectrometer with the respective standard deviation and average beam divergences and horizontal-vertical divergence ratio for RUN 7 and the simulated beam with the baseline parameters (Table 3.3).

	Spectrometer				**"First imager"**		
RUN	**Mean charge (std)**		Mean divergence FWHM (std)		**Mean beam divergence FWHM (std)**		Mean $\frac{\sigma'_x}{\sigma'_y}$ (std)
	Total *pC*	Slice *pC*	Slice *mrad*	Total *mrad*	Vertical *mrad*	Horizontal *mrad*	
Baseline	34	10.9	2.35	2.35	1	1	1
7	143.2 (59)	0.90 (0.34)	3.76 (1.53)	4.12 (0.81)	5.19 (3.45)	11.14 (4.52)	2.30 (0.78)

4.3.2.3 FEL capabilities of the measured electron beams

Figure 4.31 shows RUN 7 shots reference slice charge versus FWHM slice divergence. A grand number of shots are quite close the $f_{amp} = 2$ FEL working zone. Approximately 37 % of all measured shots are inside and present a mean of $f_{amp} = 3.72$ with a std of 1.66. A 30 % of these shots are close to the $f_{amp} = 2$ threshold with a mean $f_{amp} \approx 3$ and a std of 0.8. 8 % of all shots have an amplification ratio value of $f_{amp} \geq 5$ with half even reaching $f_{amp} \approx 7.4$. One shot reaches $f_{amp} \approx 14$, which is the closest shot to the $f_{amp} \geq 15$ threshold measured at the spectrometer. Stability is still an issue, a low number of days present consecutive sets with a majority of shots entering the $f_{amp} = 2$ zone (e.g., 2020/09/23) and there is no day in which the shots are consistently inside the $f_{amp} = 2$ zone for long periods of time. The higher the f_{amp} considered value, the lower the number of consecutive shots becomes. As in RUN 6, the stability of the beam parameters during long periods of time is required for transport and seed preparation, so, even though technically there are possibilities of achieving FEL amplification with the spectrometer shots, the lacking capacity of delivery of consecutive "good" shots, the decrease of laser power with time and other experimental imperfections makes the $f_{amp} \geq 15$ threshold a necessity to try to observe any FEL. In the best conditions only one shot got close to $f_{amp} = 15$ thus, further LPA electron beam slice charge and divergence are required.

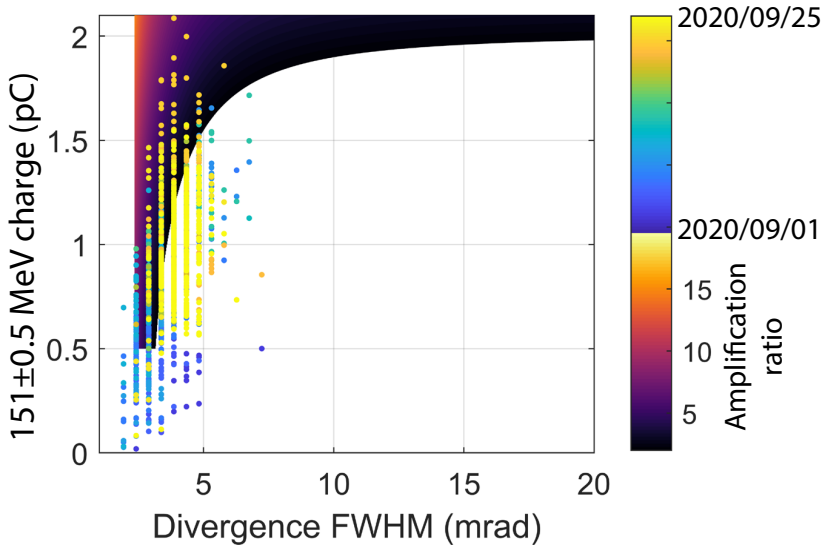

FIGURE 4.31: Slice charge versus FWHM divergence measured at the spectrometer for RUN 7. Shots sorted versus time when the series was taken according to the dots colormap with dark blue (yellow) corresponding to the start (end) if the RUN. Colored zone corresponding to low gain FEL zone deduced with the fit $f_{amp}(\sigma'_y, Q_{slice}) = -5.41 + 12.25\sigma'^{-2}_y + 2.2Q^{1.744}_{slice}$ (with Q_{slice} the slice charge and $f_{amp} \geq 2$) of the FEL radiation power achieved by a flat-top electron beam of 4 % energy spread with $\epsilon = 1$ mm.mrad and different initial divergences and beam slice charge obtained via simulations (Figures 3.14, 3.15) [201]

4.4 Summary

TABLE 4.8: Beam total and slice FWHM divergence, experimental charge average and f_{amp} with the respective standard deviation for each experimental campaign measured at the spectrometer and "first imager" and the simulated beam with the baseline parameters (Table 3.3).

		Spectrometer				**"First imager"**			f_{amp}		
RUN	Slice	**Mean charge (std)**		Mean divergence FWHM (std)		**Mean beam divergence FWHM (std)**		**Mean $\frac{\sigma'_x}{\sigma'_y}$ (std)**	$f_{amp} > 2$ shots	Mean f_{amp} (std)	Max f_{amp}
		Total	Slice	Slice (FWHM)	Total (FWHM)	Vertical (FWHM)	Horizontal (FWHM)				
	MeV	*pC*	*pC*	*mrad*	*mrad*	*mrad*	*mrad*				
Baseline	176 ± 0.5	34	10.9	2.35	2.35	1	1	1	—	146	—
4	176 ± 0.5	193 (97)	0.19 (0.18)	6.53 (1.29)	9.47 (3.33)	2.03 (1.42)	2.40 (2.46)	1.10 (0.52)	0	0	0
4 (gas cell)	176 ± 0.5	120.3 (66.8)	0.07 (0.11)	7.35 (2.87)	11.65 (3.03)	2.87 (2.19)	3.96 (3.64)	1.41 (0.47)	0	0	0
4 (gas jet)	176 ± 0.5	280.7 (110.5)	0.27 (0.23)	5.26 (2.08)	7.68 (2.37)	4.73 (2.28)	6.48 (3.43)	1.45 (1.10)	0	0	0
5	161 ± 0.5	107.7 (23.3)	0.55 (0.19)	4.54 (1.29)	4.9 (1.23)	7.64 (0.78)	9.11 (2.89)	1.21 (0.40)	3	3.5 (0.08)	3.5
6	151 ± 0.5	114.3 (35.7)	0.58 (0.18)	4.11 (4.63)	3.97 (0.65)				48	3.55 (1.13)	7.2
7	151 ± 0.5	143.2 (59.0)	0.90 (0.34)	3.76 (1.53)	4.12 (0.81)	5.19 (3.45)	11.14 (4.52)	2.30 (0.78)	504	3.72 (1.66)	14

Table 4.8 presents the RUNs electron beam initial parameters. Since the first RUN, the electron beam parameters were far from the baseline of the COXINEL line, as expected due to the use of ionization injection instead of colliding pulse scheme. At RUN 4 the reference slice charge is three times lower than the baseline and the divergence around 2.5 times higher. The initial tests with a gas cell gave a poorer electron beam and due to time constrains the gas jet target was exclusively used afterwards. At each subsequent RUN, the LPA system was improved and the reference energy reduced (from 176 MeV to 161 MeV and finally to 151 MeV) bringing the electron beam initial parameters closer to the requirements for FEL. After the laser power upgrade for RUN 7, a 37 % of the shots presented a value of f_{amp} superior to 2 and were candidates for FEL but none of them achieved the $f_{amp} \geq 15$ threshold. In addition, the low capacity for consecutive generation of shots with these conditions and the significant laser power loss during extended periods of use made the chances to achieve FEL low, leading to a necessary improvement of the beam parameters to approach the aimed $f_{amp} \geq 15$ threshold. Even though the laser stability was improved at each RUN, the production of the same beam characteristics during relatively long periods of time, which is needed for the FEL search, was not reached. Nevertheless, every RUN the electron beam could be properly transported until to the undulator. The increase of laser power while aiming at the same reference energy, as seen in the upgrade of RUN 7, substantially improves the electron beam charge and divergence taking the beam closer to the FEL. There are multiple ways to further improve the LPA, e.g., optimizing more the actual system, installing a laser feedback system to better diagnose the laser

instabilities and correlate with the LPA beam observed or by doing an additional upgrade of the laser.

4.5 Conclusion

Chapter 4 reports on the measured electron beam parameters at the sources. The ionization injection scheme (Section 2.3.2.4) for LPA was utilized thanks to its simple configuration and stability making it more suitable for a practical use for FEL. Unfortunately, its performance during the LPA experiments was lower than the initially planned collision pulse scheme (Section 2.3.2.5), previously rejected due to its complex setup and need for high laser stability. The laser system underwent multiple optimizations and improvements and the data shows a steady improvement (divergence down to 1.5 mrad RMS and reference energy charge up to 2 pC/MeV). Therefore, the ionization injection scheme would be useful for the FEL through several improvements.

Chapter 5

Ionization injection performance

In LPA, multiple schemes to inject the electrons into the wakefield exist. The ionization injection offers an experimentally simple and fairly robust way to trigger the injection and accelerate the electrons with a single laser. In the ionization injection scheme (Section 2.3.2.4), the laser is responsible of the ionization of the gas producing the plasma and the generation of the density perturbation leading to the wakefield structure to accelerate the electrons. The simplicity of the scheme principle hides various phenomena that interact with each other, e.g., laser depletion rate increase due to ionization, changes in density along the laser. The ionization process adds another complexity level to the dynamics, that makes fundamental the use of simulations and experiments for a proper understanding. Experiments require of specialized laser facilities and complete 3D simulations of large numbers of processors and memory working in parallel that can only be obtained on supercomputer facilities (more than a hundred hours with thousands cores). Therefore, numerous 2D simulations can be done with limited computational resources while obtaining a qualitative picture of the wakefield process. Multiple general studies of the ionization injection LPA scheme have been performed for high a_0 values [38]. As no previous study of the COXINEL experiment ionization injection LPA setup has been done, it is pertinent to simulate it in order to better understand its performance and what to expect. This chapter focuses on a more restricted experimental like parameter range of the simulated LPA system, with densities around $5 \times 10^{18}\ cm^{-3}$, a gas mixture of He and N_2 and a laser of $a_0 = 1.5$. The final objective of the analysis is to find the LPA parameters permitting to reach the best possible energy spread, desired electron energy slice transverse phase-space and charge, the most important beam parameters for a possible FEL application. The simulations have been done with the PIC code PICLS provided by Y. Sentoku [65, 66], Institute of Laser Engineering, Osaka University (Section 2.4). The PICLS code is well adapted for the interaction between high power lasers and dense matter and also for the lower plasma densities as utilized here ($10^{18}\ cm^{-3}$). At the same time the code has been carefully done and tested to deal with ionization of atoms due to the laser pulse [66]. The simulations have been done on the cluster of professor Sentoku group and at the "computing centre for research and technology" (CCRT) under the CEA DAM, Paris, France through its partnership with synchrotron SOLEIL.

5.1 Gas target effect on the produced beam

The LPA system can be divided in two main parts: the gas target and the laser system. For the optimization of the produced electron beam parameters one can modify the gas (e.g., density, density distribution shape, gas mixture) or the laser (e.g., focus position, power). In this section the consequences caused by variations on the gas are studied.

The used simulation parameters presented in Table 5.1 were chosen to resemble experimental conditions. The laser pulse is linearly polarized (transverse x direction) with the parameters at Table 5.1 and focused at the gas entrance. As the initial laser spot size and focus position is constant for all simulations the laser may not be matched with the plasma density and therefore, it will not be properly guided (Section 2.3.6). The simulation grid is of 1000×800 points for a window of $100\ \mu m \times 80\ \mu m$ in the longitudinal z and transverse y directions respectively, and a time step of 0.33 fs. The grid was selected to have an equilibrium between available computer resources (around 9 days per simulation) and capacity to resolve the wakefield acceleration phenomena. Higher resolutions were tested in a single case and the results agreed with the used resolution. The input normalized density is defined as:

$$n_{e,norm} = (n_e / n_c) * (2\pi)^2 \tag{5.1}$$

TABLE 5.1: Laser and plasma initial simulation parameters: laser pulse duration ($\tau_{L,FWHM}$), spot size ($d_{L,FWHM}$), laser wavelength (λ_L), normalized density ($n_{e,norm}$), gas species concentration.

Simulated laser parameters				**Simulated plasma parameters**		
a_0	λ_L	$\tau_{L,FWHM}$	$d_{L,FWHM}$	$n_{e,norm}$	He	N_2
1.5	800 nm	31 fs	11 μm	0.20	99 %	1 %

5.1.1 Density entrance and exit gradient effect

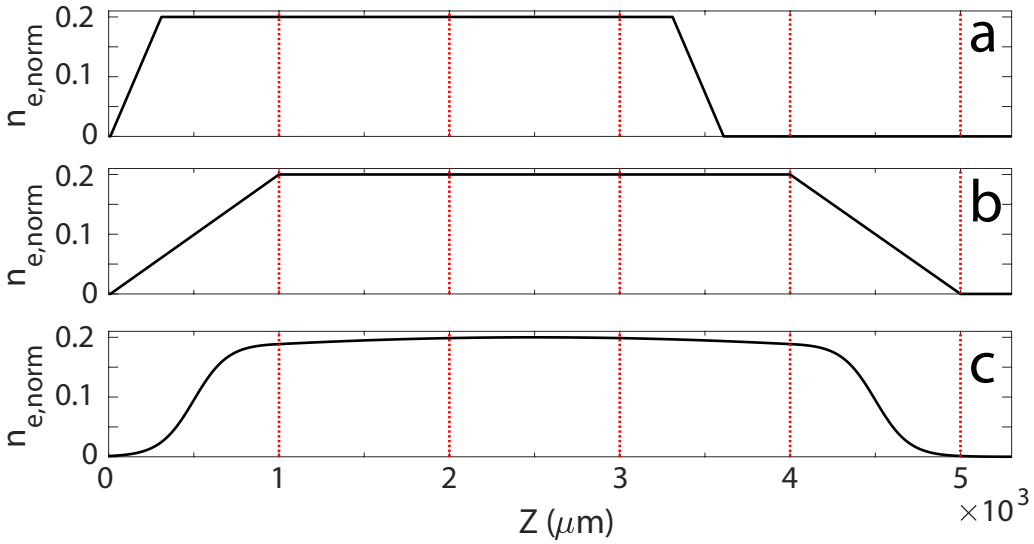

FIGURE 5.1: Steep (a), long (b) and smooth (c) longitudinal gas profiles used in simulations.

Experimentally, the density distribution seen by the laser rises with a slope until the maximum gas density is reached and vice versa at the exit of the gas target. Different gas target configurations produce distinct ramps, e.g., a gas cell can generate a uniform flat-top like distribution with a steep density rise and fall while an open gas jet has longer density slopes and not completely linear. To analyze the extent of the influence of density longitudinal distribution ramps the three cases are considered in Figure 5.1. Figure 5.1a (b) presents a steep (long) flat-top density distributions with an up and down ramp of 300 μm (1000 μm) and a constant density section of 3 mm. Figure 5.1c shows a smoother distribution with an up and down ramp defined by the function $f(s) = \frac{a}{1+be^{cs}}$ of 1 mm length and a central section of 3 mm of the form $h(s) = \frac{1}{4a}(cosh(\frac{s-b}{2a}))^{-2}$ with a, b and c the parameters responsible for the shape form and values. The simulations are done for the entire gas profile distance and an extra 30 μm in vacuum to be able to observe the electron beam that enters the transport line.

5.1.1.1 Laser pulse evolution

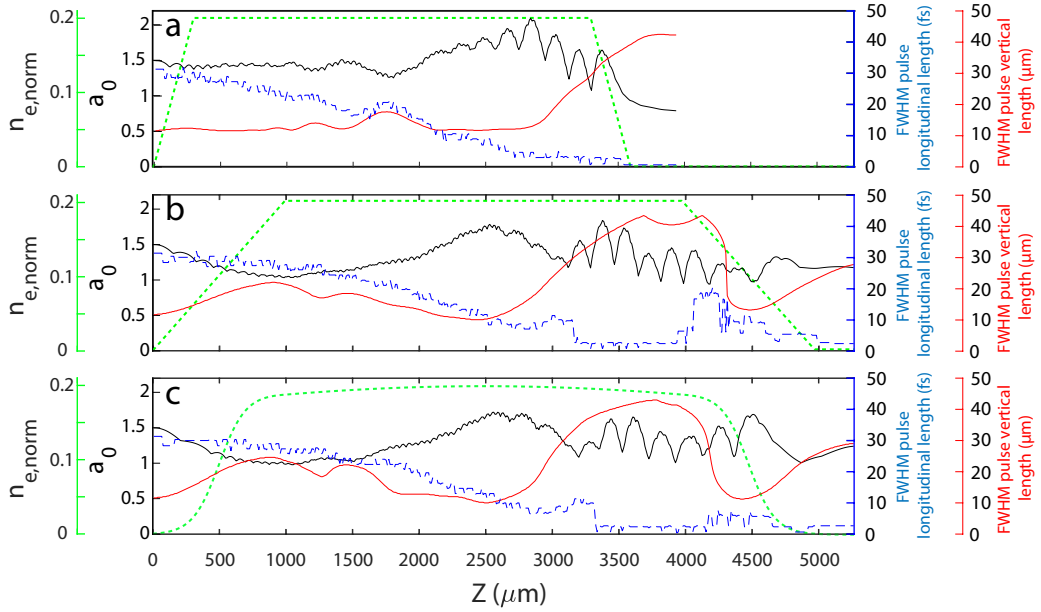

FIGURE 5.2: Simulated laser (black) a_0, (red) FWHM spot size and (blue) FWHM longitudinal length evolution along the (green) gas density profile of (a) Figure 5.1a, (b) Figure 5.1b and (c) Figure 5.1c, initial parameters of Table 5.1.

Figure 5.2 exhibits the simulated laser spot size, length and a_0 evolution along the different gas density profiles. In the steep flat-top distribution (Figure 5.2a), the laser a_0 shows a slow oscillation of increasing (decreasing) amplitude (frequency) that starts after 1 mm of propagation inside the gas and continues until the vacuum. The slow oscillation results from the transverse focusing and defocusing of the laser pulse due to an imperfect guiding. A better guiding could be obtained by optimizing the matching between the laser spot size and plasma density. After 2.5 mm, a fast a_0 oscillation overlaps the slow one reaching amplitudes of $\approx a_0 \pm 0.5$ and stops at the gas-vacuum interface. The highest a_0 amplitude is 2.1 at the position 2.86 mm. The laser spot size stops oscillating during 1 mm and then rises when the a_0 rapid oscillations appear. The laser pulse longitudinal length falls during the entire process due to pulse compression, etching and ionization.
In the long flat-top distribution (Figure 5.2b), the a_0 slow oscillation starts from the gas ramp with a low constant frequency along the propagation inside the gas. The slow oscillation can be correlated to the laser pulse focus spot transverse size until 3 mm into the gas. Its amplitude is considerably higher than in the steep flat-top case one, thus, the matching condition is also affected by the density profile ramp. Akin to the steep flat-top case, the rapid a_0 oscillation starts at approximately 2.8 mm of changing amplitude. The highest achieved a_0 value is 1.84 at the position 3.38 mm, i.e., a 14 % lower than the steep flat-top case. A transverse size growth to up to 4 times the initial one starts with the rapid a_0 oscillations. At the down-ramp, the laser pulse transverse size is again focused to values close to the initial one before starting to diverge in the vacuum.
The smoother distribution (Figure 5.2c) behaves similarly to the long flat-top distribution case. The slow and rapid a_0 oscillations appear at the same positions however, the peak a_0 is achieved at 2.56 mm, i.e., before the rapid oscillation, with a value of 1.72. Moreover, the rapid oscillation amplitude increases again at the gas down-ramp leading to a second a_0 peak at 4.51 mm with a value of 1.69. The transverse spot size exhibits a smother decrease during the down-ramp compared to the long flat-top distribution case. The pulse longitudinal length evolution at the down-ramp is also less drastic. Clear differences are observed on the laser dynamics due to the density distribution up and down-ramps that affects its self-focusing and maximum reached a_0, with its highest being achieved for the shortest up-ramp.

5.1.1.2 Electron beam injection and acceleration

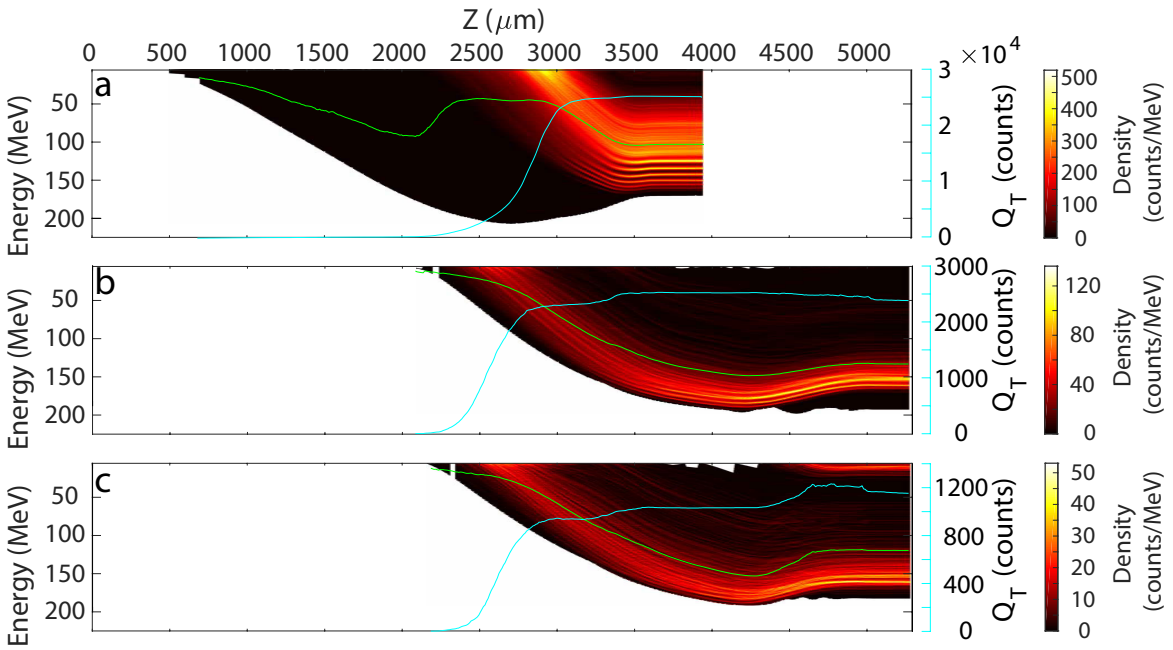

FIGURE 5.3: Simulated electron beam energy distribution evolution (surface plot), (cyan solid line) total charge and (green line) total beam mean energy along the gas density profiles of (a) Figure 5.1a, (b) Figure 5.1b and (c) Figure 5.1c, initial parameters of Table 5.1.

In the steep flat-top distribution (Figure 5.3a), an early small injection occurs after only 0.7 mm and the main injection event happens at approximately 2 mm, at the same time that the rapid a_0 oscillations begin and a_0 rises above 1.5 (Figure 5.3a). The injection continues for 1 mm until saturation, 0.3 mm before the down-ramp, saturating at 2.5×10^4 macroelectrons (97.6 % of them in the first wake). Due to the grand number of particles injected at the last $\approx$ 1.3 mm of the gas, the interaction length between the wake and the electrons is short and the final mean energy of the total electron beam is 101 MeV. In the long flat-top distribution (Figure 5.3b), there is also two injection events. Most of the charge is injected at the middle of the density profile, i.e., position 2.1 mm. After 1 mm the first injection stops reaching 2312 macroelectrons (94 % in the first wake), i.e., an order of magnitude under the steep flat-top case. The second injection event coincides with the apparition of rapid a_0 oscillations at $\approx$ 3.2 mm and stops after 0.3 mm when a_0 achieves its peak. During this injection only $\approx$ 200 additional macroelectons are injected with around half in the first wake. The macroelectrons are steadily accelerated until the down-ramp where the energy slightly decreases reaching a mean of 140 MeV. The smoother distribution (Figure 5.3c) presents a similar evolution to the long flat-top distribution case during the first injection event. The saturation charge is of only 940 macroparticles, less than half the long flat-top case one. The second event increases the charge by 10 %. A third injection event occurs at the start of the down-ramp (4.3 mm) for 0.3 mm in which 200 macroparticles between 5-40 MeV are injected in the wakes behind the first one. As this event occurs at the down-ramp, the new injected particles are not accelerated and remain between 4-45 MeV. Therefore, the mean energy of the produced total electron beam is of only 116 MeV due to the late injections of low energy electrons. However, by considering only the first wake electrons, the mean energy is of 144 MeV.

By shortening the up-ramp one can delay the injection time and significantly rise the maximum charge. Nevertheless, the plasma should be longer to leave enough acceleration length. Increasing the up and down-ramp permits the injection to happen earlier with small injection events occurring later. Thus, the electrons can accelerate to higher energies thanks to longer available acceleration lengths. However, the number of injected macroparticles is reduced by more than an order of magnitude.

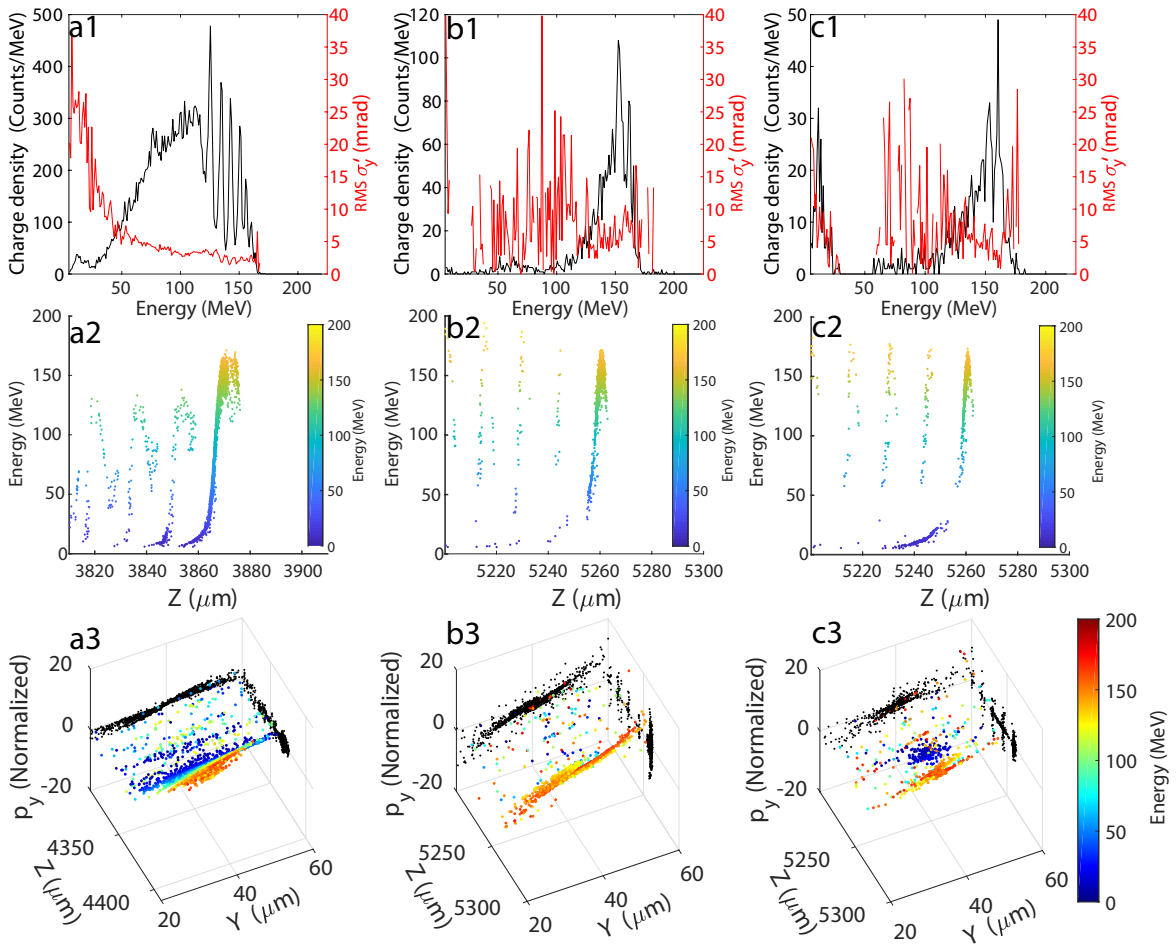

FIGURE 5.4: Simulated (a1, b1, c1) electron beam (black) energy distribution and (red) RMS divergence, (a2, b2, c2) particles longitudinal energy distribution and (a3, b3, c3) spatial and phase positions of the beam electrons 30 μm after the gas density distributions of (a) Figure 5.1a, (b) Figure 5.1b and (c) Figure 5.1c, initial parameters of Table 5.1.

Figure 5.4 shows the energy, divergence and longitudinal distribution of the total electron beam after 30 μm propagation in vacuum for the different density profiles. The steep flat-top distribution (Figure 5.4a1) provides a high energy spread (Table 5.2) energy distribution with a strong modulation for the energies between 116 MeV and 165 MeV. The RMS transverse beam divergence goes from 2 mrad for the high energies to around 20 mrad for the low energy tail.

The long flat-top (smoother) distribution has an energy spread around the high energy peak ≈ 5 (≈ 10) times lower than the steep flat-top case. In either case, no density modulation appears. The RMS transverse divergences around the main peak go from 2 mrad at 117 ± 0.5 MeV to 10 mrad at 168.5 ± 0.5 MeV in the steep flat-top case. The smoother distribution case shows lower values around the main peak with 5.9 mrad at 134.5 ± 0.5 MeV and 4.77 mrad at 166.5 ± 0.5 MeV. The longitudinal macroelectrons positions (Figure 5.4a-c2-3) show that the injection happens at least up to the fourth wake, but, most of the charge is always on the first one. For the steep flat-top case, a considerable amount of charge is inside the second wake. In the smoother profile case, the third injection event of low energy macroelectrons extends along tens of μm because it occurs at the end of the down-ramp were the wake is longer.

TABLE 5.2: Simulated electron beam parameters 30 μm after the gas density distributions of Figure 5.1a, Figure 5.1b and Figure 5.1c, initial parameters of Table 5.1. Parameters: maximum energy (E_{max}), most populated ±0.5 energy slice (E_{peak}), E_{peak} slice divergence ($\sigma'_{y,peak}$), E_{peak} slice transverse size ($\sigma_{y,peak}$), energy spread around E_{peak} ($\sigma_{\gamma,peak}$), E_{peak} ±0.5 slice charge ($Q_{E_{peak}\pm0.5}$), Total beam charge (Q_T), Total beam transverse ($\sigma_{y,total}$) and longitudinal size ($\sigma_{s,total}$). Best $E_{peak} \pm 0.5$ MeV slice parameters (blue).

Gas profile	E_{max} MeV	E_{peak} MeV	$\sigma'_{y,peak}$ mrad (RMS)	$\sigma_{y,peak}$ μm (RMS)	$\sigma_{\gamma,peak}$ MeV (FWHM)	$Q_{E_{peak}\pm0.5}$ Counts/MeV	Q_T Counts	$\frac{Q_{E_{peak}\pm0.5}}{Q_T} \times 100$ %	$\sigma_{y,total}$ μm (RMS)	$\sigma_{s,total}$ μm (RMS)
Steep flat-top (Figure 5.1a)	165	125.5	2.92	1.17	94	478	25368	1.88	1.81	3.86
Long flat-top (Figure 5.1b)	193.5	152.5	4	3.61	21.5	108	2381	4.53	4.84	8.87
Smoother (Figure 5.1c)	182.5	160.5	0.96	0.71	11	49	1153	4.25	4.32	12.5

In the three density profiles cases the macroelectrons need around 1 mm to reach 150 MeV and around 1.7 mm for 200 MeV. Thus, to accelerate as high as possible the major number of macroeletrons the main injection event has to occur sooner than 1.7 mm before the down-ramp. The length increase of the initial up-ramp shows an advancement in time of the main injection and reduction of energy spread at the expenses of the maximum charge. While the energy spread can be manipulated in a latter stage, the energy slice charge needs to be enough for generation FEL radiation. Other parameters of the LPA system (e.g., gas density, laser power) can be modified in order to increase the acceleration while avoiding considerable charge drops.

5.1.2 Density parameter scan

The consequences of a change in plasma density are difficult to ascertain as the plasma frequency depends on it (Section 2.1). Therefore, most non-linear phenomena are proportional to the plasma density (e.g., relativistic self-focusing, dephasing length, depletion length) so, a complete analytical study of the plasma density effect is not possible. In this section, three different densities are simulated with the same gas profile (Figure 5.1c) to study their effects on the beam injection, acceleration and distribution.

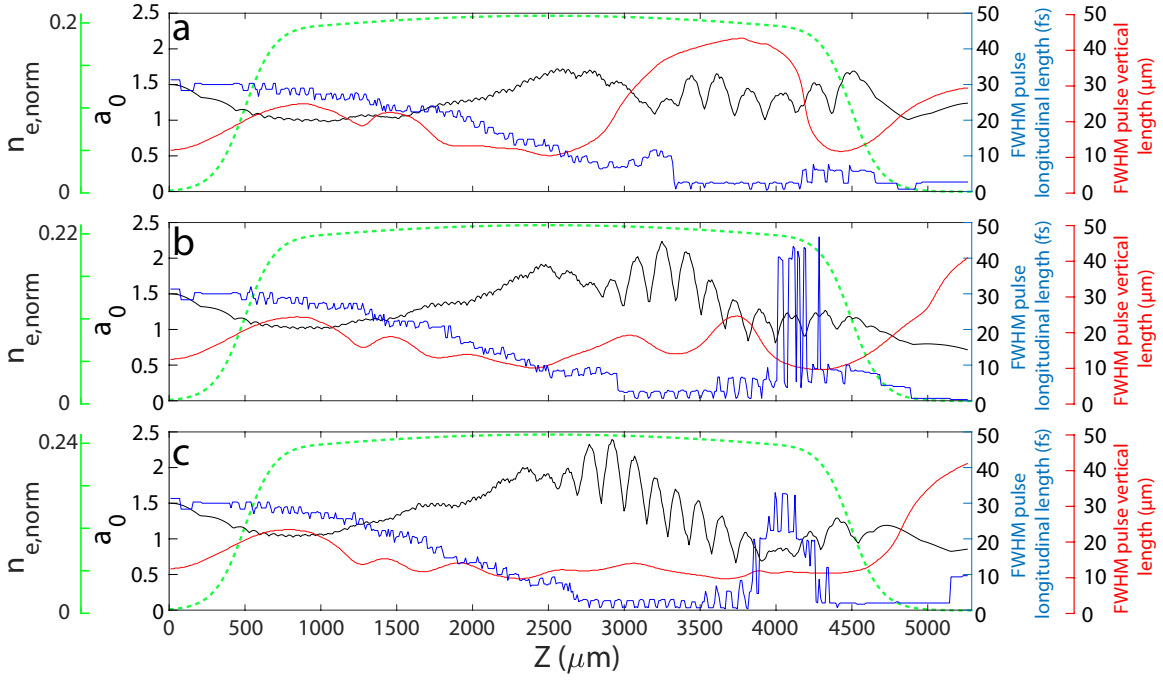

FIGURE 5.5: Simulated laser (black) a_0, (red) FWHM vertical size and (blue) FWHM longitudinal length evolution along the (green) gas density profile of Figure 5.1c, initial parameters of Table 5.1, maximum $n_{e,norm}$ (a) 0.2, (b) 0.22 and (c) 0.24.

All three case present vertical beam size oscillation due to non optimized laser spot matching with the plasma (Figure 5.5), however, by increasing the density, the oscillation amplitude falls. For the $n_{e,norm} = 0.24$ case (Figure 5.5c), the vertical beam size oscillates between 8.8 μm and 13 μm after 1.2 mm. The a_0 slow and rapid oscillations increase their frequency with the rise of density. Moreover, the rapid oscillations start earlier

for higher density, i.e., -0.3 mm per 0.02 $n_{e,norm}$. The reached maximum a_0 considerably grows going from 1.72 for 0.2 $n_{e,norm}$ to 2.24 (2.39) for 0.22 (0.24) $n_{e,norm}$. The laser depletion due to the higher particle ionization reduces a_0 linearly after its peak until the down-ramp for $n_{e,norm}$ above 0.2.

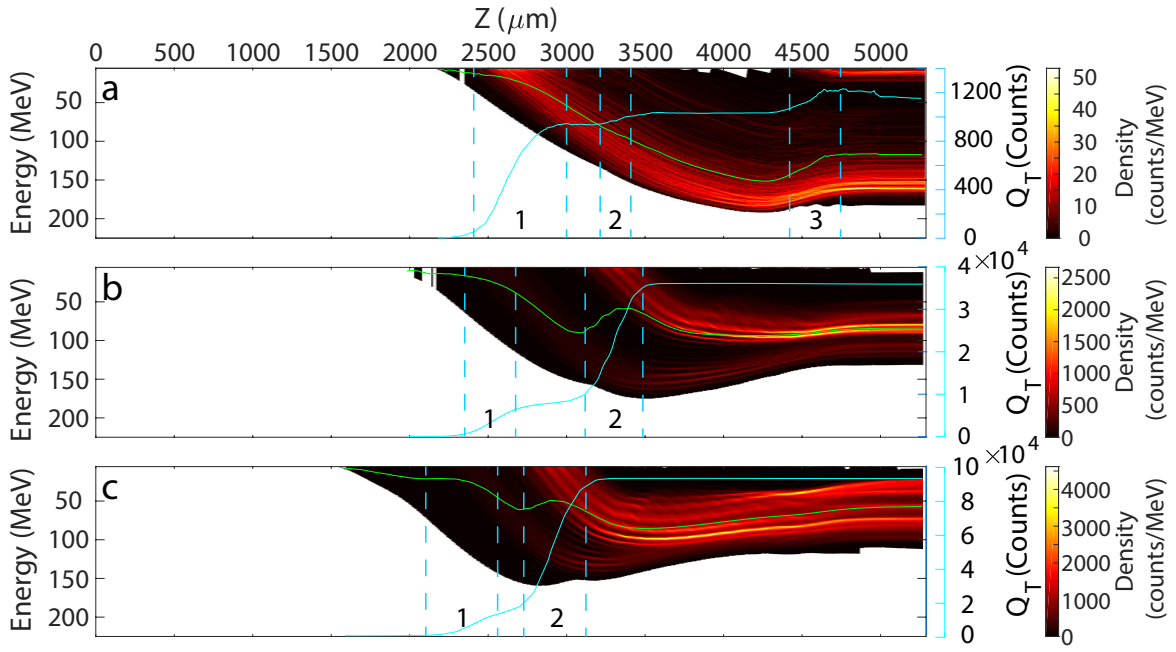

FIGURE 5.6: Simulated electron beam energy distribution evolution, (cyan solid line) total charge and (green line) total beam mean energy along the gas density profile of Figure 5.1c, initial parameters of Table 5.1, maximum $n_{e,norm}$ (a) 0.2, (b) 0.22 and (c) 0.24. (dotted cyan lines) Numbered main injection events zones.

Figure 5.6 presents the injection and acceleration along the gas for the different plasma densities. For $n_{e,norm}$ above 0.2 the low energies injection occurring at the middle of the down-ramp does not happen (Figure 5.6b, c). As the a_0 peak is reached earlier for higher $n_{e,norm}$ values (Figure 5.5) the two first major injection events also happen sooner. For 0.2 $n_{e,norm}$ most of the macroelectrons are injected in the first event (Figure 5.6a zone 1) while above 0.2 $n_{e,norm}$, the second event is more important, i.e., $\approx$ 85 % of the final charge (Figure 5.6c). The acceleration length drops with the $n_{e,norm}$ increase and thus the achieved maximum energy of the macroelectrons. The higher beam loading, deforming the wakefield, in conjunction to the laser beam depletion rate could be the cause of the fall of the acceleration length.

Figure 5.6 shows the spatial macroelectrons distribution and their transverse momentum at different positions for the three gas density cases. In the 0.2 $n_{e,norm}$ case, the macroelectrons are injected in all visible wakes, but mainly in the first one (Figure 5.6a1). During acceleration the beam slowly drifts to the wakefield transverse limits (Figure 5.6a2) and as soon as they enter the down-ramp the macroelectrons start to quickly oscillate transversely causing the energies below $\approx$ 100 MeV to be defocus becoming a cloud of particles behind the electron beam (Figure 5.6a3, a4). The origin of this behavior are the beam loading, especially the in the first wake, and the quick decrease in density on the down-ramp which expands the wake size until it disappears allowing for the macroelectrons to oscillate further. At the gas-vacuum interface (Figure 5.6a4) the first wake macroelectrons and the ones not lost during the down-ramp see a significant fall in transverse momentum. Increasing $n_{e,norm}$ improves the transversal focusing of the first wake macroelectrons substantially while worsening the rest of the wakes one due to the beam loading increase. For 0.22 $n_{e,norm}$ at the beginning of the down-ramp (Figure 5.6b2) the secondary wakes macroelectrons form a heavily transversely oscillating cloud while the first wake beam remains well focused. At the gas-vacuum interface, the first wake beam transverse size rises by a couple of μm and does not suffer significant longitudinal size change. Further increasing $n_{e,norm}$ to 0.24 causes an earlier transverse defocus of the secondary wakes macroelectrons. In addition, the longitudinal size and transverse size and momentum at the gas-vacuum interface rise with respect to the 0.22 $n_{e,norm}$ case (Figure 5.6c4) because of the larger charge.

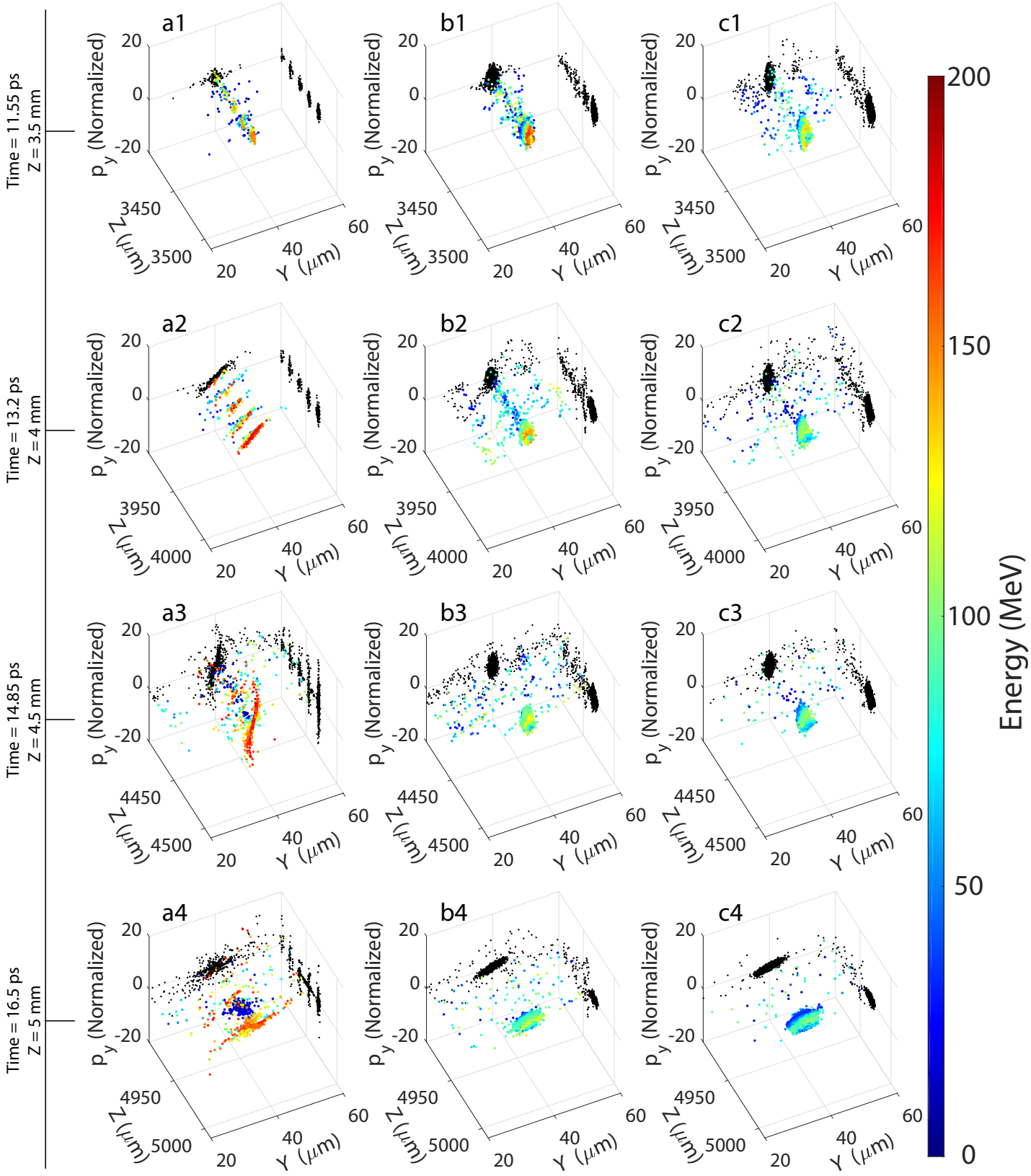

FIGURE 5.7: Simulated particles normalized transverse momentum in space and 2D projection (black dots) while accelerating (3.5 mm) (a1, b1, c1), at the down-ramp start (4 mm) (a2, b2, c2), middle of the down-ramp (4.5 mm) (a3, b3, c3) and plasma-vacuum interface (5 mm) (a4, b4, c4). Gas density profile of Figure 5.1c, initial parameters of Table 5.1, maximum $n_{e,norm}$ (a) 0.2, (b) 0.22 and (c) 0.24.

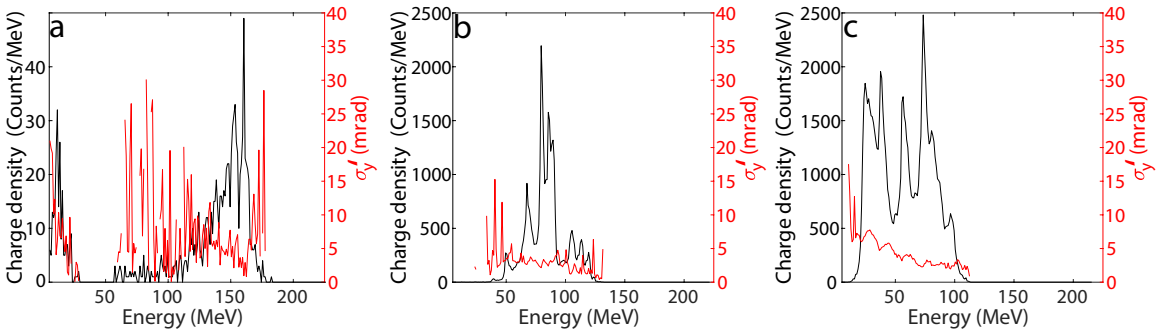

FIGURE 5.8: Simulated electron beam (black) energy distribution and (red) RMS divergence 30 μm after propagation through the gas density profile of Figure 5.1c, initial parameters of Table 5.1, maximum $n_{e,norm}$ (a) 0.2, (b) 0.22 and (c) 0.24.

The total beam energy distribution and divergence after 30 μm propagation in vacuum in Figure 5.8 exhibits a big difference between the three $n_{e,norm}$ cases. The most populated energies (E_{peak}) quickly fall with the increase of $n_{e,norm}$ (Table 5.3). The 0.22 $n_{e,norm}$ case shows a E_{peak} energy half the 0.2 $n_{e,norm}$ one. The lowest E_{peak} RMS transverse divergence is obtained in the 0.2 $n_{e,norm}$ (Table 5.3), however, the divergence distribution per energy presents variations of more than 15 mrad for the low and high energy tails around E_{peak}. Increasing $n_{e,norm}$ rises the stability of the divergence and reduces the higher energies divergence down to 0.4 mrad (0.88) for 130 MeV (112.5) in the 0.22 (0.24) $n_{e,norm}$ case. The best charge per MeV of E_{peak} is achieved for 0.22 $n_{e,norm}$ with ≈ 6 % of the total charge in it.

TABLE 5.3: Simulated electron beam parameters 30 μm after the gas density distribution of Figure 5.1c, initial parameters of Table 5.1. Parameters: maximum energy (E_{max}), most populated ± 0.5 energy slice (E_{peak}), E_{peak} slice divergence ($\sigma'_{y,peak}$), E_{peak} slice transverse size ($\sigma_{y,peak}$), energy spread around E_{peak} ($\sigma_{\gamma,peak}$), E_{peak} ± 0.5 slice charge ($Q_{E_{peak}\pm 0.5}$), Total beam charge (Q_T), Total beam transverse ($\sigma_{y,total}$) and longitudinal size ($\sigma_{s,total}$). Best $E_{peak} \pm 0.5$ MeV slice parameters (blue).

$n_{e,norm}$	E_{max} MeV	E_{peak} MeV	$\sigma'_{y,peak}$ mrad (RMS)	$\sigma_{y,peak}$ μm (RMS)	$\sigma_{\gamma,peak}$ MeV (FWHM)	$Q_{E_{peak}\pm 0.5}$ Counts/MeV	Q_T Counts	$\frac{Q_{E_{peak}\pm 0.5}}{Q_T} \times 100$ %	$\sigma_{y,total}$ μm (RMS)	$\sigma_{s,total}$ μm (RMS)
0.24	112.5	73.5	2.34	1.27	12.5	2481	92524	2.68	2.25	2.45
0.22	131.5	79.5	2.15	1.15	12	2195	35921	6.11	1.63	2.71
0.20	182.5	160.5	0.96	0.71	11	49	1153	4.25	4.32	12.5
0.18	163.5	-	-	-	-	-	57	-	-	-

In this configuration, the increase of density allows the laser to self-focus better and sooner inside the gas thus reaching higher a_0 values. However, because of beam loading and laser depletion the acceleration length is also shorter for $n_{e,norm}$ values above 0.2, therefore, the reached energies are significantly reduced but the charge rises. The peak energy slice transverse phase-space degrades with the density.

5.1.3 Gas mixture ratio parameter scan

The modification of the percentage of the high Z component (N_2) of the gas mixture may deeply the LPA dynamics. Rising the high Z component concentration enhances the number of possible injected electrons after ionization. The plasma density seen by the laser pulse during propagation should not be altered in a noticeable way due to the low concentrations of N_2. The effect of a gas mixture components concentration on the resulting electron beam is studied in this section. The initial simulation parameters of Table 5.1 and the gas longitudinal profile Figure 5.1c are used for the following simulations while utilizing the N_2 concentration values 1, 2 and 3 %.

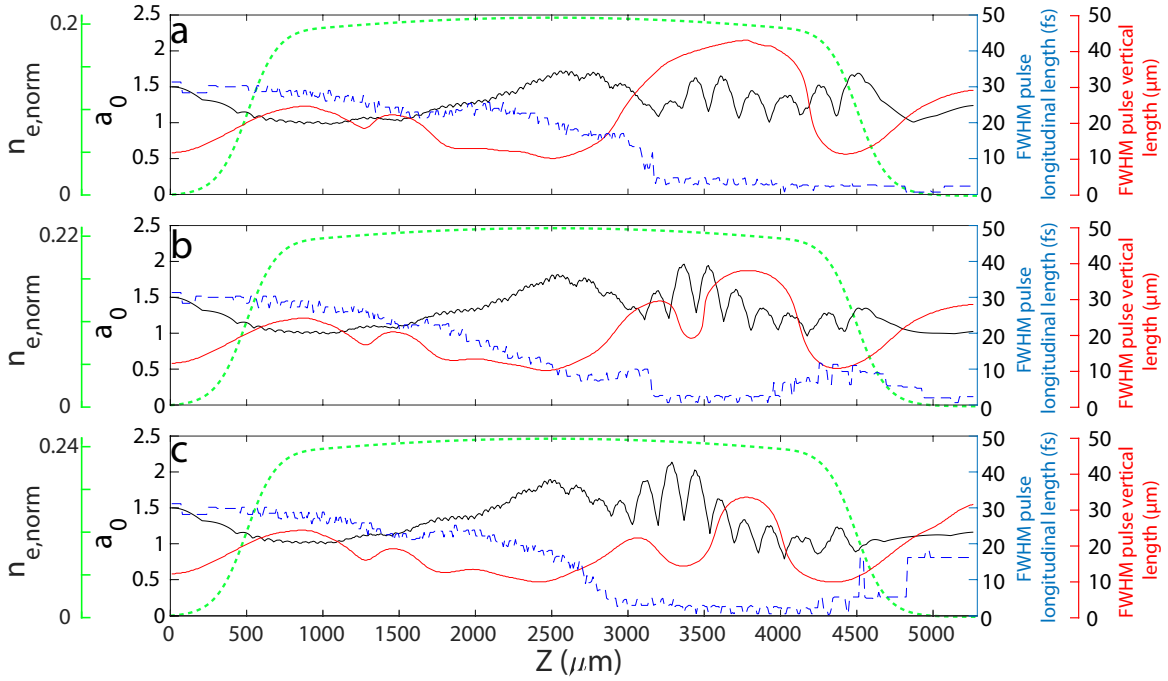

FIGURE 5.9: Simulated laser (black) a_0, (red) FWHM vertical size and (blue) FWHM longitudinal length evolution along the (green) gas density profile of Figure 5.1c, initial parameters of Table 5.1, 0.2 $n_{e,norm}$, (a) 1 %, (b) 2 % and (c) 3 % N_2.

The vertical laser size matching with the plasma improves for high concentrations (Figure 5.9). The 3 % case (Figure 5.9c) resembles the matching improvement obtained with the 0.22 $n_{e,norm}$ case (Figure 5.5b). a_0 slow oscillation frequency and the start of the rapid oscillations advance by ≈ 0.1 mm per 1 % increase in N_2 concentration. The focus improvement leads to an increase in the reached maximum a_0, with the 2 % (3 %) case achieving 1.96 (2.14) at 3.37 mm (3.29 mm). After the a_0 peak for N_2 concentrations above 1 %, a_0 decreases quickly due to the higher number particles ionized and injected into the wakes.

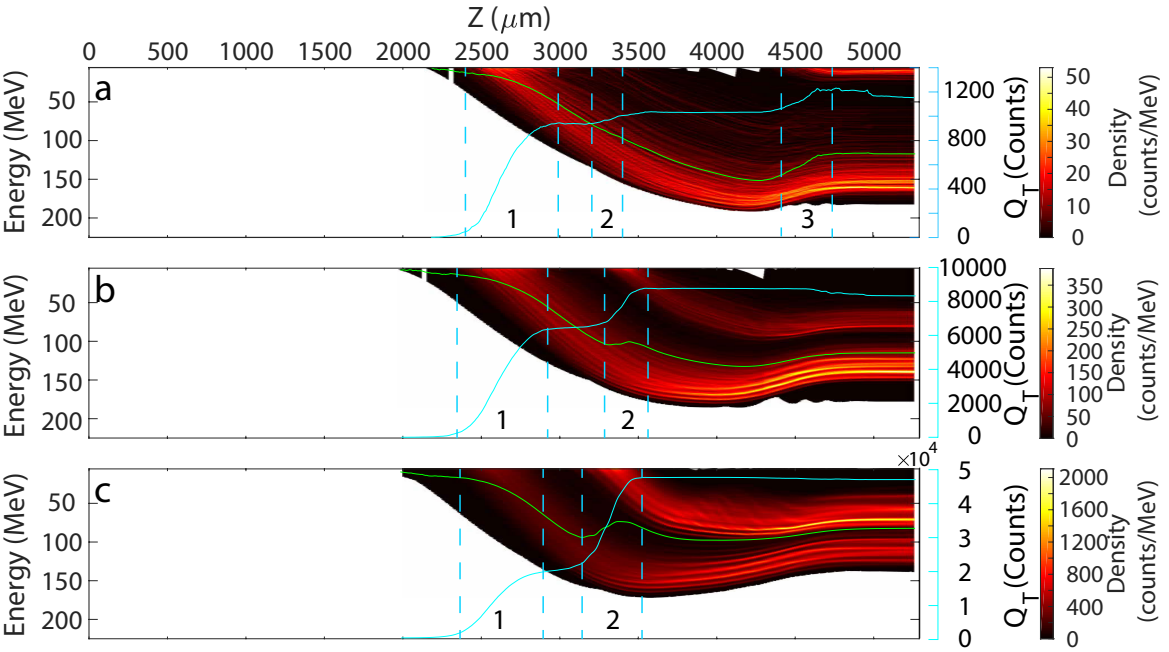

FIGURE 5.10: Simulated electron beam energy distribution evolution, (cyan solid line) total charge and (green line) total beam mean energy along the gas density profile of Figure 5.1c, initial parameters of Table 5.1, 0.2 $n_{e,norm}$, (a) 1 %, (b) 2 % and (c) 3 % N_2. (dotted cyan lines) Numbered main injection events zones.

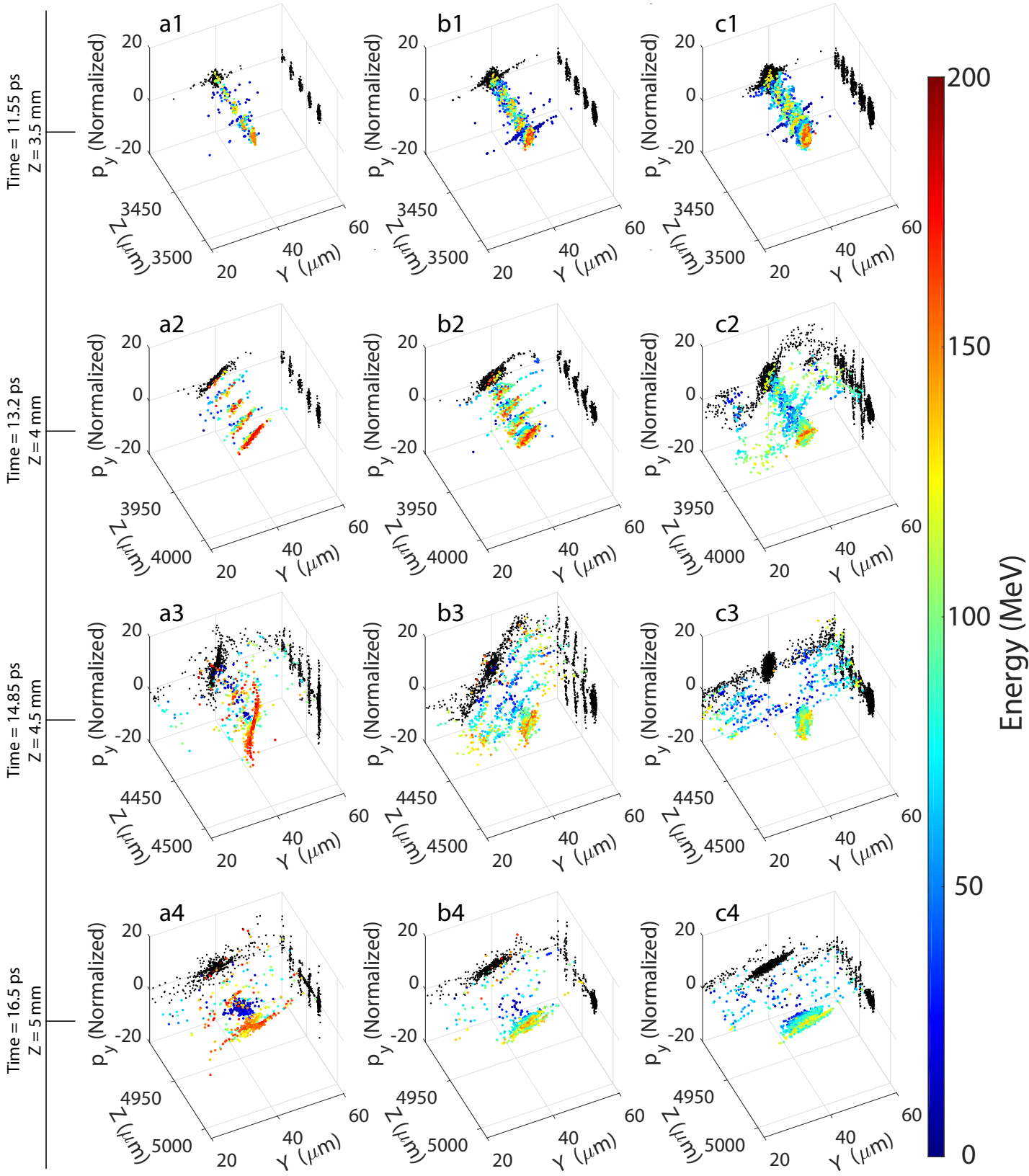

FIGURE 5.11: Simulated particles normalized transverse momentum in space and 2D projection (black dots) while accelerating (3.5 mm) (a1, b1, c1), at the down-ramp start (4 mm) (a2, b2, c2), middle of the down-ramp (4.5 mm) (a3, b3, c3) and plasma-vacuum interface (5 mm) (a4, b4, c4). Gas density profile of Figure 5.1c, initial parameters of Table 5.1, 0.2 $n_{e,norm}$, (a) 1 %, (b) 2 % and (c) 3 % N_2.

Figure 5.10 shows the beam density distribution and mean energy evolution along the gas. The injection zones position barely change with the increase of N_2 concentration because the a_0 is similar between them

(Figure 5.9). However, as the a_0 peak in the rapid oscillations part (Figure 5.9) increases so does the number of macroelectrons injected in the second injection event (Figure 5.10), leading to the second injection becoming more important than the first one. For the 3 % N_2 case (Figure 5.10c) the first injection saturates at 2×10^4 counts and the second one at 4.73×10^4, i.e., approximately 47 times higher than the 1 % N_2 final total charge (Figure 5.10a). Due to the second injection proximity to the down-ramp and the growth in the number of macroelectrons injected in it, the rise of the N_2 concentration causes a significant fall of the total beam mean energy. The macroeelctrons entering the wakes in the first injection also suffer from a lower acceleration due to beam loading and laser depletion (Figure 5.9).

Figure 5.11 presents the injected macroelectrons spatial position and transverse momentum for the different N_2 concentrations. The rise of N_2 % substantially worsens the transverse phase-space of the secondary wakes but improves the first wake beam one. During the acceleration, the 2 and 3 % cases secondary beams (Figure 5.11b1, c1) present already a higher transverse momentum compared to the 1 % case (Figure 5.11a1) and the lower energies start to oscillate spatially in the transverse direction. The oscillations only degenerate along the down-ramp. At the gas-vacuum interface the secondary wakes beams defocus slower in the transverse and longitudinal directions for high N_2 concentrations compared to the 1 % case (Figure 5.11b4, c4).

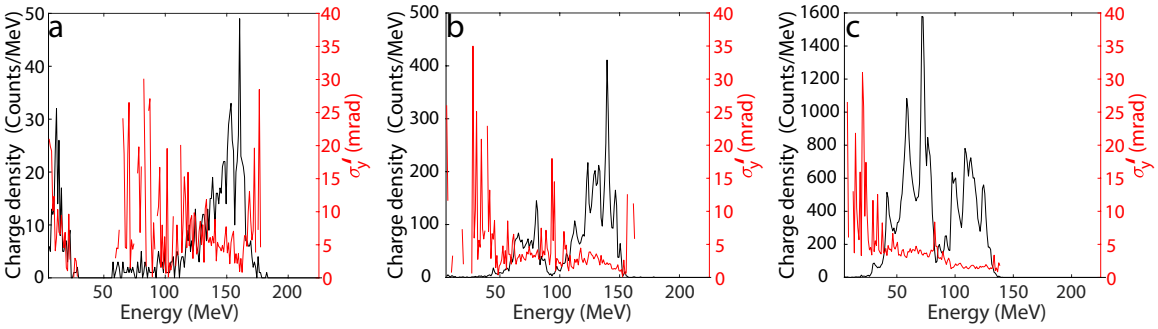

FIGURE 5.12: Simulated electron beam energy distribution and RMS divergence 30 μm after propagation through the gas density profile of Figure 5.1c, initial parameters of Table 5.1, 0.2 $n_{e,norm}$, (a) 1 %, (b) 2 % and (c) 3 % N_2.

The final total beam energy and divergence distribution in Figure 5.12 exhibit important differences between concentration cases. The increase of injected macroelectrons at the second injection event (Figure 5.10) causes the apparition of a peak around 70 MeV that becomes dominant for the 3% N_2 concentration case (Figure 5.12c). The high peak energy and maximum energy of the distributions fall with the rise of N_2 concentration (Table 5.4). The high energy peak divergence is bigger for the 2 and 3 % N_2 concentration cases compared to the 1 % one (Table 5.4), however, along the entire energy distribution the later offers much higher divergences (Figure 5.12). The same occurs regarding the longitudinal and transverse sizes (Table 5.4). The energy spread increases with the N_2 concentration, achieving for the 3 % N_2 case around the high energy peak 3 times the 1 % N_2 case one (Table 5.4).

TABLE 5.4: Simulated electron beam parameters 30 μm after the gas density distributions of Figure 5.1c, initial parameters of Table 5.1. Parameters: maximum energy (E_{max}), most populated ±0.5 energy slice (E_{peak}), E_{peak} slice divergence ($\sigma'_{y,peak}$), E_{peak} slice transverse size ($\sigma_{y,peak}$), energy spread around E_{peak} ($\sigma_{\gamma,peak}$), E_{peak} ±0.5 slice charge ($Q_{E_{peak}\pm0.5}$), Total beam charge (Q_T), Total beam transverse ($\sigma_{y,total}$) and longitudinal size ($\sigma_{s,total}$). Best $E_{peak} \pm 0.5$ MeV slice parameters (blue).

N_2 %	E_{max} MeV	E_{peak} MeV	$\sigma'_{y,peak}$ mrad (RMS)	$\sigma_{y,peak}$ μm (RMS)	$\sigma_{\gamma,peak}$ MeV (FWHM)	$Q_{E_{peak}\pm0.5}$ Counts/MeV	Q_T Counts	$\frac{Q_{E_{peak}\pm0.5}}{Q_T} \times 100$ %	$\sigma_{y,total}$ μm (RMS)	$\sigma_{s,total}$ μm (RMS)
3	140.5	108.5	1.50	0.96	29.5	781	46642	1.67	1.68	3.27
2	167.5	139.5	2.23	1.25	23.5	411	8327	4.93	1.95	4.77
1	182.5	160.5	0.96	0.71	11	49	1153	4.25	4.32	12.5

The increase of the N_2 concentration rises substantially the beam charge however, the late injection event gains more importance leading to a high number of counts in energies below 100 MeV and increasing the energy spread around the energy distribution peak. The total beam size and transverse divergence improve with high

N_2 concentration but the energy distribution peak ±0.5 MeV slice transverse size and divergence worsens by up to a factor 3 compared to the 1 % N_2 case.

5.1.4 Beam total charge and mean energy dependence on gas density and mixture ratio

The interplay between the variations of $n_{e,norm}$ and N_2 concentration cannot be studied with a couple cases and a range of parameters has to be treated. In this section, the total final beam charge (30 μm after gas) and mean energy results for parameters in Table 5.1 and $n_{e,norm}$ 0.16, 0.18, 0.2, 0.22, 0.24 and N_2 concentrations 1, 2, 3, 4 % are used to map the obtainable results by fitting the simulations (in total 14 points). While the total beam charge and main energy can be easily defined and compared, some parameters tied to the energy distribution cannot be directly compared in a meaningful way. Therefore, such a mapping is not possible.

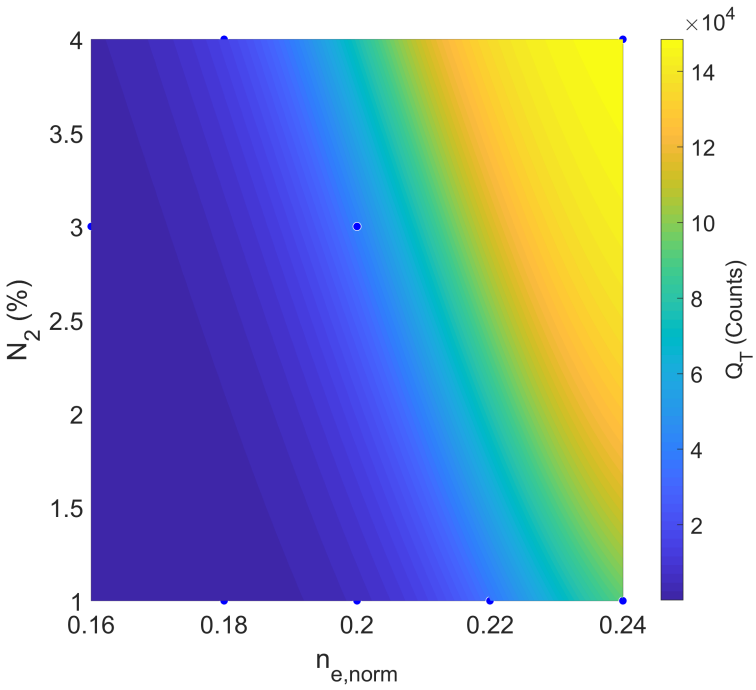

FIGURE 5.13: Final (30 μm after gas) total beam charge versus gas density and N_2 concentration percentage fitted surface via Equation 5.2 from simulations results (blue dots) and the rest of the initial parameters of Table 5.1.

The density results fit should comply with the following limits cases about the dependence on $n_{e,norm}$: The total beam charge cannot rise to infinity and in vacuum no injection occurs. Following the two $n_{e,norm}$ constrains the fit found has a form similar to the product of two logistic functions (Figure 5.13):

$$Q_T(N_2, \frac{n_e}{n_c}) = \frac{C_a + C_b N_2}{(1 + C_c e^{-C_d N_2})(1 + C_e e^{-C_f \frac{n_e}{n_c} - C_g N_2})} \tag{5.2}$$

with the C terms fitted constants with their value shown in Table 5.5. The C terms are related to the laser and other plasma parameters (e.g. profile) and the complexity of the system makes really difficult to explore all of these fitted constants.

TABLE 5.5: Constans values of the fit Equation 5.2.

$C_a = 15 \times 10^4$	$C_b = 319.15$	$C_c = 1.12246$	$C_d = 1.294$
$C_e = 1.69 \times 10^{11}$	$C_f = 109.4$	$C_g = 0.9495$	

The fit can be separated in two terms. One is purely dependent on the N_2 concentration ($\frac{C_a + C_b N_2}{1 + C_c e^{-C_d N_2}}$) and the second one ($\frac{1}{1 + C_e e^{-C_f \frac{n_e}{n_c} - C_g N_2}}$) exhibits both variables N_2 and $n_{e,norm}$. The charge increase is faster through a

$n_{e,norm}$ increase than a N_2 concentration one. Equation 5.2 is valid inside the parameter range of Figure 5.2 and below. For higher values it still needs to be tested but it should still work well for at least one more step of 1 % and 0.02 N_2 and $n_{e,norm}$.

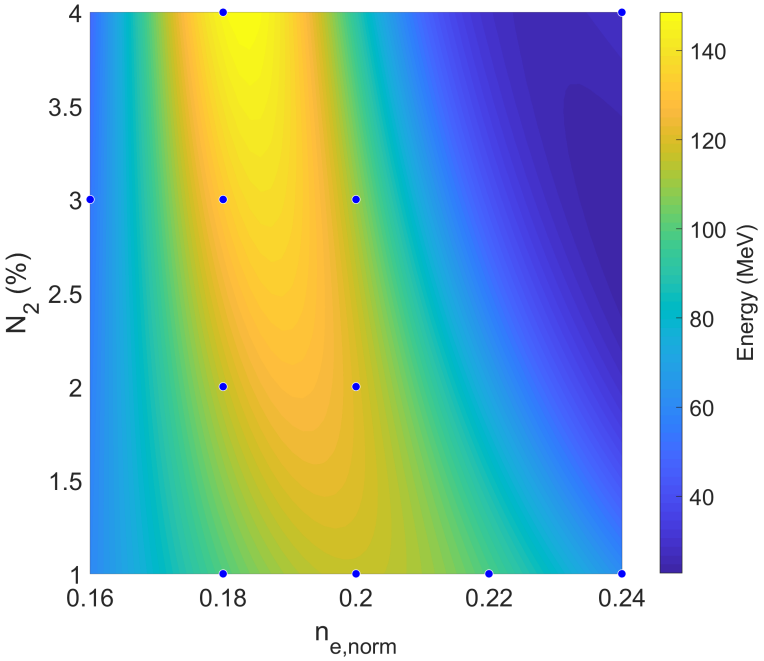

FIGURE 5.14: Final (30 μm after gas) mean total beam energy versus gas density and N_2 concentration percentage fitted surface via Equation 5.3 from simulations results (blue dots) and the rest of the initial parameters of Table 5.1.

For the total beam mean energy the only limit case the fit has to comply with is that in vacuum the mean energy is zero. The mean energy shows a more complex dependence in gas density and N_2 concentration. The fit found (Figure 5.14) is:

$$E_{mean}(N_2, \frac{n_e}{n_c}) = (C_a + C_b N_2) e^{-((-C_c - C_d N_2)\frac{n_e}{n_c} + C_e + C_f N_2)^2} + (C_g \frac{n_e}{n_c} N_2 - C_h N_2 - C_i \frac{n_e}{n_c}) \tag{5.3}$$

with the C terms fitted constants with their value shown in Table 5.6. As in Equation 5.2 the C terms are related to the laser and other plasma parameters.

TABLE 5.6: Constans values of the fit Equation 5.3.

$C_a = 107$	$C_b = 9.67296$	$C_c = 12.2562$	$C_d = 7.86133$
$C_e = 2.66859$	$C_f = 1.251$	$C_g = 115.2$	$C_h = 19.37$
$C_i = 20.15$			

The first term $((C_a + C_b N_2) e^{-((-C_c - C_d N_2)\frac{n_e}{n_c} + C_e + C_f N_2)^2})$ gives the general shape of the map. The effect over the mean energy of a change of $n_{e,norm}$ is determined by the N_2 concentration, e.g., for $n_{e,norm} = 0.2$ the highest mean energy is reached at low N_2 concentrations while the opposite occurs for 0.18 $n_{e,norm}$. The first term alone does not give good results for the point $n_{e,norm} = 0.24$ and $N_2 = 4$ %. The term $(C_g \frac{n_e}{n_c} N_2 - C_h N_2 - C_i \frac{n_e}{n_c})$ was found to correct and improve the fit accuracy.

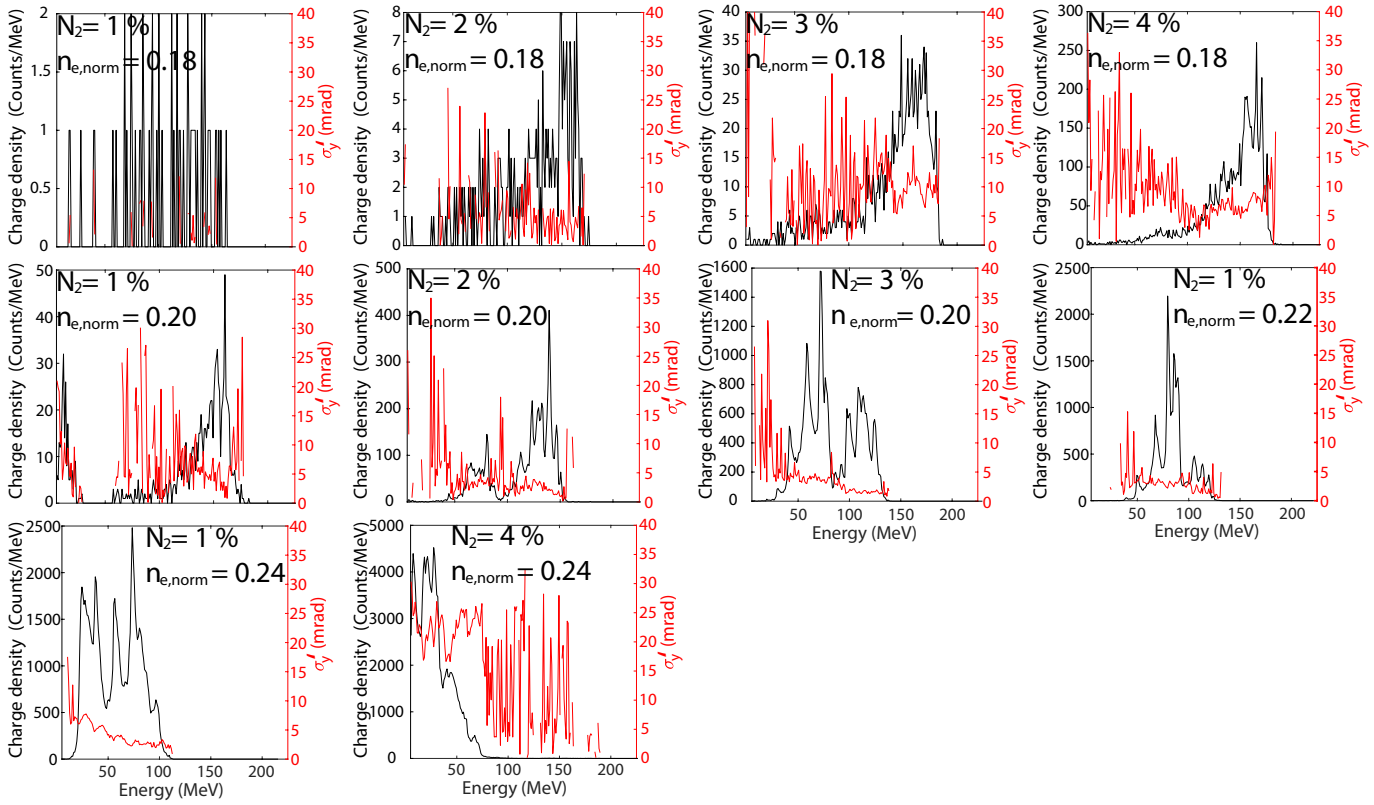

FIGURE 5.15: Final (30 μm after gas) beam energy distribution and divergence for the different $n_{e,norm}$ and N_2 concentration and the rest of the initial parameters of Table 5.1 simulated configurations.

The increase of plasma density has a deeper impact on the energy distribution Figure 5.15 than the gas mixture. The N_2 concentration growth for a fixed density rises the charge without affecting significantly the energy distribution shape. For densities equal or above 0.2 (Figure 5.10), the second injection event close to the down-ramp becomes increasingly important with the rise in N_2 concentration leading to most populated energy slice being in the low energies. Regarding the most populated 1 MeV energy slice, low densities give higher energy but with poor slice charge and divergence. The charge can be improved with the increase of the N_2 concentration but the slice divergence significantly worsens, e.g., for $n_{e,norm} = 0.18$ the increase from 2 % to 3 % N_2 doubles the slice divergence. So, if high energy is required a low density with N_2 concentrations above 2 % is more appropriate. If low slice divergence is also necessary then the density should be slightly increased while keeping the N_2 concentrations equal to 1, even though the charge severely falls.

TABLE 5.7: Simulated electron beam parameters 30 μm after the gas density distributions of Figure 5.1c, the different $n_{e,norm}$ and N_2 concentration and the rest of the initial parameters of Table 5.1. Parameters: maximum energy (E_{max}), most populated ±0.5 energy slice (E_{peak}), E_{peak} slice divergence ($\sigma'_{y,peak}$), E_{peak} slice transverse size ($\sigma_{y,peak}$), energy spread around E_{peak} ($\sigma_{\gamma,peak}$), E_{peak} ±0.5 slice charge ($Q_{E_{peak}\pm0.5}$), Total beam charge (Q_T), Total beam transverse ($\sigma_{y,total}$) and longitudinal size ($\sigma_{s,total}$). Best $E_{peak} \pm 0.5$ MeV slice parameters (blue).

$n_{e,norm}$	N_2 %	E_{max} MeV	E_{peak} MeV	$\sigma'_{y,peak}$ mrad (RMS)	$\sigma_{y,peak}$ μm (RMS)	$\sigma_{\gamma,peak}$ MeV (FWHM)	$Q_{E_{peak}\pm0.5}$ Counts/MeV	Q_T Counts	$\frac{Q_{E_{peak}\pm0.5}}{Q_T} \times 100$ %	$\sigma_{y,total}$ μm (RMS)	$\sigma_{s,total}$ μm (RMS)
0.18	1	163.5	-	-	-	-	-	57	-	3.39	16.63
0.18	2	174.5	163.5	3.76	1.97	18	8	302	2.65	4.91	19.24
0.18	3	186.5	169.5	6.98	4.20	36.5	34	1526	2.23	6.43	15.65
0.18	4	188.5	165.5	7.15	5.00	19	260	7430	3.5	4.93	10.12
0.20	1	182.5	160.5	0.96	0.71	11	49	1153	4.25	4.32	12.5
0.20	2	167.5	139.5	2.23	1.25	23.5	411	8327	4.93	1.95	4.77
0.20	3	140.5	108.5	1.50	0.96	29.5	781	46642	1.67	1.68	3.27
0.22	1	131.5	79.5	2.15	1.15	12	2195	35921	6.11	1.63	2.71
0.24	1	112.5	73.5	2.34	1.27	12.5	2481	92524	2.68	2.25	2.45
0.24	4	189.5	27.5	19.17	4.16	33	4521	147848	3.06	5.40	8.50

5.2 Laser power effect on the produced electron beam

Another way to drastically change the produced beam is by modifying the laser parameters, e.g., laser spot size, focus position, polarization, laser power. Regardless of the interest of an in depth study of the laser parameters, such analysis is out of the scope of this thesis. In the following a quick analysis of the effect of an increase of initial the laser $a_{0,initial}$ on the resulting electron beam is done. As the density $n_{e,norm} = 0.18$ and 2 % N_2 (Table 5.7) gave the best ensemble of high energy and low divergence with a low charge, in this section, the change due to an increase in the laser power from $a_{0,initial}$ 1.5 to $a_{0,initial}$ 1.75 is studied for those parameters.

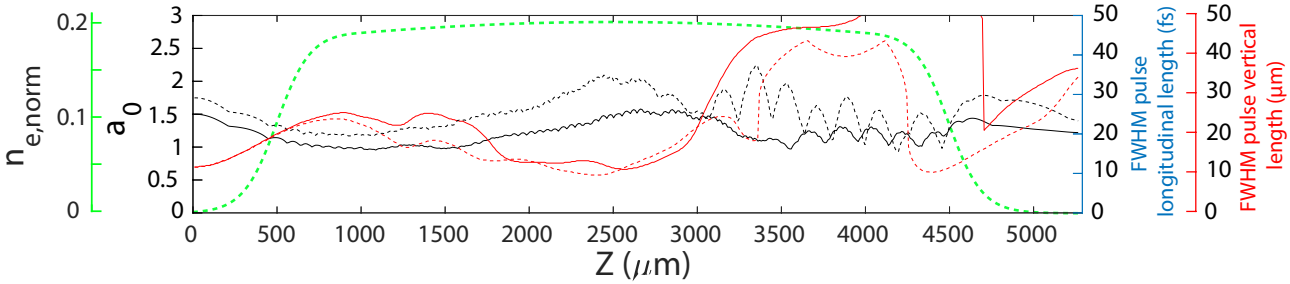

FIGURE 5.16: Simulated laser (black) a_0 and (red) FWHM vertical size evolution along the (green) gas density profile of Figure 5.1c. Simulation parameters: Table 5.1 with $a_{0,initial}$ 1.5 (solid line), 1.75 (dotted line), $n_{e,norm} = 0.18$, 2 % N_2.

Figure 5.16 presents the laser beam vertical size and a_0 evolution along the gas profile. The laser vertical focusing improves with the increase of a_0, especially at the a_0 rapid oscillation zone. The slow a_0 oscillations frequency slightly falls and its amplitude rises. The rapid oscillations start significantly advances by 0.4 mm with a much higher amplitude. The highest reached a_0 for the high (low) initial laser power case is 2.25 (1.58) at 3.35 mm (2.66 mm).

For $a_{0,initial}$ =1.5 a long injection of 1 mm length occurs and saturates at 353 macroelectrons. During the down-ramp a 14 % of the charge is lost due to not properly injected macroelectrons (Figure 5.17a). The increase of $a_{0,initial}$ to 1.75 exhibits a continuous weak injection from ≈ 1.8 mm and then two major injection events occur at ≈ 2.2 mm and ≈ 3.2 mm (Figure 5.17b). The first (second) event extends for 0.7 mm (0.28 mm) and saturates at 8.91×10^4 (1.12×10^5). In the middle of the down-ramp (4.51 mm), a sudden strong injection in the secondary wakes, especially the third and fourth ones, occurs doubling the total number of macroparticles, however, 80% of these newly added particles are immediately lost (Figure 5.17b). The $a_{0,initial}$ =1.75 case exhibits a better acceleration and the end distribution has a maximum electron energy of 225.5 MeV.

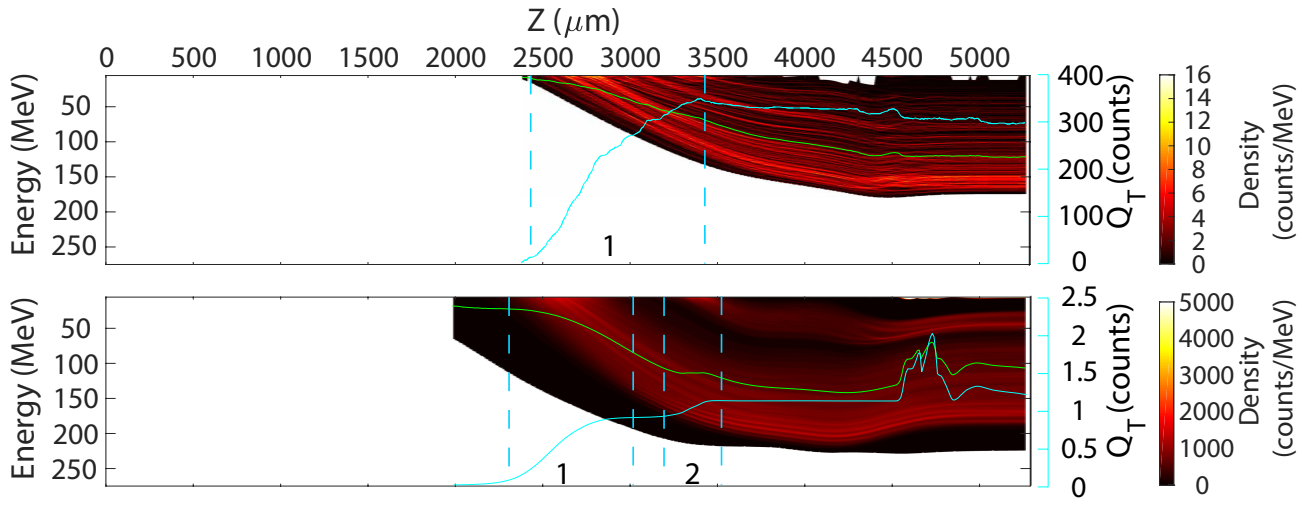

FIGURE 5.17: Simulated electron beam energy distribution evolution, (cyan solid line) total charge and (green line) total beam mean energy along the gas density profile of Figure 5.1c. Simulation parameters: Table 5.1 with $a_{0,initial}$ 1.5 and 1.75, $n_{e,norm}$ = 0.18, 2 % N_2. (dotted cyan lines) Numbered main injection events zones.

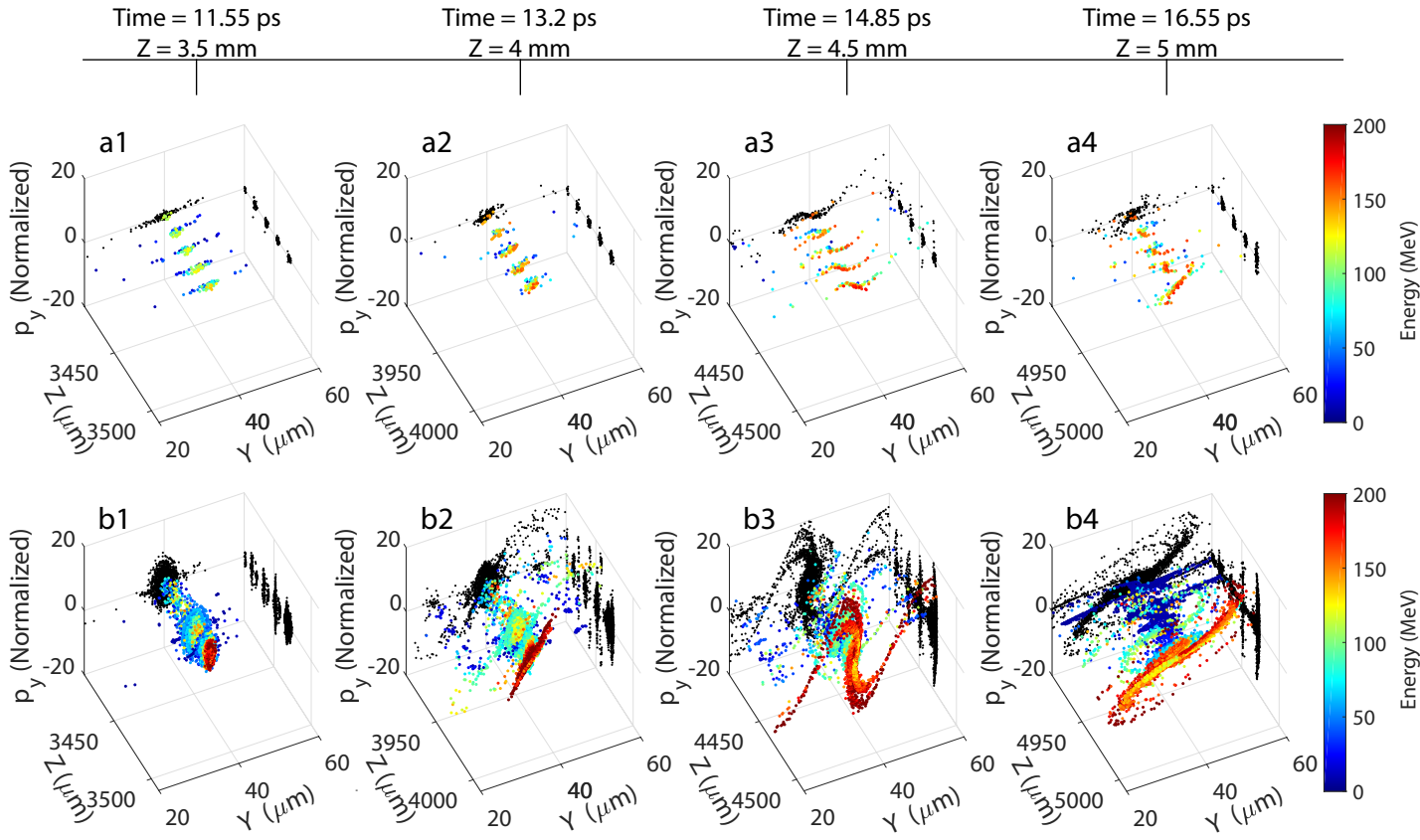

FIGURE 5.18: Simulated particles normalized transverse momentum in space and 2D projection (black dots) while accelerating (3.5 mm) (a1, b1), at the down-ramp start (4 mm) (a2, b2), middle of the down-ramp (4.5 mm) (a3, b3) and plasma-vacuum interface (5 mm) (a4, b4). Gas density profile of Figure 5.1c. Simulation parameters: Table 5.1 with $a_{0,initial}$ 1.5 (a) and 1.75 (b), $n_{e,norm}$ = 0.18, 2 % N_2.

Figure 5.18 presents the transverse phase-space and longitudinal position of the injected macroelectrons. In the $a_{0,initial}$ =1.75 case, the macroelectrons occupy always a bigger area in the transverse phase-space than the $a_{0,initial}$ =1.5 ones due to its much higher charge (Figure 5.18a1, b1). The down-ramp causes a violent transverse oscillation of the macroelectrons in the $a_{0,initial}$ =1.75 case that continues during its entire length (Figure 5.18b2, b3, b4). The transverse oscillations also happen in the $a_{0,initial}$ =1.5 case but they are much weaker (Figure

5.18a2, a3). The macroelectrons of the third injection in the $a_{0,initial}$ =1.75 case populate a wide transverse and longitudinal length behind the first wake but they have a low transverse momentum at the gas-vacuum interface (Figure 5.18b4).

Figure 5.19 and Table 5.8 compare the final beam energy distribution and divergence between the $a_{0,initial}$ =1.5 and $a_{0,initial}$ =1.75 cases for multiple N_2 concentration and $n_{e,norm}$. The rise of $a_{0,initial}$ causes a complete change in the energy distribution, a major increase in charge and energy spread and decreases the total beam transverse and longitudinal size. Regarding the energy, for $n_{e,norm}$ = 0.18 the most populated energy and maximum energies increase with $a_{0,initial}$ but for $n_{e,norm}$ = 0.20 only the maximum energy for the 2 % N_2 grows (Table 5.8). The most populated energy (E_{peak}) ±0.5 MeV slice divergence for $n_{e,norm}$ = 0.18 ($n_{e,norm}$ = 0.20) improves (worsens) with the increase in $a_{0,initial}$ and the effect is further enhanced by the rise of N_2 concentration. The E_{peak} slice transverse size considerably grows with $a_{0,initial}$, reaching a ≈ 2 times rise for the $n_{e,norm}$ = 0.20 with 2 % N_2.

Regarding possible FEL application, the best result is given by $n_{e,norm}$=0.18 and 1 % N_2 concentration. It offers a wide range of energies with a charge much higher than the $n_{e,norm}$=0.2 and 1 % N_2 case and a lower average divergence between 100-200 MeV. Therefore, the $n_{e,norm}$=0.18 and 1 % N_2 permits to work in a larger range of energies.

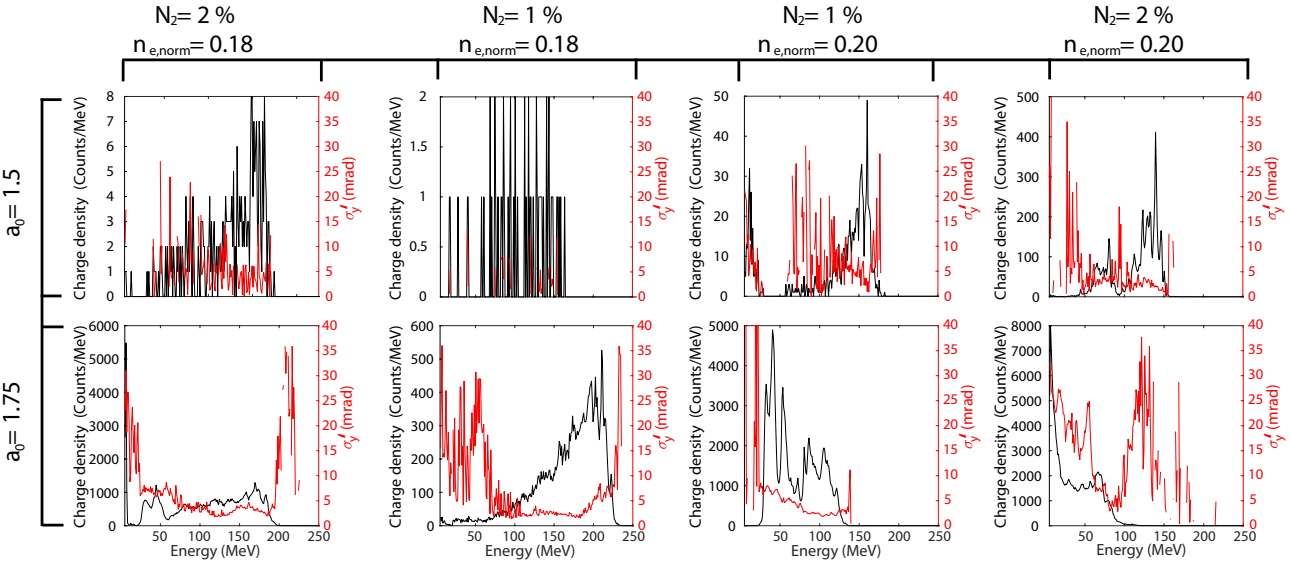

FIGURE 5.19: Simulated electron beam energy distribution and RMS divergence 30 μm after propagation through the gas density profile of Figure 5.1c. Simulation parameters: Table 5.1 with $a_{0,initial}$ 1.5 and 1.75, $n_{e,norm}$ = 0.18,0.2 and 1 %, 2 % N_2.

5.3 Summary

Simulations reveal an important effect of the gas mixture on the acceleration and also on the total charge. Their effect has been fitted from 2D PIC simulations giving highly non-linear expressions. The density up and down ramps shape and slope can also affect the produced beam. A 0.25 increase on $a_{0,initial}$ modifies significantly the energy distribution shape and transverse phase-space while enhancing the electron injection and acceleration which permits to explore lower gas densities. For FEL the desired beam energy slice transverse phase-space, charge and energy spread are fundamental (Section 2.6.3). A simple ionization injection LPA does not seem to be able to go under mrad (RMS) and approximately 10 % relative energy spread which were also observed experimentally (Chapter 4). The lowest slice divergence are around the most populated energy slice while the higher and lower energies show up to 30 times more. The best compromise between energy distribution, energy spread and slice divergence are found for $n_{e,norm}$=0.18 (0.20) and 1 % (1 %) N_2 and $a_{0,initial}$=1.75 (1.5). Experimental optimizations seem to agree with the simulations about the density and N_2 concentration. Nevertheless, for a real comparison with experiment 3D simulations are needed, but, due to the lack of computational resources it could not be done. The difference between the most populated energy slice parameters and the total beam ones shows the need of diagnostics able to target the desired energy slice for the undulator radiation to truly understand the capacity of an LPA system for such applications. The ionization injection simple setup here presented can probably be significantly improved, e.g., gas profile length, asymmetric

down and up ramps [34], better laser spot matching and focus position. Some of these improvements are already done experimentally (laser focus and matching optimization). Moreover, the addition of a density shock to the density profile [34, 36, 37] could help control the injection timing and allow for longer acceleration but its experimental implementation would require of the creation of more complex gas targets and a proper simulation study which are out of the scope of this thesis.

TABLE 5.8: Simulated electron beam parameters 30 μm after the gas density distributions of Figure 5.1c. Simulation parameters: Table 5.1 with $a_{0,initial}$ 1.5 and 1.75, $n_{e,norm}$ = 0.18,0.2 and 1 %, 2 % N_2. Parameters: maximum energy (E_{max}), most populated ±0.5 energy slice (E_{peak}), E_{peak} slice divergence ($\sigma'_{y,peak}$), E_{peak} slice transverse size ($\sigma_{y,peak}$), energy spread around E_{peak} ($\sigma_{\gamma,peak}$), E_{peak} ±0.5 slice charge ($Q_{E_{peak}\pm0.5}$), Total beam charge (Q_T), Total beam transverse ($\sigma_{y,total}$) and longitudinal size ($\sigma_{s,total}$). Best $E_{peak} \pm 0.5$ MeV slice parameters (blue).

N_2	$a_{0,initial}$	E_{max} MeV	E_{peak} MeV	$\sigma'_{y,peak}$ mrad (RMS)	$\sigma_{y,peak}$ μm (RMS)	$\sigma_{\gamma,peak}$ MeV (FWHM)	$Q_{E_{peak}\pm0.5}$ Counts/MeV	Q_T Counts	$\frac{Q_{E_{peak}\pm0.5}}{Q_T} \times 100$ %	$\sigma_{y,total}$ μm (RMS)	$\sigma_{s,total}$ μm (RMS)
					$n_{e,norm}$ **= 0.18**						
1	1.5	163.5	-	-	-	-	-	57	-	3.39	16.63
	1.75	245.5	210.5	4.95	4.51	47	526	28789	1.83	3.44	3.43
2	1.5	174.5	163.5	3.76	1.97	18	8	302	2.65	4.91	19.24
	1.75	225.5	169.5	3.26	2.60	85	1294	119958	1.08	3.22	15.25
					$n_{e,norm}$ **= 0.20**						
1	1.5	182.5	160.5	0.96	0.71	11	49	1153	4.25	4.32	12.5
	1.75	142.5	105.5	2.04	1.27	36.5	1945	167495	1.16	2.21	3.17
2	1.5	167.5	139.5	2.23	1.25	23.5	411	8327	4.93	1.95	4.77
	1.75	215.5	66.5	6.93	2.64	74	2151	167994	1.28	5.05	6.67

5.4 Conclusion

In order to interpret the experimentally characterized electron beam, 2D PIC simulations of an experimental like ionization injection scheme LPA system have been carried out for different gas densities ($3x10^{18}$ cm^{-3} to $6x10^{18}$ cm^{-3}), gas ratio (1 % to 4 %) and laser power (a_0 = 1.5 to 1.75). The results reveal that the optimum configuration is around $4.5x10^{18}$ cm^{-3} and 1 % of N_2 yielding divergence and energy spread around 2 mrad and 10 % respectively.

Chapter 6

Electron beam transport with typical measured electron beam parameters

The LPA measured electron beam charge and divergence (Chapter 4) are far from the baseline case (Table 3.3) for which the COXINEL line was designed as expected due to the utilization of the ionization injection scheme instead of the colliding pulse. The transport of the baseline beam with an ideal "slit-undulator" or "supermatching" optics cannot be experimentally reproduced (Section 3.1.2.1.1.1-3.1.2.1.2, Table 3.3). Therefore, a beam closer to the experimental results has to be considered for the transport and its characteristics at the undulator. The study of the electron beam and quadrupole misalignment effects permit to understand the capabilities of the COXINEL line and its monitoring. In this chapter, the transport of an "experimental like" beam is first compared to the baseline case. Then, the sensibility to initial beam deviations and to QUAPEVA errors is studied numerically. Lastly, the deviations are experimentally identified from the transverse shape at the imagers and reproduced by simulations.

6.1 Modelling for a realistic electron beam

6.1.1 Transport comparison between baseline and realistic electron beam parameter cases

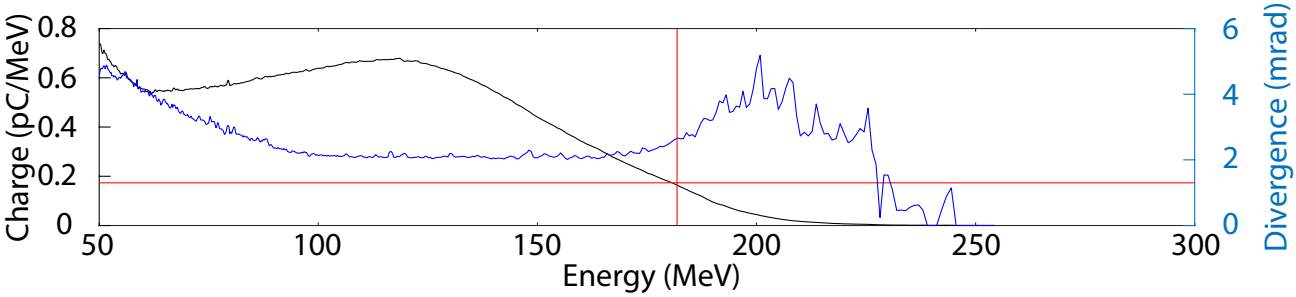

FIGURE 6.1: Initial beam energy distribution (black) and vertical (blue) RMS divergence for energy slices of ±0.5 MeV, spectrometer resolution. Average over a set of 20 distributions from the second set taken the 2017/11/30 [196].

The experimental like beam considered for the following analysis is presented in Table 6.1, with a reference slice FWHM divergence set to 4.7 mrad and the beam energy distribution the one of Figure 6.1 (Figure 4.8c), except stated otherwise. For the following simulations the initial electron beam is composed of a single bunch and not by multiple bunches as seen in the PIC simulation (Chapter 5). Due to the lack of information at the spectrometer about emittance and bunch length, the values of the baseline parameters are kept (Table 6.1).

TABLE 6.1: Baseline and experimental like study case parameters at the source of the COXINEL line design.

Case	Horizontal divergence σ'_x	Vertical divergence σ'_y	Horizontal emittance ϵ_x	Vertical emittance ϵ_y	bunch length σ_s	Beam charge	Energy Distribution
	mrad **(RMS)**	*mrad* **(RMS)**	*mm.mrad* **(RMS)**	*mm.mrad* **(RMS)**	μm	pC	
Baseline	1	1	1	1	1	34	Flat-top
Experimental like beam	2	2	1	1	1	100	Figure 4.8c

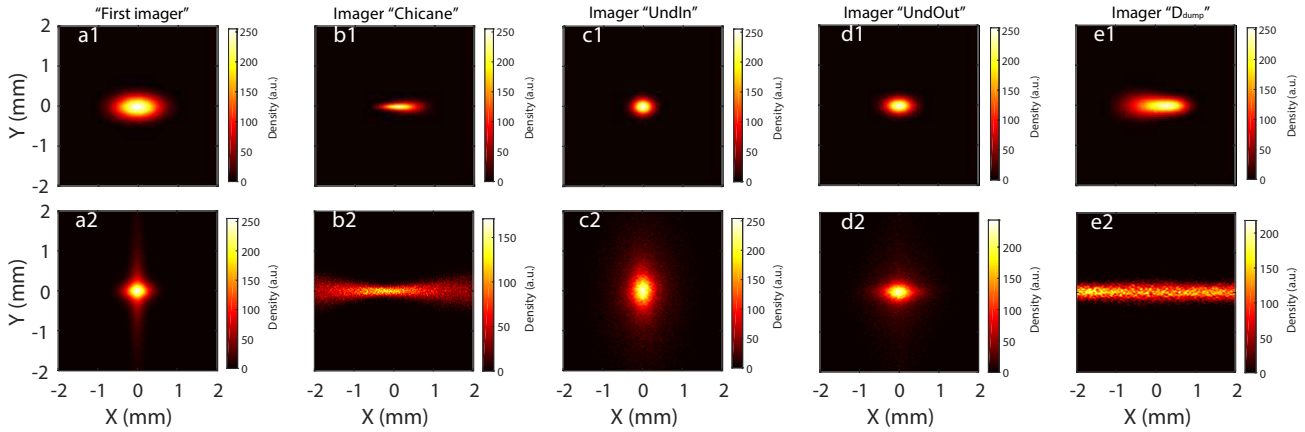

FIGURE 6.2: Simulated transversal shape along the COXINEL line for (a1, b1, c1, d1, e1) the baseline and (a2 , b2, c2, d2, e2) experimental like beam (Table 6.1) with the "supermatching" optics.

The simulated transport with the "supermatching" optics of the baseline and the experimental like beams (Table 6.1) in Figure 6.2 show the difference in the transversal shape caused by the increase in divergence and energy spread. From the "first imager" (Figure 6.2a) the increased energy spread causes the cross shape to appear while in imager "Chicane" (Figure 6.2b) and "D_{dump}" (Figure 6.2e) the beam horizontally extends much longer than in the baseline beam case. The higher divergence of the experimental case rises significantly the transversal beam size in all imagers.

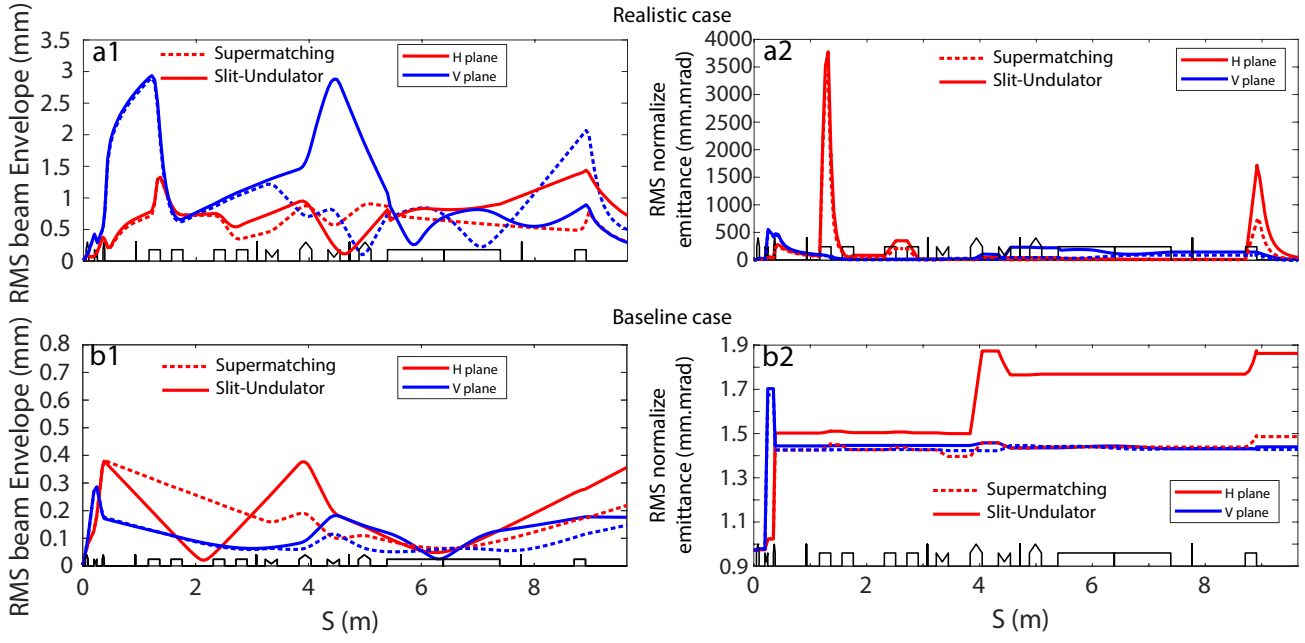

FIGURE 6.3: (a1, b1) Simulated horizontal (red), vertical (blue) beam envelope and (a2, b2) beam emittance evolution along the line for the line for the "supermatching" (dashed line) and "slit-undulator" (solid line) optics, (a) experimental like beam, with ϵ_{RMS} =1 mm.mrad, $\sigma'_{y,RMS,i} = 2$ mrad and $\sigma'_{x,RMS,i} =$ 2 mrad and (b) baseline, with ϵ_{RMS} =1 mm.mrad, $\sigma'_{y,RMS,i} = 1$ mrad and $\sigma'_{x,RMS,i} = 1$ mrad (Table 6.1).

Figure 6.3a1, b1 compares the beam envelope of the experimental like and the baseline case. In the experimental like case, the sizes are increased by an order of magnitude. The increase of the divergence and energy spread is catastrophic for the beam quality. The emittance evolution along the line in Figure 6.3a2, b2 shows an increase of more than two orders of magnitude of the emittance compared to the baseline case (Figure 3.6) in the "supermatching" and "slit-undulator" optics.

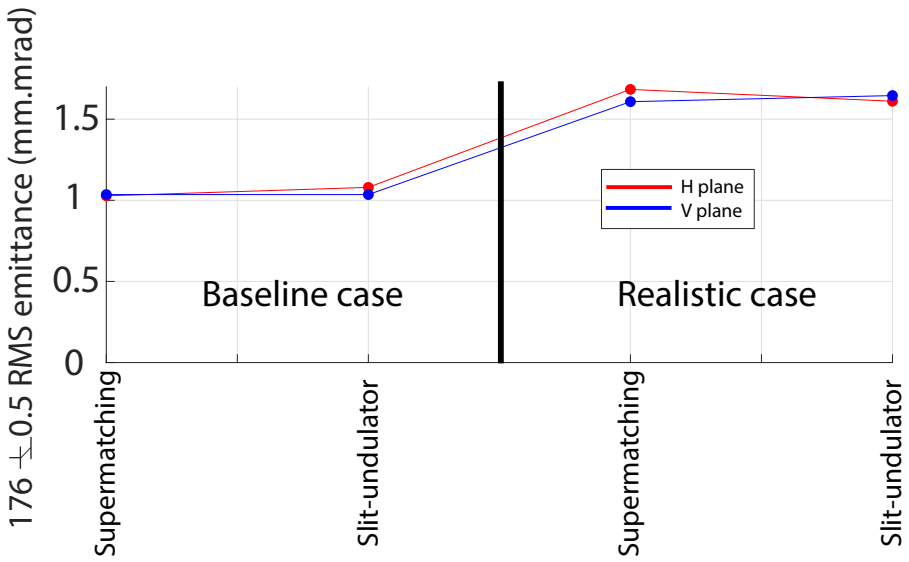

FIGURE 6.4: Simulated 176 ± 0.5 MeV slice horizontal (red) and vertical (blue) beam emittance evolution along the line for the "supermatching" (dashed line) and "slit-undulator" (solid line) optics, (a) the experimental like beam and (b) the baseline, with ϵ_{RMS} =1 mm.mrad, $\sigma'_{y,RMS,i} = 2$ mrad and $\sigma'_{x,RMS,i} = 2$ mrad (Table 6.1).

The transverse emittance for the 176 ± 0.5 MeV slice at the undulator center sees an increase of a factor ≈ 1.6 between the baseline and the realistic case (Figure 6.4).

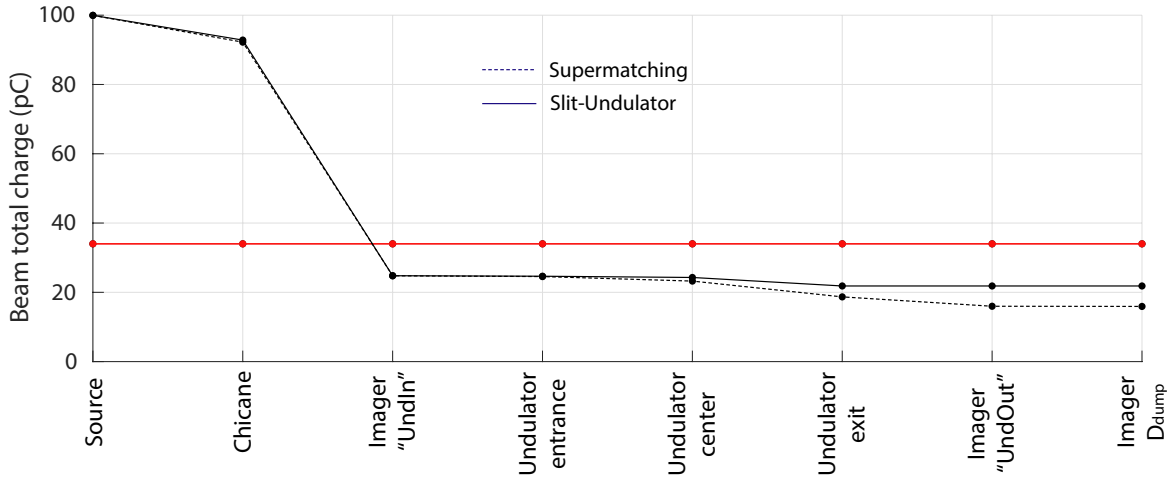

FIGURE 6.5: Simulated total beam charge evolution along the line for the "supermatching" and "slit-undulator" optics, the baseline beam (red) experimental like beam (black), with ϵ_{RMS} =1 mm.mrad, $\sigma'_{y,RMS,i} = 2$ mrad and $\sigma'_{x,RMS,i} = 2$ mrad (Table 6.1).

Table 6.2 compares the beam parameters for the baseline and experimental like cases at the undulator center for the "supermatching" and "Slit-undulator" optics. The beam longitudinal and transversal sizes increases by an order of magnitude with respect to the baseline case when using the experimental like beam. The vertical (horizontal) emittance increases by two (one) orders of magnitude with respect to the baseline case. In both cases, the reference 176 ± 0.5 MeV slice charge is conserved. However, the total charge in Figure 6.5 suffers an important loss of ≈ 60 % of low and high energies due to the vertical aperture at the chicane (Figure 3.2).

Therefore, the experimental like beam transport differs significantly from the baseline one and the electron total beam and 176 ± 0.5 MeV slice parameters at the undulator center are worse (Figure 6.4, 6.5).

TABLE 6.2: Baseline and experimental like simulated (Table 6.1) transport parameters at the undulator center for the "supermatching" and "slit-undulator" optics.

Optics	**Beam distribution**	**Longitudinal Size** σ_s	**Horizontal Size** σ_x	**Vertical Size** σ_y	**Horizontal emittance** ϵ_x	**Vertical emittance** ϵ_y	**Slice Charge**
		mm **(RMS)**	*mm* **(RMS)**	*mm* **(RMS)**	*mm.mrad* **(RMS)**	*mm.mrad* **(RMS)**	*pC*
Supermatching	Baseline	0.025	0.064	0.062	1.44	1.43	10.89
	Experimental	0.55	0.63	0.72	16.64	84.67	0.26
Slit-Undulator	Baseline	0.025	0.052	0.29	1.77	1.44	10.89
	Experimental	0.52	0.82	0.68	15.28	111.9	0.26

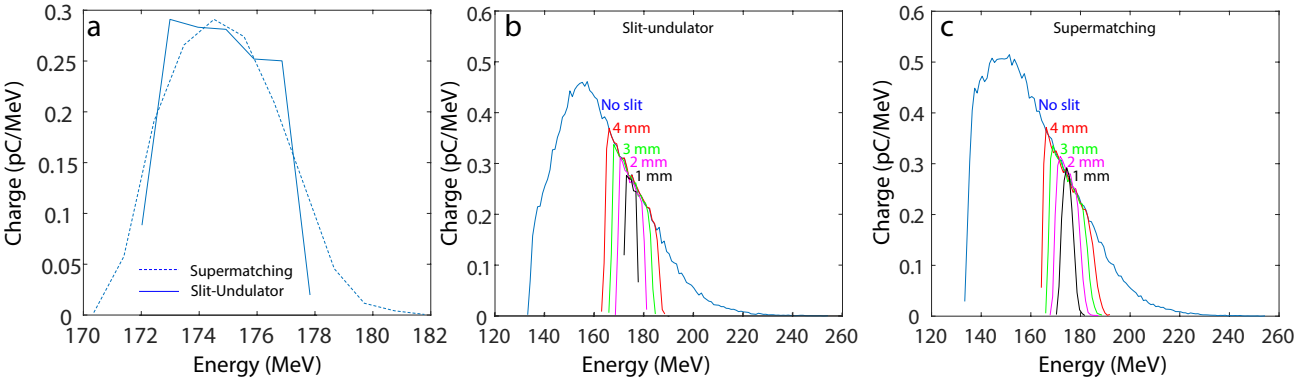

FIGURE 6.6: (a) Simulated beam energy distribution at the undulator center for the (b) "slit-undulator" and (c) "supermatching" optics with the slit open, 4, 3, 2 and 1 mm and (a) comparison for the slit closed at 1 mm. Parameters: experimental like beam, ϵ_{RMS} =1 mm.mrad, $\sigma'_{y,RMS,i}$ = 2 mrad and $\sigma'_{x,RMS,i} = 2$ mrad (Table 6.1).

The slit can still be used effectively in the experimental like beam case as shown for the 1 mm slit in Figure 6.6a. For "slit-undulator" optics, the slit cuts exactly the energies leaving for the 1 mm slit a energy range of 175 ± 3 MeV. With the "supermatching" optics energy can still be selected in the slit, but, less precisely, e.g., high and low energy tails in the distribution (Figure 6.6a). Figure 6.6b, c presents the experimental like case electron beam energy distribution at the undulator center for the "slit-undulator" and "supermatching" optics and different slit apertures. The slit at 4 mm cuts substantially the distribution reducing the energy range from approximately 135 to 250 MeV (no slit case) to 164 to 187 MeV. The distribution energy range is reduced with the slit opening by a rate of ≈ 2 MeV/mm at each side of the distributions. For the "slit-undulator" optics the distribution energy decrease is fairly equitable in the higher and lower energies with respect to the reference one, i.e., 176 MeV here. While for the "supermatching" optics is more irregular.

The realistic beam shows less optimal parameters than the initial baseline, however, simulations show that the COXINEL line can still transport the reference energy and compensate the initial divergence.

6.1.2 COXINEL FEL estimation via simulation

The measured LPA beams (Sections 4.3.2.1, 4.3.1) and PIC simulations show beam parameters and energies distributions significantly different from the baseline case (Section 3.1.4). Therefore, new start-to-end simulations should be done with a realistic beam. The input beam energy distribution and parameters (Table 6.3) are obtained from the PIC simulation results for $n_{e,norm}$=0.18, $a_{0,initial}$=1.75, N_2 concentrations of 1 % and 2 % (Figure 5.19, Table 5.8). As the charge is not available from the 2D PIC simulations (Section 5.2), a total charge of 100 pC is here utilized. Due to the lack of 3D information from the simulation both transverse divergences are taken as equal.

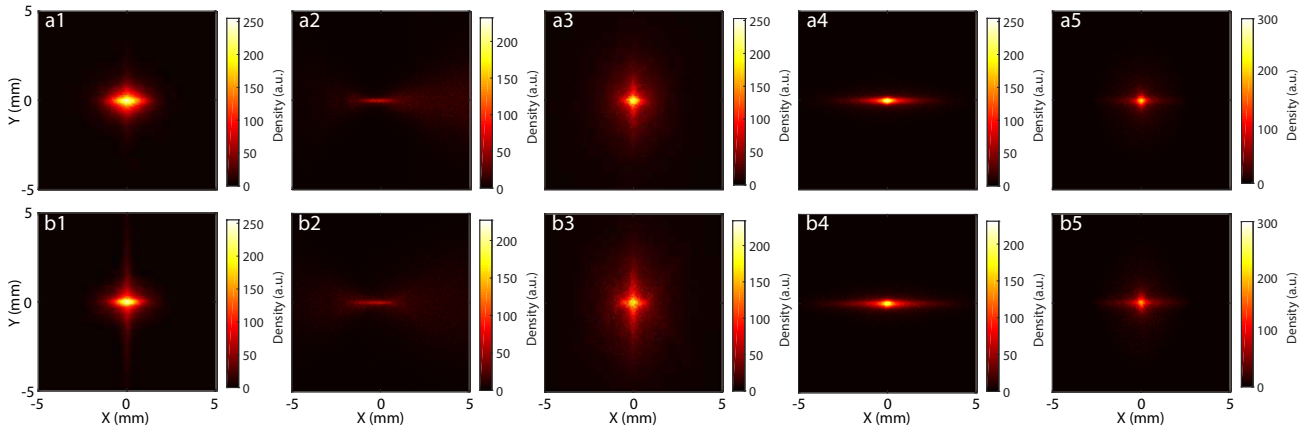

FIGURE 6.7: Simulated electron beam transverse shape at the (a1, b1) first imager, (a2, b2) "Chicane", (a3, b3) "UndIn", (a4, b4) undulator entrance and (a5, b5) "UndOut". Energy distribution from $a_{0,initial}$=1.75, $n_e = 4.56 \times 10^{18}$ and (a) 1 %, (b) 2 % N_2 concentration (Figure 5.19) PIC simulation, $Q_T = 100$ pC.

The transverse shape along the line of the 2 % N_2 concentration case (Figure 6.7b) presents a less focused and more visible cross shapes compared to the 1 % N_2 concentration case (Figure 6.7a) due to the electron beam higher divergence and energy spread (Table 5.8).

TABLE 6.3: Gain length, noise power and average SASE power calculated from the Ming Xie equations (Section 2.6.2). Energy distribution from $a_{0,initial}$=1.75, $n_e = 4.56 \times 10^{18}$ and 1 % and 2 % N_2 concentration (Figure 5.19) PIC simulation.

PIC simulation parameters			Source parameters		Undulator parameters				Radiation		
$n_{e,norm}$	$a_{0,initial}$	N_2 concentration	$Q_{151,source}$	$\sigma'_{source,151,RMS}$	$Q_{151,und}$	$\epsilon_{x,und,151,RMS}$	$\sigma_{s,und,151,RMS}$	$\sigma_{x,und,151,RMS}$	L_{gain} (m)	$P_{SASE,mean}$ (W)	P_{noise} (W)
0.18	1.75	1 %	0.58 pC	2.29 mrad	0.58 pC	7 mm.mrad	30.89 fs	2.07 mm	2.23×10^{5}	8.17×10^{-10}	1.32×10^{-3}
$n_{e,norm}$	$a_{0,initial}$	N_2 concentration	$Q_{151,source}$	$\sigma'_{source,151,RMS}$	$Q_{151,und}$	$\epsilon_{x,und,151,RMS}$	$\sigma_{s,und,151,RMS}$	$\sigma_{x,und,151,RMS}$	L_{gain} (m)	$P_{SASE,mean}$ (W)	P_{noise} (W)
0.18	1.75	2 %	0.635 pC	4.11 mrad	0.635 pC	63.75 mm.mrad	44.20 fs	3.05 mm	7.67×10^{5}	1.12×10^{-10}	5.93×10^{-4}

The SASE radiation power deduced with the Ming Xie equations (Section 2.6.2) in Table 6.3 show values considerably inferior to the noise power and three orders of magnitude lower than the degraded baseline like case (Table 3.4). The low charge density around 0.6 pC/MeV is the origin of the worsening in mean SASE power. From these results the FEL SASE configuration cannot be achieved with these LPA electron beam parameters which reinforces the need to use of the seeded FEL configuration in COXINEL.

6.2 Sensitivity to electron beam parameters

Beam parameter deviations from the baseline degrade the transport thus, the effects have to be investigated on the experimental like beam case.

6.2.1 Transversal characteristics

Five initial beam transversal parameters are studied in the following (the transversal size, divergence, σ'_x/σ'_y ratio, the pointing and displacement).

6.2.1.1 Effect of the initial beam transverse size

During transport, the chromatic emittance growth is dominated by the beam initial divergence (see Section 3.1.1.1). However, numerous additional terms (Equation 3.9) have a linear or quadratic dependence on the beam size, which can affect the emittance. For a fixed initial divergence, an increase of the initial beam size translates into an equal change in the initial emittance (Equation 2.134); neglecting the correlation terms. In the following numerical study, the initial emittance is changed while keeping the divergence constant. For the "slit-Undulator" optics, closing the slit only allows energies close to the reference energy to be transported (Section 3.1.1.3.2) and at 1 mm opening corresponds to approximately to an energy slice 175 ± 3 MeV (Figure 6.6), thus, if such slice is not affected the reference slice 175 ± 0.5 MeV is not either.

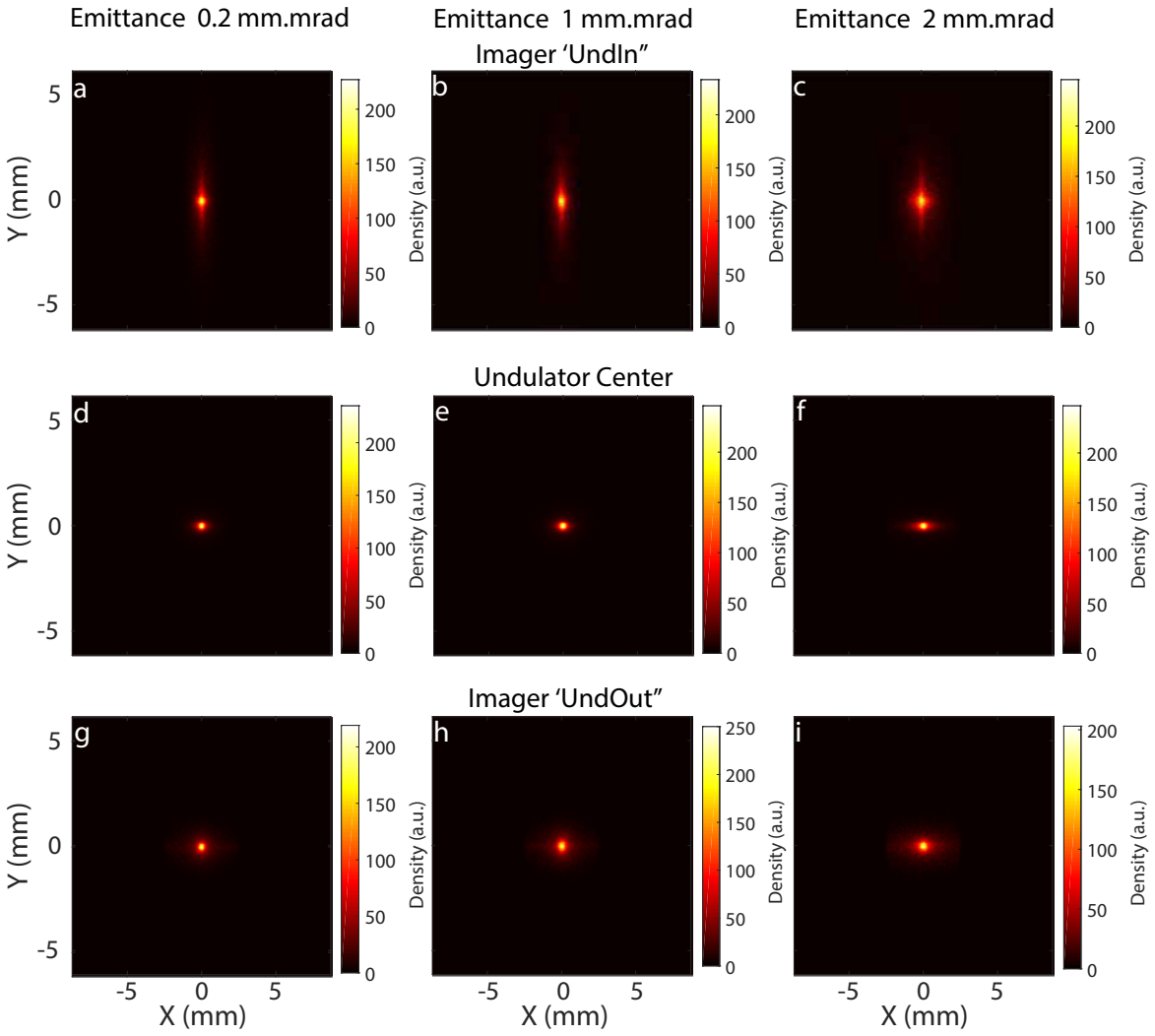

FIGURE 6.8: Simulated transverse beam shape at the imager (a-c) "UndIn", (d-f) undulator center and (g-i) "UndOut" for the "slit-undulator" optics. Initial beam distribution of Figure 4.8c with $\sigma'_{y,RMS} = 2$ mrad, $\epsilon_{RMS} = 0.2$, 1, 2 mm.mrad, $\sigma_s = 10^{-6}$ m and $\sigma'_x/\sigma'_y = 1$.

The simulated transversal shape at imagers "UndIn", UndOut" and at the undulator center is presented in Figure 6.8. The increase of the initial beam size yields an increase of the beam size along the line. The cross shape arms at imager "UndIn" do not increase in size equally. The vertical arm suffers a higher diffusion of the intensity but the area covered by the beam does not change much. The horizontal arm due to its tighter focus for the emittance value 0.2 mm.mrad increases much more. The same behavior appears in the imager "UndOut", but, with a better focus thanks to the optics (Figure 3.20).

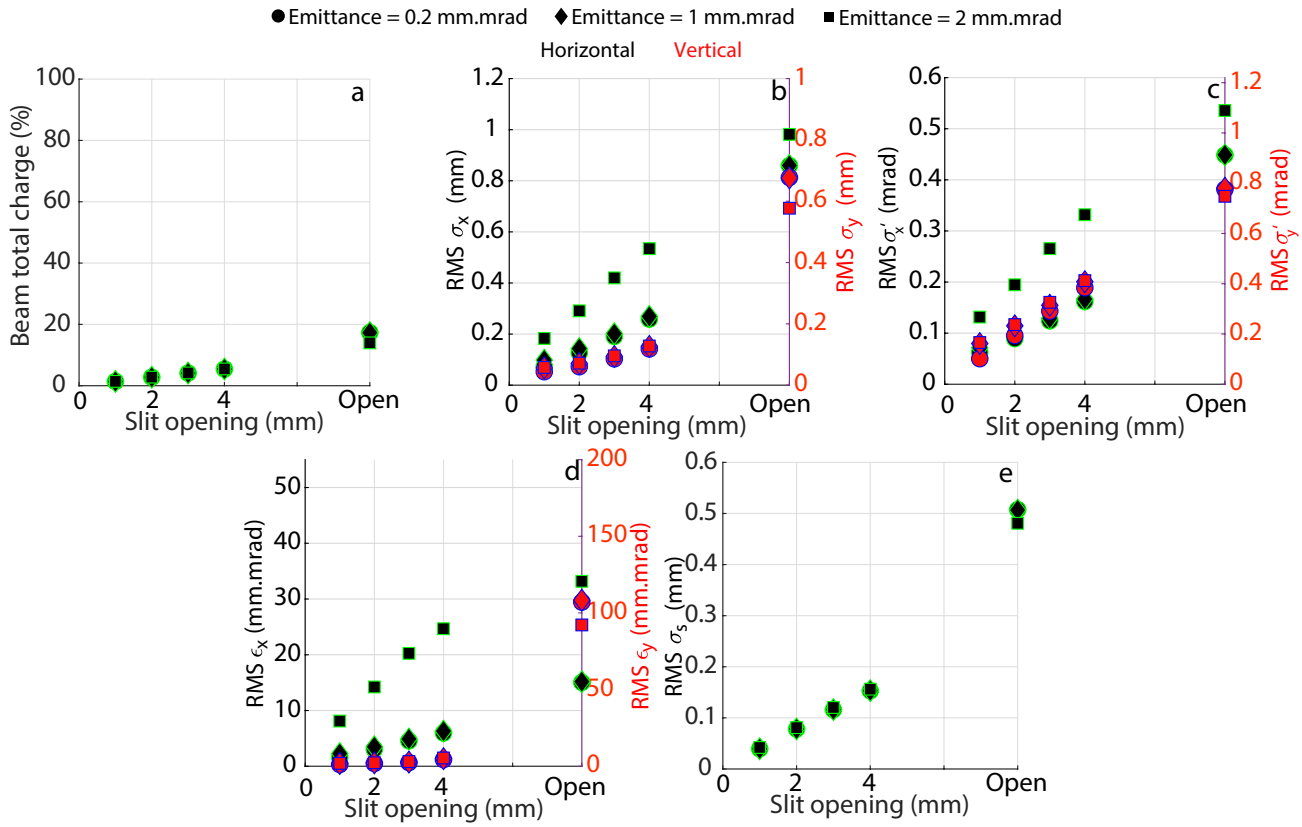

FIGURE 6.9: Simulated beam horizontal (black) and vertical (red) (b,e) $\sigma_{x,y,s}$, (c) $\sigma'_{x,y}$, (d) $\epsilon_{x,y}$ and (a) total charge versus slit opening at the undulator center for the "slit-undulator" optics. Initial beam of Figure 4.8c with $\sigma'_{y,RMS} = 2$ mrad, $\epsilon_{RMS} = 0.2$ (circle), 1 (diamond), 2 mm.mrad (square), $\sigma_s = 10^{-6}$ m and $\sigma'_x/\sigma'_y = 1$.

Figure 6.9 and Table 6.4 compares the transport of the electron beam at the undulator center (Figure 6.8d-f) for different values of the initial emittance with a fixed initial divergence without initial size-divergence correlation. The further increase of the initial emittance from 1 to 2 mm.mrad yields a more important effect in the transport of the total beam and the reference slice. For emittances equal or below 1 mm.mrad there is no electron loss, but for 2 mm.mrad, a 3.3 % of the total beam charge is lost at the undulator center (Figure 6.9a). In the three cases, the reference slice (slit closed to 1 mm) charge does not change, thus, the loss corresponds to higher and lower energies.

The difference in size and divergence of the total beam (slit open) between an emittance of 0.2 and 1 mm.mrad is mostly negligible. For $\epsilon = 2$ mm.mrad, the total beam (vertical) horizontal size decreases (increases) (Figure 6.9b, Table 6.4) and the vertical divergence barely changes while the horizontal divergence rises (Figure 6.9c, Table 6.4). The sudden decrease for $\epsilon = 2$ mm.mrad of the vertical direction is caused by the charge loss due to the line vertical aperture.

The horizontal (vertical) emittance of the total beam grows (drops) by ≈ 2 (0.85) times with respect to the 0.2 mm.mrad cases (Figure 6.9d). For the 176 ± 3 MeV slice (slit closed to 1 mm, see Figure 6.6), the horizontal (vertical) size and divergence increase by 1.34 (1.27) and 1.14 (1.59) times respectively for the 1 mm.mrad emittance case. The horizontal size and divergence double for the 2 mm.mrad (Figure 6.9c,d), which is expected in the horizontal direction as the initial size is also twice the 1 mm.mrad case one. The changes on the 176 ± 3 MeV slice size and divergence in the 1 mm.mrad lead to a reference slice horizontal (vertical) emittance of 2.26 mm.mrad (1.81 mm.mrad) (Figure 6.9d, Table 6.4). For the 2 mm.mrad case, the reference slice horizontal emittance is four times the one of the 1 mm.mrad emittance case while the vertical remain similar (Figure 6.9d, Table 6.4).

The longitudinal size is not affected (Figure 6.9e, Table 6.4). For the "supermatching" optics, the total beam (slit 1 mm) transverse horizontal and vertical size at the undulator center are 0.64 mm (0.2 mm) and 0.73 mm (0.2) respectively. Therefore, the beam is even bigger than in for the "slit-undulator" optics.

Thus, the initial beam size can indeed cause noticeable transport degradation. In the vertical direction, the main issue quickly becomes the particle loss due to the line aperture instead of the chromatic emittance growth terms in Equation 3.9.

TABLE 6.4: Figure 6.9 values of the simulated beam size σ, divergence σ', emittance ϵ and total charge (Q_T) versus slit opening and their ratio to the 0.2 mm.mrad case ($\frac{X_{\epsilon_i}}{X_{\epsilon_i=0.2}}$) for 1 mm an open slit at the undulator center for the "slit-undulator" optics. Initial beam Figure 4.8c with $\sigma'_{y,RMS} = 2$ mrad, $\epsilon_{RMS} = 0.2$ mm.mrad, 1 mm.mrad, 2 mm.mrad, $\sigma_s = 10^{-6}$ m and $\sigma'_x/\sigma'_y = 1$.

Parameter (RMS)	$\epsilon_{initial}$ (mm.mrad)	**Slit opening (mm)**						
		1 $\frac{X_{\epsilon_i}}{X_{\epsilon_i=0.2}}$	1	2	3	4	Open	Open $\frac{X_{\epsilon_i}}{X_{\epsilon_i=0.2}}$
σ_x (mm)	0.2	1	0.073	0.127	0.191	0.259	0.860	1
	1	1.34	0.098	0.143	0.202	0.269	0.860	1
	2	2.51	0.183	0.291	0.420	0.534	0.982	1.14
σ_y (mm)	0.2	1	0.044	0.060	0.086	0.118	0.677	1
	1	1.27	0.056	0.071	0.094	0.126	0.676	1
	2	1.32	0.058	0.072	0.096	0.128	0.577	0.85
σ'_x (mrad)	0.2	1	0.062	0.089	0.124	0.162	0.449	1
	1	1.14	0.071	0.097	0.129	0.166	0.449	1
	2	2.11	0.131	0.195	0.265	0.332	0.536	1.19
σ'_y (mrad)	0.2	1	0.102	0.194	0.291	0.384	0.776	1
	1	1.59	0.162	0.232	0.314	0.408	0.780	1
	2	1.63	0.166	0.237	0.326	0.412	0.748	0.96
ϵ_x (mm.mrad)	0.2	1	1.58	3.04	4.56	5.96	15.04	1
	1	1.43	2.26	3.49	4.88	6.30	15.17	1
	2	5.13	8.11	14.22	20.25	24.67	33.18	2.21
ϵ_y (mm.mrad)	0.2	1	1.15	1.83	2.40	4.35	107.07	1
	1	1.57	1.81	2.21	2.73	4.95	108.35	1.01
	2	1.63	1.88	2.28	3.05	5.39	92.18	0.86
Q_T (%)	0.2	1	1.39	2.77	4.12	5.44	17.35	1
	1	1	1.39	2.77	4.12	5.45	17.31	1
	2	1.01	1.41	2.79	4.17	5.46	13.97	0.80
σ_s (mm)	0.2	1	0.039	0.078	0.116	0.153	0.507	1
	1	1	0.039	0.078	0.116	0.153	0.507	1
	2	1.08	0.042	0.081	0.120	0.156	0.481	0.95

For the reference 176 ± 0.5 slice MeV at the undulator center (Table 6.5) the vertical focusing of the optics and undulator limits the vertical chromatic emittance growth while the horizontal emittance rises by a factor ≈ 4 for an initial emittance increase of 1 mm.mrad. The charge is conserved in all cases.

TABLE 6.5: Values of the simulated beam 176 ± 0.5 MeV slice emittance ϵ and charge (Q_{slice}) without slit at the undulator center for the "slit-undulator" optics. Initial beam Figure 4.8c with $\sigma'_{y,RMS} = 2$ mrad, $\epsilon_{RMS} = 0.2$ mm.mrad, 1 mm.mrad, 2 mm.mrad, $\sigma_s = 10^{-6}$ m and $\sigma'_x/\sigma'_y = 1$.

Parameter	**Unit**	$\epsilon_{initial}$		
(RMS)		(mm.mrad)		
		0.2	1	2
ϵ_x	mm.mrad	0.41	1.62	3.21
ϵ_y	mm.mrad	0.41	1.52	1.59
Q_{slice}	pC	0.26	0.26	0.26

6.2.1.2 Effect of the initial divergence

A high initial divergence can be catastrophic for the FEL generation (Figure 3.14) and for the transport (Equation 3.6). To be able to simulate high divergence cases without losing the beam during transport, an initial emittance of 0.2 mm.mrad is used instead of 1 mm.mrad.

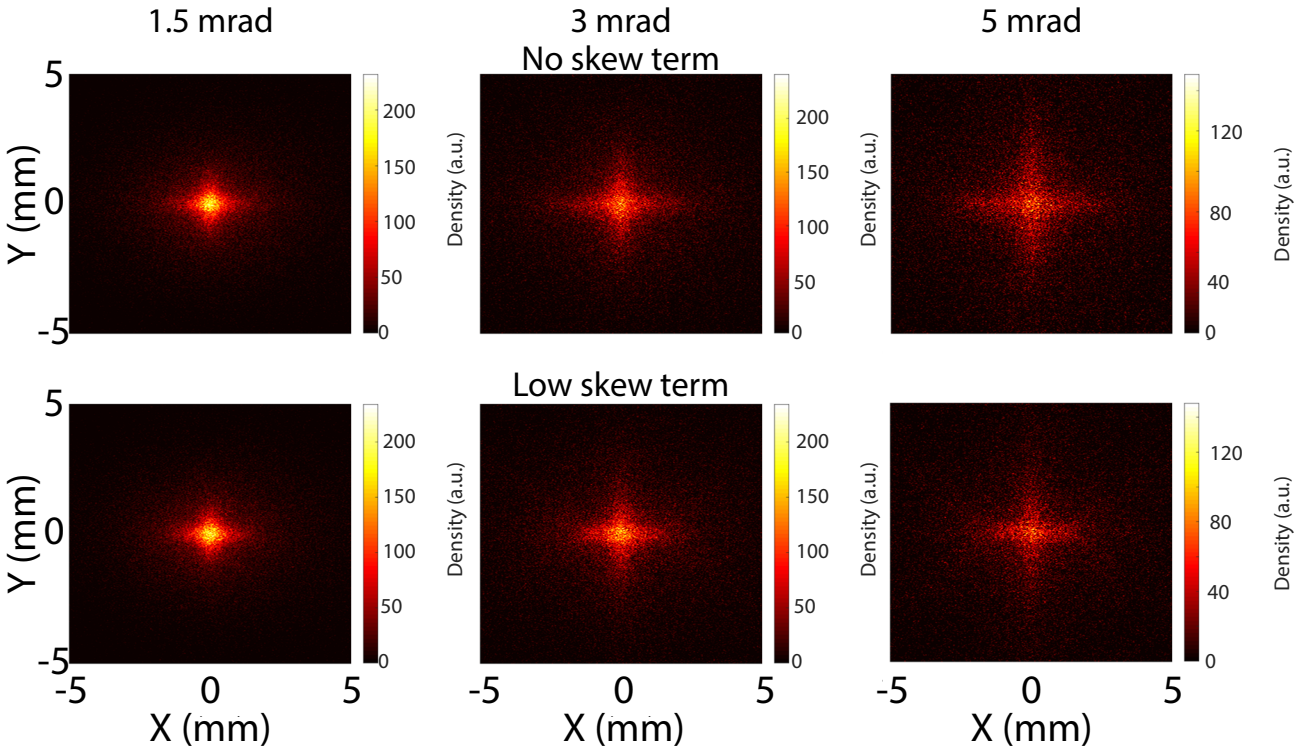

FIGURE 6.10: Simulated transverse image at imager "UndIn" for initial RMS divergences 1.5 mrad, 3 mrad and 5 mrad with and without low skew (Table 3.8) for the electron distribution of Figure 4.8c, ϵ_{RMS} = 0.2 mm.mrad, Q_t = 100 pC, divergence ratio 1.56, macroparticles=0.5×10^6, $\sigma_s = 10^{-6}$ m with the "supermatching" optics.

To investigate further the influence of the initial electron beam divergence on the transport, multiple initial vertical divergences $\sigma'_{y,i}$ with the same vertical and horizontal divergence ratio of 1.56 are used. The simulated transverse shape at imager "UndIn" for the different initial divergences (1.5, 3 and 5 mrad) in Figure 6.10 show the diffusion of the cross shape when the divergence is increased even for the focused energy. The addition of a low skew term a_2 degrades further the beam and the cross shape arms start to disappear due to the high and low energies defocusing.

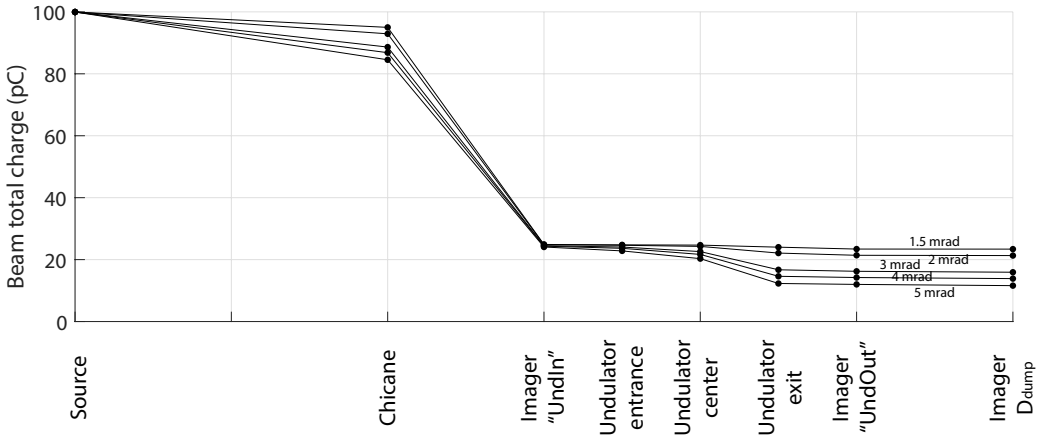

FIGURE 6.11: Total beam charge along the line for the initial divergences σ'_y = 1.5, 2, 3, 4 and 5 mrad with electron distribution of Figure 4.8c, σ'_x/σ'_y = 1.56, ϵ_{RMS} = 0.2 mm.mrad, Q_t = 100 pC, macroparticles=0.5×10^6, $\sigma_s = 10^{-6}$ m, with "supermatching" optics.

The total beam charge for the "supermatching" optics in Figure 6.11 largely decreases along the line with the rise of the initial divergence. The total charge is reduced to a 24% for the initial vertical divergence 1.5 mrad and each additional mrad increase reduces the charge by 2% , except from 2 mrad to 3 mrad where decreases by 6%. The 176 ± 0.5 MeV slice charge suffers less than 1% loss for the 5 mrad case.

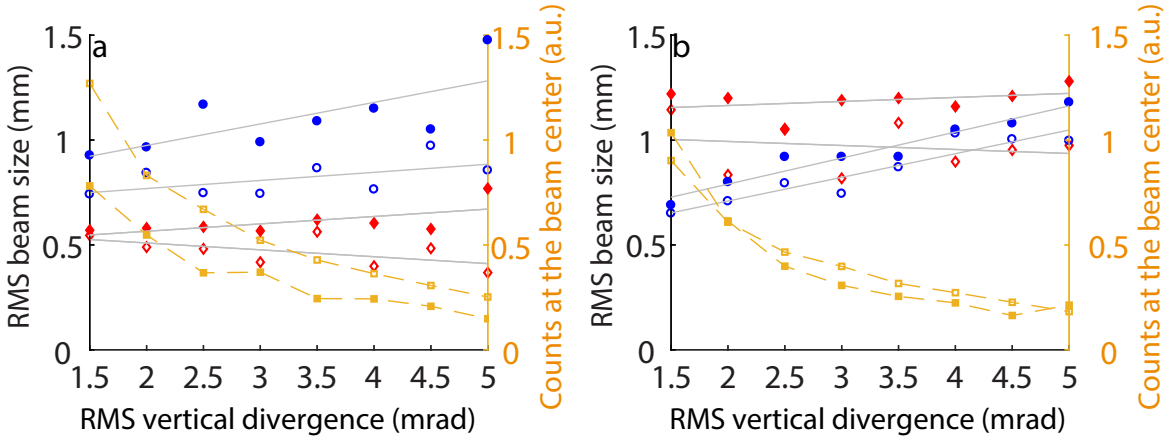

FIGURE 6.12: Counts at the center of the beam (*square*), horizontal (*diamond*), and vertical (*circle*) RMS beam size versus initial divergence for the low (**void symbols**) and high (**filled symbols**) skew (Table 3.8) for the electron distribution of Figure 4.8c, $\epsilon_{RMS} = 0.2$ mm.mrad, $Q_t = 100$ pC, macroparticles=0.5×10^6, $\sigma_s = 10^{-6}$ m, (**a**) before with the "undulator-entrance" optics and (**b**) after the undulator with the "undulator-exit" optics. Each point averaged over 5 repetitions of the simulation.

The effect of the divergence on the transport gets more detrimental in presence of a skew term a_2 (Equation 2.140) in the quadrupoles (Equation 3.10). Low (a_2=-0.007, 0.027, 0.003 $T.mm$) and high (a_2=0.073, -0.325, 0.362 $T.mm$) a_2 cases are simulated in Figure 6.12. For low a_2 (see Table 3.8, Figure 6.12a) at the undulator entrance, when the initial divergences grows, the horizontal size remains similar, the vertical size slightly increases and the focused charge rapidly decreases. When the beam is transported at the undulator exit (Figure 6.12b), the behavior is similar, with a larger growth of vertical size. For high a_2 (see Table 3.8) (Figure 6.12a) in the undulator entrance, the vertical and horizontal sizes rise. The charge focusing at 1.5 mrad divergence is much lower than for the low a_2 case and reaches the same level as for 2.5 mrad. When the beam exits the undulator (Figure 6.12b), both beam sizes increase and the charge dependence is similar to the low a_2 case. The 176 ± 0.5 MeV slice charge loss due to the low skew term a_2 increases by only 1 % with respect to the no skew case. The QUAPEVA triplet can compensate divergences superior to the baseline but the reference slice focus quickly degrades. Moreover, as the skew term increases, the ability to handle the initial divergence is reduced.

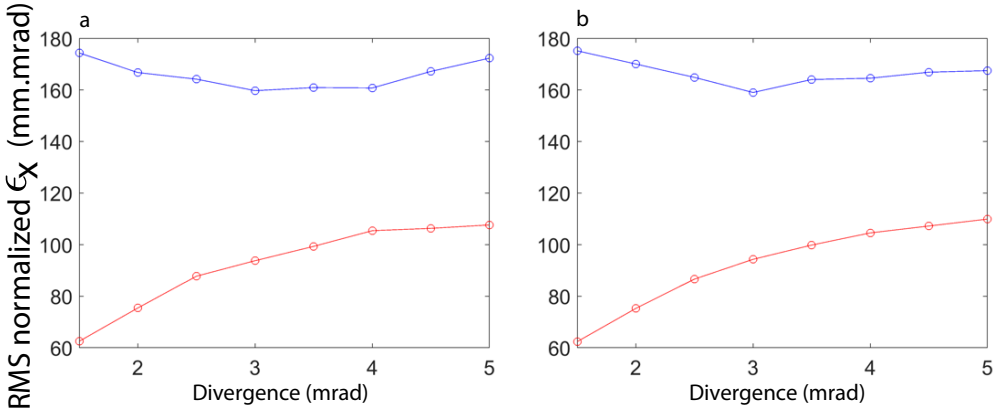

FIGURE 6.13: Vertical (**blue**) and horizontal (**red**) normalized emittance versus the initial vertical divergence at the undulator center for the low (**a**) and high (**b**) skew case (Table 3.8) with the low divergence electron distribution (see Figure 4.8c), $\epsilon_{RMS} = 0.2$ mm.mrad, $Q_t = 100$ pC, divergence ratio 1.56, macroparticles=0.5×10^6, $\sigma_s = 10^{-6}$ m and the "supermatching" optics.

The horizontal emittance at the undulator center presented in Figure 6.13a,b rapidly increases with the divergence, going from 62 mm.mrad (62 mm.mrad) for $\sigma'_y = 1.5$ mrad to 107 mm.mrad (110 mm.mrad) for $\sigma'_y = 5$ mrad for the low (high) a_2 skew term. The vertical emittance decreases until $\sigma'_y = 3$ mrad and then starts to increase by a small amount, because of particle loss on the vertical aperture of the undulator associated to the increase of the divergence.

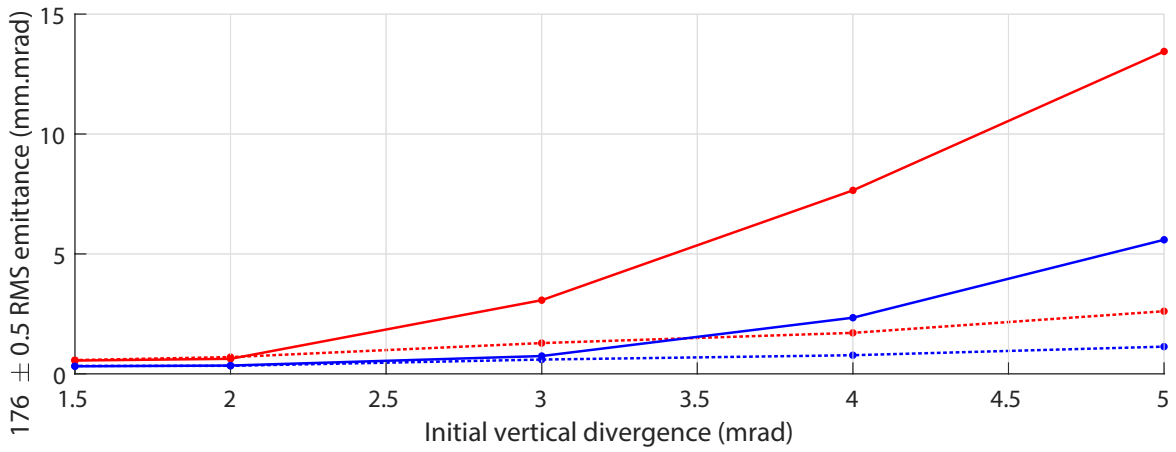

FIGURE 6.14: 176 ± 0.5 MeV slice vertical (**blue**) and horizontal (**red**) normalized emittance versus the initial vertical divergence at the undulator center for (dashed line) null and (solid line) low skew a_2 case (Table 3.8) with the low divergence electron distribution (see Figure 4.8c), $\epsilon_{RMS} = 0.2$ mm.mrad, $Q_t = 100$ pC, divergence ratio 1.56, macroparticles=0.5×10^6, $\sigma_s = 10^{-6}$ m and the "supermatching" optics.

The 176 ± 0.5 MeV slice emittance in Figure 6.14 significantly increases for divergence above 2 mrad, e.g., horizontal (vertical) emittance of 0.59 mm.mrad (0.34 mm.mrad) for $\sigma'_{y,initial} = 1.5$ mrad rises to 2.62 mm.mrad (1.14 mm.mrad) for $\sigma'_{y,initial} = 5$ mrad. The addition of a low skew term a_2 manifests for divergences above 2 mrad and increases the 176 ± 0.5 MeV slice transverse emittance by ≈ 5 times with respect to the null a_2 case.

The increase in divergence degrades the beam transport and a higher skew term a_2 accentuates the effect. Above 2 mrad the 176 ± 0.5 MeV slice substantially worsens affecting the FEL generation (Equation 2.172, 2.179). At the undulator, for RMS divergences superior to 2 mrad, the particle loss dominates the total beam emittance evolution and decreases the beam charge.

6.2.1.3 Effect of the initial divergence σ'_x/σ'_y ratio

The asymmetry present in the transverse wavefront imprints on the induced wakefield. Such asymmetry in the wakefield causes differences between the horizontal and vertical electron beam divergence and size. The measured ratio between the horizontal and vertical divergences ranges from 1.2 to higher than 2 (Section **??**). Therefore, the effect of the σ'_x/σ'_y ratio change on the transport is studied, by altering the horizontal divergence. Figure 6.15 presents the simulated transverse shape at undulator entrance, center and exit. When σ'_x/σ'_y rises, the imager "UndIn" cross shape horizontal arm length grows. The vertical size is also not affected after the undulator therefore, the increase in the horizontal divergence exclusively modifies the horizontal focusing. At the undulator center, the beam does not change in the vertical direction. At imager "UndOut", the change in the ratio between the transverse divergences can be distinguished from a transversal initial beam size variation, as it does not show a circular size increase (Figure 6.8) and instead a clear horizontal beam size difference is observed (Figure 6.15) as long as the beam vertical size is within the line aperture limits.

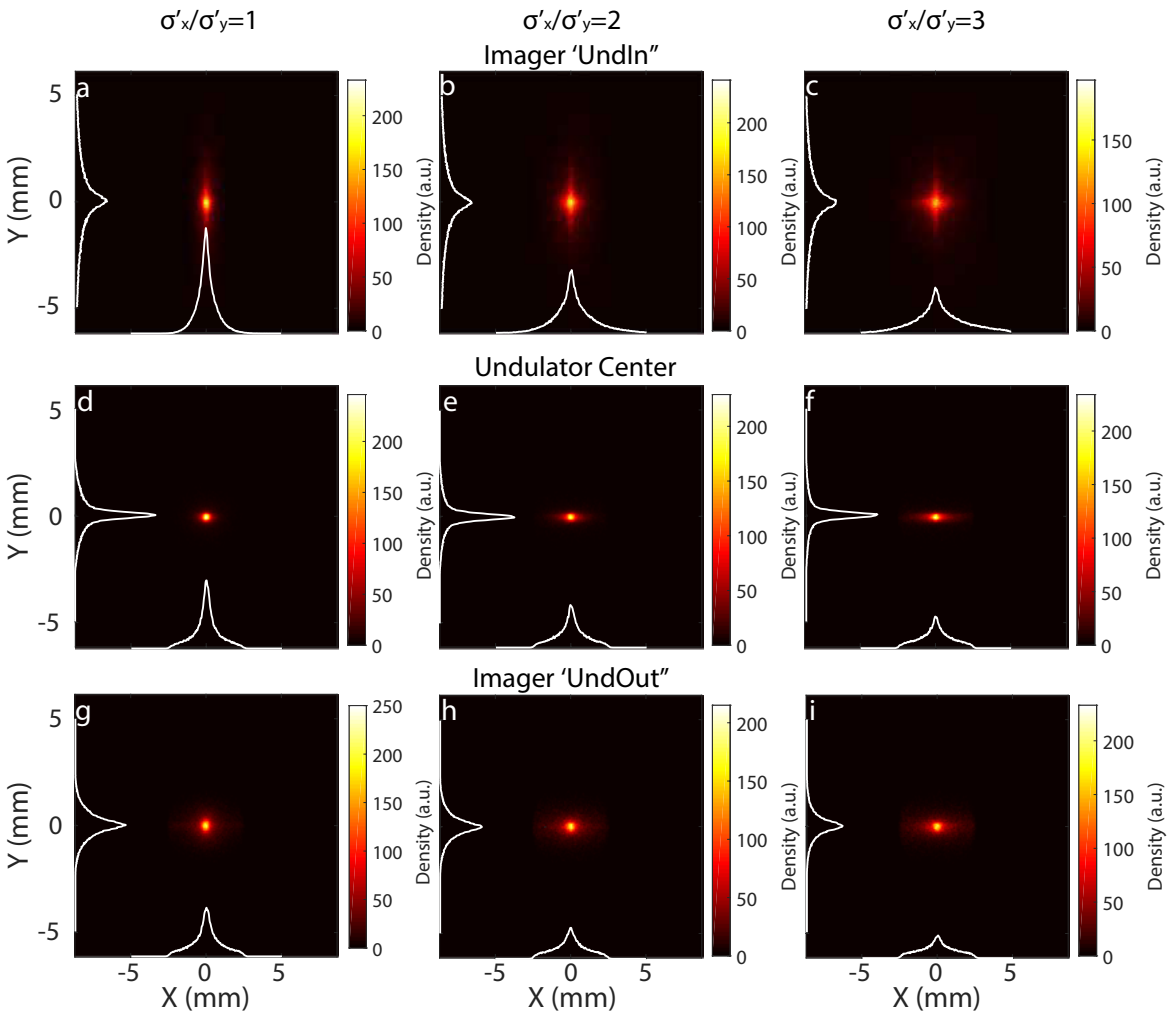

FIGURE 6.15: Simulated transverse beam shape and axis projection at the imager (a-c) "UndIn", (d-f) undulator center and (g-i) imager "UndOut" for the "slit-undulator" optics. Initial distribution Figure 4.8c with RMS $\sigma'_{y,RMS} = 2$ mrad, $\epsilon_{RMS} = 1$ mm.mrad, $\sigma_s = 10^{-6}$ m and $\sigma'_{x,i}/\sigma'_{y,i} = 1, 2, 3$.

Figure 6.16 shows the beam parameters at the undulator center for different initial divergence $\sigma'_{x,i}/\sigma'_{y,i}$ ratio. Due to a bigger horizontal divergence, the horizontal size increases substantially (see Figure 6.16a) and the horizontal emittance also grows. Even for the 175 ± 3 MeV slice (slit closed 1 mm), the horizontal size is more than twice larger, as found during RUN 7 (Figure 4.30, Section 4.3.2.2). The horizontal emittance at the undulator center for a change from a ratio of 1 to 2 (3) sees a 4 (8) times increase with the slit (see Figure 6.16c). The longitudinal beam size σ_s does not change (see Figure 6.16e). The beam charge when the slit is inserted does not vary for different ratios (Figure 6.16d). In the case of the total beam (open slit), higher horizontal divergence causes a loss of electrons due to the line aperture (see Figure 6.16d), so, the beam parameters do not follow the same proportionality as for an inserted slit. The transport line optics does not add strong correlation between the horizontal and vertical divergences.

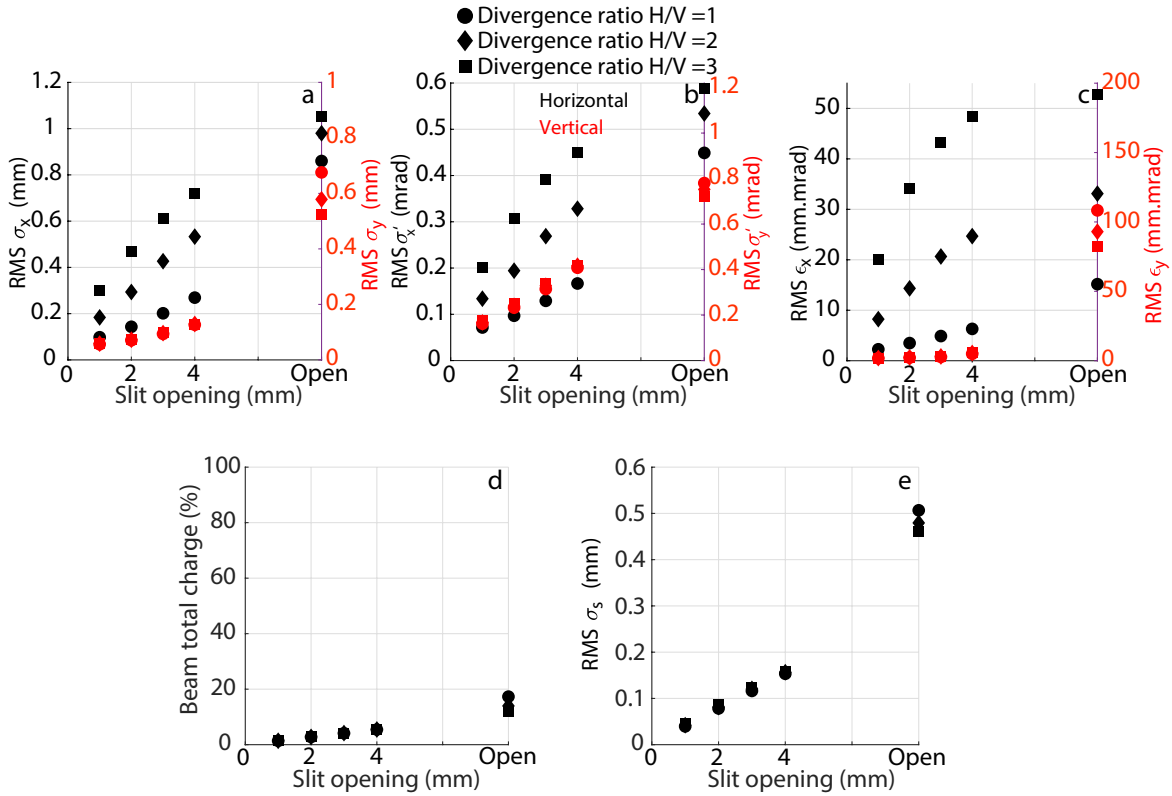

FIGURE 6.16: Simulated total beam horizontal (black) and vertical (red) (a,e) σ, (b) σ', (c) ϵ and (d) charge versus slit opening at the center of the undulator for the "slit-undulator" optics with different slit openings. Initial beam of Figure 4.8c with $\sigma'_{y,RMS} = 2$ mrad, $\epsilon_{RMS} = 1$ mm.mrad, $\sigma_s = 10^{-6}$ m and $\sigma'_{x,i}/\sigma'_{y,i} = 1$ (*circle*), 2 (*diamond*), 3 (*square*).

6.2.1.4 Beam pointing effect

The laser shot-to-shot pointing that has been experimentally observed (Figure 4.2b) can deviate the LPA electron beam from the beam axis. Changes in laser pointing can make some electrons divergence increase, decrease or even become null. As an electron beam traveling off axis does not pass through the magnetic center of the different magnetic elements of the line, the seen magnetic field differs from the initial design, e.g., additional dipolar term appear in the quadrupole magnetic field. To tackle the shot-to-shot pointing, the beam pointing compensation method is used (Section 3.1.2.1.2.2)[12].

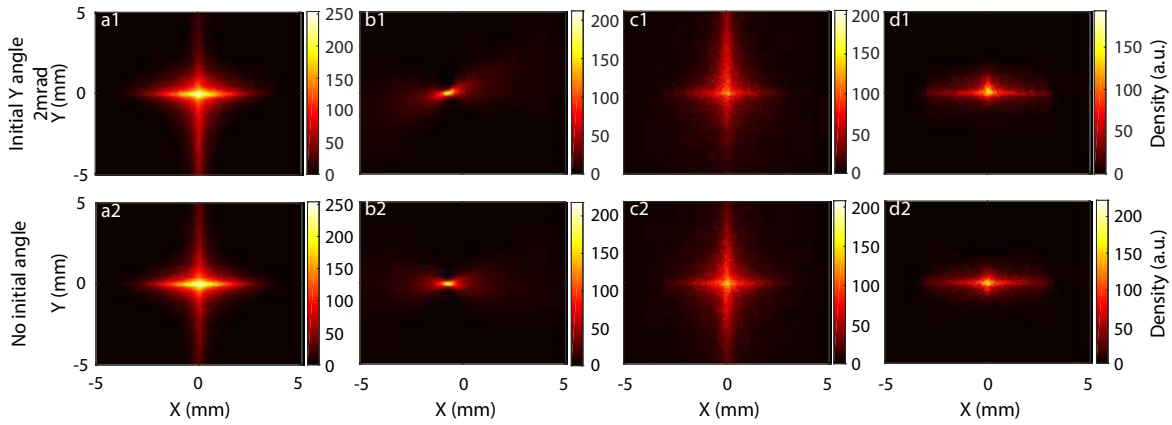

FIGURE 6.17: Simulated transverse beam shape along the transport line on screens located after QUAPEVAS (a1-2), in the middle of the chicane (b1-2), undulator entrance (c1-2) and undulator exit (d1-2), for an on-axis beam (a-d2) and for a beam with 2 mrad vertical pointing (a-d1), transported with the "slit undulator" optics with the average beam (Figure 4.8c), $\epsilon_{x,i,RMS}$,$\epsilon_{y,i,RMS}$=0.2 mm.mrad, $\sigma'_{y,i,RMS} = 2$ mrad, $\sigma'_{x,i,RMS} = 3.12$ mrad.

Figure 6.17 shows the transverse beam shape along the transport line with the "undulator slit" optics for the on-axis beam (Figure 6.17a-d2) and for a 2 mrad vertical pointing case (Figure 6.17a-d1). The pointing substantially defocuses the beam in the same direction along the line compared to the on-axis case, especially in the middle of the chicane where the tilted beam potentially worsens the energy selection capabilities of the slit (Figure 6.17b1). Table 6.6 presents the beam characteristics at the center of the undulator for the total beam and the 176±0.5 MeV slices, for two initial beam cases. For the beam distribution of Figure 4.8c without slit, from an initial total charge of 100 pC only 28 pC (26 pC) arrives at the center of the undulator in the case without pointing (with 2 mrad pointing). For the 176±0.5 MeV slice, the charge is mostly conserved. The longitudinal size, horizontal and vertical emittance at the undulator center are one order of magnitude lower compared to the total beam. With a 2 mrad vertical pointing, the vertical emittance ϵ_y at the center of the undulator increases for the total beam and the 176±0.5 MeV slice. For a flat-top beam centered at 176 MeV of energy spread σ_γ=5% with the slit opened at 3.6 mm, the emittance in the 176±0.5 MeV slice is approximately half the one in the beam distribution of Figure 4.8c case with and without pointing. With a 2 mrad vertical pointing the slice vertical emittance sees a 1.4 times increase. In both cases, an emittance rise of the total beam and 176±0.5 MeV slice due to pointing is confirmed.

TABLE 6.6: RMS bunch length σ_s, charge Q, RMS ϵ_x and RMS ϵ_y at the undulator center in the case of the "undulator slit" optics, the initial distribution Figure 4.8c, for the total beam, for 176±0.5 MeV slice and for the case of a flat-top beam of 176±5% MeV, with $\epsilon_{x,i,RMS}$,$\epsilon_{y,i,RMS}$=0.2 mm.mrad, $\sigma'_{y,i,RMS} = 2$ mrad, Q_i=100 pC, $\sigma'_{x,i} = 3.12$ mrad.

Beam distribution	*Beam part*	*Slit* (mm)	*Pointing* ($mrad$)	σ_s (μm)	Q (pC)	ϵ_x ($mm\ mrad$)	ϵ_y ($mm\ mrad$)
Figure 4.8c	Total beam	—	0	0.40	28.4	112.4	454.3
			2	0.38	26.6	112.1	489.2
Figure 4.8c	176±0.5 MeV	—	0	0.013	0.5	9.2	3.1
			2	0.014	0.48	9.2	3.5
Flat-top beam	176±0.5 MeV	3.6	0	0.01	0.48	4.6	1.4
			2	0.01	0.48	4.6	2

6.2.1.5 Beam displacement effect

In addition to shot-to-shot pointing, the laser transversal drift due to optics heating can induce a transverse beam origin position shift. Figure 6.18 presents three cases of initial beam transverse position: a displacement of 50 μm in the horizontal direction, an on-axis case and a shift of 50 μm in the vertical direction. In the horizontal axis displacement case, the focus of the beam in the chicane is not affected. A horizontal slight shift occurs and could affect the energy selection by the slit, especially when closed to small apertures. At the undulator entrance and center, the beam is shifted in the horizontal direction, by a larger amount for further positions down the line. For a vertical direction displacement of 50 μm, in the chicane the beam position shifts vertically, the focusing is affected and a tilt appears. A change in the vertical beam position is more critical for the beam transport due to the chicane and undulator magnets aperture (i.e., the magnets are positioned at the top and bottom with respect to the reference path). In addition, the dipole magnetic field seen by the electrons change in the vertical direction. At the undulator entrance and center, the tilt disappears however, the beam transverse position shift increases.

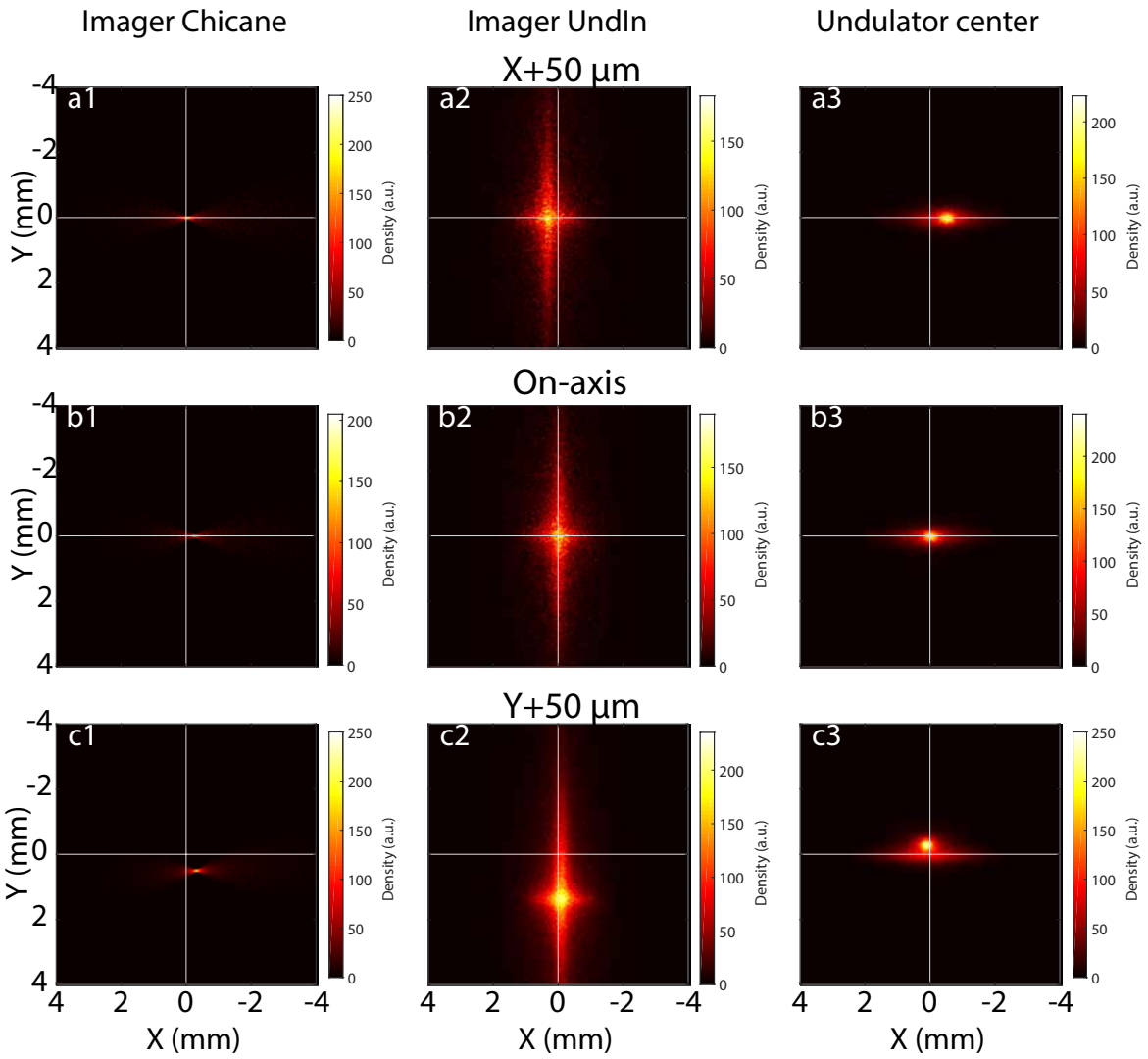

FIGURE 6.18: Simulated transverse beam shape along the transport line on screens (a1-c1) "Chicane", (a2-c2) "UndIn" and (a3-c3) at the undulator center, for an initial beam displacement of (a) x+50 μm, (c) y+50 μm and (b) on-axis beam, transported with the "slit undulator" optics with a Gaussian beam centered at 176 MeV, $\epsilon_{x,i}$, $\epsilon_{y,i}$=1 mm.mrad, $\sigma'_{y,i,RMS}$,$\sigma'_{x,i,RMS}$ = 2 mrad, σ_γ = 40 %.

Figure 6.19 shows the simulated beam parameters at the undulator center for different initial displacements with the "undulator-slit" optics without slit. The total charge is slightly reduced for every displacement, however, the reference slice charge is mostly conserved. The shifts at imager "Chicane" produce a reference slice charge loss when the slit is closed. Vertical and horizontal total beam sizes (divergence) variations of the order of 10 μm (0.02 mrad) with respect to the on-axis case are found. These small changes due to an initial displacement can amount to variations of 10 % of the emittance (Equation 2.134) at the undulator center in the horizontal and vertical directions. For the "undulator-slit" optics simulations, an initial displacement of 100 μm in the vertical or horizontal direction causes the beam to go completely out of the line. Up to a certain displacement, the COXINEL line can compensate it through the displacement of the QUAPEVA triplet (BPAC) 3.1.2.1.2.2.

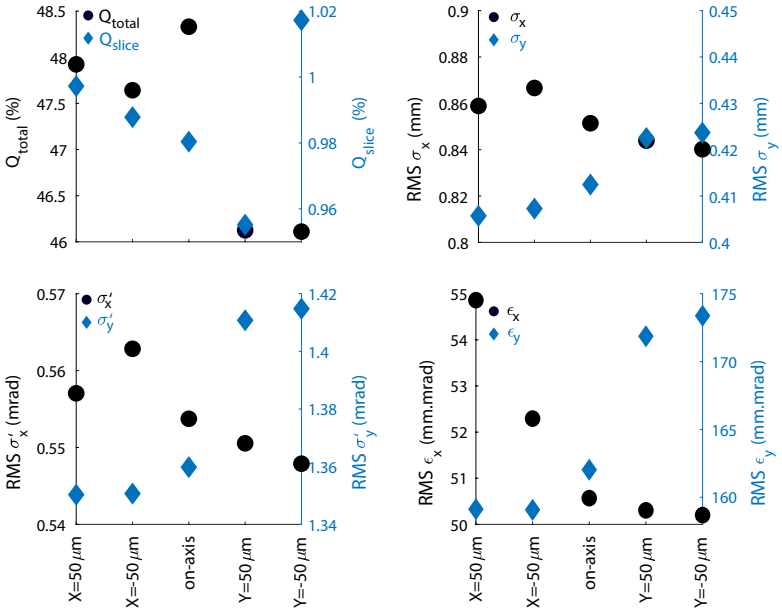

FIGURE 6.19: Simulated transport beam total and slice charge, size, divergence and emittance at the undulator center, for an initial beam displacement of x+50 μm, x-50 μm, y+50 μm, y-50 μm and on-axis beam, transported with the "undulator-slit" optics with a Gaussian beam centered at 176 MeV, $\epsilon_{x,i}$,$\epsilon_{y,i}$=1 mm.mrad, $\sigma'_{y,i,RMS}$,$\sigma'_{x,i,RMS}$ = 2 mrad, σ_γ = 40 %.

6.2.2 Effect of deviation of the longitudinal characteristics

Two main parameters affect the beam longitudinal distribution, the initial longitudinal beam size and the energy spread.

6.2.2.1 Effect of the initial longitudinal beam size

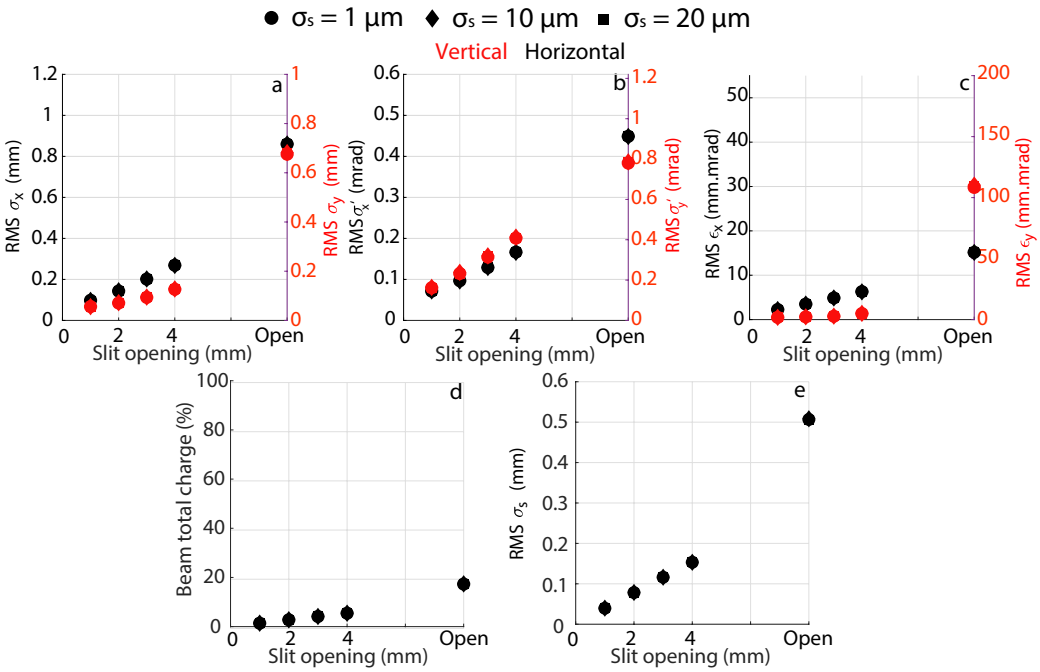

FIGURE 6.20: Simulated beam (a,e) size σ, (b) divergence σ', (c) emittance ϵ and (d) total charge versus slit opening at the undulator center for the "slit-undulator" optics. initial beam Figure 4.8c with RMS $\sigma'_{y,i,RMS}$ = 2 mrad, ϵ_{RMS} = 0.2 mm.mrad, 2×10^6 macroparticles, $\sigma_s = 10^{-6}$ (circle), 10^{-5} (diamond) and 2×10^{-5} m (square) and $\sigma'_x/\sigma'_y = 1$.

The maximum LPA electron beam longitudinal size is determined by the wakefield radius (Equation 2.90) and is thus limited by the plasma wavelength (Equation 2.56), which is proportional to the laser power and plasma density. For densities of the order of $10^{18}\ cm^{-3}$ and a_0 of 1.5, the longitudinal beam sizes are of the order of μm [157]. Figure 6.20 shows the different beam parameters at the center of the undulator for different initial beam longitudinal sizes $\sigma_{s,i}$. The beam divergence $\sigma'_{x,y}$, size $\sigma_{x,y}$, emittance $\epsilon_{x,y}$, length σ_s and charge remain the same due to different $\sigma_{s,i}$. The chicane increases the bunch length by $2-3$ orders of magnitude (FIgure **??**), thus, for μm initial size electron beams after the chicane every case becomes similar, negating any effect it could have on the following transport.

The LPA electron beam can show in some configurations a modulation in the density distribution along the longitudinal axis [238]. Figure 6.21 compares the transport of electron beams with initial Gaussian (Figure 6.21a1) and sinusoidally modulated (Figure 6.21b1, c1) longitudinal distributions. At the middle of the chicane, the modulation is already completely suppressed due to its induced elongation (Figure 6.21a2-c2). So, the beam arriving at the center of the undulator is the same (Figure 6.21a4-c4).

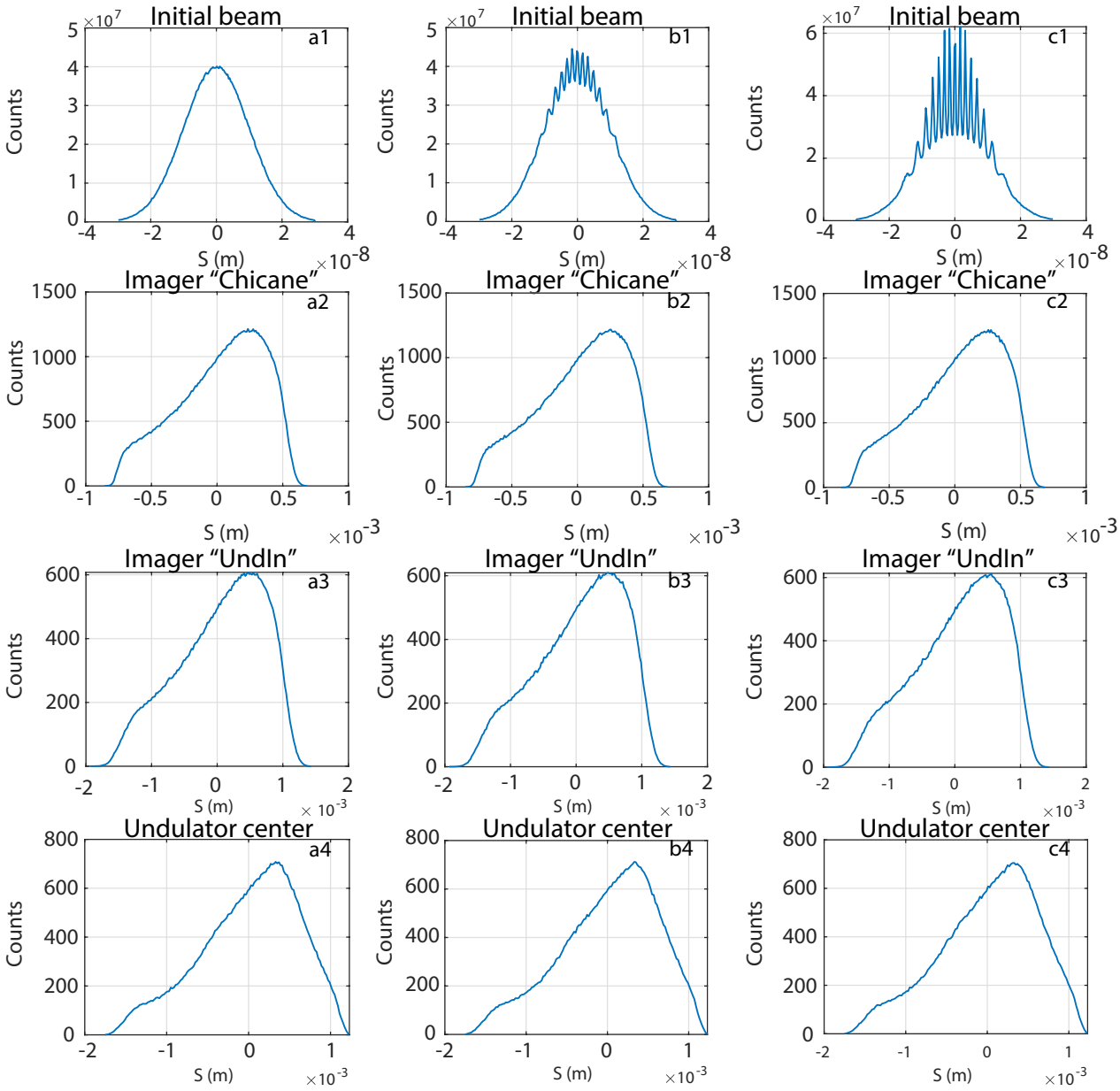

FIGURE 6.21: Simulated beam longitudinal distribution at the source, imager "Chicane", "UndIn" and undulator center with the undulator optics. Initial Gaussian distribution in the phase space 6D with $\sigma'_{y,RMS} = 1.5$ mrad, $\epsilon_{RMS} = 0.01$ mm.mrad, $\sigma_s = 10^{-8}$ m and $\sigma'_x/\sigma'_y = 1$.

6.2.2.2 Effect of the initial energy spread

The initial energy spread deteriorates significantly the beam quality by increasing the chromatic emittance growth during transport (Section 3.1.1.1).

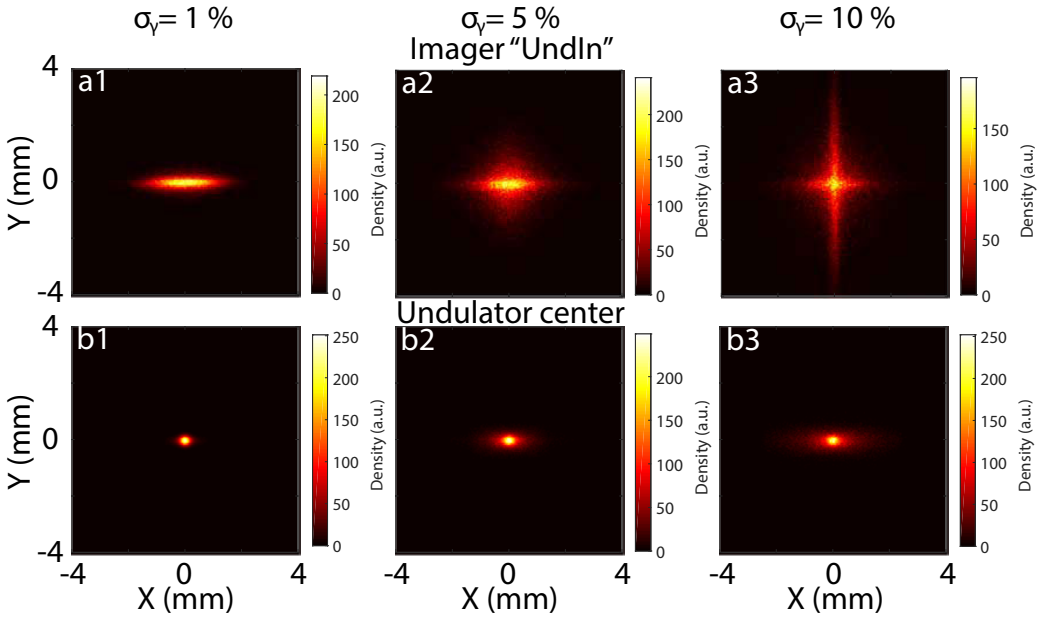

FIGURE 6.22: Simulated transversal shape of the electron beam at imager "UndIn" and the undulator center for the low a_2 skew terms (Table 3.8) and the optics "slit-undulator" without slit using flat-top electron beams for FWHM energy spread 1 %, 5 % and 10 % with 176 MeV central energy, RMS $\sigma'_{y,i} = 2$ mrad, RMS $\sigma'_{x,i} = 3.12$ mrad, and $\epsilon_{y,i}$,$\epsilon_{x,i}$ = 0.2 mm.mrad.

Figure 6.22 presents the simulated beam transversal shape at imager "UndIn" and the undulator center for different initial energy spreads. For energy spreads $\geq$ 5 % the cross shape appears at the undulator entrance. At the undulator center, the larger energy spread causes an horizontal elongation of the beam.

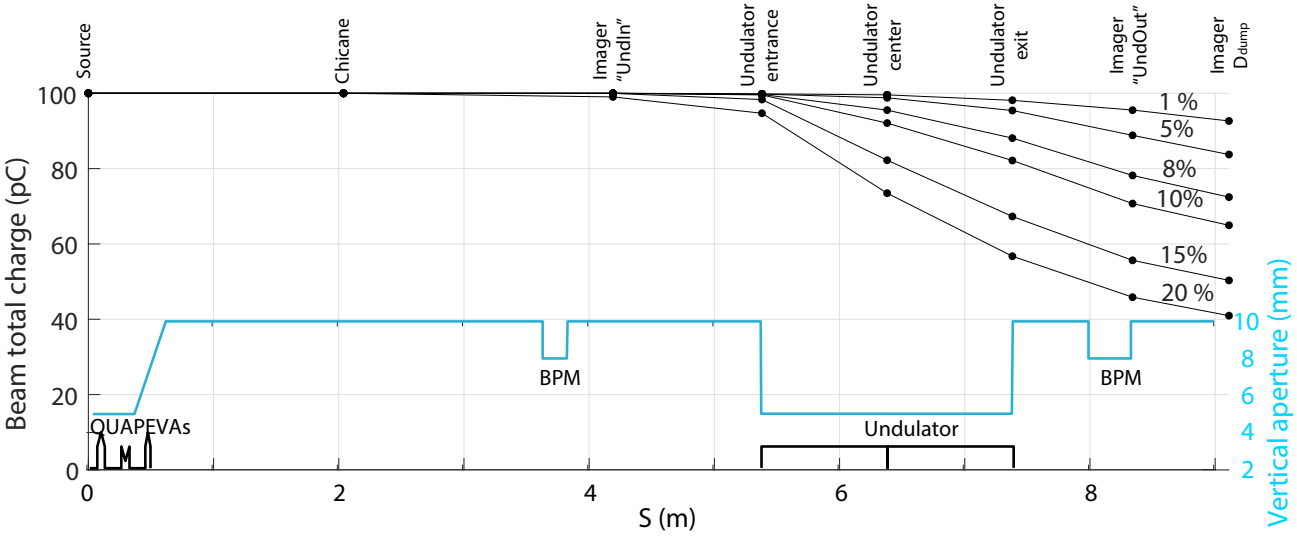

FIGURE 6.23: Line vertical aperture (blue) and simulated total beam charge evolution along the line for the low a_2 skew terms (a_2= -0.007, 0.027, 0.003 $T.mm$, Table 3.8) and the optics "slit-undulator" without slit using flat-top electron beams for different energy spreads with 176 MeV central energy, RMS $\sigma'_{y,i} = 2$ mrad, RMS $\sigma'_{x,i} = 3.12$ mrad, and $\epsilon_{y,i}$,$\epsilon_{x,i}$ = 0.2 mm.mrad [178].

The total beam charge evolution along the line in Figure 6.23 shows how an energy spread lower or equal to 5 % originates a beam loss greater or equal to 10 % at the undulator center. For an energy spread larger than 15 %, 20 % of the total beam charge is lost. The charge is lost mostly due to the undulator aperture and

it continues during the beam propagation inside the undulator, losing more than 40 % in the case of an energy spread of 20 %. Inside the undulator, for a fixed energy spread is linear, the charge decreases linearly due to the vertical beam size increase caused by the beam divergence. The reference 176 ± 0.5 slice charge drops a ≈ 7 % between the undulator entrance and exit for all energy spreads.

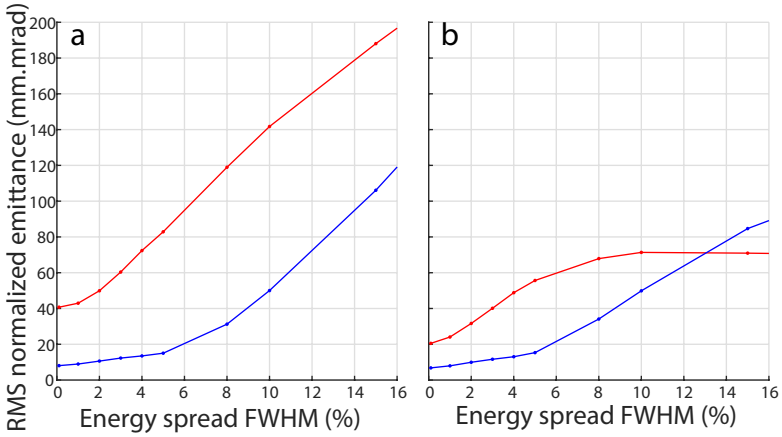

FIGURE 6.24: Simulated horizontal (**red**) and vertical (**blue**) normalized (a1, b1) emittance and (a2, b2) longitudinal size of the total electron beam at (a) the undulator entrance and (b) center for the low a_2 skew terms (a_2= -0.007, 0.027, 0.003 *T.mm*, Table 3.8), the optics "slit-undulator" without slit and an initial flat-top electron beam for different energy spread with 176 MeV central energy, RMS $\sigma'_{y,i} = 2$ mrad, RMS $\sigma'_{x,i} = 3.12$ mrad, and $\epsilon_{y,i}$,$\epsilon_{x,i} = 0.2$ mm.mrad [178].

Figure 6.24a1 presents the total beam emittance for different initial beam energy spreads at the undulator entrance. For σ_γ larger than 1%, the chromatic emittance starts to dominate. From the monochromatic beam ($\sigma_\gamma = 0$) to 5% energy spread, the emittance has a linear dependence versus energy spread at the undulator entrance and center, as shown in the chromatic term (see Equation 3.6, $\epsilon^2_{x,1} \approx \epsilon^2_{x,0} + L^2_{drift}\sigma'^4_{x,0}\sigma^2_\gamma$). At the undulator entrance (center), ϵ_x rises linearly with the energy spread with a slope of 10.22 mm.mrad/% (7.5 mm.mrad/%) (Figure 6.24a1,b1). ϵ_y also increases with a slope of 1.45 mm.mrad/% (1.73 mm.mrad/%). For σ_γ higher than 5%, the lower and higher energies vertically defocus at the undulator and are then cut by its physical aperture (larger than 5 mm). At the undulator entrance, the vertical emittance slope increases to 11.7 mm.mrad/%, while at the undulator center, the electron loss makes ϵ_x converges around ≈ 70 mm.mrad and ϵ_y increases faster with a slope of 6.1 mm.mrad/%. For the 176 ± 0.5 MeV slice, the horizontal (vertical) emittance at the undulator center is of 20.72 mm.mrad (6.91 mm.mrad). Figure 6.24a2, b2 presents the total bunch longitudinal length at the undulator entrance and center versus initial energy spread. The electron beam loss for energy spreads greater or equal to 5 % causes the bunch longitudinal length to shorten at the undulator center when compared to the undulator entrance. The initial energy spread of the electron beam increases considerably the emittance however, for values larger than 5 % FWHM, significant electron losses occur inside the undulator due to its vertical aperture.

the increase of the initial divergence, beam transverse size and energy spread with respect to the baseline case noticeably degrade the emittance at the undulator location (Section 3.1.1.1), e.g., a rise from 1 mm.mrad to 2 mm.mrad can double the undulator center emittance. In addition, the limited line aperture causes total beam charge losses for initial divergences, emittance and energy spreads superior to 1.5 mrad, 1 mm.mrad or 1 % respectively. However, the 176 ± 0.5 MeV slice charge is conserved up to 2 mrad, ≈ 2 mm.mrad or 1 %. Initial beam displacement and pointing increase further both emittance and charge loss and a 100 μm displacement in any transverse direction can cause the beam to go out of the line. Because of the chicane longitudinal elongation of the beam the initial longitudinal bunch size does not affect the transport.

6.3 Sensitivity to quadrupole errors

The QUAPEVA magnets can present imperfections with respect to the model, inherent to their assembly. They can also be slightly misaligned with respect to the LPA electron beam due to changes in the LPA system after alignment or to the vacuum, as the change in pressure can cause parts to move. Effect of the QUAPEVA triplet imperfections are here studied.

6.3.1 Skew magnetic multipolar terms

Even after careful design, assembly and correction the QUAPEVA triplet can still present a non-zero multipolar skew term a_2 (Equation 2.140, Section 3.2.2.1), thus, the effects of the skew quadrupole term on the optics should be studied to establish a tolerance level for proper transport. Three measured quadrupolar skew term a_2 cases of the QUAPEVA triplet presented in Table 3.8 are compared in this section. The high a_2 corresponds to the QUAPEVA triplet until RUN 4 and the low a_2 to RUN 5 onward. For this study, another initial experimental beam energy distribution result of a single shot done the 2017/03/28, RUN 3 (Figure 6.25) is considered. Table 6.7 shows the two used configurations, a "Low divergence case" (distribution of Figure 4.8c) and a "High divergence case" (distribution of Figure 6.25).

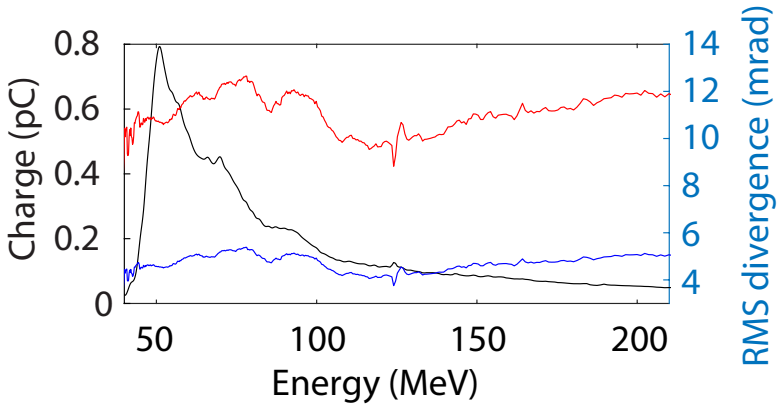

FIGURE 6.25: Initial beam electron distribution (black), vertical (blue) and horizontal (red) RMS divergence measured from a single shot (2017/03/28 shot 1) [178].

TABLE 6.7: Initial input beam parameters for the low (Figures 4.8c) and high (Figure 6.25) divergence beam cases [178].

Low and high divergence initial simulation parameters	**Symbol**	**Value**		**Unit**
Case		**Low Divergence Case** Figure 4.8c	**High Divergence Case** Figure 6.25	
Emittance	$\epsilon_{x,i}$ $\epsilon_{y,i}$	0.2	0.2	mm.mrad (RMS)
Ratio	$\sigma'_{x,i}/\sigma'_{y,i}$	1.56	2.35	
Vertical divergence at 176 MeV	$\sigma'_{y,i}$	2.0	5	mrad (RMS)
Horizontal divergence at 176 MeV	$\sigma'_{x,i}$	3.12	11.75	mrad (RMS)
Bunch longitudinal length	$\sigma_{s,i}$	10^{-6}	10^{-6}	m (RMS)
Charge	Q_T	100	100	pC
Slice charge	Q_slice	0.2	0.1	pC/MeV
Number of macro particles	N	10^6	10^6	

6.3.1.1 Skew term effect at the imagers before and after the undulator

Figure 6.26 presents the simulated transport of the low initial divergence electron beam (Table 6.7) at the undulator entrance. For an ideal quadrupole ($a_2 = 0$), the horizontal (vertical) RMS beam size is 0.52 ± 0.02 mm (0.80 ± 0.10 mm) (Figure 6.26a). With a small skew quadrupole term (a_2= -0.007, 0.027, 0.003 $T.mm$) (Table 3.8, Figure 6.26b), the beam remains well centered and focused, with a horizontal (vertical) RMS beam size of 0.52±0.05 mm (0.72 ± 0.08 mm), i.e., slightly smaller vertically than for an ideal quadrupole ($a_2 = 0$). For high a_2 (a_2= 0.073, -0.325, 0.362 $T.mm$) (Table 3.8, Figure 6.26c), the beam exhibits a tilted cross shape, resulting from the change of gradient angle (see Equation (2.141)). A substantial decrease in intensity occurs when a_2 is enhanced to the high a_2 value at the undulator entrance. The same changes occur at the undulator exit, with a different tilt due to the high a_2. Figure 6.26g–l presents simulations using an input beam with a divergence three times larger and smaller charge density for the energy of interest (high divergence beam case, Table 6.7). For $a_2 = 0$ (see Figure 6.26g), the beam is well focused. For a slight increase of a_2 (Table 3.8), the beam remains similarly focused. A larger increase of a_2 (Table 3.8) (see Figure 6.26i) leads to a defocused tilted cross. Figure 6.26j–l shows a reduction of intensity due to the undulator vertical aperture (Section 6.2.1.2).

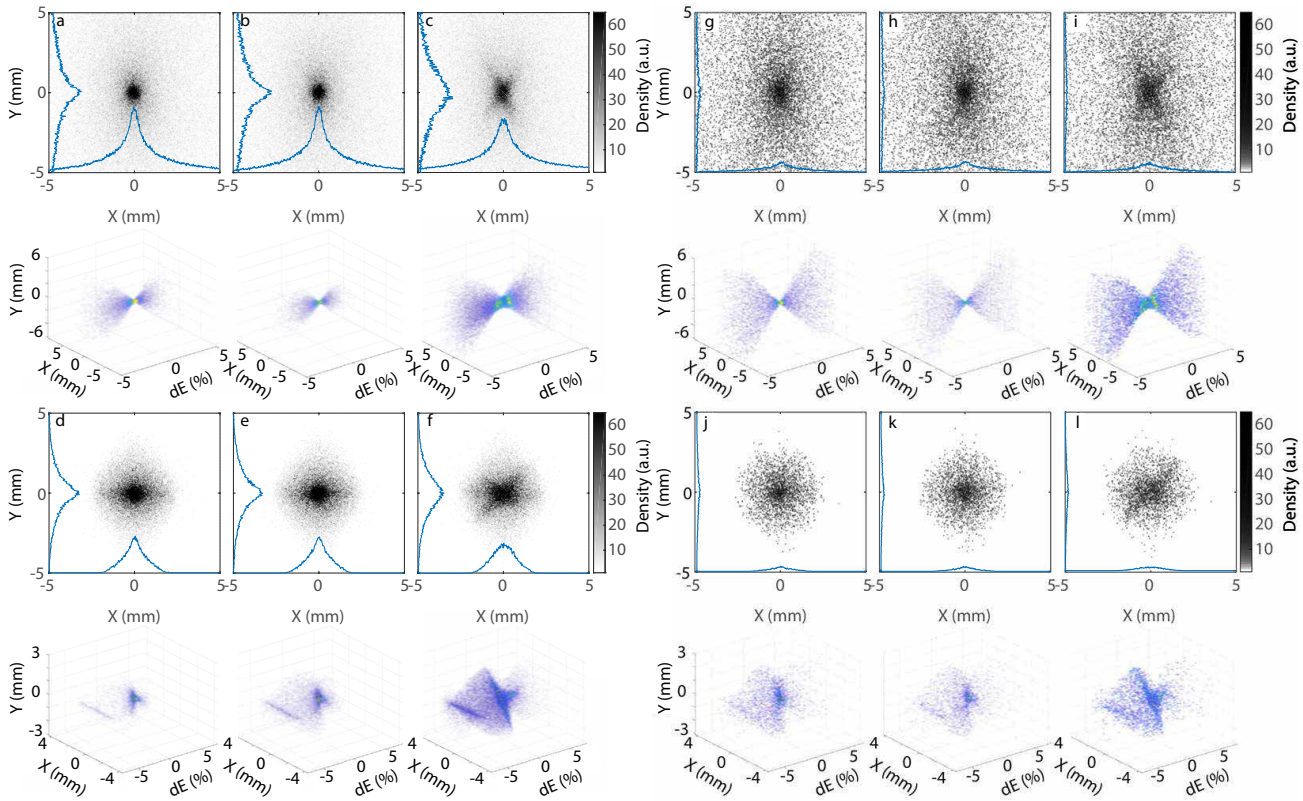

FIGURE 6.26: Electron beam transversal shape and vertical–horizontal position per energy at the screens before (**a**–**c**,**g**–**i**) and after (**d**–**f**,**j**–**l**) the undulator for low (**b**,**e**,**h**,**k**), high (**c**,**f**,**i**,**l**), and null (**a**,**d**,**g**,**j**) a_2 terms (values of Table 3.8). (**a**–**f**) Low divergence electron beam distribution (Figure 4.8c) with $\sigma'_{y,i}$ = 2 mrad, $\sigma'_{x,i}$ = 3.12 mrad, and $\epsilon_{x,i}$,$\epsilon_{y,i}$ = 0.2 mm.mrad (see Table 6.7). (**g**–**l**) High divergence electron beam distribution (Figure 6.25) with an initial $\sigma'_{y,i,RMS}$ = 5 mrad, $\sigma'_{x,i,RMS}$ = 11.75 mrad, and $\epsilon_{x,i}$,$\epsilon_{y,i}$ = 0.2 mm.mrad (see Table 6.7). Transport with the "undulator entrance" optics and "undulator exit" optics [178].

The corresponding intensities and beam sizes for the different cases are shown in Table 6.8. The transport becomes much less efficient for higher initial divergence. At the undulator entrance, the high divergence beam case with null a_2 presents bigger sizes than the low divergence beam with high a_2 case. However, the sizes between both beam cases are closer at the undulator exit. For a low divergence beam, the intensity drops to 0.8 (0.5) at the screen before (after) the undulator for the high a_2 value. In the high divergence case, the highest pixel intensity achieved is 0.2 (0.14) for the low (high) a_2 case and decreases until 0.14 (0.11) at the undulator exit. For a high divergence beam (see Figure 6.25), the charge arriving to the undulator is a small fraction of the initial one.

TABLE 6.8: Counts at the center of the beam, RMS horizontal and vertical beam size for a_2 = 0, the low (a_2= -0.007, 0.027, 0.003 $T.mm$) and high (a_2= 0.073, -0.325, 0.362 $T.mm$) a_2 (Table 3.8) and beam distributions on the screen before and after the undulator. Each point averaged over 5 repetitions of the simulation [178].

Skew Term	**Low Divergence Beam**			**High Divergence Beam**		
	$\sigma_{x,RMS}$ **(mm)**	$\sigma_{y,RMS}$ **(mm)**	**Beam Center Counts (a.u.)**	$\sigma_{x,RMS}$ **(mm)**	$\sigma_{y,RMS}$ **(mm)**	**Beam Center Counts (a.u.)**
Undulator entrance ("undulator-entrance" optics)						
$a_2 = 0$	0.52	0.80	1.00	0.63	1.08	0.20
Low	0.51	0.72	1.16	0.60	1.20	0.20
High	0.63	1.01	0.78	0.98	1.98	0.14
Undulator exit ("undulator-exit" optics)						
$a_2 = 0$	0.95	0.73	0.76	0.92	0.99	0.17
Low	0.95	0.76	0.75	0.85	1.01	0.14
High	1.22	0.83	0.50	1.31	0.97	0.11

6.3.1.2 Skew term effect at the undulator center on beam emittance

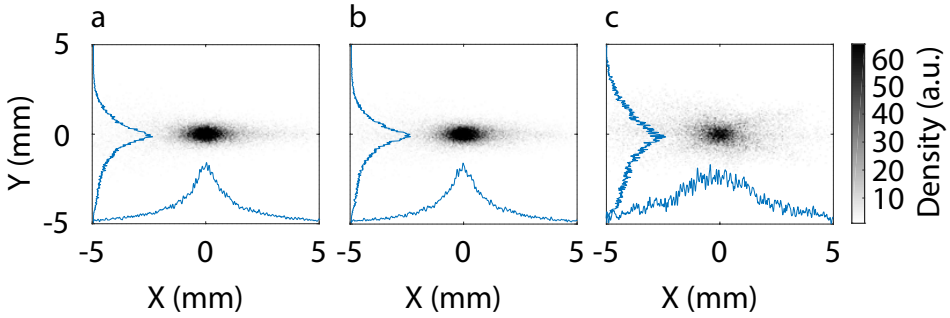

FIGURE 6.27: Simulated transversal beam shape at the undulator center for (**a**) $a_2 = 0$, the (**b**) low (a_2= -0.007, 0.027, 0.003 *T.mm*) and (**c**) high (a_2= 0.073, -0.325, 0.362 *T.mm*) a_2 (Table 3.8). 'Slit-undulator' optics (slit open to 3.2 mm corresponding to a slice of 176 ± 7 MeV). Initial low divergence beam distribution of Figure 4.8c with $\sigma'_{y,i,RMS} = 2$ mrad, $\sigma'_{x,i,RMS} = 3.12$ mrad $\epsilon_{y,i,RMS}$,$\epsilon_{x,i,RMS} = 0.2$ mm.mrad [178].

Figure 6.27 shows the transversal beam shape versus a_2 at the undulator center. For $a_2 = 0$, the beam (see Figure 6.27a) is focused (total beam horizontal size 0.67 mm and vertical size 0.37 mm RMS). For the low a_2 (Table 3.8), the beam (see Figure 6.27b) is slightly defocused (total beam RMS horizontal (vertical) size of 0.73 mm (0.38 mm)). For the high a_2 (Table 3.8), the beam (see Figure 6.27c) exhibits a vertical and horizontal focusing redistribution per energy of the beam and a small tilt. The total beam emittance at the center of the undulator (see Table 6.9) increases by a small amount from $a_2 = 0$ ($\epsilon_x = 103$ mm.mrad $\epsilon_y = 30$ mm.mrad) to low a_2 ($\epsilon_x = 119$ mm.mrad $\epsilon_y = 35$ mm.mrad), with a factor 1.2 (1.16) horizontally (vertically). The total beam charge is $\approx 2.8\%$ of the initial beam one for the null and low a_2, which corresponds to a ±3.5 MeV slice around the reference energy after being cut by the slit. For the high a_2 case, the emittance increase is more important, the horizontal (vertical) emittance is 2.73 (6.71) times larger than the low a_2 case and the charge decreases to 1.4% of the initial beam one. Table 6.9 shows the emittance and charge for the 176 ± 0.1 MeV slice of a flat top beam of central energy 176 MeV and $\sigma_\gamma = 10\%$, at the center of the undulator. The emittance quickly increases with the presence of the a_2 skew term. From $a_2 = 0$ to low a_2, an increase of 10 (4.7) times of the horizontal (vertical) emittance takes place, and for the high a_2 skew term, an additional increase by a factor 1.7 (5.7) horizontally (vertically) occurs. The 176±0.1 MeV slice horizontal (vertical) emittance at the undulator center is 2.4 (1.2) times the initial emittance. The rise of the skew term a_2 enhances the horizontal (vertical) emittance at the undulator center by a factor ≈ 10 (≈ 5) for the low a_2 case and an additional factor 1.7 (5.7) for the high a_2 case.

TABLE 6.9: Horizontal and vertical normalized emittance and charge percentage arriving of the electron beam at the undulator center for a_2=0, low (a_2= -0.007, 0.027, 0.003 *T.mm*) and high (a_2= 0.073, -0.325, 0.362 *T.mm*) a_2 (Table 3.8) cases. Simulation using the low divergence initial beam distribution (Figure 4.8c), 176±0.1 MeV slice of a $\sigma_\gamma = 10\%$ flat top beam with $\sigma'_{y,i,RMS} = 2$ mrad, $\sigma'_{x,i,RMS} = 3.12$, initial charge 100 pC, mrad $\epsilon_{y,i,RMS}$,$\epsilon_{x,i,RMS}$=0.2 mm.mrad, transported with the "slit-undulator" optics (slit closed to 3.2 mm corresponding to a slice of 176±7 MeV). Each point averaged over 5 repetitions of the simulation [178].

	Total beam			**176±0.1 MeV slice**		
Skew Term	$\epsilon_{x,RMS}$ **(mm.mrad)**	$\epsilon_{y,RMS}$ **(mm.mrad)**	**Charge (%)**	$\epsilon_{x,RMS}$ **(mm.mrad)**	$\epsilon_{y,RMS}$ **(mm.mrad)**	**Charge (%)**
$a_2 = 0$	103	30	2.82	0.48	0.24	0.3
Low a_2 case	119	35	2.79	4.83	1.14	0.3
High a_2 case	328	234	1.37	8.29	6.56	0.3

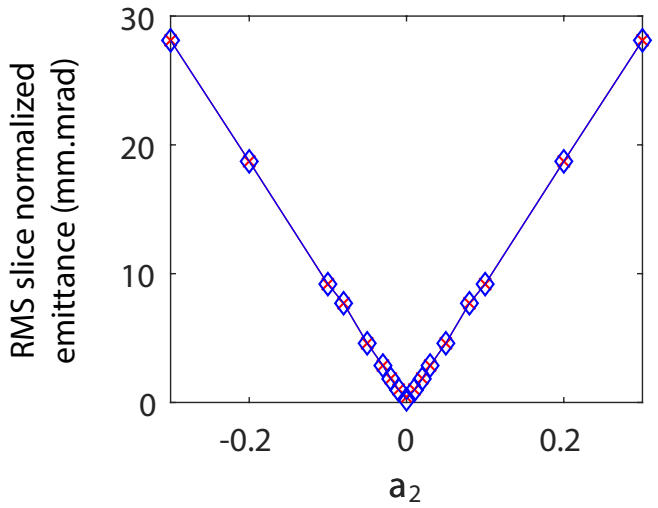

FIGURE 6.28: Simulated slice 176 ± 0.1 MeV horizontal (x) and vertical ($\diamond$) RMS normalized emittance of the electron beam at the undulator center versus QUAPEVA 2 a_2 skew term with the "slit-undulator" optics and the slit open to 3.2 mm. Simulation using a flat-top beam with $\sigma'_{y,i,RMS} = 2$ mrad and $\sigma'_{x,i,RMS} = 3.12$ mrad, $\epsilon_{y,i,RMS}$,$\epsilon_{x,i,RMS} = 0.2$ mm.mrad [178].

Figure 6.28 shows the transverse emittance at the undulator center for a 176 ± 0.1 MeV beam with the 'slit-undulator' optics while changing the skew component of QUAPEVA2 and considering the others ideal. For $a_2 = 0$, the 176 ± 0.1 MeV slice horizontal (vertical) emittance from the source to the center of the undulator is 0.41 mm.mrad (0.28 mm.mrad). For a_2 up to ±0.03, the slice horizontal (vertical) emittance increases by a factor of 68 (116), reaching a value of 28 mm.mrad, following a linear dependence versus a_2, as expected from the second term of Equation (3.10). Even small a_2 terms can significantly degrade the beam, one should keep the skew term a_2 as close to zero as possible, especially for high divergence electron beams.

6.3.1.3 Experimental observation of quadrupole skew term induced rotation

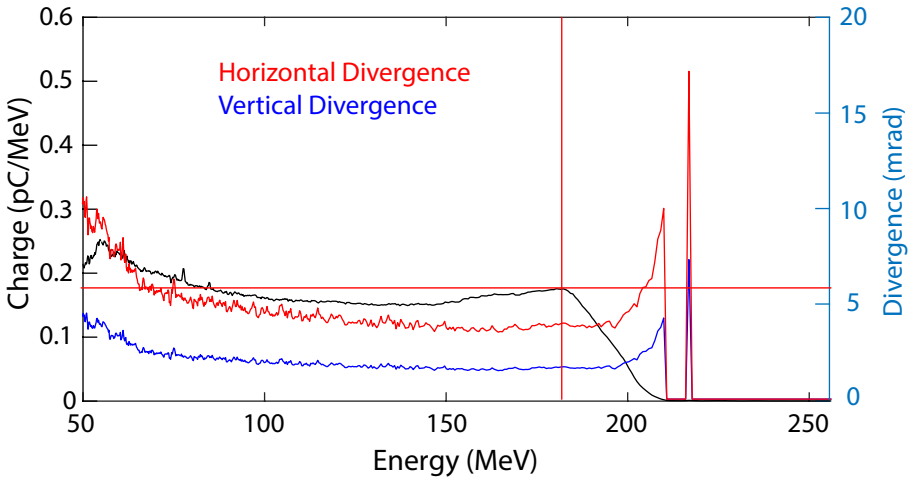

FIGURE 6.29: Initial beam electron distribution (black), vertical (blue) and horizontal (red) RMS divergence measured from a single shot (2017/11/27 set 2 shot 6) [196].

The cross shape observed at the imagers due to the large beam energy spread allows for an easy diagnostic of the tilt caused by the skew term a_2. In order to reproduce some of the measurements in simulation, one uses the single shot beam energy distribution of Figure 6.29, close in time to the data. It presents a 176 ± 1 MeV charge of 0.18 pC/MeV and a vertical (horizontal) divergence of 2.3 mrad (4 mrad).

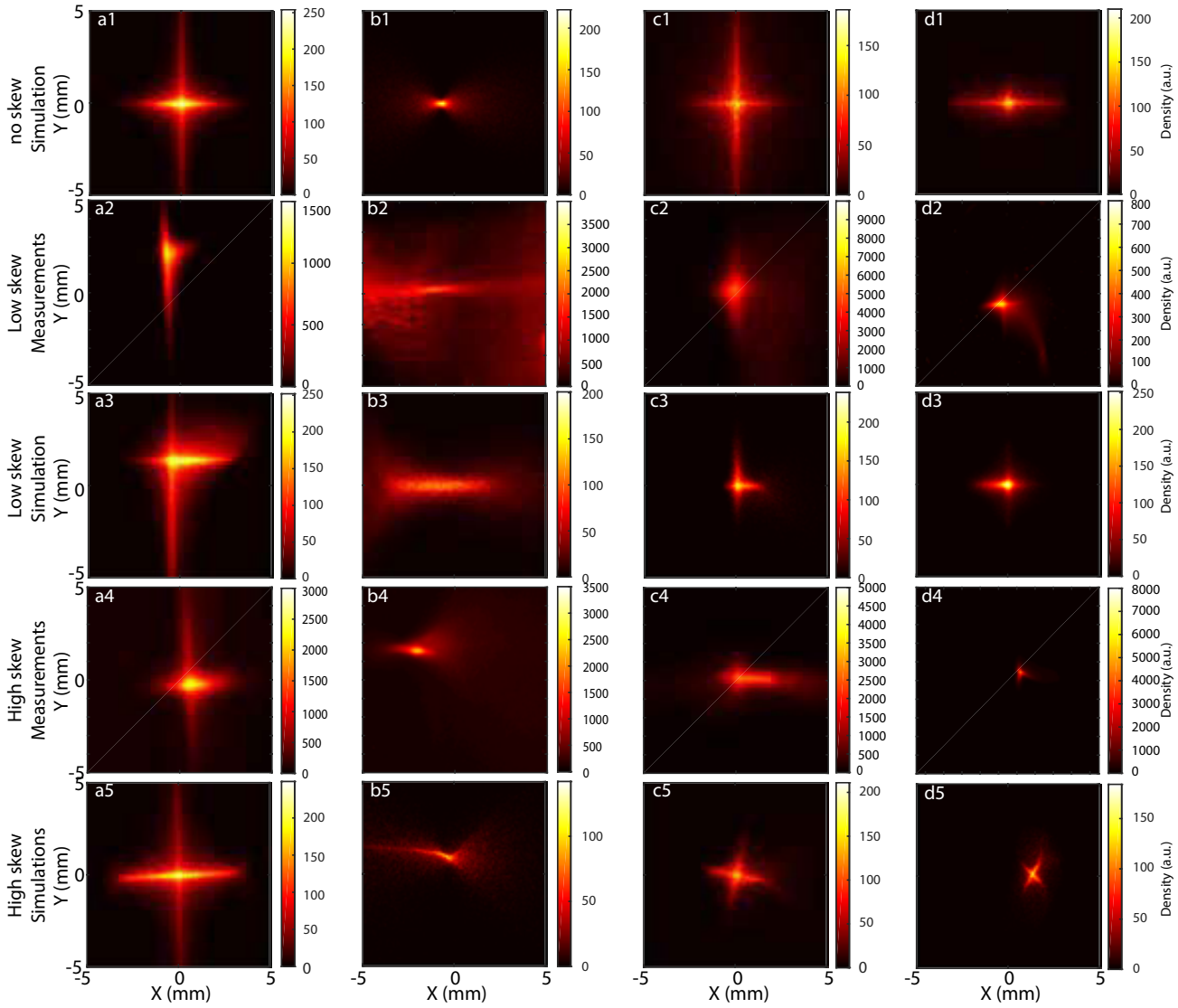

FIGURE 6.30: Transverse beam shape along the transport line at screen after QUAPEVAS (a1-5), in the middle of the chicane (b1-5), undulator entrance (c1-5) and undulator exit (d1-5) measured (a-d2, a-d4) and simulated (a-d1, a-d3, a-d5), with no (a-d1), low (a-d2-3) and high (a-d4-5) roll angle (Table 3.8), the optics "undulator slit" for (a1-3) and (b-d1), "Chicane" for (a4-5) and (b2-5), "undulator entrance" (c2-3), "undulator center" (c4-5) and (d4-5), "undulator exit" (d2-3) for the average beam (Figure 4.8c) (a-d1, a-d3) and single-shot (Figure 6.29) (a-d5). Parameters: $\epsilon_{x,i,RMS}$,$\epsilon_{y,i,RMS}$=0.2 mm.mrad, $\sigma'_{y,i,RMS} = 2$ mrad, $\sigma'_{x,i,RMS} = 3.12$ mrad for (a-d1-3) and $\sigma'_{x,i,RMS} = 4.7$ mrad for (a-d4-5). QUAPEVAs High roll angles: 3.3 mrad, -9 mrad, -9.4 mrad. Low roll angles: -0.3 mrad, 0.7 mrad, 0.05 mrad [196].

Figure 6.30 compares simulations and measurements of the transverse beam shape at the four screens along the line for different roll angle θ_{skew} values caused by a_2 (Equation 2.141). Figure 6.30a1-d1 presents the transport simulation with "slit-undulator" optics without roll angle and the initial beam distribution of Figure 4.8c. The beam is well focused vertically at the slit to achieve an accurate electron energy selection and in both directions at the center of the undulator, while at the undulator entrance and exit, the different focus for the electron energies leads to a cross shape. In the low roll angle case (Table 3.8), measurements (Figure 6.30a-d2) are well reproduced by simulations (Figure 6.30a-d3). Table 6.10 compares the beam RMS horizontal and vertical sizes found in simulation and experiment (Figure 6.30a,c,d2-3). The difference can result from the fluctuations of the beam distribution. In the presence of the high roll angle (Table 3.8), the beam suffers from a tilt that causes dispersion, affects the emittance (Equation 3.10) and degrades the transport [178]. The simulation is able to reproduce the shape of the beam along the line (Figure 6.30a-d4-5) using the initial distribution of Figure 6.29.

TABLE 6.10: Simulated and measured transverse beam shape (Figure 6.30a,c,d2-3) RMS horizontal (σ_x) and vertical (σ_y) sizes for the low roll angle case (Table 3.8).

		Simulation		Measurement	
Figures	**Position**	$\sigma_{x,RMS}$	$\sigma_{y,RMS}$	$\sigma_{x,RMS}$	$\sigma_{y,RMS}$
		mm	*mm*	*mm*	*mm*
Figure 6.30a2-3	After QUAPEVAs	1.16	3.11	1.49	0.86
Figure 6.30c2-3	Undulator entrance	1.16	1.19	1.03	1.58
Figure 6.30d2-3	Undulator exit	0.75	0.69	1.29	0.93

6.3.2 Dodecapolar terms

TABLE 6.11: Simulated σ_y, σ'_y and $\epsilon_{x,y}$ at the undulator center for the "undulator" optics and for the dodecapolar term b_{12} 0 T.mm, 0.02 T.mm, 0.1 T.mm and 0.4 T.mm. Simulations done for the "undulator" optics with initial Gaussian beam centered around 176 MeV, $\sigma'_{x,y,RMS} = 2$ mrad, $\epsilon_{x,y,RMS} = 1$ mm.mrad, $\sigma_s = 1$ μm and $\sigma_\gamma = 40$ %.

Parameter	σ_y **(mm, RMS)**				σ'_y **(mrad, RMS)**				ϵ_x **(mm.mrad, RMS)**				ϵ_y **(mm.mrad, RMS)**			
b_{12} (T.mm)	0	0.02	0.1	0.4	0	0.02	0.1	0.4	0	0.02	0.1	0.4	0	0.02	0.1	0.4
Value	0.88	0.87	0.88	0.93	0.47	0.47	0.47	0.81	31.62	31.59	31.67	35.86	140.68	140.72	141.08	209.93

The influence of the higher order terms of the QUAPEVAs on the electrons beam transport is studied. Multipolar terms up to the dodecapolar one (order 12) b_{12} are identified on the QUAPEVAs [195]. A b_{12} of 0.02 T.mm has been measured. Table 6.11 shows the values of σ_y, σ'_y and $\epsilon_{x,y}$ at the undulator center for the undulator optics for b_{12} of 0, 0.02, 0.1 and 0.4 T.mm with the other multipolar terms equal to 0. The addition of a b_{12} of 0.02 T.mm and 0.1 T.mm does not affect σ_y, σ'_y of the total beam and sligthly increases ϵ_y by 0.028 % and 0.28 % respectively. For b_{12}=0.4 T.mm, a clear σ'_y and ϵ_y (σ_y and ϵ_x) increase above 40 % can be appreciated (around 10 %) with respect to the $b_{12} = 0$ T.mm values. So, the beam parameters are not affected by the QUAPEVAs b_{12} term. Figure 6.31 presents the simulated transversal shapes at the chicane, the undulator entrance and center for b_{12} 0, 0.02, 0.4 T.mm. For $b_{12} = 0.02$ T.mm only tiny changes in the position of electron energies occur (Figure 6.31b1, b2, d1, d2), thus, the lack of effect on the transport is confirmed. For $b_{12} = 0.4$ T.mm, a horizontal defocusing in the energies with a correlation to the vertical position can be clearly observed along the line (Figure 6.31b3, d3, f3). However, this effect starts to be noticeable for a b_{12} of around 10 times the 0.02 T.mm measured at the QUAPEVAs.

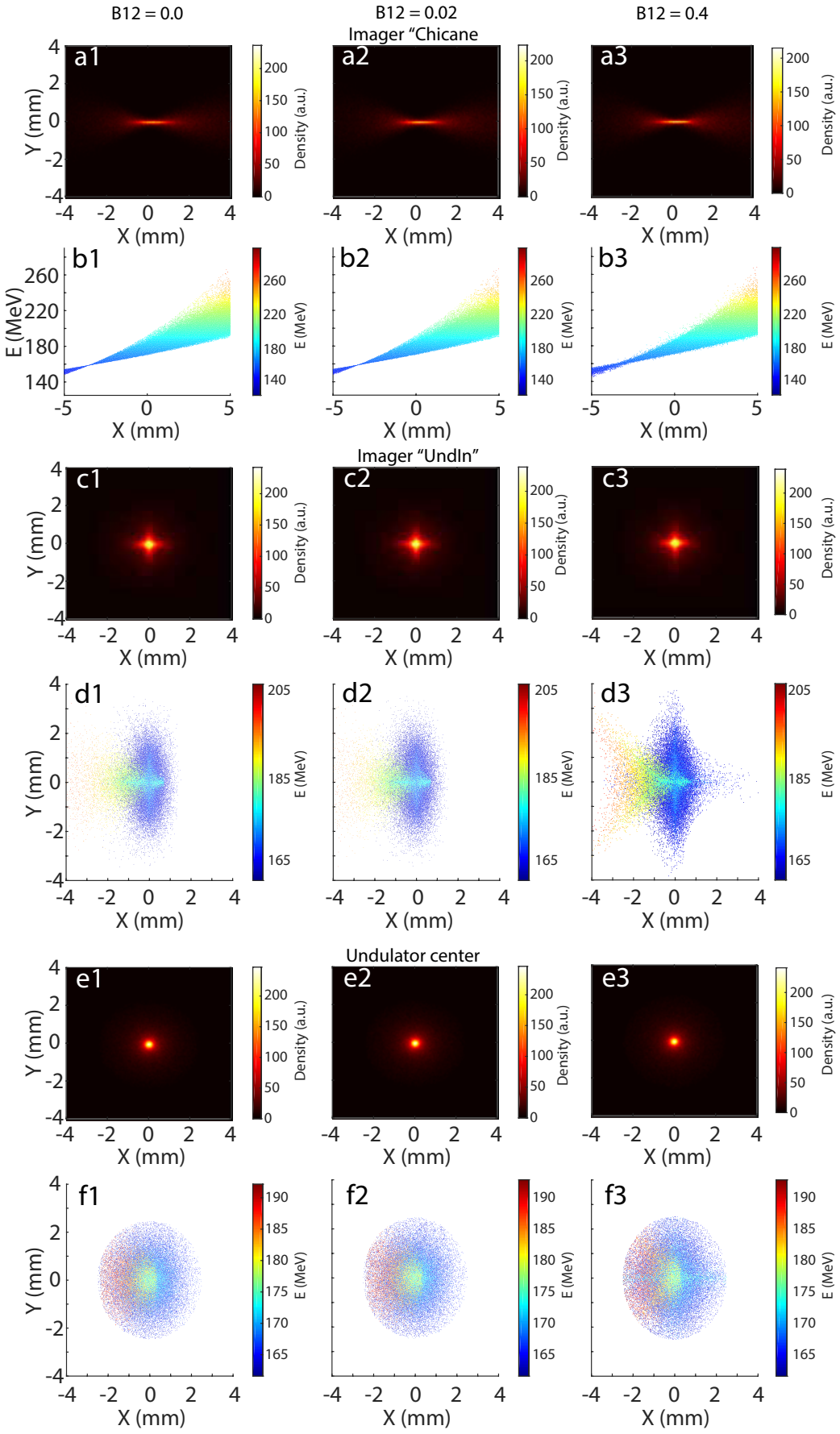

FIGURE 6.31: Simulated transversal shape at (a1-3) imager "Chicane", (c1-3, d1-3) imager "UndIn" and (e1-3, f1-3) the undulator center and (b1-3) energy versus horizontal position at imager "Chicane" for the b_{12} (a1-f1) 0 T.mm, (a2-f2) 0.02 T.mm and (a3-f3) 0.4 T.mm. Simulation done for the "supermatching" optics with initial 6D gaussian beam centered around 176 MeV, $\sigma'_{x,y,RMS} = 2$ mrad, $\epsilon_{x,y,RMS} = 1$ mm.mrad, $\sigma_s = 1\ \mu m$ and $\sigma_\gamma = 40$ %.

6.3.3 QUAPEVAs displacement

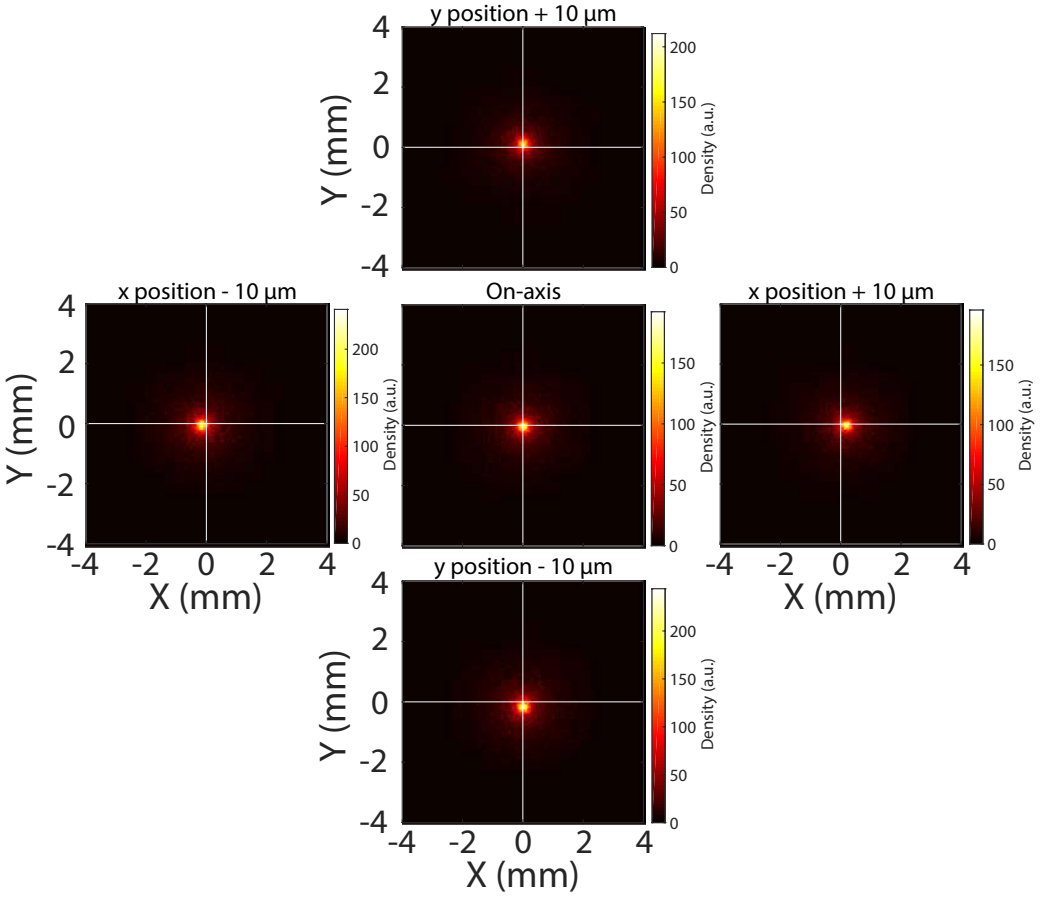

FIGURE 6.32: Simulated transverse beam shape at the undulator center for the QUAPEVA triplet displacement of 0 μm and ± 10 μm in horizontal and vertical. Simulation done for the "undulator" optics with initial 6D gaussian beam centered around 176 MeV, $\sigma'_{x,y,RMS} = 2$ mrad, $\epsilon_{x,y,RMS} = 1$ mm.mrad, $\sigma_s = 1$ μm and $\sigma_\gamma = 40$ %.

In the case of an on-axis beam, a displacement of the QUAPEVA triplet in either the horizontal or vertical direction causes a translation in the same direction of the focused beam at the undulator center as shown in Figure 6.32. Figure 6.33 shows the variation of the beam parameters for different QUAPEVA triplet translation cases. For transversal deviations larger than 10 μm, the electrons start to impinge in the line elements and thus, some charge of the total beam is lost (Figure 6.33a). For displacements of more than 150 μm, the beam cannot be transported until the center of the undulator and most of the charge is lost. All vertical and horizontal displacements show an increase in total beam size (Figure 6.33b), especially when charge starts to be lost. In addition, mixing of the energies in the transverse plane occurs. The total beam vertical divergence (Figure 6.33c) doubles for all displacements except for the horizontal 200 μm one where it triples. The total beam horizontal divergence increases significantly with the horizontal shifts however, the vertical displacements do not substantially affect it. Therefore, the total beam vertical emittance Figure 6.33d) rises for all displacements while the total beam horizontal emittance increase for horizontal shifts and drops for vertical shifts. The reference 176 ± 0.5 MeV slice charge starts to decrease for displacements higher than 100 μm and for a shift of 200 μm, all slice charge is lost. Thus, even misalignments of the order of tens of μm have an impact in the parameters of percent levels, and quickly the beam can be unable to arrive to the center of the undulator.

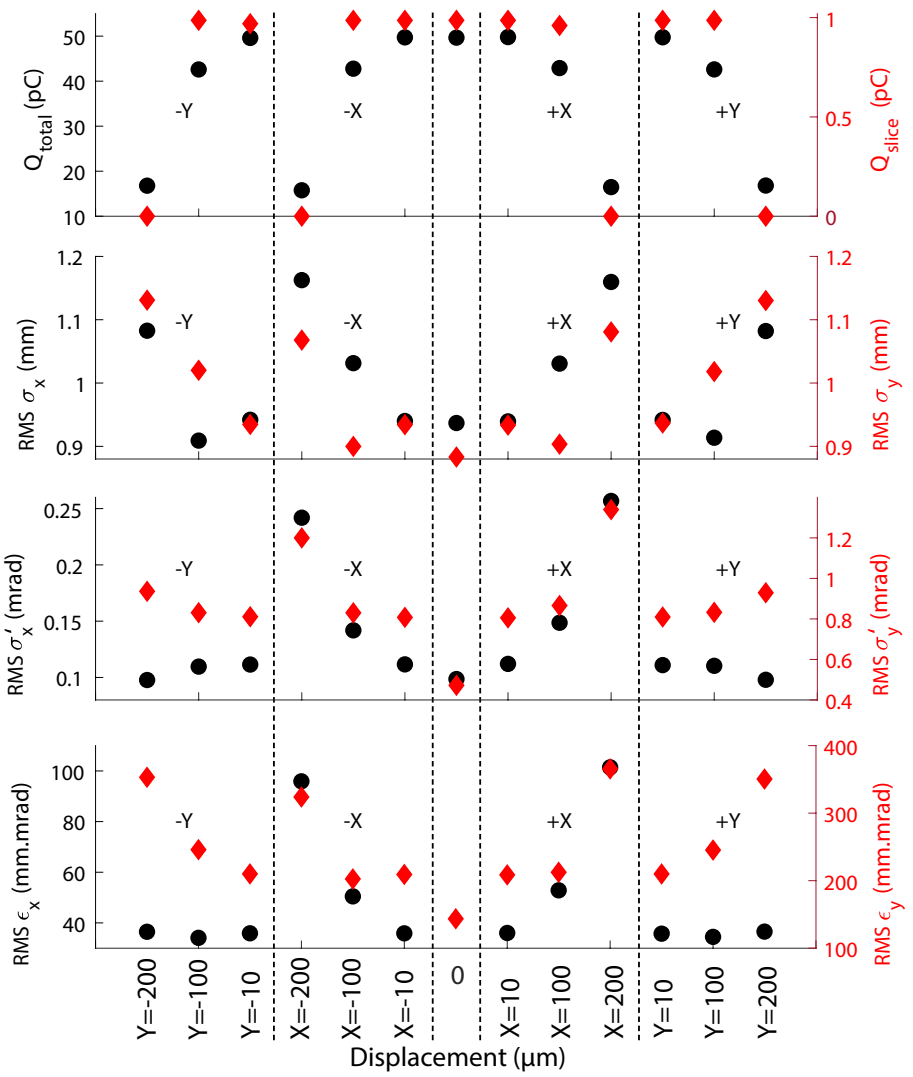

FIGURE 6.33: Simulated total beam charge, $\sigma_{x,y}$, $\sigma'_{x,y}$ and $\epsilon_{x,y}$ at the undulator center for the QUAPEVA triplet individual displacement of 0 μm (square), 10 μm (star) and -10 μm (diamond) in horizontal and 10 μm (six point star) and -10 μm (circle) vertical. Simulation done for the undulator optics with initial 6D gaussian beam centered around 176 MeV with $\sigma'_{x,y,RMS} = 2$ mrad, $\epsilon_{x,y,RMS} = 1$ mm.mrad, $\sigma_s = 1$ μm and $\sigma_\gamma = 40$ %.

6.3.4 QUAPEVA gradient chromatic effects on the transport

The QUAPEVAs gradient offers a wide range of variations (Section 3.2.2.1). When designing optics, the calculation of the QUAPEVA triplet gradients is based on the reference energy selected and where it should be focused. A slight deviation on the gradient can affect the effectiveness of the transport [178, 207]. In the following, the effects of a gradient deviation on a QUAPEVA on the transport is studied.

6.3.4.1 Numerical study

The influence of the gradient change of the strongest QUAPEVA (the second one) is investigated in Figure 6.34, where the evolution of the beam transverse distribution at the undulator entrance versus gradient is presented for the "undulator-entrance" optics (see Figure 3.8c). For the reference setting gradient, the beam displays a vertically and horizontally focused spot on the screen, especially for the energies around 176 ± 1 MeV. For the larger gradient, the vertical–horizontal position per energy plot indicates that the high energies get vertically focused, while the central and lower energies are focused in the horizontal plane. In consequence, the pattern observed on the screen exhibits a cross shape. By decreasing the gradient, the opposite occurs, the lower energies being the ones focused vertically and the rest being focused horizontally as appreciated in the transverse position per energy plot. The width and density in the cross arms are uneven due to the difference in electron density per energy (see Figure 4.8c).

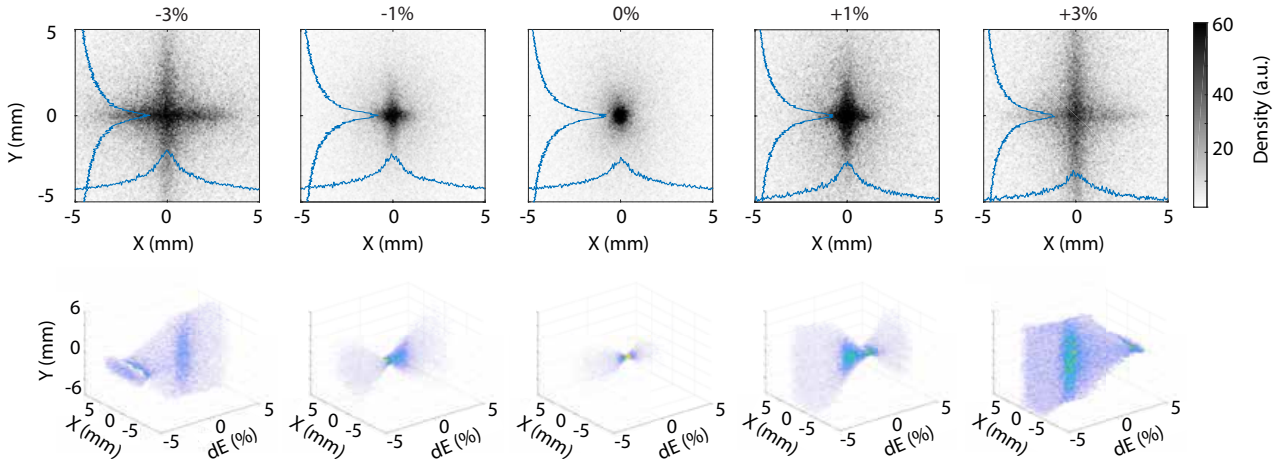

FIGURE 6.34: Electron beam transverse shape (**top**) and corresponding vertical–horizontal position per energy (**bottom**) at the undulator exit for the relative gradient change of QUAPEVA 2 of ±3, ±1, and 0%. Case of "undulator entrance" optics with the low divergence beam distribution (Figure 4.8c and Table 6.7), $\epsilon_{x,i}$,$\epsilon_{y,i,RMS}$=0.2 mm.mrad, $\sigma'_{y,i,RMS} = 2$ mrad, $\sigma'_{x,i,RMS} = 3.12$ mrad [178].

Figure 6.35a shows the maximum vertical and horizontal RMS beam sizes and the peak intensity at the center of the beam for the different gradients with the "undulator entrance" optics. When the beam is not properly focused (+1%), the beam size increases, and the intensity is reduced by a factor of two. Figure 6.35b presents the effectiveness of the transport at the undulator center versus QUAPEVA 2 gradient in the case of the "supermatching" optics. When the gradient is reduced, the charge arriving at the center of the undulator is slightly increased because the lower energy electrons are focused on the horizontal plane avoiding the loss due to the vertical aperture of the undulator. When the gradient is increased by 3%, the charge is halved because of high energy electron loss on the undulator vertical aperture (see Figure 3.8e). The horizontal emittance slightly changes from −3% to +3%, and the vertical one grows by a factor of 1.5 for the 1% case.

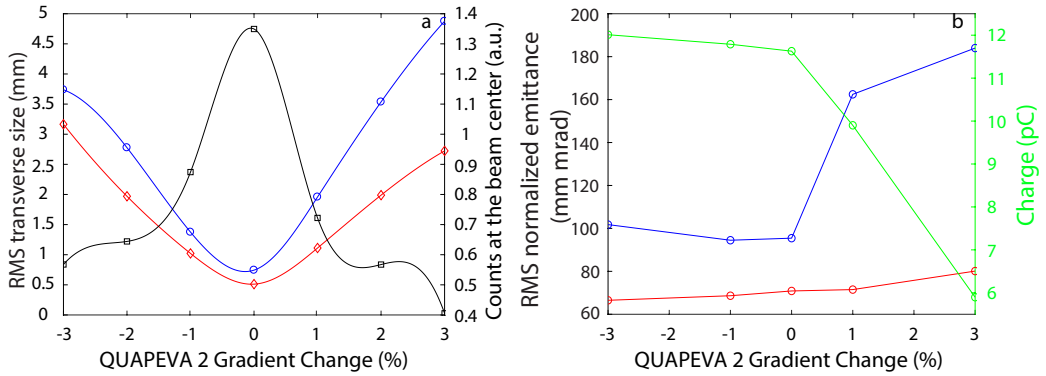

FIGURE 6.35: (**a**) Horizontal (diamond) and vertical (circle) RMS beam size and counts at the center of the beam (square) for the "undulator entrance" optics (each point averaged over 5 repetitions of the simulation) and (**b**) beam vertical (circle) and horizontal (circle) normalized emittance and total charge (circle) at the undulator center for the optics "supermatching", for the relative gradient change of QUAPEVA 2 using the low divergence initial beam distribution (Figure 4.8c and Table 6.7) with $\sigma'_{y,i,RMS} = 2$ mrad, $\sigma'_{x,i,RMS} = 3.12$ mrad, and $\epsilon_{x,i,RMS}$, $\epsilon_{y,i,RMS} = 0.2$ mm.mrad [178].

6.3.4.2 Experimental QUAPEVA gradient effect before the undulator

The effect of a gradient deviation on QUAPEVA 2 has been observed experimentally. Figure 6.36a-e1 presents the influence of the gradient for the average beam of Figure 4.8c with the "undulator entrance" optics. The measurements (Figure 6.36a-e2) show a good agreement with their simulated counterparts. For the optimum gradient, the beam has a measured horizontal (vertical) beam size of σ_x=430 μm (σ_y=270 μm) to be compared to the simulated one of σ_x=490 μm (σ_y=670 μm). The vertical size σ_y difference between measurement and simulation is probably due to the inherent unknowns of the experimental parameters of each shot.

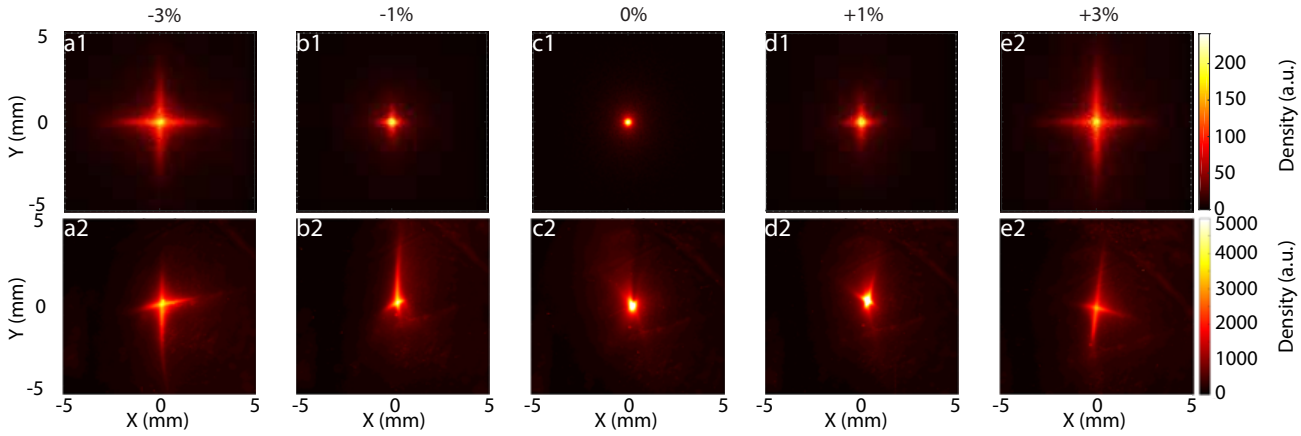

FIGURE 6.36: Electron beam transverse shape simulated for the average beam distribution (a1-e1) with the "undulator entrance" optics and measurement (a2-e2) at the undulator entrance for the relative gradient change of QUAPEVA 2 of +3% (a), +1% (b), 0% (c), -1% (d) and -3% (e). Simulation case with the average beam distribution Figure 4.8c, $\epsilon_{x,i,RMS}$,$\epsilon_{y,i,RMS}$=0.2 mm.mrad, $\sigma'_{y,i,RMS}$ = 2 mrad, $\sigma'_{x,i,RMS}$ = 3.12 mrad.

Most of the QUAPEVA deviations can heavily affect the transport and the beam parameters at the undulator center, nevertheless, they are easily identifiable with the imagers and corrected thanks to the QUAPEVA design and implementation on the line (motorized stage and variable gradient) with the exception of the skew magnetic multipolar term a_2 that cannot be corrected during operation.

6.4 Experimental beam transverse shape analysis

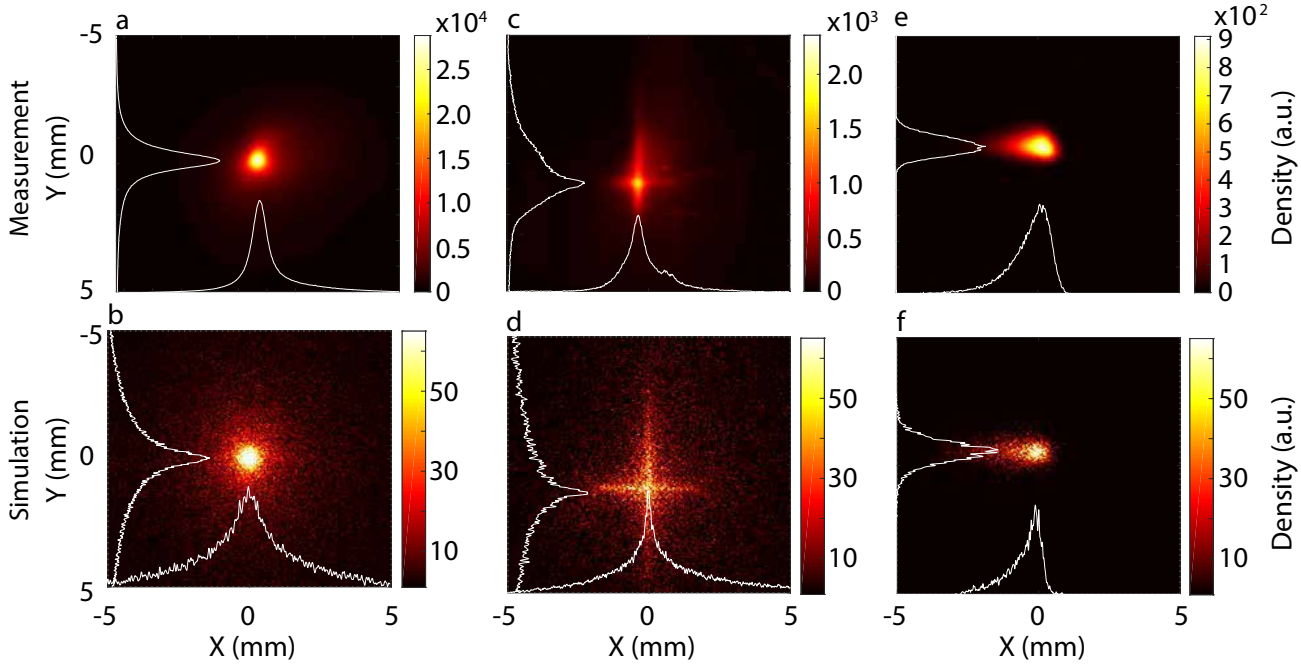

FIGURE 6.37: Transverse beam shape at the undulator entrance: measurements of RUN 4 taken the (**a**) 2017/11/07, (**c**) 2017/11/27 and (**e**) 2017/11/30 and simulations (**b**,**d**,**f**) with the low skew a_2 case (a_2= -0.007, 0.027, 0.003; Table 3.8), $\sigma'_{y,i,RMS}$ = 2 mrad, $\sigma'_{x,i,RMS}$ = 3.12 mrad, $\epsilon_{y,i,RMS}$,$\epsilon_{x,i,RMS}$ = 0.2 mm.mrad. (**a**,**b**) "Undulator entrance" optics, QUAPEVA 1: 103.27 T/m, QUAPEVA 2: −115.65 T/m, QUAPEVA 3: 94.94 T/m, (**c**,**d**) QUAPEVA 1: 103.27 T/m, QUAPEVA 2: −121.99 T/m, QUAPEVA 3: 94.94 T/m. (**e**,**f**) With the "slit-undulator" optics, a horizontal pointing of 5 mrad and the slit in the chicane closed at 1 mm (177 ±2 MeV). Shot-to-shot pointing for (**a**,**c**,**e**): 0.005 ± 0.01 mrad, −0.09 ± 0.06 mrad, and 0.17 ± 0.49 mrad (0.03 ± 0.02 mrad, 0.10 ± 0.08 mrad, −0.18 ± 0.01 mrad) in the horizontal (vertical) direction.

The parameter tolerance study on the transversal beam shape allows for a better analysis of the observed imperfections at the imagers during experiments.

Figure 6.37a,b compares the measurements at the undulator entrance and simulation. The RMS beam sizes (σ_x = 0.52 mm σ_y = 0.64 mm) are similar to the simulated ones (σ_x = 0.52 mm σ_y = 0.65 mm). The slight difference may arise from the uncertainty of the initial distribution. A change of 6 T/m in QUAPEVA 2 from the configuration of Figure 6.37c,d causes the horizontal and vertical focusing redistribution, leading to a cross shape (see Figure 6.37c). The characteristic cross due to the gradient of QUAPEVA 2 is well reproduced in simulation (see Figure 6.37d). Figure 6.37e,f compares measurements and simulations at the undulator exit and shows similar experimental (σ_x = 0.77 mm σ_y = 0.50 mm) and simulation RMS beam size (σ_x = 0.74 mm σ_y = 0.35 mm). Experimentally, the transversal shape is the result of multiple parameters deviating from the baseline, however, only a few are dominant.

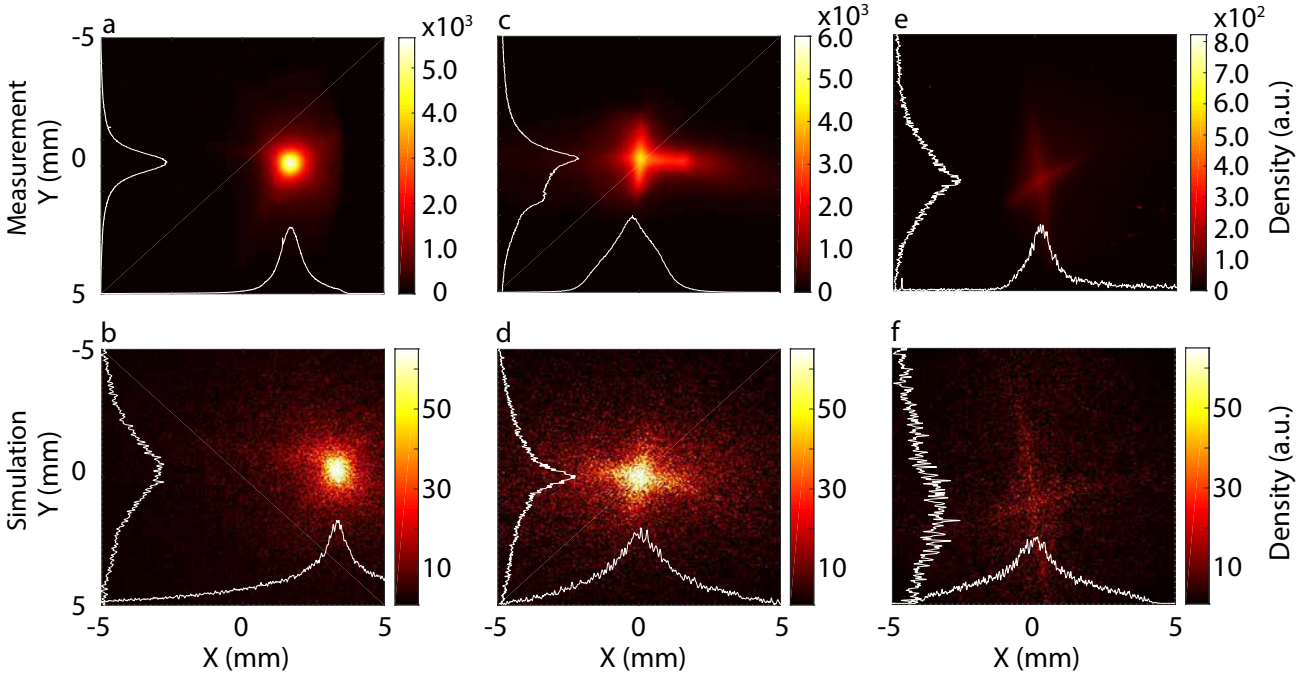

FIGURE 6.38: Transverse beam shape at the undulator entrance: measurements of RUN 3 taken the (**a**) 2017/03/24, (**c**) 2017/03/30 and (**e**) 2017/03/03 and simulations (**b**,**d**,**f**). Simulations done with the high skew a_2 case (a_2= 0.073, -0.325, 0.362; Table 3.8), $\epsilon_{y,i,RMS}$,$\epsilon_{x,i,RMS}$ = 0.2 mm.mrad. (**a**,**b**) With $\sigma'_{y,i,RMS}$ = 2 mrad, $\sigma'_{x,i,RMS}$ = 4.7 mrad and the "Undulator entrance" optics. (**c**,**d**) With $\sigma'_{y,i,RMS}$ = 2 mrad, $\sigma'_{x,i,RMS}$ = 4.7 mrad and the "supermatching" optics. (**e**,**f**) With $\sigma'_{y,i,RMS}$ = 2.5 mrad, $\sigma'_{x,i,RMS}$ = 5.9 mrad and the "Undulator exit" optics. Shot-to-shot pointing for (**a**,**c**,**e**): 0.85 ± 0.03 mrad, 0.13 ± 0.15 mrad, and 0.07 ± 0.02 mrad (−0.03 ± 0.05 mrad, −0.03 ± 0.04 mrad, 0.18 ± 0.04 mrad) in the horizontal (vertical) direction.

Figure 6.38 compares measured and simulated transverse beam profiles at the undulator entrance for some RUN 3 shots. Similar round shapes are observed (Figure 6.38a,b), corresponding to a tight focus. The RMS experimental ($\sigma_{y,RMS}$ = 1.31 mm $\sigma_{x,RMS}$ = 1.58 mm) and simulated ($\sigma_{y,RMS}$ = 0.87 mm $\sigma_{x,RMS}$ = 2.32 mm) beam sizes differ slightly, probably because of an improper initial electron beam distribution. The cross shape with a tilt observed during measurements (Figure 6.38c,d,) is well reproduced by simulations. A good agreement between measurements and simulations is also found on the beam slopes at the undulator exit (see Figure 6.38e,f). The cross pattern is rotated to the opposite side with respect to Figure 6.38c,d, because of the focusing effect of the undulator.

Figure 6.39 presents measurements shots belonging to sets taken at imagers "Chicane", "UndIn" and "UndOut" one after the other with the "supermatching" optics taken during RUN 7. Simulation and measurement show a good agreement and all the features of the beam can be reproduced. In the imager "UndOut" (Figure 6.39c1) the cross appears however, an additional low intensity beam appears to its right that does not appear in the simulation. The secondary beam probably corresponds to a low energy secondary beam as observed in the "first imager" during RUN 7 (Figure C).

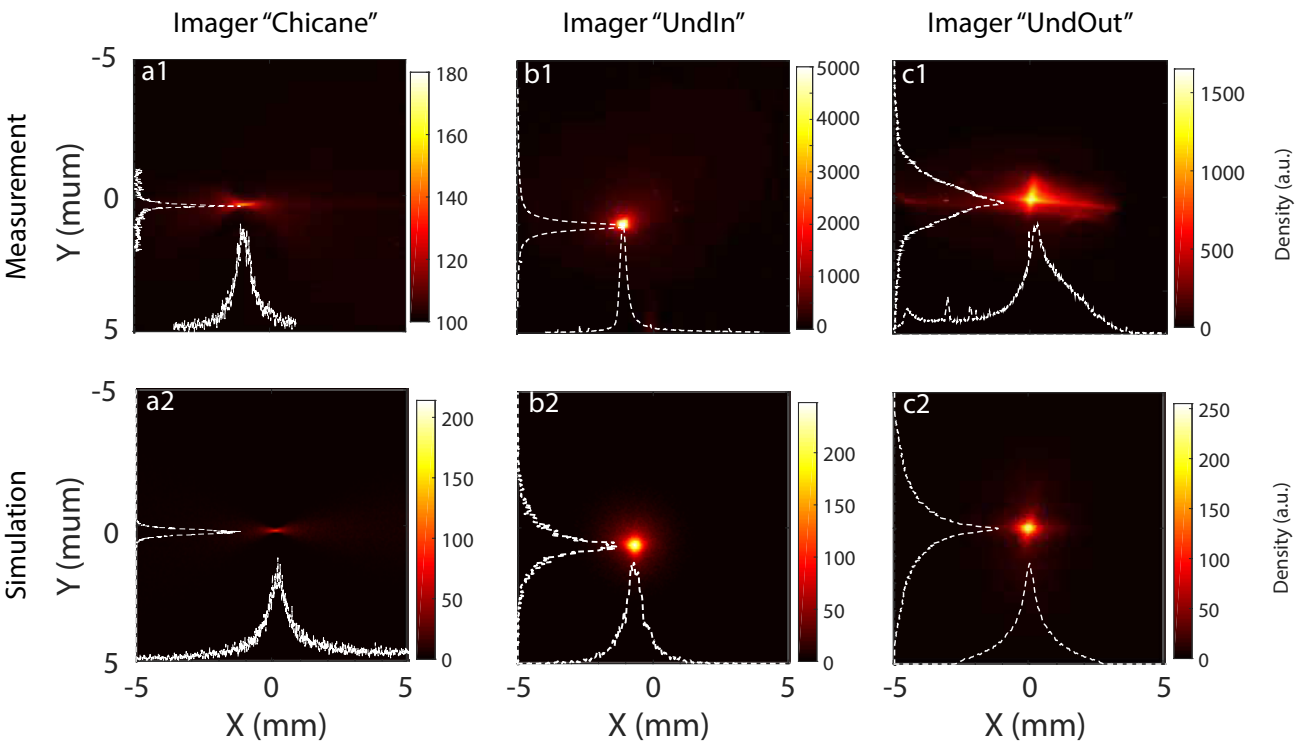

FIGURE 6.39: Transverse beam shape at the imager (**a**) "chicane", (**b**) "UndIn" and (**c**) "UndOut" (**a1, b1, c1**) taken during RUN 7 the 25/09/2020 at 14/22/23, 14/28/02 and 14/30/17 respectively and (**a2, b2, c2**) simulated with "supermatching" optics. Simulations done with the low skew a_2 case (Table 3.8), $\epsilon_{y,i,RMS}$,$\epsilon_{x,i,RMS}$ = 1 mm.mrad, with $\sigma'_{y,i,RMS} = 2$ mrad, (**a2, b2**) $\sigma'_{x,i,RMS} = 2$ mrad and (**c3**) 4 mrad. Initial vertical pointing (**a2**) -1 mrad and (**b2**) 3 mrad, horizontal pointing (**c2**) 2 mrad. Initial horizontal displacement (**a2**) -30 μm; horizontal (**b2**) -50 μm and vertical 50 μm.

6.5 Summary

In this chapter the effect on the transport of a realistic beam and multiple deviations from the ideal case have been studied. For a realistic case the 176 ± 0.5 MeV slice (total beam) emittance increases by a factor 1.6 (two orders of magnitude) compared to the baseline.

Initial beam divergences above 2 mrad degrade substantially the transport increasing the total and reference slice emittance. The addition of a skew term a_2 in the QUAPEVA magnets further enhances the chromatic emittance growth, even for low a_2 values. QUAPEVA triplet displacement below mm distances can severely change the beam optics but through it one can compensate the beam initial pointing and displacements (BPAC). Percent variations in the QUAPEVA magnetic gradient can modify the focused energy. Charge loss of the 176 ± 0.5 MeV slice can be observed for initial beam or QUAPEVAs displacements. Measurements of the different RUNs have been reproduced via simulation. Deducing the main parameters causing the transverse shape observed is enough to find a good agreement between simulation and experiment. This study shows the capabilities of the COXINEL line to identify relative deviations in the initial beam parameters and QUAPEVA during experiment which is of grand importance for LPA based FEL experiments as the beam stability is not yet comparable to the ones of classic accelerators. The possible origin of the irregularities of the observed transverse beam shape with respect to the baseline can be deduced thanks to the knowledge about the electron beam and its transport in realistic cases. Mostly the initial pointing and divergence dominate the beam transverse shape. The identification of the beam irregularities has been here done by hand and confirmed by transport simulations (Section 6.4), however, such process could be made completely automatic by the use of a neural network based on policy gradient [239] or Q-learning [240, 241]. Even though the line can transport a range of beam parameters, the transport of a low charge and high emittance beam makes the production of FEL more difficult (Section 3.1.2.2.3). Moreover, for seeded FEL the spatial overlapping is required and beam divergence, size or transversal ratio changes can significantly degrade it.

6.6 Conclusion

In view of the large discrepancy between measured and expected electron beam performance, extensive tracking simulations from the source to the undulator for multiple initial set of realistic beam parameters and QUAPEVA misalignments have been carried. The study show the transport and monitoring capabilities of the COXINEL line and results in the potential of identification during experiment of beam irregularities from the imagers measurements.

Chapter 7

On-line monitoring of the LPA electron beam along the transport

The electron beam characterization in the COXINEL line is not limited to the source. Thanks to the multiple imagers, BPMs and ICTs along the line the beam charge, position and transverse profile can be measured at multiple locations. The diagnosis of the LPA beam performances along the line and at the undulator center is important. In this chapter, the measured total charge along the line (Figure 7.1) (the ICTs and imager "UndOut") is analyzed, the beam initial emittance measurement (imager "Chicane") is validated and the experimental results studied, the energy distribution passing through the undulator is monitored (imager "D_{dump}").

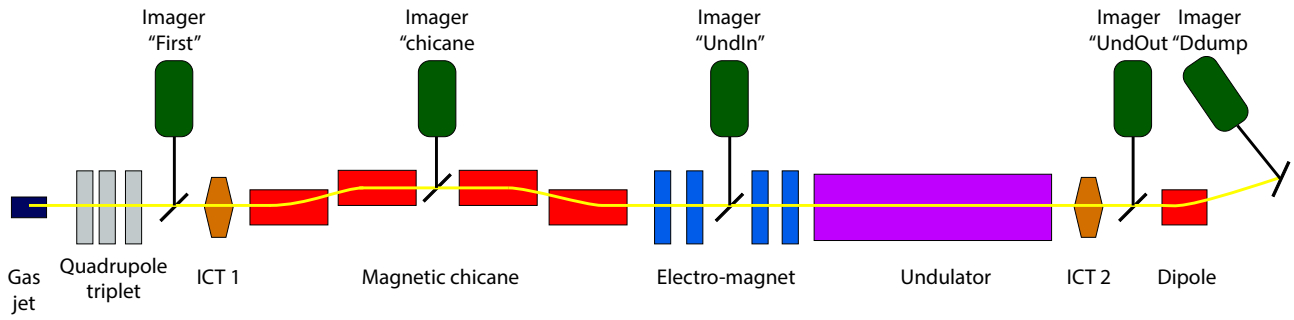

FIGURE 7.1: COXINEL transport line scheme. Left to right: Gas jet (blue), electron beam (yellow), triplet of QUAPEVAs (grey), ICT (orange), chicane (red), a second set of electro-magnetic quadrupoles (blue), undulator (purple), ICT (orange), dipole dump (red), CCD cameras (green) and imagers along the line (black).

7.1 Total electron beam charge evolution along the line

The total beam charge along the COXINEL line can be measured via the two ICTs and two BPMs positioned before and after the undulator without perturbing the beam. In this section, the evolution of the total beam charge evolution along the undulator is analyzed.

7.1.1 Integrated current transformer before the undulator

ICT1 (70 cm after the quadrupole triplet (Figure 7.1)) can give an approximated measurement of the total charge of the beam arriving to the undulator.

Diagnostic	Total charge Mean (std) (pC)							
	RUN 4				RUN 6		RUN 7	
Gas target	Gas cell		Gas jet		Gas jet		Gas jet	
Spectrometer	120.3	(66.8)	280.7	(110.5)	114.3	(35.7)	143.2	(59)
ICT1	11.30	(5.64)	35.47	(25.29)	137.03	(100.69)	359.02	(237.38)
ICT2	2.03	(1.76)	2.86	(4.11)	8.98	(3.56)	12.42	(4.55)

TABLE 7.1: Measured total beam charge at the electron spectrometer, ICT1 (4.61 m before the undulator) and ICT2 (0.78 m after the undulator) during RUNs 4, 6 and 7.

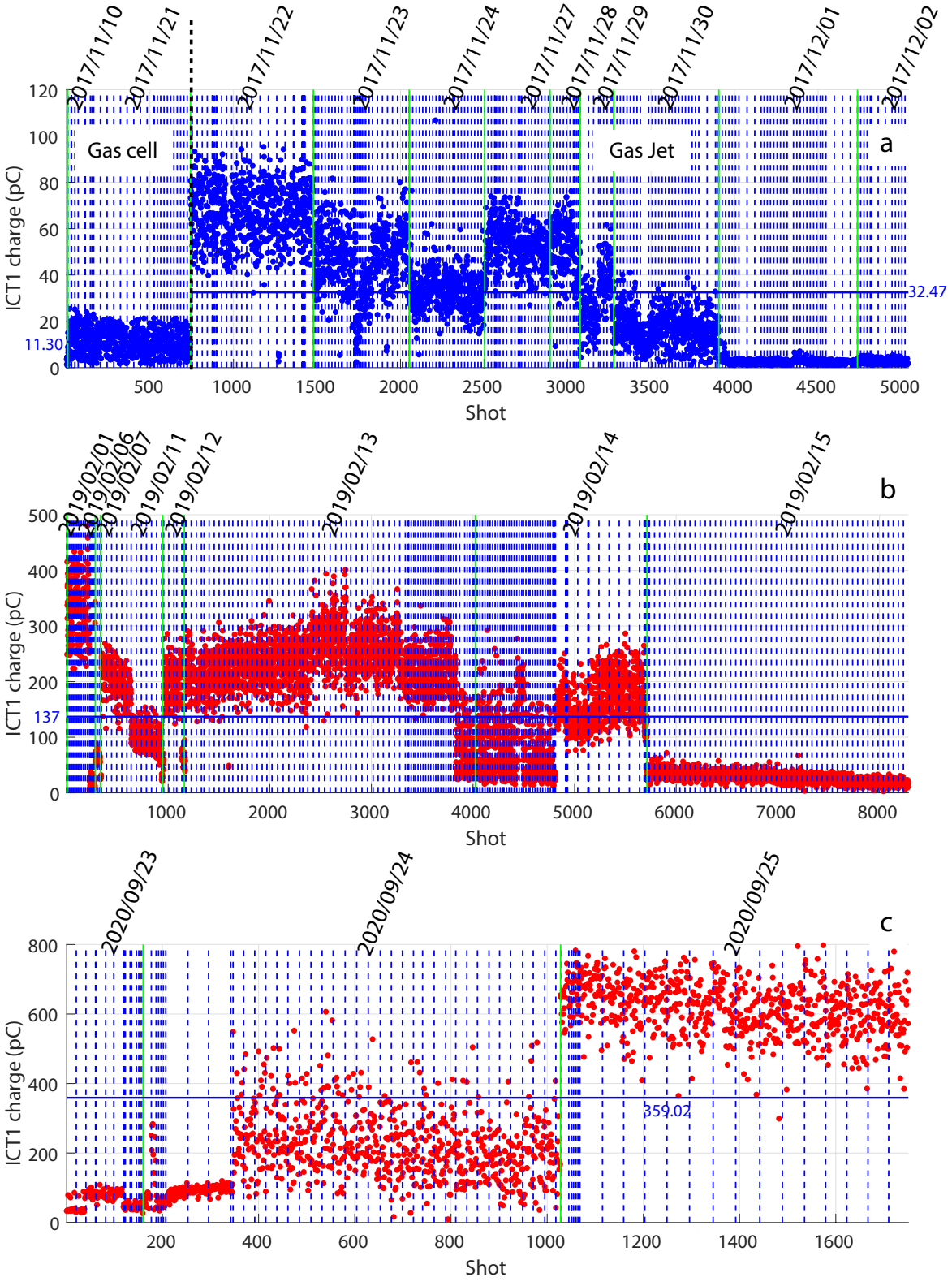

FIGURE 7.2: Measured total beam charge before the undulator at the first ICT1 during RUNs 4 (a), 6 (b) and 7 (c) in chronological order, separated by gas target (dotted black line), day (green line) and series (dotted blue line).

Figure 7.2a presents the total charge before the undulator data taken during RUN 4 for the gas cell configuration (2017/11/10 and 2017/11/21) and the gas jet one (2017/11/22 - 2017/12/02). In the gas cell (jet) case, the measured total charge fluctuates from close to 1 pC to 25 pC (1 pC to 90 pC). While the total beam charge does not significantly vary with time in the gas cell case, it clearly falls in the the gas jet case because

of the laser degradation in time during experiment. During some days (e.g., 2017/11/30 and 2017/12/01), the LPA system is re-optimized after certain time, leading to a sudden total charge increase. The mean measured total charge for the gas cell (jet) case (Table 7.1) is around 10 times lower than the electron spectrometer one (Section 4.1.2). The discrepancy can be explained by the degradation in time of the LPA system, as the data shown here are taken after the electron beam transport optimization process.
Figure 7.2b presents the total charge before the undulator data measured on ICT1 taken during RUN 6. Day by day the measured total charges changed substantially, going from a range of 140-400 pC (2019/02/13) to 10-80 pC (2019/02/15). The total charge also decreases during the day due to laser degradation with time. The numerous jumps in charge range occurring the 2019/02/14 are caused by the multiple re-optimizations of the LPA system (Section 4.3.1). Both averages are close, within ≈ 20 pC, but the one measured at the ICT1 presents a ≈ 3 times higher standard deviation than the spectrometer one (Table 7.1). RUN 6 (referen energy decrease to 151 MeV) average total charge at the undulator entrance is more than 10 times higher than the one of RUN 4, confirming a significant improvement result of the LPA electron beam enhancement (Section 4.3.1).
Figure 7.2c displays the RUN 7 (laser power increase) data measured on ICT1 starting from 2020/09/23 when it was calibrated. From day to day the total charge increases substantially thanks to LPA system optimization going from ≈ 80 pC (2020/09/23) up to 700 pC (2020/09/25). However, during the day, the fall of total charge due to laser degradation is clearly seen. The ICT1 average is more than twice the spectrometer one (Table 7.1). The spectrometer charge during the 2020/09/23-24-25 is around 175 pC (Section 4.3.2) however, at the ICT1, the average of each day varies considerably. The measured averages on ICT1 the 2020/09/23-24 are not far from the spectrometer ones but the 2020/09/25 presents an increase of close to 3 times the average of the previous date. Discrepancy between spectrometer and ICT1 charge can result from the presence of electrons below 45 MeV, the energy detection limit of the spectrometer, the possible secondary electrons created by the plasma and seen by ICT1 (e.g., low vacuum ionization, arcs) or decay of the beam charge between measurements. The high average total charge and std for the ICT1 is caused by the 2020/09/25 charge values. RUN 7 sees an significant improvement over RUN 6 total charge at ICT 1 by the laser power increase, i.e., ≈ 3 times higher average total charge.

7.1.2 Integrated current transformer after the undulator

ICT2, positioned 0.78 m after the undulator, can provide a direct monitoring of the beam total charge passing through the undulator, of interest for the FEL.

Figure 7.3 exhibits the total charge after the undulator at ICT2. In the case of RUN 4 (Figure 7.3a), for the gas cell case (2017/11/10-21) the total charge varies between 0.2 pC and 7.5 pC. The degradation of the laser is not visible however, at the end of the 2017/11/21 the total charge drops considerably, as in the spectrometer data (Section 4.1.2). The gas jet data shows clearly the total charge decrease due to laser degradation in time with the sudden increases of charge due to LPA source re-optimization, e.g., 2017/11/22-23-37. The gas jet case total charge continues to display a higher charge in average than the gas cell one (Table 7.1). The total charge after the undulator measured by ICT2 for the gas cell (jet) is reduced by a factor ≈ 5.5 (≈ 12) with respect to the ICT1. The significant drop in total charge between the ICTs can be explained by the beam high divergence, energy spread and initial pointing deviating from the baseline parameters (Sections 6.2.1.2, 6.2.2.2, 6.2.1.4) and leading to electron beam losses along the line. During RUN 4, by the time the beam transport is optimized, the total beam charge arriving at the undulator is 10 times lower than the one measured at the spectrometer due to non reference energies particles loss and laser degradation over time. A total charge ≈ 100 smaller than the one measured at the spectrometer crosses the undulator however, the reference slice charge is the only important for undulator radiation experiments.

The total charge measured after the undulator at ICT2 during RUN 6 (Figure 7.3b) present a linear decrease versus time, due to the laser degradation. Even after re-optimization of the LPA system, the total charge performance at the start of the day could not be recovered. Even from one day to another, the charge does not significantly increase. From the 2019/02/12 (8 - 23 pC) to the 2019/02/15 (1 - 13 pC) the total charge divided by more than 2. The total charge drops by around 15 times from ICT1 to ICT2 (Table 7.1) due to particle loses along the transport. Despite such a charge loss, the measured charge at ICT2 is 3 times larger than the one of RUN 4 because of the LPA parameters improvements and reduction of the reference energy to 151 MeV from 176 MeV.

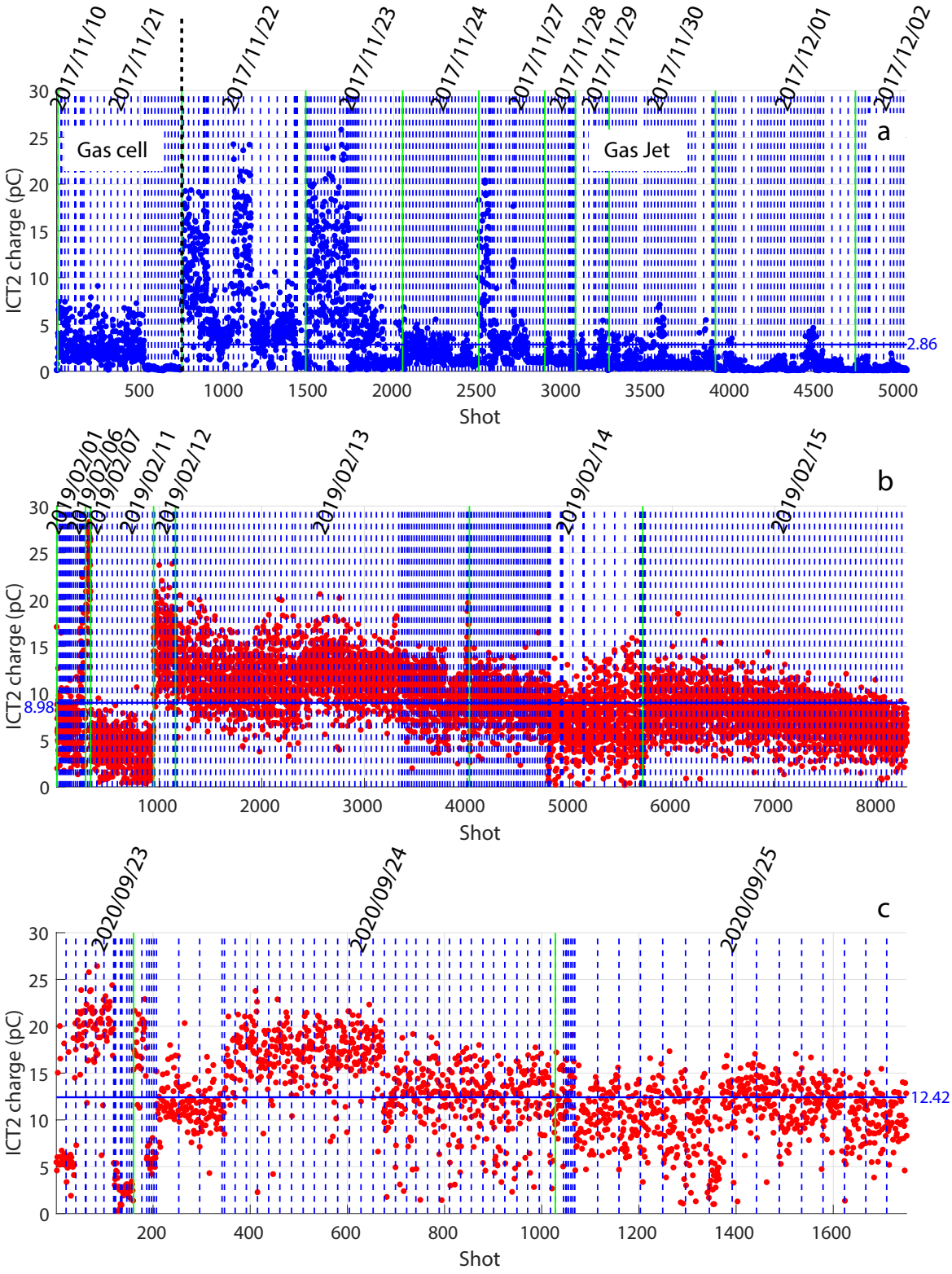

FIGURE 7.3: Measured total beam charge after the undulator at the second ICT during RUN 4 (a), 6 (b) and 7 (c) in chronological order, day (green line) and series (blue dotted line).

In case of RUN 7 (Figure 7.3c), a slight charge decrease with time due to laser degradation appears, e.g., 2020/09/25, however, it is not as pronounced as in previous RUNs and it can be compensated to certain extent via re-optimizations of the LPA system. RUN 7 offers a rise of 1.4 times of the average total charge at ICT2 with respect to RUN 6 (Table 7.1). Even though the total charge at ICT1 is much higher than in previous RUNs (Table 7.1), especially the 2020/09/25, it is mainly lost during the transport to ICT2, leaving 3.46 % after the

undulator. So the charge rise observed before the undulator the 2020/09/25 could be caused by a large quantity of low energy electrons that are lost due to vertical aperture.

7.2 Imager "Chicane" inside the magnetic chicane

Based on the principles of emittance measurements through quadrupole gradient variation shown in [242, 243], the initial beam vertical emittance [217] can be measured using imager "chicane", providing an additional source of information of the beam characteristics. In this section, the method is elaborated, validated by simulations and the measurements during RUN 7 are presented.

7.2.1 Concept

The beam size can be expressed versus the Twiss parameters (Equations 2.126, Section 2.5.2) as in [242]:

$$\sigma(s_1)^2 = M_{11}^2 \epsilon \beta_{s_0} - 2M_{11}M_{12}\epsilon\alpha_{s_0} + M_{12}^2\epsilon\gamma_{s_0} \tag{7.1}$$

with M_{ij} the ij element of the transport matrix from position s_0 to s_1. Through consecutive measurements of the beam size at the s_1 position for various M_{ij} while varying the quadrupoles strength the emittance can thus be measured (so-called "quadrupole scan method" [244]). However, this emittance measurement method does not easily apply to the LPA case. Indeed, the initially low emittance of LPA electron beam at the plasma vacuum surface (Section 3.1.1.1) (ϵ of the order of mm.mrad) rapidly increases during transport as Equation 3.10 (quadratic dependence with the beam divergence σ' and linear one with the energy spread σ_γ). Thus, the emittance evolution of the beam is dominated by the divergence and the energy spread. Besides, the shot-to-shot fluctuations of the beam parameters due to laser or gas changes. Both of these behaviors potentially cause the beam Twiss parameters to change during a series of shots, therefore, making a multi-shot based measurement [242] very difficult.

Nevertheless, the principle of the method can still be used after modifying the measurement procedure to a single shot measurement [217]. In the middle of a magnetic chicane, because of the dispersion introduced by the dipole, the energy spread translates into a transverse displacement and the beam can be sorted by electron energy (Equation 3.25, Section 3.2.2.6). The size of the different slices can thus be measured (which is similar to the measurement for different quadrupole gradients). Through a numerical fit and the knowledge of the transport matrix from source to the measurement position, one can obtain the beam size, divergence and hence the emittance, provided the resolution of the measurement is sufficient. In the case of a chicane that sorts horizontally the electrons by energy, the transport matrix in the vertical direction is (Equation 2.120, Section 2.5.1):

$$\begin{pmatrix} y_1 \\ y_1' \end{pmatrix} = \left[\begin{pmatrix} R_{33}R_{34} \\ R_{43}R_{44} \end{pmatrix} + \delta \begin{pmatrix} R_{336}R_{346} \\ R_{436}R_{446} \end{pmatrix} \right] \begin{pmatrix} y_0 \\ y_0' \end{pmatrix} = R_z \begin{pmatrix} y_0 \\ y_0' \end{pmatrix} \tag{7.2}$$

With $\delta = \frac{E-E_0}{E_0}$ (Equation2.100), E the particle energy, E_0 the target energy, the sub-index 1 and 0 corresponding to the middle of the chicane and the source positions respectively and x, y the horizontal and vertical transverse axis respectively. The vertical beam matrix can be written as (Equation 2.133, Section 2.5.3):

$$\Sigma_y = \begin{pmatrix} \sigma_y^2 \sigma_{yy'} \\ \sigma_{yy'}\sigma_{y'}^2 \end{pmatrix} \tag{7.3}$$

with σ_y the vertical beam size, $\sigma_{y'}$ the vertical beam divergence and $\sigma_{yy'}$ the correlation term between divergence and size. From Equation 7.3 the vertical emittance ϵ_y can be defined as (Equation 2.134, Section 2.5.3):

$$\epsilon_y = det(\Sigma_y)^{1/2} = \sqrt{\sigma_y^2\sigma_{y'}^2 - \sigma_{yy'}^2} \tag{7.4}$$

As once the electron beam exits the plasma, the effect of the wakefield is no longer there and as the charge is sufficiently small to prevent the beam to explode (at least for μm beam sizes), one can assume that at the source there is no correlation, and Equation 7.4 becomes simply

$$\epsilon_y = \sigma_y \sigma_{y'} \tag{7.5}$$

When the beam is transported from the source to the measurement position at the middle of the magnetic chicane the new size $\sigma_{y,1}$, divergence $\sigma_{y',1}$ and correlation term $\sigma_{yy',1}$ per beam energy slice can be calculated from the source values.

$$\Sigma_{y,1} = R_y \Sigma_{y,0} R_y^t \tag{7.6}$$

Which results in

$$\sigma_{y,1}^2 = \sigma_{y,0}^2 (R_{33} + \delta R_{336})^2 + R_{346}^2 \delta^2 \sigma_{y',0}^2 \tag{7.7}$$

$$\sigma_{y',1}^2 = \sigma_{y,0}^2 (R_{43} + \delta R_{436})^2 + R_{44}^2 \sigma_{y',0}^2 \tag{7.8}$$

$$\sigma_{yy',1} = \sigma_{y,0}^2 (R_{33} + \delta R_{336})(R_{43} + \delta R_{436}) + \delta R_{44} R_{346} \sigma_{y',0}^2 \tag{7.9}$$

Due to the nature of the source-to-image optics (S2I) design [179], $det(R_y) = 1$, $R_{44} = 1/R_{33}$. The relative energy is $\delta = x/D_x$, with x the horizontal position and D_x the dipole dispersion. Since $R_{336} << 1$, δR_{336} can be neglected.

$$\sigma_{y,1}^2 = \sigma_{y,0}^2 R_{33}^2 + R_{346}^2 \sigma_{y',0}^2 (x/D_x)^2 \tag{7.10}$$

Thus, from a single measurement of the beam at the middle of the magnetic chicane, one can obtain $\sigma_{y,0}$, $\sigma_{y',0}$ and $\epsilon_{y,0}$.

7.2.2 Validation of the concept via simulation in an ideal case

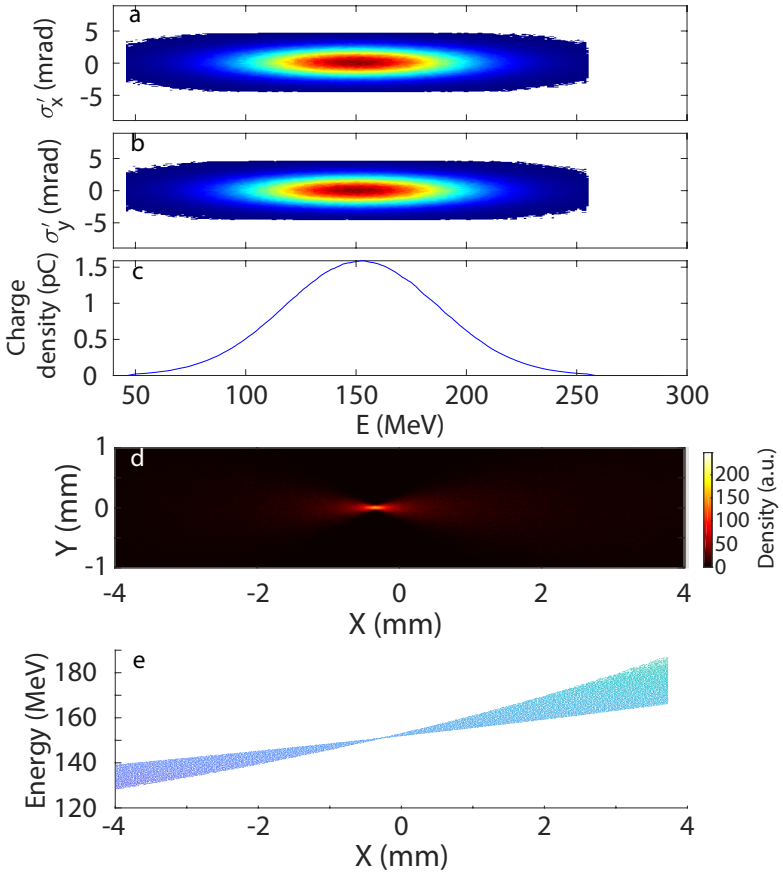

FIGURE 7.4: Initial beam (a, b) divergence and (c) energy distribution used as input for the trasport simulation, (d) result at imager 2 and (e) the electron energies horizontal position at imager 2. Initial parameters; $\epsilon_{RMS} = 1$ $mm.mrad$, $\sigma'_{RMS} = 1.5$ $mrad$, $\sigma_{s,RMS} = 1$ μm, $\sigma_\gamma = 40$ %, reference energy of 151 MeV, undulator slit optics and simulated imager 2 vertical and horizontal resolution of 2.5 $\mu m/px$ and 2.3 $\mu m/px$ respectively.

Figure 7.4a,b,c show the electron beam Gaussian energy and divergence distribution used for the following transport simulations, with the reference energy being 151 MeV (initial beam parameters $\epsilon = 1$ mm.mrad, $\sigma'_{source} = 1.5$, $\sigma_{source} = 1\ \mu m$, $\sigma_\gamma = 40$ %). The beam after transport to imager "chicane" using the "slit-undulator" optics shown in Figure 7.4d,e present a vertically focused zone, where the energy of interest is, and wings on each side, where higher (right) and lower (left) energy electrons are, forming a butterfly figure. The deduced vertical divergence $\sigma'_{y,s}$ and vertical size $\sigma_{y,s}$ at the initial Gaussian beam by the covariant matrix method (Appendix A) are 1.49 mrad (3.52 mrad) and 2.15 μm (5.07 μm) RMS (FWHM) respectively for the 151 ± 0.5 MeV slice. In imager "chicane" (Figure 7.4d), deducing the vertical size of 1 MeV electron energy slices by the covariant matrix and using Equation 7.10 yields the same values of source vertical 151 ± 0.5 MeV slice size and divergence (1.49 mrad and 2.15 μm RMS). Therefore, the method principle works for an ideal imager "chicane" diagnostic.

7.2.3 Aligned electron beam

The method is first tested in the case of an aligned beam without pointing errors. The method validation via simulations has been done also in experimental like conditions (see Appendix D).

7.2.3.1 Imager "chicane" vertical slice size analysis

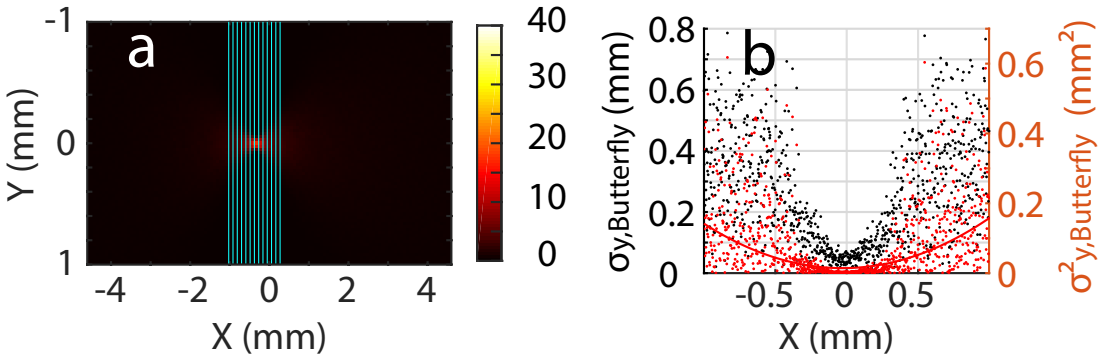

FIGURE 7.5: (a) Transport simulation at imager "chicane" and example of some 1 grid unit width vertical slices (blue lines) and (b) result of FWHM vertical slice size. Initial parameters; $\epsilon_{RMS} = 1$ *mm.mrad*, $\sigma'_{RMS} = 1.5$ *mrad*, $\sigma_{RMS} = 1\ \mu m$, $\sigma_\gamma = 40$ %, reference energy of 151 MeV, "slit-undulator" optics and simulated imager "chicane" vertical and horizontal resolution of 2.5 μm/grid-unit and 2.3 μm/grid-unit respectively.

The simulated image is divided in a squared grid. Figure 7.5 shows the steps to obtain the source vertical divergence $\sigma'_{y,chicane}$ and vertical size $\sigma_{y,chicane}$ from imager "chicane". At each vertical slice of 1 grid-unit width (see Figure 7.5a) inside a horizontal window centered around the most focused spot (reference energy) the FWHM vertical size $\sigma_{y,butterfly}$ is determined (see Figure 7.5b). The data of vertical size $\sigma_{y,butterfly}$ versus horizontal position x can be fitted with an equation of the form of Equation 7.10, and thus, the initial vertical size and divergence $\sigma'_{y,chicane}$ and $\sigma_{y,chicane}$ are deduced. For the imager "chicane" simulations, two grid sizes are used; a "high resolution" case, where vertical and horizontal grid-unit size are equivalent to 1 μm/grid-unit each and a "low resolution" case, where the vertical and horizontal grid-unit size are equivalent to 2.5 μm/grid-unit and 2.3 μm/grid-unit respectively.

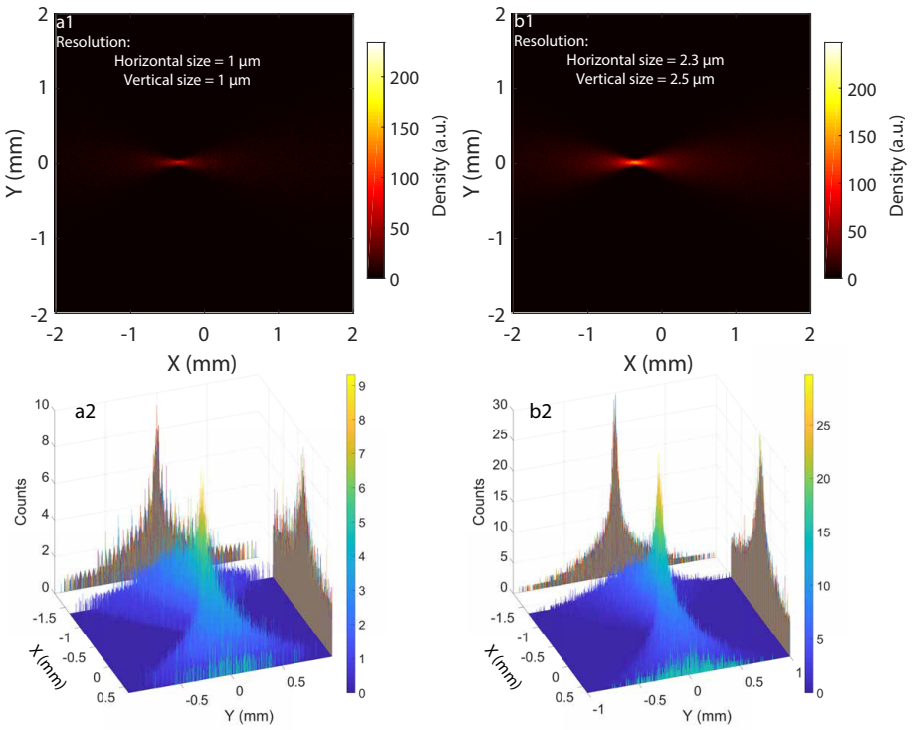

FIGURE 7.6: Figure 7.4 beam simulated transport to imager "chicane" using a (a) resolution of 1 μm/grid-unit (high resolution) and (b) a resolution of 2.5 μm/grid-unit (low resolution). Initial parameters; ϵ_{RMS} = 1 $mm.mrad$, σ'_{RMS} = 1.5 $mrad$, σ_{RMS} = 1 μm, σ_γ = 40 %, reference energy of 151 MeV, "slit-undulator" optics.

Figure 7.6a shows the high resolution case example. Due to the lower grid-unit surface, the highest achieved counts per grid-unit, at the center of the beam, is of 9 counts (see Figure 7.6a2). For the low resolution case (Figure 7.6b2), the higher grid-unit surface causes a higher electron count per grid-unit, so, the distribution wings can be seen more clearly and the maximum counts per grid-unit is of 29. As seen in Figure 7.6a2, b2, the data presents a lot of peaks, even more in the high resolution case (Figure 7.6a1, b1), that can cause a wrong measurement of the FWHM size, requiring data smoothing or Gaussian fit to avoid errors.

7.2.3.2 Vertical slice size methods comparison

Figure 7.7 present the reference slice vertical divergence analysis process in a simulation case raw data and for a Gaussian fit treatment method. For a total horizontal aperture of 0.5 mm (Figure 7.7a1-c1) centered at the reference energy position, the analysis of the raw image yields a FWHM source vertical divergence and size of $\sigma'_{y,chicane,FWHM}$ = 1.41 mrad and $\sigma_{y,chicane,FWHM}$ = 4.13 μm, which are far from the initial beam values of 3.52 mrad and 5.07 μm FWHM (Table 7.2). Figure 7.7c1 shows a high variability of the vertical size $\sigma_{y,butterfly}$. Consecutive slices measurements can give completely different size values in occasions due to the peaks of intensity (Figure 7.6). To mitigate this, the slice can be fitted by a Gaussian obtaining directly the RMS values [242] (Figure 7.7a2-c2). The consecutive slice size variation is gone and the RMS vertical divergence and size (Table 7.2) are only a 0.7 % and 7.04 % respectively higher than the exact values.

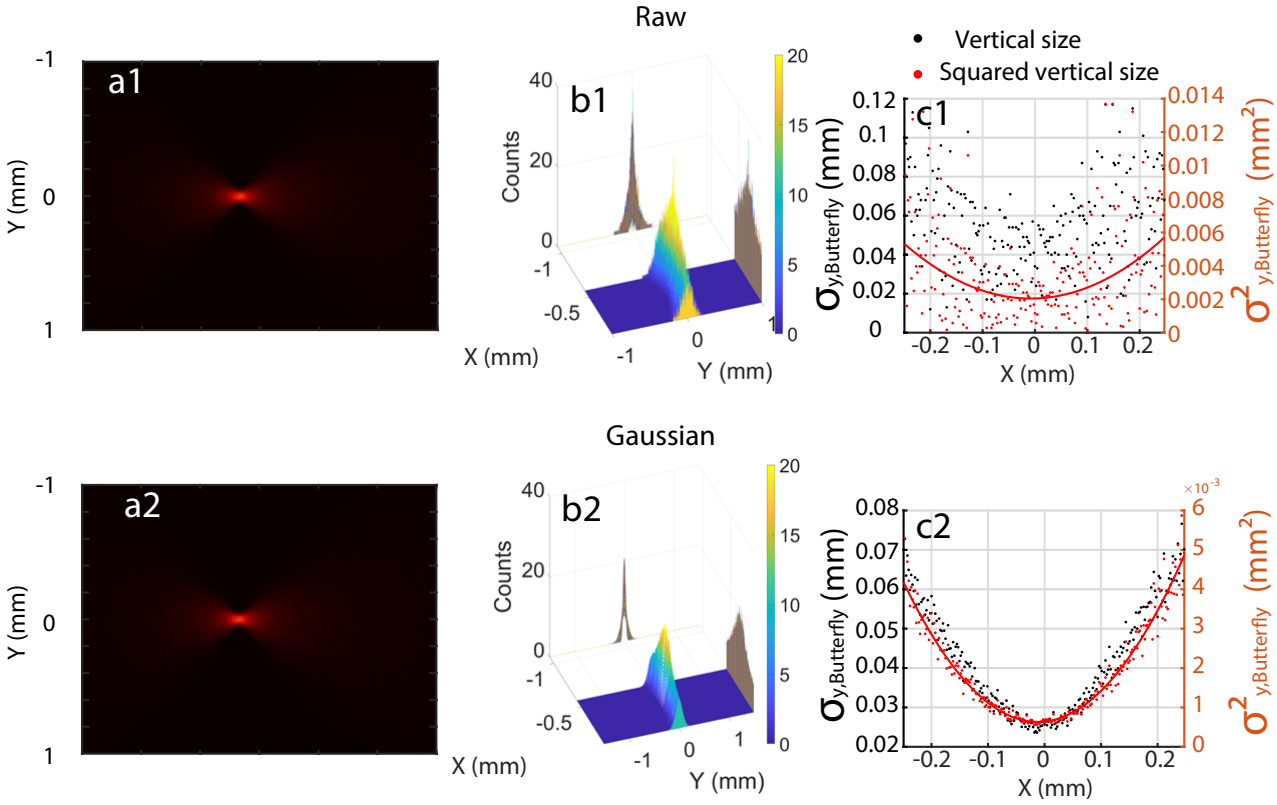

FIGURE 7.7: (a) Simulated transported beam at imager "chicane", (b) 3D view surface of the transversal shape and (c) 1 grid-unit width vertical slices size values and squared size. (a-c1) RAW image and (a-c2) RMS vertical gaussian fit treatment and σ_y and σ'_y resulting from it. Initial parameters; Figure 7.4, $\epsilon_{RMS} = 1$ *mm.mrad*, $\sigma'_{RMS} = 1.5$ *mrad*, $\sigma_{RMS} = 1$ μm, $\sigma_{\gamma,FWHM} = 40$ %, reference energy of 151 MeV and "slit-undulator" optics. The "low resolution" case for imager "chicane" is used.

Figure	Method	Value type	$\sigma'_{y,chicane}$ *mrad*	$\frac{\sigma'_{y,chicane}}{\sigma'_{y,s}}$	$\sigma_{y,chicane}$ μm	$\frac{\sigma_{y,chicane}}{\sigma_{y,s}}$
Figure 7.4a, b, c	Ideal	FWHM	3.52	1	5.07	1
		RMS	1.49	1	2.15	1
Figure 7.7a1-c1	RAW	FWHM	1.41	0.4	4.13	0.82
Figure 7.7a2-c2	Gaussian fit	RMS	1.5	1.01	2.31	1.07

TABLE 7.2: Vertical divergence $\sigma'_{y,chicane}$ and size $\sigma_{y,chicane}$ values deduced from the simulated imager "chicane" and relative difference versus source ($\sigma'_{y,s}$, $\sigma_{y,s}$) for the Gaussian fit method shown at Figure 7.7. Initial parameters; Figure 7.4, $\epsilon_{RMS} = 1$ *mm.mrad*, $\sigma'_{RMS} = 1.5$ *mrad*, $\sigma_{RMS} = 1$ μm, $\sigma_\gamma = 40$ %, reference energy of 151 MeV and "slit-undulator" optics. The "low resolution" case for imager "chicane" is used.

Method	Resolution case	$\sigma'_{y,img2}/\sigma'_{y,source}$	$\sigma_{y,img2}/\sigma_{y,source}$	$\frac{\sigma'_{y,img2}}{\sigma'_{y,source}} \times \frac{\sigma_{y,img2}}{\sigma_{y,source}}$
Gaussian fit	High resolution	1.02	1.07	1.09
	Low resolution	1.03	1.05	1.08

TABLE 7.3: $\sigma'_{y,chicane}/\sigma'_{y,s}$ and $\sigma_{y,chicane}/\sigma_{y,s}$ results relative to the source values from the simulated imager "chicane" with high resolution (2.3μm/grid-unit x 2.5μm/grid-unit) and low resolution (1μm/grid-unit x 1μm/grid-unit) and horizontal apertures of 0.5 mm for the Gaussian fit method. Initial parameters; Figure 7.4, $\epsilon_{RMS} = 1$ *mm.mrad*, $\sigma'_{RMS} = 1.5$ *mrad*, $\sigma_{RMS} = 1$ μm, $\sigma_\gamma = 40$ %, reference energy of 151 MeV and "slit-undulator" optics.

Table 7.3 compares the vertical divergence and size for the Gaussian method applied on the two resolution cases for a fixed horizontal aperture of 0.5 mm. In the focused zone of the beam at imager "chicane", the intensity above FWHM vertical zone size is of about 46 μm, thus, the length in grid-units for the high (low)

resolution case is of ≈ 46 grid-units (≈ 20 grid-units), which is enough to deduce the vertical size. The decrease in resolution from the high case to the low case improves slightly the vertical size accuracy.

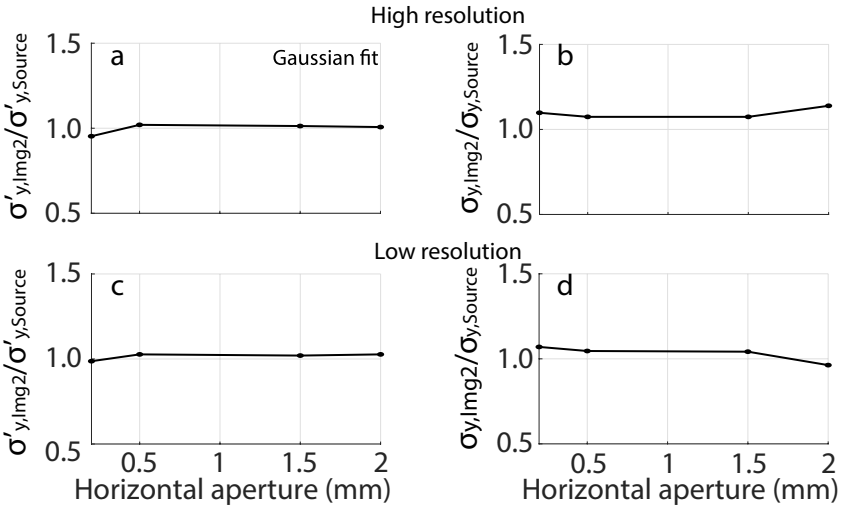

FIGURE 7.8: (a, c) $\sigma'_{y,chicane}/\sigma'_{y,s}$ and (b, d) $\sigma_{y,chicane}/\sigma_{y,s}$ results relative to the source values from the simulated imager "chicane" with (a, b) high resolution (1 μm/grid-unit x 1 μm/grid-unit) and (c, d) low resolution (2.3 μm/grid-unit x 2.5 μm/grid-unit) and different horizontal apertures for the Gaussian fit method. Initial parameters; Figure 7.4, $\epsilon_{RMS} = 1$ $mm.mrad$, $\sigma'_{RMS} = 1.5$ $mrad$, $\sigma_{RMS} = 1$ μm, $\sigma_\gamma = 40$ %, reference energy of 151 MeV and "slit-undulator" optics.

Figure 7.8 presents the effects of the variation of the horizontal aperture on the ratios $\sigma_{y,chicane}/\sigma_{y,s}$ and $\sigma'_{y,chicane}/\sigma'_{y,s}$ obtained at imager "chicane" for high (1 x 1 μm/grid-unit) and low (2.5 x 2.3 μm/grid-unit) resolution. In the high resolution case (Figure 7.8a,b), the Gaussian fit gives an accurate value of the vertical divergence $\sigma'_{y,chicane}$ for all horizontal apertures, within 4.5 % from the source value $\sigma'_{y,s}$. The values of the vertical size $\sigma_{y,chicane}$ are less accurate but still within 9.5 % from the source value $\sigma_{y,s}$ except at 2 mm horizontal aperture, where the accuracy is reduced by a 4 % due to the lower signal far from the beam center. Both the vertical divergence and size values found remain fairly stable for the multiple horizontal apertures.
Figure 7.8c,d shows the low resolution case (2.5 x 2.3 μm/grid-unit). The Gaussian fit sees an improvement in accuracy of % levels in both vertical divergence and size, while still being stable for all horizontal apertures. So, in the low and high resolution for a perfect beam and imager case, the Gaussian fit performs well, i.e., within percent from the real value.

7.2.4 Electron beam with initial pointing

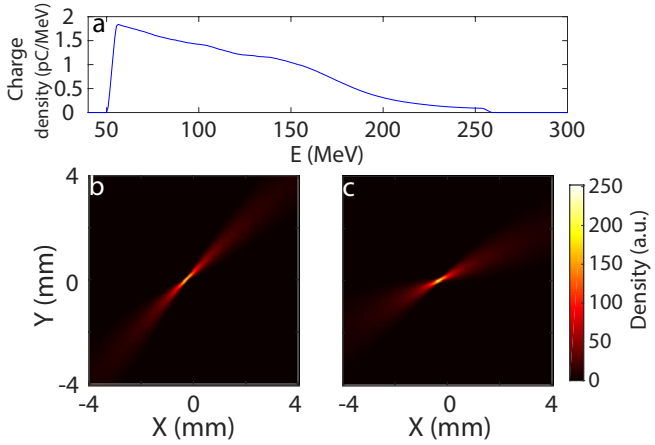

FIGURE 7.9: Transport simulation to imager "chicane". Simulation parameters: "slit-undulator" optics, initial (b) 6 mrad and (c) 3 mrad vertical pointing, $\sigma'_{x,RMS} = 1$ mrad, $\sigma'_{y,RMS} = 1$ mrad, $\epsilon_{RMS} = 1.0$ mm.mrad and (a) initial energy distribution.

The variations of the laser can cause the appearance of vertical pointing producing images like the ones shown in Figure 7.9, where the beam is rotated. Considering a simplified transport matrix from the source to imager "chicane", the transport can be calculated via the matrices for the different drifts, QUAPEVAs and dipoles (Section 2.5.4):

$$M_{drift} = \begin{pmatrix} 1 & l_d & 0 & 0 & 0 & 0 \\ 0 & 1 & 0 & 0 & 0 & 0 \\ 0 & 0 & 1 & l_d & 0 & 0 \\ 0 & 0 & 0 & 1 & 0 & 0 \\ 0 & 0 & 0 & 0 & 1 & 0 \\ 0 & 0 & 0 & 0 & 0 & 1 \end{pmatrix}; M_{QAP,i} = \begin{pmatrix} 1 & 0 & 0 & 0 & 0 & 0 \\ -k_i & 1 & 0 & 0 & 0 & 0 \\ 0 & 0 & 1 & 0 & 0 & 0 \\ 0 & 0 & k_i & 1 & 0 & 0 \\ 0 & 0 & 0 & 0 & 1 & 0 \\ 0 & 0 & 0 & 0 & 0 & 1 \end{pmatrix};$$
$$M_{Dipole,i} = \begin{pmatrix} cx_i & sx_i/k_i & 0 & 0 & 0 & r_{16,i} \\ -k_i \times sx_i & cx_i & 0 & 0 & 0 & r_{26,i} \\ 0 & 0 & 1 & l_{d,i} & 0 & 0 \\ 0 & 0 & 0 & 1 & 0 & 0 \\ r_{51,i} & r_{52,i} & 0 & 0 & 1 & r_{56,i} \\ 0 & 0 & 0 & 0 & 0 & 1 \end{pmatrix} \tag{7.11}$$

with l_i the element length, k_i the magnetic strength, the index i as the element index, $cx_i = cos(k_i * l_i)$, $sx_i = sin(k_i * l_i)$. An initial pointing in the electron beam modifies its divergence as:

$$\sigma'_{y,0,total} = \sigma'_{y,0} + \sigma'_{y,0,pointing} \tag{7.12}$$

Calculating the transport of such beam from the source to imager "chicane" yields a vertical size of:

$$\begin{aligned} \hat{\sigma}_{y,1} = \sigma'_{y,0,total} f_{1,(k_{Q1},k_{Q2},k_{Q3},l_{Source,Q1},l_{Q1,Q2},l_{Q2,Q3},l_{Q3,dip1},l_{dip1},l_{dip1,dip2},l_{dip2},l_{dip2,IMGchic})} \\ + \sigma_{y,0} f_{2,(k_{Q1},k_{Q2},k_{Q3},l_{Q1,Q2},l_{Q2,Q3},l_{Q3,dip1},l_{dip1},l_{dip1,dip2},l_{dip2},l_{dip2,IMGchic})} \end{aligned} \tag{7.13}$$

with f_1 and f_2 functions dependent on the transport line elements parameters, $\sigma_{y,0}$ and $\sigma'_{y,0}$ the initial electron values at the source, $Q1, Q2, Q3, dip1, dip2$ and $IMGchic$ corresponding to the different QUAPEVAs, dipoles and imager "chicane". From Equation 7.11 the found f_1 is:

$$\begin{aligned} f_1 = l_{Q2,Q3} + (l_{dip2,IMGchic} + l_{dip1,dip2})[1 + k_1 l_{Source,Q1} - k_2(1 + k_3 l_{Q2,Q3})(l_{Q1,Q2} + l_{Source,Q1} \\ + k_1 l_{Q1,Q2} l_{Source,Q1}) + k_3(l_{Q1,Q3} + l_{Q2,Q3} + l_{Source,Q1} k_1 l_{Q1,Q2} l_{Source,Q1} + k_1 l_{Q2,Q3} l_{Source,Q1})] \\ + l_{Q3,dip1} + k_3 l_{Q2,Q3} l_{Q3,dip1} + l_{Q1,Q2}(1 + k_3 l_{Q3,dip1} - k_2(l_{Q2,Q3} + l_{Q3,dip1} + k_3 l_{Q2,Q3} l_{Q3,dip1})) + \\ l_{Source,Q1}[1 + k_3 l_{Q3,dip1} - k_2(l_{Q2,Q3} + l_{Q3,dip1} + k_3 l_{Q2,Q3} l_{Q3,dip1}) + k_1(l_{Q1,Q2} + l_{Q2,Q3} \\ + l_{Q3,dip1} k_3 l_{Q1,Q3} l_{Q3,dip1} + k_3 l_{Q2,Q3} l_{Q3,dip1} - k_2 l_{Q1,Q2}(l_{Q2,Q3} + l_{Q3,dip1} + k_3 l_{Q2,Q3} l_{Q3,dip1}))] \end{aligned} \tag{7.14}$$

Using Equation 7.12 in Equation 7.13 gives:

$$\hat{\sigma}_{y,1} = (\sigma'_{y,0} + \sigma'_{y,0,pointing}) f_1 + \sigma_{y,0} f_2 = \sigma_{y,1} + \sigma'_{y,0,pointing} f_1 \tag{7.15}$$

with $\sigma_{y,1} = \sigma'_{y,0} f_1 + \sigma_{y,0} f_2$ the vertical size value at imager "chicane" in the case of a transport with $\sigma'_{y,0,total} = \sigma'_{y,0}$. Due to the used Equation 7.11, a precise evaluation of f_1 is preferred using the real COXINEL transport matrix. Thus, an initial constant pointing for all particles of a beam modifies the positions by a value that depends on the electron energy, lattices parameters and pointing. For the reference energy and close energies, one can consider this value constant for a given pointing, so, the changes of the size of the vertical slices containing mostly these energies are the same. In consequence, when one fits the vertical slices sizes at imager "chicane" the absolute value of the size is affected by the initial pointing but the divergence, i.e., the shape of the fit, remains unchanged.

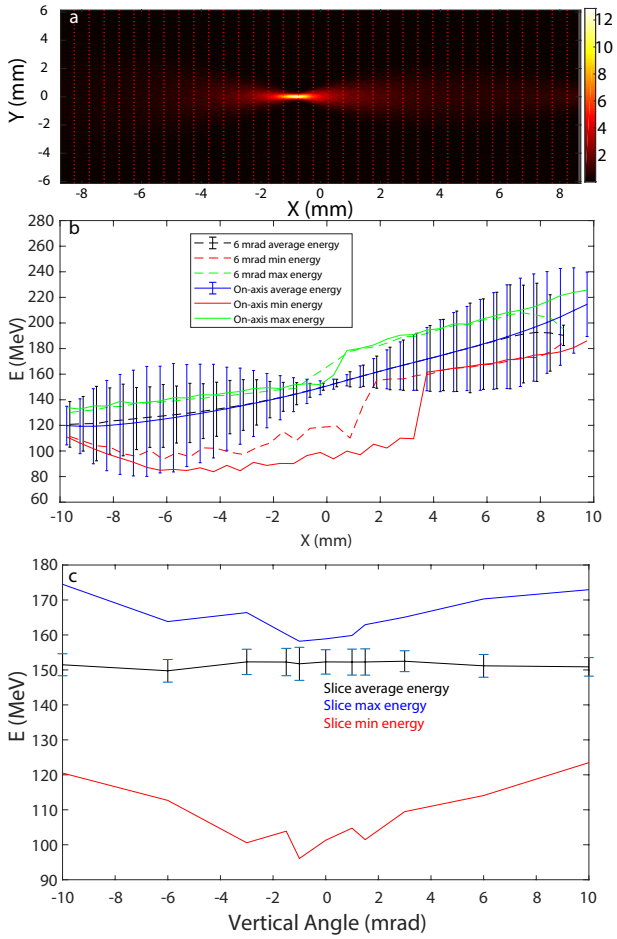

FIGURE 7.10: (a) Simulated image at imager "chicane" with the x axis slice divisions (red dotted line). (b) Maximum electron energy (blue), minimum energy (red) and electron energy mean square error (error bar) of ± 0.25 mm vertical slices for an (solid lines) on-axis and (dashed lines) 6 mrad initial vertical pointing beam. (c) Electron maximum (blue), minimum (red) energy and energy mean square error (error bar) of the ± 0.25 mm vertical slice at the mean energy 151 MeV. Simulation parameters: "slit-undulator" optics, $\sigma_{x,RMS} = 1.5$ mrad, $\sigma_{z,RMS} = 2.34$ mrad, $\epsilon_{RMS} = 0.2$ mm.mrad, initial beam of Figure 7.9a.

The consequences of a 6 mrad vertical pointing in the beam horizontal energy distribution is shown in Figure 7.10, where the image is divided in vertical slices of ±0.25 mm along the horizontal axis (Figure 7.10a). Figure 7.10b presents the calculations of the maximum, minimum and mean electron energy for each slice for the 6 mrad initial pointing and the on-axis case (Figure 7.4c). The pointing causes some electrons of high and low energies to disappear due to impinging the different elements of the transport line, thus, the aligned beam spans over a 80-225 MeV range with respect to 90-210 MeV for the 6 mrad initial pointing case. The quantity of electrons with energies below 151 MeV is specially affected by the rotation as can be seen when comparing the minimum energy curves (red dashed and solid lines in Figure 7.10b). The average electron energy per horizontal position remains fairly unchanged but the mean squared error (MSE) changes. The slice with lowest MSE changes from the 151 MeV slice (aligned case) to the 149 MeV one (6 mrad pointing case). Thus, the angle affects the energies involved in a spatial vertical slice, most importantly in the focused energy of interest. Figure 7.10c shows in more detail the change of the energies of the electrons inside the slice where the energy of interest is the average energy for multiple initial pointing angles. The vertical pointing makes higher energy electrons contribute more and lower energy electrons disappear. In a real measurement, the range of electron energies, inside a vertical slice of 1 pixel width is higher than it should be.

7.2.4.1 Pointing correction

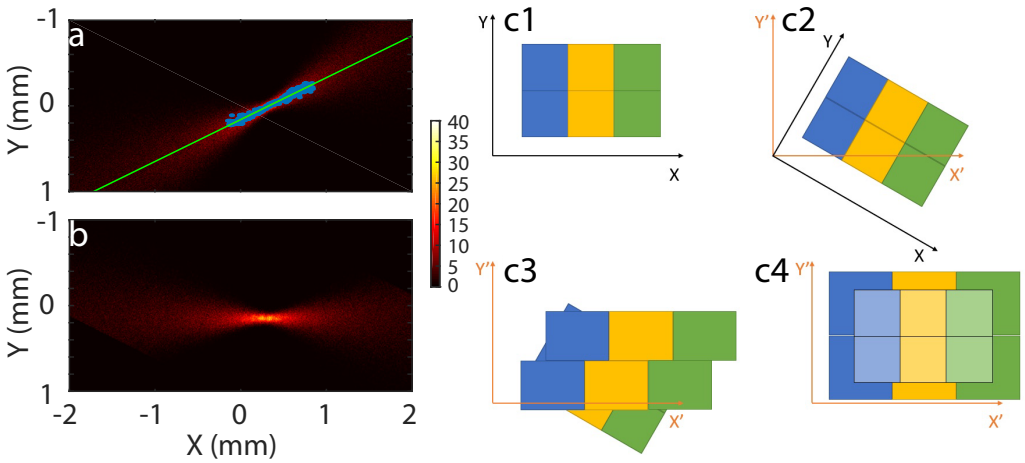

FIGURE 7.11: (a) Simulated transversal beam shape at imager "chicane" with vertical 1 grid-unit width slices most intense grid-unit (blue dot) and linear fit of the most intense grid-unit (green line). (b) Result after the rotation of the image by the angle created between the linear fit and the horizontal axis. Simulation parameters: "slit-undulator" optics, initial 3 mrad vertical pointing, $\sigma'_{x,RMS} = 1$ mrad, $\sigma'_{y,RMS} = 1$ mrad, $\epsilon_{RMS} = 1.0$ mm.mrad and energy distribution Figure 7.9a. (c1, c2, c3, c4) Steps to rotate the image at imager "chicane" to compensate initial beam pointing. 2 by 3 grid-units example. The different colors represent the grid-unit wide vertical slices.

To tackle the energy mixing and vertical slice size $\sigma_{y,butterfly}$ increase, the image can be rotated by the necessary angle to straighten the beam with respect to the horizontal axis as shown in Figure 7.11. First, the image is separated in vertical slices of 1 grid-unit width inside a certain horizontal aperture centered at the highest intensity zone of the beam, i.e., reference energy (see Figure 7.11a). At each vertical slice, the most intense grid-unit is located (Figure 7.11a blue dots). Secondly, the intense grid-units are used to do a linear fit (Figure 7.11a green line), and from it the angle of rotation is calculated (see Figure 7.11a). Then, the image and the vertical and horizontal axis are rotated by the angle calculated from the fit (see Figure 7.11b). The rotation process has some subtleties (Figure 7.11). The grid-units are initially well organized in the reference axis X and Y (Figure 7.11c1). Then the entire image is rotated with respect to the center of the image, and the center of each grid-unit is expressed in the new axis X' and Y' (Figure 7.11c2). However, in this new axis, the sides of the grid-units are not parallel to the new axis so, new grid-units of non equal side lengths are generated by interpolation (Figure 7.11c3). These new grid-units sides lengths are calculated to cover as best as possible the area of the previous grid-unit and their center is not necessarily aligned with the previous and next line/column of grid-units. Finally, new grid-units with their center aligned to the other lines and columns are generated by interpolation with sides length equal to the previous grid-unit longer side length (Figure 7.11c4). Thus, after the rotation process, the resolution of the image is proportionally reduced to the angle of rotation.

7.2.4.2 Effect of the pointing correction on the emittance

Case	Methods	$\sigma_{y,img2,151\pm0.5}$ (μm) $[\frac{\sigma_{y,chicane,151\pm0.5}}{\sigma_{y,s,151\pm0.5}}]$		$\sigma'_{y,chicane,151\pm0.5}$ $(mrad)$ $[\frac{\sigma'_{y,chicane,151\pm0.5}}{\sigma'_{y,s,151\pm0.5}}]$	
		None	Image rotation	None	Image rotation
Source		7.87 FWHM (3.37 RMS)	—	3.44 FWHM (1.46 RMS)	—
3 mrad	Gaussian fit (RMS)	3.61 [1.07]	3.29 [0.98]	1.47 [1.01]	1.20 [0.82]
6 mrad	Gaussian fit (RMS)	3.92 [1.16]	2.85 [0.85]	1.54 [1.05]	0.72 [0.49]

TABLE 7.4: Simulated transport to imager "chicane" vertical divergence $\sigma_{y,chicane}$ and size $\sigma'_{y,chicane}$ values with and without rotation treatement. Simulation parameters: "slit-undulator" optics, initial 6 mrad and 3 mrad vertical pointing (Figure 7.9b,c), $\sigma'_{x,RMS} = 1$ mrad, $\sigma'_{y,RMS} = 1$ mrad, $\epsilon_{RMS} = 1.0$ mm.mrad and energy distribution Figure 7.9a.

Table 7.4 presents the analysis of the simulated transverse distribution on imager "chicane" for the Gaussian fit method and the post-treatment "image rotation". The vertical beam size values $\sigma_{y,chicane}$ lose accuracy with the

increase of initial pointing. However, the vertical divergence is barely affected by the pointing. Applying the "image rotation" post-treatment improves the vertical size result but the enhancement is inversely proportional to the initial pointing value. For the vertical divergence the post-treatment significantly worsens the value. Therefore, for an initial pointing below 4 mrad the rotation post-treatment can improve the accuracy substantially, nevertheless, for higher values the correction becomes weaker. The vertical beam divergence $\sigma'_{y,chicane}$ directly measured before any post-treatment is barely affected by the initial pointing even in the case of 6 mrad. The image rotation only worsens the obtained $\sigma'_{y,chicane}$. The results are in agreement with Equation 7.15, thus, when pointing is present experimentally, a measurement with and without the "image rotation" post-treatment should be done to obtain the vertical size $\sigma_{y,chicane}$ and divergence $\sigma'_{y,chicane}$ respectively.

7.2.4.3 Pointing value deduction from imager "chicane"

As shown in Figure 7.9 and Equation 7.15, the pointing has a linear effect in the electrons position which allows for its measurement from the tilt present at imager "chicane" transversal beam shape. An initial vertical pointing can shift the imager "chicane" coordinates $(\sigma_{x,1}, \sigma_{y,1})$ of an electron to $(\sigma_{x,1}, \hat{\sigma_{y,1}})$ (Equation 7.15). Considering that the pointing does not affect $\sigma_{x,1}$, $f_1 = r_{34}$ for the exact transport matrix calculation, the value of $\sigma_{x,1}$ is of the same order of $\sigma_{y,0,pointing}$, the angle between the on-axis position and the one with pointing with respect to the origin $(0,0)$ can be simplified as:

$$\theta_{angle,chicane} = arctan(\frac{\hat{\sigma}_{y,1} - \sigma_{y,1}}{\sigma_{x,1}}) = arctan(\frac{\sigma'_{y,0,pointing} f_1}{\sigma_{x,1}}) \approx \sigma'_{y,0,pointing} \frac{f_1}{\sigma_{x,1}} + o(x^2) \tag{7.16}$$

e.g., for an electron in the horizontal position $\sigma_{x,1} = f_1 = 4.3\ mm$, the initial pointing is approximately the angle between the beam transversal center, the electron position and its projection on the horizontal axis.

Through calculation of the exact transport from the source to the imager "chicane", for the "chicane" and "slit-undulator" optics transport matrix parameters, the relation between initial source pointing and the beam rotation angle at imager "chicane" can be found (Figure 7.12):

$$Angle = Pointing * a - b \tag{7.17}$$

with $a = 0.1234$ and $b = 0.0053$.

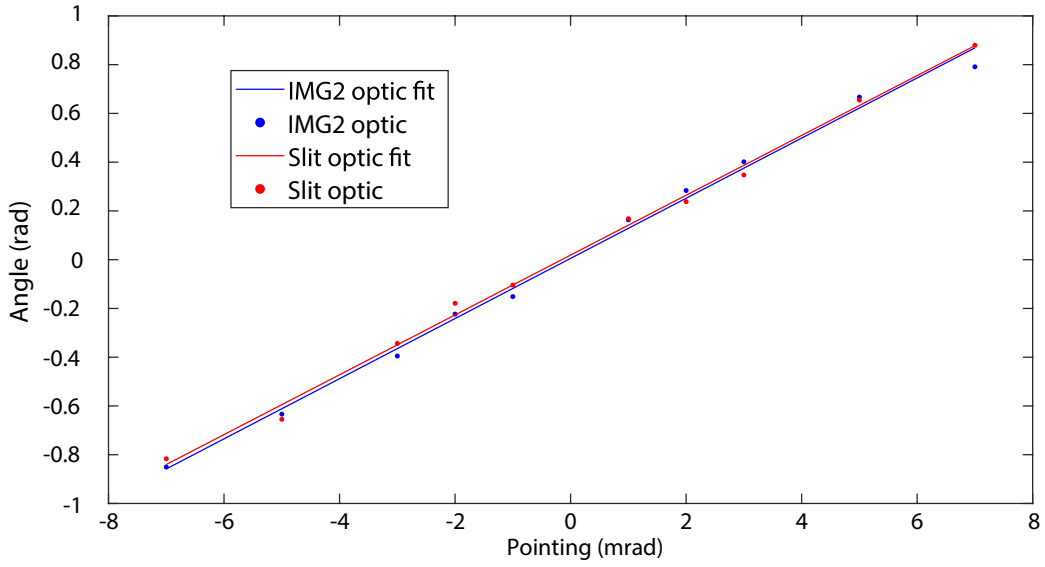

FIGURE 7.12: Relation between angle of the beam at imager "chicane" and initial vertical pointing for "chicane" optics and "slit-undulator". The fit used is $Angle = Pointing * a - b$ with $a = 0.1234$ and $b = 0.0053$.

7.2.5 Measurement of emittance and beam pointing

During RUN 7 a significant amount of data was taken in imager "chicane" with the different camera lenses setups to find their limits and an accurate value of the emittance in the COXINEL transport line. For the vertical slice size measurement at imager "chicane", the Gaussian fit method has been used.

7.2.5.1 Image treatment

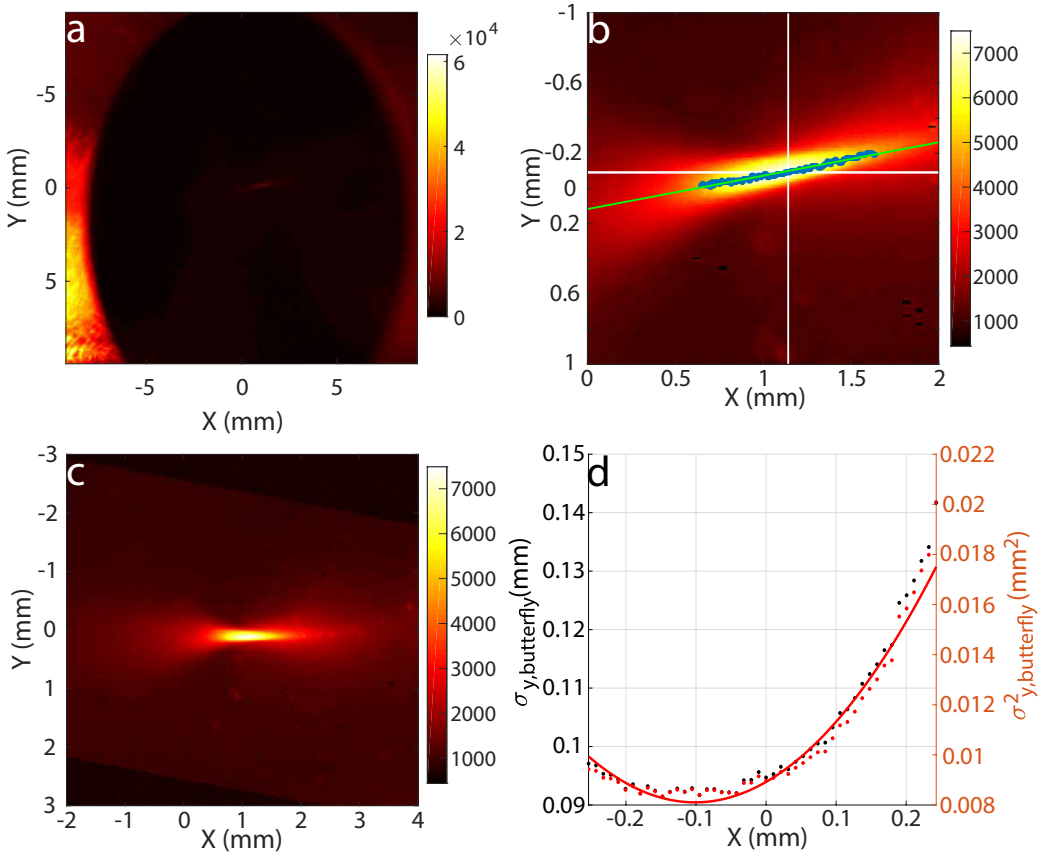

FIGURE 7.13: (a) Original image, (b) image after "mediafilter" and hotspot cleaning treatment and angle measurement by fitting vertical slices maxima position, (c) image rotated and (d) vertical slices vertical size $\sigma_{y,butterfly}$ and its square $\sigma^2_{y,butterfly}$. Sigma Macro lens used.

Figure 7.13 presents the treatment applied to experimental results. The image from the camera output in Figure 7.13a, is zoomed where the beam impinges, a media filter is applied to clean hotspots, a code identifies remaining hotspots and reduce them to sorrounding signal levels (Figure 7.13b). The maximum intensity points are found by a vertical pixel slice sweep. Then, by fitting these points, the beam angle with respect to the horizontal axis is found. For the image rotation post-treatment, an artificial rotation of the beam angle (Figure 7.13c) is applied to horizontally straighten (see Figure 7.11, Table 7.4). The $\sigma_{y,butterfly}$ of each pixel width vertical slice is calculated with the previously explained Gaussian fit methods. The squared vertical slice size $\sigma^2_{y,butterfly}$ versus position data is fitted with a polynomial of second order as in Equation 7.10 (Figure 7.13d).

7.2.5.2 Measurements

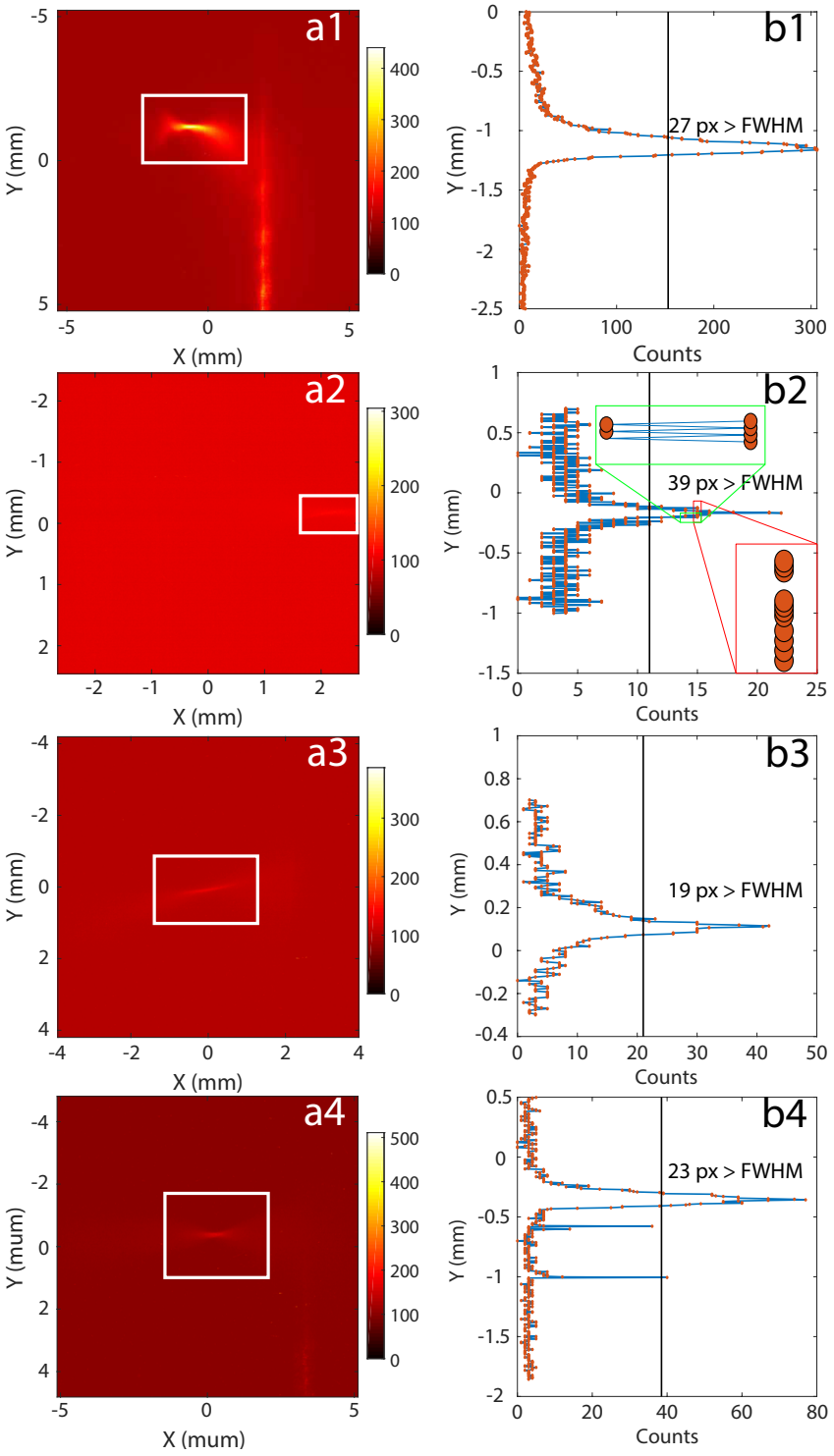

FIGURE 7.14: (a) Measured transverse shape at Imager "chicane" and (b) 1 pixel width vertical slice going through the beam center projection after background treatment taken during RUN 7 with the (a1, b1) Trioptic S1 (5.2 x 5.1 $\mu m/px$) shot 17 from the set 2020/09/02 14:50:53, (a2, b2) Navitar S1 (2.6 x 2.4 $\mu m/px$; $S/N = 1.25$) shot 7 from the set 2020/09/02 17:49:39, (a3, b3) Navitar S3 (3.8 x 4.1 $\mu m/px$; $S/N = 1.25$) shot 4 from the set 2020/09/04 16:14:56, (a4, b4) Trioptic S3 (5 x 4.7 $\mu m/px$; $S/N = 2.47$) shot 1 from the set 200/09/11 15:17:29.

Following the simulation results, the experimental beam transverse distribution data on imager "chicane" is treated for an horizontal aperture of 0.5 mm. During RUN 7, the three different lenses and different configurations (see Table D.2) were used.

Figure 7.14a1, b1 presents an example of 1 pixel width vertical line projection for a shot with the Trioptic S1 lens. At the center of the beam, after background treatment there are 27 pixels with an intensity over the FWHM (Table 7.5). No signal or resolution limitation can be observed in this configuration. For the Navitar S1 lens (Figure 7.14a2, b2) the peak of the signal is more than 10 times lower the Trioptic S1 one (Table 7.5) and only 18 counts over the noise. The lens high resolution yields approximately 1.5 times more pixels of intensity above FWHM however, two limitations related to resolution and signal-to-noise ratio can be clearly observed. Clusters of pixels with the same counts are observed frequently, of up to 8 consecutive pixels (Figure 7.14b2 red insert). Consecutive pixel counts oscillation can be seen and are more frequent the further one gets from the intensity peak (Figure 7.14b2 green insert), due to the low signal to noise ratio. Neglecting the redundant pixels, the ones above FWHM intensity are only around half the Trioptic S1 case (Table 7.5). The Navitar S3 (Figure 7.14a3, b3) presents less intensity oscillation due to its lower resolution than the Navitar S1. However, there are still numerous the clusters of consecutive pixels with equal value. The number of non redundant pixels of intensity aboive FWHL is even smaller than the Navitar S1 case. The Trioptic S3 (Figure 7.14a4, b4) exhibits a peak intensity 4 times lower than the Trioptic S1 and 15 % less pixels above FWHM intensity (Table 7.5). Multiple clusters of consecutive pixels with same intensity appear making the number of non-redundant pixels similar to the Navitar S1 but with much more intensity over the noise. While the Navitar offers the highest resolution, the lack of signal makes the number of useful pixels over FWHM lower than the Trioptics due to oversampling. Therefore, an accurate initial slice vertical size measurement is difficult to obtain. The Trioptics offer a good resolution-signal performance for measurements and no limitations are observed.

Objective	Config	px calibration	S/N	Peak Counts	$px > FWHMcounts$	Non-redundant px	dates (2020)	Shots	$\sigma_{y,butterfly}$ mm	
									Mean	Std
Sigma	S1	8.5 x 9.2 $\mu m/px$	21.69	-	-	-	Start of RUN 7 - 9/02 14:17:02	36	0.25	0.07
Trioptic	S1	5.2 x 5.1 $\mu m/px$	6.23	300	27	27	9/02 14:18:09 - 9/02 14:50:53	18	0.20	0.05
	S2	5 x 4.6 $\mu m/px$	6.26	-	-	-	9/02 15:29:34 - 9/02 15:18:31	2	0.14	0.001
Navitar	S1	2.6 x 2.4 $\mu m/px$	1.25	22	39	17	9/02 16:06:25 - 9/02 17:09:54	9	0.07	0.05
	S2	2.6 x 2.4 $\mu m/px$	1.22	-	-	-	9/02 17:24:44 - 9/02 17:49:39	122	0.11	0.04
	S3	3.8 x 4.1 $\mu m/px$	1.25	45	19	10	9/03 14:19:42 - 9/04 16:24:19	52	0.14	0.08
Trioptic	S3	5 x 4.7 $\mu m/px$	2.47	78	23	16	9/10 15:53:53 - End of RUN 7	269	0.13	0.06

TABLE 7.5: Macro lenses and configurations used during RUN 7 (Table D.2) with their respective number of shots analyzed and FWHM $\sigma_{y,butterfly}$ mean and std.

Figure 7.15a and Table 7.5 shows the minimum vertical slice size $\sigma_{y,butterfly}fit$. The vertical pixel sizes observed with the Trioptics S1 and S2 are close to half the Sigma Macro lens pixel size. The resolution change is reflected in the minimum vertical slice size $\sigma_{y,butterfly}$ (Table 7.5). Two shots having only been recorded for the second configuration, std is low (Table 7.5) The Navitar S1 and S2 present a difference in average minimum vertical slice size $\sigma_{y,butterfly}$ of 0.04 mm (Table 7.5) caused by the difference in quantity of data (Table 7.5). The less zoomed Navitar S3 sees an increase of the average minimum slice size $\sigma_{y,butterfly}$ of 0.03 mm over the second Navitar configurations (Table 7.5). The small change of minimum average vertical slice size $\sigma_{y,butterfly}$ between the Navitar S1 and S3 (0.03 mm, Table 7.5) suggests that there is no resolution limitation. The last lens used was the Trioptic in its third configuration (5 x 4.7 $\mu m/px$; $S/N = 2.47$). Minimum sizes of ≈ 80 μm (e.g. 2020/09/10) have been measured with the Trioptics S3. Based on the results of the Trioptic S2 and Figure 7.14, all Trioptic cases offer a good performance and the higher resolution of the Navitar does not show better results than the Trioptic.

Figure 7.15b presents the pointing measured at imager "chicane". The pointing stability varies day-by-day, and in average the pointing is -0.79 mrad. The beam pointing is found to be able to jump by several mrad from shot to shot, with in some instances jumping by 5 mrad. The rotation post-treatment should improve the vertical size measurement for most shots.

Figure 7.15c shows the source beam vertical size $\sigma_{y,chicane}$ measured at imager "chicane" with the Gaussian fit method, the image rotation post-treatment (Table D.2). For the Sigma Macro lens (Figure 7.15 zone 1), the decrease of vertical size $\sigma_{y,chicane}$ of 5 % due to the image rotation is in agreement with the simulations (Table 7.4). the Trioptic S1 (S2) configuration (Figure 7.15c zones 2 and 3) present an average beam vertical size a $\approx$ 28% ($\approx$ 49%) lower compared to the Sigma Macro lens. The change in value is significant enough to relate it to the lens and not to laser variations. The Navitar configurations (Figure 7.15c zones 4, 5 and 6) low signal-to-noise ratio supposes a limitation that affects the vertical size measurement accuracy and makes the post-treatment impossible. For the Trioptic S3 (Figure 7.15c zone 7) the rotation post-treatment rises the slice vertical size $\sigma_{y,chicane}$ due to its low efficiency, however, as the pointing during the shots was under 3.5 mrad (Figure 7.15b), the value before post-rotation should be within 5 % of the real value.

The ratio between the vertical beam size results without and with image rotation post-treatment are shown in Table 7.6. The high signal-to-noise ratio configurations; Sigma Macro, Trioptic S1 and S2 show results close to the simulations. The low signal to noise ratio configurations, i.e., Navitar and Trioptic S3, show an

important increase in the beam vertical size after image rotation. The Trioptic S3 configuration presents a 20 % increase after rotation. There is a strong correlation between the signal-to-noise ratio and the effectiveness of the image rotation post treatment (Chapter D.3). The Navitar configurations and Trioptic S3 are limited in this respect. Therefore, only the Trioptics S1 and S2 configurations should be considered as proper measurements not hampered by any limitation. The obtained values with the Trioptic S3 before the rotation post-treatment should be some percent less accurate due to the pointing below 3.5 mrad thus, the vertical divergence and the vertical size before post-treatment can be considered correct .

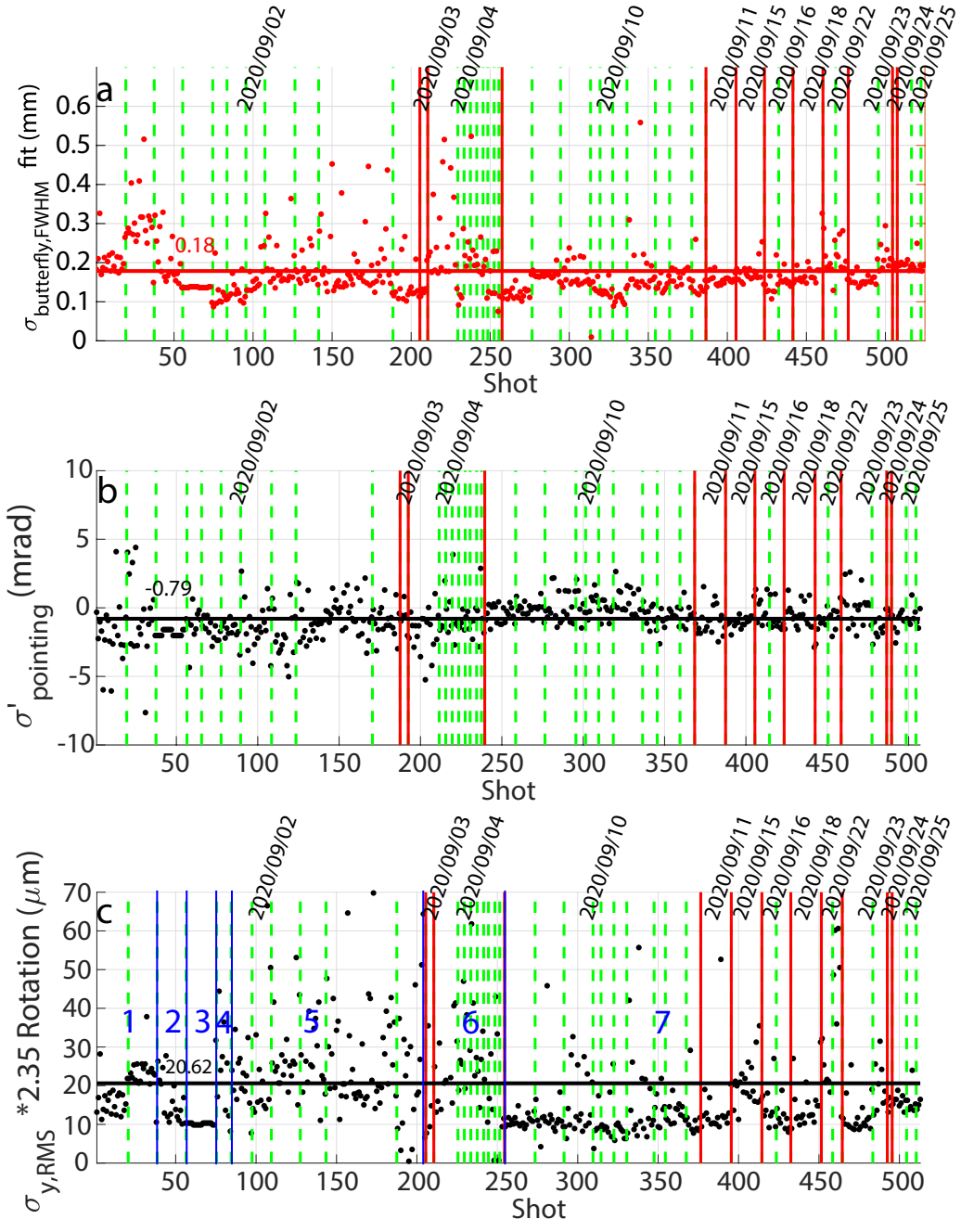

FIGURE 7.15: (a) Minimum FWHM vertical slice size after fit (Equation 7.10) $\sigma_{y,butterfly}fit$, measured at imager "chicane". All shots of RUN7. (b) Vertical beam pointing and average value (black) calculated via fit (Figure 7.12) from imager "chicane" measurements. All shots of RUN7. (c) Vertical size FWHM with Image rotation post-treatment and the Gaussian fit method, measured at imager 2 chronologically sorted and separated by series (green line), days (red line) and lens (blue line). All shots of the second part of RUN7 with an analysis horizontal aperture of 0.5 mm. The lens configurations used are (1) Sigma Macro lens (8.5 x 9.2 $\mu m/px$; $S/N = 21.69$), (2) Trioptic S1 (5.2 x 5.1 $\mu m/px$; $S/N = 6.23$), (3) Trioptic S2 (5 x 4.6 $\mu m/px$; $S/N = 6.26$), (4) Navitar S1 (2.6 x 2.4 $\mu m/px$; $S/N = 1.25$), (5) Navitar S2 (2.6 x 2.4 $\mu m/px$; $S/N = 1.22$), (6) Navitar S3 (3.8 x 4.1 $\mu m/px$; $S/N = 1.25$) and (7) Trioptic S3 (3.8 x 4.1 $\mu m/px$; $S/N = 1.25$)

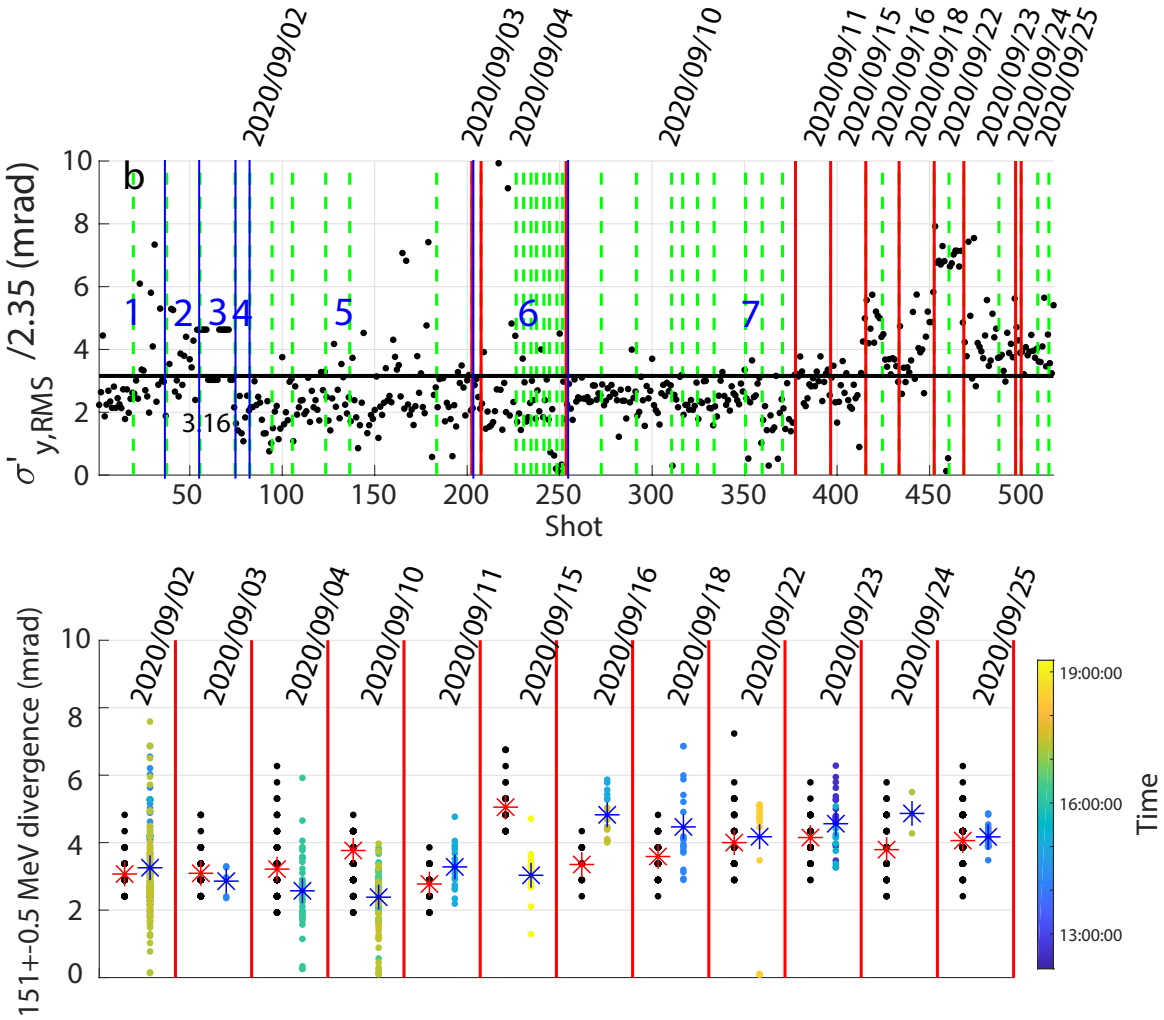

FIGURE 7.16: (a) FWHM vertical divergence using the Gaussian fit method, measured at imager "chicane" chronologically sorted and separated by series (green line), days (red line) and lens (blue line). All shots of RUN7 with an analysis horizontal aperture of 0.5 mm. Lens configurations: (1) Sigma Macro lens (8.5 x 9.2 μm; $S/N = 21.69$), (2) Trioptic S1 (5.2 x 5.1 μm; $S/N = 6.23$), (3) Trioptic S2 (5 x 4.6 μm; $S/N = 6.26$), (4) Navitar S1 (2.6 x 2.4 μm; $S/N = 1.25$), (5) Navitar S2 (2.6 x 2.4 μm; $S/N = 1.22$), (6) Navitar S3 (3.8 x 4.1 μm; $S/N = 1.25$) and (7) Trioptic S3 (3.8 x 4.1 μm; $S/N = 1.25$). (b) Vertical (circle) single shot and day average (star) divergence FWHM (black) measured at the spectrometer and (colored by time of the day) at imager "chicane" with the Gaussian method organized by day. All shots of RUN7 with an analysis horizontal aperture of 0.5 mm.

Figure 7.16a shows the vertical beam divergence $\sigma'_{y,chicane}$ measured at imager "chicane" with the Gaussian fit method without the image rotation post-treatment. The vertical beam divergence $\sigma'_{y,chicane}$ measurements are not affected by the change of lenses (Table 7.6). Figure 7.16b presents the comparison of the vertical divergence measured at imager "chicane" and at the electron spectrometer. The day averages between both diagnosis are similar with around a 0.25 mrad difference for most days. During the 2020/09/10, 2020/09/15 and 2020/09/16 both diagnostics differ by 1.4 mrad, 2 mrad and 1.4 mrad respectively, which is probably caused by the time difference and the number of shots done between measurements. The vertical beam divergence $\sigma'_{y,chicane}$ measured are inside the range of values observed from the spectrometer (Section 4.3.2). Table 7.6 shows the average emittance $\epsilon_{y,chicane,RMS}$ for each lens and configuration.

The measured average value of the RUN 7 RMS emittance is of 3.2 mm.mrad (2.8 mm.mrad with Trioptic S3 data) with an std of 1.5 mm.mrad (1.2 mm.mrad), approximately 3 times higher than the COXINEL baseline parameters.

Objective (Figure 7.15c, 7.16a zone)	px to μm calibration	S/N	Limitation	Post-treatment (Shots)	$\sigma'_{y,chicane}$ mrad mean	std	$\sigma_{y,chicane}$ μm mean	std	$\frac{\sigma_{y,chicane}}{\sigma_{y,chicane,Rotated}}$	ϵ_y mm.mrad $FWHM/2.35^2$
Sigma (1)	8.5 x 9.2 $\mu m/px$	21.69	Resolution limited	None (36)	3.01	1.27	20.81	8.53		-
				Rotation (37)			19.79	5.59	1.05	-
Trioptic (2)	5.2 x 5.1 $\mu m/px$	6.23		None (18)	4.88	4.08	18.16	11.69		4.74
				Rotation (18)			16.27	5.76	1.12	4.25
Trioptic (3)	5 x 4.6 $\mu m/px$	6.26		None (2)	3.96	0.81	10.48	0.12		2.22
				Rotation (2)			10.14	0.24	1.03	2.15
Navitar (4)	2.6 x 2.4 $\mu m/px$	1.25	S/N limited	None (8)	1.81	0.54	9.14	1.91		-
				Rotation (9)			25.88	10.65	0.35	-
Navitar (5)	2.6 x 2.4 $\mu m/px$	1.22	S/N limited	None (120)	2.96	3.37	14.34	7.26		-
				Rotation (121)			26.33	13.75	0.55	-
Navitar (6)	3.8 x 4.1 $\mu m/px$	1.25	S/N limited	None (51)	2.54	1.75	14.68	8.69		-
				Rotation (49)			38.41	39.04	0.38	-
Trioptic (7)	5 x 4.7 $\mu m/px$	2.47	S/N limited	None (265)	3.25	1.41	12.32	4.71		2.14
			for rotation	Rotation (260)			15.61	10.77	0.79	-

TABLE 7.6: Measured initial average and std FWHM vertical divergence, size and emittace at imager "chicane" with and without image rotation post-treatment and using Gaussian fit method for each lens (Table D.2) during RUN 7. (red) Limited configurations (green) not limited ones.

7.3 Total electron beam charge measured via imagers "UndIn" and "UndOut"

Imager "UndIn", before the undulator (Figure 7.1) checks the electron beam focusing and position that enters the undulator (Sections 3.1.2.1.2.1, 6.4). Imager "UndOut" is used to monitor the electron beam after the undulator. No charge loss occurs between imager "UndOut" and ICT2 thanks to their proximity (17 cm) (Section 6.1.1), which permits the imager calibration. The monitoring of the electron beam with the imager located around the undulator is required. In this section imager "UndOut" data is analyzed.

7.3.1 Measured data treatment and calibrations

Due to the intrinsic camera noise, plasma radiation and possible reflections arriving to the imager, the raw image is treated to better isolate the electron beam signal from the rest. After treatment, imager "UndOut" total counts are calibrated to pC by correlating them to the measured charge at ICT2.

7.3.1.1 Modeled beam on Imager "UndOut"

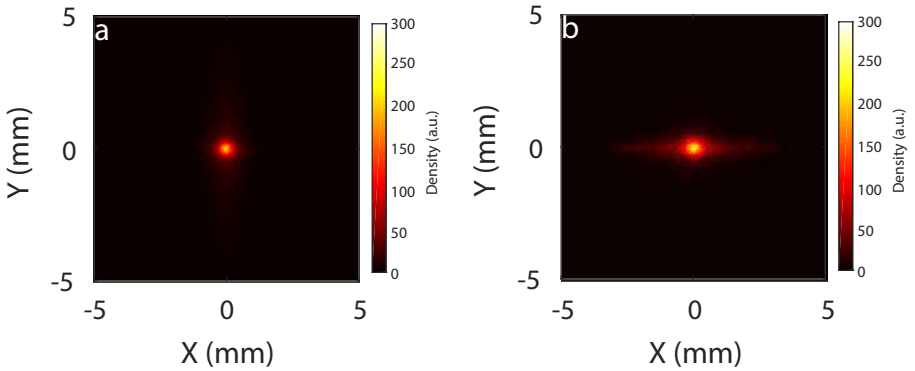

FIGURE 7.17: Simulated beam transverse shape at imager "UndOut" for the (a) "supermatching" and (b) "slit-undulator" optics. Experimental like beam (Figure 4.8c), with ϵ_{RMS} =1 mm.mrad, $\sigma'_{y,RMS,i} = 2$ mrad and $\sigma'_{x,RMS,i} = 2$ mrad

For all COXINEL optics (Section 3.1.2.1), the transverse beam size after the undulator increases. As the imager "UndOut" is 96 cm away to the undulator exit, the envelope expansion does not completely defocus the beam. In imager "UndOut", the transport with a flat-top beam of 5 % energy spread in the "supermatching" optics exhibits a cross shape while the "slit-undulator" presents a vertically focused beam with faint horizontal trails (Section 3.1.2.1). For a experimental like beam (Table 6.1) the "supermatching" optics case (Figure 7.17a) shows a round spot with a faint cross with uneven horizontal and vertical branches. $\approx$ 22 % of the total beam

charge arrives at imager "UndOut" while the reference energy slice is conserved along the entire line (Figure 6.5, Section 6.1.1). In the "slit-undulator" optics case, the transverse beam shape (Figure 7.24b) coincides with the one observed in the flat-top case (Section 3.1.2.1), i.e., vertically focused with faint horizontal trails. The total charge arriving after the undulator is ≈ 20 % (Figure 6.5, Section 6.1.1) of the initial one.

7.3.1.1.1 Raw data treatment

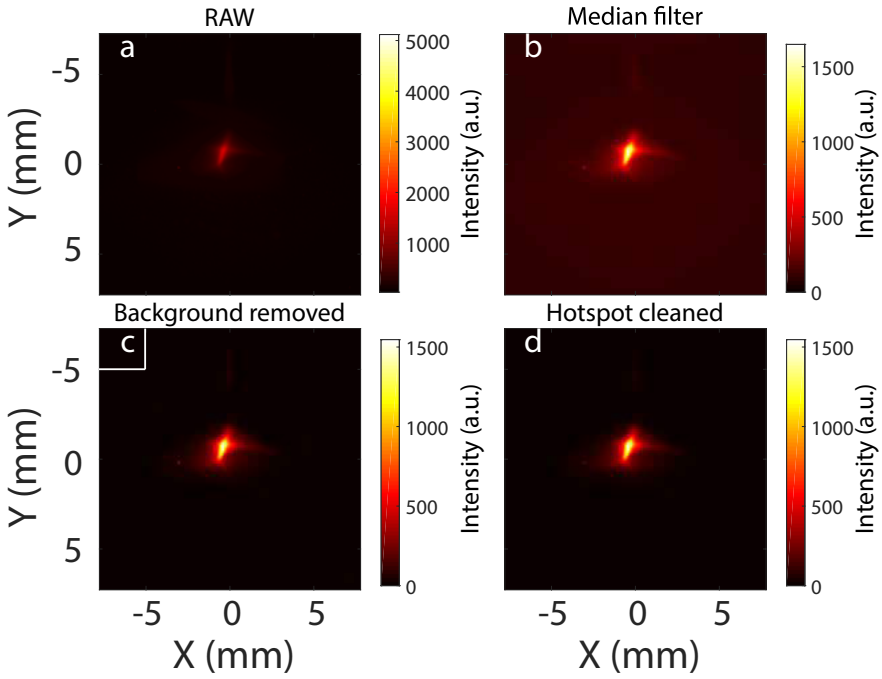

FIGURE 7.18: Measured transverse beam shape at the imager "UndOut" (a) raw data, (b) after a median filter, (c) background removal and (d) hotspot cleaning. Shot done the 2020/09/23 at RUN 7.

Figure 7.18 presents the post-treatment applied to the measurements of imager "UndOut". First, the vertical and horizontal axis are converted from pixel to mm (Figure 7.18a). Second, a median filter is applied to the image (Figure 7.18b). Then, from an area without beam of 300×300 pixels (Figure 7.18c white square) an average background count is deduced and subtracted to all pixels (Figure 7.18c). Finally, the hotspots are identified and reduced to its surrounding pixel counts (Figure 7.18d).

7.3.1.1.2 Calibration

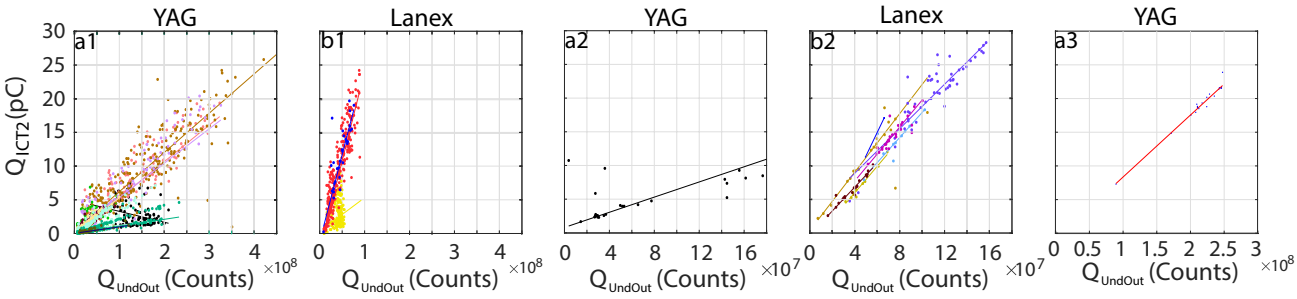

FIGURE 7.19: Charge measured after the undulator at the ICT2 versus imager "UndOut" total counts after image treatment and (line) linear fits for count/pC calibration with the (a) YAG and (b) Lanex screens. Run (a1, b1) 4, (a2, b2) 6 and (a3) 7 data each color representing a day. RUN 4 (a1, b1): 2017/11/21 (YAG black, Lanex yellow), 2017/11/22 (YAG pink, Lanex red), 2017/11/23 (YAG brown, Lanex blue), 2017/11/24 (YAG green), 2017/11/27 (YAG purple), 2017/11/28 (YAG yellow), 2017/11/29 (YAG crimson), 2017/11/30 (YAG light green), 2017/12/01 (YAG emerald), 2017/12/02 (YAG dark brown). RUN 6 (a2, b2): 2019/02/01 (Lanex blue), 2019/02/06 (YAG black, Lanex brown), 2019/02/07 (Lanex purple), 2019/02/11 (Lanex light brown), 2019/02/12 (Lanex cyan), 2019/02/13 (Lanex pink), 2019/02/14 (Lanex crimson). RUN 7 (a3): 2020/09/23.

After the measurement post-treatment, the beam charge is calibrated using ICT2 data. The charge data of ICT2 versus the imager "UndOut" counts in Figure 7.19 show a linear correlation between them therefore, the calibration can be achieved by doing a linear fit:

$$Q_{ICT2}[pC] = Q_{img}[counts] \times p_1 + p_2 \tag{7.18}$$

with p_1 and p_2 the linear fit terms and Q_{img} the total number of counts and Q_{ICT2} the charge in pC at ICT2. Each day the fit parameters p_1 and p_2 vary because of the slight LPA conditions. LPA changes can cause variations on the background and thus on the number of counts measured at the imager for the same total beam charge. The linear fit shows a non-zero p_2 parameter caused by the inability to perform a perfect background cleaning. The two screens of imager "UndOut" (Lanex, YAG), that offer different quantum efficiency, are calibrated.

During RUN 4, most shots show high divergences (above 5 mrad) and low charges at the spectrometer (Section 4.1.2.1). Therefore, one can expect a big loss of charge along the line and a highly transversal dispersed beam making difficult the measurement at imager "UndOut". Figure 7.19a1, b1 and Table 7.7 present the calibrations of each day and screen of RUN 4. 356 shots have been taken with the gas cell (2017/11/21) at imager "UndOut" however, clouds of data are present (Figure 7.19a1 black dots and Figure 7.19b1 yellow dots) that prevent a proper calibration. For the gas jet (after 2017/11/21) YAG data, the fit parameter p_1 varies from 10^{-8} to 5.8×10^{-8} from day to day. The difference in photon efficiency between the YAG and Lanex screens is noticeable, i.e., an order of magnitude. Figure 7.19a2,b2 and Table 7.7 present the linear fit calibrations of imager "UndOut" via the ICT2 of each day of RUN 6. The fit values are of the same order of magnitude that the ones of RUN 4. The difference between the Lanex and YAG screen is around one order of magnitude. During RUN 7 only the YAG screen was used for the measurements at imager "UndOut". The fit parameter p_1 during RUN 7 (Figure 7.19a3, Table 7.7) is 1.64 times higher than the RUN 6 or 4 higher ones, probably due to the change in background radiation caused by the increase in laser power.

RUN 4				RUN 6				RUN 7			
Screen	Day	Fit parameters		Screen	Day	Fit parameters		Screen	Day	Fit parameters	
		p_1	p_2			p_1	p_2			p_1	p_2
		(pC/counts)	(pC)			(pC/counts)	(pC)			(pC/counts)	(pC)
Lanex	2017/11/21	4.98×10^{-8}	0.48	Lanex	2019/02/01	3.47^{-7}	-5.92	YAG	2020/09/23	9.19^{-8}	-0.84
	2017/11/22	2.65×10^{-7}	-2.44		2019/02/06	2.17^{-7}	0.37				
	2017/11/23	2.57×10^{-7}	-1.18		2019/02/07	1.65^{-7}	2.31				
					2019/02/11	1.96^{-7}	-1.87				
					2019/02/12	1.86^{-7}	-0.70				
					2019/02/13	2.00^{-7}	-0.29				
					2019/02/14	1.77^{-7}	-0.27				
				YAG	2019/02/06	5.63^{-8}	0.80				
YAG	2017/11/21	-1.61×10^{-8}	4.9								
	2017/11/22	5.42×10^{-8}	-0.17								
	2017/11/23	5.81×10^{-8}	0.45								
	2017/11/24	4.31×10^{-8}	0.50								
	2017/11/27	5.09×10^{-8}	0.24								
	2017/11/28	4.43×10^{-8}	0.43								
	2017/11/29	5.09×10^{-8}	0.20								
	2017/11/30	7.69×10^{-9}	0.45								
	2017/12/01	1.02×10^{-8}	0.1								
	2017/12/02	9.50×10^{-9}	0.03								

TABLE 7.7: Calibration fit (Equation 7.18) parameters of imager "UndOut" with ICT2 for the different RUNs.

7.3.2 Evolution of the electron beam transverse profile

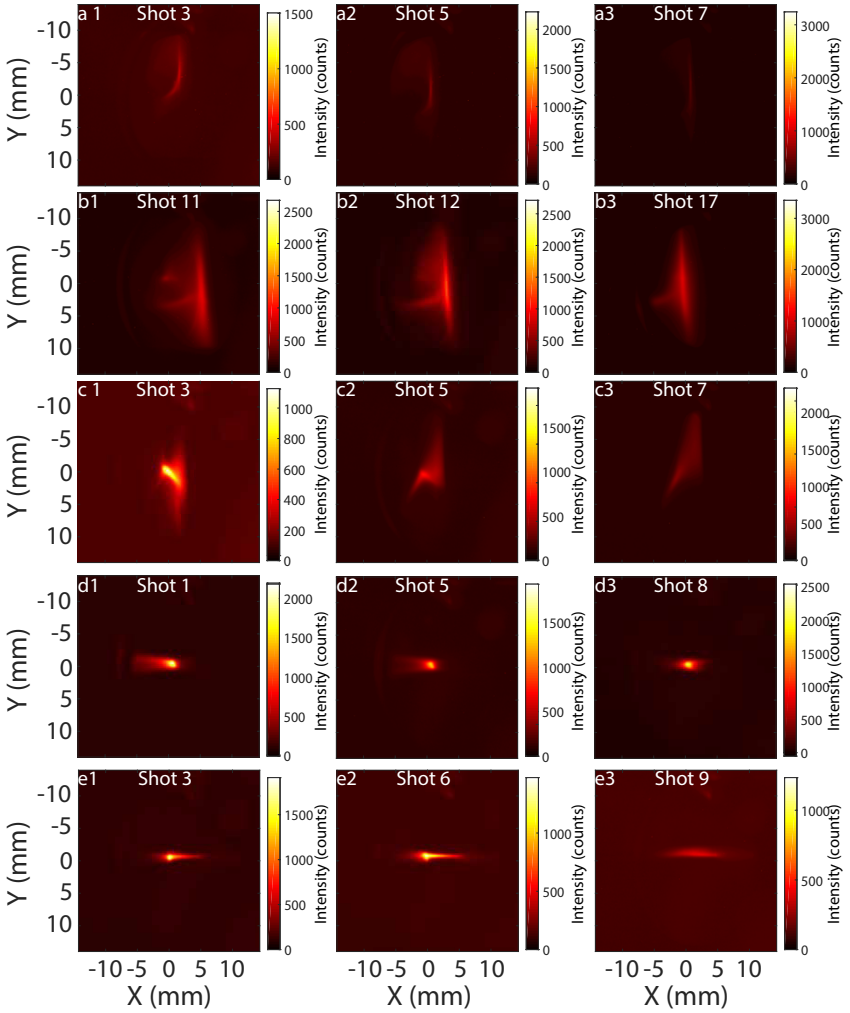

FIGURE 7.20: Examples of measurements at imager "UndOut" from the series taken the (a1, a2, a3) 2017/11/21-19:58:12, (b1, b2, b3) 2017/11/21-19:28:12, (c1, c2, c3) 2017/11/27-16:04:26, (d1, d2, d3) 2017/11/28-18:20:28 and (e1, e2, e3) 2017/12/01-18:17:10 with the "D_{dump}" (a, b) optics, "slit-undulator" optics (c), "undulator-exit" (d, e) and the gas cell (a, b) and jet (c, d, e) target during RUN 4.

Figure 7.20 shows some shots at imager "UndOut" with the gas cell (2017/11/06 - 2017/11/21) belonging to its "best" sets and jet (2017/11/21 - 2017/12/02) target of RUN 4. The beam signal is of $\approx$ 300 counts and the beam is not stable. In the 2017/11/21-19:58:12 set, the beam shape is a not well focused and exhibits a bent vertical line (Figure 7.20a1, a2, a3). The 2017/11/21-19:28:12 shape is close to a not well focused cross (Figure 7.20b1, b2, b3) with in occasions an extra round beam on top of the horizontal line (Figure 7.20b1). In the series 2017/11/ 27-16:04:26 (Figure 7.20c1, c2, c3) taken with the "undulator-exit" optics, the beam is focused in a elongated spot however, a vertical faint line (to the right of the spot) can be differentiated. The elongated spot changes its angle with respect to the horizontal axis shot-to-shot. Even though the beam is not well focused, the intensity can achieve $\approx$ 700 counts, i.e., above twice the gas cell one. The series 2017/11/28-18:20:28 (Figure 7.20d1, d2, d3) taken with the "slit-undulator" optics presents a well focused spot with horizontal wings as seen in simulation (Figure 7.24a1). The beam achieves maximum intensities of above 2000 counts. The series 2017/12/01-18:17:10 (Figure 7.20e1, e2, e3) taken with the "slit-undulator" optics shows a more irregular focused spot with horizontal wings. In occasions the beam defocuses causing a long horizontal line with low counts per pixel. When the beam is well focused the max counts/pixel are above 1500 counts/pixel while when the beam defocuses it decreases to around 500 counts/pixel.

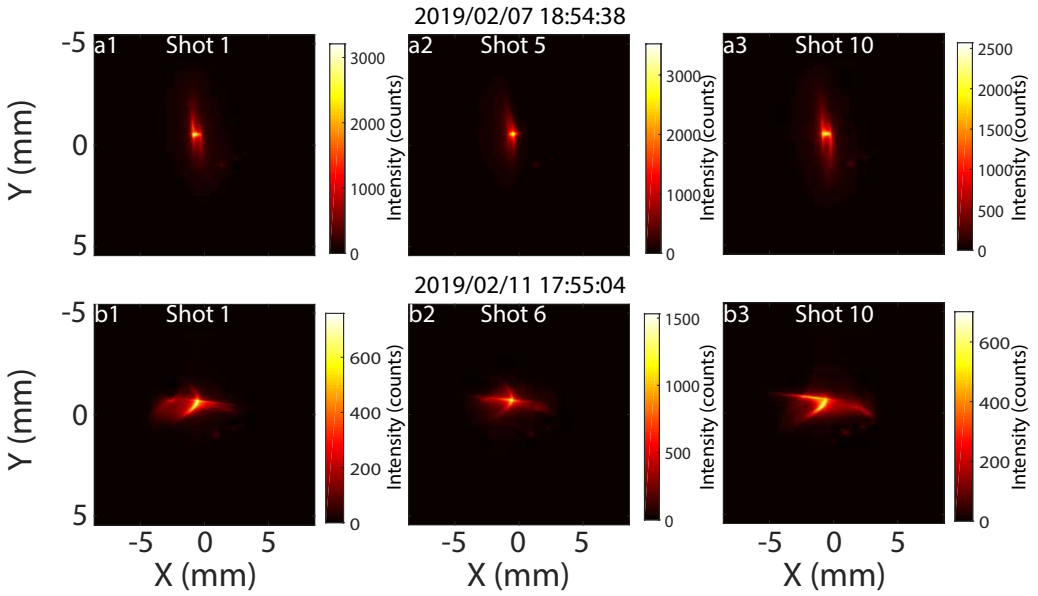

FIGURE 7.21: Examples of measurements at imager "UndOut" from the series taken the (a1, a2, a3) 2019/02/07-18:54:38 and (b1, b2, b3) 2019/02/11-17:55:04 with the "slit-undulator" and "supermatching" optics respectively during RUN 6.

In RUN 6, the set taken the 2019/02/07-18:54:38 with the "slit-undulator" optics at the imager "UndOut" exhibits focused round spot in all shots with a maximum intensity of around 2500 counts and two vertical faint lines on both sides that could be caused by lower or higher energies with a different initial transverse position to the main electron beam. The set 2019/02/11-17:55:04 taken with the "supermatching" optics in Figure 7.21b has a bent cross shape (Figure 3.16) due to initial beam pointing. The maximum intensity is of around 800 counts.

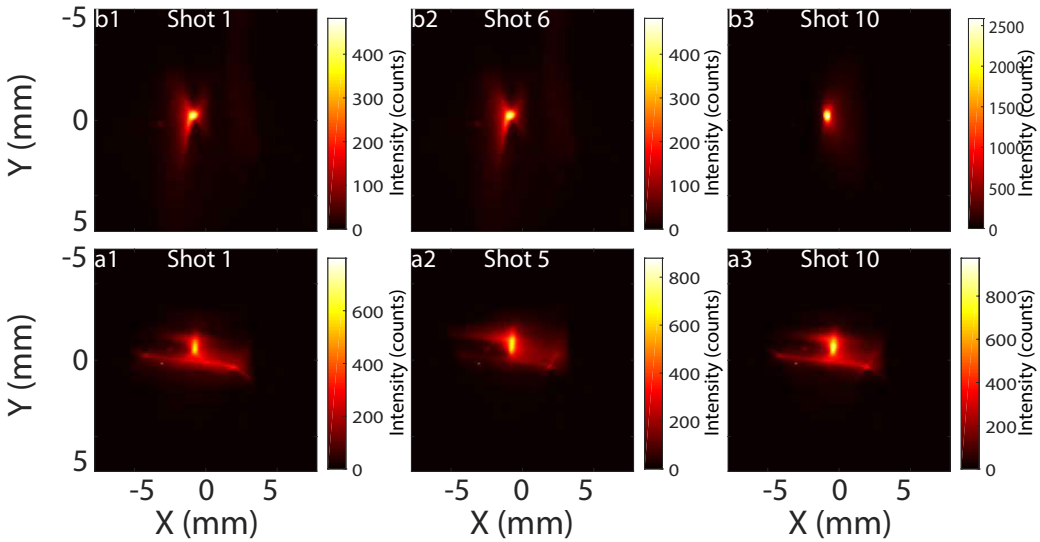

FIGURE 7.22: Examples of measurements at imager "UndOut" from the series taken the (a1, a2, a3) 2020/03/12-18:51:04 and (b1, b2, b3) 2020/09/17-17:44:48 with the "slit-undulator" and "supermatching" optics respectively during RUN 7.

During RUN 7, the "slit-undulator" optics set of the 2020/03/12-18:51:04 (Figure 7.22a) has a well focused spot with left and right low intensity wings. A high intensity shot-to-shot variation occurs, with maximum pixel intensity values going from 400 counts to 2000 counts. The 2020/09/17-17:44:48 set shows the expected cross shape for the "supermatching" optics but an additional deformed low intensity cross appears to the right of the main one. The secondary cross is probably caused by an additional electron beam of low charge and different energy from the reference one. The maximum intensity in this set is of $\approx$ 800 counts.

7.3.3 Evolution of the deduced charge from the imager

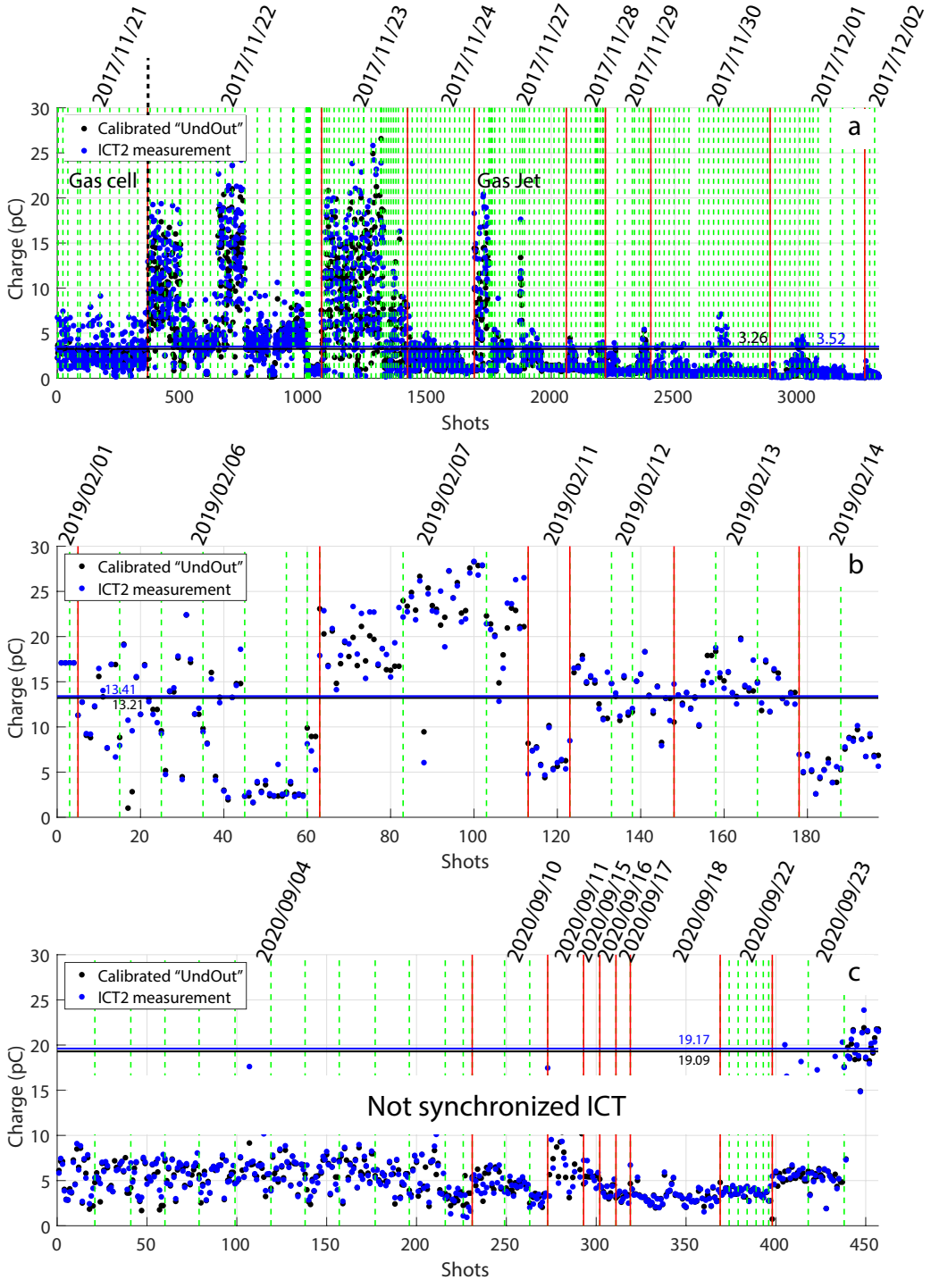

FIGURE 7.23: Measured total beam charge after the undulator on (blue) the ICT2 and (black) at the calibrated imager "UndOut" during RUN 4 (a), 6 (b) and 7 (c) in chronological order, separation by configuration (black dotted line), day (red line) and series (green line).

Figure 7.23 exhibits the simultaneously measured total charge on ICT2 and calibrated imager "UndOut" for the different RUNs. During RUN 4, for the gas cell (jet) target (Figure 7.23a) the difference between the mean total charge at the ICT2 and imager "UndOut" (Table 7.8) is of a factor 1.3 (1.35). The mean total charge on imager "UndOut" is in agreement with ICT2 (Table 7.8). The small difference between them arise from the shot-to-shot variations in background counts on the imager. The calibrated imager "UndOut" agrees within 0.2

pC with ICT2 results in RUN 6 (Figure 7.23b, Table 7.8). The agreement during RUN 7 between the calibrated imager "UndOut" and the ICT2 is within 0.08 pC (Figure 7.23c, Table 7.8).

Diagnostic	Total charge Mean (std) (pC)							
	RUN 4				RUN 6		RUN 7	
Gas target	Gas cell		Gas jet		Gas jet		Gas jet	
Spectrometer	120.3	(66.8)	280.7	(110.5)	114.3	(35.7)	143.2	(59)
ICT1	11.32	(6.10)	35.13	(25.01)	64.45	(107.04)	82.42	(8.35)
ICT2	1.98	(1.46)	2.48	(3.36)	13.40	(6.68)	19.17	(3.4)
Imager "UndOut"	2.58	(0.51)	3.34	(4.26)	13.21	(6.73)	19.09	(3.28)

TABLE 7.8: Measured total beam charge at the electron spectrometer, ICT1 (4.61 m before the undulator) and ICT2 (0.78 m after the undulator) during RUNs 4, 6 and 7.

The calibrated imager "UndOut" can be used to monitor the total charge with ICT2 reliably with a daily calibration. The simultaneously measured total charge after the undulator at imager "UndOut" and ICT2 rises with each RUN up to 19 pC. In average more than 80 % of the total charge at ICT1 is lost by the time it reaches imager "UndOut". As the measured transverse shape at imager "UndOut" agrees with what is found by simulation, it is assumed that the reference energy slice charge is not significantly affected.

7.4 Electron beam charge and energy distribution at the undulator

Imager "D_{dump}" (77 cm after "UndOut") can provide additional information on the electron beam quality.

7.4.1 Simulation charge study at the dipole dump

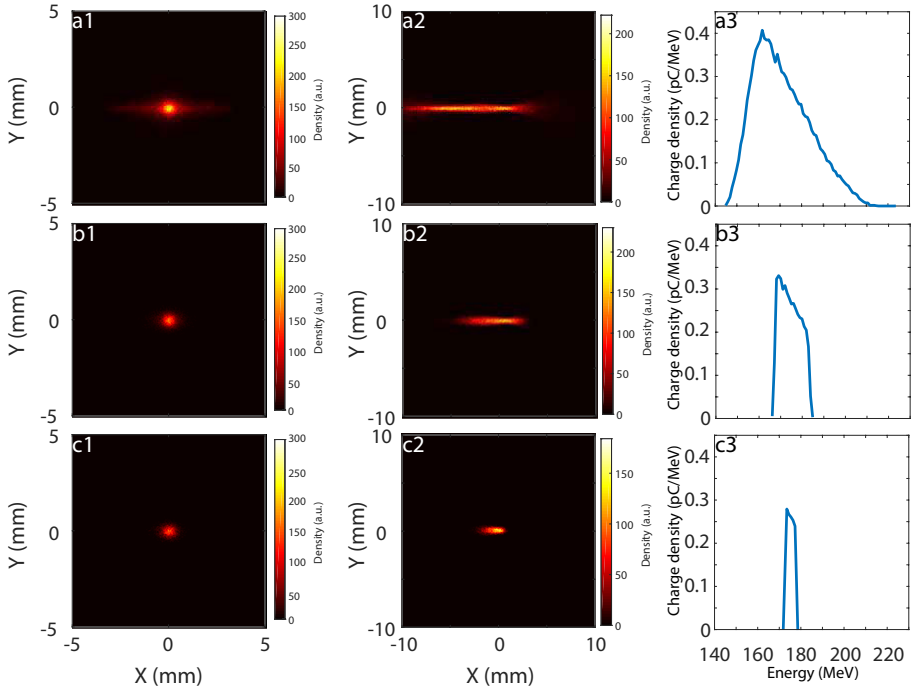

FIGURE 7.24: Simulated beam transverse shape at imager "UndOut" (a1, b1, c1) and "D_{dump}" (a2, b2, c2) and energy distribution at "D_{dump}" (a3, b3, c3). Case of the "slit-undulator" optics: (a1, a2, a3) slit open (145-220 MeV), slit opened at (b1, b2, b3) 3 (165-190 MeV) and (c1, c2, c3) 1 mm (170-179 MeV). Experimental like beam (Figure 4.8c), with ϵ_{RMS} =1 mm.mrad, $\sigma'_{y,RMS,i} = 2$ mrad and $\sigma'_{x,RMS,i} = 2$ mrad

Figure 7.24 presents the simulated transport of the experimental like beam (Table 6.1) with the "slit-undulator" optics and for different energy selection cases.

In the case of the "slit-undulator" optics with an experimental like beam (Table 6.1) (Figure 7.24), at imager "D_{dump}", a long beam with two tightly vertically focused zones is observed (Figure 7.24a2). The beam horizontally extends along a 20 mm range (145- 220 MeV) and the right focused zone corresponds to the reference energy slice (Figure 7.24a3). The total charge reduces to 20 % of the initial one at the undulator exit and to 19.5 % at the dump location (Figure 6.5, Section 6.1.1) . The reference slice charge is conserved along the entire line. Closing the slit to 3 mm (Figure 7.24a2,b2,c2) (1 mm (Figure 7.24a3,b3,c3)) limits the energy distribution to 165-190 MeV (170-179 MeV) and reduces the horizontal beam size.

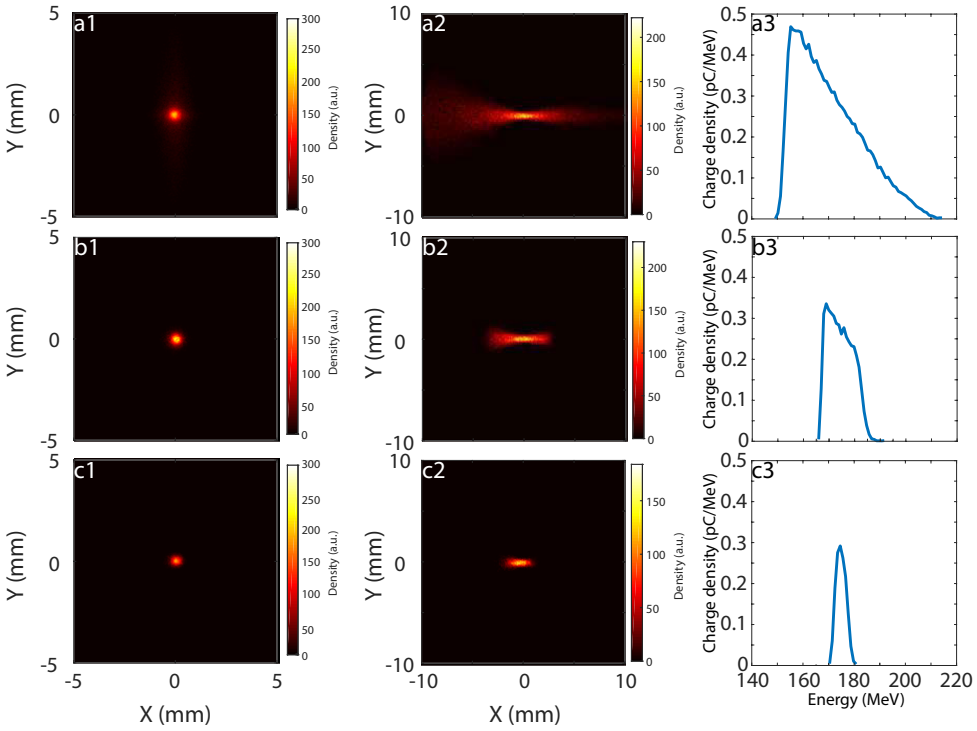

FIGURE 7.25: Simulated beam transverse shape at imager "UndOut" (a1, b1, c1) and "D_{dump}" (a2, b2, c2) and energy distribution at "D_{dump}" (a3, b3, c3). Case of the "supermatching" optics: (a1, a2, a3) slit open (150-210 MeV), slit opened at (b1, b2, b3) 3 (170-192 MeV) and (c1, c2, c3) 1 mm (170-181 MeV). Experimental like beam (Figure 4.8c), with ϵ_{RMS} =1 mm.mrad, $\sigma'_{y,RMS,i} = 2$ mrad and $\sigma'_{x,RMS,i} = 2$ mrad

In the case of the "supermatching" optics simulations with an experimental like beam (Table 6.1), $\approx$ 22 % of the total beam arrives at the end (Figure 6.5, Section 6.1.1), without any loss between the undulator exit and the dipole dump. The reference energy slice is conserved along the entire line. At imager "D_{dump}", an asymmetric butterfly with a higher dispersion at the left wing than at the right one (Figure 7.25b1) appears. The energy range arriving at the end of the line spans from 150 MeV to 210 MeV (Figure 7.25a3) slightly shorter than the "slit-undulator" optics case. The slit is less precise in the energy selection in the "supermatching" optics (Figure 7.25a3,b3,c3) than in the "slit-undulator" one (Figure 7.24a3,b3,c3).

Imager "D_{dump}" for an on-axis is shown in Section 3.2.2.6. The effect of an initial electron beam vertical (horizontal) displacement of 30 μm (Figure 7.26a1, a2, a3) (60 μm (Figure 7.26b1, b2, b3)) on imager "D_{dump}" shape and energies horizontal distribution is compared to the on-axis case (Figure 7.26c1, c2, c3) with the "supermatching" optics. The vertical displacement tilts the butterfly (Figure 7.26a1) but neither the horizontal energy positions (Figure 7.26a2) nor the energy distribution (Figure 7.26a3) are affected. The reference energy slice charge remains unchanged but the total beam one decreases by an extra 1 % with respect to the on-axis case corresponding to the low energies of the distribution (Figure 7.26a3, c3). The horizontal displacement shifts the energies horizontal positions by 0.56 mm, i.e., $\approx$ 2.3 MeV. With a 60 μm displacement, higher energies arrive to the imager and the total and reference energy slice charge are the same as in the on-axis case (Figure 7.26a3, b3, c3). Figure 7.26d, e exhibits the effects of an initial beam pointing on imager "D_{dump}". A 2 mrad initial vertical pointing vertically bends the butterfly, especially for the energies below 190 MeV (Figure 7.26d1), and the position of the reference energy slice slightly shifts (Figure 7.26d2). The total beam charge at the undulator dump is halved (i.e., $\approx$ 11 % the initial total charge) with respect to the on-axis case, while the reference energy slice remains the same (Figure 7.26c3, d3). A 2 mrad initial horizontal pointing increases the transverse defocus at imager "D_{dump}" (Figure 7.26e1) and substantially shifts the energies horizontal positions by 1.27 mm, i.e.,

≈ 3.5 MeV (Figure 7.26e2). The energy distribution loses part of the high and low tails reducing the energy range to approximately 155 – 210 MeV (Figure 7.26e3). While an initial displacement can affect the energies horizontal position, the initial pointing dominates. Experimentally (Figure 7.15b), vertical pointings of up to 4 mrad are common and probably similar horizontal ones occur.

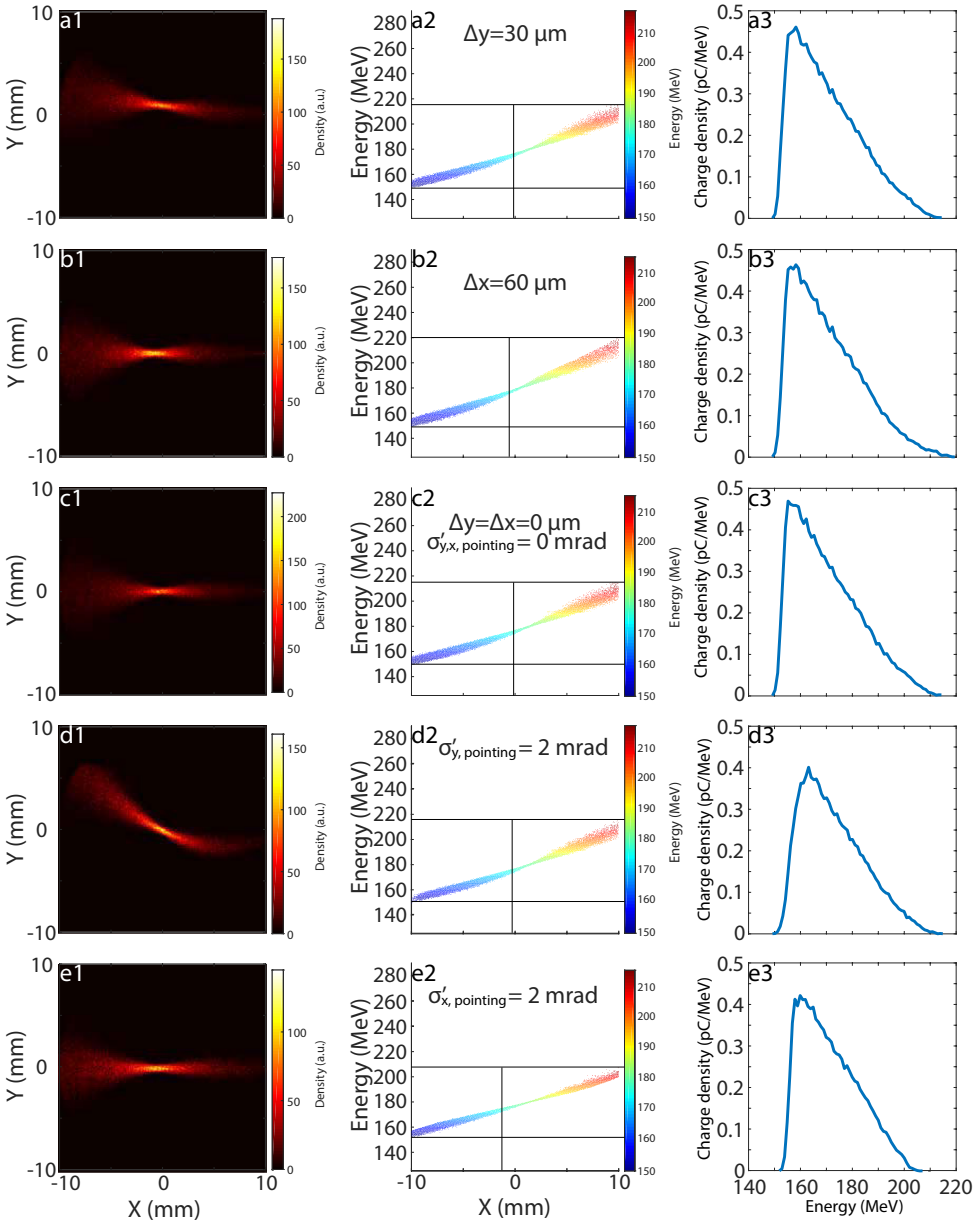

FIGURE 7.26: Simulated beam transverse shape (a1, b1, c1, d1, e1), energy versus horizontal position (a2, b2, c2, d2, e2) and energy distribution (a3, b3, c3, d3, e3) at "D_{dump}". Case of the "supermatching" optics; slit open, on-axis beam (c1, c2, c3), with initial vertical displacement of 30 μm (a1, a2, a3), with a horizontal displacement 60 μm (b1, b2, b3), initial vertical pointing of 2 $mrad$ (d1, d2, d3), horizontal pointing 2 $mrad$ (e1, e2, e3). Experimental like beam (Figure 4.8c), with ϵ_{RMS} =1 mm.mrad, $\sigma'_{y,RMS,i} = 2$ mrad and $\sigma'_{x,RMS,i} = 2$ mrad

7.4.2 Raw data treatment

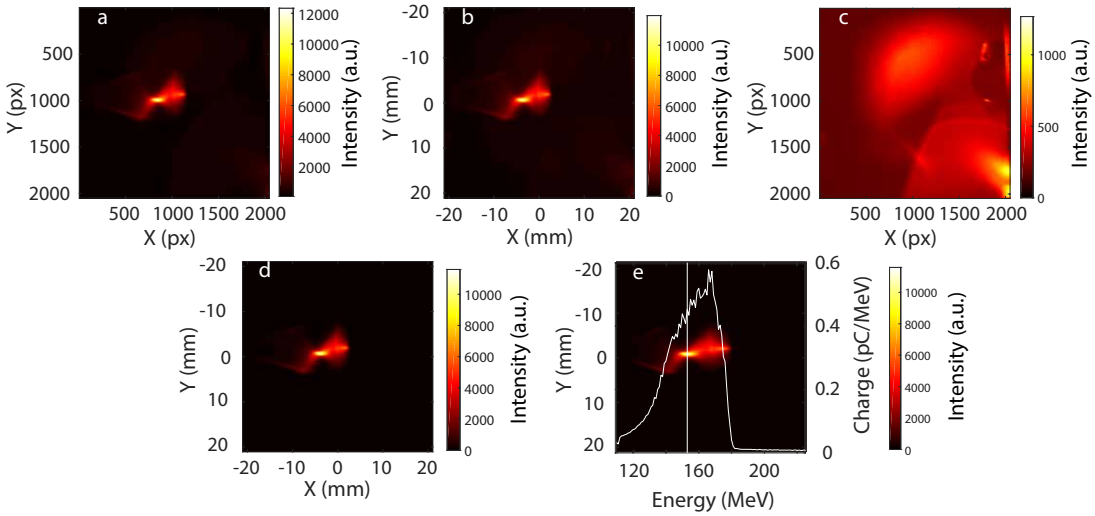

FIGURE 7.27: Measured transverse beam shape at the imager "D_{dump}" (a) raw data, (b) after a median filter, (c) used background image, (d) image after background subtraction, (d) image after horizontal axis energy calibration and (white line plot) energy distribution per MeV. Shot done the 2020/09/24 at RUN 7.

Figure 7.27 presents the imager "D_{dump}" measurement post-treatment of the raw image (Figure 7.27a). First, a median filter is applied and the axis are converted to mm (Figure 7.27b). Second, from a previously taken background image (Figure 7.27c) the shot background is erased (Figure 7.27d). Finally, the calibration calculated from the dipole equation (Section 3.2.2.6) is applied (conversion horizontal axis distances in mm to energy in MeV). Even if there is a horizontal displacement the center of the observed butterfly at imager "D_{dump}" should correspond to the reference energy slice as the optics are design for it. If the center is not clear (e.g., "slit-undulator" Figure 7.24) the energy axis position from the calibration is used (Section 3.2.2.6).

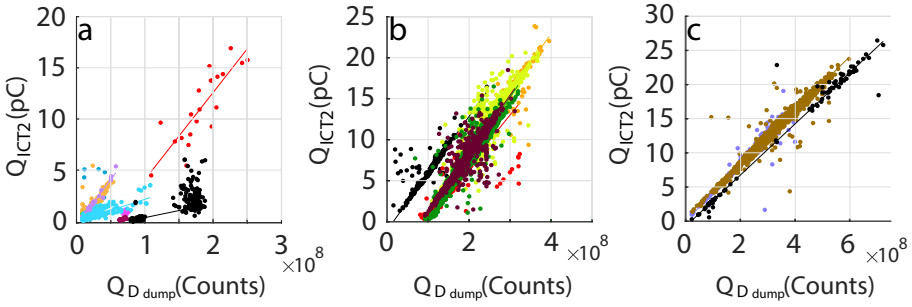

FIGURE 7.28: Charge measured after the undulator at the ICT2 versus imager "D_{dump}" total counts after image treatment and (line) linear fit count/pC calibration ($Q_{ICT2}[pC] = Q_{img}[counts] \times p_1 + p_2$). Run 4 (a) gas cell (black dots) and gas jet, RUN 6 (b) and RUN 7 (c) data, colors representing different days. RUN 4 (a): 2017/11/21 (black), 2017/11/22 (red), 2017/11/23 (blue), 2017/11/24 (orange), 2017/11/28 (pink), 2017/11/29 (yellow), 2017/11/30 (purple), 2017/12/01 (cyan), 2017/12/02 (crimson). RUN 6 (b): 2019/02/06 (black), 2019/02/11 (red), 2019/02/12 (orange), 2019/02/13 (green), 2019/02/14 (dark green), 2019/02/15 (brown). RUN 7 (c): 2020/09/23 (black), 2020/09/24 (brown), 2020/09/25 (purple).

The simultaneously measured ICT2 charge and imager "D_{dump}" counts present a linear correlation (Figure 7.28). Therefore, to calibrate imager "D_{dipole}" counts to pC a linear fit is used (Equation 7.18). Each day, the calibrations present differences in the fit parameters p_1 and p_2 (Table 7.9) as in imager "UndOut" case (Table 7.7). The p_2 parameter is non-zero due to the impossibility of a perfect background removal. Figure 7.28a and Table 7.9 show each day calibrations of imager "D_{dump}" during RUN 4. The gas cell data (2017/11/21) are more dispersed than the gas jet ones. The fit slope per day varies between 1.6×10^{-8} and 9×10^{-8} pC/counts. Close to 8000 shots were taken during RUN 6 at imager "D_{dipole}". The line fit calibrations per day during RUN 6 in Figure 7.28b show slope values between 6.2×10^{-8} and 7.4×10^{-8} pC/counts (Table 7.9). Figure 7.28c

shows the calibration of imager "D_{dipole}" via a linear fit during RUN 7. The fit slope values for each day go from 3.7×10^{-8} (2020/09/23) to 4.2×10^{-8} pC/counts (2020/09/25), the most stable of all the RUNs.

RUN 4			RUN 6			RUN 7		
Day	Fit parameters		Day	Fit parameters		Day	Fit parameters	
	p_1 (pC/counts)	p_2 (pC)		p_1 (pC/counts)	p_2 (pC)		p_1 (pC/counts)	p_2 (pC)
2017/11/21	1.38×10^{-8}	0.89	2019/02/06	6.94×10^{-8}	-1.05	2020/09/23	3.74×10^{-8}	-0.72
2017/11/22	8.51×10^{-8}	-4.33	2019/02/11	6.20×10^{-8}	-5.58	2020/09/24	3.91×10^{-8}	0.60
2017/11/23	3.33×10^{-8}	0.43	2019/02/12	6.88×10^{-8}	-4.64	2020/09/25	4.19×10^{-8}	-0.03
2017/11/24	6.73×10^{-8}	0.20	2019/02/13	7.30×10^{-8}	-5.86			
2017/11/28	2.10×10^{-8}	-0.46	2019/02/14	7.40×10^{-8}	-7.00			
2017/11/29	5.56×10^{-8}	0.22	2019/02/15	7.17×10^{-8}	-6.07			
2017/11/30	8.99×10^{-8}	-0.31						
2017/12/01	2.13×10^{-8}	0.02						
2017/12/02	1.62×10^{-8}	-0.90						

TABLE 7.9: Calibration fit (Equation 7.18) parameters of imager "D_{dump}" with ICT2 for the different RUNs.

7.4.3 Analysis of the electron beam transverse profile on the dipole dump along the RUNs

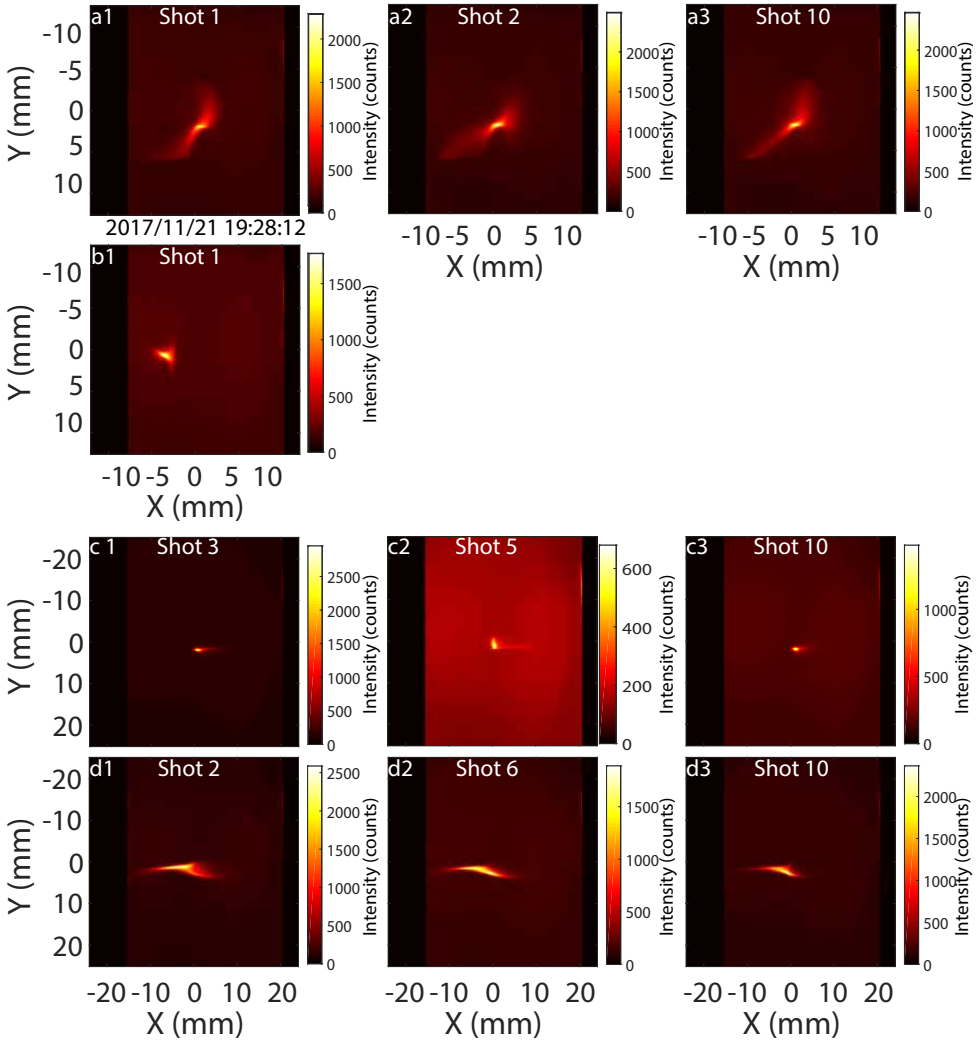

FIGURE 7.29: Examples of measurements at imager "D_{dump}" from the series taken the (a1, a2, a3) 2017/11/21-18:50:36 and (b1) 2017/11/21-20:07:47 with the "undulator-exit" optics, gas cell target and (c1, c2, c3) 2017/12/01-17:01:22 and (d1, d2, d3) 2017/11/24-20:12:49 with the "slit-undulator" optics and the gas jet target during RUN 4.

RUN 4 examples of measurements at imager "D_{dump}" for the gas cell LPA in Figure 7.29a1, a2, a3, b1 shows a tilted and bent butterfly. In addition, horizontal position shifts can be observed from shot-to-shot (Figure 7.29a1, a2, a3). The maximum intensity per pixel at the beam center is around 1800 counts. Figure 7.29c, d present some measurements at imager "D_{dump}" for the gas jet LPA. For the set 2017/11/29-17:54:59 (Figure 7.29c1, c2, c3) a focused spot with a much less intense right wing appears. The maximum intensity per pixel of the beam varies shot-to-shot between 600-2000 counts. In the set 2017/12/01-16:33:24 (Figure 7.29d1, d2, d3) a vertically focused line is observed with some focusing changes shot-to-shot. The maximum intensity per pixel at the beam center is around 2000 counts

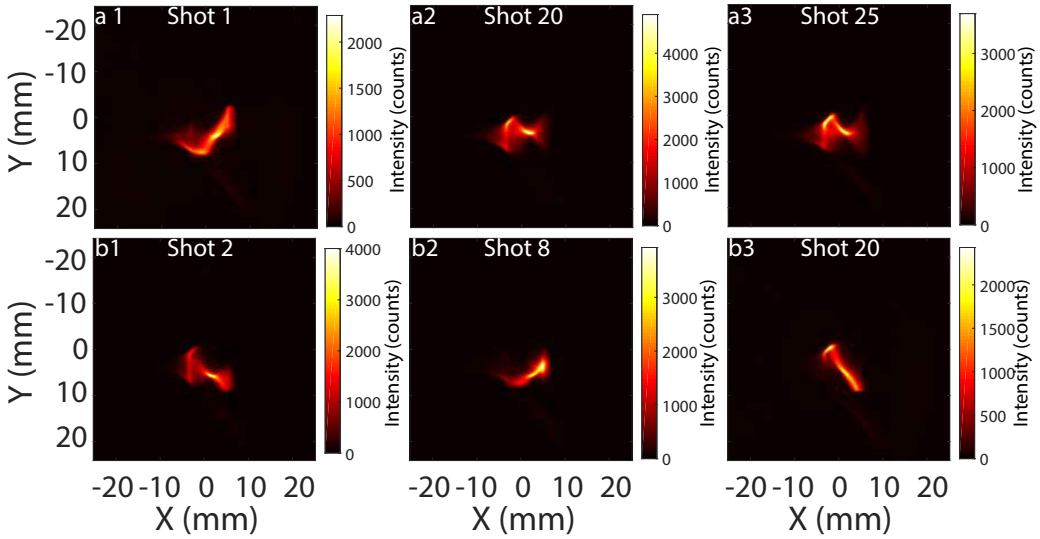

FIGURE 7.30: Examples of measurements at imager "D_{dump}" from the series taken the (a1, a2, a3) 2019/02/14-00:54:58 and (b1, b2, b3) 2019/02/12-21:56:27 with the "supermatching" optics during RUN 6.

During RUN 6, at imager "D_{dump}" with the "supermatching" optics, the bent butterfly shape has been consistently obtained (Figure 7.30). The bent is mainly caused by initial vertical pointing (Figure 7.26d) and the change in the direction of the bent is in agreement with the pointing measured in imager "Chicane" (Figure 7.15b). The beam maximum pixel intensity is around 2000 and 3000 counts.

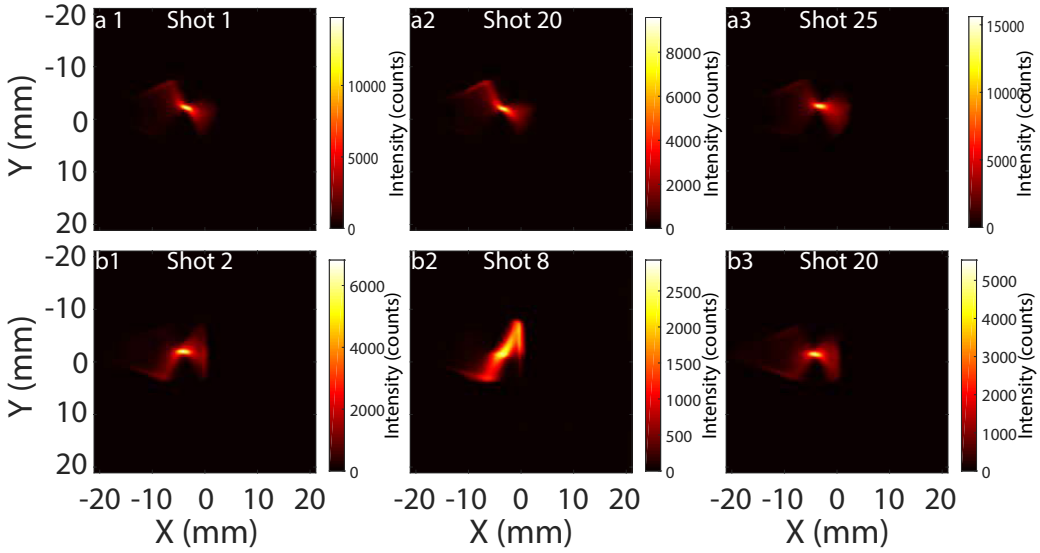

FIGURE 7.31: Examples of measurements at imager "D_{dump}" from the series taken the (a1, a2, a3) 2020/09/24-16:11:38 and (b1, b2, b3) 2020/09/25-19:37:34 with the "supermatching" optics and the gas cell target during RUN 7.

Similarly to RUN 6, the transverse shape observed at imager "D_{dump}" during RUN 7 in Figure 7.31 presents a bent butterfly due to pointing (Figure 7.15b) and the beam maximum pixel intensity is around 2500 counts.

7.4.4 Analysis of the total charge on the dipole dump along the RUNs

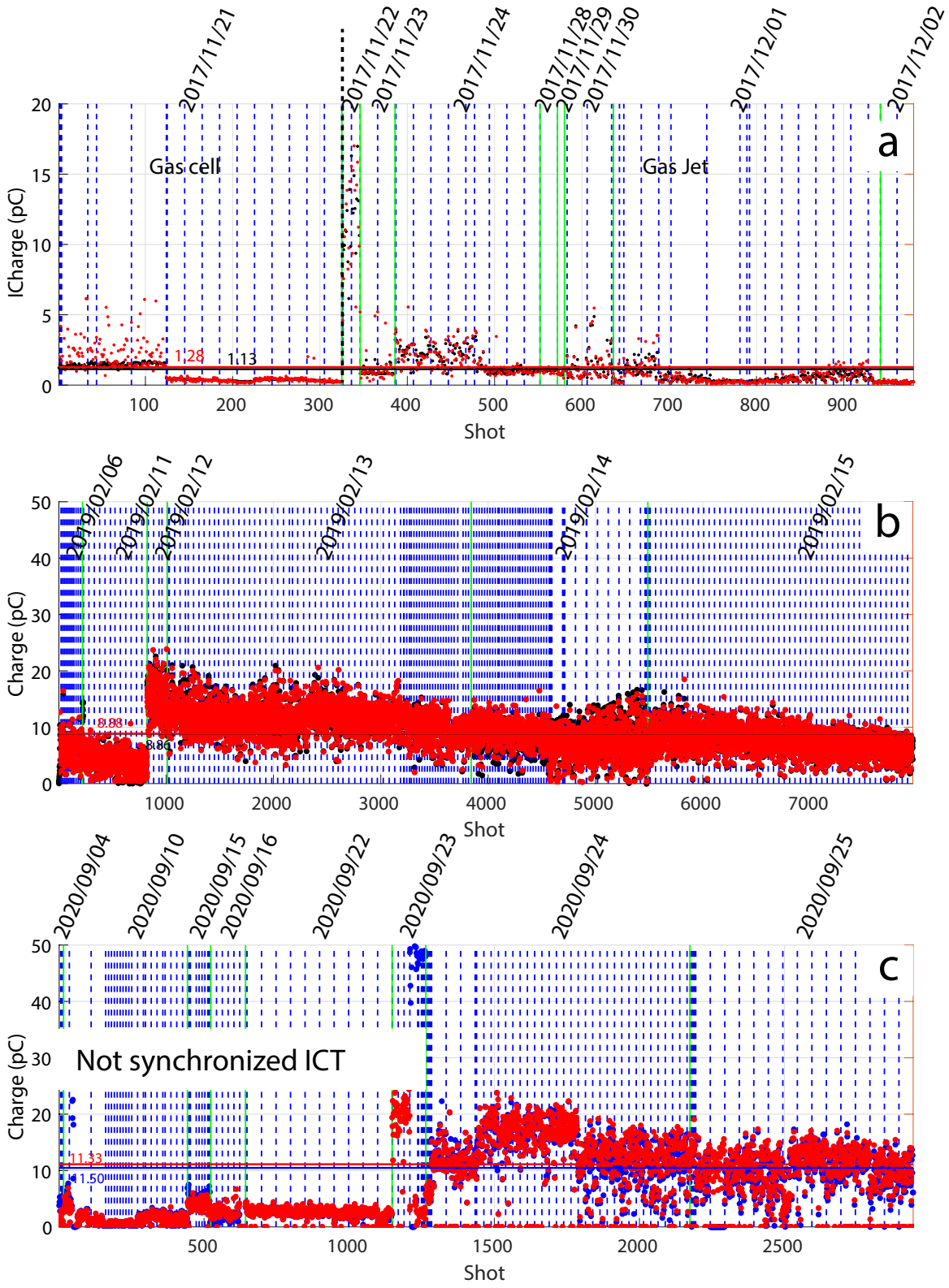

FIGURE 7.32: Measured total beam charge at (red) ICT2 and (black) at the calibrated imager "D_{dump}" during RUN 4, 6 and 7 in chronological order, separation by configuration (black dotted line), day (red line) and series (dotted green line).

Figure 7.32a presents the simultaneously measured total charge at the ICT2 and imager "D_{dump}" taken at RUN 4. The calibrated "D_{dump}" values agrees within 0.15 pC with the ICT2 ones (Table 7.10). During the imager

"D_{dump}" shots, the laser degradation in time reaches its maximum and no significant decrease in total charge is noticed. When the radiation generation experiments start, the total beam charge is less than 5 pC, with the exception of the 2017/11/22 in which it was between 5 pC and 17 pC (Figure 7.32a). During RUN 6, the high number of imager "D_{dump}" shots (Figure 7.32b) gives a mean total charge difference between the calibrated imager "D_{dump}" and ICT2 of 0.02 pC. In RUN 7, after the undulator (Figure 7.32c), no significant difference is found between the 09/24 and 09/25 beam charge as already shown in Section 7.1.2. The mean total charge between the calibrated imager "D_{dump}" and ICT2 differs by 0.2 pC and is 8 pC lower than the imager "UndOut" one due to laser degradation over time. The RUN 7 mean charge after the undulator is ≈ 1.3 times (Table 7.10) the RUN 6 one, which reflects the better beam energy distribution.

Diagnostic	Total charge Mean (std) (pC)							
	RUN 4				RUN 6		RUN 7	
	Gas cell		Gas jet		Gas jet		Gas jet	
Spectrometer	120.3	(66.8)	280.7	(110.5)	114.3	(35.7)	143.2	(59)
ICT2	1.07	(1.20)	1.10	(1.89)	8.88	(3.39)	11.33	(5.10)
"D_{dump}"	0.77	(0.55)	1.31	(2.05)	8.86	(3.34)	11.50	(4.51)

TABLE 7.10: Average and standard deviation of the spectrometer data and the simultaneously measured ICT1, ICT2 and imager "D_{dump}" for RUNs 4, 6 and 7.

7.4.4.1 Charge density evolution along the different RUNs

The charge density deduced from dipole dump imager is now analysed. The reference energy slice charge corresponding to the vertical slice cutting the center of the butterfly and the maximum slice charge are taken (Section 7.4.2) as the energies horizontal position can shift due to pointing and initial displacements. The maximum slice charge value is the possible top limit for complex images, e.g., Figure 7.29d1.

Figure 7.33a presents the maximum and 176 ± 0.5 slice charge for all imager "D_{dump}" shots corresponding to undulator radiation during RUN 4. For the gas cell (jet) target case, the 176 ± 0.5 MeV slice charge value is approximately 7 (27) times lower than the spectrometer one (Table 7.11). Even taking the highest slice charge, its average is 2 (5) times lower the than the spectrometer one. Only during the 2017/11/22 the reference energy slice offered confirmed values superior to 0.1 pC/MeV at the end of the line. As by simulation (Section 6.2.1.2), the reference energy slice charge loss is under 1 % for the measured divergences, the loss origin must come from laser degradation and initial beam pointing. Thus, even when the best case scenario is considered (highest slice charge on imager "D_{dump}), the 176 ± 0.5 MeV slice charge is significantly less that the average just after the LPA optimization (electron spectrometer). During RUN 6, the mean 151 ± 0.5 MeV slice and maximum slice charge at imager "D_{dump}" in Figure 7.33b shows a significant improvement over RUN 4 results. The 151 ± 0.5 MeV slice achieves up to 0.6 pC/MeV the 2019/02/12 and most commonly oscillates between 0.5 pC/MeV and 0.1 pC/MeV. The 151 ± 0.5 MeV slice mean is half the measured at the electron spectrometer (Table 7.11) which can be due to laser degradation over time. Therefore, the reference energy slice charge conditions used for radiation generation search experiments is, as in RUN 4, at best in the low range of values measured at the spectrometer (Section 4.3.1.2). The RUN 7 151 ± 0.5 MeV slice charge after the undulator (Figure 7.33c) measured during the FEL search experiments is in average the same as the RUN 6 one, although their difference at the spectrometer data showed a 1.3 increase (Section 4.4). Compared to RUN 7 spectrometer measurements (Section 4.3.2.3), the slice charge is on the level of the worst spectrometer shots and even the maximum charge slice measured is far from the mean 0.9 pC/MeV found on it (Table 7.11).

Diagnostic	Parameter	Units	RUN 4		RUN 6	RUN 7
			Cell	Jet		
Spectrometer	Q_{slice} (std)	pC/MeV	0.07 (0.11)	0.27 (0.23)	0.58 (0.18)	0.9 (0.34)
"D_{dump}"	Q_{slice} (std)	pC/MeV	0.01 (0.004)	0.01 (0.03)	0.26 (0.1)	0.27 (0.11)
"D_{dump}"	$Q_{Max,slice}$ (std)	pC/MeV	0.03 (0.02)	0.05 (0.07)	0.55 (0.21)	0.36 (0.14)

TABLE 7.11: Mean and std reference slice charge Q_{slice} measured at the spectrometer and "D_{dump}" and highest slice charge ($Q_{Max,slice}$) during the different RUNs.

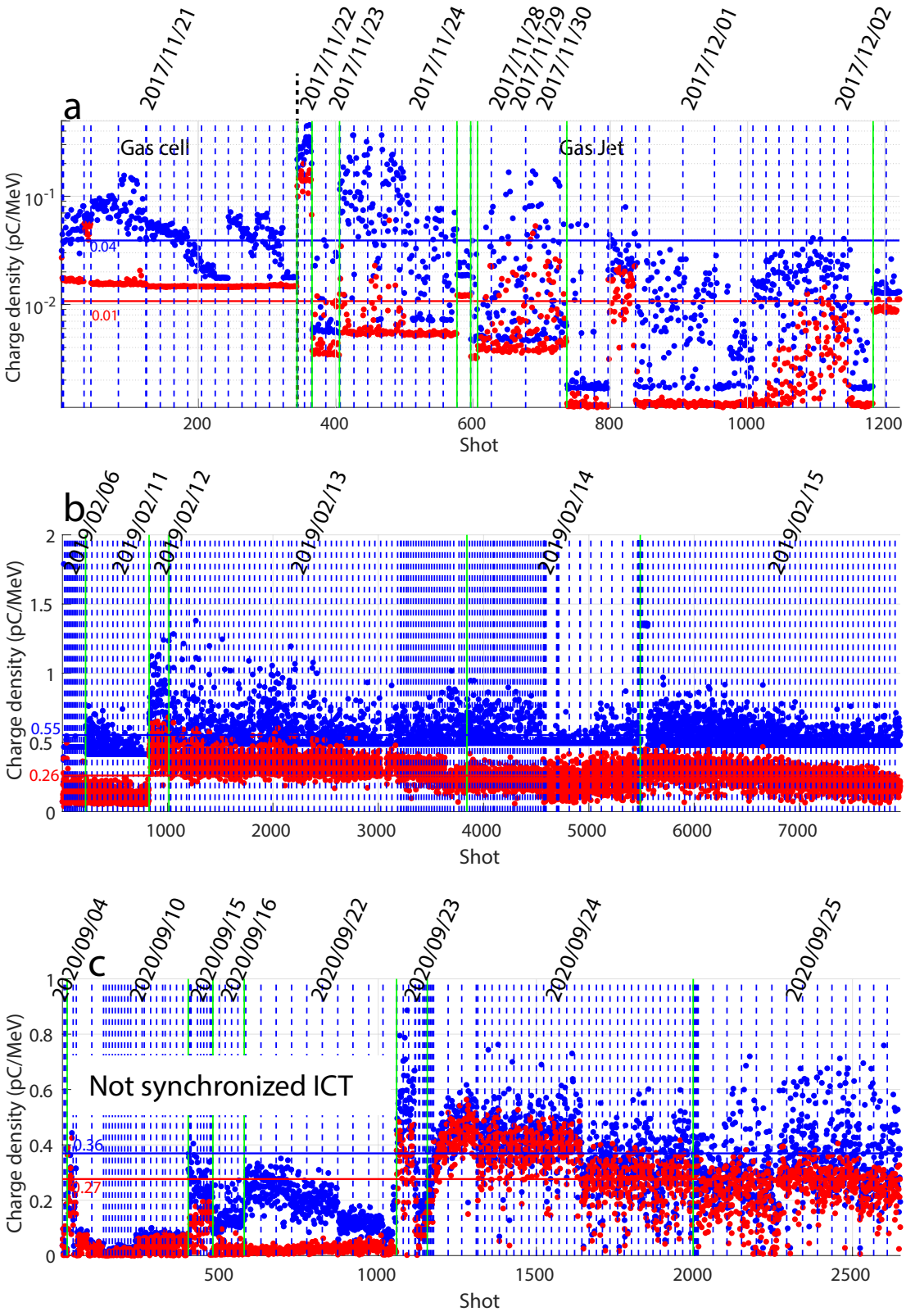

FIGURE 7.33: Measured (red) 176 ± 0.5 (a) and MeV 151 ± 0.5 MeV (b, c) slice and (blue) 1 MeV maximum slice charge at the calibrated imager "D_{dump}" during RUN 4 (a), 6 (b) and 7 (c) in chronological order, separation by configuration (dotted black line), day (green line) and series (dotted blue line). RUN 4 vertical axis in log (a).

7.5 Comparison of the different measurements methods

7.5.1 Total charge and charge density

In addition to their use for beam transport, the diagnostics permit to track the beam parameters evolution from the source to the line exit. The measurements at imager "D_{dump}" enable to observe the reference energy slice charge going through the undulator, of interest for judging the possibility of obtaining FEL. Table 7.12 summarizes the total and reference slice charge for the different RUNs. Each RUN, the total charge before the undulator (ICT1) has been substantially increased (Table 7.12) thanks to the improvements in the LPA source (higher charge, better energy distribution, lower divergence (2 mrad RMS)) and transport (Section 4.4). However, most of the charge correspond to energies outside the reference slice one and thus, after the undulator more than 80 % is lost. As the transport is well optimized for the reference energy slice, even for high divergences, e.g. 5 mrad RMS (Section 6.2.1.2), its charge is mostly conserved to the end of the line at imager "D_{dump}". The best measured mean reference slice charge on imager "D_{dump}" during FEL radiation search are around 0.26 pC/MeV during RUN 6 and 7, less than half the measured mean at the electron spectrometer. Therefore, the beam used for undulator radiation experiments is worse than the spectrometer ones, and realistically no shot was inside the low gain FEL zone even after the laser power upgrade in RUN 7 (Section 4.3.2.3). The difference can be attributed to the laser degradation over time (from the LPA optimization to the transport and seed) and initial beam pointing. The low reference energy slice charge, RMS divergence above 2 and the laser stability heavily hinders the chances of FEL radiation and must be improved in order to achieve the FEL based LPA demonstration.

Diagnostic	Parameter	Units	RUN 4		RUN 6	RUN 7
			Cell	Jet		
Source						
Spectrometer	Q_T (std)	pC	120.3 (66.8)	280.7 (110.5)	114.3 (35.7)	143.2 (59)
	Q_{slice} (std)	pC	0.07 (0.11)	0.27 (0.23)	0.58 (0.18)	0.9 (0.34)
Before the Undulator						
ICT1	Q_T (std)	pC	11.30 (5.64)	35.47 (25.29)	137.03 (100.69)	359.02 (237.38)
After the Undulator						
ICT2	Q_T (std)	pC	2.03 (1.76)	2.86 (4.11)	8.98 (3.56)	12.42 (4.55)
'UndOut"	Q_T (std)	pC	2.58 (0.51)	3.34 (4.25)	13.21 (6.73)	11.50 (4.51)
"D_{dump}"	Q_T (std)	pC	0.77 (0.55)	1.31 (2.05)	8.86 (6.73)	14.18 (11.96)
	Q_{slice} (std)	pC/MeV	0.01 (0.004)	0.01 (0.03)	0.26 (0.1)	0.27 (0.11)

TABLE 7.12: Mean and std total beam charge Q_T and reference slice charge Q_{slice} measured at the spectrometer, ICTs, imager "UndOut" and "D_{dump}" during the different RUNs.

7.5.2 Reference energy slice vertical size, divergence and emittance

The possibility of achieving an accurate single shot emittance measurement through the measurement of the beam transversal shape at a screen at the middle of a magnetic chicane has been explored theoretically and via simulations in different cases. The measurement has been applied experimentally for different lenses configurations and multiple vertical slice size $\sigma_{y,butterfly}$ measuring methods. Moreover, it has been found that through the observation of the observed tilt of the butterfly like transverse beam shape on imager "chicane" the initial beam vertical pointing can be obtained accurately.

By simulation, the capacity to obtain a vertical beam size $\sigma_{y,chicane}$ and divergence $\sigma'_{y,chicane}$ value within % levels of the source value has been confirmed even with the inclusion of experimental like noise and electron beam energy distributions. The accurate correction of the vertical beam size $\sigma_{y,chicane}$ when the beam presents an initial pointing below 5 mrad via an artificial image rotation post-treatment has also been demonstrated. For an initial pointing larger than 5 mrad the error in the vertical divergence is above 14 % thus, is not acceptable.

The Sigma Macro lens (8.5 x 9.2 μm; $S/N = 21.69$) shows some consecutive pixel sudden intensity variation at the peak of the central vertical slices caused by the combination of low resolution and high efficiency, thus, giving consistently a ≈ 21.5 μm vertical beam size $\sigma_{y,img2}$ in RUN 7. The Navitar S1 (2.6 x 2.4 μm; $S/N = 1.25$), S2 (2.6 x 2.4 μm; $S/N = 1.22$) and S3 (3.8 x 4.1 μm; $S/N = 1.25$) lens configurations high resolutions and low signal to noise ratios produces an oversampling and consecutive pixel intensity variation that reduces the number of pixels to effectively around a third, making them worse than the Trioptic (5.2 x 5.1 μm; $S/N = 6.23$, 5 x 4.6 μm; $S/N = 6.26$, 5 x 4.7 μm; $S/N = 2.47$) and Sigma Macro (8.5 x 9.2 μm; $S/N = 21.69$) configurations. The image rotation post-treatment has been found useful and in agreement with simulations for the lens configurations

with a signal to noise ratio above 6 (Sigma Macro (8.5 x 9.2 μm; $S/N = 21.69$), Trioptic S1 (5.2 x 5.1 μm; $S/N = 6.23$) and Trioptic S2 (5 x 4.6 μm)

The optimal lens configurations for this measurement are the Trioptic S1 and S2 which are the only ones that do not exhibit oversampling or high consecutive pixel intensity variation and also are compatible with the image rotation post-treatment. The Trioptic S3 configuration can be also considered accurate without the without rotation post-treatment due to the low pointing found during its shots. The obtained vertical divergence is in agreement with the spectrometer and "First imager" ones. The average vertical emittance found with the Trioptic S1 and S2 (S1, S2 and S3) data is of 3.2 mm.mrad (2.8 mm.mrad) with an std of 1.5 mm.mrad (1.2 mm.mrad), three times the COXINEL baseline beam one.

Diagnostic	Post-treatment	$\sigma'_{y,initial,151\pm0.5}$ mrad		$\sigma_{y,initial,151\pm0.5}$ μm		ϵ_y mm.mrad
		mean	std	mean	std	$FWHM/2.35^2$
Spectrometer		3.76	1.53			
"First imager"		5.19	3.45			
Imager "chicane" Trioptic S1	Rotation	4.88	4.08	16.27	5.76	4.25
Imager "chicane" Trioptic S2	Rotation	3.96	0.81	10.14	0.24	2.15
Imager "chicane" Trioptic S3	None	3.25	1.41	12.32	4.71	2.14

TABLE 7.13: Average and std FWHM initial 151 ± 0.5 slice vertical divergence, size measured and emittace measured at the spectrometer, "first imager" and imager "chicane" during RUN 7.

7.6 Conclusion

The electron beam total charge evolution along the line has measured and it agrees with the transport simulations. Using the imager "D_{dump}" after the undulator, a measurement of the beam energy distribution at the undulator has been done revealing the slice charge at the FEL gain medium and its loss due to laser power degradation over time. Accurate initial beam emittance and a new initial vertical pointing measurement have been successfully implemented using the imager "chicane" .

Chapter 8

Conclusion

8.1 Thesis summary

The theoretical background needed to tackle the LPA based FEL problematic has been presented in chapter 2. The main plasma parameters and dynamics have been introduced. Then, the laser mathematical definition has been reported and the equations of the laser-plasma interaction developed with the multiple non-linear phenomena that it entails (relativistic self-focusing, pulse compression, self-modulation). The conditions in which a laser can cause particle acceleration are fulfilled inside a plasma which leads to the laser plasma acceleration scheme are explained through the Lawson-Woodward theorem. The concept of the laser caused plasma density perturbation called wakefield due to the laser strong ponderomotive force, its analytical definition and the different LPA electron injection schemes are shown. The concepts of laser depletion, dephasing between the laser and electrons and maximum energy exchange in LPA are presented and the basic equations elaborated. The state of the art in LPA is summarized highlighting the achieved parameters important for a FEL application, i.e., divergence, charge, emittance and energy spread. The particle in cell principle and main calculation loop is explained. The equations describing the electron dynamics for different magnetic field structures are then developed. The Twiss parameters and the concept of emittance for an electron beam have been defined. The calculation of the propagation of electron beams through different magnetic elements via transport matrices and its Hamiltonian counterpart are reported. The FEL principle and base equations have been summarized and the three configurations (Resonator, Self amplified spontaneous emission, seeded) presented. The low and high FEL regimes and the conditions that they bring to the electron beam have been introduced. The FEL state of the art is presented and the shortcomings of the current LPA electron beams for FEL use is discussed.

The LPA based FEL is being searched experimentally in the COXINEL line with the LPA system of "Salle jeune" at LOA. The COXINEL line aims at qualifying LPA by the FEL application in the UV range from a baseline electron beam set of parameters (reference electron energy of 176 MeV, 1 mrad RMS divergence, 1 mm.mrad RMS emittance, 1 % energy spread and 34 pC total charge). The experiment and its components are introduced in chapter 3. The fast degradation of the beam quality due to the chromatic emittance growth during transport through a drift and magnetic elements is developed analytically. It is shown how the initial beam divergence and energy spread dominate the chromatic emittance growth, i.e., a beam of 1 mrad initial divergence, 1 % energy spread and 0.2 mm.mrad initial emittance can quadruplicate its emittance in just 3.5 cm during a drift. Therefore, the COXINEL line has to transport the electron beam from the source to the undulator while compensating its initial divergence, manipulating and focusing it at the undulator. The COXINEL line achieves the three functions via classic magnetic devices such as dipoles and quadrupoles. Following the electron beam path, the COXINEL line has first a triplet of specially designed variable gradient quadrupoles (QUAPEVA) to compensate the initial divergence. A magnetic chicane with a slit follows that serves two purposes, to elongate the electron beam and to select the desired energy range. A set of four electromagnetic quadrupoles to focus the electron beam on the undulator. After the undulator a dipole dump evacuates the electrons. The numerous motorized components and variable field magnets permits the design of multiple optics of the line. The diagnostic-oriented optics and the undulator-radiation oriented ones are introduced and their effect on the transverse beam along the line analyzed via simulations with the baseline parameters. A study of the beam transport and undulator radiation for a baseline beam and with slight deviations is realized. Through the Ming Xie equations calculations and GENESIS code simulations it is shown that with the baseline beam FEL amplification can be achieved. A fall of slice charge or increase in divergence from the baseline parameters quickly reduces the amplification or completely nullifies it.

I participated in four experimental campaigns of COXINEL where I transported the beam during the experiment and analyzed the data from the multiple electron beam diagnostics along the line. The beam at the source is diagnosed with the spectrometer (energy distribution, charge and vertical divergence) and the first imager

(horizontal and vertical divergence), as presented in chapter 4. During these four experimental campaigns the line and LPA system have been improved, the on-target laser power has been noticeably enhanced for the last campaign. However, the experimental electron beam was always far from the initially expected baseline parameters deduced from colliding pulse injection done before COXINEL (RMS reference slice divergence of 1 mrad and slice charge of 10.3 pC). Due to robustness issues in the used laser system, the colliding pulse injection was not possible and the ionization injection was utilized instead, invalidating the expected baseline parameters. At each campaign the electron beam parameters improved but even after the laser power upgrade the mean reference slice RMS divergence and charge were 1.6 mrad and 0.9 pC respectively. The parameters obtained were close to be usable for low gain FEL but the deficiencies in laser stability reduced even further any possibility of it. Improvements on the LPA system beam parameters and stability are still needed to be able to produce FEL.

In chapter 5, I expand on the ionization injection scheme of LPA used in COXINEL, chosen due to its stability and robustness compared to the colliding pulse scheme, and explore its performance via PIC simulations with experimental like parameters utilizing the PICLS code as no previous analysis was done for the COXINEL experiment. The effect of different down and up ramps of the gas profile have been simulated and significant effect on the electron injection in the wakefield and acceleration has been found. Shorter up-ramp permits the injection of a high charge and a longer one gives a lower energy spread and higher electron energies. A gas density range from $4 \times 10^{18}\ cm^{-3}$ to $6 \times 10^{18}\ cm^{-3}$ has shown that the increase of density leads to a much higher charge injection and lower electron energies. Moreover, different high Z gas (N_2) concentration (from 1 % to 4 %) have been explored. The rise of N_2 concentration does not affect the energy distribution shape but reduces the reached electron energies, substantially increases the number of late injected electrons and worsens the transverse phase-space. A total beam charge and mean energy expression depending of the gas density and N_2 concentration have been fitted from the simulation results. The charge dependence is straightforward as it grows with higher density and N_2 quantity. The mean energy is not a monotonic function of the density but it is of the N_2 concentration. Finally, the effect of an increase on the laser power has been simulated for multiple gases. Even a small laser power rise shows a substantial boost in energy, charge and energy spread. The energy distribution is heavily changed. As for FEL, the energy spread, reference energy slice charge and divergence are the most important parameters and the low density ($4.5 \times 10^{18}\ cm^{-3}$) and 1 % N_2 concentration configuration presented the best results in that regard. Nonetheless, the mean divergences around the most populated energy peak is at best around 2 mrad and the energy spreads around 10 %, i.e., far from the usual used electron beams for FEL. The result seem to be comparable with experiment to certain extent.

As the experimental electron beams were far from the expected baseline parameters a new study of the transport in COXINEL with an experimental like electron beam and the effects of deviations from the ideal case was needed. In chapter 6, the transport of the experimental like and baseline beams has been compared. The experimental like beam reference slice can still be properly transported with the COXINEL line without losing charge, however, the focusing due to the initial divergence causes the emittance at the undulator to be above 1.6 times the baseline case one. A start to end simulation with Ming Xie equations to estimate the SASE FEL capabilities exhibits the impossibility of FEL with such initial electron beam parameters. I carried an extensive study of the transport degradation due to quadrupole field imperfections and initial beam parameter deviations (pointing, displacements, divergence, beam size, beam length). RMS initial divergences above 2 mrad and energy spreads superior to 2 % substantially worsens the transport increasing the total and reference slice emittance. The presence of initial beam pointing or displacement further degrades the transport and originate total charge loss. The presence of dipolar skew terms in the QUAPEVA triplet enhances the chromatic emittance growth. Small variations on the QUAPEVA triplet position or magnetic gradient can severely change the beam optics but they can be used to compensate the initial pointing and displacement of the electron beam. The possible origin of the irregularities of the observed transverse beam shape with respect to the baseline can be deduced thanks to the knowledge about the electron beam and its transport in realistic cases. Mostly the initial pointing and divergence dominate the beam transverse shape. Transverse shape measurements of different campaigns have been reproduced via simulation. The misalignment study shows the capability of the COXINEL line to adjust to highly non-ideal cases and also the capabilities of the monitoring of the beam along the transport to detect such imperfections.

The COXINEL line can act also as a electron beam diagnostic during transport thanks to its multiple imagers and integrated current transformers (ICT). Two ICTs are positioned at the start of the line and after the undulator and five imagers are after the QUAPEVA triplet, in the middle of the chicane, before and after the undulator and after the dipole dump. In chapter 7, I monitor the beam parameters along the line with the ICTs and imagers. In addition to the electron spectrometer the total charge along the line can be followed by the ICTs. The measurements exhibit a clear decrease of total charge with time due to laser degradation and around 80 % of the initial beam charge is lost during transport, corresponding to lower and higher energies with respect to the reference one. Via the ICT after the undulator, I calibrated the imagers after the undulator to

be able to measure the electron beam charge on them. A good agreement in the total charge is found between the ICT and the imagers results. The measurements after the dipole dump are the only current way to observe the reference energy slice charge going through the undulator which permits the judgment of the real capacity to generate FEL. It has been found that even though in every experimental campaign the reference slice charge increased, the value arriving at the undulator during FEL search experiments were considerably lower than the spectrometer ones due mainly to laser degradation with time. A single shot emittance diagnostic was prepared and tested during the last experimental campaign using the imager at the center of the magnetic chicane. The horizontal energy sorting of the focused electron beam at the center of the chicane permits to identify the reference slice position. By measuring the reference slice vertical size at the imager it is possible calculate the slice divergence and size at the source through the transport matrix. Therefore, the vertical emittance can be deduced. Moreover, it has been found that the transverse shape tilt observed at the middle of the chicane gives a way to determine an accurate initial vertical pointing value. The initial pointing (up to 6 mrad) is found to be able to affect the vertical size measurement but not the divergence one. So, to correct it I have made an image rotation post-treatment. The method has been validated by simulations. Experimentally, different CCD camera objectives (Sigma, Navitar and Trioptics) with different photon sensitivity and resolution have been tested and it has been found that the Trioptics one offers an emittance measurement without any apparent limitation. The mean reference slice RMS vertical divergence and size found during the last experimental campaign were 2 mrad and 6 μm leading to an average initial vertical emittance of 3.2 mm.mrad, 3 times higher than the baseline case. A SASE FEL calculation with the Ming Xie equations for a transported initial reference slice with the obtained average experimental parameters (0.27 pC/MeV, 2 mrad RMS, 3.2 mm.mrad RMS) results in a mean radiation power of the order of 10^{-28} W therefore, there was no possibility of FEL generation. The achieved capacity to properly characterize the important electron macro bunch parameters at the source and at the undulator is a milestone for LPA based FEL and can be applied to other experimental facilities.

8.2 Conclusion

The electron beam parameters significantly improved from the first RUN of COXINEL with the best recorded single-shot charge density and divergence of the reference energy slice being 2.1 pC/MeV and 3 mrad RMS at the electron spectrometer and 0.6 pC/MeV at the undulator with an emittance above 2.14 mm.mrad RMS during RUN 7. However, the beam characteristics are still far from the initial baseline capable of FEL (established from colliding pulse scheme (Section 2.3.2.5) LPA experiments) of 10.3 pC/MeV, 1 mrad RMS and RMS emittance of 1 mm.mrad. To achieve the demonstration of LPA based FEL, it became clear that the reference slice charge would need to be further improvement.

Despite the lack of FEL generation, this work presents a step forward towards the qualification of FEL generation with an LPA source. The main accomplishments here presented are:

- Through careful systematic tolerance studies in the case of electron beam realistic parameters and quadrupole misalignment a better understanding of the transversal beam dynamics has been achieved. This knowledge permits to extract more information about the beam parameters from the transverse beam shape diagnostics and to predict beam behavior further down-stream.
- The electron beam has been characterized along the transport line including measurements of emittance, electron beam charge density at the undulator and a new vertical beam pointing measurement. Such results have shown that even though the state-of-the-art LPA beam does not still meet the required performance for FEL, its properties have been successfully improved with the transport line.

The results exhibit the importance of the transport and the monitoring of the beam and are of interest not only for LPA based FEL search experiments in general but also for other LPA uses, e.g., synchrotron radiation, LPA staging. It was found that FEL amplification strongly depends on the beam parameters thus, its accurate transport and diagnosis is of great importance.

8.3 Outlook

Even though the LPA based FEL demonstration hasn't been achieved yet anywhere, some further improvements of the LPA could make it a reality in the years to come. Experiment and PIC simulations done during the thesis show that the increase of laser power yielded the most notable rise of charge density. Therefore, further increasing the laser power on target is a direct approach to improve the COXINEL experiment capabilities. The stability

of the laser being also an issue, the implementation of a feedback loop to correct the slow degradation and drift of the laser with time could considerably help in keeping the best beam possible during the FEL search. Other laboratories have realized the importance of the laser stability for such application and steps towards its improvement are being done [8], including the utilization of new computing advances in machine learning to detect the origin and necessary corrections. In the ionization injection, the beam loading and acceleration cannot be easily manipulated in a simple gas jet as a continuous injection is inherent to this scheme, however, the tailoring of the gas target density profile could offer a better control of the energy spread, energy, divergence and charge density while only requiring the addition of a carefully designed gas jet in the COXINEL experiment. As simulations show clear FEL generation with the baseline parameters, the use of the COXINEL line in a laser facility capable of using the LPA colliding scheme pulse, as initially planned, could permit the demonstration.

Chapter 9

Articles and conferences

9.1 Publications

9.1.1 First author publications

- 2020 **Espinos, D. O.**, Ghaith, A., Loulergue, A., Andre, T., Kitegi, C., Sebdaoui, M., ... & Lestrade, A. (2020). COXINEL transport of laser plasma accelerated electrons. Plasma Physics and Controlled Fusion.
- 2019 **Oumbarek Espinos, D.**, Ghaith, A., André, T., Kitégi, C., Sebdaoui, M., Loulergue, A., ... & Lestrade, A. (2019). Skew Quadrupole Effect of Laser Plasma Electron Beam Transport. Applied Sciences, 9(12), 2447.
- 2018, **Oumbarek Espinos, D.**, Zhidkov, A., & Kodama, R. (2018). Langevin equation for coulomb collision in non-Maxwellian plasmas. Physics of Plasmas, 25(7), 072307.

9.1.2 Other publications

- 2020, Roussel, E., Andre, T., Andriyash, I., Blache, F., Bouvet, F., Corde, S., **Oumbarek Espinos, D.**, ... & Kononenko, O. (2020). Energy spread tuning of a laser-plasma accelerated electron beam in a magnetic chicane. Plasma Physics and Controlled Fusion.
- 2020, Ghaith, A., **Oumbarek, D.**, Labat, M., Kononenko, O., Loulergue, A., Roussel, E., ... & Couprie, M. E. (2020, August). Characterization of undulator radiation from a compact laser plasma acceleration source. In Advances in Computational Methods for X-Ray Optics V (Vol. 11493, p. 114930Y). International Society for Optics and Photonics.
- 2020 Ghaith, A., **Oumbarek-Espinos, D.**, André, T., Roussel, E., Loulergue, A., Labat, M., ... & Couprie, M. E. (2020, July). Control of undulator radiation using a Laser Plasma Acceleration Source. In Journal of Physics: Conference Series (Vol. 1596, No. 1, p. 012045). IOP Publishing.
- 2020, Ghaith, A., Loulergue, A., **Oumbarek, D.**, Marcouillé, O., Valléau, M., Labat, M., ... & Couprie, M. E. (2020). Electron Beam Brightness and Undulator Radiation Brilliance for a Laser Plasma Acceleration Based Free Electron Laser. Instruments, 4(1), 1.
- 2019, Ghaith, A., **Oumbarek, D.**, Roussel, E., Corde, S., Labat, M., André, T., ... & Smartsev, S. (2019). Tunable High Spatio-Spectral Purity Undulator Radiation from a Transported Laser Plasma Accelerated Electron Beam. Scientific Reports, 9(1), 1-12.
- 2019, Ghaith, A., **Oumbarek, D.**, Kitégi, C., Valléau, M., Marteau, F., & Couprie, M. E. (2019). Permanent Magnet-Based Quadrupoles for Plasma Acceleration Sources. Instruments, 3(2), 27.
- 2019, Weikum, M., Koester, P., Martins, J., Mangles, S., Walczak, R., Khikhlukha, D., ... **Oumbarek Espinos, D.**, ... & Petrillo, V. (2019). JACoW: Status of the Horizon 2020 EuPRAXIA conceptual design study.
- 2019, F. Marteau, P. N' gotta, C. Benabderrahmane, A. Ghaith, M. Valleau, ⋯**D. Oumbarek**, O. Cosson, F. Forest, P. Jivkov, J. L. Lancelot and M.E. Couprie, "Variable high gradient permanent magnet quadrupole (QUAPEVA)", applied physic letters

9.2 Posters and talks

- 06/05/2019 **Talk**, "Transport of a laser plasma accelerated electron beam on COXINEL" , LPAW2019, Split, Croatia
- 04/2019 **Poster**, "Skew quadrupole effect of laser plasma electron beam transport", HEDS2019, Yokohama, Japan
- 05/2018 **Poster**, "LPA Generated Electron Bunch Transport in a Manipulation Line" , PHENIICS Fest, Paris, France
- 04/2018 **Poster**, "LPA Generated Electron Bunch Transport in a Manipulation Line" , HEDS2018, Yokohama, Japan
- 21/08/2017 **Talk**, "New method of molecular dynamics simulation method for plasma collision", National institute for quantum and radiological science and technology, Nara, Japan
- 04/2019 **Poster**, "Studies on the COXINEL transport line: strong focusing with permanent magnet quadrupoles" , HEDS2017, Yokohama, Japan

Appendix A

Variance-Covariance Matrix Method

The variance is a measure of the variation of a parameter for an ensemble of values. For n values of a parameter X the variance function is defined as:

$$\sigma^2_{(X)} = \frac{1}{n-1}\sum_{i=1}^{n}(x_i - \overline{x})^2 \tag{A.1}$$

with $\overline{x}$ the mean of the X values and i the value index. The covariance is the measure of the variation of two parameters together and it is given by:

$$\sigma(X,Y) = \frac{1}{n-1}\sum_{i=1}^{n}(y_i - \overline{y})(x_i - \overline{x}) \tag{A.2}$$

For a system of N variables a matrix of covariants $C \in \mathbb{R}^{NxN}$ can be created

$$C = \begin{pmatrix} \sigma(X_1,X_1) & \sigma(X_1,X_2) & \dots & \sigma(X_1,X_N) \\ \sigma(X_2,X_1) & \sigma(X_2,X_2) & \dots & \sigma(X_2,X_N) \\ \vdots & \vdots & \ddots & \vdots \\ \sigma(X_N,X_1) & \sigma(X_N,X_2) & \dots & \sigma(X_N,X_N) \end{pmatrix} \tag{A.3}$$

with the diagonal of C being the variance of each variable.

For a 6D phasespace (σ_x, σ'_x, σ_y, σ'_y, σ_s and σ_γ) of an electron beam one can calculate the 6x6 variance-covariance matrix:

$$C = \begin{pmatrix} \sigma(\sigma_x,\sigma_x) & \sigma(\sigma_x,\sigma'_x) & \sigma(\sigma_x,\sigma_y) & \sigma(\sigma_x,\sigma'_y) & \sigma(\sigma_x,\sigma_s) & \sigma(\sigma_x,\sigma_\gamma) \\ \sigma(\sigma'_x,\sigma_x) & \sigma(\sigma'_x,\sigma'_x) & \sigma(\sigma'_x,\sigma_y) & \sigma(\sigma'_x,\sigma'_y) & \sigma(\sigma'_x,\sigma_s) & \sigma(\sigma'_x,\sigma_\gamma) \\ \sigma(\sigma_y,\sigma_x) & \sigma(\sigma_y,\sigma'_x) & \sigma(\sigma_y,\sigma_y) & \sigma(\sigma_y,\sigma'_y) & \sigma(\sigma_y,\sigma_s) & \sigma(\sigma_y,\sigma_\gamma) \\ \sigma(\sigma'_y,\sigma_x) & \sigma(\sigma'_y,\sigma'_x) & \sigma(\sigma'_y,\sigma_y) & \sigma(\sigma'_y,\sigma'_y) & \sigma(\sigma'_y,\sigma_s) & \sigma(\sigma'_y,\sigma_\gamma) \\ \sigma(\sigma_s,\sigma_x) & \sigma(\sigma_s,\sigma'_x) & \sigma(\sigma_s,\sigma_y) & \sigma(\sigma_s,\sigma'_y) & \sigma(\sigma_s,\sigma_s) & \sigma(\sigma_s,\sigma_\gamma) \\ \sigma(\sigma_\gamma,\sigma_x) & \sigma(\sigma_\gamma,\sigma'_x) & \sigma(\sigma_\gamma,\sigma_y) & \sigma(\sigma_\gamma,\sigma'_y) & \sigma(\sigma_\gamma,\sigma_s) & \sigma(\sigma_\gamma,\sigma_\gamma) \end{pmatrix} \tag{A.4}$$

The square root of the variance-covariance matrix diagonal (in red) gives the RMS values of each variable for the electron beam.

Appendix B

Spectrometer calibration

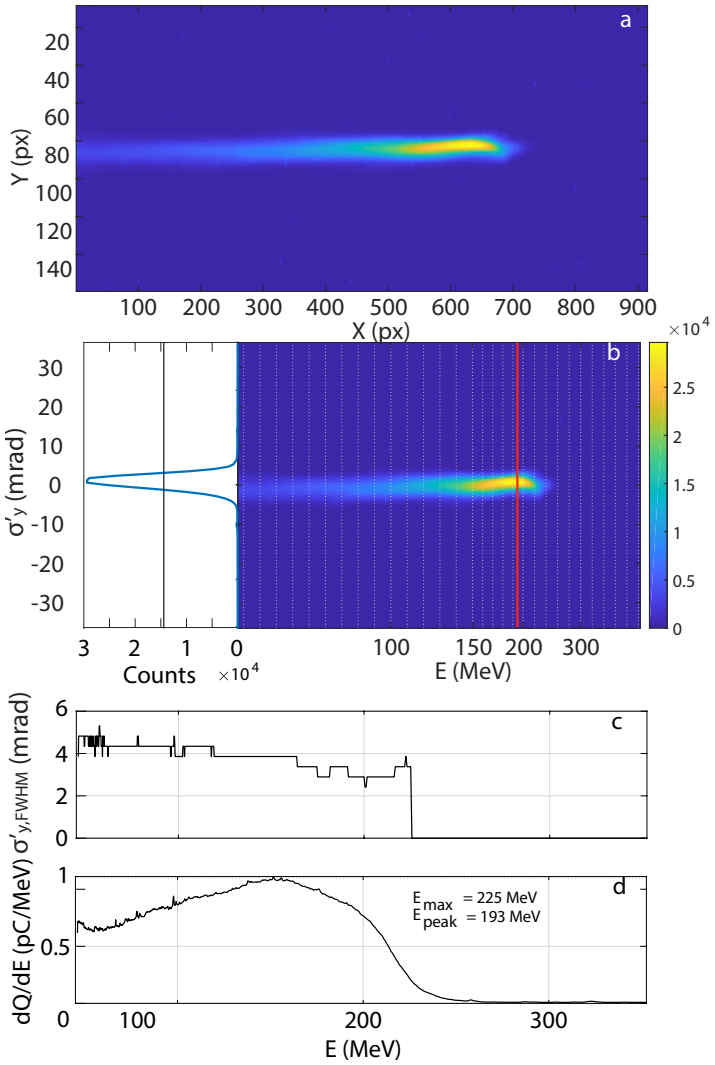

FIGURE B.1: 2020/09/14 set 1 shot 1 (a) raw image captured the by the CCD camera at the electron spectrometer, (b) after axis calibration and measured vertical divergence projection corresponding to the red vertical line, (c) vertical divergence per energy slice and (d) energy distribution.

Figure B.1a shows an example of an experimental raw image before calibration. The camera pixel to mm factor α is found by imaging a ruler. Measuring the distance from the gas jet to the screen $L_{jet/screen}$ (Figure 3.26) and by considering the source as a point ($\sigma_{y,0} = 0$), one can calibrate the vertical axis of the image to divergence in mrad as:

$$\sigma'_y = \sigma_{y,pixel} * \alpha / L_{jet/screen} \tag{B.1}$$

with $\sigma_{y,pixel}$ the pixel vertical size. Under the same point-source assumption and calculating the electron horizontal path through the dipole per energy (Equation 3.25), one can deduce the horizontal pixel to electron energy calibration is calibrated as shown in Figure B.1b, with the vertical slice projection for the reference energy 176 MeV enabling to evaluate the FWHM slice vertical divergence for each 1 MeV slice. Figure B.1c presents the resultant slice vertical divergence per energy. An approximation of the vertical beam divergence can be deduced via the weighted mean of the 1 MeV slice vertical divergences. The weights are based on the charge of the slices. Then, a median filter is applied to the image and a noise of ≈ 125 counts, previously measured without electron beam, is subtracted from the image. The count to pC factor is calibrated by imaging the screen being affected by a known radioactive source [245]. The total charge per energy slice distribution is then calculated via the count/pC factor (Figure B.1d). The energy resolution of the spectrometer varies for different energies due to the non linear proportionality of ρ on the electron energy (Equation 3.25). Figure B.2 presents the pixel to energy calibration of the spectrometer image taken by the CCD camera in the case of RUN 7 (2020/09/01 - 2020/09/25). Due to the different curvature per energy the spectrometer offers a higher resolution in the lower energies (Figure B.1b) [207]. Energies under 50 MeV cannot arrive to the lanex imager, thus, are not seen by the spectrometer.

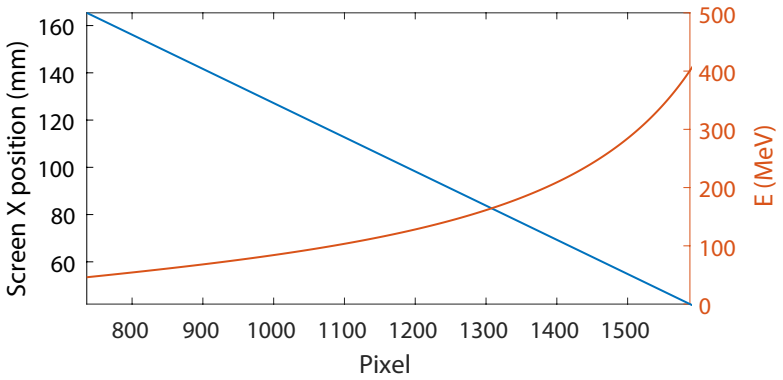

FIGURE B.2: Electron spectrometer lanex screen calibration from pixel to mm and electron energy MeV as of RUN 7

The calibrations are done considering that the electron beam goes through the line reference trajectory. If the beam horizontal position before the dipole is shifted it could affect the energy position in the spectrometer screen. A shift of 0.15 mm (i.e., 1 pixel) in the horizontal position on the lanex screen causes an energy axis shift from 0.12 MeV for the lower energies to 3.17 MeV for the higher energies. For the reference energies 176 MeV or 151 MeV, a horizontal shift from the reference trajectory of $\Delta\sigma_{x,spectro} = 0.4$ mm causes an spectrometer energy axis position shift of ≈ 1 MeV.
If the initial beam presents a horizontal pointing of $\sigma'_{x,point}$, the drift from the source to the screen yields a horizontal position shift of:

$$\sigma_{x,spectro} = \sigma_{x,0} + (\sigma'_{x,0} + \sigma'_{x,point}) * L \tag{B.2}$$

with L the drift length (Equation 2.136, neglecting any dipole magnetic field variation caused by changes in the horizontal position. For example, for $L = 200$ mm, $\sigma'_{x,point} = 2$ mrad, reference energy 151 MeV and the calibration in Figure B.2, the screen position shift due to the pointing from a zero pointing case is $\Delta\sigma_{x,spectro} = 0.4$ mm, i.e., an energy axis shift of ≈ 1 MeV. The slice charge change due to an error of 1 MeV in the position of the reference energy depends on the beam energy distribution shape. For a large energy spread broad Gaussian or flat top like energy distribution such error is negligible, but, for distributions presenting a peak around the reference energy, the error could be considerable.

Appendix C

"First imager" data treatment and analysis

The data from the spectrometer gives for each shot an approximate charge of the electron bunch, energy distribution of the electrons and the energies slices vertical divergence σ'_y. Nevertheless, the information about the horizontal divergence σ'_x cannot be measured directly. In direct observation of the LPA beam, one can see at the "first imager" (60 cm after the source) the electron beam after propagation through a drift (Chapter 3, Section 3.1.1.3.1), and the size evolution is given by Equation 2.136. Let L_d be the drift length, considering the initial size as much smaller than the size after propagation to the "first imager" ($\sigma_{x,beam}(Source) \approx \sigma_{y,beam}(Source) \ll \sigma_{y,x,beam}(img1)$), the expression for the horizontal and vertical beam sizes at the "first imager" $\sigma'_{x,y,beam}(img1)$ becomes:

$$\begin{aligned} \sigma_{x,beam}(img1) &\approx \sigma'_{x,beam}(Source)L_d \\ \sigma_{y,beam}(img1) &\approx \sigma'_{y,beam}(Source)L_d \end{aligned} \tag{C.1}$$

with the index $img1$ and $Source$ indicating the values at the "first imager" and the plasma-vacuum interface respectively. In addition, the source divergences can be related via a ratio between the transversal sizes at the "first imager":

$$\begin{aligned} \frac{\sigma_{x,beam}(img1)}{\sigma_{y,beam}(img1)} &\approx \frac{\sigma'_{x,beam}(Source)}{\sigma'_{y,beam}(Source)} \\ \sigma'_{x,beam}(Source) &\approx \frac{\sigma_{x,beam}(img1)}{\sigma_{y,beam}(img1)}\sigma'_{y,beam}(Source) \end{aligned} \tag{C.2}$$

Therefore, both divergences and a relation between them can be evaluated from the "first imager". The method with the approximation done in Equations C.1 and C.2 is tested in a numeric case.

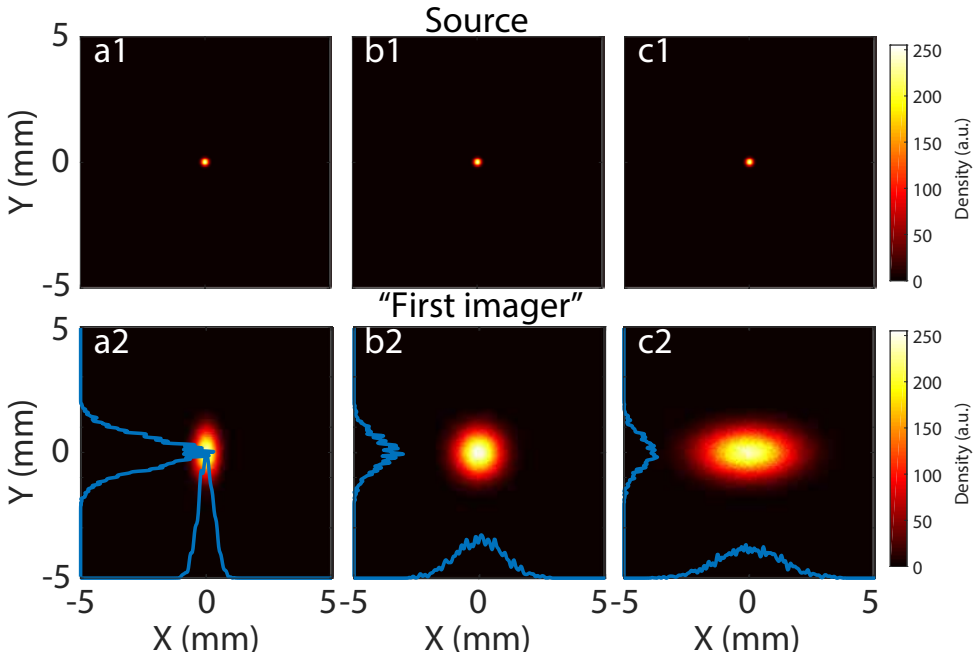

FIGURE C.1: Simulated transport of the electron beam at the source (a1-c1) and at the "first imager" (a2-c2) for $\frac{\sigma'_{x,beam}}{\sigma'_{y,beam}} = 0.5$ (a), 1 (b) and 2 (c). The initial beam used is the one in Figure 3.3a with $\epsilon_{RMS} = 1$ mm.mrad, $\sigma'_{y,RMS} = 1$ mrad, $\sigma_s = 1\ \mu m$ and $\sigma_\gamma = 15$ %.

After simulating the propagation of the beam shown in Figure 3.3a (Chapter 3, Section 3.1.1.3.1) in the cases of initial $\frac{\sigma'_{x,beam}}{\sigma'_{y,beam}} = 0.5$, 1 and 2 as shown in Figure C.1, the FWHM sizes of the projections of the horizontal line and vertical line at the beam center ($X = 0$ and $Y = 0$ respectively in this case) are calculated. The change of the ratio can be clearly visually appreciated in the beam size on the simulated "first imager". Table C.1 shows the results of the "first imager" for the simulations shown in Figure C.1. A good agreement is found between the input ratios and divergences and the ones deduced from the "first imager". Thus, the method seems to give accurate enough results with the approximation used in Equations C.1 and C.2.

Figure	$\sigma'_{x,source}$ mrad RMS	$\sigma'_{y,source}$ mrad RMS	$\sigma_{x,IMG1}$ mm FWHM	$\sigma_{x,IMG1}$ mm FWHM	$\sigma'_{x,source,deduced}$	$\sigma'_{y,source,deduced}$ mrad RMS	$\frac{\sigma'_{x,IMG1}}{\sigma'_{y,IMG1}}$ mrad RMS
C.1a	0.5	1	0.72	1.38	0.49	0.93	0.52
C.1b	1	1	1.5	1.46	1.01	0.99	1.02
C.1c	2	1	2.76	1.44	1.86	0.97	1.92

TABLE C.1: Deduced beam divergences and $\frac{\sigma'_x}{\sigma'_y}$ at the "first imager" for the simulated cases at Figure C.1

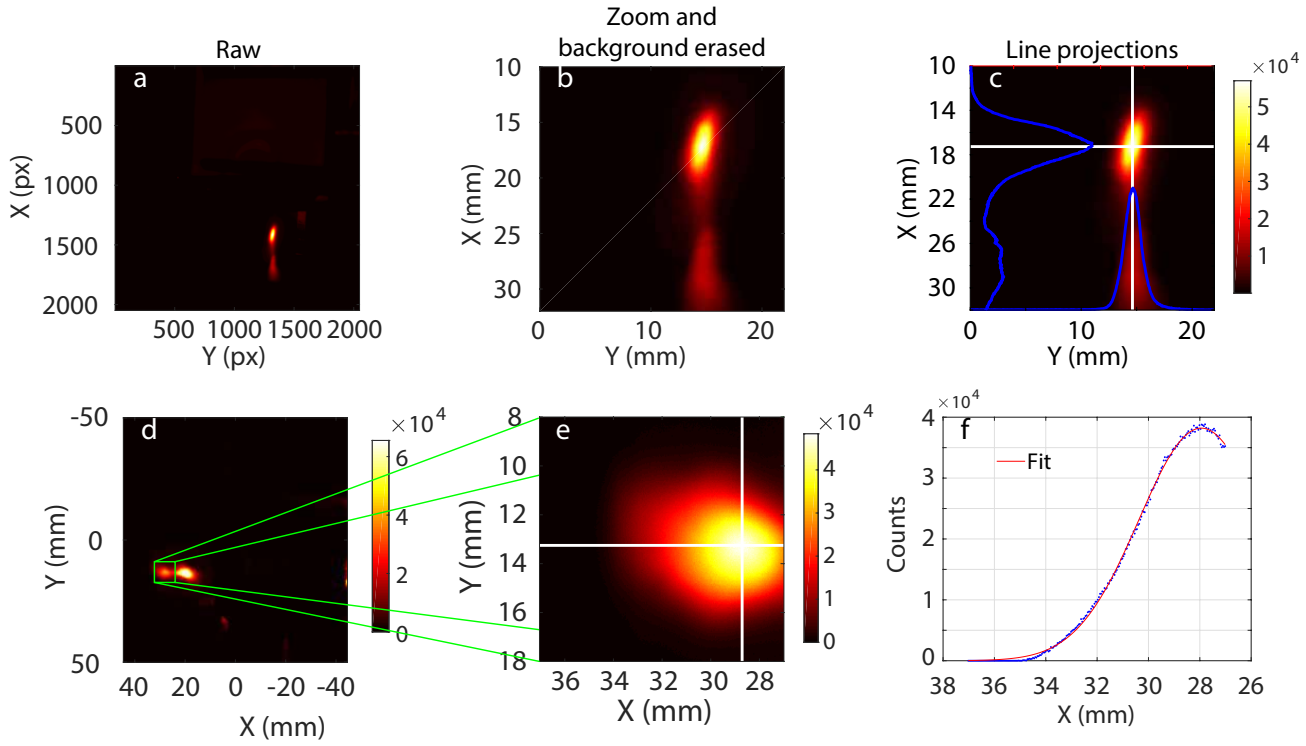

FIGURE C.2: Experimental measurement at the "first imager" corresponding to (a, b, c) shot 3 of the 2020/09/04 11:11:08 set and to (d, e, f) shot 6 of the 2020/09/23 12:42:18 set. (a, d) Shows the raw image, (b, e) the image zoomed around the beam and after background treatment and (c, f) presents in addition the vertical and horizontal projections passing through the beam center and (f) the Gaussian fit.

Experimentally, the "first imager" is back imaged by a CCD camera (Chapter 3, Section 3.2.3.1.4) and the image obtained has to be rotated by 90° to correspond to the real horizontal and vertical directions (Figure C.2a). Firstly, the background is treated by calculating the average count per pixel from a 50x50 pixels zone without beam (or any anomalies), and subtracting this value to all pixels (Figure C.2b). Then, a Gaussian filter is applied. After, by using a 10x10 pixel size box, the zone of maximum average intensity is found, giving the main beam center (Figure C.2c). Finally, the FWHM beam size is calculated from the vertical and horizontal line projections (Figure C.2c). Figure C.2 measured divergence ratio is 2.49 and the FWHM beam horizontal (vertical) divergence is 6.56 mrad (2.64 mrad). In numerous occasions, two beams are observed on the "first imager" (Figure C.2d). When the two beams can be clearly separated, one can consider that the most focused one should correspond to the energy of interest and higher energies (Figure C.2e), because the lower energies have a higher divergence (Section 5.2) and after the LPA system optimization, the energies equal or higher to the reference one are the ones with low divergence. Due to the closeness of both beams, the tail of the horizontal projection is not always visible, making difficult a direct deduction of the FWHM size. In such cases, the visible projection is fitted with a Gaussian and the FWHM size is calculated from the fit (Figure C.2f). For this shot the measured divergence ratio is 1.45 and the beam horizontal (vertical) divergence is 8.28 mrad (5.7 mrad).

Appendix D

Simulation validation of the single-shot emittance measurement in experimental conditions

Experimentally the diagnostic presents multiple limitations in addition to the resolution like noise and quantum efficiency. An study of the experimental diagnostic configurations available and the effect of noise is realized in this section.

D.1 Experimental level noise

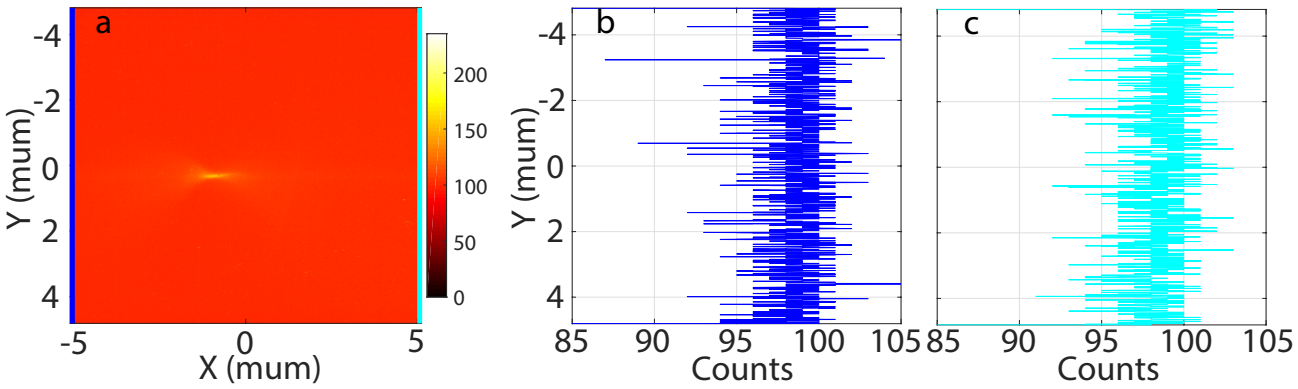

FIGURE D.1: (a) Measurement at imager "chicane" taken the 2020/09/25 at 14:22:23 after a median filter, (b, c) 1 pixel vertical slice projection of the first (dark blue) and last (cyan) slice of the image.

Figure D.1a presents a measurement at imager "chicane", where the camera shows a random noise between ≈ 93 and ≈ 104 counts with an average of 98 counts (Figure D.1b,c). The minimum counts of ≈ 93 is due to the camera sensor. The noise could affect the measurements, especially for objectives with a low efficiency.

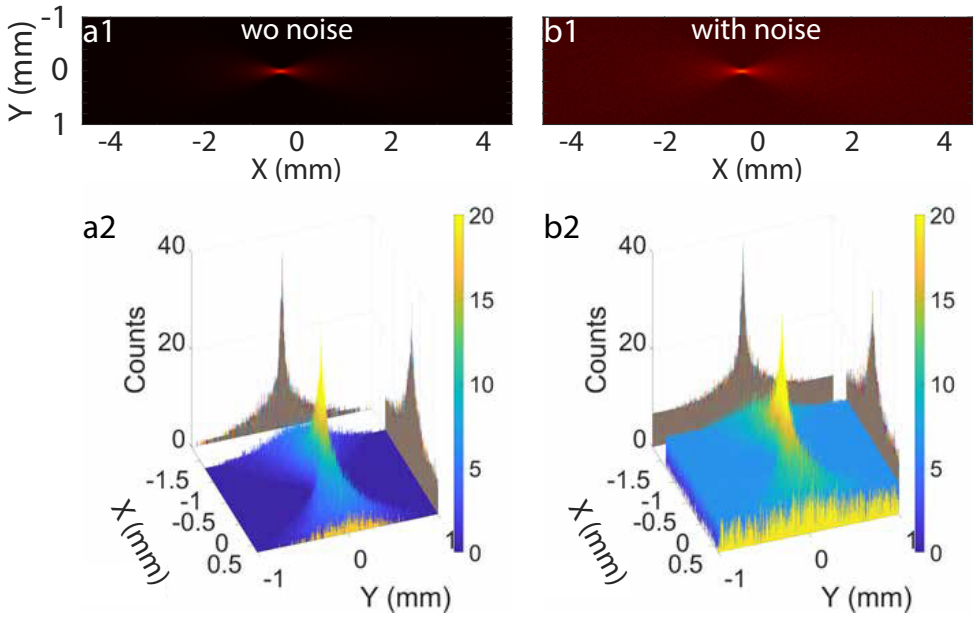

FIGURE D.2: Figure 7.4 simulated beam transport to imager "chicane" (a) without and (b) with random noise between 0 and 7 counts. Initial parameters; $\epsilon_{RMS} = 1$ *mm.mrad*, $\sigma'_{RMS} = 1.5$ *mrad*, $\sigma_{RMS} = 1$ μm, $\sigma_\gamma = 40$ %, reference energy of 151 MeV and "slit-undulator" optics. "Low resolution" case (2.3 μm/grid-unit horizontal x 2.5 μm/grid-unit vertical) for imager "chicane".

In order to test the noise effect on the measurement, a noise between 0 and 7 counts is added to the simulated transport at imager "chicane" (Figure D.2). Figure D.2b2 shows how the noise drowns the intensity of the wings of the beam. To treat this background noise, a vertical line-by-line approach has been taken. At each 1 grid-unit width vertical slice of the image, an average count per grid-unit is calculated from top and bottom column grid-units, so that the grid-units representing the beam intensity can be avoided as much as possible. Then, the average of each line is subtracted from the same line grid-units.

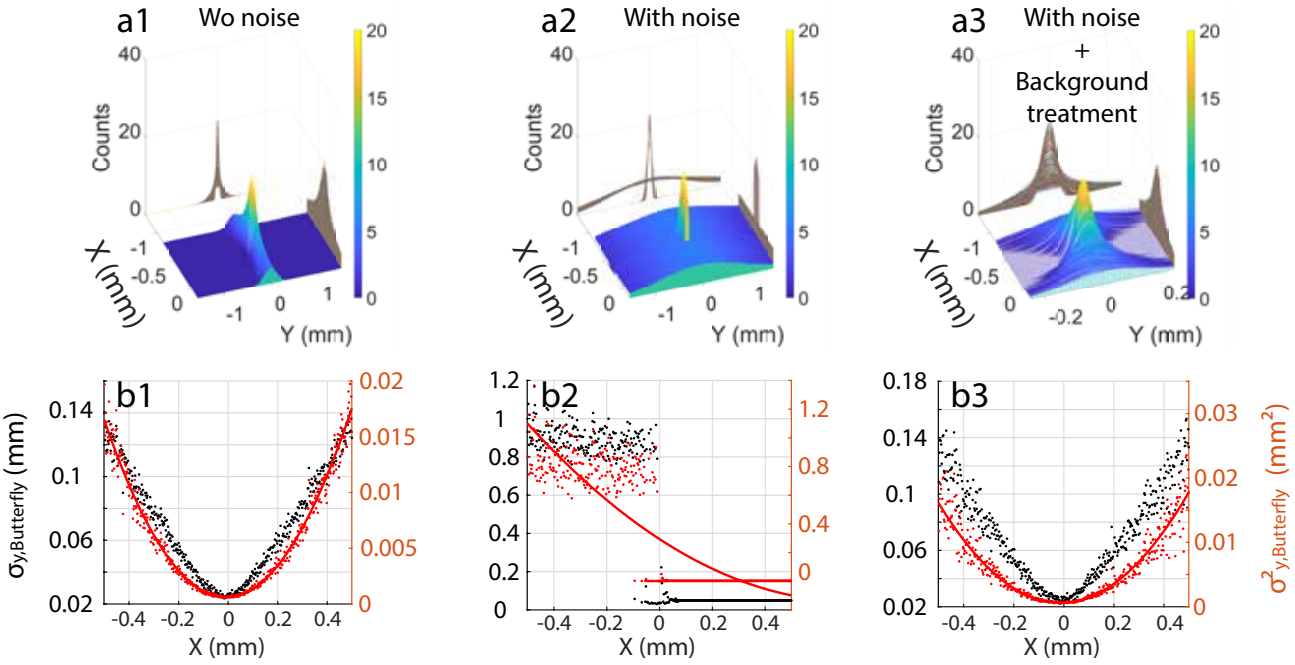

FIGURE D.3: (a1-a3) Simulated transported beam at imager "chicane" and (b1-b3) vertical slice size using the Gaussian fit method (a1-b1) without (a2-b2), with noise (random between 0 to 7 counts) and (a3-b3) with noise plus line by line background treatment. Initial parameters; Figure 7.4, $\epsilon_{RMS} = 1$ *mm.mrad*, $\sigma'_{RMS} = 1.5$ *mrad*, $\sigma_{RMS} = 1$ μm, $\sigma_\gamma = 40$ %, reference energy of 151 MeV and "slit-undulator" optics. The "low resolution" case (2.3 μm/grid-unit horizontal x 2.5 μm/grid-unit vertical) for imager "chicane" with noise between 0 and 7 counts.

Figure D.3 compares the Gaussian fit method without (Figure D.3a1, b1), with noise (Figure D.3a2, b2) and with noise plus background treatment (Figure D.3a3, b3) in the "low resolution" case (Figure 7.6b). Table D.1 shows the obtained vertical divergence $\sigma'_{y,chicane,RMS}$ and size $\sigma_{y,chicane,RMS}$ values at the source. When noise is added to the image (Figure D.3a2), the Gaussian fit is incapable of identifying the beam signal, with the exception of the most focused zone, as expected. Thus, the Gaussian fits are broad and the resulting $\sigma'_{y,chicane}$ and $\sigma_{y,chicane}$ values are nowhere close (Figure D.3b2, Table D.1) to the values at the source. If after the addition of noise, the image background is treated line-by-line and then the Gaussian fit is done (Figure D.3a3), the results improve substantially (Table D.1). One can still see a broader fit at the wings, nevertheless, around a horizontal aperture of 0.5 mm (Figure D.3b3), the vertical size measurements are close to the case without noise (Figure D.3b1). For the Gaussian fit with low resolution case of the imager (Figure 7.6b), noise can be countered effectively with a background treatment, but, for horizontal apertures above 1 mm the accuracy is affected.

Noise	Figure	$\sigma'_{y,chicane,RMS}$ (mrad)	$\sigma_{y,chicane,RMS}$ (μm)
	7.4a, b, c (Source)	1.49	2.15
Without noise	D.3a	1.53	2.22
With noise	D.3b	6.2	45.4
With noise + background treatment	D.3c	1.51	2.36

TABLE D.1: Simulated transported beam at imager "chicane" vertical divergence and size obtained using the gaussian fit method without noise, with noise (0 to 7 counts) and with noise coupled to a line by line background treatement. Initial parameters; Figure 7.4, $\epsilon_{RMS} = 1$ *mm.mrad*, $\sigma'_{RMS} = 1.5$ *mrad*, $\sigma_{RMS} = 1$ μm, $\sigma_\gamma = 40$ %, reference energy of 151 MeV and undulator slit optics. The "low resolution" case (2.3 μm x 2.5 μm) for imager 2 with noise between 0 and 7 counts.

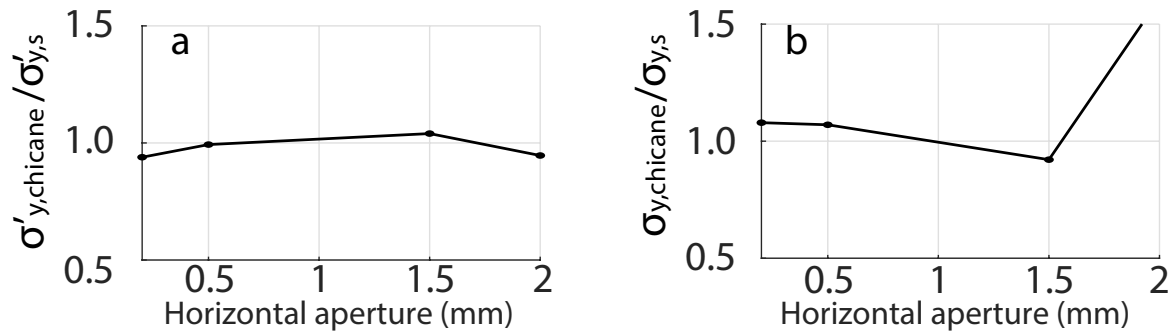

FIGURE D.4: (a) $\sigma'_{y,chicane}/\sigma'_{y,s}$ and (b) $\sigma_{y,chicane}/\sigma_{y,s}$ deduced results from the simulated imager "chicane" transport for the low resolution case (2.3 μm/grid-unit horizontal x 2.5 μm/grid-unit vertical), with artificial noise between 0 and 7 counts per grid-unit and background treatment. Initial parameters; Figure 7.4, $\epsilon_{RMS} = 1$ *mm.mrad*, $\sigma'_{RMS} = 1.5$ *mrad*, $\sigma_{RMS} = 1$ μm, $\sigma_\gamma = 40$ %, reference energy of 151 MeV and undulator slit optics.

Figure D.4 shows the $\sigma'_{y,chicane}/\sigma'_{y,s}$ and $\sigma_{y,chicane}/\sigma_{y,s}$ for the Gaussian fit method with (0 to 7 counts) noise for the low resolution case (2.3 μm/grid-unit horizontal x 2.5 μm/grid-unit vertical). The Gaussian fit, after background treatment is able to get accurate results for horizontal apertures of less or equal 1.5 mm, with a maximum difference from the source values of 4 % and 8 % for the vertical divergence $\sigma'_{y,chicane}$ and size $\sigma_{y,chicane}$ respectively (see Figure D.4c, d).

The noise can drown the signal, especially at the butterfly wings but, can be compensated by a line-by-line background treatment. Taking into account the resolution limit introduced by the YAG screen with the Sigma lens (Chapter 3.2.3.1.4.1), the experimental resolution is lower than the low resolution case (Figure 7.6b) used for these simulations. Thus, experimentally the utilization of the Gaussian fit method to measure $\sigma_{y,butterfly}$ should offer a good enough accuracy for horizontal apertures of less than 1.5 mm.

D.2 Experimental diagnostic resolution and signal-to-noise ratio

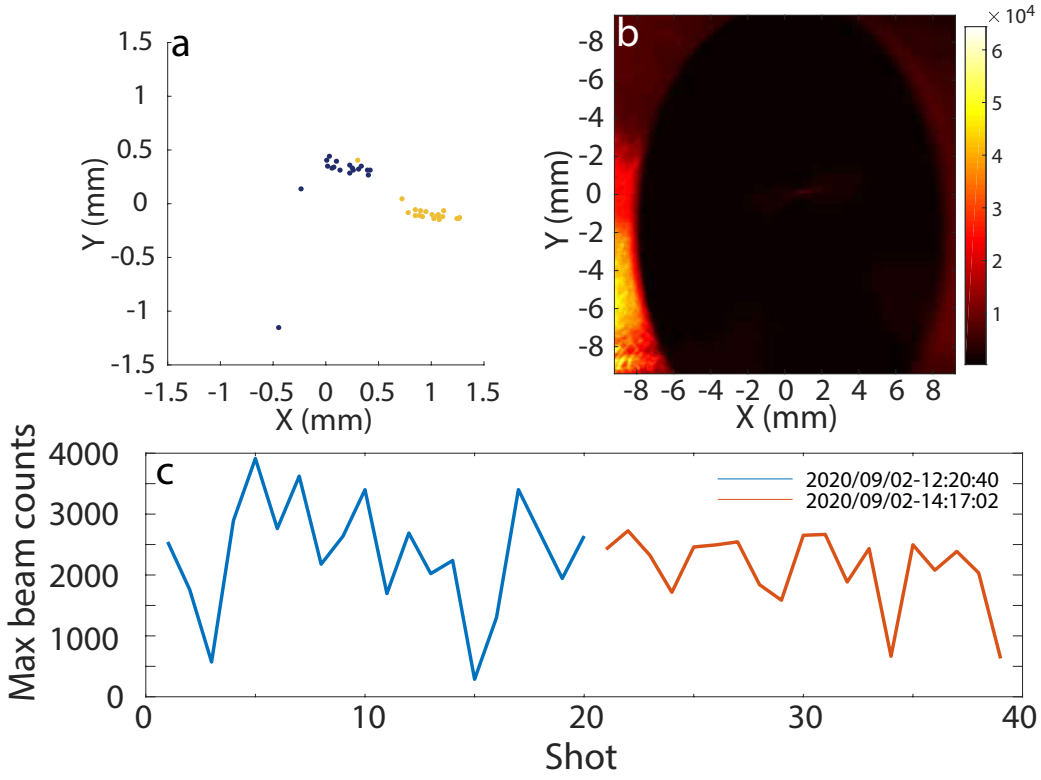

FIGURE D.5: Measured (a) position of the center of the beam taken the 2020/09/02 at 12:20:40 and 14:17:02 and (b) field of view using the Sigma lens in the beam at imager "chicane" of the first shot of the set 2020/09/02 at 12:20:40. (c) Maximum counts per pixel in the beam at imager "chicane" with the Sigma Macro lens during taken the 2020/09/02 at 12:20:40 and 14:17:02.

The resolution can be increased by a rise of the magnification, that can be achieved by changing the lens in front of the camera (Table 3.16). Imager "chicane" setup until RUN 7 used the Sigma Macro lens with a field of view of 17x17 mm (Figure D.5b), however, after the electron transport optimization (BPAC), the electron beam stays inside an area below 2x2 mm (Figure D.5a), thus, lower FOV lenses can be used.

The efficiency of the objectives, defined as the counts per time per surface, should also be taken into account. Figure D.5c presents the maximum pixel counts in the beam measured with the Sigma Macro lens, the average counts of all days is $\approx$ 2700, with a maximum achieved of 4000 counts and a minimum of 350 counts. The efficiency of the TRIOPTIC objective (Apo Rodagon D 120) is one order of magnitude smaller than the Sigma [218] (Table 3.16), so, it should be still enough for measurements. By using the TRIOPTIC lens at minimum zoom one can image an area big enough to not lose the beam under normal circumstances and decrease σ_{opt}. In this case, the 30 μm caused by the σ_{gran} of the YAG screen becomes the limiting factor of the resolution. For the NAVITAR lens case the efficiency is close to 2 orders of magnitude lower, therefore, the signal-to-noise ratio is expected to be low with possibilities to drown the beam signal in the noise.

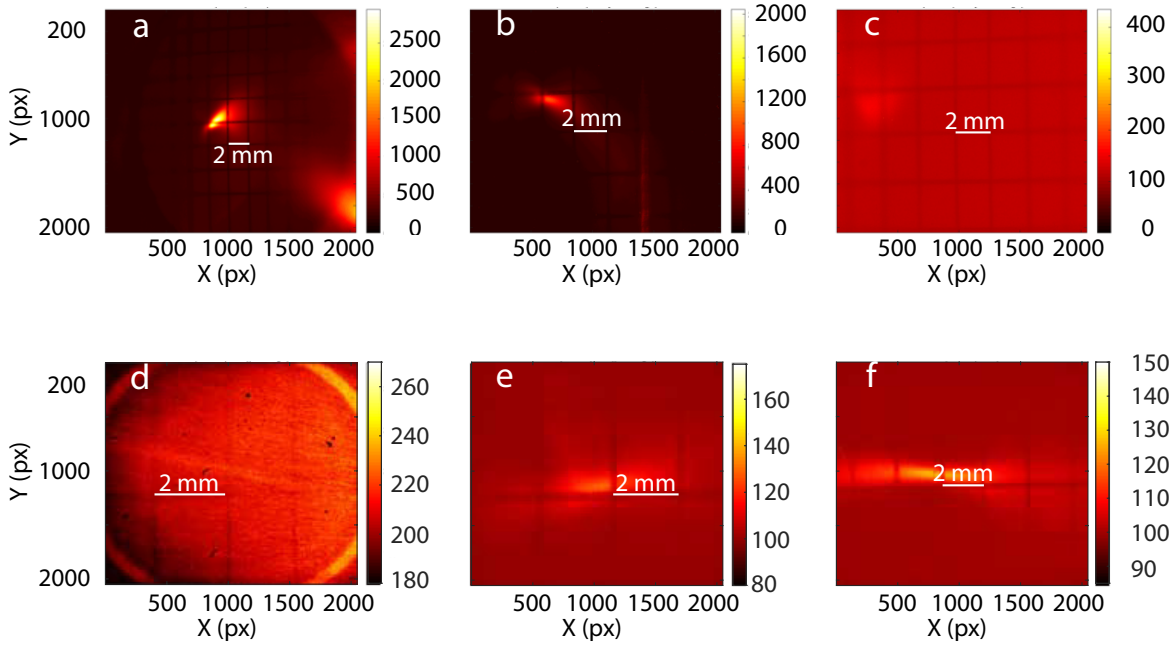

FIGURE D.6: Imager "chicane" calibration with a Lanex screen for the (a) Sigma lens (shot 8 of set 2020/09/02 14:20:14), (b) Trioptic lens first configuration (shot 10 of set 2020/09/02 14:48:09), (c) Trioptic lens third configuration (shot 2 of set 2020/09/02 15:29:34), (d) Navitar lens first configuration (shot 3 of set 2020/09/02 16:06:25), (d) Navitar lens second configuration (shot 6 of set 2020/09/03 17:24:44) and (f) Navitar lens third configuration(shot 3 of set 2020/09/03 14:19:42) during RUN 7.

During the entirety of RUN 7, the three different macro lenses were used (Table D.2). The Trioptic and the Navitar (Table D.2) permit to adjust the level of zoom, so, three configurations of each were tested. Figure D.6 presents the calibration data from pixel to μm using a lanex screen with 2 mm x 2 mm squares pattern. As the exact square size is known, one can deduce the real size of an image pixel. The Sigma presents the lowest resolution (8.5 μm x 9.2 μm) (Figure D.6a). The Trioptic has a much better resolution in both axis in all its configurations, with factors going from 5.2 to 5.0 μm (4.7 to 4.1 μm) horizontally (vertically) (Figure D.6b, c; Table D.2). The Navitar gives the best resolution (2.6 μm x 2.4 μm; 2.6 μm x 2.4 μm), achieving half of the best Trioptics factor (5 μm x 4.6 μm), in its most zoomed configuration (Figure D.6d, e; Table D.2). Due to the small area imaged by the Navitar zoomed configuration, a third less zoomed Navitar configuration was tested with a factor of 3.8 μm (4.1 μm) in the horizontal (vertical) direction (Figure D.6f).

Objective	Config	Dates (2020)	Calibration					S/N
			μm per px		M_{opt}		efficiency	
			Horizontal	Vertical	Horizontal	Vertical	$Counts/ms/mm^2$	
Sigma	S1	Start of RUN 7 - 9/02 14:17:02	8.5	9.2	0.42	0.17	0.9	21.69
Trioptic	S1	9/02 14:18:09 - 9/02 14:50:53	5.2	5.1	0.97	0.31	0.15	6.23
Trioptic	S2	9/02 15:29:34 - 9/02 15:18:31	5	4.6	1.01	0.34	0.15	6.26
Trioptic	S3	9/10 15:53:53 - End of RUN 7	5	4.7	1.01	0.33	0.15	2.47
Navitar	S1	9/02 16:06:25 - 9/02 17:09:54	2.6	2.4	1.94	0.65	0.02	1.25
Navitar	S2	9/02 17:24:44 - 9/02 17:49:39	2.6	2.4	1.94	0.65	0.02	1.22
Navitar	S3	9/03 14:19:42 - 9/04 16:24:19	3.8	4.1	1.33	0.38	0.02	1.25

TABLE D.2: Macro lenses and configurations used during RUN 7 with their respective horizontal and vertical size per pixel and M_{opt}, efficiency and maximum signal to noise ratio S/N and the dates during which they were used.

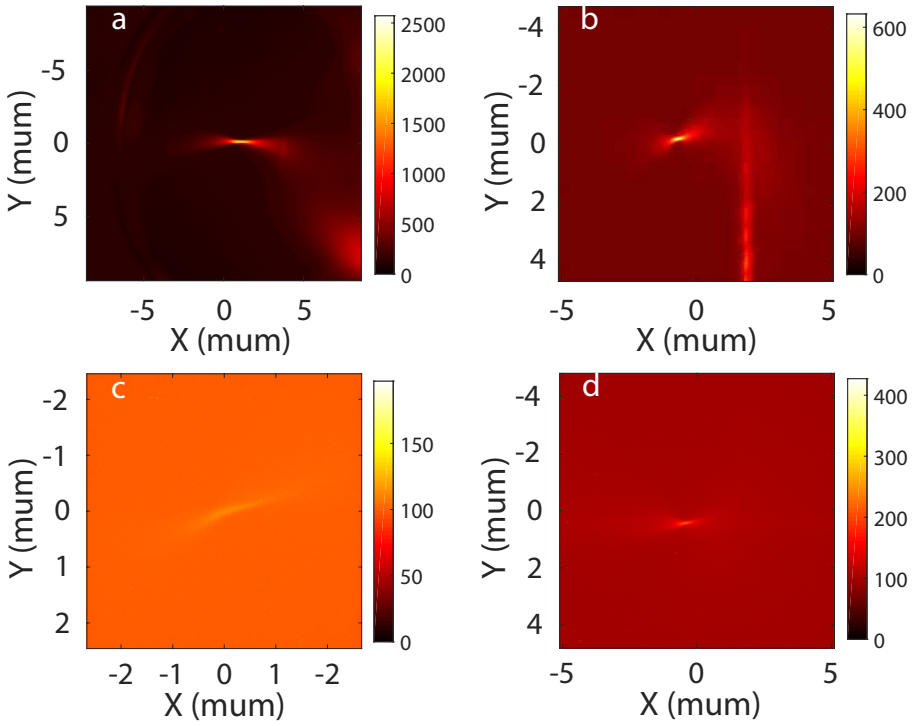

FIGURE D.7: Imager "chicane" measured during experiment with the (a) Sigma lens (shot 1 2020/09/02 12:20:40), (b) Trioptic first (shot 1 2020/09/02 15:18:31) and (d) third (shot 2 2020/09/02 17:38:28) configurations and (c) Navitar second configuration (2020/09/16 17:48:58) lenses (Table D.2, Figure D.6).

Table D.2 presents the efficiency and maximum beam signal-to-noise ratio for each lens configuration. The Sigma Macro lens has the highest efficiency [246] ($\approx 0.8\ Counts/ms/mm^2$) (Figure D.7a) and a signal-to-noise ratio of 21.69. The Trioptics efficiency is around an order of magnitude lower [246] ($\approx 0.15\ Counts/ms/mm^2$) than the Sigma Macro one. The signal-to-noise ratio is around 6.24, around 3.5 times lower than the Sigma Macro. For the third configuration of the Trioptics, a filter added in front of it to clean some parasitic light, reduced the efficiency to levels closer to the Navitar (Figure D.7d), resulting in a signal-to-noise ratio of 2.47. The Navitar shows the lowest efficiency, with close to two orders of magnitude less than the Sigma Macro [246] ($\approx 0.01\ Counts/ms/mm^2$) (Figure D.7b, c). The efficiency is also the lowest with a signal-to-noise ratio of 1.25.

The Sigma Macro offers the best signal to noise ratio S/N in expenses of the resolution while the Navitar has a high resolution but with a low efficiency (signal to noise ratio is of only 1.25). The Trioptics presents a middle ground, high resolution and signal-to-noise levels superior to 2.4, enough to separate the beam from the noise.

D.3 Simulation validation with an experimental like beam

The energy distribution of the beam being experimentally not Gaussian (Chapter 4), it is appropriate to check if the results with the Gaussian beam simulation hold true for a realistic beam energy distribution. In the following section, the emittance measurement method at imager "chicane" is studied with a realistic energy distribution and divergence beam taking into account the camera noise and resolution. The considered electron beam (Figure D.8a,b,c) is averaged from 20 shots measured at the electron spectrometer, with $\epsilon_{RMS} = 1\ mm.mrad$, $\sigma'_{RMS} = 1.5\ mrad$, $\sigma_{s,RMS} = 1\ \mu m$. After generating a 6D phasespace using these parameters with 5×10^5 particles, the covariant matrix method gives 1.46 mrad (3.44 mrad) and 3.19 μm (7.52 μm) RMS (FWHM) respectively for the 151 ± 0.5 MeV slice for the initial distribution at the source. Propagating this beam to imager "chicane" with the slit optics results in Figure D.8d,e.

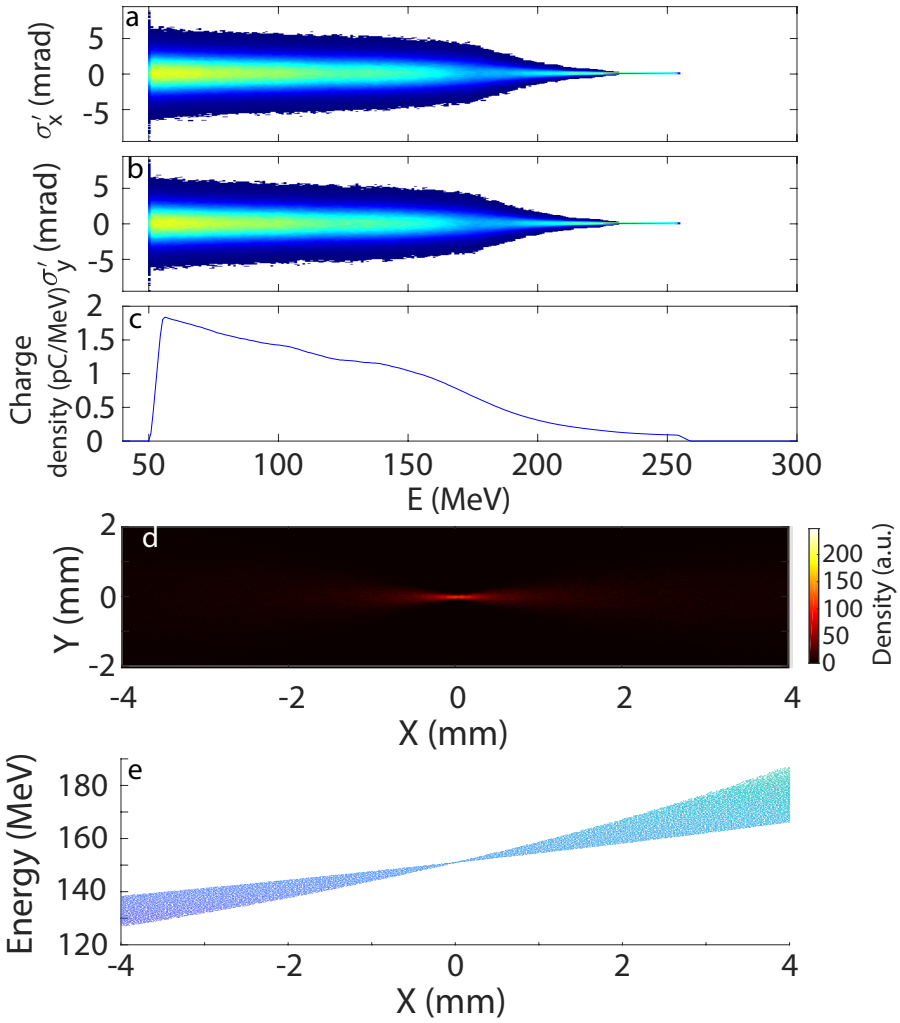

FIGURE D.8: Initial beam's (a, b) divergence and (c) energy distribution used, calculated from an average of 20 experimental shots. Simulated transport (d) result at imager "chicane" and (e) energies horizontal positions with the "slit-undulator" optics. Initial parameters; $\epsilon_{RMS} = 1$ *mm.mrad*, $\sigma'_{RMS} = 1.5$ *mrad*, $\sigma_{RMS} = 1$ μm and reference energy of 151 MeV.

The simulated transported beam at imager "chicane" is analyzed for the Gaussian fit with the imager "chicane" resolutions of 1x1 μm/grid-unit, 2x2 μm/grid-unit, 2.3x2.3 μm/grid-unit and 4.6x4.6 μm/grid-unit. Table D.3 shows the results of the vertical divergence $\sigma'_{y,chicane}/\sigma'_{y,s}$ and size $\sigma_{y,chicane}/\sigma_{y,s}$ ratios for the fixed horizontal aperture 0.5 mm. The Gaussian fit gives accurate results for both ratios in all resolutions. The worst case of divergence and size are 1.06 and 1.10 respectively.

	Without noise		With noise	
$\sigma_{y,x,res}$ μm/grid-unit	$\sigma'_{y,chicane,RMS}$ $(\sigma'_{y,chicane}/\sigma'_{y,s})$	$\sigma_{y,chicane,RMS}$ $(\sigma_{y,chicane}/\sigma_{y,s})$	$\sigma'_{y,chicane}/\sigma'_{y,s}$	$\sigma_{y,chicane}/\sigma_{y,s}$
1	1.44 (0.99)	3.51 (1.10)	0.67	1.09
2	1.46 (1.00)	3.51 (1.10)	0.43	1.18
2.3	1.55 (1.06)	3.41 (1.07)	1.05	1.08
4.6	1.46 (1.00)	3.48 (1.09)	0.91	1.11

TABLE D.3: $\sigma'_{y,chicane}/\sigma'_{y,s}$ and $\sigma_{y,chicane}/\sigma_{y,s}$ results from the simulated imager "chicane" transport for horizontal aperture 0.5 mm, for the resolutions of 1 μm/grid-unit, 2 μm/grid-unit, 2.3 μm/grid-unit and 4.6 μm//grid-unit, the Gaussian fit method and withou, with noise up to 7 counts per grid-unit. Initial beam Figure D.8c parameters; $\epsilon_{RMS} = 1$ *mm.mrad*, $\sigma'_{RMS} = 1.5$ *mrad*, $\sigma_{RMS} = 1$ μm, reference energy of 151 MeV and "slit-undulator" optics.

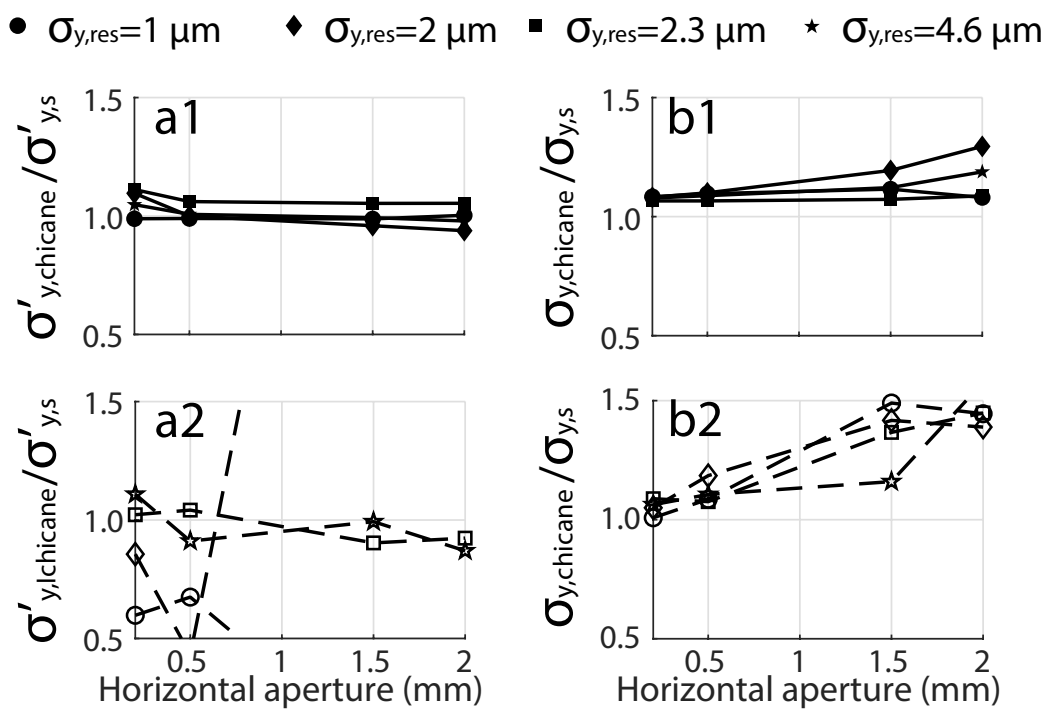

FIGURE D.9: (a) $\sigma'_{y,chicane}/\sigma'_{y,s}$ and (b) $\sigma_{y,chicane}/\sigma_{y,s}$ results from the simulated imager "chicane" transport for the resolutions 1 μm/grid-unit (circle), 2 μm/grid-unit (diamond), 2.3 μm/grid-unit (square) and 4.6 μm/grid-unit (star) and the Gaussian fit treatment method (a1, b1) without, (a2, b2) with noise up to 7 counts per grid-unit. Initial beam Figure D.8c parameters; $\epsilon_{RMS} = 1$ $mm.mrad$, $\sigma'_{RMS} = 1.5$ $mrad$, $\sigma_{RMS} = 1$ μm, reference energy of 151 MeV and "slit-undulator" optics.

Figure D.9a1, b1 shows the analysis of $\sigma'_{y,chicane}/\sigma'_{y,s}$ and $\sigma_{y,chicane}/\sigma_{y,s}$ extended to different horizontal apertures. As in the Gaussian beam case (Figure D.2), the Gaussian fit method performs well. For the vertical divergence $\sigma'_{y,chicane}$, only for resolutions larger than 2 μm, and horizontal apertures lower of equal to 0.5 mm the accuracy decreases. Regarding the vertical beam size $\sigma_{y,chicane}$ (Figure D.9b1), the Gaussian fit shows a limit in accuracy, being incapable of getting a result under 1.08. The highest resolution gives the best accuracy for the Gaussian fit. Table D.3 shows the analysis at the simulated distribution on imager "chicane" with added noise, background treatment and a 0.5 mm horizontal aperture. The Gaussian fit shows a stable and accurate result of the vertical size ratio $\sigma_{y,chicane}/\sigma_{y,s}$. The vertical divergence ratio $\sigma'_{y,chicane}/\sigma'_{y,s}$ starts giving acceptable results for vertical resolutions larger than $\sigma_{y,res} = 2.3$ μm. The initial low counts per pixel in the high resolution case mixed with the noise makes the wings of the transverse beam shape difficult to fit therefore, yielding not accurate vertical divergence values. Figure D.9a2, b2 shows the analysis of the simulated distribution on imager "chicane" with noise added extended to multiple horizontal apertures and background treatment. The noise deeply impacts the accuracy, especially for horizontal apertures larger than 0.5 mm. With background treatment, for resolutions above 2 μm/grid-unit and apertures below or equal to 0.5 mm, the Gaussian fit method achieves values between 1 and 1.10, in both $\sigma'_{y,chicane}/\sigma'_{y,s}$ and $\sigma_{y,chicane}/\sigma_{y,s}$.

For the noisy imager "chicane" case (Figure D.9a2, b2), the analysis has a lower precision compared to the same conditions for a Gaussian beam case (Figure D.4). The noise accentuates the difference between the multiple horizontal apertures and resolutions. For more complex energy distributions of the beam, horizontal apertures below or equal 0.5 mm should be used to obtain accurate results. The simulations show that the low signal-to-noise and high resolution of the Navitar lens might not be able to deliver accurate results.

Appendix E

Langevin equation for coulomb collision in non-Maxwellian plasmas (2018)

Langevin equation for coulomb collision in non-Maxwellian plasmas

Driss Oumbarek Espinos,[1] Alexei Zhidkov,[2] and Ryousuke Kodama[2,3]
[1]*Synchrotron-Soleil, Saint-Aubin, Gif-sur-Yvette 91192, France*
[2]*Photon Pioneers Center, Osaka University, 2-1 Yamadaoka, Suita, Osaka, Japan*
[3]*Graduate School of Engineering, Institute of Laser Engineering, Osaka University, 2-8 Yamadaoka, Suita, Osaka, Japan*

(Received 12 February 2018; accepted 10 July 2018; published online 26 July 2018)

The Langevin equation method is developed for the simulation of elastic collisions in non-Maxwellian plasmas by particle methods. The properties of random processes are shown to allow splitting not only of collisions between different compounds but even splitting inside a compound. The latter drastically simplifies extension of the method for colliding plasmas. The method is also verified by obtaining characteristics of runaway electron generation under an external electric field and under an external magnetic field. *Published by AIP Publishing.*
https://doi.org/10.1063/1.5025743

I. INTRODUCTION

Plasma physics is present in a grand number of phenomena that are still not yet completely understood. One of the problems of plasmas is the overwhelming number of interactions happening within them and between the plasma and external fields, which mainly give rise to two problems. The plasma is a highly nonlinear medium due to the coupling between different interactions and the different phenomena that occur at different timescales as proposed by Bogoliubov's hierarchy in which four time scales are differentiated: correlation, kinetic, hydrodynamics, and diffusion. In order to eliminate the difficulties occurring due to the nonlinearity, computer simulation is used, while the multiple time scales remain to be a challenge.

Two kinds of simulations are used, hydrodynamic and kinetic simulations. Hydrodynamic simulation is widely used for laser-matter interaction,[1] instabilities in plasmas[2] among other cases, while kinetic simulation is used for some discharge plasmas, low density plasmas, and more generally, collisional plasmas. However, lots of situations require simulations that take into account multiple timescales in order to simulate the complex plasma behavior, for example, the guiding channel creation via discharge plasma and the plasma-picosecond laser pre-pulse interaction with an external magnetic field.[3]

Research in this kind of multi-scale simulations started not long ago with different proposals, for example, the division of the computational domain (physical space) into kinetic and continuum sub-domains based on some continuum breakdown criteria[4,5] or the decomposition in velocity space, treating fast and slow particles separately.[6] But in the midst of these advances, a complete method to treat the collision between electrons, ions, and neutrals is still needed. Some methods made for gases will require extra work in order to try to adapt to plasmas, like the Direct Simulation Monte Carlo (DSMC) method.[7] The most used method to treat these collisions is the Monte Carlo Method (MCM) proposed by Takizuka and Abe,[8] however, this method reveals itself limited in multiple instances, being unable to conserve mean velocities or to provide, for example, the electron runaway flux for plasma in a constant electric field, conductivity, etc. Other studies for initial Maxwellian particle distributions have proven the shortcomings of the Monte Carlo treatment of collisions to obtain kinetic properties,[9–13] studies in which heat flux, thermalization time, and accuracy issues amongst others were shown.

In this paper, a way to simulate collision for use in particle-in-cell (PIC) and valid for non-Maxwellian distribution plasmas is given based on the Langevin Equation Method (LEM). The Langevin equation is the result of treating the dynamics of non-equilibrium systems with the theory of Brownian motion in the velocity space. In the Langevin equation, the force caused by a heat bath is expressed as the total effect of a systematic part and a fluctuating stochastic part of zero mean

$$\frac{dv}{dt} = -\gamma v + \delta F(t)$$
$$\langle \delta F(t) \rangle = 0, \quad \left\langle \delta F_i(t) \delta F_j(t') \right\rangle = 2C\delta_{ij}\delta(t-t'), \qquad (1)$$

with v being the instantaneous velocity, j and i the subindexes indicating the Cartesian component, δ being the Kronecker and Dirac deltas, respectively, C being a constant representing the importance of this fluctuating force, and $\langle \ldots \rangle$ being the average. The $\delta(t-t')$ delta function shows that there is no correlation between collisions in any distinct time intervals dt_1 and dt_2. This absence of time correlation is a consequence of the separation of time scales. Therefore, any memory between forces at different times will be forgotten due to the great number of collisions.

In order to use the LEM, both terms have to be calculated with ion and electron populations with different temperatures, which reflect the random nature of collisions in plasma in an accurate manner. The usefulness of LEM for collision simulations for near- Maxwellian electrons has been shown in Ref. 14. This technique has been used in kinetic PIC simulations.[15,16] The feasibility of LEM for non-Maxwellian plasma, consisting of various compounds, many ion components, and/or colliding plasmas, is yet to be explored.

In the first part of this paper, the Langevin collision terms for the different binary collisions are calculated for a plasma with ion temperature T_I and electron temperature T_e by using the Grad approximations for both population distribution functions (DFs), then a code based on these equations is used to simulate electron and ion collisions with and without an external field (electric and magnetic). In the last part, a method of simplification of non-Maxwellian DF is proposed and tested in simulations of collisions. Finally using this LEM, a simulation of different plasma collisions is done.

II. FOKKER-PLANCK AND LANGEVIN EQUATION LINK

The Fokker-Planck equation (FPE) is widely used to study collisional relaxation of plasmas.[11] The FPE is expressed as follows:

$$\frac{\partial \mathbf{f}}{\partial t} + \mathbf{v}\nabla \mathbf{f} + \frac{\boldsymbol{a}}{m}\nabla_{\mathbf{v}}\mathbf{f} = \left(\frac{\mathrm{d}\mathbf{f}}{\mathrm{dt}}\right)_{coll}, \tag{2}$$

with f being the particle DF, $\mathbf{v}$ the velocity, $\boldsymbol{a}$ the acceleration, m the mass, ∇ the gradient in space, $\nabla_{\mathbf{v}}$ the gradient in velocity space, and $\left(\frac{\mathrm{df}}{\mathrm{dt}}\right)_{coll}$ the collision term. The FPE describes the evolution of the DF in phase-space and time. Nevertheless, this equation is difficult to use for studying the plasma-vacuum interface; for example, for self-consistent description of laser-plasma interaction.[13] PIC simulations are far more suitable for that purpose. However, in PIC simulations, particles are treated individually, and a change in velocity space of a particle will be caused not only by the external fields but also by collisions with other particles. The equation for a charged particle can be written as

$$\frac{\mathrm{d}\mathbf{v_k}}{\mathrm{dt}} = \frac{\mathrm{q_k}}{\mathrm{M_k}}\left[\mathbf{E}(\boldsymbol{r_k}) + \frac{\mathbf{v_k}}{\mathrm{c}} \times \mathbf{H}(\boldsymbol{r_k})\right] + \mathbf{P_k}(\mathbf{v_k}), \tag{3}$$

where $\mathbf{v_k}$ is the velocity, $\boldsymbol{r_k}$ **is** the position, $\mathrm{q_k}$ is the charge, and $\mathrm{M_k}$ is the mass of the particle k. E and H are the electric and magnetic fields and $\mathbf{P_k}$ is a term describing collision between the particle k and the other species in the medium, taking into account elastic and inelastic collisions. This collisional term should be chosen in a proper way to provide conformity between a solution of FPE (2) and a sampling DF of assembly of particles moving in accordance with Eq. (3).

The collisional term in the FPE is determined by velocity correlation functions[14,17]

$$\langle \Delta v_i \rangle^{\alpha\beta}, \ \langle \Delta v_i \Delta v_j \rangle^{\alpha\beta}, \ \langle \Delta v_i \Delta v_j \Delta v_l \rangle^{\alpha\beta}, \ldots, \tag{4}$$

with $\langle \Delta v_i \rangle = \frac{1}{N}\sum_{v=1}^{N} \Delta v_{i_v}$ and α, β being the scattered and scattering particle species, respectively.

At distances of the order of the Debye length, the first two correlation functions diverge logarithmically for the coulomb case and the rest of the functions converge and are negligibly small in comparison. For this reason, only the two first correlations should be taken into account, which is interpreted as not taking into account close collisions (Fokker-Planck approximation).

The collisional term in the FPE can be written as

$$\left(\frac{\partial f_\alpha}{\partial t}\right)_{coll} = -\frac{\partial}{\partial v_i}\sum_{\beta}\left(A_i^{\alpha\beta} f_\alpha - \frac{1}{2}B_{ik}^{\alpha\beta}\frac{\partial f_\alpha}{\partial v_k}\right), \tag{5}$$

with $A_i^{\alpha\beta}$ and $B_{ij}^{\alpha\beta}$ being the called Fokker plank coefficients (FPCs). This expression describes the effects of the collisions for a particle in plasma through a stochastic differential equation (SDE) with a drag diffusion term.

The FPC $A_i^{\alpha\beta}$ describes a change of position of the distribution in velocity space and the FPC $B_{ij}^{\alpha\beta}$ describes the rate-of-change of the dimension and shape of the distribution in velocity space and their expressions are

$$\begin{aligned}
A_i^{\alpha\beta}(\mathbf{v}_\alpha) &= \lim_{\Delta t\to 0}\frac{1}{\Delta t}\langle \Delta v_i \rangle^{\alpha\beta} = N_\beta \int \mathrm{f}_\beta(\mathbf{v}_\beta) w_i^{\alpha\beta} d\mathbf{v}_\beta \\
B_{ij}^{\alpha\beta}(\mathbf{v}_\alpha) &= \lim_{\Delta t\to 0}\frac{1}{\Delta t}\langle \Delta v_i \Delta v_j \rangle^{\alpha\beta} = N_\beta \int \mathrm{f}_\beta(\mathbf{v}_\beta) w_{ij}^{\alpha\beta} d\mathbf{v}_\beta
\end{aligned} \tag{6}$$

$$w_i^{\alpha\beta} = -\frac{\mu_{\alpha\beta}}{M_\alpha}(v_{i\alpha} - v_{i\beta})|\mathbf{v_\alpha} - \mathbf{v_\beta}|\sigma_1(|\mathbf{v_\alpha} - \mathbf{v_\beta}|)$$

$$\begin{aligned}
w_{ij}^{\alpha\beta} = &\left(\frac{\mu_{\alpha\beta}}{M_\alpha}\right)^2 |\mathbf{v_\alpha} - \mathbf{v_\beta}|^3 \\
&\times \left[\delta_{ij}\frac{\sigma_2}{2} + \frac{(v_{i\alpha} - v_{i\beta})(v_{j\alpha} - v_{j\beta})}{|\mathbf{v_\alpha} - \mathbf{v_\beta}|^2}\left(2\sigma_1 - \frac{3}{2}\sigma_2\right)\right],
\end{aligned} \tag{7}$$

with N_β being the density of scattering species and σ_k being the cross-section moment of order k given by the kinetic gas theory as

$$\sigma_k = \int \left(1 - \cos^k(\theta)\right) d\theta. \tag{8}$$

The cross-section σ_1 is the diffusion cross-section, and σ_2 is the deflection cross-section. Each cross-section moment is related to some physical quantity: σ_1 with the loss of particle velocity in elastic scattering and σ_2 with viscosity and thermal conductivity.[18] This illustrates that the FP approximation, taken here, is valid for our purposes but in certain cases, higher orders should be calculated.

In the case of coulomb particles, it can be shown that taking the Debye length as the maximum collision parameter, we have

$$\begin{aligned}
\sigma_1(|\mathbf{v_\alpha} - \mathbf{v_\beta}|) &= \frac{1}{2}\sigma_2(|\mathbf{v_\alpha} - \mathbf{v_\beta}|) = \frac{4\pi e_\alpha^2 e_\beta^2 \Lambda}{\mu_{\alpha\beta}^2 |\mathbf{v_\alpha} - \mathbf{v_\beta}|^4} \\
\Lambda &= ln\left(\frac{2e_\alpha^2 e_\beta^2}{3(T_\beta + T_\alpha)}\sqrt{\frac{T_\beta T_\alpha |e_\beta e_\alpha|}{4\pi(T_\beta n_\beta + T_\alpha n_\alpha)}}\right),
\end{aligned} \tag{9}$$

where $\mu_{\alpha\beta} = \frac{M_\alpha M_\beta}{M_\alpha + M_\beta}$ is the reduced mass and Λ is the coulomb logarithm with n as the mean density and T as the mean temperature.

With the collision term in the form of a SDE, Eq. (5) can be linked with the LE general expression (1).[17,19] However, in this case, the stochastic part $\delta F(t)$ should be treated carefully due to the FPC B being a symmetric tensor of 2nd rank with 2 non-degenerated roots.

For a Maxwellian distribution, the general form of the FPC B becomes

$$B_{ij} = B_1\delta_{\mathrm{ij}} - B_2\frac{v_i v_j}{\mathbf{v}^2}, \tag{10}$$

where B_1 and B_2 are matrixes 3×3. And the roots can be simplified as

$$\begin{aligned}\left(B_{\pm}^{\frac{1}{2}}\right)_{ij} &= \left(B_1\delta_{\mathrm{ij}} - B_2\frac{v_i v_j}{\mathbf{v}^2}\right)^{\frac{1}{2}} \\ &= \left(\sqrt{B_1}\delta_{\mathrm{ij}} - \left(\sqrt{B_1} \pm \sqrt{B_1 - B_2}\right)\frac{v_i v_j}{\mathbf{v}^2}\right); \quad B_1 - B_2 \geq 0.\end{aligned} \tag{11}$$

In previous studies, the collisions were treated omitting one of the roots,[20] which results in a serious mistreatment of electron-electron and ion-ion collisions.

By taking into account both roots, a slightly different expression from Eq. (1) is obtained[19]

$$\mathbf{P_k}(\mathbf{v_k}) = -\boldsymbol{f_k} - (\boldsymbol{\xi}\mathbf{x}\mathrm{d_k} + \boldsymbol{\eta}\mathbf{x}\mathrm{g_k}), \tag{12}$$

where $a\mathbf{x}b$ is the matrix multiplication between a and b, $\boldsymbol{f}$ is a regular acceleration, while $(\boldsymbol{\xi}\mathbf{x}\mathrm{d_k} + \boldsymbol{\eta}\mathbf{x}\mathrm{g_k})$ is the fluctuation acceleration. The terms $\boldsymbol{f}$, d, and g depend on the DF of the scattering particles. $\boldsymbol{\xi}$ and $\boldsymbol{\eta}$ are two random vectors used to describe the random character of collisions in plasma. These random numbers have the following characteristics.

$$\begin{aligned}&\langle\xi_{\mathrm{i}}(\mathrm{t})\rangle = 0 \quad \langle\xi_{\mathrm{i}}(\mathrm{t})\xi_{\mathrm{k}}(\mathrm{t}+\Delta\mathrm{t})\rangle = \delta_{\mathrm{ik}}\delta(\Delta\mathrm{t}) \\ &\langle\xi_{\mathrm{i}}(\mathrm{t})\eta_{\mathrm{k}}(\mathrm{t}+\Delta\mathrm{t})\rangle = 0 \quad \int_{\mathrm{t}}^{\mathrm{t}+\Delta\mathrm{t}}\xi_{\mathrm{k}}\mathrm{dt}' = \mathrm{p_k}\sqrt{\Delta\mathrm{t}},\end{aligned} \tag{13}$$

where $\mathrm{p_k}$ is a random number normally distributed of zero mean and dispersion equal to 1.

By integration of Eq. (3) for a velocity component, the expressions of $\langle\Delta v_i\rangle$ and $\langle\Delta v_i\Delta v_j\rangle$ are deduced, in this case for $\langle\Delta v_i\Delta v_j\rangle$, we stop at third order in velocity. Substituting the velocity correlations in equation Eq. (6) and using the properties of the random vectors in Eq. (13), one is able to express $\boldsymbol{f}$, d, and g by the FPC

$$\begin{aligned}f_i &= A_i - \chi\sum_{l,j}(d_{lj} + g_{lj})\frac{\partial(d_{ij} + g_{ij})}{\partial v_l} \\ d_{ij} &= \frac{1}{\sqrt{2}}\left(B_+^{\frac{1}{2}}\right)_{ij}; \quad g_{ij} = \frac{1}{\sqrt{2}}\left(B_-^{\frac{1}{2}}\right)_{ij},\end{aligned} \tag{14}$$

where $B_{\pm}^{\frac{1}{2}}$ are the roots of the FPC $B^{\alpha\beta}$. The term f can be now identified as the force of dynamical friction experienced by particles α in a medium of β particles and d and g as the diffusion tensor for particles α in a medium of β.[14,17]

The parameter χ is a parameter chosen to conserve the energy in elastic collisions. For electron-ion collisions: $\chi_{ei} = \frac{1}{2}$; for electron-electron collisions: $\chi_{ee} = 0$.

III. FULLY IONIZED PLASMA

In order to calculate the force (12) from Eq. (6), first the distribution of the scattering particles is defined. Electrons in the plasma collide with other electrons and also with the different species of ions. For the electrons, an 8th grad approximation[21] moving Maxwellian is used with the electron mean velocity $\mathbf{u}_\beta = \frac{1}{N}\sum_{k=1}^{N}\mathrm{v}_{\beta\mathrm{k}}$, with N being the number of electrons

$$\begin{aligned}f_e(\mathbf{v_e}, \mathrm{T_e}) = \frac{1}{\pi^{3/2}v_{te}^3}e^{-\frac{(\mathbf{v_e}-\mathbf{u_e})^2}{v_{Te}^2}}\Bigg[1 - \sum_{m,n}\frac{\sigma_{mn}}{v_{Te}^2} \\ \times\left(\frac{2(\mathrm{v_{en}} - \mathrm{u_{e_n}})(\mathrm{v_{em}} - \mathrm{u_{e_m}})}{v_{Te}^2} - \delta_{mn}\right) \\ - \frac{\mathbf{q}(\mathbf{v_e} - \mathbf{u})}{v_{Te}^4}\left(1 - \frac{2(\mathbf{v_e} - \mathbf{u_e})^2}{v_{Te}^2}\right)\Bigg],\end{aligned} \tag{15}$$

where N_e is the electron density, $v_{Te} = \frac{2}{3}\left\langle(\mathbf{v_e} - \mathbf{u_e})^2\right\rangle$ is the thermal velocity of the electron population, $\mathbf{q} = \left\langle(\mathbf{v_e} - \mathbf{u_e})^2(\mathbf{v_e} - \mathbf{u_e})\right\rangle$ is the heat flux, and $\sigma_{mn} = \frac{v_{Te}^2}{2}\delta_{mn} - \left\langle(\mathrm{v_{en}} - \mathrm{u_{e_n}})(\mathrm{v_{em}} - \mathrm{u_{e_m}})\right\rangle$ is the viscosity. In this case, due to the objective of calculating the conductivity and runaway generation, the term viscosity is neglected. However, the derivation process will be the same if this term was included.

For the ions, fully ionized plasma and an ion population with an arbitrary thermal velocity and a Maxwellian DF is used

$$\mathrm{f_{ion}}(\mathbf{v_I}, \mathrm{T}_I) = \frac{1}{\pi^{3/2}v_{TI}^3}e^{-\left(\frac{(\mathbf{v_I}-\mathbf{u_I})^2}{v_{TI}^2}\right)}. \tag{16}$$

In case of considering multiple ion species, we could approximate it in some cases as a single species of charge $Z = \frac{1}{N}\sum_{k=1}^{N}\mathrm{Z_k}$, with N being the number of species of ions and in a similar manner for the ion mass.

For an initial electron distribution like (15) and an initial ion distribution like (16), the FPC can be calculated from Eq. (6) for electron-electron and electron-ion collision

$$\begin{aligned}A_i^{\mathbf{e}\beta}(\mathbf{v_e}, \mathrm{T}_\beta) &= -N_\beta\int \mathrm{f}_\beta(\mathbf{v}_\beta)\frac{1}{m_e}(\mathbf{v_{e_i}} - \mathbf{v}_{\beta_i})\frac{4\pi Z_\beta^2 e_e^4\Lambda}{\mu_{e\beta}|\mathbf{v_e} - \mathbf{v}_\beta|^3}d\mathbf{v}_\beta \\ B_{ij}^{\mathbf{e}\beta}(\mathbf{v_e}, \mathrm{T}_\beta) &= N_\beta\int \mathrm{f}_\beta(\mathbf{v}_\beta)\frac{1}{m_e^2}\frac{4\pi Z_\beta^2 e_e^4\Lambda}{|\mathbf{v_e} - \mathbf{v}_\beta|} \\ &\quad\times\left[\frac{|\mathbf{v_e} - \mathbf{v}_\beta|^2\delta_{ij} - (\mathbf{v_{e_i}} - \mathbf{v}_{\beta_i})(\mathbf{v_{e_j}} - \mathbf{v}_{\beta_j})}{|\mathbf{v_e} - \mathbf{v}_\beta|^2}\right]d\mathbf{v}_\beta,\end{aligned} \tag{17}$$

via the fact that $\frac{\partial}{\partial\mathbf{v}}\left(\frac{1}{|\mathbf{v}|}\right) = \frac{-\mathbf{v}}{|\mathbf{v}|^3}$ and $\frac{\partial}{\partial\mathbf{v}}\left(\frac{\partial|\mathbf{v}|}{\partial\mathbf{v}}\right) = \frac{|\mathbf{v}||\mathbf{v}|\widehat{I-\mathbf{vv}}}{|\mathbf{v}|^3}$ the FPC can be rewritten by using electrostatic potential-like functions $H_{(\mathbf{v_e})}^{\mathbf{e}\beta}$ and $G_{(\mathbf{v_e})}^{\mathbf{e}\beta}$ also called Rosenbluth potentials[14,22]

$$\begin{aligned}H_{(\mathbf{v_e})}^{\mathbf{e}\beta} &= -\frac{m_e}{\mu_{e\beta}}\int f_\beta(\mathbf{v}_\beta)\frac{1}{|\mathbf{v_e} - \mathbf{v}_\beta|}d\mathbf{v}_\beta \\ G_{(\mathbf{v_e})}^{\mathbf{e}\beta} &= \int f_\beta(\mathbf{v}_\beta)|\mathbf{v_e} - \mathbf{v}_\beta|d\mathbf{v}_\beta,\end{aligned} \tag{18}$$

$$A_i^{ei} = \Gamma_{eI}\frac{\partial H_{(\mathbf{v_e})}^{eI}}{\partial\mathbf{v_e}} \quad B_{ij}^{ei} = \Gamma_{eI}\frac{\partial^2 G_{(\mathbf{v_e})}^{eI}}{\partial\mathbf{v_e}\partial\mathbf{v_e}}, \tag{19}$$

$$A_i^{ee} = \Gamma_{ee}\frac{\partial H_{(\mathbf{v_e})}^{ee}}{\partial\mathbf{v_e}} \quad B_{ij}^{ee} = \Gamma_{ee}\frac{\partial^2 G_{(\mathbf{v_e})}^{ee}}{\partial\mathbf{v_e}\partial\mathbf{v_e}}, \tag{20}$$

which satisfy following relations:

$$\nabla^2_{v_e} G = 2H\frac{\mu_{eI}}{m_e} \quad \nabla^2_{v_e} H = -4\pi f_{ion}(\mathbf{v_e})\frac{m_e}{\mu_{eI}}. \tag{21}$$

Then by using Eq. (18) in Eq. (19) and Eq. (20), we obtain the FPC for e-e and e-I collision which gives the collision term Eq. (12). After calculation, the e-e collision term is

$$\begin{aligned}\mathbf{P_{e-e}}(\mathbf{v_e}, \boldsymbol{T_e}) = &+\sqrt{\frac{N_e}{|\omega_e| v_{Te}}\frac{2\pi e^4\Lambda}{m_e^2}}\left[\sqrt{\Omega(\omega_e)}\left(\boldsymbol{\xi} - \frac{\boldsymbol{\omega_e}(\boldsymbol{\omega_e}\boldsymbol{\xi})}{|\boldsymbol{\omega_e}|^2}\right) - \left(\sqrt{2G(\omega_e)}\right)\frac{\boldsymbol{\omega_e}(\boldsymbol{\omega_e}\boldsymbol{\xi})}{|\boldsymbol{\omega_e}|^2}\right]\\ &+\sqrt{\frac{N_e}{|\omega_e| v_{Te}}\frac{2\pi e^4\Lambda}{m_e^2}}\left[\sqrt{\Omega(\omega_e)}\left(\boldsymbol{\eta} - \frac{\boldsymbol{\omega_e}(\boldsymbol{\omega_e}\boldsymbol{\eta})}{|\boldsymbol{\omega_e}|^2}\right) + \left(\sqrt{2G(\omega_e)}\right)\frac{\boldsymbol{\omega_e}(\boldsymbol{\omega_e}\boldsymbol{\eta})}{|\boldsymbol{\omega_e}|^2}\right]\\ &-\frac{4\pi e^4\Lambda}{m_e^2}\left[\frac{2\boldsymbol{\omega_e}}{|\omega_e| v_{Te}^2} N_e G(\omega_e) - \left(\frac{4(\mathbf{q}\boldsymbol{\omega_e})\boldsymbol{\omega_e}}{5v_{Te}^5}\right) N_e \Phi'(\omega_e)\right].\end{aligned} \tag{22}$$

For e-I collision,

$$\begin{aligned}\mathbf{P_{e-i}}(\mathbf{v_e}, \mathrm{T_I}) = &\sqrt{\frac{\Gamma_{ei}}{2|\boldsymbol{\omega_{eI}}| v_{Tion}}}\left[\sqrt{\Omega(\omega_{eI})}\left(\boldsymbol{\Psi} - \frac{\boldsymbol{\omega_{eI}}(\boldsymbol{\omega_{eI}}\boldsymbol{\Psi})}{|\boldsymbol{\omega_{eI}}|^2}\right) - \frac{\boldsymbol{\omega_{eI}}(\boldsymbol{\omega_{eI}}\boldsymbol{\Psi})}{|\boldsymbol{\omega_{eI}}|^2}\sqrt{2G(\omega_{eI})}\right]\\ &+\sqrt{\frac{\Gamma_{ei}}{2|\boldsymbol{\omega_{eI}}| v_{Tion}}}\left[\sqrt{\Omega(\omega_{eI})}\left(\boldsymbol{\zeta} - \frac{\boldsymbol{\omega_{eI}}(\boldsymbol{\omega_{eI}}\boldsymbol{\zeta})}{|\boldsymbol{\omega_{eI}}|^2}\right) + \frac{\boldsymbol{\omega_{eI}}(\boldsymbol{\omega_{eI}}\boldsymbol{\zeta})}{|\boldsymbol{\omega_{eI}}|^2}\sqrt{2G(\omega_{eI})}\right] + \Gamma_{ei}\frac{m_e}{\mu_{ei} v_{Tion}^2}\frac{2\boldsymbol{\omega_{eI}}}{|\boldsymbol{\omega_{eI}}|}G(\omega_{eI})\\ &-\frac{\Gamma_{ei}}{\boldsymbol{\omega_{eI}}}\frac{\boldsymbol{\omega_{eI}}}{|\boldsymbol{\omega_{eI}}|^4 v_{Tion}^4}\left[2|\boldsymbol{\omega_{eI}}|^2 v_{Tion}^2 G(\omega_{eI}) + \left(\boldsymbol{\omega}_{eI}^2 - \frac{1}{2}\right)\mathrm{G}(\omega_{eI})\left[|\mathbf{v_e} - \boldsymbol{u_i}|^2\right]\right].\end{aligned} \tag{23}$$

And finally for i-i collision,

$$\begin{aligned}\mathbf{P_{I-I2}}(\mathbf{v_I}, \mathrm{T_{I_2}}) = &-\Gamma_{II_2}\frac{M_I}{\mu_{II_2}}\frac{2\omega_{II_2}}{v_{TI_2}^2|\omega_{II_2}|}G(\omega_{II_2}) - \sqrt{\frac{\Gamma_{II_2}}{2\omega_{II_2} v_{TI_2}}}\left[\sqrt{\Omega(\omega_{II_2})}\left(\boldsymbol{\xi} - \frac{\omega_{II_2}(\omega_{II_2}\boldsymbol{\xi})}{|\omega_{II_2}|^2}\right) - \sqrt{2G(\omega_{II_2})}\frac{\omega_{II_2}(\omega_{II_2}\boldsymbol{\xi})}{|\omega_{II_2}|^2}\right.\\ &\left.+\sqrt{\Omega(\omega_{II_2})}\left(\boldsymbol{\eta} - \frac{\omega_{II_2}(\omega_{II_2}\boldsymbol{\eta})}{|\omega_{II_2}|^2}\right) + \sqrt{2G(\omega_{II_2})}\frac{\omega_{II_2}(\omega_{II_2}\boldsymbol{\eta})}{|\omega_{II_2}|^2}\right],\end{aligned} \tag{24}$$

with $\boldsymbol{u_\beta}$ being the mean velocity of the species β, Ψ, ζ, ξ, and η random numbers of mean 0 and dispersion $\frac{1}{\sqrt{2}}$, Φ and $\Phi'(w) = \frac{2}{\sqrt{\pi}}e^{-w^2}$ being the error function and its derivative, $G(w) = \frac{\Phi(w) - w\Phi'(w)}{2w^2}$ the Chandrasekhar function, $\Omega(w) = \Phi(w) - G(w)$, $\boldsymbol{\omega_{eI}} = \frac{(\mathbf{v_e} - \boldsymbol{u_I})}{v_{TI}}$, $\boldsymbol{\omega_{II_2}} = \frac{(\mathbf{v_I} - \boldsymbol{u_{I_2}})}{v_{TI_2}}$, $\boldsymbol{\omega_e} = \frac{(\mathbf{v_e} - \mathbf{u})}{v_{Te}}$, and $\Gamma_{\alpha\beta} = \frac{4\pi e_\alpha^2 e_\beta^2 \Lambda}{m_\alpha^2}$.

It can be observed that in the 1D case, the terms of the form $\boldsymbol{\xi} - \frac{(\mathbf{v_e} - \mathbf{u})((\mathbf{v_e} - \mathbf{u})\boldsymbol{\xi})}{|\mathbf{v_e}|^2}$ become 0. This is because here the Fokker-Planck equation is being used to treat the collisions in plasma, which means that the interactions are mainly due to Coulomb force, thus to a "long" range force. So, every particle interacts simultaneously with many others (those in a Debye sphere), but most binary interactions are weak. This is the fundamental difference between the Fokker-Planck and Boltzmann equation, in the Boltzmann equation, the interactions are violent and binary, and between two collisions, the particles are not under the action of any force and move along a rectilinear path. Boltzmann is in fact a model based on a classical kinetic theory from a neutral gases point of view.

For the limit case where $T_i = 0$ for the ion population,

$$\begin{aligned}\mathbf{P_{e-i}}(\mathbf{v_e}, 0) = &\sqrt{\frac{\Gamma_{ei}}{2|\mathbf{v_e}|}}\left[\left(\boldsymbol{\Psi} - \frac{\mathbf{v_e}(\mathbf{v_e}\boldsymbol{\Psi})}{|\mathbf{v_e}|^2}\right) + \left(\boldsymbol{\zeta} - \frac{\mathbf{v_e}(\mathbf{v_e}\boldsymbol{\zeta})}{|\mathbf{v_e}|^2}\right)\right]\\ &-\Gamma_{ei}\frac{\mathbf{v_e}}{2|\mathbf{v_e}|^3},\end{aligned} \tag{25}$$

which translates to a static ion population which only causes a change in the direction for the electrons conserving their momentum after collision and a small friction. So, this collision term can be used for temperatures T_i inferior to the electron population temperature. This result is the same as what is obtained in the case of considering initially the ion DF as a delta.[19]

IV. RUNAWAY ELECTRONS

In order to test the accuracy of the code, a simulation of the simplest case, $T_i = 0$ is carried, and compared with the

theoretical results.[23] Only Eqs. (22) and (25) with $q = 0$ are taken into account. To transform these equations into dimensionless units $\tau = t\upsilon_{ei0}$ with $\upsilon_{ei0} = \frac{e^4}{m_e^2 v_{Te0}^2}\frac{4\pi\Lambda Z^2 N_i}{v_{Te0}}$ being the electron-ion collision frequency at time 0 is used for time and for velocity $\mathbf{v} = \frac{\mathbf{V}}{v_{Te0}}$ with $v_{Te0} = \sqrt{\frac{2}{3}\left\langle (\mathbf{v}_0 - \mathbf{u}_0)^2 \right\rangle}$ being the thermal velocity of the electron population at time 0. The dimensionless electric field is then $\alpha = \frac{E}{E_D}$ with $E_D = \frac{v_{Te0}\upsilon_{ei0}m_e}{e} = \frac{2\pi\Lambda Z^2 N_i e^3}{T_{e0}}$, where $T_{e0} = \frac{1}{2}m_e v_{Te0}^2$. E_D is the Dreicer field.

The flux of runaway electron is mainly parallel to the direction of the electric field. In order to calculate the number of runaway electrons produced in υ_{ei} unit of time, j_0, the following equation[24] is used:

$$\left(\frac{j_0}{\upsilon_{ei}}\right)(t) \approx \frac{\frac{v_{Te}}{\Delta T}\int_t^{t+\Delta T} n_{(v_1<v<v_2,t')}dt'}{2\pi(v_2 - v_1)N}\alpha, \tag{26}$$

where $\Delta T = \frac{0.3}{\upsilon_{ei}}$ is the time interval of integration, $n_{(v_1<v<v_2,t')}$ is the number of electrons with a module velocity in the interval $[v_1, v_2]$, $v_1, v_2 > 1/\sqrt{\alpha}$, and N the total number of electrons. When the velocity of a particle increases, the collision frequency sharply falls, hence, friction becomes negligibly small for high energetic particles. In the simulation code, the electrons acquiring velocities larger than v_2 are considered as escaped, ergo they will be no more in interaction with the rest, and a new electron will be reintroduced in its place. The new electron will be initialized with the electron population thermal velocity.

For the calculation of random numbers of mean 0 and dispersion equal to 1, a low-discrepancy Sobol number generator is used.

The initial parameters of the first simulations are $N = 10\,000$ electrons, the normalized electric field $\alpha = 0.01$ on the x axis, the normalized time step $\Delta\tau = 0.02$, $Z = 1$, $v_1 = 6$, and $v_2 = 10$.

The first thing one can notice is that for a field of $\alpha = 0.02$ or less, the Ohmic heating is not enough to increase temperature sufficiently in such time period [see Fig. 1(c)]. Figure 1(b) shows that the Spitzer conductivity is around 0.92, which is an 8% difference with the expected theoretical result of 1 but is close enough. Finally, the DF [see Fig. 1(a)] at the end of the simulation exhibits a Maxwellian centered in 0 as the initial distribution, confirming that the collisions with 0 or low electric field conserve the Maxwellian as expected.

In the next simulation, the initial parameters are $N = 6000$, $\Delta\tau = 0.045$ and the normalized electric field $\alpha = 0.1$, 0.08, *and* 0.06 on the x axis, while the rest of the parameters remain as before.

The DF at every time step, the mean velocity, the temperature of the electron population, and the runaway flux are obtained from the simulation. The results obtained are compared to those obtained by Kulsrud *et al.*[23] For $\alpha = 0.1$, 0.08, and 0.06, the runaway fluxes in Ref. 23 are 1×10^{-3}, 3.2×10^{-4}, *and* 5.4×10^{-5}, respectively. The first thing one can appreciate is that the convergence time for each α is different, this is mainly because the lower the electric field is the slower the electrons will gain energy but it also depends on the velocity range chosen for Eq. (25), this range has to be chosen carefully, if the interval is too small, important fluctuations will appear even at later times but if it is too big particles that are not really runaways and are just entering this interval and going back to the main Maxwellian will be taken as runaway. Figure 2(b) shows that the values obtained from simulation are in agreement with those from Ref. 23, with the less precise result being for $\alpha = 0.06$ which shows that for fields lower than 0.06, more resolution in time and more particles could be needed for more precise results.

To test the statistics, a simulation for $\alpha = 0.1$ on the x axis, normalized time step $\Delta\tau = 0.045$, $Z = 1$, $v_1 = 6$, and $v_2 = 10$ and $N = 1000$, 3000, 5000, and 10 000 is shown in Fig. 2(a). For $N = 1000$, the results are still good but a clear fluctuation can be appreciated due to the low statistics. With the use of less than 1000, the results become too inaccurate so in this case, the minimum limit will be 1000 particles. On the other hand, when we increase the number of particles, the results get more accurate the more particles we use, as expected. A good equilibrium between time and accuracy is found between 1000 and 10 000 but depending on other uses, more particles could be needed. While for a simulation like the one done in this work, time is not really an important

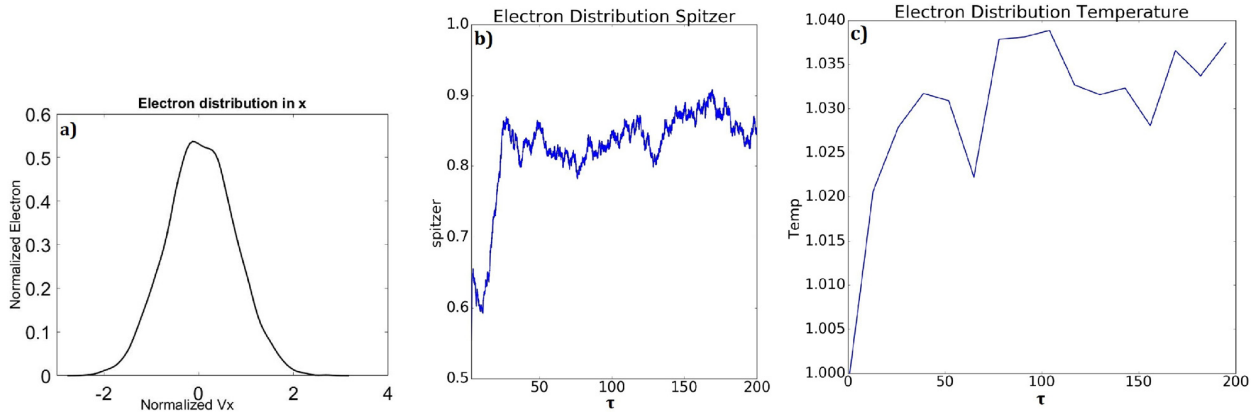

FIG. 1. (a) Electron distribution in the X direction, (b) normalized Spitzer, and (c) normalized electron population temperature for $\alpha = 0.01$ on the x axis, $\Delta\tau = 0.02$, $Z = 1$, $v_1 = 6$, and $v_2 = 10$.

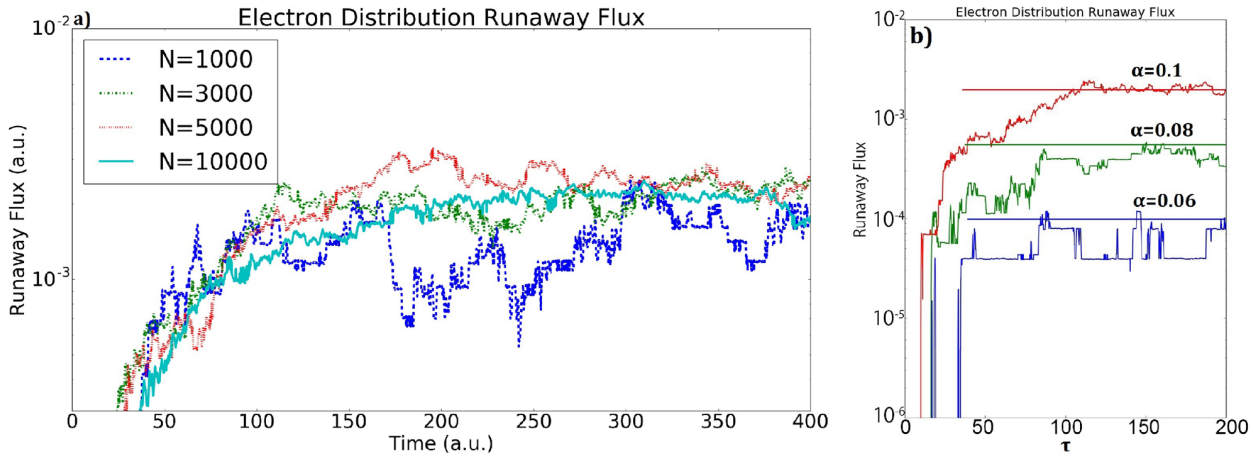

FIG. 2. (a) Comparison of the results for $\alpha = 0.1$ with N = 1000, 3000, 5000, and 10 000. (b) Comparison of results for N = 6000 and $\alpha = 0.1$, 0.08, and 0.06.

factor, in the case of the application of this method in conjunction with PIC will make it more of a factor to take into account.

A simulation to test the evolution of the electron population for an ion population of higher Z is done for Z= 1, 2, 3, and 10.

Again, the results are compared with those given in Ref. 23. For this simulation, the parameters chosen are $\boldsymbol{\alpha} = 0.1$, T_{ion}=0, q = 0, $\Delta\tau = 0.045$, and $N = 6000$. While a good enough agreement between the theory and results for Z= 1, 2, 3, and 10 is found (see Fig. 3), from Z = 10, large variations for each time step can be appreciated and also, that the time for convergence is higher, this is assumed to be due to not having enough statistics.

One limitation of this method is the incapacity of the calculation of the Spitzer conductivity when the external electric field is too low.

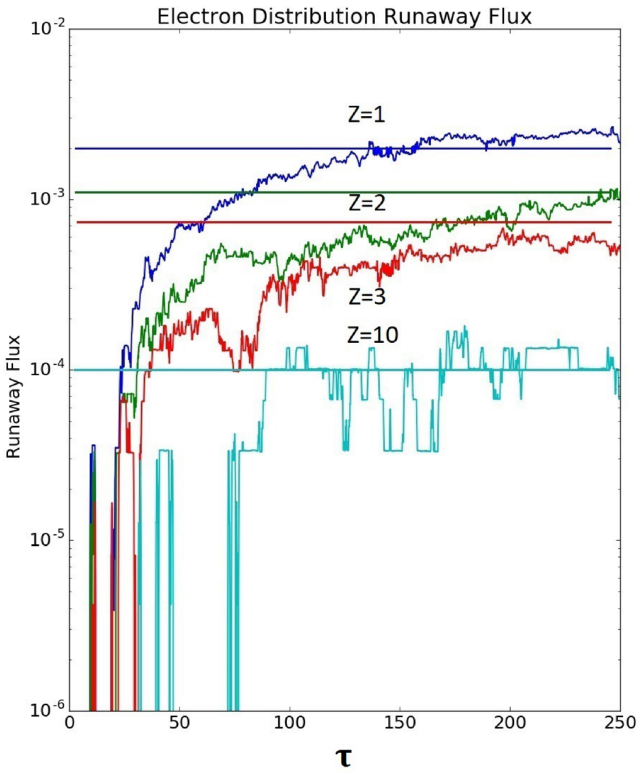

FIG. 3. Simulation results of the runaway flux for $\boldsymbol{\alpha} = 0.1$ in the x direction and Z = 1, 2, 3, and 10 compared with the results given in Ref. 17 (straight lines).

V. ELECTRON KINETICS IN EXTERNAL MAGNETIC FIELDS

The application of a magnetic field is a delicate matter that could importantly affect the way that the collisions occur due to the appearance of anisotropy in the direction of the magnetic field. In this section, the application of a normalized magnetic field is tested by adding the force $\mathbf{V} \times \mathbf{H}$. The magnetic field applied is considered not too high to drastically change the way that the interactions occur in the plasma. The normalization is done as follows, $\frac{\mathbf{V}}{v_{Te0}} \times \frac{\mathbf{eB}}{v_{ei0} m_e c} = \mathbf{v} \times \boldsymbol{\beta}$. Four cases are treated, first a magnetic field parallel to the electric field and then a magnetic field perpendicular to the electric field, both of them will be done with high and low alpha. For this simulation, the initial parameters $\boldsymbol{\alpha} = 0.1$ and 0.01, T_{ion}=0, $q = 0$, $\Delta\tau = 0.045$, $N = 6000$, and $\beta_x, \beta_y = 0$, 0.1, 0.15, 0.25, *and* 0.5 are used.

For β_x, the magnetic force is parallel to the electric force so only a cyclotronic movement on the plane Y0Z occurs. Because of that, the acceleration by the electric field is not affected and it is what the simulations confirm. On the other hand, for β_y, a cyclotronic movement on the plane X0Z happens which causes the electron to accelerate and decelerate in the x direction periodically. Figure 4 shows the results of the simulations for $\boldsymbol{\alpha} = 0.01$ for different β_y. As Figs. 4(a) and 4(b) show, the stronger the β_y is, the lower the conductivity in x and the mean velocity due to this cyclotron movement.

In the case of a strong electric field of $\boldsymbol{\alpha} = 0.1$ in the x direction and the magnetic force $\mathbf{v} \times \boldsymbol{\beta}$ which again should only affect the acceleration if the $\boldsymbol{\beta}$ is perpendicular to x, simulations confirm once more that if β_x is applied, no change to the acceleration process of the electrons appears. On the other hand, when we apply β_y, it can be observed how the cyclotron movement in x opposes the acceleration due to the $\boldsymbol{\alpha}$ to the extent that if β_y is strong, enough acceleration is no longer possible. In the runaway electron flux, this

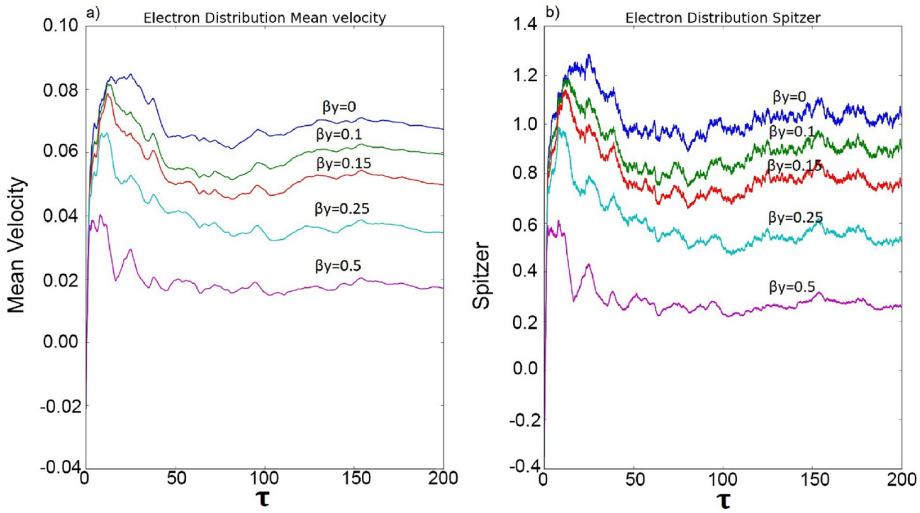

FIG. 4. (a) Mean velocity and (b) Spitzer conductivity changes for $\Delta\tau = 0.045$, $N = 6000\,\alpha = 0.01$ and $\beta_y = 0$, 0.1, 0.15, 0.25, *and* 0.5.

phenomenon can be clearly seen [see Fig. 5(a)]. For $\beta_y = 0.5$, the runaway flux becomes 0. Figure 5(b) shows that for that temperature, the convergence value becomes lower with a higher β_y.

VI. COLLIDING PLASMAS

The term colliding plasmas here refers to the kind of strong collisions between plasma species or different plasmas that cause the plasma to evolve into a non-Maxwellian distribution.

A challenging modern problem is the collision of dense plasma species. A typical sample of such objects is found in the two foils irradiated by the two contra-propagating high-power laser pulse case. Ion-ion collisions play a key role in such plasma dynamics and kinetics. It is clear that the ion velocity distribution, characterized initially by a set of temperatures and mean velocities, becomes essentially non-Maxwellian during the encounter. Simulation of such a process can be done with the use of LEM.

One of the most important advantages of the LEM is the capacity to simulate the collision between different populations, in theory no matter how many they are. This gives more flexibility for non-Maxwellian plasma simulations and in general plasma collisions. One of the most powerful tools that this allows is the capacity of separating a complex DF into a sum of Maxwellian distributions with different parameters, when mathematically possible. So, instead of calculating the FPC $A^{\alpha\beta}$ and $B^{\alpha\beta}$ with a complex $f_\beta(\mathbf{v})$ from scratch, the simulation could be done as a collision between different populations with Maxwellian distribution.

This means that for a $f_\beta(\mathbf{v})$ separable in a sum Maxwellian

$$f_\beta(\mathbf{v}) = \sum_k f_k(\mathbf{v}) = N \sum_k \frac{1}{\pi^{3/2} v_{Tk}^3} e^{-\frac{(\mathbf{v}-\mathbf{u}_\mathbf{k})^2}{v_{Tk}^2}}. \tag{27}$$

Then, $A_i^{\alpha\beta}$ and $B_{ij}^{\alpha\beta}$ will become

$$\begin{aligned} A_i^{\alpha\beta} &= \int\int_{v(t)}^{v(t+\Delta t)} N \sum_k \left(-f_k(\mathbf{v}) \frac{\mu_{\alpha k}}{M_\alpha} (v_{i\alpha} - v_{ik}) |\mathbf{v_e} - \mathbf{v_k}| \right. \\ &\quad \left. \times \sigma_1(|\mathbf{v}_\alpha - \mathbf{v_k}|) \right) d\mathbf{v} \\ B_{ij}^{\alpha\beta} &= \int\int_{v(t)}^{v(t+\Delta t)} N \sum_k \left(f_k(\mathbf{v}) |\mathbf{v}_\alpha - \mathbf{v_k}|^3 \frac{4\pi e_\alpha^2 e_k^2 \Lambda}{m_\alpha^2 |\mathbf{v}_\alpha - \mathbf{v_k}|^4} \right. \\ &\quad \left. \times \left[\delta_{il} - \frac{(v_{i\alpha} - v_{ik})(v_{l\alpha} - v_{lk})}{|\mathbf{v}_\alpha - \mathbf{v_k}|^2} \right] \right) d\mathbf{v}. \end{aligned} \tag{28}$$

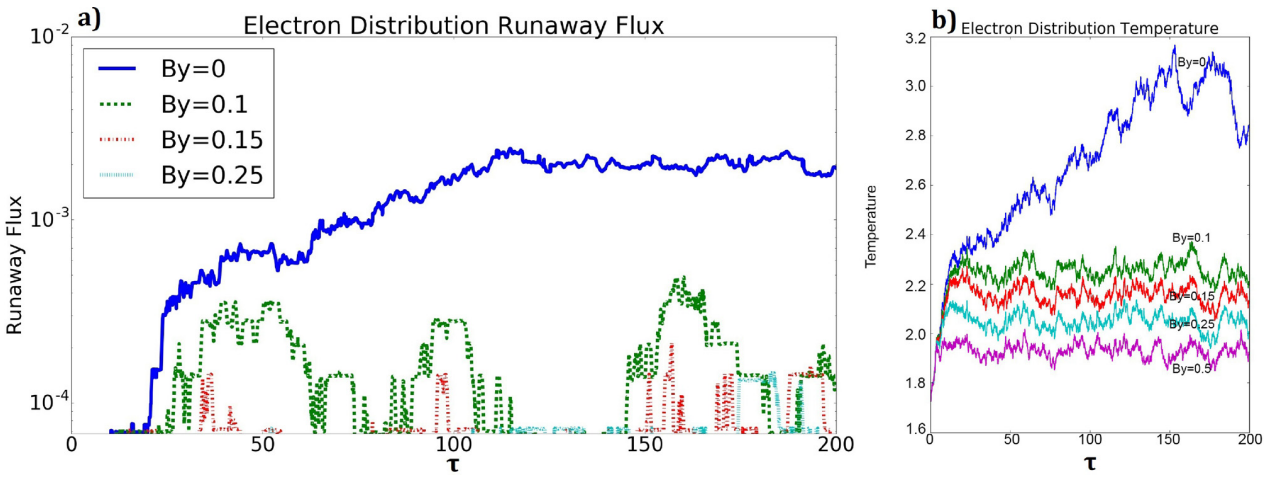

FIG. 5. (a) Runaway flux changes for $\Delta\tau = 0.045$, $N = 6000\,\alpha = 0.1$, and $\beta_y = 0$, 0.1, 0.15, 0.25, *and* 0.5. (b) Temperature of the electron distribution for the same parameters.

As it can be observed in Eq. (28), the FPC of the initial distribution can also be separated into a sum of FPC for each Maxwellian. The problem in this case is that the matrix $B^{\alpha\beta}$ is not the same as for the Maxwellian case, here the number of roots increases

$$B_{ij}^{\alpha\beta} = \left(B_{a1}\delta_{ij} - B_{a2}\frac{v_{ai}v_{aj}}{\mathbf{v_a^2}}\right) + \left(B_{b1}\delta_{ij} - B_{b2}\frac{v_{bi}v_{bj}}{\mathbf{v_b^2}}\right). \quad (29)$$

In Eq. (29) is shown the result for the case in which the distribution is divided into 2 Maxwellian a and b with different mean velocities. By comparing Eq. (29) with Eq. (10), it can be appreciated that the matrix has increased significantly in complexity. Even though the use of LE with the matrix $\boldsymbol{B}$ containing the distribution f being far from the Maxwellian is possible and stable,[25] necessary calculations of Eq. (27) with a 3D sampling distribution of particles make the method impractical.

Another simpler way to separate is directly consider a set of Maxwellian DF with different temperatures and mean velocities, as completely independent populations, which means that there is no need to recalculate any new FPC, from that point each of the collision terms already obtained in Eqs. (22)–(24) can be used again. This will end up in a different collision term per Maxwellian with uncorrelated random numbers for each.

In order to give a proof of this second simplification way, a simulation of collisions between electrons and ions is carried, but in this case, the ion population will be divided into n subpopulations of N/n ions. These subpopulations have the same characteristics. This means that instead of a population of electrons colliding with a population of ions, the population of electrons collides with n populations of ions, but the collisions are still treated with Eq. (25). The simulation parameters are $\boldsymbol{\alpha} = 0.01$, T_{ion}=0, $q = 0$, $\Delta\tau = 0.045$, and $N = 10\,000$.

Some care about the random numbers has to be taken because the scheme used to treat the collisions with each subpopulation along with the random number variance can change, so a square root of n will appear at the variance, $\sigma_k = \sqrt{\frac{n}{N_k}\sum_i (x_i - \mu)^2} = \sqrt{n}\sigma$. However, by treating each collision with each sub-population independently, and because $\mathbf{P_{e-i}}(\mathbf{v_e}, 0) \propto \sqrt{\frac{N_k}{n}}\boldsymbol{\zeta}$, the $\sqrt{n}$ term is canceled.

In Fig. 6 are presented the results of this simulations for n = 1, 5, 6, and 10. The results show that even with a division of the population into 10 subpopulations, the results are still close to those obtained by a single population which shows that it is possible to treat a DF this way. Nevertheless, there is a difference between the results, and this could be attributed to the need for more statistics the more we divide the initial population.

An interesting application is the case of collision of two electron beams with the same module mean velocity but in the reverse direction. This is modeled as two electron populations with Maxwellian distribution of initial normalized temperature of 1 moving into each other and colliding. Only the collision between electrons is considered, inside the Maxwellian and with the other population, without any external field, so only Eq. (23) is needed. If we let a system like this evolve, the final electron distribution should be a single Maxwellian.

In the simulation, two Maxwellian distributions of electrons with $\mathbf{u}_{e1} = \mathbf{u}$ and $\mathbf{u}_{e2} = -\mathbf{u}$ and the simulation parameters $\boldsymbol{\alpha} = 0$, $T_{e1} = T_{e2}$, $q = 0$, $\Delta\tau = 0.04$, $N_i = 1500$, and normalized $\mathbf{u} = \mathbf{3}, \mathbf{5}$, and $\mathbf{7}$ are considered.

Starting with the case $\mathbf{u} = \pm\mathbf{5}$, Fig. 7(a) shows how the initial DF of two Maxwellian distributions of mean velocity +5 and −5 start interacting with each other until both populations merge into a single Maxwellian of mean velocity 0. Both populations maintain a Maxwellian form during the entire process which further justifies the use of Eq. (23), as can be observed for $\tau = 250$.

Figures 7(b) and 7(c) show how the mean velocity decreases and transforms into temperature until convergence at 16 which is the expected maximum temperature for the final state, taking into account the factor $\frac{3}{2}$ in our definition of v_{Te}. Figure 7(c) also shows the temperature of one population for $\mathbf{u} = \mathbf{3}$ and $\mathbf{7}$ and one can see that the temperature of convergence is consistent with the expectations and also how the higher the time needed to converge is, the higher the initial mean velocity separation is. For $\mathbf{u} = \mathbf{3}$, the convergence occurs at around τ =90 while for $\mathbf{u} = \mathbf{5}$ and $\mathbf{u} = \mathbf{7}$, it occurs at $\tau = 300$ and $\tau = 700$, respectively.

As it has been just proven, the treatment as separated independent populations gives good results and it is simple enough that one can avoid the recalculation of the FPC $B_{ij}^{\alpha\beta}$ as written in Eq. (28), giving this method a lot more flexibility for use in non-Maxwellian distributions and multiple distributions interactions. This LEM then can be used, for

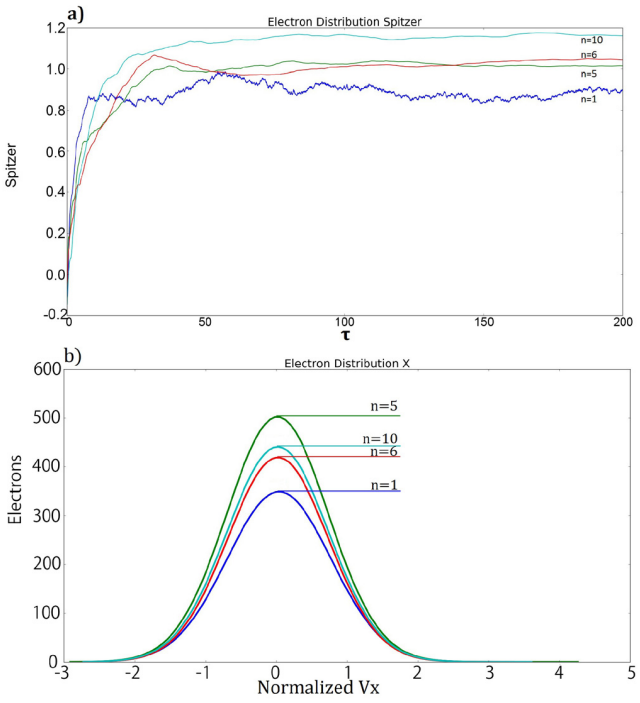

FIG. 6. (a) Spitzer conductivity results for the simulation parameters $\boldsymbol{\alpha} = 0.01$, T_{ion}=0, q = 0, $\Delta\tau = 0.045$, $N = 10\,000$, and n = 1, 5, 6, and 10. (b) Electron distribution on the x direction for the same parameters.

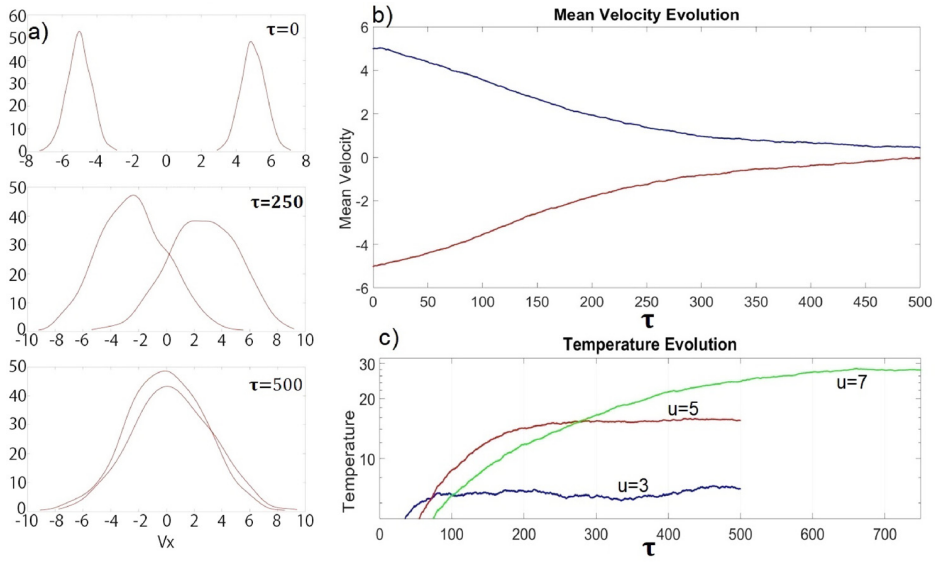

FIG. 7. (a) Distribution function in V_x evolution in time for $\boldsymbol{u} = \pm\mathbf{5}$ at $\tau = 0$, 250, *and* 500. (b) Evolution in time of the mean velocity for both populations for $\boldsymbol{u} = \pm\mathbf{5}$. (c) Evolution in time of one population temperature for $\boldsymbol{u} = \mathbf{3}, \mathbf{5}$, and $\mathbf{7}$.

example, in PIC simulations for coaxial plasma accelerator colliding plasmas experiments[26] in which the behavior of the electron density and the interactions at the collision zone of the plasma sheaths are important. In laser-plasma research, there also exists an interest in collision between plasmas and non-Maxwellian distributions and some examples are laser irradiated double foil experiments,[27] as already mentioned, and indirect-drive inertial confinement fusion[28] and PIC simulations for these cases could benefit from this LEM.

VII. CONCLUSIONS

In conclusion, we have demonstrated the high ability of the Langevin equation method for calculations of plasma kinetics using particles even for non-Maxwellian plasmas. This method is shown to be quite efficient for calculation of both rough (thermalization) and sensitive (electron runaway) collisional processes in plasmas. This has been demonstrated by direct simulations of plasma conductivity with and without magnetic fields.

It has been shown that the presentation of Langevin equation as a set of random processes

$$\mathbf{P}(\mathbf{v}) = \sum_{\alpha} \boldsymbol{\psi}_{\alpha} \times \boldsymbol{D}_{\alpha},$$

with ψ_α as a Gaussian random process and $\boldsymbol{D}_\alpha$ as a matrix derived with use of a Maxwellian distribution having sampling temperature and mean velocity, allows an easy inclusion of elastic collisions in particle simulation even in non-Maxwellian plasmas. As has been demonstrated, such an approach can be extended for collisions between different plasma species if their particle velocity distribution can be expressed as a set of Maxwell-like ones with sampling temperature and mean velocity calculated directly for every part of the species.

This way of calculation of collisions in plasma clearly distinguishes the difference between the mean velocity of particles and their temperature. This feature is extremely important in the simulation of energetic particle generation in numerous physical processes, like runaway generations from lightning, beam charge effects during transport or acceleration, plasma shockwaves and for collisions between different plasmas, and many others. Besides, the particle simulation with the Langevin equation allows a simple and natural link between kinetics and hydrodynamics methods.

[1]K. Cassou, S. Kazamias, A. Klisnick, D. Ros, P. Zeitoun, E. Oliva, P. Velarde, C. Garcia, and F. Ogando, X-Ray Lasers **2006**, 275–285 (2007).
[2]A. Ghizzo, M. M. Shoucri, P. Bertrand, M. Feix, and E. Fijalkow, Phys. Lett. A **129**(8–9), 453–458 (1988).
[3]N. Nakanii, T. Hosokai, K. Iwasa, S. Masuda, A. Zhidkov, N. Pathak, H. Nakahara, Y. Mizuta, N. Takeguchi, and R. Kodama, Phys. Rev. ST-AB **18**(2), 021303 (2015).
[4]V. I. Kolobov and R. R. Arslanbekov, in *5th International Conference of Numerical Modeling of Space Plasma Flows (ASTRONUM 2010)* (2011), Vol. 444, p. 223.
[5]S. Tiwari, A. Klar, and S. Hardt, J. Comput. Phys. **228**(18), 7109–7124 (2009).
[6]L. D. Tsendin, Phys.-Usp. **53**(2), 133–157 (2010).
[7]G. A. Bird, "Molecular gas dynamics," NASA STI/Recon Technical Report A, 1976, Vol. 76.
[8]T. Takizuka and H. Abe, J. Comput. Phys. **25**(3), 205–219 (1977).
[9]C. D. Decker, W. B. Mori, and J. M. Dawson, Phys. Plasmas **1**(12), 4043–4049 (1994).
[10]Y. Sentoku *et al.*, J. Phys. Soc. Jpn. **67**(12), 4084–4088 (1998).
[11]T. D. Arber, K. Bennet, C. S. Brady, A. Lawrence-Douglas, M. G. Ramsay, N. J. Sircombe, P. Gillies, R. G. Evans, H. Schmitz, and A. R. Bell, Plasma Phys. Controlled Fusion **57**(11), 113001 (2015).
[12]M. M. Turner, Phys. Plasmas **13**(3), 033506 (2006).
[13]A. Zhidkov and A. Sasaki, Phys. Rev E **59**, 7085 (1999).
[14]B. A. Trubnikov, *Reviews of Plasma Physics*, edited by M. A. Leontovich (Consultants Bureau, New York, 1965), Vol. 1, p. 105.
[15]A. M. Dimits, B. I. Andris, R. E. Caflish, M. S. Rosin, and L. F. Ricketson, J. Comput. Phys. **242**, 561–580 (2013).
[16]D. S. Lemons, D. Winske, W. Daughton, and B. Albright, J. Comput. Phys. **228**, 1391–1403 (2009).
[17]D. Ferry, *Semiconductor Transport* (CRC Press, 2000).
[18]S. Chapman and T. G. Cowling, *The Mathematical Theory of Non-uniform Gases: An Account of the Kinetic Theory of Viscosity, Thermal Conduction and Diffusion in Gases* (Cambridge University Press, 1970).

[19]A. G. Zhidkov, Phys. Plasmas **5**(2), 385–389 (1998).
[20]M. F. Ivanov and V. F. Shvets, Sov. Phys. Doklady **23**, 130 (1978), available at http://adsabs.harvard.edu/abs/1978SPhD...23..130I.
[21]H. Grad, Commun. Pure Appl. Math. **2**(4), 331–407 (1949).
[22]M. N. Rosenbluth, W. M. MacDonald, and D. L. Judd, Phys. Rev. **107**(1), 1 (1957).
[23]R. M. Kulsrud, Y. C. Sun, N. K. Winsor, and H. A. Fallon, Phys. Rev. Lett. **31**(11), 690 (1973).
[24]A. V. Gurevich, Sov. Phys. JETP **12**(5), 904–912 (1961), available at http://jetp.ac.ru/cgi-bin/e/index/e/12/5/p904?a=list.
[25]D. A. Zhidkov, "Non-linear Langevin equation for a system of Coulomb particles," Tech. Phys. (in press).
[26]J. Wiechula, A. Schönlein, M. Iberler, C. Hock, T. Manegold, B. Bohlender, and J. Jacoby, AIP Adv. **6**, 075313 (2016).
[27]P. Glas and M. Schnurer, Laser Part. Beams **9**, 501 (1991).
[28]J. Lindl, Phys. Plasmas **2**, 3933–4024 (1995).

References

[1] J. M. Madey, "Stimulated emission of bremsstrahlung in a periodic magnetic field", *Journal of Applied Physics*, vol. 42, no. 5, pp. 1906–1913, 1971.

[2] T. Tajima and J. M. Dawson, "An electron accelerator using a laser", *IEEE Transactions on Nuclear Science*, vol. 26, no. 3, pp. 4188–4189, 1979.

[3] D. Strickland and G. Mourou, "Compression of amplified chirped optical pulses", *Optics communications*, vol. 55, no. 6, pp. 447–449, 1985.

[4] A. Gonsalves, K Nakamura, J Daniels, C Benedetti, C Pieronek, T. De Raadt, S Steinke, J. Bin, S. Bulanov, J Van Tilborg, *et al.*, "Petawatt laser guiding and electron beam acceleration to 8 gev in a laser-heated capillary discharge waveguide", *Physical review letters*, vol. 122, no. 8, p. 084 801, 2019.

[5] J. Faure, Y. Glinec, A Pukhov, S Kiselev, S Gordienko, E Lefebvre, J.-P. Rousseau, F Burgy, and V. Malka, "A laser–plasma accelerator producing monoenergetic electron beams", *Nature*, vol. 431, no. 7008, pp. 541–544, 2004.

[6] C. Geddes, C. Toth, J Van Tilborg, E Esarey, C. Schroeder, D Bruhwiler, C Nieter, J Cary, and W. Leemans, "High-quality electron beams from a laser wakefield accelerator using plasma-channel guiding", *Nature*, vol. 431, no. 7008, pp. 538–541, 2004.

[7] W. Leemans, A. Gonsalves, H.-S. Mao, K Nakamura, C Benedetti, C. Schroeder, C. Tóth, J Daniels, D. Mittelberger, S. Bulanov, *et al.*, "Multi-gev electron beams from capillary-discharge-guided subpetawatt laser pulses in the self-trapping regime", *Physical review letters*, vol. 113, no. 24, p. 245 002, 2014.

[8] A. R. Maier, N. M. Delbos, T. Eichner, L. Hübner, S. Jalas, L. Jeppe, S. W. Jolly, M. Kirchen, V. Leroux, P. Messner, *et al.*, "Decoding sources of energy variability in a laser-plasma accelerator", *Physical Review X*, vol. 10, no. 3, p. 031 039, 2020.

[9] M. Couprie, "The lunex5 project", in *Mid-Infrared Coherent Sources*, Optical Society of America, 2018, JT5A–4.

[10] J. Filhol, A Nadji, J. Besson, P Brunelle, L Cassinari, M. Couprie, J. Denard, C Herbeaux, N Hubert, J. Lamarre, *et al.*, "Operation and performance upgrade of the soleil storage ring", in *PAC*, vol. 9, 2015, pp. 2312–21 314.

[11] C. Rechatin, J. Faure, A. Ben-Ismaïl, J Lim, R. Fitour, A Specka, H Videau, A. Tafzi, F. Burgy, and V. Malka, "Controlling the phase-space volume of injected electrons in a laser-plasma accelerator", *Physical review letters*, vol. 102, no. 16, p. 164 801, 2009.

[12] T André, I. Andriyash, A Loulergue, M Labat, E Roussel, A Ghaith, M Khojoyan, C Thaury, M Valléau, F Briquez, *et al.*, "Control of laser plasma accelerated electrons for light sources", *Nature communications*, vol. 9, no. 1, pp. 1–11, 2018.

[13] A. Ghaith, A. Loulergue, D. Oumbarek, O. Marcouillé, M. Valléau, M. Labat, S. Corde, and M.-E. Couprie, "Electron beam brightness and undulator radiation brilliance for a laser plasma acceleration based free electron laser", *Instruments*, vol. 4, no. 1, p. 1, 2020.

[14] J. C. Maxwell, *A treatise on electricity and magnetism*. Oxford: Clarendon Press, 1873, vol. 1.

[15] M. W. Kunw, "Lecture notes on irreversible processes in plasmas", 2021. [Online]. Available: https://www.astro.princeton.edu/~kunz/Site/AST554/AST554_lecture_notes_Kunz.pdf.

[16] "Applications of high intensity laser pulses", *LMU, Munchen*, 2017. [Online]. Available: https://www.physik.uni-muenchen.de/lehre/vorlesungen/sose_17/applications_of_high-intensity_laser-pulses/vorlesung/lasermatter.pdf.

[17] L. Keldysh *et al.*, "Ionization in the field of a strong electromagnetic wave", *Sov. Phys. JETP*, vol. 20, no. 5, pp. 1307–1314, 1965.

[18] *Electron work function of the elements*. [Online]. Available: https://public.wsu.edu/~pchemlab/documents/Work-functionvalues.pdf.

[19] V. Krainov, "Theory of barrier-suppression ionization of atoms", *Journal of Nonlinear Optical Physics & Materials*, vol. 4, no. 04, pp. 775–798, 1995.

[20] L. Boltzmann, ""studien über das gleichgewicht der lebendigen kraft zwischen bewegten materiellen punkten" [studies on the balance of living force between moving material points]", *Task Technical Report*, 58: 517-560, 1868.

[21] J. Lawson, "Lasers and accelerators", *IEEE Transactions on Nuclear Science*, vol. 26, no. 3, pp. 4217–4219, 1979.

[22] P. Gibbon, *Short pulse laser interactions with matter: an introduction*. World Scientific, 2005.

[23] C. E. Max, J. Arons, and A. B. Langdon, "Self-modulation and self-focusing of electromagnetic waves in plasmas", *Physical Review Letters*, vol. 33, no. 4, p. 209, 1974.

[24] G.-Z. Sun, E. Ott, Y. Lee, and P. Guzdar, "Self-focusing of short intense pulses in plasmas", *The Physics of fluids*, vol. 30, no. 2, pp. 526–532, 1987.

[25] J. Faure, Y. Glinec, J. Santos, F Ewald, J.-P. Rousseau, S Kiselev, A Pukhov, T Hosokai, and V. Malka, "Observation of laser-pulse shortening in nonlinear plasma waves", *Physical review letters*, vol. 95, no. 20, p. 205 003, 2005.

[26] A Modena, Z Najmudin, A. Dangor, C. Clayton, K. Marsh, C Joshi, V. Malka, C. Darrow, C Danson, D Neely, *et al.*, "Electron acceleration from the breaking of relativistic plasma waves", *nature*, vol. 377, no. 6550, pp. 606–608, 1995.

[27] T. Tajima and J. M. Dawson, "Laser electron accelerator", *Physical Review Letters*, vol. 43, no. 4, p. 267, 1979.

[28] N. E. Andreev and L. M. Gorbunov, "Laser-plasma acceleration of electrons", *Physics-Uspekhi*, vol. 42, no. 1, pp. 49–53, 1999.

[29] V Malka, "Plasma wake accelerators: Introduction and historical overview", *arXiv preprint arXiv:1705.09584*, 2017.

[30] K. Schmid, A. Buck, C. M. Sears, J. M. Mikhailova, R. Tautz, D. Herrmann, M. Geissler, F. Krausz, and L. Veisz, "Density-transition based electron injector for laser driven wakefield accelerators", *Physical Review Special Topics-Accelerators and Beams*, vol. 13, no. 9, p. 091 301, 2010.

[31] H. Suk, N. Barov, J. B. Rosenzweig, and E Esarey, "Plasma electron trapping and acceleration in a plasma wake field using a density transition", in *The Physics Of High Brightness Beams*, World Scientific, 2000, pp. 404–417.

[32] A. Gonsalves, K. Nakamura, C. Lin, D. Panasenko, S. Shiraishi, T. Sokollik, C. Benedetti, C. Schroeder, C. Geddes, J. Van Tilborg, *et al.*, "Tunable laser plasma accelerator based on longitudinal density tailoring", *Nature Physics*, vol. 7, no. 11, pp. 862–866, 2011.

[33] A. Brantov, T. Z. Esirkepov, M Kando, H Kotaki, V. Y. Bychenkov, and S. Bulanov, "Controlled electron injection into the wake wave using plasma density inhomogeneity", *Physics of Plasmas*, vol. 15, no. 7, p. 073 111, 2008.

[34] J Faure, C Rechatin, O Lundh, L Ammoura, and V Malka, "Injection and acceleration of quasimonoenergetic relativistic electron beams using density gradients at the edges of a plasma channel", *Physics of Plasmas*, vol. 17, no. 8, p. 083 107, 2010.

[35] P Tomassini, M Galimberti, A Giulietti, D. Giulietti, L. Gizzi, L Labate, and F. Pegoraro, "Production of high-quality electron beams in numerical experiments of laser wakefield acceleration with longitudinal wave breaking", *Physical Review Special Topics-Accelerators and Beams*, vol. 6, no. 12, p. 121 301, 2003.

[36] T.-Y. Chien, C.-L. Chang, C.-H. Lee, J.-Y. Lin, J Wang, and S.-Y. Chen, "Spatially localized self-injection of electrons in a self-modulated laser-wakefield accelerator by using a laser-induced transient density ramp", *Physical review letters*, vol. 94, no. 11, p. 115 003, 2005.

[37] J. Kim, N Hafz, and H Suk, "Electron trapping and acceleration across a parabolic plasma density profile", *Physical Review E*, vol. 69, no. 2, p. 026 409, 2004.

[38] C McGuffey, A. Thomas, W Schumaker, T Matsuoka, V Chvykov, F. Dollar, G Kalintchenko, V Yanovsky, A Maksimchuk, K Krushelnick, *et al.*, "Ionization induced trapping in a laser wakefield accelerator", *Physical Review Letters*, vol. 104, no. 2, p. 025 004, 2010.

[39] E Oz, S Deng, T Katsouleas, P Muggli, C. Barnes, I Blumenfeld, F. Decker, P Emma, M. Hogan, R Ischebeck, *et al.*, "Ionization-induced electron trapping in ultrarelativistic plasma wakes", *Physical review letters*, vol. 98, no. 8, p. 084 801, 2007.

[40] J. Couperus, R Pausch, A Köhler, O Zarini, J. Krämer, M Garten, A Huebl, R Gebhardt, U Helbig, S Bock, *et al.*, "Demonstration of a beam loaded nanocoulomb-class laser wakefield accelerator", *Nature communications*, vol. 8, no. 1, pp. 1–7, 2017.

[41] B. Pollock, C. Clayton, J. Ralph, F Albert, A Davidson, L Divol, C Filip, S. Glenzer, K Herpoldt, W Lu, *et al.*, "Demonstration of a narrow energy spread, 0.5 gev electron beam from a two-stage laser wakefield accelerator", *Physical review letters*, vol. 107, no. 4, p. 045 001, 2011.

[42] J. Wang, J. Feng, C. Zhu, Y. Li, Y. He, D. Li, J. Tan, J. Ma, and L. Chen, "Small energy spread electron beams from laser wakefield acceleration by self-evolved ionization injection", *Plasma Physics and Controlled Fusion*, vol. 60, no. 3, p. 034 004, 2018.

[43] D. Umstadter, S.-Y. Chen, A Maksimchuk, G Mourou, and R Wagner, "Nonlinear optics in relativistic plasmas and laser wake field acceleration of electrons", *Science*, vol. 273, no. 5274, pp. 472–475, 1996.

[44] E. Esarey, P. Sprangle, J. Krall, and A. Ting, "Self-focusing and guiding of short laser pulses in ionizing gases and plasmas", *IEEE journal of quantum electronics*, vol. 33, no. 11, pp. 1879–1914, 1997.

[45] J. Faure, C. Rechatin, A Norlin, A. Lifschitz, Y Glinec, and V. Malka, "Controlled injection and acceleration of electrons in plasma wakefields by colliding laser pulses", *Nature*, vol. 444, no. 7120, pp. 737–739, 2006.

[46] G Fubiani, E Esarey, C. Schroeder, and W. Leemans, "Beat wave injection of electrons into plasma waves using two interfering laser pulses", *Physical Review E*, vol. 70, no. 1, p. 016 402, 2004.

[47] X Davoine, E Lefebvre, J. Faure, C. Rechatin, A. Lifschitz, and V. Malka, "Simulation of quasimonoenergetic electron beams produced by colliding pulse wakefield acceleration", *Physics of Plasmas*, vol. 15, no. 11, p. 113 102, 2008.

[48] V. Malka, J. Faure, C. Rechatin, A. Ben-Ismaïl, J. Lim, X. Davoine, and E Lefebvre, "Laser-driven accelerators by colliding pulses injection: A review of simulation and experimental results", *Physics of Plasmas*, vol. 16, no. 5, p. 056 703, 2009.

[49] C. Rechatin, J. Faure, A. Lifschitz, X. Davoine, E Lefebvre, and V. Malka, "Quasi-monoenergetic electron beams produced by colliding cross-polarized laser pulses in underdense plasmas", *New Journal of Physics*, vol. 11, no. 1, p. 013 011, 2009.

[50] C. Rechatin, X. Davoine, A. Lifschitz, A. B. Ismail, J Lim, E Lefebvre, J. Faure, and V. Malka, "Observation of beam loading in a laser-plasma accelerator", *Physical review letters*, vol. 103, no. 19, p. 194 804, 2009.

[51] W. Lu, M Tzoufras, C Joshi, F. Tsung, W. Mori, J Vieira, R. Fonseca, and L. Silva, "Generating multi-gev electron bunches using single stage laser wakefield acceleration in a 3d nonlinear regime", *Physical Review Special Topics-Accelerators and Beams*, vol. 10, no. 6, p. 061 301, 2007.

[52] L. Gorbunov and V. Kirsanov, "Excitation of plasma waves by an electromagnetic wave packet", *Sov. Phys. JETP*, vol. 66, no. 2, pp. 290–294, 1987.

[53] P Sprangle, G Joyce, E Esarey, and A Ting, "Laser wakefield acceleration and relativstic optical guiding", in *AIP Conference Proceedings*, American Institute of Physics, vol. 175, 1988, pp. 231–239.

[54] J. Rosenzweig, B Breizman, T Katsouleas, and J. Su, "Acceleration and focusing of electrons in two-dimensional nonlinear plasma wake fields", *Physical Review A*, vol. 44, no. 10, R6189, 1991.

[55] A. Pukhov and J. Meyer-ter Vehn, "Laser wake field acceleration: The highly non-linear broken-wave regime", *Applied Physics B*, vol. 74, no. 4, pp. 355–361, 2002.

[56] W. Lu, C. Huang, M. Zhou, W. Mori, and T Katsouleas, "Nonlinear theory for relativistic plasma wakefields in the blowout regime", *Physical review letters*, vol. 96, no. 16, p. 165 002, 2006.

[57] W Lu, C Huang, M Zhou, M Tzoufras, F. Tsung, W. Mori, and T Katsouleas, "A nonlinear theory for multidimensional relativistic plasma wave wakefields", *Physics of Plasmas*, vol. 13, no. 5, p. 056 709, 2006.

[58] I Kostyukov, A Pukhov, and S Kiselev, "Phenomenological theory of laser-plasma interaction in "bubble" regime", *Physics of Plasmas*, vol. 11, no. 11, pp. 5256–5264, 2004.

[59] C. Clayton, K.-C. Tzeng, D Gordon, P Muggli, W. Mori, C Joshi, V. Malka, Z Najmudin, A Modena, D Neely, *et al.*, "Plasma wave generation in a self-focused channel of a relativistically intense laser pulse", *Physical review letters*, vol. 81, no. 1, p. 100, 1998.

[60] C Gahn, G. Tsakiris, A Pukhov, J Meyer-ter Vehn, G Pretzler, P Thirolf, D Habs, and K. Witte, "Multi-mev electron beam generation by direct laser acceleration in high-density plasma channels", *Physical Review Letters*, vol. 83, no. 23, p. 4772, 1999.

[61] W. P. Leemans, B. Nagler, A. J. Gonsalves, C. Tóth, K. Nakamura, C. G. Geddes, E. Esarey, C. Schroeder, and S. Hooker, "Gev electron beams from a centimetre-scale accelerator", *Nature physics*, vol. 2, no. 10, pp. 696–699, 2006.

[62] H.-P. Schlenvoigt, K Haupt, A Debus, F Budde, O Jäckel, S Pfotenhauer, H Schwoerer, E Rohwer, J. Gallacher, E Brunetti, *et al.*, "A compact synchrotron radiation source driven by a laser-plasma wakefield accelerator", *Nature Physics*, vol. 4, no. 2, pp. 130–133, 2008.

[63] C. K. Birdsall and A. B. Langdon, *Plasma physics via computer simulation*. CRC press, 2004.

[64] W. Kruer, *The physics of laser plasma interactions*. CRC Press, 2019.

[65] Y. Sentoku and A. J. Kemp, "Numerical methods for particle simulations at extreme densities and temperatures: Weighted particles, relativistic collisions and reduced currents", *Journal of Computational Physics*, vol. 227, no. 14, pp. 6846–6861, 2008.

[66] R Mishra, P Leblanc, Y Sentoku, M. Wei, and F. Beg, "Collisional particle-in-cell modeling for energy transport accompanied by atomic processes in dense plasmas", *Physics of Plasmas*, vol. 20, no. 7, p. 072 704, 2013.

[67] D. Oumbarek Espinos, A. Zhidkov, and R. Kodama, "Langevin equation for coulomb collision in non-maxwellian plasmas", *Physics of Plasmas*, vol. 25, no. 7, p. 072 307, 2018.

[68] Y. Kitagawa, Y. Sentoku, S. Akamatsu, W. Sakamoto, R. Kodama, K. A. Tanaka, K. Azumi, T. Norimatsu, T. Matsuoka, H. Fujita, *et al.*, "Electron acceleration in an ultraintense-laser-illuminated capillary", *Physical review letters*, vol. 92, no. 20, p. 205 002, 2004.

[69] Y Mori, Y Sentoku, K Kondo, K Tsuji, N Nakanii, S Fukumochi, M Kashihara, K Kimura, K Takeda, K. Tanaka, *et al.*, "Autoinjection of electrons into a wake field using a capillary with attached cone", *Physics of Plasmas*, vol. 16, no. 12, p. 123 103, 2009.

[70] T. Z. Esirkepov, "Exact charge conservation scheme for particle-in-cell simulation with an arbitrary form-factor", *Computer Physics Communications*, vol. 135, no. 2, pp. 144–153, 2001.

[71] N. Chauvin, *Transverse beam dynamics, master 2 grands instruments*, 2016.

[72] M Martini, "An introduction to transverse beam dynamics in accelerators", Tech. Rep., 1996.

[73] M. Reiser and P. O'Shea, *Theory and design of charged particle beams*. Wiley Online Library, 1994, vol. 312.

[74] K. L. Brown, "First and second order matrix theory for the design of the beam transport systems and charged particle spectrometers", Stanford Linear Accelerator Center, Calif., Tech. Rep., 1971.

[75] G. W. Hill, "On the part of the motion of the lunar perigee which is a function of the mean motions of the sun and moon", *Acta mathematica*, vol. 8, no. 1, pp. 1–36, 1886.

[76] G. Floquet, "Sur les équations différentielles linéaires à coefficients périodiques", in *Annales scientifiques de l'École normale supérieure*, vol. 12, 1883, pp. 47–88.

[77] K. Floettmann, "Some basic features of the beam emittance", *Physical Review Special Topics-Accelerators and Beams*, vol. 6, no. 3, p. 034 202, 2003.

[78] J. Liouville, "Note sur la théorie de la variation des constantes arbitraires.", fre, *Journal de Mathématiques Pures et Appliquées*, pp. 342–349, 1838. [Online]. Available: http://eudml.org/doc/234417.

[79] A. Madur, "Contribution à la métrologie magnétique des multipôles d'accélérateurs: Les quadrupôles du synchroton soleil", PhD thesis, Vandoeuvre-les-Nancy, INPL, 2006.

[80] A. Milanese, *An introduction to magnets for accelerators*, Jan. 2017. [Online]. Available: https://indico.cern.ch/event/590390/contributions/2381025/attachments/1401281/2140074/JAI_course_Jan_2017.pdf.

[81] K. Hwang and S. Lee, "Dipole fringe field thin map for compact synchrotrons", *Physical Review Special Topics-Accelerators and Beams*, vol. 18, no. 12, p. 122 401, 2015.

[82] L. Nadolski, "Application de l'analyse en fréquence à l'etude de la dynamique des sources de lumière", PhD thesis, Université Paris Sud-Paris XI, 2001.

[83] W. R. Hamilton, "On the application to dynamics of a general mathematical method previously applied to optics", *British Association Report*, vol. 513, p. 1834, 1834.

[84] H. Motz, "Applications of the radiation from fast electron beams", *Journal of Applied Physics*, vol. 22, no. 5, pp. 527–535, 1951.

[85] R. M. Phillips, "The ubitron, a high-power traveling-wave tube based on a periodic beam interaction in unloaded waveguide", *IRE Trans. Electron Devices*, vol. 7, no. 4, pp. 231–241, 1960. [Online]. Available: http://cds.cern.ch/record/439952.

[86] L. R. Elias, W. M. Fairbank, J. M. Madey, H. A. Schwettman, and T. I. Smith, "Observation of stimulated emission of radiation by relativistic electrons in a spatially periodic transverse magnetic field", *Physical Review Letters*, vol. 36, no. 13, p. 717, 1976.

[87] D. A. G. Deacon, L. R. Elias, J. M. J. Madey, G. J. Ramian, H. A. Schwettman, and T. I. Smith, "First operation of a free-electron laser", *Phys. Rev. Lett.*, vol. 38, pp. 892–894, 16 1977. DOI: 10.1103/PhysRevLett.38.892. [Online]. Available: https://link.aps.org/doi/10.1103/PhysRevLett.38.892.

[88] L. Elias and J. Madey, "Superconducting helically wound magnet for the free-electron laser", *Review of Scientific Instruments*, vol. 50, no. 11, pp. 1335–1341, 1979.

[89] Y. Ivanyushenkov, E Baynham, T Bradshaw, S Carr, J Rochford, B. Shepherd, J. Clarke, O. Malyshev, D. Scott, J. Dainton, *et al.*, "Development of a superconducting helical undulator for a polarised positron source", in *Proceedings of the 2005 Particle Accelerator Conference*, IEEE, 2005, pp. 2295–2297.

[90] G Dattoli, M Del Franco, M Labat, P. Ottaviani, and S Pagnutti, "Introduction to the physics of free electron laser and comparison with conventional laser sources", *Free Electron Lasers*, 2012.

[91] C. Pellegrini and S. Reiche, "Lasers, free-electron", *digital Encyclopedia of Applied Physics*, 2003.

[92] G. Brown, K Halbach, J. Harris, and H. Winick, "Wiggler and undulator magnets—a review", *Nuclear Instruments and Methods in Physics Research*, vol. 208, no. 1-3, pp. 65–77, 1983.

[93] P. Schmüser, "Fel theory for pedestrians", in *Lecture at Heraeus seminar Free-electron lasers: From fundamentals to applications*, 2012.

[94] J. S. Nodvick and D. S. Saxon, "Suppression of coherent radiation by electrons in a synchrotron", *Physical Review*, vol. 96, no. 1, p. 180, 1954.

[95] A. Wolski, "Introduction to free electron lasers", 2014. [Online]. Available: https://indico.cern.ch/event/279729/contributions/1626355/attachments/512320/707051/FreeElectronLasers.pdf.

[96] C.-C. Shih and S.-M. Shih, "Advanced free electron laser resonator", *Nuclear Instruments and Methods in Physics Research Section A: Accelerators, Spectrometers, Detectors and Associated Equipment*, vol. 304, no. 1-3, pp. 788–791, 1991.

[97] M Marsi, M Trovo, R. Walker, L Giannessi, G Dattoli, A Gatto, N Kaiser, S Günster, D Ristau, M. Couprie, *et al.*, "Operation and performance of a free electron laser oscillator down to 190 nm", *Applied physics letters*, vol. 80, no. 16, pp. 2851–2853, 2002.

[98] B Faatz, N Baboi, V Ayvazyan, V Balandin, W Decking, S Duesterer, H. Eckoldt, J Feldhaus, N Golubeva, M Koerfer, *et al.*, "Flash ii: A seeded future at flash", *Proceedings of IPAC, Kyoto, Japan*, 2010.

[99] E. Schneidmiller, B Faatz, M Kuhlmann, J. Rönsch-Schulenburg, S Schreiber, M Tischer, and M. Yurkov, "First operation of a harmonic lasing self-seeded free electron laser", *Physical Review Accelerators and Beams*, vol. 20, no. 2, p. 020 705, 2017.

[100] M. Svandrlik, E. Allaria, L. Badano, F. Bencivenga, C. Callegari, F. Capotondi, D. Castronovo, P. Cinquegrana, M. Coreno, R. Cucini, *et al.*, "The fermi seeded fel facility: Operational experience and future perspectives", in *6th Int. Particle Accelerator Conf.(IPAC'15), Richmond, VA, USA, May 3-8, 2015*, JACOW, Geneva, Switzerland, 2015, pp. 1538–1541.

[101] J. Rosenzweig, D Alesini, G Andonian, M Boscolo, M Dunning, L Faillace, M Ferrario, A Fukusawa, L Giannessi, E Hemsing, *et al.*, "Generation of ultra-short, high brightness electron beams for single-spike sase fel operation", *Nuclear Instruments and Methods in Physics Research Section A: Accelerators, Spectrometers, Detectors and Associated Equipment*, vol. 593, no. 1-2, pp. 39–44, 2008.

[102] C Pellegrini, "High power femtosecond pulses from an x-ray sase-fel", *Nuclear Instruments and Methods in Physics Research Section A: Accelerators, Spectrometers, Detectors and Associated Equipment*, vol. 445, no. 1-3, pp. 124–127, 2000.

[103] K Zhukovsky, "Two-frequency undulator in a short sase fel for angstrom wavelengths", *Journal of Optics*, vol. 20, no. 9, p. 095 003, 2018.

[104] G Lambert, T Hara, D Garzella, T Tanikawa, M Labat, B Carre, H Kitamura, T Shintake, M Bougeard, S Inoue, *et al.*, "Injection of harmonics generated in gas in a free-electron laser providing intense and coherent extreme-ultraviolet light", *Nature physics*, vol. 4, no. 4, pp. 296–300, 2008.

[105] J. M. Dawson, "Plasma particle accelerators", *Scientific American*, vol. 260, no. 3, pp. 54–61, 1989.

[106] M. Born and E. Wolf, "Principles of optics pergamon press", *Chap*, vol. 3, no. 1, p. 118, 1980.

[107] R Bonifacio, C Pellegrini, and L. Narducci, "Collective instabilities and high-gain regime free electron laser", in *AIP Conference Proceedings*, American Institute of Physics, vol. 118, 1984, pp. 236–259.

[108] Z. Huang and K.-J. Kim, "Three-dimensional analysis of harmonic generation in high-gain free-electron lasers", *Physical Review E*, vol. 62, no. 5, p. 7295, 2000.

[109] K.-J. Kim, "An analysis of self-amplified spontaneous emission", *Nuclear Instruments and Methods in Physics Research Section A: Accelerators, Spectrometers, Detectors and Associated Equipment*, vol. 250, no. 1-2, pp. 396–403, 1986.

[110] A. Kondratenko and E. Saldin, "Generating of coherent radiation by a relativistic electron beam in an ondulator", *Part. Accel.*, vol. 10, pp. 207–216, 1980.

[111] J. Madey, "Relationship between mean radiated energy, mean squared radiated energy and spontaneous power spectrum in a power series expansion of the equations of motion in a free-electron laser", *Il Nuovo Cimento B (1971-1996)*, vol. 50, no. 1, pp. 64–88, 1979.

[112] J. M. Madey and C. Pellegrini, "Free electron generation of extreme ultraviolet coherent radiation", in *Topical Meeting on Free Electron Generation of Extreme Ultraviolet Coherent Radiation (1983: Brookhaven National Laboratory)*, American Institute of Physics, 1984.

[113] T. Orzechowski, "B. anderson, wm fawley, d. prosnitz, et scharle-mann, s. yarema, d. hopkins", *AC Paul, AM Sessler, and JS Wurtele, Phys. Rev. Lett*, vol. 54, p. 889, 1985.

[114] D. A. Edwards and M. J. Syphers, *An introduction to the physics of high energy accelerators*. John Wiley & Sons, 2008.

[115] S Krinsky and L. Yu, "Output power in guided modes for amplified spontaneous emission in a single-pass free-electron laser", *Physical Review A*, vol. 35, no. 8, p. 3406, 1987.

[116] G. T. Moore, "High-gain small-signal modes of the free-electron laser", *Optics communications*, vol. 52, no. 1, pp. 46–51, 1984.

[117] K.-J. Kim, "Three-dimensional analysis of coherent amplification and self-amplified spontaneous emission in free-electron lasers", *Phys. Rev. Lett.*, vol. 57, pp. 1871–1874, 15 1986. DOI: 10.1103/PhysRevLett.57.1871. [Online]. Available: https://link.aps.org/doi/10.1103/PhysRevLett.57.1871.

[118] R. Bonifacio, C. Pellegrini, and L. Narducci, "Collective instabilities and high-gain regime in a free electron laser", *Optics Communications*, vol. 50, no. 6, pp. 373–378, 1984, ISSN: 0030-4018. DOI: https://doi.org/10.1016/0030-4018(84)90105-6. [Online]. Available: https://www.sciencedirect.com/science/article/pii/0030401884901056.

[119] M. Xie, "Design optimization for an x-ray free electron laser driven by slac linac", in *Proceedings Particle Accelerator Conference*, IEEE, vol. 1, 1995, pp. 183–185.

[120] L.-H. Yu and S. Krinsky, "Amplified spontaneous emission in a single pass free electron laser", *Nuclear Instruments and Methods in Physics Research Section A: Accelerators, Spectrometers, Detectors and Associated Equipment*, vol. 285, no. 1, pp. 119–121, 1989, ISSN: 0168-9002. DOI: https://doi.org/10.1016/0168-9002(89)90436-1. [Online]. Available: https://www.sciencedirect.com/science/article/pii/0168900289904361.

[121] Y. H. Chin, K.-J. Kim, and M. Xie, "Three-dimensional theory of the small-signal high-gain free-electron laser including betatron oscillations", *Phys. Rev. A*, vol. 46, pp. 6662–6683, 10 1992. DOI: 10.1103/PhysRevA.46.6662. [Online]. Available: https://link.aps.org/doi/10.1103/PhysRevA.46.6662.

[122] L.-H. Yu, S Krinsky, and R. Gluckstern, "Calculation of universal scaling function for free-electron-laser gain", *Physical review letters*, vol. 64, no. 25, p. 3011, 1990.

[123] K.-J. Kim and M. Xie, "Self-amplified spontaneous emission for short wavelength coherent radiation", *Nuclear Instruments and Methods in Physics Research Section A: Accelerators, Spectrometers, Detectors and Associated Equipment*, vol. 331, no. 1-3, pp. 359–364, 1993.

[124] Z. Huang and I. Lindau, "Sacla hard-x-ray compact fel", *Nature Photonics*, vol. 6, no. 8, pp. 505–506, 2012.

[125] J Rossbach, T. F. S. Group, *et al.*, "A vuv free electron laser at the tesla test facility at desy", *Nuclear Instruments and Methods in Physics Research Section A: Accelerators, Spectrometers, Detectors and Associated Equipment*, vol. 375, no. 1-3, pp. 269–273, 1996.

[126] R Ischebeck, J Feldhaus, C. Gerth, E Saldin, P Schmüser, E Schneidmiller, B Steeg, K Tiedtke, M Tonutti, R Treusch, *et al.*, "Study of the transverse coherence at the ttf free electron laser", *Nuclear Instruments and Methods in Physics Research Section A: Accelerators, Spectrometers, Detectors and Associated Equipment*, vol. 507, no. 1-2, pp. 175–180, 2003.

[127] T Atkinson, M Dirsat, O Dressler, P Kuske, and H Rast, "Development of a non-linear kicker system to facilitate a new injection scheme for the bessy ii storage ring", *Proc. IPAC' 11*, pp. 3394–3396, 2011.

[128] M. E. Couprie, "Towards compact free electron–laser based on laser plasma accelerators", *Nuclear Instruments and Methods in Physics Research Section A: Accelerators, Spectrometers, Detectors and Associated Equipment*, vol. 909, pp. 5–15, 2018.

[129] R Prazeres, J. Ortega, F Glotin, D. Jaroszynski, and O Marcouillé, "Observation of self-amplified spontaneous emission in the mid-infrared in a free-electron laser", *Physical review letters*, vol. 78, no. 11, p. 2124, 1997.

[130] M Babzien, I Ben-Zvi, P Catravas, J.-M. Fang, T. Marshall, X. Wang, J. Wurtele, V Yakimenko, and L. Yu, "Observation of self-amplified spontaneous emission in the near-infrared and visible wavelengths", *Physical Review E*, vol. 57, no. 5, p. 6093, 1998.

[131] D. Nguyen, R. Sheffield, C. Fortgang, J. Goldstein, J. Kinross-Wright, and N. Ebrahim, "Self-amplified spontaneous emission driven by a high-brightness electron beam", *Physical review letters*, vol. 81, no. 4, p. 810, 1998.

[132] T. Ishikawa, H. Aoyagi, T. Asaka, Y. Asano, N. Azumi, T. Bizen, H. Ego, K. Fukami, T. Fukui, Y. Furukawa, *et al.*, "A compact x-ray free-electron laser emitting in the sub-ångström region", *nature photonics*, vol. 6, no. 8, pp. 540–544, 2012.

[133] A Tremaine, X. Wang, M Babzien, I Ben-Zvi, M Cornacchia, H.-D. Nuhn, R Malone, A Murokh, C Pellegrini, S Reiche, *et al.*, "Experimental characterization of nonlinear harmonic radiation from a visible self-amplified spontaneous emission free-electron laser at saturation", *Physical review letters*, vol. 88, no. 20, p. 204 801, 2002.

[134] H.-S. Kang, H. Yang, G. Kim, H. Heo, I. Nam, C.-K. Min, C. Kim, S. Y. Baek, H.-J. Choi, G. Mun, *et al.*, "Fel performance achieved at pal-xfel using a three-chicane bunch compression scheme", *Journal of synchrotron radiation*, vol. 26, no. 4, pp. 1127–1138, 2019.

[135] W. Decking, H. Weise, *et al.*, "Commissioning of the european xfel accelerator", in *Proc. 8th Int. Particle Accelerator Conf.(IPAC' 17)*, 2017, pp. 1–6.

[136] V Ayvazyan, N Baboi, I Bohnet, R Brinkmann, M Castellano, P Castro, L Catani, S Choroba, A Cianchi, M Dohlus, *et al.*, "Generation of gw radiation pulses from a vuv free-electron laser operating in the femtosecond regime", *Physical review letters*, vol. 88, no. 10, p. 104 802, 2002.

[137] S. Gold, D. Hardesty, A. Kinkead, L. Barnett, and V. Granatstein, "High-gain 35-ghz free-electron laser-amplifier experiment", *Physical review letters*, vol. 52, no. 14, p. 1218, 1984.

[138] C Lejuene and J Aubert, "Emittance and brightness: Definitions and measurements, applied charged particle optics", *Adv. Electron. Electron Phys., Suppl. A*, vol. 13, 1980.

[139] Z. Zhu, Z. Zhao, D Wang, Z Liu, R. Li, L. Yin, and Z. Yang, "Sclf: An 8-gev cw scrf linac-based x-ray fel facility in shanghai", *Proceedings of the FEL2017, Santa Fe, NM, USA*, pp. 20–25, 2017.

[140] M. Yoon, W. Hwang, D. Kim, S. Park, I Hwang, and E. Kim, "0.1 nm sase fel at the pohang accelerator laboratory," ", in *FEL 2008 conference, Gyeongju*, 2008.

[141] I. S. Ko, H.-S. Kang, H. Heo, C. Kim, G. Kim, C.-K. Min, H. Yang, S. Y. Baek, H.-J. Choi, G. Mun, *et al.*, "Construction and commissioning of pal-xfel facility", *Applied Sciences*, vol. 7, no. 5, p. 479, 2017.

[142] M. Yabashi, H. Tanaka, K. Tono, and T. Ishikawa, "Status of the sacla facility", *Applied Sciences*, vol. 7, no. 6, p. 604, 2017.

[143] C. J. Milne, T. Schietinger, M. Aiba, A. Alarcon, J. Alex, A. Anghel, V. Arsov, C. Beard, P. Beaud, S. Bettoni, *et al.*, "Swissfel: The swiss x-ray free electron laser", *Applied Sciences*, vol. 7, no. 7, p. 720, 2017.

[144] J Amann, W Berg, V Blank, F.-J. Decker, Y Ding, P Emma, Y Feng, J Frisch, D Fritz, J Hastings, *et al.*, "Demonstration of self-seeding in a hard-x-ray free-electron laser", *Nature photonics*, vol. 6, no. 10, pp. 693–698, 2012.

[145] J. MacArthur, J. Duris, Z. Huang, A. Marinelli, *et al.*, "High power sub-femtosecond x-ray pulse study for the lcls", *Proceedings of IPAC2017, Copenhagen, Denmark*, vol. 10, 2017.

[146] C. Lechner, R. Assmann, J Bödewadt, M Dohlus, N Ekanayake, B Faatz, G Feng, I Hartl, A Azima, M. Drescher, *et al.*, "Concept for a seeded fel at flash2", in *8th Int. Particle Accelerator Conf.(IPAC'17), Copenhagen, Denmark, 14â 19 May, 2017*, JACOW, Geneva, Switzerland, 2017, pp. 2607–2610.

[147] B. Faatz, M. Braune, O. Hensler, K. Honkavaara, R. Kammering, M. Kuhlmann, E. Ploenjes, J. Roensch-Schulenburg, E. Schneidmiller, S. Schreiber, *et al.*, "The flash facility: Advanced options for flash2 and future perspectives", *Applied Sciences*, vol. 7, no. 11, p. 1114, 2017.

[148] L. Giannessi, E. Allaria, L. Badano, S. Bassanese, F. Bencivenga, C. Callegari, F. Capotondi, D. Castronovo, F. Cilento, P. Cinquegrana, *et al.*, "Status and perspectives of the fermi fel facility (2019)", PhD thesis, Univerza v Novi Gorici, 2019.

[149] Z. Zhao, S. Chen, L. Yu, C. Tang, L. Yin, D Wang, Q Gu, *et al.*, "Shanghai soft x-ray free electron laser test facility", *Proceedings of IPAC2011, San Sebastián, Spain*, pp. 3011–3013, 2011.

[150] Z. Zhao, D. Wang, L. Yin, Q. Gu, G. Fang, M. Gu, Y. Leng, Q. Zhou, B. Liu, C. Tang, *et al.*, "Shanghai soft x-ray free-electron laser facility", 2019.

[151] M Ferrario, D Alesini, M Bellaveglia, M Benfatto, R Boni, M Boscolo, M Castellano, E Chiadroni, A Clozza, L Cultrera, *et al.*, "Recent results of the sparc fel experiments", *Energy*, vol. 146, no. 148, p. 150, 2009.

[152] L. Lazzarino, E Di Palma, M. Anania, M Artioli, A Bacci, M Bellaveglia, E Chiadroni, A Cianchi, F Ciocci, G Dattoli, *et al.*, "Self-amplified spontaneous emission free electron laser devices and nonideal electron beam transport", *Physical Review Special Topics-Accelerators and Beams*, vol. 17, no. 11, p. 110 706, 2014.

[153] R Prazeres, J. Berset, F Glotin, D Jaroszynski, and J. Ortega, "Optical performance of the clio infrared fel", *Nuclear Instruments and Methods in Physics Research Section A: Accelerators, Spectrometers, Detectors and Associated Equipment*, vol. 331, no. 1-3, pp. 15–19, 1993.

[154] D Oepts, A. Van der Meer, and P. Van Amersfoort, "The free-electron-laser user facility felix", *Infrared physics & technology*, vol. 36, no. 1, pp. 297–308, 1995.

[155] W. Leemans, R Duarte, E Esarey, S Fournier, C. Geddes, D Lockhart, C. Schroeder, C. Tóth, J.-L. Vay, and S Zimmermann, "The berkeley lab laser accelerator (bella): A 10 gev laser plasma accelerator", in *AIP Conference Proceedings*, American Institute of Physics, vol. 1299, 2010, pp. 3–11.

[156] S. Barber, J. van Tilborg, C. Schroeder, R. Lehe, H.-E. Tsai, K. Swanson, S. Steinke, K. Nakamura, C. Geddes, C. Benedetti, *et al.*, "Measured emittance dependence on the injection method in laser plasma accelerators", *Physical review letters*, vol. 119, no. 10, p. 104 801, 2017.

[157] O. Lundh, J Lim, C. Rechatin, L Ammoura, A. Ben-Ismaïl, X Davoine, G. Gallot, J.-P. Goddet, E Lefebvre, V. Malka, *et al.*, "Few femtosecond, few kiloampere electron bunch produced by a laser–plasma accelerator", *Nature Physics*, vol. 7, no. 3, pp. 219–222, 2011.

[158] M Scisciò, L Lancia, M Migliorati, A Mostacci, L Palumbo, Y Papaphilippou, and P Antici, "Parametric study of transport beam lines for electron beams accelerated by laser-plasma interaction", *Journal of Applied Physics*, vol. 119, no. 9, p. 094 905, 2016.

[159] F. Isono, J. van Tilborg, S. Barber, C. Geddes, H.-E. Tsai, C. Schroeder, and W. P. Leemans, "Update on bella center's free-electron laser driven by a laser-plasma accelerator", in *CLEO: Science and Innovations*, Optical Society of America, 2019, SF3I–1.

[160] G Zhou, Y Jiao, J Wu, and T Zhang, "Improving the energy-extraction efficiency of laser-plasma accelerator driven free-electron laser using transverse-gradient undulator with focusing optics and longitudinal tapering", *arXiv preprint arXiv:1608.03067*, 2016.

[161] A. H. Lumpkin, D. W. Rule, M LaBerge, and M. Downer, "Observations n microbunching of electrons in laser-driven plasma accelerators and free-electron", Fermi National Accelerator Lab.(FNAL), Batavia, IL (United States), Tech. Rep., 2019.

[162] B Hafizi and C. Roberson, "Effect of emittance and energy spread on a free-electron laser in the gain-focusing regime", *Physical review letters*, vol. 68, no. 24, p. 3539, 1992.

[163] C. Roberson and B Hafizi, "Free electron laser scaling with emittance and energy spread", *Nuclear Instruments and Methods in Physics Research Section A: Accelerators, Spectrometers, Detectors and Associated Equipment*, vol. 331, no. 1-3, pp. 365–370, 1993.

[164] M.-E. Couprie *et al.*, "An application of laser plasma acceleration: Towards a free-electron laser amplification", *Plasma Physics and Controlled Fusion*, vol. 58, no. 3, p. 034 020, 2016.

[165] S Kuschel, D Hollatz, T Heinemann, O Karger, M. Schwab, D Ullmann, A Knetsch, A Seidel, C Rödel, M Yeung, *et al.*, "Demonstration of passive plasma lensing of a laser wakefield accelerated electron bunch", *Physical Review Accelerators and Beams*, vol. 19, no. 7, p. 071 301, 2016.

[166] J. Van Tilborg, S Steinke, C. Geddes, N. Matlis, B. Shaw, A. Gonsalves, J. Huijts, K Nakamura, J Daniels, C. Schroeder, *et al.*, "Active plasma lensing for relativistic laser-plasma-accelerated electron beams", *Physical review letters*, vol. 115, no. 18, p. 184 802, 2015.

[167] J Van Tilborg, S. Barber, H.-E. Tsai, K. Swanson, S Steinke, C. Geddes, A. Gonsalves, C. Schroeder, E Esarey, S. Bulanov, *et al.*, "Nonuniform discharge currents in active plasma lenses", *Physical Review Accelerators and Beams*, vol. 20, no. 3, p. 032 803, 2017.

[168] A. Madur, P. Brunelle, A. Nadji, and L. S. Nadolski, "Beam based alignment for the storage ring multipoles of synchrotron soleil", in *Proceedings of EPAC*, 2006, pp. 1939–1941.

[169] H Ego, M Hara, Y Kawashima, Y Ohashi, T Ohshima, H Suzuki, I Takeshita, and H Yonehara, "Suppression of the coupled-bunch instability in the spring-8 storage ring", *Nuclear Instruments and Methods in Physics Research Section A: Accelerators, Spectrometers, Detectors and Associated Equipment*, vol. 400, no. 2-3, pp. 195–212, 1997.

[170] K Soutome, K Kaneki, Y Shimosaki, M Takao, and H Tanaka, "Non-linear optimization of storage ring lattice for the spring-8 upgrade", *Energy [GeV]*, vol. 6, p. 8, 2016.

[171] A. Mostacci, M Bellaveglia, E Chiadroni, A Cianchi, M Ferrario, D Filippetto, G Gatti, and C Ronsivalle, "Chromatic effects in quadrupole scan emittance measurements", *Physical Review Special Topics-Accelerators and Beams*, vol. 15, no. 8, p. 082 802, 2012.

[172] S. D. Fartoukh and O. Napoly, "Quadrupolar wakefield induced single-bunch emittance growth in linear colliders", Tech. Rep., 1994.

[173] M.-E. Couprie, T. Andre, and I. Andriyash, "Coxinel: Towards free electron laser amplification to qualify laser plasma acceleration", *Reza Kenkyu*, vol. 45, no. 2, pp. 94–98, 2017.

[174] T. André, I. Andriyash, S. Bielawski, F. Blache, F. Bouvet, F. Briquez, S. Corde, M.-E. Couprie, Y. Dietrich, J.-P. Duval, *et al.*, "Electron transport on coxinel beam line", in *8th Int. Particle Accelerator Conf.(IPAC'17), Copenhagen, Denmark, 14â 19 May, 2017*, JACOW, Geneva, Switzerland, 2017, pp. 1688–1691.

[175] M Khojoyan *et al.*, "Transport studies of LPA electron beam towards the FEL amplification at COXINEL", *Nucl. Instr. Meth. Phys. Res. A*, vol. 829, pp. 260–264, 2016.

[176] M Labat, A Loulergue, T Andre, I. Andriyash, A Ghaith, M Khojoyan, F Marteau, M Valléau, F Briquez, C Benabderrahmane, *et al.*, "Robustness of a plasma acceleration based free electron laser", *Physical Review Accelerators and Beams*, vol. 21, no. 11, p. 114 802, 2018.

[177] T. André, I. Andriyash, C. Basset, C. Benabderrahmane, P. Berteaud, S. Bielawski, S. Bonnin, F. Bouvet, F. Briquez, L. Cassinari, *et al.*, "First electron beam measurements on coxinel", in *7th International Particle Accelerator Conference (IPAC' 16), Busan, Korea*, 2016, pp. 712–715.

[178] D. Oumbarek Espinos, A. Ghaith, T. André, C. Kitégi, M. Sebdaoui, A. Loulergue, F. Marteau, F. Blache, M. Valléau, M. Labat, *et al.*, "Skew quadrupole effect of laser plasma electron beam transport", *Applied Sciences*, vol. 9, no. 12, p. 2447, 2019.

[179] A Loulergue, M Labat, C Evain, C Benabderrahmane, V. Malka, and M. Couprie, "Beam manipulation for compact laser wakefield accelerator based free-electron lasers", *New Journal of Physics*, vol. 17, no. 2, p. 023 028, 2015.

[180] F Marteau, A Ghaith, P N'Gotta, C Benabderrahmane, M Valléau, C Kitegi, A Loulergue, J Vétéran, M Sebdaoui, T André, *et al.*, "Variable high gradient permanent magnet quadrupole (quapeva)", *Applied Physics Letters*, vol. 111, no. 25, p. 253 503, 2017.

[181] A. Ghaith, C Kitegi, T André, M Valléau, F Marteau, J Vétéran, F Blache, C Benabderrahmane, O Cosson, F Forest, *et al.*, "Tunable high gradient quadrupoles for a laser plasma acceleration based fel", *Nuclear Instruments and Methods in Physics Research Section A: Accelerators, Spectrometers, Detectors and Associated Equipment*, vol. 909, pp. 290–293, 2018.

[182] M Mirzaie, S Li, M Zeng, N. Hafz, M Chen, G. Li, Q. Zhu, H Liao, T Sokollik, F Liu, *et al.*, "Demonstration of self-truncated ionization injection for gev electron beams", *Scientific reports*, vol. 5, p. 14 659, 2015.

[183] A. Goers, S. Yoon, J. Elle, G. Hine, and H. Milchberg, "Laser wakefield acceleration of electrons with ionization injection in a pure n5+ plasma waveguide", *Applied Physics Letters*, vol. 104, no. 21, p. 214 105, 2014.

[184] T Seggebrock, A. Maier, I. Dornmair, and F Grüner, "Bunch decompression for laser-plasma driven free-electron laser demonstration schemes", *Physical Review Special Topics-Accelerators and Beams*, vol. 16, no. 7, p. 070 703, 2013.

[185] P Antici, A Bacci, C Benedetti, E Chiadroni, M Ferrario, A. Rossi, L Lancia, M Migliorati, A Mostacci, L Palumbo, *et al.*, "Laser-driven electron beamlines generated by coupling laser-plasma sources with conventional transport systems", *Journal of Applied Physics*, vol. 112, no. 4, p. 044 902, 2012.

[186] A. Maier, A. Meseck, S. Reiche, C. Schroeder, T. Seggebrock, and F. Gruener, "Demonstration scheme for a laser-plasma-driven free-electron laser", *Physical Review X*, vol. 2, no. 3, p. 031 019, 2012.

[187] M.-E. Couprie, A Loulergue, M Labat, R Lehe, and V. Malka, "Towards a free electron laser based on laser plasma accelerators", *Journal of Physics B: Atomic, Molecular and Optical Physics*, vol. 47, no. 23, p. 234 001, 2014.

[188] P Emma, K Bane, M Cornacchia, Z Huang, H Schlarb, G Stupakov, and D Walz, "Femtosecond and subfemtosecond x-ray pulses from a self-amplified spontaneous-emission–based free-electron laser", *Physical review letters*, vol. 92, no. 7, p. 074 801, 2004.

[189] M Scisciò, M Migliorati, L Palumbo, and P Antici, "Design and optimization of a compact laser-driven proton beamline", *Scientific reports*, vol. 8, no. 1, pp. 1–11, 2018.

[190] X. Zhu, D. R. Broemmelsiek, and Y.-M. Shin, "Theoretical and numerical analyses of a slit-masked chicane for modulated bunch generation", *Journal of Instrumentation*, vol. 10, no. 10, P10042, 2015.

[191] J Payet, A Chance, A Loulergue, A Ropert, F Meot, J. Filhol, J. Laclare, L Farvacque, and T Aniel, "Beta code", *CEA, SACLAY*, 2001.

[192] K. Flöttmann, "Astra, a. a space charge tracking algorithm. astra, 2007. available online: Http://www.desy.de/ mpyflo/",

[193] M Borland and E. APS, "A flexible sdds-compliant code for accelerator simulation, report no", *APS LS-287*, 2000.

[194] I. Agapov, G. Geloni, S. Tomin, and I. Zagorodnov, "Ocelot: A software framework for synchrotron light source and fel studies", *Nuclear Instruments and Methods in Physics Research Section A: Accelerators, Spectrometers, Detectors and Associated Equipment*, vol. 768, pp. 151–156, 2014.

[195] A. Ghaith, "Towards compact and advanced free electron laser", These de doctorat dirigee par Couprie, Marie-Emmanuelle Physique des accelerateurs Universite Paris-Saclay (ComUE) 2019, PhD thesis, 2019. [Online]. Available: http://www.theses.fr/2019SACLS333.

[196] D. O. Espinos, A. Ghaith, A. Loulergue, T. André, C. Kitégi, M. Sebdaoui, F. Marteau, F. Blache, M. Valléau, M. Labat, *et al.*, "Coxinel transport of laser plasma accelerated electrons", *Plasma Physics and Controlled Fusion*, vol. 62, no. 3, p. 034 001, 2020.

[197] S. Reiche, "Genesis 1.3: A fully 3d time-dependent fel simulation code", *Nuclear Instruments and Methods in Physics Research Section A: Accelerators, Spectrometers, Detectors and Associated Equipment*, vol. 429, no. 1-3, pp. 243–248, 1999.

[198] I. A. Andriyash, R. Lehe, and V. Malka, "A spectral unaveraged algorithm for free electron laser simulations", *Journal of Computational Physics*, vol. 282, pp. 397–409, 2015.

[199] I. Agapov, G. Geloni, S. Tomin, and I. Zagorodnov, "Ocelot: A software framework for synchrotron light source and fel studies", *Nuclear Instruments and Methods in Physics Research Section A: Accelerators, Spectrometers, Detectors and Associated Equipment*, vol. 768, pp. 151–156, 2014.

[200] M. Couprie, C Benabderrahmane, P Berteaud, F Briquez, L Chapuis, O Chubar, T Elajjouri, F Marteau, J. Filhol, C Kitegi, *et al.*, "A panoply of insertion devices at soleil for a wide spectral range and flexible polarisation", in *AIP Conference Proceedings*, American Institute of Physics, vol. 1234, 2010, pp. 519–522.

[201] M Labat, "Task 1.4. fel simulations for run6", Tech. Rep., 2019.

[202] I. Basistiy, M. Soskin, and M. Vasnetsov, "Optical wavefront dislocations and their properties", *Optics Communications*, vol. 119, no. 5-6, pp. 604–612, 1995.

[203] H. Baumhacker, G. Pretzler, K. J. Witte, M. Hegelich, M. Kaluza, S. Karsch, A Kudryashov, V Samarkin, and A Roukossouev, "Correction of strong phase and amplitude modulations by two deformable mirrors in a multistaged ti: Sapphire laser", *Optics letters*, vol. 27, no. 17, pp. 1570–1572, 2002.

[204] I. Zemzemi, "Calcul haute-performance et simulation numérique pour l'accélération d'électrons par sillage laser avec des profils laser réalistes", 2020.

[205] N Nakanii, T Hosokai, K Iwasa, N. Pathak, S Masuda, A. Zhidkov, H Nakahara, N Takeguchi, Y Mizuta, T. Otsuka, *et al.*, "Effect of halo on the stability of electron bunches in laser wakefield acceleration", *EPL (Europhysics Letters)*, vol. 113, no. 3, p. 34 002, 2016.

[206] S. Corde, O Kononenko, and C. a. Thaury, *As reported by measurements done by laboratoire d' optique appliquée team.*

[207] T. Andre, "Transport et manipulation d'électrons produits par interaction laser plasma sur la ligne COXINEL", Theses, Université Paris-Saclay, Dec. 2018. [Online]. Available: https://tel.archives-ouvertes.fr/tel-02072265.

[208] M. Chen, E. Esarey, C. Geddes, E Cormier-Michel, C. Schroeder, S. Bulanov, C Benedetti, L. Yu, S Rykovanov, D. Bruhwiler, *et al.*, "Electron injection and emittance control by transverse colliding pulses in a laser-plasma accelerator", *Physical Review Special Topics-Accelerators and Beams*, vol. 17, no. 5, p. 051 303, 2014.

[209] S. Corde, C. Thaury, A. Lifschitz, G. Lambert, K. T. Phuoc, X Davoine, R Lehe, D Douillet, A. Rousse, and V. Malka, "Observation of longitudinal and transverse self-injections in laser-plasma accelerators", *Nature Communications*, vol. 4, no. 1, pp. 1–7, 2013.

[210] G Lebec, J Chavanne, C. Penel, *et al.*, "Stretched-wire measurements of small bore multipole magnets", *Phys. Rev. Spec. Top. Accel. Beams*, vol. 15, 2012.

[211] C Benabderrahmane, M Valléau, A Ghaith, P Berteaud, L Chapuis, F Marteau, F Briquez, O Marcouillé, J.-L. Marlats, K Tavakoli, *et al.*, "Development and operation of a pr 2 fe 14 b based cryogenic permanent magnet undulator for a high spatial resolution x-ray beam line", *Physical Review Accelerators and Beams*, vol. 20, no. 3, p. 033 201, 2017.

[212] M. Labat, M. El Ajjouri, N. Hubert, T. Andre, A. Loulergue, and M.-E. Couprie, "Electron and photon diagnostics for plasma acceleration-based fels", *Journal of synchrotron radiation*, vol. 25, no. 1, pp. 59–67, 2018.

[213] *Hamamatsu.* [Online]. Available: https://www.hamamatsu.com/jp/en/product/type/C13440-20CU/index.html.

[214] R. C. Webber, "Tutorial on beam current monitoring", in *AIP Conference Proceedings*, American Institute of Physics, vol. 546, 2000, pp. 83–104.

[215] "Turbo integrating current transformer. url http://www.bergoz.com/en/turbo-ict-bcm-rf-0.", Bergoz, Tech. Rep.

[216] B. Keil, R. Baldinger, R. Ditter, W. Koprek, R. Kramert, F. Marcellini, G. Marinkovic, M. Roggli, M. Rohrer, M. Stadler, *et al.*, "Design of the swissfel bpm system", *Proc. IBIC*, vol. 13, 2013.

[217] T. Andre, "Transport et manipulation delectrons produits par interaction laser plasma sur la ligne coxinel", These de doctorat dirige par Couprie, Marie-Emmanuelle Physique des accelerateurs Universite Paris-Saclay (ComUE) 2018, PhD thesis, 2018. [Online]. Available: http://www.theses.fr/2018SACLS602.

[218] M. Labat, M.-E. Couprie, A. Loulergue, and E. Roussel, "Task 1.4. tests on imagers for single shot emittance measurements", *Task Technical Report*, 2020.

[219] *Sigma macro 105 mm f2.8 ex dg os hsm.* [Online]. Available: https://www.sigma-global.com/jp/lenses/105_28_os/.

[220] *Apo rodagon d 120.* [Online]. Available: https://www.eureca.de/files/pdf/lenses/qioptiq/Apo-Rodagon-D-120.pdf.

[221] *Navitar 12x.* [Online]. Available: https://navitar.com/products/imaging-optics/high-magnification-imaging/12x-zoom/.

[222] *Horiba*. [Online]. Available: https://www.horiba.com/uk/scientific/products/optical-spectroscopy/spectrometers-monochromators/ihr/ihr320-imaging-spectrometer-198/.

[223] M Labat, S Bielawski, A Loulergue, S. Corde, M. Couprie, and E. Roussel, "Interferometry for full temporal reconstruction of laser-plasma accelerator-based seeded free electron lasers", *New Journal of Physics*, vol. 22, no. 1, p. 013 051, 2020.

[224] J.-y. Zhang, J. Y. Huang, H Wang, K. Wong, and G. Wong, "Second-harmonic generation from regeneratively amplified femtosecond laser pulses in bbo and lbo crystals", *JOSA B*, vol. 15, no. 1, pp. 200–209, 1998.

[225] L DiMauro, A Doyuran, W Graves, R Heese, E. Johnson, S Krinsky, H Loos, J. Murphy, G Rakowsky, J Rose, *et al.*, "First sase and seeded fel lasing of the nsls duv fel at 266 and 400 nm", *Nuclear Instruments and Methods in Physics Research Section A: Accelerators, Spectrometers, Detectors and Associated Equipment*, vol. 507, no. 1-2, pp. 15–18, 2003.

[226] M. Lewenstein, P. Balcou, M. Y. Ivanov, A. L' huillier, and P. B. Corkum, "Theory of high-harmonic generation by low-frequency laser fields", *Physical Review A*, vol. 49, no. 3, p. 2117, 1994.

[227] P. Salieres, A. L'Huillier, and M. Lewenstein, "Coherence control of high-order harmonics", *Physical Review Letters*, vol. 74, no. 19, p. 3776, 1995.

[228] E Constant, D Garzella, P Breger, E Mével, C. Dorrer, C Le Blanc, F Salin, and P Agostini, "Optimizing high harmonic generation in absorbing gases: Model and experiment", *Physical Review Letters*, vol. 82, no. 8, p. 1668, 1999.

[229] M. Frolov, N. Manakov, T. Sarantseva, and A. F. Starace, "Analytic formulae for high harmonic generation", *Journal of Physics B: Atomic, Molecular and Optical Physics*, vol. 42, no. 3, p. 035 601, 2009.

[230] *Femtokits for third harmonic generation of ti:sapphire laser, eksma optics*. [Online]. Available: https://eksmaoptics.com/femtoline-components/femtoline-nonlinear-laser-crystals/femtokits-for-third-harmonic-generation-of-ti-sapphire-laser/.

[231] R. Santra and A. Gordon, "Three-step model for high-harmonic generation in many-electron systems", *Physical review letters*, vol. 96, no. 7, p. 073 906, 2006.

[232] M. Grishin, *Advances in Solid State Lasers: Development and Applications*. BoD–Books on Demand, 2010.

[233] *Pompe primaire edwards nxds20i*. [Online]. Available: https://shop.edwardsvacuum.com/products/a73801983/view.aspx.

[234] *Pompe turbomoléculaire pfeiffer vacuum hipace 80*. [Online]. Available: https://www.pfeiffer-vacuum.com/en/products/vacuum-generation/turbopumps/hybrid-bearing/hipace-80/?detailPdoId=32024.

[235] *Faro laser tracker*. [Online]. Available: https://www.faro.com/fr-fr/produits/metrologie-industrielle/faro-laser-tracker/.

[236] *Leica geosystems*. [Online]. Available: https://leica-geosystems.com/fr-FR.

[237] *Wyler clinotronic plus*. [Online]. Available: http://www.symetrie.fr/fr/instruments/niveaux-electroniques-wyler/clinotronic-plus/2240.

[238] J Couperus and U Schramm, *Private communications*.

[239] D. Silver, G. Lever, N. Heess, T. Degris, D. Wierstra, and M. Riedmiller, "Deterministic policy gradient algorithms", in *International conference on machine learning*, PMLR, 2014, pp. 387–395.

[240] C. J. Watkins and P. Dayan, "Q-learning", *Machine learning*, vol. 8, no. 3-4, pp. 279–292, 1992.

[241] B. O'Donoghue, R. Munos, K. Kavukcuoglu, and V. Mnih, "Combining policy gradient and q-learning", *arXiv preprint arXiv:1611.01626*, 2016.

[242] R. Weingartner, S. Raith, A. Popp, S Chou, J. Wenz, K. Khrennikov, M. Heigoldt, A. R. Maier, N. Kajumba, M. Fuchs, *et al.*, "Ultralow emittance electron beams from a laser-wakefield accelerator", *Physical Review Special Topics-Accelerators and Beams*, vol. 15, no. 11, p. 111 302, 2012.

[243] S. Barber, J Van Tilborg, C. Schroeder, R Lehe, H. Tsai, K. Swanson, S Steinke, K Nakamura, C. Geddes, C Benedetti, *et al.*, "Parametric emittance measurements of electron beams produced by a laser plasma accelerator", *Plasma Physics and Controlled Fusion*, vol. 60, no. 5, p. 054 015, 2018.

[244] K. McDonald and D. Russell, "Methods of emittance measurement", in *Frontiers of particle beams; observation, diagnosis and correction*, Springer, 1989, pp. 122–132.

[245] A. Buck, K Zeil, A. Popp, K. Schmid, A Jochmann, S. Kraft, B Hidding, T Kudyakov, C. Sears, L. Veisz, *et al.*, "Absolute charge calibration of scintillating screens for relativistic electron detection", *Review of Scientific Instruments*, vol. 81, no. 3, p. 033 301, 2010.

[246] M. Labat and M.-E. Couprie, "Task 1.4. fel simulations for run 7", *Task Technical Report*, 2020.

[247] "Smooth() function documentation", in, MATLAB. [Online]. Available: https://fr.mathworks.com/help/curvefit/smooth.html#mw_ad6b65fd-4dac-46c4-a649-a7a0b301eb80.

[248] A. Gurevich, "Enhancement of rf breakdown field of superconductors by multilayer coating", *Applied Physics Letters*, vol. 88, no. 1, p. 012 511, 2006.